



**TECHNISCHE UNIVERSITÄT MÜNCHEN**

Fakultät für Chemie

**Advanced Characterization for Proton Exchange  
Membrane Fuel Cells – Elucidating the Correlation  
between Catalyst Activity, Selectivity, and  
Durability**

Björn Marcel Stühmeier

Vollständiger Abdruck der von der Fakultät für Chemie der Technischen Universität  
München zur Erlangung des akademischen Grades eines

Doktors der Naturwissenschaften (Dr. rer. nat.)

genehmigten Dissertation.

Vorsitzender: Prof. Dr.-Ing. Kai-Olaf M. Hinrichsen

Prüfer der Dissertation:

1. Prof. Dr. Hubert A. Gasteiger
2. Prof. Dr. Klaus Köhler
3. Prof. Dr. David P. Wilkinson

Diese Dissertation wurde am 10.03.2022 bei der Technischen Universität München  
eingereicht und durch die Fakultät für Chemie am 19.04.2022 angenommen.



---

*A scientist in his laboratory is not only a technician: he is also a child placed before natural phenomena which impress him like a fairy tale.*

Marie Curie



# Abstract

The long-term durability of proton exchange membrane fuel cells (PEMFCs) remains a major challenge for automotive and heavy-duty applications. In this context, this PhD thesis aims to further our understanding of the activity, selectivity, and durability of commercial and novel catalyst materials by employing various electrochemical characterization methods. Thus, this work will cover three main topics: appropriate measurement techniques, novel catalyst concepts, and cathode degradation.

First, the two most commonly used techniques for the investigation of PEMFC catalysts, namely the rotating disk electrode (RDE) and the membrane electrode assembly (MEA) setup, are discussed regarding their capabilities and limitations for the application-relevant characterization of catalyst materials. Here, appropriate measurement protocols for the characterization of low-loaded electrodes and the investigation of the hydrogen oxidation and evolution reaction mechanism are established.

Then, novel catalyst concepts based on metal oxide support materials are explored, whereby in a first study, a method to reduce oxide thin films is investigated. Subsequently, the effect of a strong metal-support interaction (SMSI) on the surface oxide formation and the hydrogen oxidation activity of platinum group metals is scrutinized. Hereby, Pt/TiO<sub>x</sub>/C is found to be selective for the hydrogen oxidation reaction (HOR) while the oxygen reduction reaction (ORR) is suppressed. Furthermore, for a Ru/TiO<sub>x</sub>/C catalyst, it could be shown for the first time that SMSI effects can stabilize the HOR activity of ruthenium at potentials above 0.1 V.

Finally, the durability of the cathode catalyst layer is investigated in two studies that focus on the implementation of the HOR-selective anode catalyst as a mitigation strategy for start-up/shut-down (SUSD) induced cathode degradation and on the correlation between the cathode roughness factor ( $rf$ ) and the H<sub>2</sub>/air performance during voltage cycling based accelerated stress tests (ASTs).



# Kurzzusammenfassung

Die erfolgreiche Anwendung von Protonenaustauschmembran-Brennstoffzellen im Automobilbereich ist aktuell noch immer durch deren begrenzte Lebensdauer stark eingeschränkt. In diesem Zusammenhang, befasst sich diese Doktorarbeit mit der Aktivität, Selektivität und Stabilität von kommerziellen und neu entwickelten Katalysatormaterialien unter Verwendung verschiedener elektrochemischer Charakterisierungsmethoden. Der Schwerpunkt der Arbeit liegt daher auf den folgenden drei Themengebieten: Die Erarbeitung geeigneter Messmethoden, die Entwicklung neuer Katalysatorkonzepte und die Untersuchung der Kathodendegradation.

Deshalb werden zuerst die Vor- und Nachteile der beiden am häufigsten für die Analyse von Brennstoffzellenkatalysatoren verwendeten Versuchsaufbauten, die rotierende Scheibenelektrode (RDE) und die Membran-Elektrodeneinheit (MEA), verglichen. Zusätzlich werden Protokolle sowohl für die Untersuchung von anwendungsrelevanten, niedrigbeladenen Elektroden als auch des Reaktionsmechanismus der Wasserstoffoxidation und -entwicklung etabliert.

Anschließend werden neue Katalysatorkonzepte auf der Basis oxidischer Trägermaterialien betrachtet, wobei in einer ersten Studie die Reduktion von oxidischen Dünnschichten mittels des Polyolprozesses erforscht wird. In weiteren Studien wird die starke Wechselwirkung zwischen oxidischen Trägermaterialien und Platingruppenmetall-Nanopartikeln untersucht, wobei eine Modifikation der Oberflächenoxidation von Pt und Ru zu Änderungen im Wasserstoffoxidationsverhalten führt. Für  $\text{TiO}_x$ -getragertes Platin ( $x \leq 2$ ) wird eine bisher weitestgehend unbekannte Selektivität für die Wasserstoffoxidation (im Vergleich zur Sauerstoffreduktion) beobachtet, wohingegen für Ruthenium erstmals eine Wasserstoffoxidationsaktivität oberhalb von 0,1 V gezeigt werden kann.

Abschließend wird in zwei Studien die Degradation des Kathodenkatalysators untersucht. Zum einen wird dabei das schadensminimierende Potenzial des selektiven Pt/ $\text{TiO}_x$ /C Katalysators im Falle von Start/Stop-induzierter Kohlekorrosion auf der Kathode untersucht. Zum anderen wird eine allgemeingültige Korrelation zwischen dem Potenzialzyklen-induzierten Verlust aktiver Platinoberfläche und der Leistungsfähigkeit der  $\text{H}_2$ /Luft-Brennstoffzelle etabliert.



# Acknowledgements

First and foremost, I want to express my deepest gratitude to my supervisor **Prof. Hubert Gasteiger**. Ever since I started my journey at your chair in 2015, it was a pleasure to work with you and to be inspired by your passion and curiosity about electrochemistry. You have taught me to pursue any scientific question that sparks my interest and to critically analyze all experimental results with an open mind, which has greatly shaped this thesis. During all those years, you have always had an open ear to discuss a scientific or personal issue and somehow you have even found the time to read this thesis on an incredibly short notice. Without your guidance, support, and encouragement, I would certainly not be the scientist that I am today. Thank you.

A special thanks goes to my former supervisors **Dr. Hany El-Sayed** and **Dr. Jan Schwämmlein** who introduced me to electrochemistry and became good friends in the years that followed. You have taught me the planning and the execution of individual experiments as well as full project, been incredible role-models for the supervision of students and showed me the importance of a healthy work-life balance. I was always happy to work with you in various projects ever since. Furthermore, I want to thank **Dr. Tim Fellingner** who was my mentor during my PhD and who always offered advice when I needed it.

Certainly, this work would not have been possible without a lot of other people to whom I would like to say thank you. The co-authors of the joint publications, **Timon Lazaridis**, **Markus Pietsch**, **Robin Schuster**, **Ana Marija Damjanović**, and **Roberta Della Bella**, have greatly contributed to the success of this thesis and I want to thank you for the great working atmosphere and productiveness during our joint projects.

Another big acknowledgement is directed to my fellow researchers that I had the pleasure to supervise during their studies for a Bachelor's thesis, a Master's thesis, or as a student researcher. Not only did you work with extraordinary motivation and contributed significantly to the outcome of this thesis, but you also became great friends that I am happy to meet in research or in private: **Nhat Long Tran Pham**, **Markus Pietsch**, **Robin Schuster**, and **Ida Keussen**.

I also do not want to miss on acknowledging the great working atmosphere which was created by all members of the Chair of Technical Electrochemistry during working

---

hours as well as during leisure activities. Special thanks goes to **Konstantin Weber** for the endless hours we spent getting the new cell design to work as smoothly as possible and for the beautiful hiking trips in snow and ice. **Stefan Oswald** has not only been a great conference and lion spotting buddy, but also the tireless organizer of Schafkopf sessions. Whenever I was at risk to loose myself in too much lab or paper work, **Louis Hartmann** would organize a social get-together and make sure that my work-life balance would be re-adjusted. Furthermore, I want to thank **Anne Berger**, **Matthias Kornherr**, **Matthias Ernst**, **Christian Sedlmeier**, **Felix Riewald**, and **Tobias Kutsch** for great discussions, board game sessions, lunch breaks, and motor bike trips.

Additionally, I would like to acknowledge the help of **Daniel Henschel**, **Mohammad Fathi Tovini**, and **Roberta Della Bella** for their great efforts of proof-reading this thesis.

Finally, I want to thank my family and my friends who have supported me throughout my life. I am deeply grateful to my parents, **Angelika and Udo Stühmeier**, who have always supported me, believed in me, and provided me with the opportunity to follow my dreams. Thank you. I also want to thank my brothers, **Patrick** and **Daniel**, who have greatly enriched my life.

And finally, I want to acknowledge the support and motivation from my close friends that have always been there for me when I was struggling through hard times or enjoying the good times (which luckily were more frequent). A special thanks goes to **Thomas Biller**, **Ockert Malan**, and **Katharina Freyer** whom I can rely on whenever I need them the most.

# Contents

<b>Abstract</b>	<b>i</b>
<b>Kurzzusammenfassung</b>	<b>iii</b>
<b>Acknowledgements</b>	<b>v</b>
<b>List of Acronyms</b>	<b>ix</b>
<b>1. Introduction</b>	<b>1</b>
1.1. Proton Exchange Membrane Fuel Cell (PEMFC) . . . . .	2
1.1.1. 3-Layer Membrane Electrode Assembly (MEA) . . . . .	5
1.1.2. H <sub>2</sub> /Air Performance . . . . .	6
1.1.3. MEA Durability . . . . .	9
1.2. Rotating Disk Electrode (RDE) vs Membrane Electrode Assembly (MEA) Measurement Configurations . . . . .	14
1.2.1. RDE Measurements . . . . .	15
1.2.2. MEA Measurements . . . . .	17
1.2.3. Bridging Techniques . . . . .	19
1.3. Strong Metal-Support Interaction (SMSI) . . . . .	19
1.4. Thesis Outline . . . . .	23
<b>2. Experimental Methods</b>	<b>25</b>
2.1. Synthesis of Novel Catalyst Materials . . . . .	25
2.2. Low-Roughness Factor MEA Measurements . . . . .	28
2.2.1. CO-Stripping Measurements . . . . .	28
2.2.2. O <sub>2</sub> -Limiting Current Measurements . . . . .	37
2.2.3. H <sub>2</sub> -Pump Measurements . . . . .	40
2.3. Optimized Procedure for 5 cm <sup>2</sup> MEA Characterization . . . . .	41
<b>3. Published Work</b>	<b>45</b>
3.1. Measurement Methods to Determine Catalyst Activity/Performance . .	45
3.1.1. Investigation of PGM-Based Electrocatalysts by RDE vs MEA .	46
3.1.2. PEMFC-Based Hydrogen-Pump Measurements for the Investi- gation of the HOR/HER Kinetics . . . . .	60
3.2. Novel Catalyst Concepts for PEMFCs . . . . .	73
3.2.1. Metal Oxide Thin-Film Reduction via the Polyol Process . . . .	73
3.2.2. SMSI-Induced HOR-Selectivity of Pt/TiO <sub>x</sub> Catalysts . . . . .	83

3.2.3. Suppression of the Ruthenium Surface Oxide Formation by SMSI Effects . . . . .	91
3.3. PEMFC Cathode Durability Aspects . . . . .	106
3.3.1. Mitigation of SUSD-Induced Cathode Degradation in PEMFCs via HOR-Selective Anodes . . . . .	106
3.3.2. Correlation Between Voltage Cycling-Induced Cathode Degradation and H <sub>2</sub> /Air Performance Losses . . . . .	125
<b>4. Conclusions</b>	<b>143</b>
<b>References</b>	<b>149</b>
<b>List of Figures</b>	<b>169</b>
<b>A. Curriculum Vitae and Publication List</b>	<b>173</b>

# List of Acronyms

<b>Abbreviation</b>	<b>Description</b>
AEMFC	Anion Exchange Membrane Fuel Cell
AST	Accelerated Stress Test
BPP	Bipolar Plate
CE	Counter Electrode
COR	Carbon Oxidation Reaction
CV	Cyclic Voltammetry
<i>ECSA</i>	Electrochemically Active Surface Area
EDX	Energy Dispersive X-ray Spectroscopy
EG	Ethylene Glycol
EIS	Electrochemical Impedance Spectroscopy
FET	Floating Electrode Technique
FF	Flow Field
GDE	Gas Diffusion Electrode
GDL	Gas Diffusion Layer
HCD	High Current Density
HER	Hydrogen Evolution Reaction
HFR	High Frequency Resistance
HOR	Hydrogen Oxidation Reaction
$H_{\text{upd}}$	Hydrogen Underpotential Deposition
MEA	Membrane Electrode Assembly
MFC	Mass Flow Controller
MPL	Microporous Layer
OCP	Open Circuit Potential
OCV	Open Circuit Voltage
OER	Oxygen Evolution Reaction
ORR	Oxygen Reduction Reaction
PEMFC	Proton Exchange Membrane Fuel Cell
PEMWE	Proton Exchange Membrane Water Electrolyzer
PGM	Platinum Group Metal
PTFE	Polytetrafluoroethylene
R(R)DE	Rotating (Ring) Disk Electrode

RE	Reference Electrode
<i>rf</i>	Roughness Factor
RHE	Reversible Hydrogen Electrode
SEM	Scanning Electron Microscopy
SHE	Standard Hydrogen Electrode
SMSI	Strong Metal-Support Interaction
SOFC	Solid Oxide Fuel Cell
SOV	Shut Off Valve
SUSD	Start-Up/Shut-Down
TEM	Transmission Electron Microscopy
<i>TS</i>	Tafel Slope
UPL	Upper Potential Limit
WE	Working Electrode
XPS	X-ray Photoelectron Spectroscopy

# 1. Introduction

While the COVID-19 crisis and the resulting economic standstill has led to a short-term reduction in greenhouse gas emissions, climate change remains one of the defining issues of the 21st century.<sup>1-6</sup> The required transition to carbon-neutral power production will require more efficient ways of transporting and storing energy due to the strong regional differences in the availability of hydro/tidal power and geothermal, wind, and solar energy sources as well as short-term and seasonal fluctuations in the availability of the latter two. Here, hydrogen will play a crucial role as chemical energy storage medium.<sup>7</sup> In this context, the key technologies are the electrochemical generation and conversion of hydrogen according to eq. 1.1. Water electrolyzers generate "green" hydrogen from non-carbon emitting energy sources, while fuel cells convert the chemical energy of hydrogen back into electricity, thereby powering stationary and mobile applications.



Depending on the application, several types of fuel cells are employed. These include solid oxide fuel cells (SOFCs) that operate at high temperatures ( $\gg 500\text{ }^\circ\text{C}$ ). SOFCs offer a compact design and have the advantage to be tolerant towards reformat gas. In addition, they are able to operate with a wide range of hydrocarbon fuels, and their high-quality waste heat can be used for district heating. However, due to the high operating temperatures, slow start-up and limited operational flexibility, SOFCs are mostly limited to stationary applications, like in combined cycle power plants or for power and heat generation in residential areas.<sup>8</sup> At low temperatures ( $< 120\text{ }^\circ\text{C}$ ), fuel cell systems have been developed using either acidic or alkaline electrolytes.<sup>9</sup> In alkaline environment, the most advanced technology is based on anion exchange membrane fuel cells (AEMFCs).<sup>9</sup> The benefit of operating at high pH is that the increased stability of non-noble metals enables the use of non-platinum group metal (non-PGM) catalysts for the oxygen reduction reaction (ORR), which are significantly more cost-effective in comparison to the PGM-based catalysts required in acidic environment. However, this advantage is mostly theoretical, since the sluggish hydrogen evolution reaction (HER)

and hydrogen oxidation reaction (HOR) kinetics require substantially larger amounts of platinum for the anode catalyst layer in the alkaline environment.<sup>10,11</sup> Most importantly, the limited ionomer/membrane durability and the vulnerability to CO<sub>2</sub> in the gas feed pose major challenges for AEMFC systems that to date limit their technical feasibility.<sup>12,13</sup> For mobile applications, the most promising fuel cell technology are low temperature proton exchange membrane fuel cells (PEMFCs) that have proven their market readiness by the introduction of several fuel cell electric vehicles (FCEVs) over the last decade.<sup>9,14–16</sup>

In the following, a short overview of the working principle, the used materials, and the remaining performance and durability issues of state-of-the-art PEMFCs, with a focus on the used catalyst materials, will be given in Section 1.1. Then, the two most commonly used techniques for the assessment of PEMFC catalysts will be compared with respect to their limitations in the evaluation of PGM-based electrocatalysts (Section 1.2), followed by an introduction to the effect of metal oxide supports on the electrochemical properties of noble metal catalysts, which is essential for the catalyst concepts presented later on (Section 1.3). The final part of the introduction will provide the reader with an outline of this thesis (Section 1.4).

## 1.1. Proton Exchange Membrane Fuel Cell (PEMFC)

In a PEMFC, the chemical energy stored in H<sub>2</sub> and O<sub>2</sub> is converted to electrical energy and heat, whereby water is produced according to eq. 1.2.



Hereby, the overall reaction can be divided into two half-cell reactions, namely the hydrogen oxidation reaction (HOR, eq. 1.3) and the oxygen reduction reaction (ORR, eq. 1.4) which take place at the anode and the cathode, respectively. In order to enable a utilization of these half-cell reactions, the compartments are separated by a proton exchange membrane.



As the name suggests, the proton can migrate through the proton exchange membrane from the anode to the cathode, while the electron has to travel through an external circuit where the resulting electrical power can be utilized. This smallest electrochemical unit consisting of anode, membrane, and cathode is called a catalyst coated membrane (CCM) or 3-layer membrane electrode assembly (MEA). The CCM is sandwiched between two gas diffusion layers (GDLs), resulting in a 5-layer MEA.

In a fuel cell stack, the 5-layer MEA is then sealed between two bipolar plates (BPP) that typically feature the flow field (FF) of the anode on one side and of the cathode on the other side, leading to a series connection of the individual cells in a stack. For cooling, a coolant channel runs within the BPP, so that each cell is cooled individually. The endplates that face the outermost cells in the stack and therefore exhibit the FF only on one side, are used as current collectors. Furthermore, they are used to mechanically stabilize the stack, whereby an electrical short of the stack must be prevented. This can be achieved either by using a non-conducting material to connect the endplates, or by using an insulating layer that separates the current collectors from a metallic housing. A single-cell setup, as it was used throughout this thesis, consists only of the endplates that include the heaters, the pressure leveling/insulation layers, a set of current collectors, the two FFs, the gaskets, and the 5-layer MEA (see fig. 1.1).

The role of the FFs is to distribute the gaseous reactants over the cell active area via channels. As the individual channels are separated by the so-called land area (with a width of  $\approx 0.5$  mm) that is required as contact area for electrical and heat conduction, the FFs cannot achieve a homogeneous distribution of the reactants to the electrode on a (sub-)micrometer-scale. Thus, the role of the GDL is to provide for a homogeneous distribution of the gaseous reactants to the electrode, for a good conduction of electrons, for efficient heat transfer, and for the removal of product water. It is therefore essential that the GDL has a high structural integrity to maintain its porosity and to enable efficient gas phase transport, while at the same time it must have a high electrical and a sufficient thermal conductivity. State-of-the-art GDLs consist of a highly porous carbon fiber substrate with a hydrophobic polytetrafluoroethylene (PTFE) coating as binder. To assist with the water management and to reduce electrical contact resistances, an electrode-facing microporous layer (MPL) consisting of PTFE-bonded carbon black is often coated on the GDL substrate.



**Figure 1.1.** Components and assembly of the 5 cm<sup>2</sup> active area PEMFC hardware that was used throughout this thesis for the characterization of PEMFC single-cells.

Since the focus of this thesis lies on the investigation of PEMFC catalysts using measurements in a liquid electrolyte based half-cell setup and in small active area ( $5 \text{ cm}^2$ ) single-cells under differential flow conditions (i.e., with stoichiometries  $\geq 10$  that enable operation under effectively gradient-free conditions but with high pressure drops of  $\approx 20 \text{ kPa}$ ), the following sections will focus exclusively on the materials, performance, and durability of the 3-layer MEA component of a PEMFC stack.

### 1.1.1. 3-Layer Membrane Electrode Assembly (MEA)

Ideally, the membrane should be electrically insulating and impermeable to gases while maintaining a high proton conductivity and structural integrity. In state-of-the-art PEMFCs, the membranes consist of a perfluorinated ionomer and a reinforcement layer, e.g., expanded PTFE (see bright stripe in the middle of fig. 1.2), that provides the structural stability required for extremely thin membranes with a thickness of  $\approx 8 - 20 \mu\text{m}$ .<sup>17-19</sup> The ionomer used in state-of-the-art PEMFCs is an ion conducting polymer with a hydrophobic backbone based on polytetrafluoroethylene (PTFE) and side chains that include immobilized perfluorosulfonic acid end groups.<sup>17</sup> In the presence of water, the hydrophilic sulfonic acid groups dissociate and create a highly acidic medium that enables facile proton transport through the well-known Grotthuss mechanism. Thus, the conductivity of the ionomer is heavily affected by its water uptake  $\lambda$  in  $\text{mol}_{\text{H}_2\text{O}} \text{mol}_{\text{SO}_3}^{-1}$  that is a function of the relative humidity ( $RH$ ) of the gas phase in contact with the membrane.

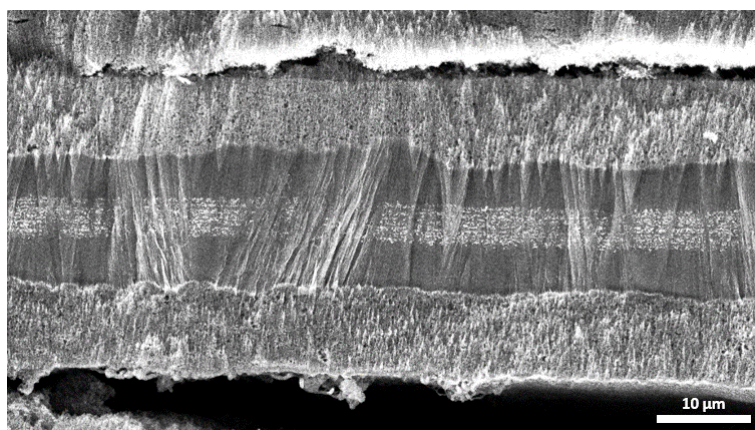


**Figure 1.2.** Cross-sectional image of a symmetrical MEA with anode and cathode loadings of  $0.1 \text{ mg}_{\text{Pt}} \text{ cm}_{\text{MEA}}^{-2}$  coated on a reinforced  $15 \mu\text{m}$  thick PFSA membrane. The image was taken by scanning electron microscopy (SEM) at  $10 \text{ kV}$  and a magnification of  $1,600\times$ .

For the electrochemical reactions within the electrodes, electrons, protons, and the

respective gas ( $\text{O}_2$  or  $\text{H}_2$ ) have to be simultaneously present at the active site(s) of the catalyst (so-called triple-phase interface). Thus, the ORR and the HOR take place on the surface of Pt (or Pt-alloy) nanoparticles that are most commonly supported on a high-structure carbon black material (resulting in a highly porous catalyst layer) with a high electrical conductivity, enabling sufficient gas and electron transport to the active site. The size of the nanoparticles is adjusted to  $\approx 2 - 5$  nm to achieve a high surface area to mass ratio, i.e., a high electrochemically accessible surface area ( $ECSA$  in  $\text{m}^2 \text{g}_{\text{Pt}}^{-1}$ ). The high porosity of the carbon support with a void volume fraction of  $\approx 80\%$ <sup>20</sup> (not considering the ionomer filled fraction) enables gas transport to the catalyst and the removal of product water to avoid flooding. The proton transport to the catalyst is achieved by a thin layer of ionomer on the catalyst surface. To achieve sufficient proton transport throughout the electrode, the ionomer-to-carbon (I/C) ratio is adjusted to  $\approx 0.6 - 1 \text{ g}_I \text{ g}_C^{-1}$  (depending on the ionomer type and the internal porosity of the carbon material), which results in the ionomer filling  $\approx 10 - 20\%$ <sup>20</sup> of the aforementioned void volume in the dry state and up to double of that volume in fully humidified conditions, depending also on the equivalent weight (EW, in  $\text{g}_I \text{ mol}_{\text{SO}_3^-}^{-1}$ ) of the ionomer.<sup>21</sup> Even though the ionomer structure is similar for the  $\approx 8 - 20 \mu\text{m}$  thick membrane, where gas transport from one to the other side is limited,  $\text{O}_2$  and  $\text{H}_2$  supply to the active site(s) of the catalyst is possible through the very thin ionomer film ( $< 10$  nm) that is believed to cover the Pt nanoparticles.<sup>22-24</sup>

### 1.1.2. $\text{H}_2$ /Air Performance

The thermodynamic equilibrium potential of the fuel cell reaction (eq. 1.2) can be calculated according to the Nernst equation (eq. 1.5) for the two individual half-cell reactions (eq. 1.3 and eq. 1.4). Here,  $E_{\text{rev}}$  is the thermodynamic cell potential at the operating conditions,  $E_0$  is the equilibrium potential of the individual reactions at standard conditions ( $25^\circ\text{C}$ ,  $101.3 \text{ kPa}$  gas partial pressure, and liquid water),  $R$  is the ideal gas constant ( $8.314 \text{ J mol}^{-1} \text{ K}^{-1}$ ),  $T$  is the temperature (in K),  $n$  is the number of transferred electrons (4 according to eq. 1.2),  $F$  is the Faraday constant ( $96485.3 \text{ A s mol}^{-1}$ ), and  $a_i$  is the activity of the gaseous reactants. Under standard conditions, the equilibrium potential is  $\equiv 0 \text{ V}$  vs the reversible hydrogen electrode (RHE) for  $\text{H}_2/\text{H}^+$  and  $\equiv 1.23 \text{ V}_{\text{RHE}}$  for  $\text{O}_2/\text{H}^+/\text{H}_2\text{O}$  (note that the RHE scale accounts for the pH-dependent Nernst-shift and the  $\text{H}_2/\text{H}^+$  equilibrium is  $\equiv 0 \text{ V}_{\text{RHE}}$  independent on the activity of protons). For  $\text{H}_2$  and  $\text{O}_2$ , the activity equals the partial pressure of the respective gases normalized to the reference gas pressure at

standard conditions (101.3 kPa), whereas for H<sub>2</sub>O, the partial pressure is normalized to the water saturation pressure at the respective temperature, i.e., the activity of water equals the *RH*.

$$E_{\text{rev}} = E_0^{\text{OER/ORR}} - E_0^{\text{HOR/HER}} + \frac{R \cdot T}{n \cdot F} \cdot \ln \left( \frac{a_{\text{O}_2} \cdot a_{\text{H}_2}^2}{a_{\text{H}_2\text{O}}^2} \right) \quad (1.5)$$

In a real system, the fuel cell potential is lowered by the so-called overpotentials and by parasitic currents. The overpotentials include kinetic overpotentials from the two reactions ( $\eta_{\text{ORR/HOR}}$ ), ohmic resistances caused by a limited proton conductivity in the membrane ( $R_{\text{membrane}}$ ) and the catalyst layers ( $R_{\text{H}^+}^{\text{eff}}$ ), as well as electrical contact resistances ( $R_{\text{contact}}$ ) and oxygen mass transport resistances ( $R_{\text{O}_2}^{\text{total}}$ ). Parasitic currents include H<sub>2</sub>-crossover ( $i_{\text{H}_2-x}$ ) and shorting currents ( $i_{\text{short}}$ ) that force an electrochemical reaction within the electrodes, even when no external current is drawn, whereby the respective kinetic overpotentials reduce the open circuit voltage (OCV) of the cell. The focus of current PEMFC materials research is therefore the minimization of the individual voltage loss contributions, while lowering the required Pt loading is essential to reduce the overall system costs.<sup>19</sup>

Overpotentials caused by the electrode kinetics are generally described by the Butler-Volmer equation (eq. 1.6).

$$i = i_0 \cdot rf \cdot \left( e^{\frac{\alpha_a \cdot F}{R \cdot T} \cdot \eta} - e^{-\frac{\alpha_c \cdot F}{R \cdot T} \cdot \eta} \right) \quad (1.6)$$

Here,  $i$  is the current density (in  $\text{A cm}_{\text{MEA}}^{-2}$ ),  $i_0$  is the exchange current density (in  $\text{A cm}_{\text{Pt}}^2$ ),  $rf$  is the roughness factor (active surface area of the catalyst with respect to the electrode area, given in  $\text{cm}_{\text{Pt}}^2 \text{ cm}_{\text{MEA}}^{-2}$ ),  $\alpha_a$  and  $\alpha_c$  are the anodic and cathodic transfer coefficients, and  $\eta$  is the overpotential (in V). As the Butler-Volmer equation considers the reaction in the anodic direction (e.g., HOR) and the backward reaction in the cathodic direction (e.g., HER) through the transfer coefficients and the overpotential, it is mostly used to describe fast reactions (i.e., reactions with a high exchange current density) that require low overpotentials. For reactions that require a high overpotential, i.e., that occur far from the equilibrium potential (e.g., ORR), the backward reaction can usually be neglected and the simplified Tafel equation (eq. 1.7)

is therefore used, with the Tafel slope being defined as  $TS = 2.303 \cdot \frac{R \cdot T}{\alpha_{a/c} \cdot F}$ .

$$|\eta| = \frac{R \cdot T}{\alpha_{a/c} \cdot F} \cdot \ln \left( \frac{|i|}{i_0 \cdot rf} \right) = TS \cdot \lg \left( \frac{|i|}{i_0 \cdot rf} \right) \quad (1.7)$$

The sign of the overpotential depends on the sign of the current, i.e., for anodic currents ( $i_a > 0$ ), a positive overpotential is obtained, whereas for cathodic currents ( $i_c < 0$ ), the overpotential is negative (note that in fuel cell studies the overpotentials of the ORR are often stated as positive numbers although they reduce the half-cell potential). On the anode side of a PEMFC, the HOR according to eq. 1.3 is extremely fast with a reported  $i_0$  of  $0.52 \pm 0.15 \text{ A cm}_{\text{Pt}}^{-2}$  (at  $80^\circ\text{C}$ ,  $90\% \text{ RH}$ , and  $100 \text{ kPa}_{\text{H}_2}$ ), so that the anode kinetics account for less than 10 mV of the total voltage losses even at high current densities of  $3 \text{ A cm}_{\text{MEA}}^{-2}$  and low anode loadings of  $0.05 \text{ mg}_{\text{Pt}} \text{ cm}_{\text{MEA}}^{-2}$  (see Section 3.1.2).<sup>25</sup> Thus, the catalyst development has concentrated on improving the cathode activity as the large kinetic ORR overpotential contributes  $\approx 300 - 400 \text{ mV}$  to the overall voltage losses. In recent years, a more holistic understanding of the ORR mechanism has been gained and, by optimizing lattice strain and electronic effects, more than ten-fold improvements in mass activity over conventional Pt/C catalysts have been demonstrated in rotating disk electrode (RDE) measurements. However, the improvement factors upon the integration of such advanced materials in MEAs are typically much lower (these discrepancies will be discussed in detail in Sections 1.2 and 3.1.1).<sup>16,26-28</sup>

Apart from the intrinsic catalytic activity of the Pt or Pt-alloy nanoparticles, the ORR activity of the catalyst in an MEA is strongly affected by the adsorption of the ionomer's sulfonate endgroups which can block some of the active sites for the ORR.<sup>29,30</sup> The magnitude of this so-called ionomer poisoning effect on the catalyst activity is mainly depending on the structure of the carbon support. In general, the ionomer cannot reach the nanoparticles that are located inside the pores of a highly porous carbon support (e.g., Ketjenblack) but it can easily access particles located on the outside of a solid carbon support without significant internal porosity (e.g., Vulcan).<sup>31</sup> Thus, catalysts supported on porous carbon show  $\approx 2$  times higher mass activities compared to solid carbon supported catalysts with a similar *ECSA*.<sup>31,32</sup> This is especially important for applications that require high electric efficiency and thus operate at low current density.<sup>16</sup>

While substantial progress has been made with respect to the catalyst kinetics, the high-power performance of a fuel cell stack is mostly defined by the high current density (HCD) operation ( $> 2 \text{ A cm}_{\text{MEA}}^{-2}$ ), where due to the logarithmic nature of the Tafel equation, the kinetic overpotentials account only for an additional  $TS$  of 70 mV (for the ORR) upon increasing the current density from  $0.5 \text{ A cm}_{\text{MEA}}^{-2}$  to  $5 \text{ A cm}_{\text{MEA}}^{-2}$ . At HCD, the consumption of oxygen in the vicinity of the catalyst and the resulting decrease in the local oxygen concentration (21% in air) at the active site(s) lead to a severe increase in the oxygen mass transport resistance and is thus seen as the major contributor to the overall voltage loss in this current regime.<sup>33</sup> This is especially pronounced for low-loaded electrodes with a low  $rf$  that require high Pt surface specific currents and therefore force a high local flux of  $\text{O}_2$  and  $\text{H}^+$  at the triple-phase interface. In catalysts with a highly porous carbon support, the necessity for  $\text{O}_2$  to pass through constricted pores to reach the Pt nanoparticles located inside the primary carbon particles, increases the oxygen mass transport resistance and annihilates the advantage of a reduced ionomer poisoning for HCD operation.<sup>31</sup> The additional voltage losses that are connected with high Pt surface specific currents are often referred to as local  $\text{O}_2$ -transport resistances and were found to scale inversely with the cathode  $rf$ .<sup>33–36</sup> In recent years, significant progress has been made in understanding the local  $\text{O}_2$ -transport resistance and in optimizing both the pore structure and the Pt particle location to achieve better HCD performance at low Pt loadings.<sup>23,31,37–40</sup>

### 1.1.3. MEA Durability

Apart from the MEA performance at beginning-of-life, the durability of the components remains a major challenge for the wide spread commercialization of PEMFC systems.<sup>41,42</sup> Hereby, many factors affect the durability of an MEA, namely cell reversal events that cause anode degradation, mechanical and chemical degradation of membrane and ionomer, corrosion of the carbon support in the cathode catalyst layer during start-up/shut-down (SUSD) or local hydrogen starvation events, and finally the loss of Pt  $ECSA$  in the cathode as a result of load cycling.<sup>18,43–47</sup>

#### Load Cycling

During fuel cell operation, the load of a PEMFC stack varies from full load with high current densities and corresponding low cathode potentials ( $\approx 0.6 - 0.7 \text{ V}_{\text{RHE}}$ ),

to low or no load and therefore high cathode potentials ( $\approx 0.85 - 0.95 V_{\text{RHE}}$ ). As a consequence of the reversible electrochemical surface oxidation of Pt that occurs across these potential regions, repeated Pt dissolution and subsequent redeposition takes place.<sup>43,48</sup> Since the Pt ions are mobile within the ionomer phase during high potential operation, this leads to a loss of *ECSA* both due to Pt nanoparticle growth by Ostwald ripening and Pt loss into the membrane phase where the Pt ions get reduced by crossover  $\text{H}_2$ , leading to the so-called Pt band formation.<sup>43,49</sup> Since these two processes are to some extent competitive and since the diffusion length plays a crucial role, the overall loss of active Pt surface area is not homogeneous across the thickness of the electrode: in the part of the electrode that is closest to the membrane, a depletion of Pt due to Pt band formation dominates, whereas in the part of the electrode that is adjacent to the GDL (and furthest from the membrane), Ostwald ripening is the predominant cause of the *ECSA* loss.<sup>43</sup> Hereby, the Pt dissolution/redeposition processes are more pronounced for smaller Pt nanoparticles that have a higher surface energy and are therefore more susceptible to Pt dissolution and the corresponding *ECSA* loss during load cycling.<sup>50</sup> The concomitant loss of cathode *rf* during load cycling leads to severe  $\text{H}_2$ /air performance penalties due to kinetic overpotentials on the one hand and, more importantly, due to additional  $\text{O}_2$ -transport losses on the other hand.<sup>51–53</sup> The load cycling induced degradation is mostly investigated by voltage cycling based accelerated stress tests (ASTs), which will be discussed in detail in Section 3.3.2.

### Start-Up/Shut-Down

While carbon is thermodynamically unstable at potentials above  $0.2 \text{ V}$  vs. the standard hydrogen electrode (SHE),<sup>54</sup> the kinetics of the carbon oxidation reaction (COR) are fortunately so slow that carbon corrosion is not a major issue during normal operation of a PEMFC.<sup>55</sup> However, during an SUSD event, the local cathode potential can rise to potentials  $> 1.2 V_{\text{RHE}}$ , where the COR kinetics are sufficiently fast for carbon corrosion to become a serious issue.<sup>44,56</sup> When a PEMFC stack remains in a long shut-down during which the gas circulation is turned off,  $\text{H}_2$  in the anode compartment first permeates through the membrane to the cathode compartment, where  $\text{H}_2$  and  $\text{O}_2$  are consumed according to eq. 1.2. Since there is usually an excess of  $\text{H}_2$  in the anode compared to  $\text{O}_2$  in the cathode (21% in air, with at the same time similar flow field volumes) compartment, this results in an intermediate state where both sides of the PEMFC are filled with a mixture of  $\text{H}_2$  and  $\text{N}_2$  ( $\text{N}_2$  permeates through the membrane from the cathode to the anode side). However, since the sealing of the

stack is not perfect, air intrudes slowly into the system whereby the remaining  $\text{H}_2$  is consumed and, after long shut-down periods, both sides of the cell are filled with air. During a subsequent start-up, the anode compartment is flushed with  $\text{H}_2$ , whereby a  $\text{H}_2/\text{air}_{\text{anode}}$ -front passes through the anode (see fig. 1.3 a) and causes a polarization of the anode between a  $\text{H}_2$ -filled segment, where the HOR takes place, and an  $\text{air}_{\text{anode}}$ -filled segment, in which ORR occurs (conceptually shown in fig. 1.3 b). Due to the poor in-plane  $\text{H}^+$ -conductivity of the catalyst layers and distances of several mm – cm between the respective anode segments, an oxidative current is forced on the adjacent cathode that is only separated by a 10 – 25  $\mu\text{m}$  thick membrane, which leads to cathode-sided carbon oxidation in the  $\text{air}_{\text{anode}}/\text{air}_{\text{cathode}}$ -filled section of the cell (so-called reverse-current mechanism, see fig. 1.3 a & b).<sup>44,57</sup>

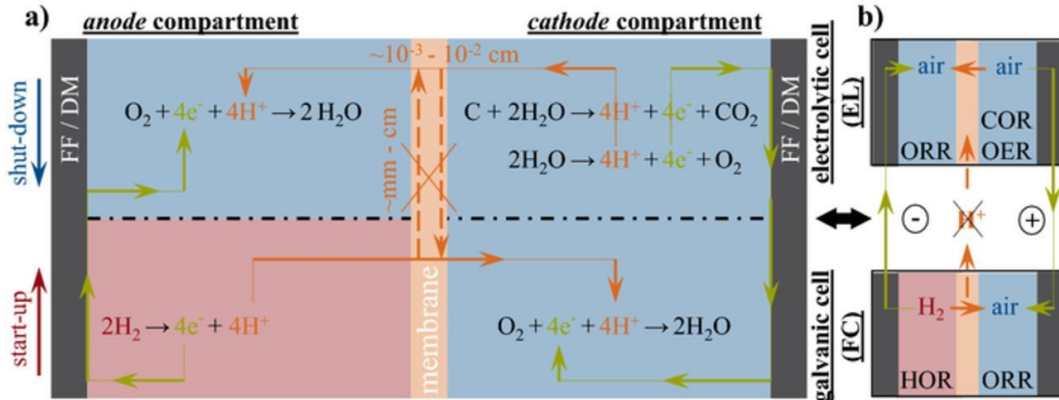


**Figure 1.3.** Schematic of a SUSD event in a PEMFC, sketching the passage of a  $\text{H}_2/\text{air}_{\text{anode}}$  front through the anode flow-field ( $\text{H}_2$ -filled regions in red, air-filled regions in blue) while the cathode flow-field is filled with air. a) Illustration of the reactions occurring during the SUSD event, with sketched pathways of electrons (in green) through the electrode, diffusion medium (DM) and flow-field (FF) as well as of protons (in orange) across the membrane; b) Conceptual separation into a fuel cell (FC) segment and an electrolytic cell (EL) segment ( $\text{H}_2$ -filled and air-filled flow-field segments are indicated in red and in blue, respectively). In-plane proton conduction is only possible within very short distances from the  $\text{H}_2/\text{air}_{\text{anode}}$  front ( $\approx 120\mu\text{m}$  for a  $20\mu\text{m}$  thick membrane) and not over extended distances, which is indicated by the crossed-out arrows. The figure is reprinted from Mittermeier *et al.* under the terms of the CC BY-NC-ND License.<sup>57</sup>

In some cases, the safety regulations of a PEMFC system require that  $\text{H}_2$  is purged from the anode side during the shut-down of the system to avoid that pure  $\text{H}_2$  is present during an uncontrolled/unmonitored period, whereby a  $\text{H}_2/\text{air}_{\text{anode}}$ -front passes through the anode during the shut-down event as well. The carbon mass loss due to SUSD events results in a structural collapse of the cathode catalyst layer already after less than 10% of the carbon mass have been corroded. This is accompanied by severe performance losses due to increasing  $\text{O}_2$  mass transport resistances and a loss

of *ECSA* due to the detachment of Pt nanoparticles from the support.<sup>44,56,58</sup> Since the carbon corrosion current during an SUSD event is linked to the ORR activity of the anode, an anode catalyst that has a reduced ORR activity while maintaining its HOR activity during normal operation was shown to reduce the cathode degradation under these conditions.<sup>59,60</sup> The development and evaluation of such a catalyst will be discussed in detail in Sections 3.2.2 and 3.3.1.

Another catalyst-based approach to mitigate SUSD-induced cathode degradation is replacing the conventional carbon supported ORR catalyst with a Pt catalyst supported on a metal oxide substrate that cannot be corroded at high potentials and should therefore be much more stable.<sup>61–66</sup> However, the low conductivity of these supports often limits their applicability in a PEMFC system.<sup>66</sup> Here, continuous metal films on high surface area supports might be a promising approach for durable and highly active electrodes,<sup>67,68</sup> but the high interfacial energy of the metal/oxide interface always results in a 3D morphology growth of the deposited metal,<sup>69</sup> thus making thin Pt films on a poorly conducting metal oxide inaccessible. However, these structures might become accessible if the outermost surface of the oxide could be reduced to form a metallic buffer layer on which the Pt thin film deposition can take place.<sup>70</sup> As the first step towards extended Pt films on a metal oxide support, a novel approach to achieve these metallic buffer layers by the surface reduction of metal oxides will be explored in Section 3.2.1.

### Local Fuel Starvation

Similar to SUSD events, local H<sub>2</sub> starvation (e.g., due to a water droplet blocking a channel of the anode FF) can result in a reverse-current event, since O<sub>2</sub> and N<sub>2</sub> permeate through the membrane from the cathode to the anode and the crossover O<sub>2</sub> undergoes ORR in the anode compartment, forcing an oxidative current on the adjacent section of the cathode.<sup>45</sup> The effect is especially detrimental as local H<sub>2</sub> starvation events take place during operation (i.e., at temperatures of  $\approx 80 - 90$  °C), where the kinetics of the COR are much higher compared to start-up events that usually occur at ambient temperature. It is therefore essential to design a FF structure that helps to avoid water accumulation in the channels and mitigates local H<sub>2</sub> starvation events. Since the reverse-current mechanism is the same in local fuel starvation and SUSD events, the same catalyst based mitigation strategies apply.

### Cell Reversal

Compared to a local H<sub>2</sub> starvation event, a cell reversal event occurs when the H<sub>2</sub> supply is interrupted to an entire cell rather than just a section of the anode. In a single-cell configuration, the resulting drop in H<sub>2</sub> partial pressure would result in a performance decay until all H<sub>2</sub> is consumed and no power can be drawn from the cell anymore. In a PEMFC stack with multiple cells, however, the cells are connected in series and therefore the same current must pass through each MEA. The cells that are supplied with H<sub>2</sub> operate as galvanic cells and increase the stack voltage, while the starved cells have to operate as electrolytic cells to sustain the applied current, i.e., an oxidative current is forced on the anode side of the MEA. Since the conventional Pt/C anode catalysts are poor oxygen evolution catalysts, this results in very high anode potentials at which carbon corrosion is very severe. Because this phenomenon occurs on a cell level and usually during HCD operation, it leads to a rapid PEMFC failure and must be avoided at all times.<sup>71,72</sup>

### Membrane and Ionomer Degradation

In general, degradation of the membrane is caused by mechanical and thermal stress and by chemical decomposition.<sup>73</sup> Mechanical failure can already occur during the cell assembly process, e.g., when large agglomerates in the catalyst layer or carbon fibers from the GDL could pierce the membrane. However, the mechanical stress induced membrane degradation typically describes the swelling and contracting of the ionomer phase of the membrane due to water uptake and release resulting from operation at high and low *RH*, respectively.<sup>17</sup> In the most extreme case, the repeated expansion and contraction of the membrane can lead to its rupture, followed by a rapid and uncontrolled heat development due to the mixing of H<sub>2</sub> and air.<sup>18,74</sup> The mechanical stability of state-of-the-art membranes is commonly enhanced by an expanded PTFE reinforcement that limits the swelling to a change in the membrane thickness and thus mitigates membrane rupture.<sup>18</sup>

Chemical degradation of the ionomer and membrane occurs mostly during OCV operation at low *RH*.<sup>75</sup> Here, the chemical degradation of the ionomer proceeds via a radical attack, whereby hydroxyl radicals ( $\bullet\text{OH}$ ) are generated by the decomposition of H<sub>2</sub>O<sub>2</sub> that is formed by the reaction between H<sub>2</sub> and O<sub>2</sub> in the presence of Pt (e.g., at the Pt band in the membrane). The decomposition of H<sub>2</sub>O<sub>2</sub> to  $\bullet\text{OH}$  radicals is strongly

accelerated by the presence of transition metal cations, such as  $\text{Fe}^{2+}$  (so-called Fenton reaction). The hydroxyl radicals can attack hydrogen atoms that are generally present at the endgroups of the ionomer's perfluorinated backbone (endgroup unzipping mechanism) or at the sulfonic acid group when the local water content of the ionomer is very low (side chain unzipping mechanism at low  $RH$ ), whereby HF is released.<sup>76</sup> As the sulfonic acid endgroup is deprotonated during operation under humidified conditions, and the endgroup unzipping mechanism can be inhibited by post-fluorination of the ionomer, the chemical degradation of the membrane occurs mostly at low  $RH$  and can therefore be mitigated to some extent by operating the PEMFC stack at high  $RH$ . Additionally, radical scavengers, such as  $\text{Ce}^{3+/4+}$ , are often used to significantly improve the membrane stability.<sup>77</sup>

## 1.2. Rotating Disk Electrode (RDE) vs Membrane Electrode Assembly (MEA) Measurement Configurations

Although the data that is most representative of the performance of a PEMFC system is obtained by MEA measurements, the development of novel catalysts, that are often synthesized in mg-quantities and undergo multiple synthesis iterations, requires a fast and easily accessible measurement technique for the initial screening of the catalyst activity and, where possible, stability. Here, the rotating disk electrode (RDE) technique is most commonly employed, as the electrode rotation in an aqueous electrolyte establishes a well-defined diffusion layer of 5 – 50  $\mu\text{m}$  that allows for a highly reproducible extraction of the kinetic parameters for the ORR, as long as the catalyst coating is uniformly distributed on the electrode disk.<sup>78,79</sup>

The RDE and MEA measurement configurations are compared in fig. 1.4, whereby the main differences between the techniques are highlighted. These include the catalyst environment, the required catalyst amounts, the experiment duration, the dominant mass transport regime and resulting transport limited current densities, and the electrolyte/catalyst ratio.

In the following, the characteristics of the two setups are briefly introduced and a discussion of the critical differences between the techniques and the implications for

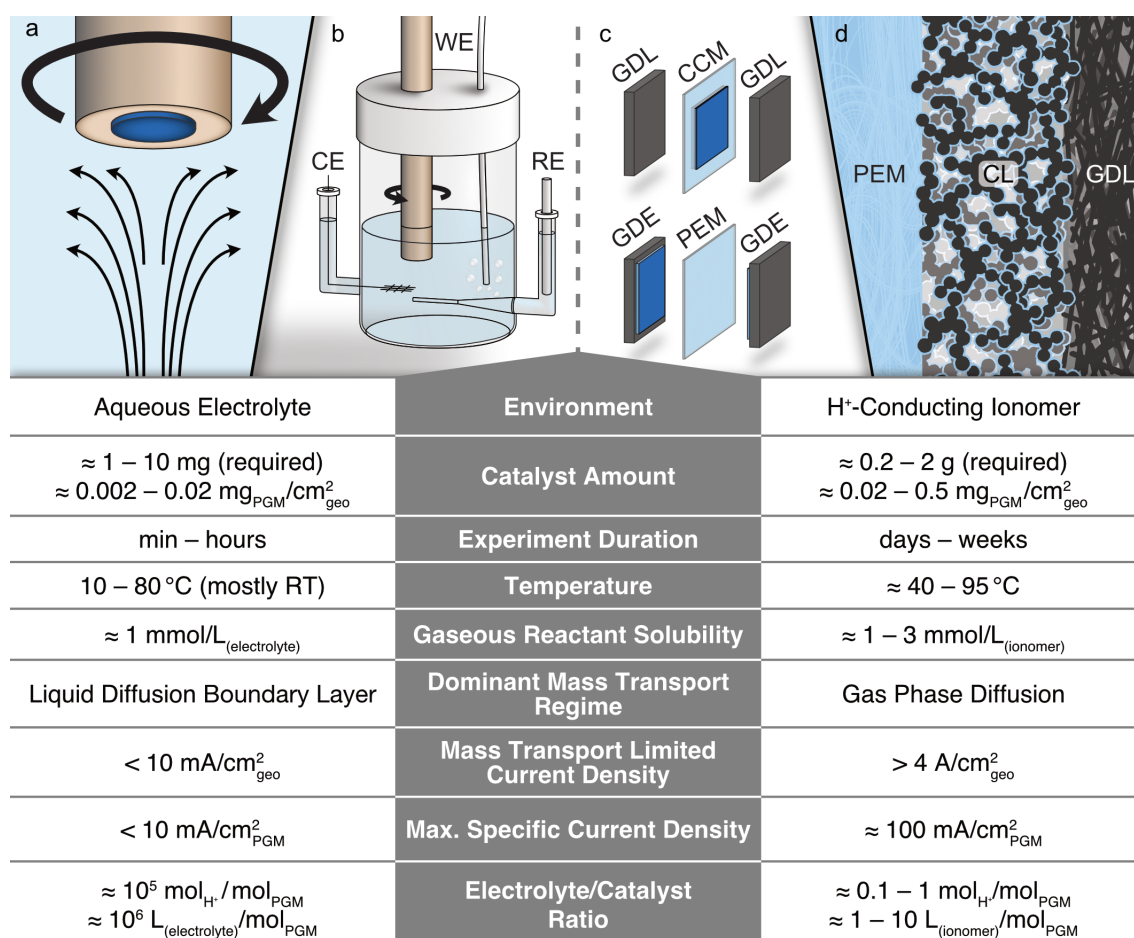


**Figure 1.4.** Comparison of RDE (left) and 5-layer MEA (right) setups, including a table that highlights the main differences between the techniques. a) Local environment of an RDE working electrode (WE); b) scheme of a 3-electrode RDE setup; c) 5-layer MEA setups consisting either of a CCM sandwiched between two GDLs or a PEM between two GDEs; d) local environment in an MEA with the porous catalyst layer (CL) consisting of catalyst particles (black) and ionomer (light blue). The table summarizes typical specifications for both setups (exceptions might apply). The figure is adapted from Lazaridis and Stühmeier *et al.* (see Section 3.1.1).<sup>28</sup>

the investigation of PEMFC catalysts will then be presented in Section 3.1.1.

### 1.2.1. RDE Measurements

The RDE technique employs a three-electrode setup (see fig. 1.4 a & b) to investigate the half-cell reactions of a PEMFC in an aqueous electrolyte (typically HClO<sub>4</sub> or H<sub>2</sub>SO<sub>4</sub>) under well defined mass transport conditions. This allows for the precise determination of the intrinsic activity of electrocatalysts that is not directly accessible by MEA measurements. Additionally, the use of a rotating ring disk electrode (RRDE) setup, where a Pt or Au ring surrounding the working electrode (WE) in close prox-

imity is used to collect side products of the reaction, e.g., H<sub>2</sub>O<sub>2</sub> during the ORR, as well as studies on single-crystal model electrodes or advanced catalyst concepts have enabled a more holistic understanding of the relevant reaction mechanisms in PEMFC systems.<sup>78,80</sup>

For RDE measurements, the catalyst (with or without binder/ionomer) is deposited as a thin layer on an electrically conductive non-porous RDE substrate, e.g., glassy carbon. Since the total amount of catalyst deposited on the WE is extremely low with  $\approx 5 - 50 \mu\text{g}_{\text{Pt}} \text{cm}_{\text{disk}}^{-2}$  on a disk with an area of 0.196 cm<sup>2</sup> (5 mm diameter), the quality of the coating has a severe impact on the reproducibility of the measurement results.<sup>79</sup> Furthermore, the cleanliness requirements for the system and especially the purity of the used electrolytes are extremely high (for details see Shinozaki *et al.*<sup>81</sup> and Kocha *et al.*<sup>82</sup>). The electrolyte can be gas-saturated, which allows for a precise determination of the electrode's *ECSA* or *rf* by hydrogen underpotential deposition (H<sub>upd</sub>) or CO-stripping (if CO is available) in N<sub>2</sub>/Ar-saturated electrolytes. Using H<sub>2</sub>-saturation enables the calibration of the reference electrode (RE) on the RHE scale by recording HER/HOR polarization curves. Finally, OER/ORR kinetics can be determined in O<sub>2</sub>-saturated environment. The rotation of the electrode results in a rotation rate dependent thickness of the diffusion boundary layer and therefore a maximum mass transport rate by diffusion that is expressed as a current plateau (so-called limiting current density, *i*<sub>lim</sub>), where the reactant concentration at the surface of the disk approaches zero.<sup>80</sup> Assuming first-order reaction kinetics, the measured current density (*i*<sub>meas</sub>) can be corrected for the change in the reactant concentration according to eq. 1.8 in order to obtain the kinetic current density (*i*<sub>kin</sub>).<sup>83</sup>

$$i_{\text{kin}} = \frac{i_{\text{lim}} \cdot i_{\text{meas}}}{i_{\text{lim}} - i_{\text{meas}}} \quad (1.8)$$

At the same time, the measured potential (*E*) must be corrected for the potential drop due to the high frequency resistance (*R*<sub>HFR</sub>) between the RDE working electrode and the reference electrode, i.e., the uncompensated solution resistance that is obtained from the high frequency intercept in electrochemical impedance spectroscopy (EIS) measurements. From this one obtains the *iR*-free potential (*E*<sub>*iR*-free</sub>, eq. 1.9).<sup>83</sup>

$$E_{\text{iR-free}} = E - i_{\text{meas}} \cdot R_{\text{HFR}} \quad (1.9)$$

Note that here the sign of *i*<sub>meas</sub> is positive for anodic and negative for cathodic re-

actions. Additionally, the potential must be corrected for the diffusion overpotential ( $\eta_{\text{diff}}$ ), i.e., for the Nernst-shift of the equilibrium potential due to the reduced reactant concentration/activity at the disk surface. Under the assumption that the concentration of protons or hydroxide ions in the bulk solution and at the disk surface is approximately the same, i.e., the concentration of H<sub>2</sub> or O<sub>2</sub> is much smaller than the concentration of the ionic charge carriers (at pH  $\leq$  2 or pH  $\geq$  12), the diffusion overpotential can be calculated according to eq. 1.10 for the HOR and according to eq. 1.11 for the ORR.<sup>83,84</sup>

$$\eta_{\text{diff}} = -\frac{R \cdot T}{2 \cdot F} \cdot \ln \left( 1 - \frac{i_{\text{meas}}}{i_{\text{lim}}} \right) > 0 \quad (1.10)$$

$$\eta_{\text{diff}} = +\frac{R \cdot T}{4 \cdot F} \cdot \ln \left( 1 - \frac{i_{\text{meas}}}{i_{\text{lim}}} \right) < 0 \quad (1.11)$$

However, the corrections are only reliable for measured current densities smaller than  $\frac{i_{\text{lim}}}{2}$  where the mass transport corrections according to eq. 1.8 are less than a factor of 2.<sup>83</sup> With these corrections, the intrinsic catalyst activity is easily accessible from RDE testing, which is therefore an essential tool for the development of novel catalysts that allows for a fast screening of small sample quantities. At this point, it should be noted that the limited mass transport rates in an RDE setup severely limit the ability to properly quantify exchange current densities that exceed  $\approx 1 - 3 \text{ mA cm}_{\text{disk}}^{-2}$ <sup>85</sup> (corresponding to the maximum mass transport limited current densities) and that the RDE technique is therefore unsuitable for the determination of HER/HOR kinetics on Pt based catalysts at low pH (for details see Chapter 3.1).<sup>10</sup>

### 1.2.2. MEA Measurements

As described above, a 5-layer MEA consists of a proton exchange membrane, anode and cathode catalyst layers, and gas diffusion layers (GDLs) (see fig. 1.4 c & d). Hereby, the CCM can either be sandwiched by GDLs, or the catalyst layer is cast onto the GDLs to form gas diffusion electrodes (GDE) that are then laminated to the membrane. These GDL/CCM/GDL or GDE/PEM/GDE units are finally sealed between two FFs to form a single-cell unit. Thus, MEA measurements are performed in a two-electrode setup, whereby both half-cell reactions (eq. 1.3 and eq. 1.4) are measured simultaneously. This is possible because the kinetics of the HOR/HER are extremely fast and the overpotential of the hydrogen side is therefore small ( $\leq 5 \text{ mV}$

for electrodes with an  $rf$  of  $\geq 45 \text{ cm}_\text{Pt}^2 \text{ cm}_\text{MEA}^{-2}$ ),<sup>25</sup> so that it can serve as both counter electrode and pseudo-reversible hydrogen reference electrode (the partial pressure of  $\text{H}_2$  is precisely controlled at all times and Nernst shift corrections can thus be applied). The porous catalyst layers allow for efficient mass transport through the gas phase and, consequently, high limiting and Pt-specific current densities can be reached, so that even the HOR/HER kinetics can be determined by using ultra-low-loaded electrodes (for details see Section 3.1.2). About 20 years ago, the intrinsic activity of a given catalyst could only be quantified approximately by MEA measurements, as one could only correct for the membrane and contact resistances by HFR measurements as well as for the  $\text{H}_2$ -crossover and shorting currents by measurements in  $\text{H}_2/\text{N}_2$  atmosphere, whereas many other voltage loss contributions were known to exist but it was not yet possible to quantify them.<sup>80,83</sup> Since then, however, significant progress has been made in understanding and evaluating the various voltage loss terms described in Section 1.1.2. Thus, it is now possible to correct for the inhomogeneous through-plane catalyst utilization,<sup>86</sup> the effective proton conduction resistance within the electrode,<sup>21</sup> and the oxygen mass transport resistance in catalyst layer, GDL, and FF.<sup>87</sup> Furthermore, novel methods have been developed to investigate the interaction between Pt nanoparticles and ionomer (e.g., by CO-displacement)<sup>88</sup> and the accessibility of Pt particles embedded in a porous carbon support (e.g., by  $RH$ -dependent CO-stripping).<sup>89</sup> Many of these voltage loss contributions that mostly affect HCD operation can only be investigated in PEMFC single-cells or short-stacks, as in other measurement configurations, such as thin-film RDE, the relevant current densities are inaccessible or the difference in local environment (liquid electrolyte vs. ionomer thin film) prevents the evaluation of relevant effects, e.g., proton conduction in micropores or local  $\text{O}_2$ -transport resistances.

However, MEAs are time consuming to manufacture, the electrochemical testing often takes multiple days per catalyst and further requires capital-intensive instrumentation capable of precisely controlling gas pressures, flow rates, relative humidities, and temperatures. Additionally, the electrode preparation requires gram-quantities of catalyst, the conditions in MEAs (catalyst/electrolyte interface, high temperatures, low pH, voltage cycles, high current densities, etc.) often result in a destabilization and incomplete utilization of optimized active sites, and the complex experimental setup implies that results are often affected by unrelated influences, e.g., from membrane, counter electrode, GDL, operating conditions, or the MEA preparation. Therefore,

MEA measurements require extraordinary care when trying to properly quantify the intrinsic activity of a given catalyst. Nevertheless, MEA testing is essential for the catalyst evaluation at higher technology readiness levels and for the understanding of MEA specific effects (for details see Section 3.1.1).

#### 1.2.3. Bridging Techniques

It should be mentioned that several techniques that bridge the gap between RDE and MEA measurements by providing high mass transport in liquid electrolytes while requiring much smaller amounts of catalyst have been developed in recent years.<sup>26</sup> Among others, these methods include the floating electrode technique (FET),<sup>90</sup> the modified rotating disk electrode (MRDE),<sup>91</sup> and the gas diffusion electrode (GDE).<sup>92–94</sup> The promise of these bridging techniques consists in their ability to closely resemble the local environment and mass transport pathways of MEAs, albeit at lower catalyst-mass requirements and technical complexity comparable to the RDE technique. However, since I did not use these techniques for this thesis, they will not be discussed in detail here and instead, the reader is referred to the works of Kwan *et al.*,<sup>91</sup> Pan *et al.*,<sup>26</sup> and Ehelebe *et al.*<sup>94</sup> regarding the use of these techniques and respective protocols.

### 1.3. Strong Metal-Support Interaction (SMSI)

In 1978, Tauster *et al.* reported for the first time on drastic changes in the chemisorption properties of group VIII noble metal particles that were supported on titanium oxide. They called this behavior the "strong metal-support interaction" (SMSI).<sup>95</sup>

In recent years, SMSI has been established as a collective term that is used to describe significant alterations of the catalytic activity and selectivity of group VIII metal nanoparticles supported on reducible oxides.<sup>96,97</sup> This includes electronic effects, the (partial) encapsulation of the metal nanoparticles by a thin layer of partially reduced oxide, spillover effects, morphology changes, and, in some cases, alloy formation.<sup>96–100</sup> A heat-treatment in reductive atmosphere or oxygen removal in ultra-high vacuum are typically required to form the SMSI,<sup>96</sup> although similar effects have been achieved electrochemically by voltage cycling.<sup>101–105</sup> Thus, in the following section, the SMSI will be discussed with respect to the electrochemical properties of oxide supported

catalysts.

Catalyst concepts based on oxide supported Pt nanoparticles have gained considerable interest over the last two decades as alternatives to conventional carbon supported catalysts.<sup>106</sup> Here, corrosion resistant oxides promise to suffer less from SUSD and cell reversal events and to facilitate an improved *EC*SA retention during voltage cycling.<sup>61,62,65,107,108</sup> Additionally, it was found that the electronic effect of the SMSI enhances the ORR activity of Pt supported on solid solutions of TiO<sub>2</sub> and the oxides of Mo,<sup>109</sup> Ru,<sup>110</sup> and Ta,<sup>111</sup> as well as on niobium, antimony, or tantalum doped tin oxides.<sup>112,113</sup>

While the electronic SMSI effect has a positive impact on the ORR activity of oxide supported Pt catalysts, the encapsulation that is often observed for SMSI systems has a detrimental effect on the ORR. This was shown conclusively in a study by Hsieh *et al.*,<sup>114</sup> where they synthesized a TiO<sub>2</sub> supported Pt catalyst that they heat-treated in H<sub>2</sub> at 200 °C. Before the heat-treatment, the catalyst showed a mass activity of 1.83 mA mg<sub>Pt</sub><sup>-1</sup> at 0.9 V<sub>RHE</sub>, whereas after SMSI formation, the activity decreased to only 1.01 mA mg<sub>Pt</sub><sup>-1</sup> due to an encapsulation of the Pt particles by TiO<sub>x</sub> (x ≤ 2), which they showed by high resolution TEM images.<sup>114</sup> The driving force for the encapsulation is generally considered to be the minimization of the total surface-energy of the system and thus, it occurs mostly when high surface-energy metal nanoparticles (e.g., Pt, Rh, Ru, or Pd) are supported on reducible low surface-energy metal oxides (e.g., TiO<sub>2</sub>, CeO<sub>2</sub>, Nb<sub>2</sub>O<sub>5</sub>, or V<sub>2</sub>O<sub>3</sub>).<sup>97,115</sup> Hsieh *et al.*<sup>114</sup> then etched the encapsulating layer by hydrofluoric acid treatment and obtained an enhanced activity of 4.23 mA mg<sub>Pt</sub><sup>-1</sup>, while solely the acid treatment without a previous reductive heat-treatment did not result in a significantly improved ORR activity. They thus confirmed that the electronic SMSI effect indeed enhances the ORR activity of Pt but that an encapsulation can have a stronger effect as a reaction barrier. Furthermore, they observed that the Pt oxidation at potentials above 0.6 V<sub>RHE</sub> is suppressed by the encapsulation, while the H<sub>upd</sub> is not, from which they concluded that the encapsulating layer must be permeable for protons but not for oxygenated species.<sup>114</sup>

Although Hsieh *et al.* were, to the best of my knowledge, the first to deconvolute the electronic SMSI effect and the encapsulation effect with respect to the ORR activity of Pt/TiO<sub>2</sub> catalysts, a hindered Pt oxidation and suppressed ORR activity of

Pt nanoparticles ( $\leq 1$  nm) supported on  $\text{TiO}_2$  had already been shown by Hayden *et al.*<sup>101,102</sup> in 2009. Banham *et al.*<sup>103</sup> found for a Pt/NbTiO<sub>2</sub> catalyst with a Pt particle size of  $\approx 7.5$  nm that the catalyst exhibited an unexpected HOR selectivity after voltage cycling between 1.0–1.4 V, i.e., the catalyst maintained its HOR activity while losing most of its ORR activity. They concluded that this effect was most likely caused by the dissolution/redeposition of the oxide that led to a selective site blocking, and proposed that this concept might be used in an anode catalyst to mitigate carbon corrosion on the cathode side during SUSD events.<sup>103</sup> Similar results were found by Gebauer *et al.* when exposing a Pt/C/TiO<sub>x</sub>N<sub>y</sub>C<sub>z</sub> catalyst to a square wave voltage cycling profile between 0.4–1.4 V, whereby the catalyst showed a surprisingly low ORR activity retention as well as suppressed Pt oxidation features.<sup>108</sup> Since then, the in-situ electrochemical SMSI formation has been observed in an increasing number of studies.<sup>104,105,116,117</sup> Thus, the correlation between a suppressed electrochemical Pt surface oxide formation, a reduced ORR activity, and the encapsulation of Pt nanoparticle is well established by now.<sup>104,105,118,119</sup>

Based on the works of Hsieh *et al.* and Banham *et al.*, we developed an HOR-selective Pt/TiO<sub>x</sub>/C catalyst for the mitigation of SUSD-induced cathode degradation (see Sections 3.2.2 and 3.3.1).<sup>118</sup> The catalyst combines the selectivity resulting from the Pt encapsulation (see fig. 1.5 b & c) with the structural advantages of a carbon support, i.e., high conductivity and low packing density that yields highly porous electrodes (see fig. 1.5 a). Furthermore, we found that due to the suppressed Pt surface oxide formation, the HOR activity of the catalyst is maintained even at potentials positive of 1.0 V<sub>RHE</sub>, where Pt surface oxide formation on conventional Pt/C catalysts results in a deactivation of the catalyst. This HOR activity retention at high anodic potentials was also observed in an earlier study by Gebauer *et al.*<sup>117</sup> and was later investigated in greater detail in our group by Geppert *et al.*<sup>119</sup> Employing this stabilization effect, we have furthermore investigated the SMSI effect on the electrochemical surface oxide formation and the HOR activity of Ru in a follow-up study (see fig. 1.5 d – g and Section 3.2.3).<sup>120</sup>

Finally, it should be noted that in 2021, Zhang *et al.*<sup>121</sup> conclusively showed the detrimental effect of  $\text{TiO}_2$  for the long term stability of a PEMFC. Unfortunately,  $\text{TiO}_2$  is not fully stable at  $\text{pH} \approx 0 - 1$ <sup>122</sup> and the dissolved ionic Ti species react with  $\text{H}_2\text{O}_2$  through a Fenton reaction and generate hydroxyl radicals ( $\bullet\text{OH}$ ) that decompose the

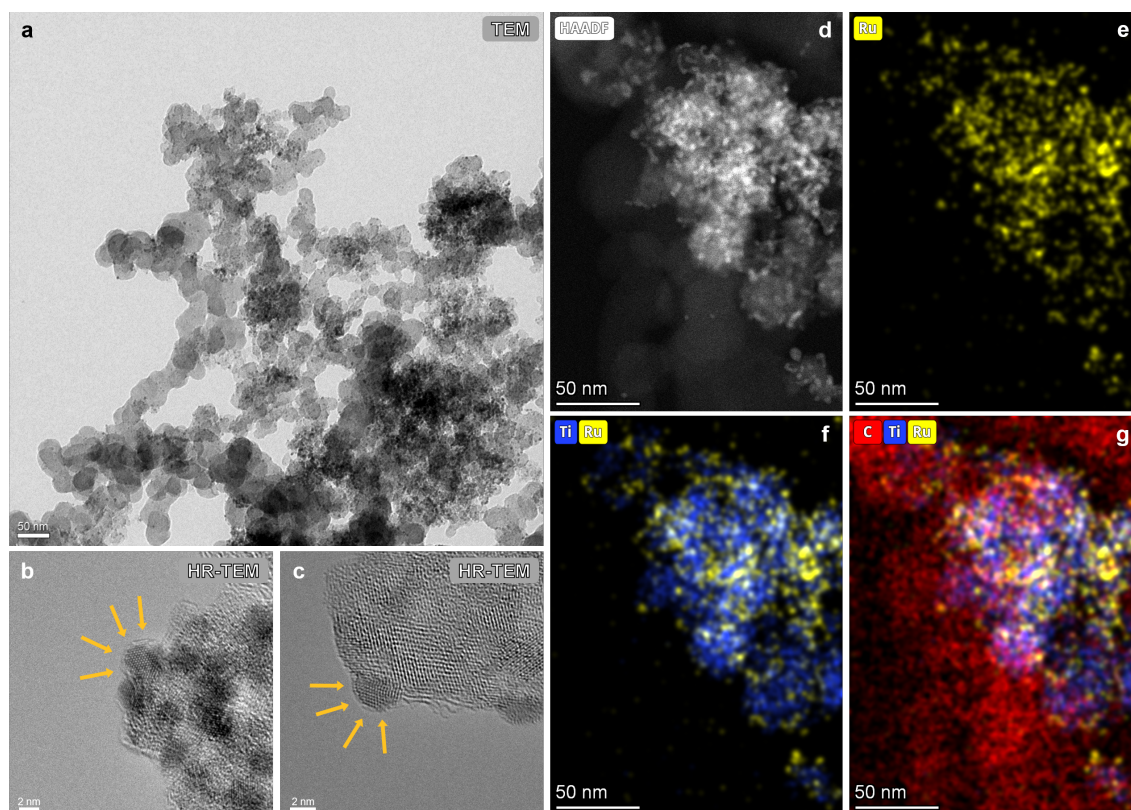


**Figure 1.5.** TEM images of Pt/TiO<sub>x</sub>/C (a – c) and Ru/TiO<sub>x</sub>/C (d – g) after the reductive heat-treatment at 400 °C in 5% H<sub>2</sub>/Ar atmosphere. a) TEM image of the Pt/TiO<sub>x</sub>/C catalyst that consists of Pt/TiO<sub>x</sub> agglomerates (characterized by their rough morphology and the dark Pt particles) supported on the Vulcan carbon structure (primary agglomerates of round and smooth carbon spheres); b & c) high resolution TEM images showing the encapsulation of the Pt particles by a thin layer of TiO<sub>x</sub> (indicated by the yellow arrows). d) Scanning transmission electron microscopy (STEM) images of the Ru/TiO<sub>x</sub>/C catalyst in high angle annular dark field (HAADF) mode whereby heavy elements appear brighter; corresponding energy dispersive X-ray spectroscopy (EDX) mappings of e) Ru, f) Ru & Ti, and g) Ru, Ti & C, showing the successful deposition of Ru on TiO<sub>x</sub>. Panels d – g adapted from Stühmeier and Schuster *et al.* (see Section 3.2.3).<sup>120</sup>

membrane.<sup>121</sup> Furthermore, we show that dissolved Ti species from the Pt/TiO<sub>2</sub>/C anode catalyst migrate to the cathode (see Section 3.3.1), where they compromise the high current density performance, which is most likely caused by the build-up of a pH gradient across the MEA that shifts the cathode equilibrium potential and results in an additional thermodynamic penalty.<sup>36</sup> Consequently, TiO<sub>2</sub> and, most likely, in extension also doped TiO<sub>2</sub> and Magneli phase materials (e.g., Ti<sub>4</sub>O<sub>7</sub>) are not suitable support materials for PEMFC catalysts. Thus, further research on employing the SMSI effect in next generation catalysts should focus on oxides that might prove to be more stable at low pH, such as WO<sub>3</sub> or Nb<sub>2</sub>O<sub>5</sub>.

## 1.4. Thesis Outline

Despite the introduction of the first commercial models of fuel cell electric vehicles in the last decade,<sup>14,15</sup> PEMFC systems still continue to face challenges with respect to the overall system performance and, arguably more important, the long-term durability.<sup>41,123</sup> Here, the current research focuses on the development of cathode catalysts with higher intrinsic activities, elucidating the mass transport limitations that affect HCD operation, the investigation of degradation mechanisms and stressors, and the development of appropriate mitigation strategies.<sup>9,16,19,123</sup> Within this research effort, the focus of this PhD thesis is to advance our understanding of the activity, selectivity, and durability of PEMFC catalyst materials by employing various electrochemical characterization methods. Thus, this work will cover three main topics: firstly, the development of suitable measurement techniques, secondly, the exploration and implementation of novel catalyst concepts, and finally, the investigation of catalyst degradation to elucidate the correlation between degradation and H<sub>2</sub>/air performance losses.

The first publication presented in Section 3.1 is a perspective that summarizes the capabilities and limitations of the RDE technique and of single-cell MEA measurements, proposing appropriate protocols for the screening and characterization of catalyst materials. Therefore, the perspective will outline the toolbox that is used throughout this thesis. Additionally, the Experimental Methods chapter (Chapter 2) will cover some of the pitfalls that come with the investigation of low-*r<sub>f</sub>* electrodes in more detail and propose an optimized procedure for the full characterization of 5 cm<sup>2</sup> single-cell PEMFCs. The second paper in Section 3.1 will then establish an experimental pro-

cedure for PEMFC based H<sub>2</sub>-pump measurements on ultra-low-loaded electrodes for the investigation of the HOR/HER kinetics and the underlying reaction mechanism.

Having established the required characterization techniques, several new catalyst concepts will be presented in Section 3.2. In the first paper, a novel method to reduce oxide thin-films in-situ with a polyol will be explored as a first step towards extended Pt (or Pt-alloy) thin films covering oxide support materials. In the second publication, we will develop a Pt/TiO<sub>x</sub>/C catalyst that combines the advantages of the SMSI effect with the high porosity and conductivity of a carbon support to achieve a catalyst that is selective for the HOR and stabilized against Pt oxidation. Based on this concept, a third study will investigate the SMSI effect on the electrochemical surface oxide formation and the HOR activity of Ru/TiO<sub>x</sub>/C.

In the final section of this thesis (Section 3.3), the hypothesized advantage of employing the HOR-selective Pt/TiO<sub>x</sub>/C catalyst on the anode side of a PEMFC for the mitigation of SUSD-induced degradation is investigated in a first study. The final work within this thesis deals with voltage cycling based ASTs and the correlation between cathode *r<sub>f</sub>* degradation and the development of the individual voltage loss contributions that affect the H<sub>2</sub>/air performance.

## 2. Experimental Methods

This chapter aims to elaborate on the reasoning behind choosing the experimental procedures presented in the individual publications in Chapter 3 and to serve as a guide for the efficient planning, execution, and evaluation of fuel cell experiments. For an introduction to the techniques used in the group of Technical Electrochemistry at the Technical University of Munich in the field of fuel cells, the reader is referred to the PhD theses of G. S. Harzer,<sup>124</sup> and J. N. Schwämmlein,<sup>125</sup> while this thesis will focus on optimized protocols and more recently resolved issues.

### 2.1. Synthesis of Novel Catalyst Materials

This section focuses on the synthesis of novel catalyst materials that utilize the unique properties of a SMSI, specifically Pt/TiO<sub>x</sub>/C ( $x \leq 2$ , whereby TiO<sub>x</sub> might be partially hydrated)<sup>118</sup> and Ru/TiO<sub>x</sub>/C. Thus, a generalized synthesis route for PGM/TiO<sub>x</sub>/C catalysts is summarized here, with a special emphasis on aspects that require special attention to ensure reproducible synthesis results but could not be discussed in detail in the respective publications. For details on the synthesis of Pt/TiO<sub>x</sub>/C and Ru/TiO<sub>x</sub>/C (e.g., reactant quantities/concentrations and temperature profiles), the reader is referred to the respective publications in Chapter 3.<sup>118,120,126</sup>

First, the titanium oxide nanoparticles are synthesized by the dropwise addition of a solution of titanium(IV)isopropoxide ( $\geq 97\%$ , Sigma Aldrich Corp.) in ethanol (EtOH, 99.8%, absolute, Sigma Aldrich Corp.) to an equal volume of high purity water (H<sub>2</sub>O, 15 M $\Omega$ ·cm, E-POD, Merck Millipore KGaA) held at 80 °C over the course of  $\approx 30$  min. Here, it is essential that the titanium(IV)isopropoxide is stored in a glove box, the ethanol is dry, and that the solution is freshly prepared on the day of the experiment to avoid the premature formation of TiO<sub>x</sub> nanocrystals that might otherwise alter the crystallite growth behavior during the synthesis. After stirring for 60 min, the volume is doubled by ethylene glycol (EG, 99.8%, anhydrous, Sigma Aldrich). Then, H<sub>2</sub>O and EtOH are slowly evaporated using a rotary evaporator (Hei-VAP Value, Hei-

dolph Instruments GmbH & CO. KG.) at 70 °C, whereby superheating (i.e., heating the solution past its boiling point, leading to a meta-stable state that might result in a sudden eruption of solvent into the rotary evaporator) must carefully be avoided and the collecting container must be emptied multiple times. After applying full vacuum for  $\approx 30$  min, a titania dispersion is obtained in the remaining EG that cannot be evaporated at 70 °C in a rotary evaporator even over night.

Meanwhile, the PGM nanoparticles are synthesized from the respective chloride salts ( $\text{RuO}_3$  or  $\text{K}_2\text{PtCl}_4$ ) by the polyol method. To speed up the dissolution of the precursor salts, grinding them to a fine powder with mortar and pestle is recommended. However, it is essential that a separate precursor mortar is used to avoid any contamination by metal nanoparticles that can lead to heterogeneous nucleation and thereby prevent the formation of a homogeneous particle size distribution.<sup>127</sup> Similarly, the glass vials used for the synthesis should be cleaned in a KOH bath and subsequently with acid to remove residual nanoparticles from previous syntheses. During the synthesis, the particle size is controlled via the pH for Pt nanoparticles and by the addition of polyvinylpyrrolidone (PVP, average  $M_w \approx 55000$ , Sigma Aldrich) for Ru nanoparticles. For adjusting the pH, fresh 1M solutions of NaOH (99.99% [metal basis], Sigma Aldrich Corp.) and  $\text{H}_2\text{SO}_4$  (95%, VWR) in EG should be used to minimize the addition of  $\text{H}_2\text{O}$ . It was observed that an old NaOH solution in EG can kick-start the reduction of the PGM precursors already at room temperature (visible by severe darkening of the solution that indicates nanoparticle formation),<sup>128</sup> which results in large primary particles and agglomerates that cannot be used for the catalysts and that are often visible by eye at the bottom of the flask. In this case, the synthesis of the PGM nanoparticles should be repeated with a fresh batch rather than continuing with the synthesis. Similarly, a glass pipette must be used to deaerate the solution with argon to avoid premature PGM precursor reduction by electrochemical displacement with a metallic syringe.

Once both solutions have cooled down to room temperature, the PGM nanoparticle suspension is added to the titania dispersion and stirred for 24 h at room temperature, whereby in the case of Pt, the pH must be adjusted to  $\leq 5$  to ensure opposite surface charges of Pt and  $\text{TiO}_x$  and consequently a successful deposition of the Pt particles on the titania support. The easiest method to check the pH is the centrifugation of a small fraction ( $\approx 1$  mL) of the dispersion, whereby a homogeneously colored deposit

and a clear solution should be obtained after the mixture has been stirred for at least 30 min. In parallel, the Vulcan carbon support is dispersed in EG by ultrasonication and subsequent stirring for 24 h to ensure a homogeneous dispersion.

Then, the solution containing PGM/TiO<sub>x</sub> is added to the Vulcan dispersion and stirred for another 48 h before the volume of the solution is doubled in volume with acetone ( $\geq 98\%$ , Sigma Aldrich Corp.), stirred for another 12 h, and centrifuged at 11000 rpm at 10 °C in an ultra-centrifuge (5810 R, Eppendorf) to separate the PGM/TiO<sub>x</sub>/C catalyst and the solvent. Here, acetone reduces the polarity of the solvent, which results in a reduced stability of the strongly surface charged nanoparticles in the dispersion and facilitates an easy separation. Subsequently, the catalyst is washed at least three times with a 50:50 mixture of acetone and water to remove EG, PVP, residual ions from the precursor salts, and the side products of the polyol process.<sup>129–131</sup> Finally, the catalyst is dried at 70 °C in air. It should be noted that when TiO<sub>x</sub> containing samples were washed with isopropanol, the solution immediately turned yellow indicating the formation of a soluble titanium complex and therefore a dissolution of the catalyst. This was exclusively observed for catalysts that had not yet been dried, but to ensure the integrity of the catalyst, any propanol should be avoided as a solvent before the sample has been heat-treated in reductive atmosphere (5% H<sub>2</sub>/Ar) to form the SMSI (see fig. 2.1).

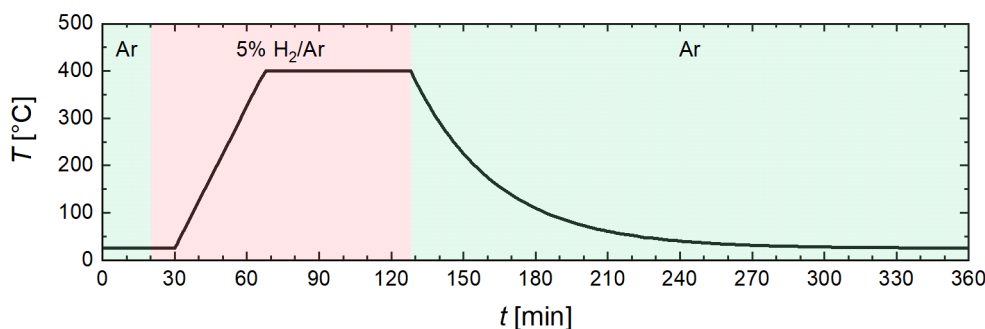


**Figure 2.1.** Temperature profile for the reductive heat-treatment of PGM/TiO<sub>2</sub>/C catalysts. First, the tube furnace is flushed with Ar (1 L min<sup>-1</sup>), followed by a temperature ramp of 10 K min<sup>-1</sup> and a 60 min hold at 400 °C in 5% H<sub>2</sub>/Ar (0.5 – 1 L min<sup>-1</sup>, depending on the sample size), and finally, the furnace is allowed to cool down in Ar atmosphere (1 L min<sup>-1</sup>).

For the heat-treatment, the tube furnace is first flushed with Ar for 20 min to remove oxygen from the system, and 10 min before starting the heating process, the gas is switched to 5% H<sub>2</sub>/Ar. The heating is conducted with a ramp of 10 K min<sup>-1</sup> and a 60 min hold at the final temperature of 400 °C. Finally, the heating is turned off and

the furnace is passively cooled down to room temperature in Ar atmosphere.

Before electrode fabrication for MEA measurements, the catalyst must further be ball milled to break down large agglomerates ( $\approx 5 - 20 \mu\text{m}$ ) that would otherwise pierce the membrane (for details see Section 3.3.1).

## 2.2. Low-Roughness Factor MEA Measurements

Typically, a single cell measurement protocol is developed and optimized for the characterization of state-of-the-art MEAs at beginning-of-test. As a result, the standard evaluation of the measured data works well for electrodes with a high  $rf$ , but might be unreliable when investigating highly degraded electrodes or electrode compositions that differ significantly from the MEAs, for which the protocol had been developed. In the following, measurements that were found to be severely affected by low  $rf$  values will be discussed and, where possible, adaptations of established protocols that deal with these difficulties will be proposed.

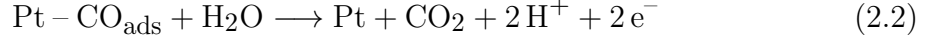
### 2.2.1. CO-Stripping Measurements

At low  $rf$  values, the  $rf$  or  $ECSA$  determination by  $H_{\text{upd}}$  is not sufficiently accurate, as it is heavily affected by  $H_2$ -crossover and the Nernst potential shifted onset of the HER. Thus, the strong affinity of CO to PGMs is often utilized in CO-stripping measurements that correlate the oxidation current of an adsorbed monolayer of CO to the PGM surface area.

#### General Procedure

In general, CO (10% CO/N<sub>2</sub>) is introduced into the single-cell PEMFC to be adsorbed on the catalyst surface at a low applied potential, e.g.,  $100 \text{ mV}_{\text{RHE}}$  (see eq. 2.1). Then, the remaining CO is removed from the system by an extensive N<sub>2</sub> purge ( $\approx 1 - 2 \text{ h}$ ), while the low potential is maintained to avoid premature CO oxidation. Once the gas phase is completely CO-free, a cyclic voltammogram (CV) is recorded from the

holding potential in anodic direction to oxidize the adsorbed CO according to eq. 2.2.



The CO oxidation results in an anodic CO-stripping peak during the first anodic scan (see red lines in fig. 2.2 a). To distinguish the CO oxidation currents from other anodic currents that occur in the same potential region, e.g., Pt oxidation and capacitive currents, a second CV scan is recorded (black line in fig. 2.2 a) and used as the baseline for the integration of the peak (gray area in fig. 2.2). For the comparison between measurements, it is often easier to discuss the baseline corrected CO-stripping peaks, i.e., the mathematical difference between the first and the second anodic scan, as shown in fig. 2.2 b. From the integrated area ( $\int i_{\text{geo}}(\text{E})d\text{E}$ , gray area), the  $rf$  can be calculated according to eq. 2.3, whereby  $\nu$  is the scan rate (in  $\text{V s}^{-1}$ ) and  $C_{\text{spec}}$  is the surface area specific charge of  $420 \mu\text{C cm}_{\text{Pt}}^{-2}$  for the oxidation of CO (two-electron transfer and linear adsorption of CO).<sup>132</sup>

$$rf = \frac{\int i_{\text{geo}}(\text{E})d\text{E}}{\nu \cdot C_{\text{spec}}} \quad (2.3)$$

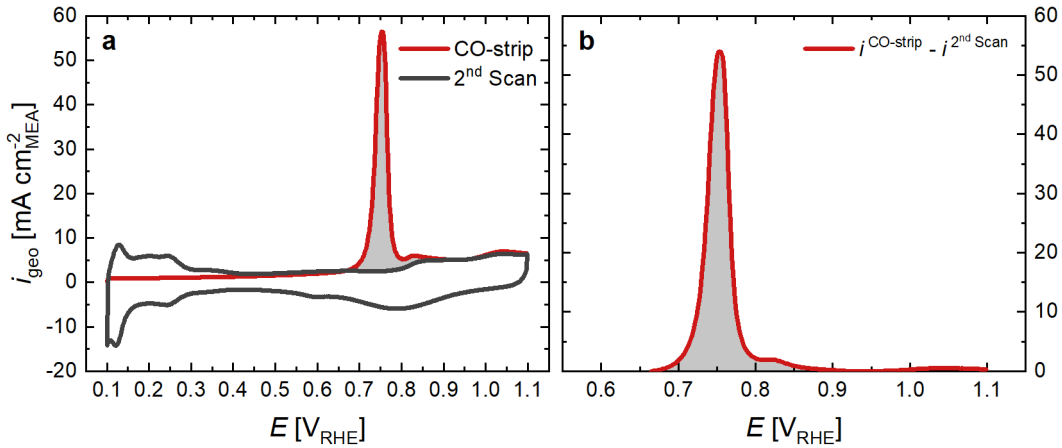


**Figure 2.2.** CO-stripping measurement for a  $0.1 \text{ mg}_{\text{Pt}} \text{ cm}_{\text{MEA}}^{-2}$  MEA with an  $rf$  of  $78 \text{ cm}_{\text{Pt}}^2 \text{ cm}_{\text{MEA}}^{-2}$ : a) CO-stripping and subsequent CV recorded at  $100 \text{ mV s}^{-1}$ ; b) baseline (second scan) corrected CO-stripping peak; the measurements were performed at  $40 \text{ }^\circ\text{C}$  and  $95\% \text{ RH}$ .

## N<sub>2</sub> Gas Purity

Before going into detail on CO-stripping measurements for low- $rf$  electrodes, the effect of the N<sub>2</sub> purge and the gas purity has to be discussed first. The test stations operate with two kinds of N<sub>2</sub>: i) N<sub>2</sub> (main) from the house line that comes from the evaporation of liquid N<sub>2</sub> from a central tank, and ii) N<sub>2</sub> (5.0, purity  $\geq 99.999\%$ ) that comes from gas bottles in the laboratory. The flow diagram of the relevant connections, valves, and mass flow controllers (MFCs) is depicted in fig. 2.3.

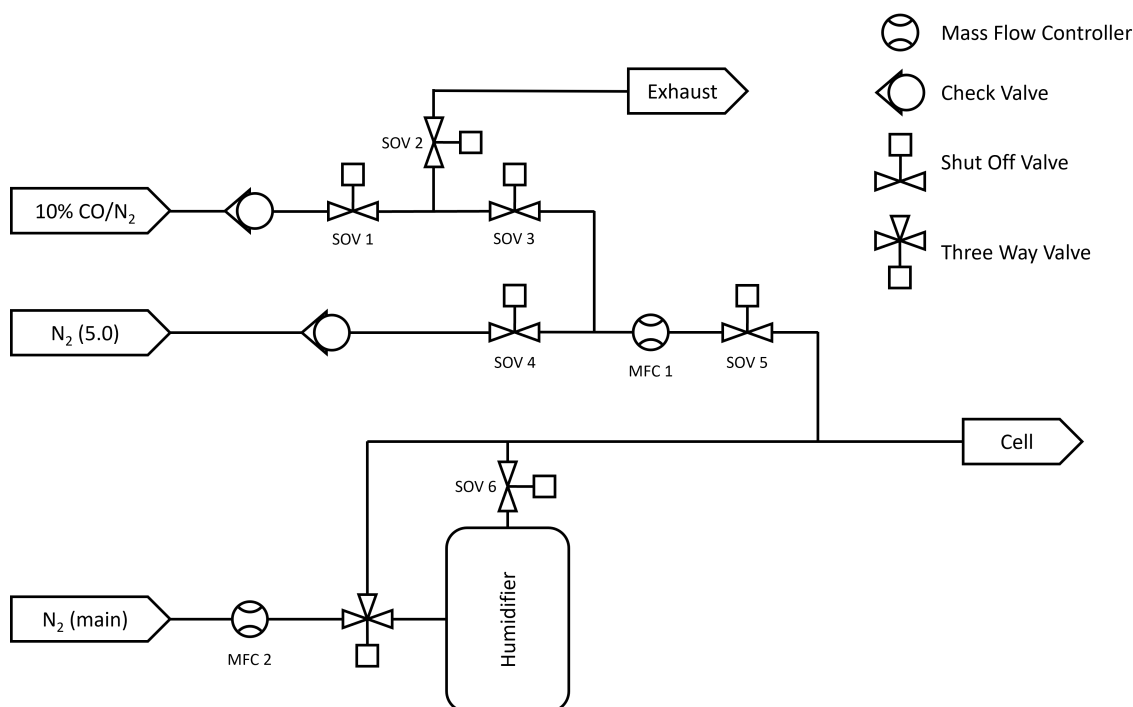


**Figure 2.3.** Simplified flow diagram of the relevant connections, valves and mass flow controllers for CO measurements. Here, N<sub>2</sub> (main) refers to N<sub>2</sub> from the house line that is obtained from a liquid N<sub>2</sub> tank, whereas N<sub>2</sub> (5.0) is obtained from gas bottles ( $\geq 99.999\%$  gas purity).

To minimize gas expenses, house line N<sub>2</sub> (main) is used almost exclusively, whereas N<sub>2</sub> (5.0) is only used for purging the CO lines and, in some instances, for cathode CVs. During the CO-saturation phase of CO experiments, CO is introduced into the system by opening the shut off valves (SOVs) 1, 3 & 5 with a flow of up to 100 nccm controlled by MFC 1. During the subsequent N<sub>2</sub> purge, SOVs 1 & 3 are closed and CO is purged from the system by opening SOVs 4 & 5. In order to remove residual CO from the dead-volume between SOV 3 and MFC 1, the line can be purged with N<sub>2</sub> (5.0) in the opposite direction by closing SOV 5 and opening SOVs 2 & 3, whereby the gas is purged directly to the exhaust. For  $\approx 30$  min, the purging procedure con-

sists of changing between this back-purge and flushing the cell with N<sub>2</sub> (5.0) every 90 s. Then, the cell is flushed with N<sub>2</sub> (main) for another  $\approx 30$  min, whereby the *RH* can be adjusted by going through the humidifier. Finally, the pressure is increased to 50 kPa<sub>g</sub> to minimize oxygen intrusion from any imperfections in the cell connection sealing and subsequently, the flow rate is reduced to 1 nccm cm<sup>-2</sup><sub>MEA</sub> and the CO-stripping CVs are recorded.

To check whether this purging procedure is effective, the gas lines were tested for residual CO after a CO-stripping experiment. Fig. 2.4 a shows the recorded CVs using the usual CO-stripping procedure, whereas fig. 2.4 c used the same procedure but without introducing CO, i.e., SOV 1 was never opened but the usual purging procedure including the potential hold was applied. While the CO-stripping peak is clearly much smaller, the fact that the peak exists at all indicates that some CO was introduced during the N<sub>2</sub> purge. Since the most likely origin of this CO is from residual CO in the lines going through MFC 1, a 12 h long purge of these lines was conducted that included switching every 30 min between the back-purge to the exhaust and flushing N<sub>2</sub> (5.0) into the cell. However, when the CO<sub>free</sub>-stripping experiment was repeated after this 12 h purging procedure, the CO-oxidation peak still remained (see fig. 2.4 e).

The origin of the adsorbed CO must therefore be the N<sub>2</sub> gases themselves, whereby the purity of the N<sub>2</sub> (main) gas is less controlled. The above described experiment was therefore repeated with N<sub>2</sub> (5.0) connected to the "N<sub>2</sub> (main)"-line in fig. 2.3. While the CO-strip itself is unaffected by this change (see fig. 2.4 b), the CO-oxidation peak is still present without an additional purge (see fig. 2.4 d), but disappears completely after the 12 h purge (see fig. 2.4 f). This indicates that the origin of adsorbed CO is indeed the combination of residual CO in the N<sub>2</sub> (5.0) lines and a CO impurity in the house line N<sub>2</sub> (main). The most likely explanation for the impurity are the similar condensation temperatures of CO and N<sub>2</sub> that might result in up to 0.3 ppm of CO in the liquid N<sub>2</sub> fraction after air liquefaction (based on the average CO level of 0.4 mg m<sup>-3</sup> in Munich in 2019).<sup>133</sup>

It should be noted that the smaller CO-oxidation peak in fig. 2.4 c compared to fig. 2.4 d is the result of a longer back-purge procedure of  $\approx 60$  min that leads to less residual CO in the N<sub>2</sub> (5.0) lines. However, as some CO will be introduced during normal FC operation with N<sub>2</sub> (main) as the main N<sub>2</sub> gas during the purge in any case and no

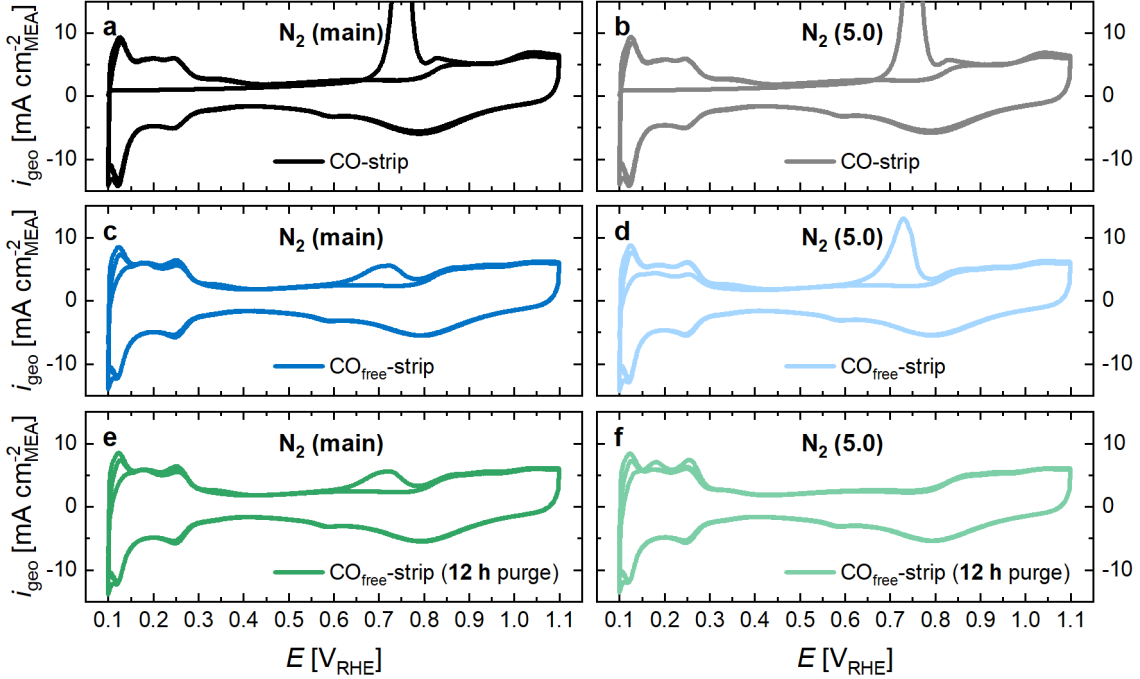


**Figure 2.4.** Investigation of the gas purity by comparing measurements with regular  $\text{N}_2$  (main) from the house line connected to the test station (left) and with  $\text{N}_2$  (5.0) connected to both  $\text{N}_2$  inlets (right); a & b) proper CO-stripping measurements including CO introduction into the system; c & d)  $\text{CO}_{\text{free}}$ -stripping experiments consisting of the full purging procedure (including potential hold) without the preceding introduction of CO; e & f)  $\text{CO}_{\text{free}}$ -stripping procedure after purging all lines for 12 h with  $\text{N}_2$  (5.0). The CO-stripping peak in the  $\text{CO}_{\text{free}}$  measurements is indicative of the remaining CO in the  $\text{N}_2$  gas lines; the measurements were performed at  $40^\circ\text{C}$  and 95%  $RH$  on cells with an active area of  $5\text{ cm}^2$ .

CO-oxidation peaks are observed in subsequent scans, the shorter purging procedure of only 30 min can be considered to be the best trade-off between experiment duration and gas purity for CO-stripping measurements. Still, when conducting experiments that are highly sensitive to CO impurities, e.g.,  $\text{H}_2$ -pump or CO-displacement measurements, full removal of any residual CO should be ensured by adding an additional back-purging procedure of  $\approx 2 - 3$  h.

While the CO impurity in the  $\text{N}_2$  (main) gas supply might affect all measurements that employ  $\text{N}_2$ , the relevance of this issue is relatively small in most cases. The amount of CO is too little to affect the measurements, as long as CO does not accumulate on the catalyst over a longer period of time. As described above, this happens only at low potentials, e.g., when there are traces of  $\text{H}_2$  in the gas mixture after having recorded anode CVs or after operation in  $\text{H}_2/\text{N}_2$  configuration for a long time (see fig. 2.5 a). In these cases, it might be required to polarize the cathode to  $\approx 0.8\text{ V}_{\text{RHE}}$  for a few

seconds to ensure the oxidation of accumulated CO prior to any sensitive measurement. However, traces of O<sub>2</sub> from O<sub>2</sub>/air operation, that remain in the cathode system even after standard purging procedures, prevent an accumulation of CO in most cases and make this a non-issue (see fig. 2.5 b).

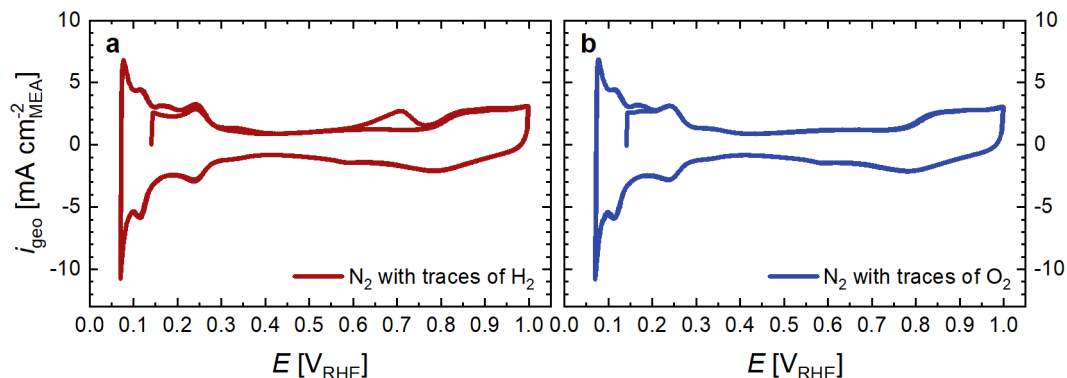


**Figure 2.5.** All three cycles of cathode CVs that were recorded after N<sub>2</sub> purges following a) anode CVs (cathode filled with 5% H<sub>2</sub>/Ar), or b) polarization curves (cathode filled with air), respectively. A CO-oxidation peak in the first scan indicates CO accumulation on the Pt surface. The CVs were recorded at 50 mV s<sup>-1</sup>, 5 nccm N<sub>2</sub> (main), 40 °C, 95% RH, and ambient pressure with 5% H<sub>2</sub>/Ar on the anode (100 nccm). The active area of the cell is 5 cm<sup>2</sup>.

### CO-Crossover

Most studies that employ CO-stripping in PEMFC single-cells focus exclusively on the cathode electrode due to the insignificant contribution of the anode's HOR kinetics to the overall voltage losses. However, during normal operation, the anode potential remains close to 0 V<sub>RHE</sub> at all times. This means that any CO reaching the anode will accumulate on the Pt surface and might result in unexpected HOR overpotentials due to CO poisoning. While this is most likely not an issue in an actual PEMFC stack as long as the H<sub>2</sub> supply is sufficiently CO-free, it might be an artificial problem induced by the measurement procedure in single-cell tests. Here, CO can be introduced to the anode by two means: i) CO-crossover during CO measurements on the cathode side (e.g., CO-stripping or CO-displacement measurements, see fig. 2.6 a), and ii) N<sub>2</sub> purges of the anode compartment (see fig. 2.6 b). It should be noted that CVs on the anode side require a preceding N<sub>2</sub> purge to remove H<sub>2</sub> from the anode compartment and a small CO-stripping peak will therefore be seen in any anode CVs, except for freshly connected cells (here the anode is filled with air and does not adsorb CO, see fig. 2.5 b).

It is therefore recommended to minimize the amount of N<sub>2</sub> purges of the anode com-

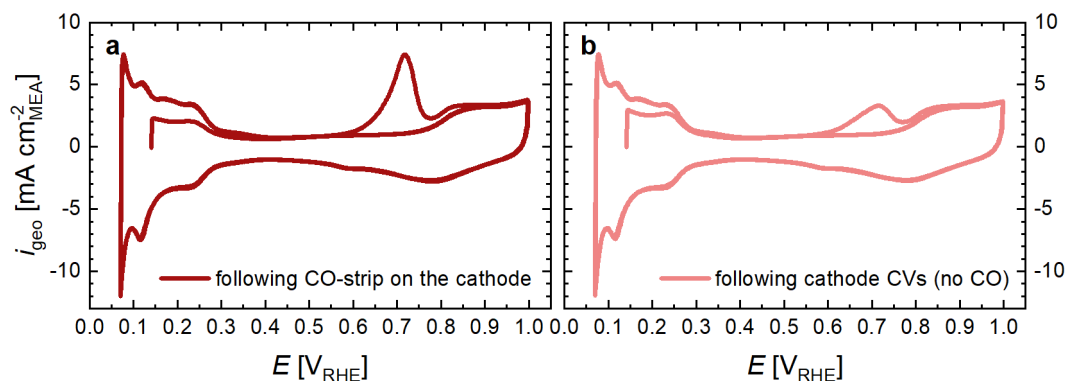


**Figure 2.6.** All three cycles of anode CVs that were recorded after a) a CO-strip on the cathode, or b) cathode CVs without CO, respectively. A CO-oxidation peak in the first scan indicates CO accumulation on the Pt surface. The anode was purged with  $N_2$  (main) for  $\approx 30$  min to remove  $H_2$  from the cell before recording the CVs at  $50 \text{ mV s}^{-1}$ ,  $5 \text{ nccm } N_2$  (main),  $40^\circ \text{C}$ ,  $95\% RH$ , and ambient pressure with  $5\% H_2/Ar$  on the cathode ( $100 \text{ nccm}$ ). The active area of the cell is  $5 \text{ cm}^2$ .

partment throughout a measurement procedure to avoid CO accumulation. Furthermore, it was found in the early stages of optimizing the testing protocol for the voltage cycling study (see Section 3.3.2) that the CO-stripping peak on the anode increased after performing multiple CO-strips on the cathode side. This indicates that CO is diffusing from the cathode through the membrane and accumulates on the anode side. It is therefore required to polarize the anode to  $\approx 0.8 V_{RHE}$  for a few seconds after CO measurements on the cathode side. Since this requires removing  $H_2$  from the anode compartment by a  $N_2$  purge, one can combine this with a CV measurement to assess the state-of-health of the anode, in which case, CO is automatically stripped from the anode catalyst's Pt surface.

### Severely Degraded Electrodes

While the conventional method of subtracting the subsequent scan as the baseline for the CO-stripping peak works well for pristine MEAs (see fig. 2.2 b), the CO-stripping peak does not return to the same baseline for severely aged MEAs (see fig. 2.7 a). A similar behavior has been observed for CO-strips at low  $RH$  ( $< 50\%$ ) on catalysts with a high fraction of Pt nanoparticles within the pores of a highly porous carbon support. Shinozaki *et al.* explained this by an insufficient availability of  $H_2O$  for the oxidation of CO according to eq. 2.2.<sup>89</sup> However, this cannot be the reason in the here presented case as the CO-strip was performed at  $95\% RH$  and the low  $rf$  of the degraded electrode means that the amount of water required for the oxidation is extremely small. Thus, there must be a different explanation for the discrepancy between the first and

the second scan. Interestingly, a similar offset of  $\approx 0.03 \text{ mA cm}_{\text{MEA}}^{-2}$  is observed between the first and the second scan during the  $\text{CO}_{\text{free}}$ -strip of a pristine MEA with the same catalyst and loading even when no CO is present in the system (see black dotted line in fig. 2.7, data taken from fig. 2.4 f). This indicates that the offset between the first and the second scan is an oxidation current that is not related to CO but rather is the result of the potential hold at  $0.1 \text{ V}_{\text{RHE}}$  for 1 h that seems to be able to reduce the catalyst surface further than what happens during the cathodic scan to  $0.07 \text{ V}_{\text{RHE}}$  at  $100 \text{ mV s}^{-1}$ . This is confirmed by a similar discrepancy between the first and the second scan that is observed in all CVs of the anode (that usually sits at  $0 \text{ V}_{\text{RHE}}$ ). Furthermore, the oxidation must take place on the carbon surface as the offset is almost identical between a pristine MEA with a cathode  $rf$  of  $78 \text{ cm}_{\text{Pt}}^2 \text{ cm}_{\text{MEA}}^{-2}$  and a severely aged electrode with an  $rf$  of  $\approx 5 \text{ cm}_{\text{Pt}}^2 \text{ cm}_{\text{MEA}}^{-2}$  (see fig. 2.7 b). Therefore, the conventional integration of the full area between the first and the second scan (gray and blue areas in fig. 2.7 combined) would lead to an overestimation of the electrode's  $rf$ .

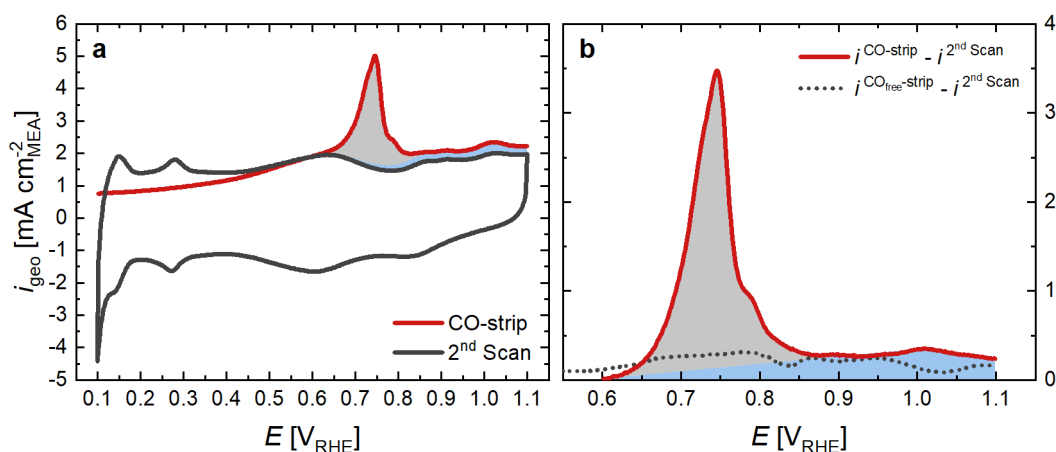


**Figure 2.7.** CO-stripping measurement of a severely degraded cathode with an  $rf$  of  $\approx 5 \text{ cm}_{\text{Pt}}^2 \text{ cm}_{\text{MEA}}^{-2}$  ( $0.1 \text{ mg}_{\text{Pt}} \text{ cm}_{\text{MEA}}^{-2}$ , after 50,000 square wave cycles between  $0.6 - 0.95 \text{ V}$  with a  $1 \text{ s}$  hold under  $\text{H}_2/\text{N}_2$  at  $80^\circ \text{ C}$  and  $95\% \text{ RH}$ , see Section 3.3.2): a) CO-strip and subsequent CV recorded at  $100 \text{ mV s}^{-1}$ ; b) CO-stripping peak corrected for the second scan as the baseline (red line) and difference between first and second scan after a  $\text{CO}_{\text{free}}$ -strip of a pristine MEA (black dotted line, data taken from fig. 2.4 f); the measurements were performed at  $40^\circ \text{ C}$  and  $95\% \text{ RH}$ . The gray area is integrated from the difference between the first and second scan in the range of  $0.6 - 1.0 \text{ V}_{\text{RHE}}$  with a linear baseline; the blue area is the difference between the gray area and a full integration of the red curve. The active area of the cell is  $5 \text{ cm}^2$ .

The most accurate way to determine the  $rf$  by CO-stripping would be to record the CO-strip and subsequently perform the same procedure without introducing CO and use the first scan of the  $\text{CO}_{\text{free}}$ -strip for the baseline correction. However, this approach

would more than double the measurement time as it is essential that all traces of CO are removed from the N<sub>2</sub> (5.0) line before the measurement is conducted. Additionally, it would not be possible to run the CO-strips at a controlled *RH*, as the N<sub>2</sub> (main) supply contains a CO contamination and must therefore be avoided. Instead, I propose the following approach to minimize the error of the *rf* determination without having to conduct a second measurement: first, one uses the second scan during the CO-stripping CVs as the baseline to obtain the baseline-corrected CO-stripping peak (red line in fig. 2.7 b); then, the baseline-corrected CO-stripping peak is integrated using a linear baseline from 0.6 – 1.0 V<sub>RHE</sub> (gray area in fig. 2.7 a & b, the integration boundaries might have to be adapted for other catalysts/MEAs). Although this approach is certainly not perfect, it avoids integrating the blue area in fig. 2.7 which, for the most part, is a measurement artifact rather than a CO oxidation feature.

### Ultra-Low-Loaded Electrodes

For ultra-low-loaded electrodes ( $\approx 1 - 2 \mu\text{g}_{\text{Pt}} \text{cm}_{\text{MEA}}^{-2}$ ), additional effects have to be considered when evaluating the CO-strip area (see fig. 2.8). Here, the subsequent CV is shifted by  $\approx 0.18 \text{ mA cm}_{\text{MEA}}^{-2}$  due to the H<sub>2</sub>-crossover current (note that an  $i_{\text{H}_2-x}$  of  $\approx 5 \text{ mA cm}_{\text{MEA}}^{-2}$  would be expected for pure H<sub>2</sub> on the anode at 80 °C and that  $\approx 0.18 \text{ mA cm}_{\text{MEA}}^{-2}$  is therefore a reasonable value for CO-stripping measurements at 40 °C with 5% H<sub>2</sub>/Ar on the anode).

However, during the CO-stripping scan, the CO blocks the active Pt surface and prevents the oxidation of crossover H<sub>2</sub>.<sup>134</sup> Thus, the conventional method of subtracting the subsequent CV as the baseline would lead to an underestimation of the ECSA due to HOR current being subtracted from the CO oxidation current (overlapping gray area in fig. 2.8 a and black dotted line in fig. 2.8 b). At the same time, the aforementioned oxidation of the carbon support would lead to an overestimation of the CO-stripping integral at potentials  $> 0.9 \text{ V}_{\text{RHE}}$  (see black dotted line in fig. 2.8 b).

While in this case, the underestimation due to H<sub>2</sub>-crossover and the overestimation due to a semi-irreversible oxidation current at high potentials would roughly balance each other out (compare red solid line and black dotted line in fig. 2.8 b), this might not always be the case and should therefore not be used as the standard procedure for the evaluation of CO-strips on ultra-low-loaded electrodes. Instead, a linear baseline should be used, whereby the potential window needs to be adapted for each catalyst.

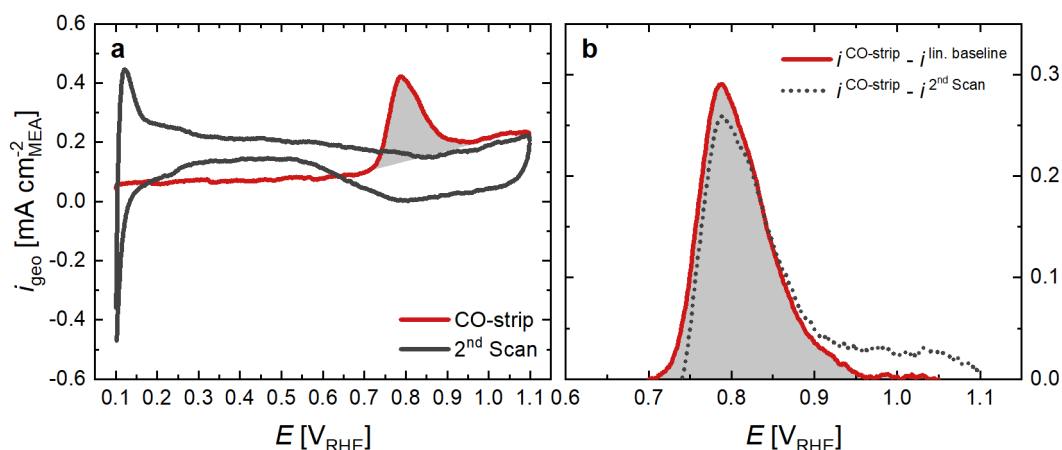


**Figure 2.8.** CO-stripping measurement of an ultra-low-loaded ( $1.4 \mu\text{gPt cm}^{-2}_{\text{MEA}}$ ) electrode (see Section 3.1.2) with an active area of  $5 \text{ cm}^2$ : a) CO-strip and subsequent CV recorded at  $50 \text{ mV s}^{-1}$  with the CO-stripping current being integrated using a linear baseline (gray area); b) comparison of the CO-stripping peak using a linear baseline ( $0.7 - 1.0 \text{ V}_{\text{RHE}}$ ) for the correction (red line) and conventionally corrected for the second scan as the baseline (black dotted line); the measurements were performed at  $40^\circ \text{ C}$  and  $95\% \text{ RH}$ . Data adapted from Stühmeier and Pietsch *et al.* (see Section 3.1.2).<sup>25</sup>

## Summary

While CO-stripping is a useful technique for the determination of the electrode *rf*, one has to keep in mind that there is no one perfect way to evaluate the CO-stripping integral. Even for conventional Pt/C catalysts that were discussed in the preceding section, the CO-stripping might be affected by one or some combination of the following factors: i) an insufficient availability of  $\text{H}_2\text{O}$  for the oxidation of CO;<sup>89</sup> ii) the purity of the used gases; iii) the semi-irreversible oxidation of the carbon support; and iv) the  $\text{H}_2$ -crossover currents. It is therefore essential to consider these effects when choosing the CO-stripping evaluation method. For CO-strips on Pt-alloy catalysts, additional factors (e.g., transition metal dissolution or adsorption) might affect the measurements and the evaluation might therefore be even more complicated. Finally, CO was found to accumulate on the anode after CO measurements were performed or during a  $\text{N}_2$  purge of the anode. Thus, the anode should be polarized to  $> 0.8 \text{ V}_{\text{RHE}}$  after CO measurements were performed on the cathode and the number of anode purges should be minimized during MEA measurements.

### 2.2.2. $\text{O}_2$ -Limiting Current Measurements

$\text{O}_2$ -limiting current measurements according to Baker *et al.*<sup>87</sup> are by now a well established method to determine the  $\text{O}_2$  mass transport resistances of a PEMFC single-cell.

Hereby, O<sub>2</sub> is diluted in N<sub>2</sub> with oxygen concentrations ( $c_{\text{O}_2}$ , dry fraction) in the range 0.5–21% to achieve a diffusion limitation. The total transport resistance ( $R_{\text{O}_2}^{\text{total}}$ ) can be calculated according to eq. 2.4 from the limiting current ( $i_{\text{lim}}$ ) by assuming a full  $4e^-$ -reduction of O<sub>2</sub> at low cell potentials (0.05–0.4 V). Ideally, in the absence of GDL flooding,  $i_{\text{lim}}$  should be directly proportional to  $c_{\text{O}_2}$  and independent of the potential. Furthermore, by varying the pressure,  $R_{\text{O}_2}^{\text{total}}$  can be separated into a pressure independent ( $R_{\text{O}_2}^{\text{PI}}$ ) and a pressure dependent ( $R_{\text{O}_2}^{\text{PD}}$ ) contribution, whereby the latter is mostly associated with the molecular diffusion in the GDL and catalyst layer (see eq. 2.5).<sup>87</sup> On the other hand,  $R_{\text{O}_2}^{\text{PI}}$  consists of various contributions, namely Knudsen diffusion in the small pores of the catalyst layer and the MPL ( $R_{\text{O}_2}^{\text{PI}}|_{rf \rightarrow \infty}$ ) as well as the so-called local O<sub>2</sub>-transport resistance ( $R_{\text{O}_2}^{\text{local}}$ ) that is a function of the  $rf$  and that is often associated with O<sub>2</sub>-diffusion in the ionomer and liquid water phase; the latter can therefore be determined by changing the electrode's  $rf$  (eq. 2.6).<sup>31, 34–36, 52, 53</sup>

$$R_{\text{O}_2}^{\text{total}} = \frac{4 \cdot F \cdot c_{\text{O}_2}}{i_{\text{lim}}} \quad (2.4)$$

$$R_{\text{O}_2}^{\text{total}} = R_{\text{O}_2}^{\text{PD}} + R_{\text{O}_2}^{\text{PI}} \quad (2.5)$$

$$R_{\text{O}_2}^{\text{PI}} = R_{\text{O}_2}^{\text{PI}}|_{rf \rightarrow \infty} + \frac{R_{\text{O}_2}^{\text{local}}}{rf} \quad (2.6)$$

The limiting current measurements are based on the assumption that, firstly, the measured current is exclusively the result of the full  $4e^-$ -reduction of all O<sub>2</sub> molecules reaching the catalyst surface and secondly, the resulting limiting current is potential independent. However, for high O<sub>2</sub> concentrations and high pressures, this is not always the case due to significant ohmic resistance contributions at high current densities that result in a significant shift of the cathode potential and thus relevant kinetic contributions (i.e., the currents are not fully mass transport limited, see Simon *et al.*<sup>135, 136</sup>). Similarly, at low O<sub>2</sub> concentrations and low pressures, the currents at 0.05 V are higher than one would expect due to a significant HER contribution (the HER/HOR equilibrium potential is shifted to positive potentials due to the low partial pressure of H<sub>2</sub>). Based on the works of Simon *et al.*,<sup>135, 136</sup> a measurement protocol was established at the chair of Technical Electrochemistry (TUM) that was found to work well for almost all MEAs. Hereby, the limiting current is recorded for 2–24% O<sub>2</sub> (7 points in total) and pressures of 170, 270, 350, & 500 kPa<sub>abs</sub> at voltages of 0.30, 0.15, 0.1, & 0.05 V (see PhD thesis of J. N. Schwämmlein<sup>125</sup>).

However, when this protocol is applied to severely degraded cathodes with an  $rf$  of  $\approx 3 \text{ cm}^2_{\text{Pt}} \text{ cm}^{-2}_{\text{MEA}}$  (see Section 3.3.2), the limiting current data are found to scatter (compare only data points in the gray area in fig. 2.9). When the measurement is repeated with data points recorded every 50 mV, a pronounced "Z-shape" form becomes visible, where the current first increases, then decreases, and finally increases again upon going from 0.4 V to 0.05 V. Greszler *et al.*<sup>36</sup> observed similar trends for a low-loaded cathode ( $0.03 \text{ mg}_{\text{Pt}} \text{ cm}^{-2}_{\text{MEA}}$ ), which they attributed to a transition from the typical  $4e^-$ -reduction of oxygen ( $\text{H}_2\text{O}$  formation) to a  $2e^-$ -reduction ( $\text{H}_2\text{O}_2$  formation), which reduces the number of electrons per oxygen molecule and therefore the mass transport limited current density.

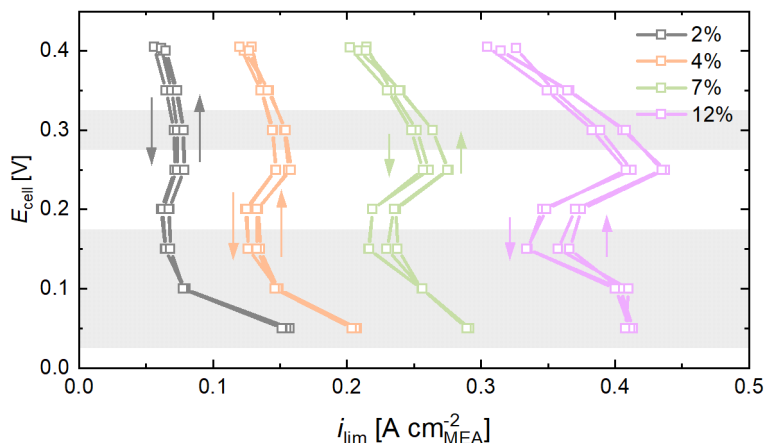


**Figure 2.9.** Limiting current measurements in the potential range between 0.4 V and 0.05 V using  $\text{O}_2$  concentrations of 2% (gray), 4% (orange), 7% (green) and 11% (magenta) in  $\text{N}_2$  (on a dry gas basis) for a cathode with an  $rf$  of  $\approx 3 \text{ cm}^2_{\text{Pt}} \text{ cm}^{-2}_{\text{MEA}}$  after 10,000 cycles of a square wave voltage cycling AST with an upper potential limit of 1.0 V and a vertex hold time of 8 s at  $80^\circ\text{C}$  in  $\text{H}_2/\text{H}_2$ . The measurements were performed at  $170 \text{ kPa}_{\text{abs}}$ ,  $80^\circ\text{C}$ , and 95%  $RH$  using 2000 nccm  $\text{H}_2$  and 5000 nccm ( $\text{O}_2$  in  $\text{N}_2$ ) on anode and cathode, respectively. For each concentration, the measurement was performed by going from 0.4 V down in potential, followed by going from 0.05 V back up (repeated twice, direction indicated by the arrows). The active area of the cell is  $5 \text{ cm}^2$ .

This is consistent with RRDE measurements showing an increasing formation of  $\text{H}_2\text{O}_2$  at low potentials with a decrease in  $ECSA$ .<sup>137</sup> Obviously, this behavior creates an ambiguity with regard to the determination of the "correct" limiting current density and thus, limiting current measurements should be performed in 50 mV steps in the full potential range (0.05–0.4 V), so that the development of the "Z-shape" can be observed and the data can be treated with the appropriate caution. Interestingly, when going from 0.05 V up to 0.4 V, an offset ( $\approx 8\%$  of the current in the downwards sequence)

towards higher current densities is observed for all conditions between 0.15 – 0.35 V (see hystereses in fig. 2.9). The origin of this offset is yet to be investigated, but it is a further indication that the  $R_{\text{O}_2}^{\text{total}}$  values obtained for electrodes with a low  $rf$  should not be considered accurate.

Based on these observations, an optimized protocol for limiting current measurements was developed. In order to ensure that deviations from the limiting current behavior related to a  $4e^-$ -ORR can be observed, the potential is recorded in 50 mV steps from 0.35 V to 0.05 V (the 0.4 V point is often still affected by kinetics and therefore unreliable). At the same time,  $\text{O}_2$  is limited to the four most reliable values (2%, 4%, 7%, and 11%) and the pressure range is reduced to 170, 270, and 400 kPa<sub>abs</sub> to minimize the required measurement time. This procedure was found to be highly reliable and capable of collecting all relevant data for a full oxygen transport resistance analysis (for details see Section 3.3.2).

### 2.2.3. H<sub>2</sub>-Pump Measurements

H<sub>2</sub>-pump measurements on ultra-low-loaded electrodes are discussed in great detail in Section 3.1.2. Thus, this section focuses only on aspects that were found to complicate the execution of the experiments or the data evaluation, but that are not reported in the experimental section of the publication.

Ideally, the OCV in H<sub>2</sub>-pump measurements should be exactly 0.0 mV, as both electrodes should experience the identical H<sub>2</sub> partial pressure, temperature, and  $RH$ . However, in practice, this is not always the case, since the cathode and anode temperatures, pressures, dew points, and flow rates are regulated mostly independently and each of these control variables have a certain error tolerance. While some of these factors are subject to random fluctuations during the measurement (e.g., the dew point and cell temperature regulation over time), other factors result (at least partially) in systematic offsets that can be accounted for. One of these factors is that the cell temperature is regulated by a single heating and cooling signal for both sides of the cell (i.e., both sides see the same heating or cooling power) but both sides have their own heating cartridge that might have slightly more or less power or a better/worse heat transfer than the other side, resulting in a constant temperature offset. Since the H<sub>2</sub>-pump measurements are extremely sensitive to these offsets, one should make sure that the heating of both sides is as even as possible. Another factor is that the anode and the

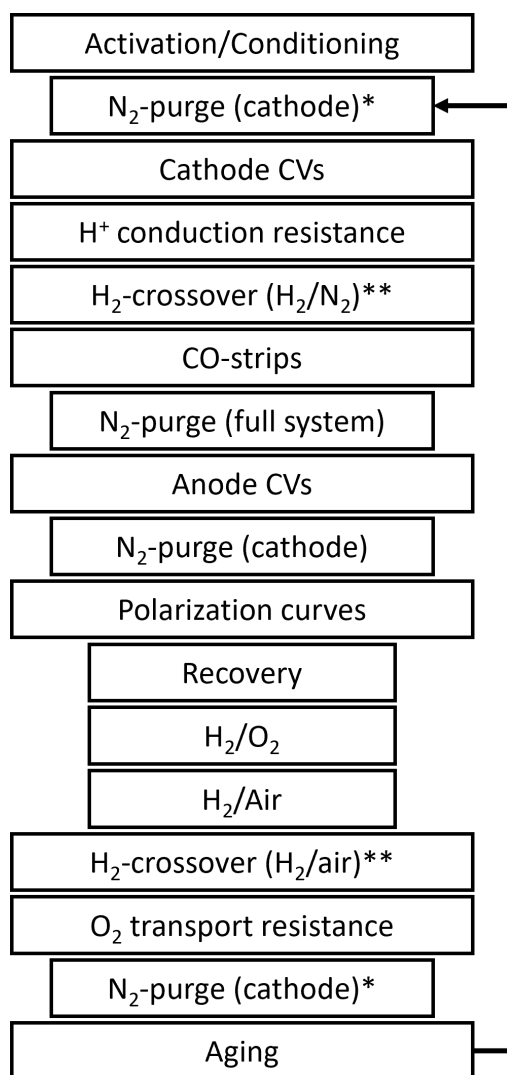
cathode have slightly different pressure drops, which might result in a Nernst-shift of the OCV. To account for this, the cell inlet pressure for each side should be adjusted to the intended cell pressure plus  $\frac{1}{2}$  of the difference between inlet and outlet pressure (in the testing script, this adjustment can be implemented by an equation at the end of the "set condition"-script once the pressure drop has stabilized at the operating conditions). Adjusting these two factors helps to reduce the OCV variations from roughly  $\pm 3$  mV to  $\pm 0.5$  mV. The galvanostatic measurements at low current densities are performed to guarantee that a sufficient amount of data points are recorded around the OCV. Finally, the remaining offset of the reversible potential can be corrected by subtracting the x-intercept (zero current) of the micropolarization fit from the measured potentials.

## 2.3. Optimized Procedure for 5 cm<sup>2</sup> MEA Characterization

Based on the findings reported in the previous section, the suggested protocol for an efficient, fast, and artifact free characterization of 5 cm<sup>2</sup> PEMFC single-cells is depicted in fig. 2.10 (for the individual procedures see Section 3.3.2).

There are some restrictions on the sequence of measurements that should be considered when planning the experimental procedure. As mentioned above, the CO-stripping characterization (or any other CO containing measurement) of the cathode results in a poisoning of the anode by CO-crossover. Therefore, all CO involving measurements should be considered as a single sequence block (even if this requires changing the humidifier and cell temperatures, which should otherwise be avoided as much as possible) and after these measurements, it is essential to perform anode CVs. Additionally, due to the presence of CO in the N<sub>2</sub> (main) line, the anode should be purged with N<sub>2</sub> exclusively before the anode CVs and all other purges of the cathode compartment should be performed with a reduced flow of H<sub>2</sub> (100 – 500 nccm) on the anode (denominated as cathode purge). Furthermore, it was found in the study by Harzer *et al.*<sup>52</sup> that it matters in which order the polarization curves are measured, and thus the polarization curves block (recovery, H<sub>2</sub>/O<sub>2</sub>, H<sub>2</sub>/air) should not be altered within a study to ensure consistent results. Note that this indicates a (small but noticeable) systematic ambiguity of the performance data related to the measurement procedure, even when all other factors are kept constant. Finally, for the determination of the

H<sub>2</sub>-crossover, two procedures are established in our group and the placement of these procedures within the measurement sequence varies due to different cathode gas compositions (N<sub>2</sub> vs. air, see Gasteiger *et al.*<sup>83</sup> and Zihrul *et al.*,<sup>138</sup> respectively).



\* For aging under H<sub>2</sub>/N<sub>2</sub> or H<sub>2</sub>/air, the cathode purge is performed before or after the aging step, respectively.

\*\* The placement of the H<sub>2</sub>-crossover measurements depends on the chosen procedure (H<sub>2</sub>/N<sub>2</sub> or H<sub>2</sub>/air by OCV-drop).

**Figure 2.10.** Optimized procedure for the characterization and full voltage loss analysis of 5 cm<sup>2</sup> PEMFC single-cells.

Obviously, the sequence of the measurements depends on the investigated system and is subject to change when new or optimized testing protocols are established or integrated. Nevertheless, in order to ensure a fast and efficient characterization, the

measurement sequence should generally be optimized with the following prioritization from high to low (and considering the above mentioned restrictions): i) minimization of gas changes that require a purge of the gas lines and the humidifier (i.e., between the categories O<sub>2</sub>-containing, inert (N<sub>2</sub> and CO-strip), and H<sub>2</sub>-containing); ii) minimization of dew point temperature changes; and iii) minimization of cell temperature changes.

Additionally, it is found that measurements conducted under fully humidified conditions (100% *RH*) in some cases result in the flooding of the cell due to the error tolerance of the anode/cathode cell and dew point temperatures. This can potentially lead to a blockage of some of the FF channels and a flooding of the catalyst layer and the GDL, thereby introducing measurement artifacts. Due to the FF design used in our group, with deep gas distribution headers at the gas inlets and outlets (see fig. 2.11), it is extremely difficult to remove condensed water once a significant amount has accumulated. Thus, it is highly recommended to perform measurements exclusively below full humidification ( $\leq 95\%$  *RH*). Exceptions to this rule are the activation/conditioning and the recovery steps that were found to be much less effective at 95% compared to 100% *RH*.



**Figure 2.11.** Picture detail of fig. 1.1 showing the cathode FF and the 5-layer MEA. The deep gas distribution headers at the gas inlet and outlet of the FF are highlighted in red.

As a final remark, in order to prove the general applicability of a chosen testing protocol, publications/studies that establish new measurement protocols are typically designed to cover a wider data space than what would strictly be required for the evaluation of the measurements. Consequently, if one of these techniques is only to be applied as part of the overall characterization of an MEA, rather than being the main focus of a study, there is often significant potential for streamlining a protocol

and reducing the required measurement time, while still maintaining all of the relevant information. Nevertheless, the relevant fraction of the initial data space might vary from system to system and it is therefore generally a good approach to use a more comprehensive protocol in the initial phase of a study. This helps to gain the necessary understanding of which data is actually required for the evaluation (e.g., the full potential range in limiting current measurements). Once the relevant data is identified, one should streamline the measurement protocol to avoid unnecessary data collection (e.g., high O<sub>2</sub> concentrations and pressures that were found to add no value to the data evaluation), especially, when performing extensive long-term measurements or many repetitions, where even 30 min of gained measurement time can add up to days.

## 3. Published Work

The perspective and journal articles comprising this thesis are thematically grouped into three categories. First, the measurement techniques that are commonly used to assess PEMFC catalyst activity and durability will be discussed (see Section 3.1), then novel catalyst concepts that employ metal oxides as support materials will be explored (see Section 3.2), and finally the degradation of the cathode catalyst layer is investigated (see Section 3.3).

### 3.1. Measurement Methods to Determine Catalyst Activity/Performance

Choosing the right measurement method and knowing its capabilities and limitations is essential for the investigation and evaluation of electrocatalysts. For proton exchange membrane based devices (PEMFC and PEMWE), the most representative method for the investigation of the electrocatalysts is based on MEAs. However, this is a time-consuming process that requires gram-quantities of catalyst as well as expensive and complex measurement equipment. Thus, convective flow-based techniques in aqueous electrolytes, such as RDEs,<sup>81,139,140</sup> the floating electrode technique (FET),<sup>26,141,142</sup> and GDEs,<sup>26,48,93,143,144</sup> are often used for the initial characterization of novel catalyst materials that are only available in milligram-quantities or to qualitatively compare the activity and durability of several catalyst candidates for MEA implementation. In the following section, the capabilities and limitations of the two most commonly used techniques, RDE and MEA, for the investigation of PGM-based electrocatalysts for PEMFC and PEMWE systems will be critically discussed. Based on this assessment, a suitable measurement protocol for the investigation of HOR/HER kinetics for PGM-based catalysts in an MEA will be established and used for the evaluation of anode catalysts throughout this thesis.

### 3.1.1. Investigation of PGM-Based Electrocatalysts by RDE vs MEA

This section presents the perspective ”Capabilities and limitations of rotating disk electrodes versus membrane electrode assemblies in the investigation of electrocatalysts” that was accepted in March 2022 and published in May 2022 in *Nature Catalysis*.<sup>28</sup> It is reprinted with permission from *Nature Catalysis* 2022. Copyright Springer Nature Limited 2022. The permanent web-link to the article is <https://doi.org/10.1038/s41929-022-00776-5>.

Cost-competitive PEMFCs and PEMWEs require highly efficient electrocatalysts for the relevant reactions, namely the HOR/HER and the ORR/OER. The activity and durability of these electrocatalysts is most commonly assessed using either RDEs or MEAs, although more recently, FETs and GDEs have been established as bridging techniques.<sup>26,48,81,92,140,142</sup> This perspective critically discusses the capabilities and limitations of the RDE technique applied to these four elementary reactions.<sup>28</sup>

Initially, the RDE and MEA setups are compared by highlighting the main differences between the techniques, namely the catalyst environment with respect to the respective electrolyte and required amounts of catalyst, the experiment duration, the dominant mass transport regime, and the electrolyte/catalyst ratio. Then, these critical differences are discussed regarding their non-reaction-specific implications for electrochemical measurements. This includes the choice of the reference electrode (RE), whereby the hydrogen electrode typically serves as the RE and the counter electrode (CE) in the two-electrode setup of an MEA, whereas a dedicated RE is used in the three-electrode setup of an RDE. Possibly the most fundamental difference between the two setups is the prevailing mass transport mode for the gaseous reactants to the active site: Although the solubility of O<sub>2</sub> and H<sub>2</sub> in the liquid electrolyte of an RDE and the ionomer phase in an MEA is similarly low ( $\approx 1 - 3 \text{ mmol L}^{-1}$ ),<sup>145</sup> the diffusion length in an RDE setup is in the range of tens of  $\mu\text{m}$ ,<sup>78</sup> whereas in an MEA, the mass transport occurs mainly in the gas phase and requires only diffusion through a nm-thin film of ionomer.<sup>24</sup> This leads to much lower accessible geometric and specific current densities in an RDE setup for the gas consuming reactions (HOR and ORR) and to artifacts by insufficient removal of gas bubbles in the case of gas evolving reactions (HER and OER). Additionally, the vastly different electrolyte/catalyst ratios between

the two setups result in different measurement sensitivities with respect to the source and effect of contaminants: While an RDE setup is highly sensitive to contaminants that can be induced by the experimental setup or by the electrolyte,<sup>81</sup> MEAs are heavily affected by contaminations coming from gas impurities (see also Section 2.2.1) and the degradation of cell and catalyst components, because ionic degradation products accumulate in the ionomer (see also Section 3.3.1).

Then, the reaction-specific limitations of the RDE setup are discussed. For the OER, it is possible to obtain activities that are comparable to MEA measurements, as long as sufficiently low loadings are employed.<sup>146,147</sup> However, the OER catalyst lifetime determined in half-cell measurements with a liquid electrolyte is  $\approx 3-4$  orders of magnitude less than that measured in a PEMWE.<sup>147-150</sup> Although there is still some debate on the topic, we believe that the formation of microscopic bubbles is one of the major reasons for the discrepancy in the stability results obtained from RDE and MEA measurements.<sup>28,148,149,151</sup>

Since the hydrogen oxidation and evolution reactions are extremely fast in an acidic environment, the slow mass transport limited rates in the RDE configuration make it impossible to obtain reliable HOR/HER kinetic data of carbon supported PGM catalysts this way, whereby even the HER is affected by H<sub>2</sub> oversaturation and bubble formation.<sup>85,152-155</sup> Consequently, high mass transport setups, such as PEMFC-based H<sub>2</sub>-pump measurements, are required for an accurate determination of the HOR/HER kinetics and also of the durability of a Pt-based catalyst. This technique is discussed in detail in the following subsection.

For the ORR in acidic electrolytes, mechanistic studies and trends in kinetics can be determined by RDE experiments.<sup>79,81,82</sup> However, in some instances, RDE-based activities overestimate those in MEAs, due to issues in stabilization/utilization of the active site and/or the enhanced negative effect of transition metal dissolution in the MEA environment.<sup>9,16,26</sup> However, a qualitative understanding of the ORR catalyst-specific degradation mechanisms (*EC*SA loss, carbon support stability) can be gained by RDE experiments, so that trends among different catalysts are also comparable to those observed in MEAs when experimental conditions are adequately chosen.<sup>156-158</sup> For a meaningful assessment of secondary degradation phenomena (e.g., transition metal dissolution, electrode structural collapse), MEA testing is inevitable.<sup>123,159</sup> The

high current density performance of ORR catalysts in a PEMFC cannot be assessed via the RDE technique, as it does not allow measurements at the relevant high specific current densities. Therefore, the influence of catalyst (support) morphology and catalyst/ionomer interaction on the high current density performance of an ORR catalyst in PEMFCs can only be determined by MEA measurements, whereby an optimization of these catalyst properties can result in up to 100 mV higher PEMFC voltages at high current densities.<sup>37,38,160</sup>

Finally, the discussed aspects for the OER, HOR, HER, and ORR regarding the transferability between RDE and MEA are summarized, whereby the main issues that prevent comparable results are highlighted and, where possible, reliable protocols for RDE and MEA measurements as well as possible alternatives using bridging techniques (e.g., GDE or FET based measurement configurations) are suggested.

#### **Author contributions**

All authors conceptualized the overall structure of this perspective. T.L., B.M.S., and H.A.E. co-wrote the manuscript, with T.L. and B.M.S. contributing the discussion of general aspects and the conclusion, H.A.E. focusing on the OER section, B.M.S. drafting the HOR/HER section, and T.L. discussing the ORR-specific aspects. All authors provided insights, contributed feedback, and edited the manuscript.



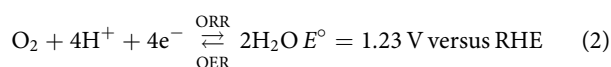
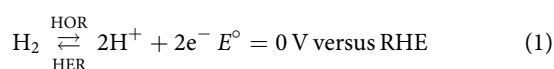
# Capabilities and limitations of rotating disk electrodes versus membrane electrode assemblies in the investigation of electrocatalysts

Timon Lazaridis<sup>1,2</sup>, Björn M. Stühmeier<sup>1,2</sup>, Hubert A. Gasteiger<sup>1</sup> and Hany A. El-Sayed<sup>1</sup>✉

**Cost-competitive fuel cells and water electrolyzers require highly efficient electrocatalysts for the respective reactions of hydrogen oxidation and evolution, and oxygen evolution and reduction. Electrocatalyst activity and durability are commonly assessed using rotating disk electrodes (RDEs) or membrane electrode assemblies (MEAs). RDEs provide a quick and widely accessible testing tool, whereas MEA testing is more complex but closely resembles the actual application. Although both experimental set-ups allow investigation of the same reactions, there are scientific questions that cannot be answered by the RDE technique. In this Perspective, we scrutinize protocols widely used to determine the activity and durability of electrocatalysts, and highlight discrepancies in the results obtained using RDEs and MEAs. We discuss where the use of RDEs is appropriate and, conversely, where it leads to erroneous interpretations. Ultimately, we show that many of the current challenges for hydrogen and oxygen electrocatalysts require MEA testing and advocate for its greater adoption in the early stages of electrocatalyst development.**

The electrochemical generation and conversion of hydrogen and its role as an energy vector are key elements in virtually all scenarios for decarbonizing future energy systems. The economic and ecologic viability of hydrogen in this context relies on the efficiency of two technologies: water electrolysis<sup>1</sup>, which generates hydrogen from electrical energy, and fuel cells, converting the chemical energy of hydrogen back into electricity, powering stationary and mobile applications<sup>2,3</sup>.

Fuel cells and water electrolyzers can operate using acidic or alkaline electrolytes, with the techniques and methodologies used to study suitable electrocatalysts generally being the same in both environments. In this Perspective, we focus exclusively on acidic proton exchange membrane fuel cells (PEMFCs) and proton exchange membrane water electrolyzers (PEMWEs), as the main challenges for anion exchange membrane systems are found in ionomer and membrane durability rather than catalyst stability. In PEMFCs, hydrogen is oxidized by a platinum electrocatalyst at the anode (hydrogen oxidation reaction (HOR)), which results in the generation of electrons and protons (equation (1)). Here,  $E^\circ$  is the standard electrode potential versus the reversible hydrogen electrode (RHE). The protons migrate through a proton-conducting membrane towards the cathode, which is also composed of Pt or a Pt-based alloy, while the electrons move to the cathode through an external circuit, generating usable electricity. Reacting with protons and electrons at the cathode, oxygen is reduced (oxygen reduction reaction (ORR)), which results in the formation of clean water (equation (2))



In PEMWEs, the above reactions proceed in the opposite direction: hydrogen is produced (equation (1)) at the cathode with the

help of a Pt electrocatalyst (hydrogen evolution reaction (HER)), while oxygen evolves from water (equation (2)) on the anode side (oxygen evolution reaction (OER)) mediated by electrocatalysts based on Ir oxide or Ru oxide.

As both PEMFCs and PEMWEs use platinum group metals (PGMs) that are expensive and scarce, it is pivotal to develop highly active and reactant-accessible catalysts to lower the required amount of noble metals. Likewise, catalyst durability must be sufficiently high to warrant the initial capital expenditure. The development of such catalysts requires reliable methods for evaluating both activity and stability. Although the data most representative of fuel cell or electrolyser system performance are obtained by membrane electrode assembly (MEA) measurements, it is very common for the initial screening of newly developed catalysts, which are available only in milligram quantities, to use convective flow-based techniques in aqueous electrolytes<sup>4</sup>. These include the rotating disk electrode (RDE)<sup>5,6</sup>, the channel flow dual electrode<sup>7</sup> and, most recently, the gas diffusion electrode (GDE)<sup>8,9</sup>. For RDE measurements, the technique most commonly used with aqueous electrolytes, only several tens of micrograms of catalyst per square centimetre geometric electrode area are deposited onto the non-porous surface of a conductive substrate electrode (for example, glassy carbon and Au) embedded in the RDE holder (Fig. 1a,b)<sup>10</sup>. The rotation of the RDE establishes a well-defined diffusion layer of 5–50  $\mu\text{m}$ , allowing the extraction of the kinetic parameters of the four fuel cell and electrolyser reactions<sup>11</sup>.

In contrast, a five-layer MEA consists of a proton exchange membrane (PEM), anode and cathode catalyst layers, and gas diffusion layers (Fig. 1c,d). The catalyst layers can be either laminated or spray-coated directly onto the membrane to form a catalyst-coated membrane that is then sandwiched by gas diffusion layers, or cast onto the latter to form gas diffusion electrodes, between which the membrane is sandwiched. For both methods, the five-layer MEA is finally sealed between two flow fields to form a single-cell unit.

<sup>1</sup>Department of Chemistry and Catalysis Research Center, Technical University of Munich, Garching, Germany. <sup>2</sup>These authors contributed equally: Timon Lazaridis, Björn M. Stühmeier. ✉e-mail: [hany.el-sayed@tum.de](mailto:hany.el-sayed@tum.de)

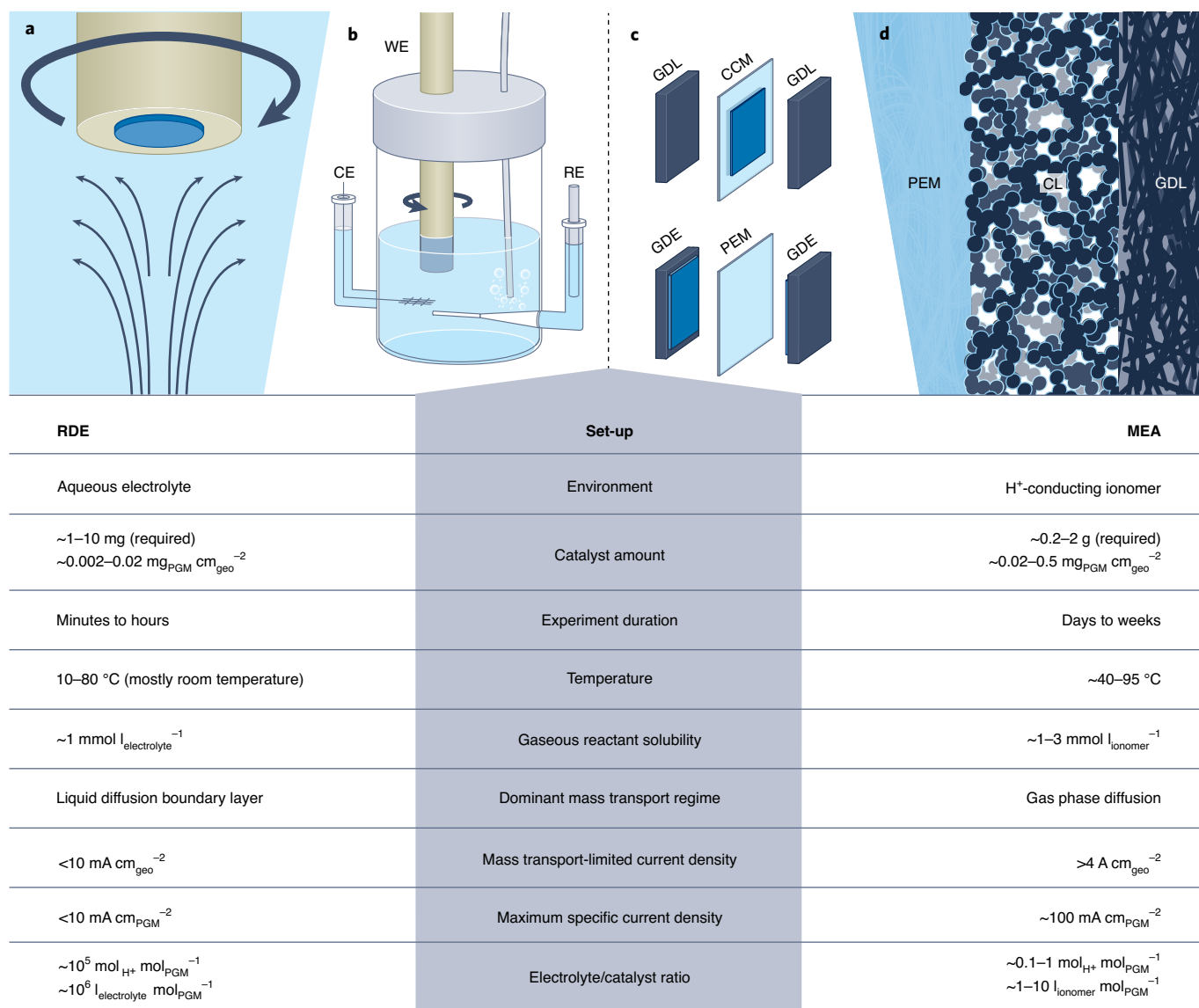


**Fig. 1 | Comparison of the RDE and five-layer MEA set-ups.** **a**, Local environment of an RDE working electrode (WE). **b**, Schematic of a three-electrode RDE set-up including a counter electrode (CE) and a reference electrode (RE). **c**, Five-layer MEA set-ups consisting either of a catalyst-coated membrane (CCM) sandwiched between two gas diffusion layers (GDLs) or a PEM between two GDEs. **d**, Local environment in an MEA, with the porous catalyst layer (CL) consisting of catalyst particles (black) and ionomer (light blue). The table summarizes typical specifications for the RDE and MEA set-ups (exceptions might apply).

These porous catalyst layers allow for efficient mass transport through the gas phase, and correspondingly, high limiting and Pt-specific current densities can be reached, albeit requiring gram quantities of catalyst powder. Also, such MEAs are time-consuming to manufacture, their electrochemical testing takes up multiple days per catalyst and further requires capital-intensive instrumentation capable of precisely controlling gas pressure, flow rate, relative humidity and temperature. Hence, the majority of novel catalyst designs are tested in RDEs, particularly in the early development stages, at small-scale synthesis.

In recent years, however, the challenges of transferring RDE-observed catalyst activity and durability to MEA experiments have moved into the limelight. This issue has been particularly prevalent in the ORR, where novel catalyst concepts, such as bimetallic, shape-controlled nanoparticles, displayed record activities in RDE experiments, but did not do nearly as well in MEA testing. Conversely, the activity of PGM-based HOR catalysts is vastly

underestimated in RDE experiments and only revealed in dedicated MEA measurements. In electrolysis, the transferability problem mainly concerns the RDE-observed stability of Ir-based OER catalysts, which is generally three to four orders of magnitude lower than what is observed in MEA experiments.

The development of standardized operating procedures, often validated across multiple laboratories, has played a key role in harmonizing RDE-observed catalyst characterization<sup>4,12,13</sup>. Particularly for ORR catalysts, state-of-the-art and novel catalysts can be reliably benchmarked, and the trends in catalyst activities mostly reflect what is observed in MEA testing. Unfortunately, the absolute mass activities obtained from the two techniques still do not match well. Although standardized protocols are not as widely used for OER catalysts, their activities can be obtained using the RDE technique, typically measured by linear sweep voltammetry, and are comparable to those obtained from MEA measurements<sup>14</sup>.

An alternative approach to reducing the gap between RDE and MEA catalyst performances is the introduction of techniques enabling high mass transport in liquid electrolytes while requiring much smaller amounts of catalyst<sup>15</sup>. These include the use of microelectrodes (50- $\mu\text{m}$ -diameter electrodes fixed on a PEM)<sup>16,17</sup>, the so-called floating electrode technique (FET, where the catalyst is cast onto a hydrophobic porous substrate floating on liquid electrolyte)<sup>18</sup> and GDEs (the electrode is placed at the liquid/gas interface)<sup>8,9,19</sup>, all of which are slowly being incorporated into electrocatalyst research. Various recent publications provide direct comparisons of these bridging techniques with RDE and MEA measurements, demonstrating their suitability as accessible intermediate techniques<sup>8,15,20</sup>. The RDE, however, remains the most commonly used technique so far.

Hence, in this Perspective, we lay out the capabilities and limitations of the RDE technique applied to the four elementary reactions of PEMFCs and PEMWEs. First, we highlight certain critical differences between the RDE and MEA set-ups, and consider their non-reaction-specific implications for electrochemical measurements. We then scrutinize, for each reaction, which catalyst properties can be reliably determined in an RDE set-up, and whether correctly determined metrics can be projected from the RDE to the MEA level. Where possible, the reader is directed to established operating procedures that ensure an artefact-free extraction of catalyst characteristics from the RDE technique. In many instances, however, no adequate protocols exist. Therefore, through this Perspective, we aim to encourage a more widespread use of MEA testing in the earlier stages of catalyst development and, where this is unfeasible, to pursue the development of rigorous protocols for bridging high mass transport techniques in aqueous electrolytes.

### Critical differences between RDE and MEA measurements

Certain properties intrinsic to RDE and MEA architectures systematically affect the evaluation of any electrocatalyst. As such, these considerations need to be taken into account for all four fuel cell and electrolyser reactions, and are discussed in this section.

**Choice of reference electrode.** While the standard potentials for the HOR/HER (equation (1)) and OER/ORR (equation (2)) reactions are typically given versus the standard hydrogen electrode (SHE; defined at activity  $a_{\text{H}^+}=1$  and pressure  $p_{\text{H}_2}=1,013$  mbar), both equilibrium reactions involve protons as reactants or products. Thus, their equilibrium potentials undergo a Nernstian pH-dependent shift, albeit at an identical rate of 0.059 mV per unit of pH in both cases. The reversible hydrogen electrode (RHE) scale accounts for this by defining the HOR/HER equilibrium potential at the given electrolyte pH and at any temperature as 0 V versus RHE. Consequently, the OER/ORR equilibrium potential always remains at 1.23 V versus RHE independent of the electrolyte pH (at 25 °C). We therefore strictly recommend using the RHE as the potential scale when reporting activities for equilibria (1) and (2), as is commonly done in the fuel cell and electrolyser literature. In this context, a precise activity determination also mandates careful calibration of the reference electrode, as potential errors of only 20 mV would correspond to a twofold change in activity for the reactions discussed here. Although this generally applies to all electrochemical set-ups, it is more easily achieved in an MEA, where the hydrogen side serves as both reference and counter electrode. The fast kinetics as well as the precise determination of the  $\text{H}_2$  partial pressure and temperature ensure that the potential can be determined reliably on the RHE scale at all times (unless the hydrogen side is investigated or severely poisoned). In an RDE, other references that are highly sensitive to changes in ion concentrations or temperature, for example, Ag/AgCl or calomel electrodes, are often used. These require calibration versus RHE by measuring the HER/HOR equilibrium potential of a platinum electrode in a  $\text{H}_2$ -saturated

electrolyte due to their different pH dependency. Note that special caution must be taken when working in electrolytes with  $2 \leq \text{pH} \leq 12$ : in this case, the local pH at the electrode surface of an RDE depends on the current density, which results in a current-dependent shift of the reversible potential for equilibria (1) and (2), so that no meaningful catalyst activities can be determined unless a buffered electrolyte is used<sup>21</sup>. In the absence of cationic contaminations (see below), a pH gradient cannot be formed in an MEA as the transfer number of protons is equal to 1 in the ionomer with the sulfonate end groups being fixed in position<sup>22</sup>.

**Governing mass transport limitations.** Possibly the most fundamental difference between the two set-ups is the prevailing mass transport limitation (see table in Fig. 1), which has direct implications for the transferability of RDE results to an MEA environment. In MEAs, reactants reach the rather thick catalyst layer (5–20  $\mu\text{m}$ ) mainly by rapid gas phase diffusion through the flow fields, the gas diffusion layers and the pores of the catalyst layer, and only ultimately need to diffuse across a nanometre-thin film of ionomer covering the catalyst particles, where the solubility of  $\text{O}_2$  and  $\text{H}_2$  is reduced to 1–3  $\text{mmol l}^{-1}$  (ref. 23). In contrast, the much thinner catalyst layer (0.1–2  $\mu\text{m}$ ) in an RDE set-up is flooded by the liquid electrolyte, and hence the diffusion length for dissolved  $\text{O}_2$  and  $\text{H}_2$  across the liquid diffusion boundary layer is in the range of tens of micrometres. For the gas-consuming reactions (HOR and ORR), this leads to much lower accessible geometric and specific current densities in an RDE set-up, preventing both meaningful assessments of HOR kinetics and high current density ORR performance on PGM catalysts. When gas evolves during the OER and HER reactions, insufficient removal of gas bubbles can additionally affect the measurements by blocking the active sites. This has severe consequences for the reliability of activity and durability measurements by RDE testing and requires special attention (detailed in the respective sections below).

The promise of the aforementioned bridging techniques (such as GDEs) lies precisely in their ability to closely resemble the local environment and mass transport pathways of an MEA, albeit at lower catalyst mass requirements and with a technical complexity comparable to the RDE technique (regarding these techniques and protocols, the reader is referred to the works of Pan et al.<sup>15</sup>, Schröder et al.<sup>8</sup>, Petzoldt et al.<sup>19</sup> and Ehelebe et al.<sup>24</sup>).

**Sources and consequences of contaminants.** In the discussion of contaminants, three possible contamination effects need to be distinguished: contaminants that poison the catalytic activity (for example,  $\text{CO}$ ,  $\text{SO}_4^{2-}$ ,  $\text{Cl}^-$ , organic molecules or redepositing metals), contaminants that affect proton transport (mostly cations) and contaminants that accelerate degradation (for example,  $\text{Fe}^{2+}$ ,  $\text{Cu}^{2+}$  or  $\text{Cl}^-$ )<sup>4,25,26</sup>. It is possible that a contaminant might fall in multiple of these categories.

Contaminants can be introduced through a contaminated set-up, electrolyte or gas supply, or come from the degradation of the catalyst and other cell components. The former case heavily affects RDE measurements due to the high electrolyte/catalyst ratio (see table in Fig. 1), where even tiny impurity concentrations can heavily poison catalyst surfaces (the reader is referred to the work of Shinozaki et al.<sup>4</sup> for details), although degradation products are inconsequential due to near-infinite dilution.

In contrast, MEAs are heavily affected by contamination coming from gas impurities and the degradation of cell components. Here, the difference in the relative proton inventories of the RDE and MEA environments results in a vastly more pronounced contamination effect due to the dissolution of transition metal (TM) ions from the catalyst in the latter. Even small amounts of dissolved  $\text{TM}^{2+}$  ions can displace a substantial fraction of the protons in the ionomer phase of an MEA due to the very low electrolyte/catalyst ratio

(see table in Fig. 1), thereby lowering the ionic conductivity in both the catalyst layer and membrane. Most importantly, at high current densities, the potential gradient-driven accumulation of  $\text{TM}^{z+}$  ions in the cathode ionomer film can eliminate a substantial fraction of the protons in the cathode catalyst layer even at  $\text{TM}^{z+}$  concentrations that do not yet reduce membrane conductivity. The associated increase in local pH shifts the cathode equilibrium potential, yielding an additional thermodynamic penalty of up to 400 mV, and currents become effectively proton transport-limited<sup>26–28</sup>.

It has been shown that the effect of catalyst poisoning can be simulated in an RDE by intentionally adding the respective contaminant to the electrolyte<sup>4,29</sup>. Estimating the expected degree of contamination due to catalyst degradation is also possible by analysing the concentration of metal ions in the liquid electrolyte, for example, by inductively coupled plasma mass spectrometry<sup>30</sup>. However, these experiments cannot adequately reproduce the pH gradient effects that are expected for a potential-driven accumulation of  $\text{TM}^{z+}$  ions in the cathode catalyst layer, or secondary effects on the MEA performance, for example, ionomer degradation as a result of  $\text{TM}^{z+}$  ions catalysing the Fenton reaction<sup>26–28</sup>.

### Oxygen evolution reaction

Electrocatalyst research in acidic water electrolysis focuses on the OER, where noble metal oxides, particularly  $\text{IrO}_2$ -based materials, are currently being used due to their superior long-time stability<sup>31</sup>. Iridium, however, is very scarce and considerably more expensive than Pt, necessitating the development of catalysts with higher OER activity and lower iridium loadings. In identifying and validating a suitable catalyst design, both activity and long-term stability are equally critical.

**Activity of  $\text{IrO}_2$ -based catalysts.** OER activities can be measured in liquid electrolytes using half-cell configurations with liquid electrolytes, such as the RDEs and flow channel approaches<sup>32–34</sup>, yielding estimated activities comparable to those obtained from MEA measurements<sup>35,36</sup>. Even though some oxide-supported OER catalysts are not very conductive, the electronic conductivity of the catalyst layer has almost no effect on the RDE-determined OER activity, as the thin catalyst layer does not require substantial electronic conduction lengths. This may, however, become relevant in the thicker catalyst layers found in MEAs. Furthermore, when in contact with a porous transport layer (PTL) that passivates at high OER potentials, poorly conductive catalysts can display low performance due to the development of a contact resistance at the PTL–CL interface. A Pt-coated PTL was found to prevent the formation of such a contact resistance, maintaining proper overall performance<sup>37</sup>.

**Stability of  $\text{IrO}_2$ -based catalysts.** OER catalyst stability measurements can be performed in the MEA configuration, but it is not feasible to evaluate the long-term stability of OER catalysts under realistic conditions due to the already very long catalyst lifetimes of 50,000–100,000 h in PEMWEs<sup>1</sup>. Therefore, accelerated stress tests (ASTs) have been devised either for cells with liquid electrolyte or for PEMWEs<sup>38,39</sup>. However, a frequent shortcoming of ASTs is that their exact acceleration factor is not known, so it is generally not possible to correlate the catalyst lifetime obtained from an AST with the lifetime in an actual electrolyser.

In half-cell measurements with a liquid electrolyte, OER catalyst lifetimes are around three to four orders of magnitude lower than those measured in a PEMWE<sup>14,35,40,41</sup>. Several hypotheses for this discrepancy have been brought forward in the literature. First, an additional contact resistance at the catalyst layer/RDE substrate interface could form, possibly by passivation of the electrode substrate<sup>38</sup>. Although it is advisable to use electrode materials that do not passivate at OER potentials, for example, Au or boron-doped diamond, rapid activity decay has also been observed on an Ir

disk, where no catalyst layer/electrode substrate interface exists<sup>42</sup>. Furthermore, the observed activity decay could be prevented by electrolyte ultrasonication, indicating that the activity decay stems from a temporary effect rather than permanent passivation. Second, continuous oxygen evolution could deplete the OER-active species through the formation of an anhydrous Ir oxide, which was concluded exclusively on the basis of RDE measurements<sup>43</sup>. If this depletion took place in a liquid electrolyte, it should similarly occur in an MEA configuration, resulting in comparably short catalyst lifetimes, which have not been observed. Third, Knöppel et al. argued that the overestimated acidity in the anode catalyst layer in MEAs and stabilization over time are responsible for the catalyst lifetime/dissolution discrepancy<sup>41</sup>. Lastly, oxygen microbubbles trapped at the surface of the RDE tip and/or within the catalyst layer could shield the catalyst's active sites. Here, the blockage of the active sites forces a potential increase, which then induces catalyst degradation<sup>40</sup>. An argument against this finding is that the accumulation of microscopic oxygen bubbles could also take place in the MEA configuration, resulting in shorter catalyst lifetime. In a comparative RDE and MEA study, bubble accumulation was observed in the MEA configuration as well, but to a much lesser extent; thus, it does not have the same detrimental effects on catalyst stability as in RDE or liquid cell tests<sup>14</sup>. The different extents of catalyst shielding by microscopic oxygen bubbles in the two configurations were attributed to the net water flux through the catalyst/membrane interface in the MEA configuration, in contrast to the RDE configuration<sup>14</sup>.

We believe that microscopic bubble formation is one of the major reasons for the discrepancy in catalyst lifetimes obtained from RDE and MEA measurements. In the following, we therefore describe how the trapping of evolved oxygen bubbles is consistent with the measurement artefacts found in various OER catalyst stability protocols. In general, such ASTs are performed using either constant current holds (chronopotentiometry), constant potential holds (chronoamperometry) or potential cycling. Although chronopotentiometry is the most commonly discussed method in the literature when using liquid electrolytes, it produces the largest errors in catalyst lifetime determination compared with the other two methods. When a constant current density ( $j$ ) is applied in an RDE set-up, the observed potential rapidly increases by one Tafel slope (TS; ~50–60 mV for the OER<sup>32,33</sup>) within a couple of minutes. This indicates that at least 90% of the electrochemically active surface area, or electrode roughness factor (rf), is lost, that is, shielded by microscopic oxygen bubbles. Equation (3) describes this relationship, with  $\eta$  being the observed overpotential and  $j_0$  being the exchange current density.

$$\eta = \text{TS} \times \left[ \log \left( \frac{j}{j_0} \times \frac{1}{\text{rf}} \right) \right] \quad (3)$$

With increasing time at constant current, further shielding-induced potential increases take place, often by three to four TS values after several hours. The rapid increase in potential due to the shielding of active sites initially only reflects reversible performance decay rather than catalyst degradation, which can be recovered by Ar purging. However, when the potential increases beyond 1.7–1.8 V, irreversible catalyst degradation by dissolution occurs. Chronopotentiometry thus starts with reversible OER degradation, but ultimately turns into irreversible degradation at high potentials, which would not occur in the absence of bubble accumulation, that is, in an MEA configuration. Therefore, chronopotentiometric OER catalyst stability measurements should strictly be limited to MEA tests, as no meaningful stability data can be obtained in liquid electrolyte cells.

The other two methods, chronoamperometry and potential cycling, do not exhibit the artefact-induced degradation that takes place during chronopotentiometry, as both keep the potential

under control. Nevertheless, the two methods result in irreversible degradation when applied to testing OER catalysts in liquid electrolytes, whereas the degradation is fully reversible in the MEA configuration. This discrepancy in catalyst degradation between the two techniques (RDE versus MEA) is still not understood, and future investigations should focus on the cause(s) of this discrepancy and whether a meaningful stability protocol in liquid cells can be established.

Recently, Petzoldt et al. demonstrated a modified RDE (MRDE) method that is capable of directly testing catalyst-coated membranes using conventional RDE techniques. In this study, the formation of microscopic bubbles and their effects on three accelerated degradation tests was investigated using RDE and MRDE<sup>19</sup>. In addition to confirming that the formation of microscopic oxygen bubbles is responsible for a major fraction of the apparent degradation in both RDE and MRDE, the authors successfully distinguished and quantified reversible degradation, due to active site blockage, and irreversible degradation, due to dissolution. The authors reported that 100% of the degradation is reversible when potential cycling or chronoamperometry protocols are applied using MRDE. When a square wave voltammetry AST was applied, however, only 50–60% of the degradation was reversible. The authors attributed the superiority of the MRDE in testing OER catalyst stability to the vastly different morphology of the catalyst-coated membrane compared with the RDE catalyst layer, with efficient removal of the microscopic bubbles in the former technique.

We thus conclude that although OER catalyst activities derived from liquid electrolyte cells and thin-film electrodes reliably match MEA-obtained values, the use of such techniques to investigate catalyst stability should be avoided. Conventional thin-film RDE ASTs display rapid reversible degradation, triggering subsequent irreversible degradation, which does not occur in MEA testing. Although several alternatives to the RDE technique have been proposed, such as GDEs and FETs, we consider MRDE the best low-tech set-up for testing OER catalyst stability because of its direct use of catalyst-coated membranes and its powerful capability to quantitatively delineate reversible and irreversible degradation in chronoamperometric ASTs<sup>8,19</sup>.

### Hydrogen oxidation and evolution reaction

For acidic systems, the HER at the cathode of a PEMWE and the HOR at the anode of a PEMFC according to equation (1) are extremely fast, with exchange current densities ( $j_0$ ) of the order of ~100 mA per cm<sup>2</sup> platinum (~100 mA cm<sub>Pt</sub><sup>-2</sup>) at room temperature<sup>44–46</sup>. Consequently, only small amounts of Pt (~0.025–0.05 mg platinum per cm<sup>2</sup> geometric area (~0.025–0.05 mg<sub>Pt</sub> cm<sub>geo</sub><sup>-2</sup>)) are required to limit the HOR/HER overpotential to only a few millivolts<sup>53,46</sup>. However, when using the RDE technique, exchange current densities that are roughly two orders of magnitude lower have typically been reported<sup>44,45</sup>. This is due to slow mass transport-limited rates ( $j_{lim}$ ) in the RDE configuration, where the HOR voltage–current density profiles directly follow the diffusion-limited current density rates ( $j_{diff}$ ) arising from the Nernstian diffusion overpotential ( $\eta_{diff}$ ; equation (4)) with the Faraday constant ( $F = 96,485$  C mol<sup>-1</sup>), the universal gas constant ( $R = 8.314$  J mol<sup>-1</sup> K<sup>-1</sup>), and the temperature ( $T$ )<sup>45,47</sup>.

$$j_{diff} = j_{lim} \left( 1 - e^{-\frac{2F}{RT} \eta_{diff}} \right) \quad (4)$$

It has been shown that Pt/C, Ir/C and Rh/C all follow the same diffusion rate-limited HOR polarization curves in 0.1M HClO<sub>4</sub> (Fig. 2a), even though their exchange current densities differ by a factor of 20 when determined from MEA-based H<sub>2</sub> pump measurements<sup>45</sup>. Similarly, no difference in the RDE-based HOR polarization curves could be observed even after poisoning 98% of a Pt(111)

single crystal surface with calix[4]arene (Fig. 2b)<sup>48</sup>. These results clearly show that it is impossible to obtain reliable HOR/HER kinetic data for carbon-supported PGM catalysts from RDE measurements in acidic electrolyte, unless the activity of the catalyst is at least two orders of magnitude lower than that of Pt/C.

When investigating HER kinetics, physical shielding effects due to bubble formation further complicate the interpretation of RDE results<sup>49,50</sup>, as discussed already for the OER, although the blockage of active sites does not directly result in a loss in the observed current response due to the fast kinetics (Fig. 2b). As a possible solution, it has been suggested that an inverted RDE could be used to facilitate the fast removal of evolved gas<sup>51</sup>. However, even when the shielding effect could be mitigated by successfully removing all microbubbles, the limited mass transport of dissolved gases leads to an ~300-fold supersaturation at the catalyst surface before bubble formation<sup>50</sup>. For PGM-based catalysts, this results in a limitation of the HER current densities by the Nernstian diffusion overpotential rather than the kinetics as well<sup>49</sup>.

Many other high mass transport set-ups developed in recent years still yield underestimated HOR/HER kinetics when compared with the values obtained from MEA-based H<sub>2</sub> pump measurements (Fig. 2c)<sup>45</sup>, thus indicating that these set-ups are still more affected by H<sub>2</sub> mass transport than MEA measurements.

It is therefore highly preferable to investigate acidic HOR/HER catalysts by means of MEA measurements. Whenever this is not feasible, researchers should either use a GDE or FET set-up or, at a minimum, perform low-loaded ( $\leq 10 \mu\text{g}_{\text{Pt}}, \text{cm}_{\text{geo}}^{-2}$ ) RDE measurements in alkaline electrolytes<sup>44,52</sup>, where HOR/HER kinetics are roughly two orders of magnitude lower and might give a reasonable estimation of activity trends<sup>47,53</sup>. This has been rationalized by the universal pH dependency of the hydrogen binding energy<sup>54</sup>. However, it is yet to be determined whether this applies to all classes of HOR/HER catalysts.

In MEA testing, it should be emphasized that HOR/HER losses are limited to a few millivolts even when using electrode loadings of ~0.025–0.05 mg<sub>Pt</sub> cm<sub>geo</sub><sup>-2</sup>, and that therefore suitably low loadings must be used to investigate the HER/HOR performance of a catalyst. Otherwise, the contributions of the HOR/HER to the overall cell potential may fall in the same range as the expected variations between measurements, or the measured HOR/HER currents are actually transport limited rather than kinetically limited<sup>55</sup>. Lastly, durability measurements of HOR/HER catalysts cannot be performed by RDE measurements as it is impossible to evaluate the loss of activity when the activity itself is concealed by mass transport limitations.

### Oxygen reduction reaction

The development of catalysts for PEMFC systems has concentrated on improving the cathode activity due to the large ORR overpotential contributing 300–400 mV to the overall voltage losses. Also, cathode performance must be maintained over the entire system lifetime, especially when aiming for heavy-duty applications where PEMFCs compete with long-lived diesel engines (>30,000 h of operation)<sup>56</sup>. As recent reviews have highlighted the current state-of-the-art in ORR catalyst development in great detail<sup>3,15,57,58</sup>, this section is focused entirely on the experimental challenges involved in investigating Pt-based ORR catalysts using RDE and MEA techniques.

**Activity and performance of novel Pt (alloy) catalysts.** RDE studies have proven valuable for understanding the factors that lead to a high ORR mass activity, identifying the most active crystallographic facets and sites, and rapidly screening alloys and advanced catalyst structures with such properties. For typical Pt(alloy)/C catalysts, joint research efforts have given rise to standardized protocols that ensure reproducible RDE-based determination of ORR activity,

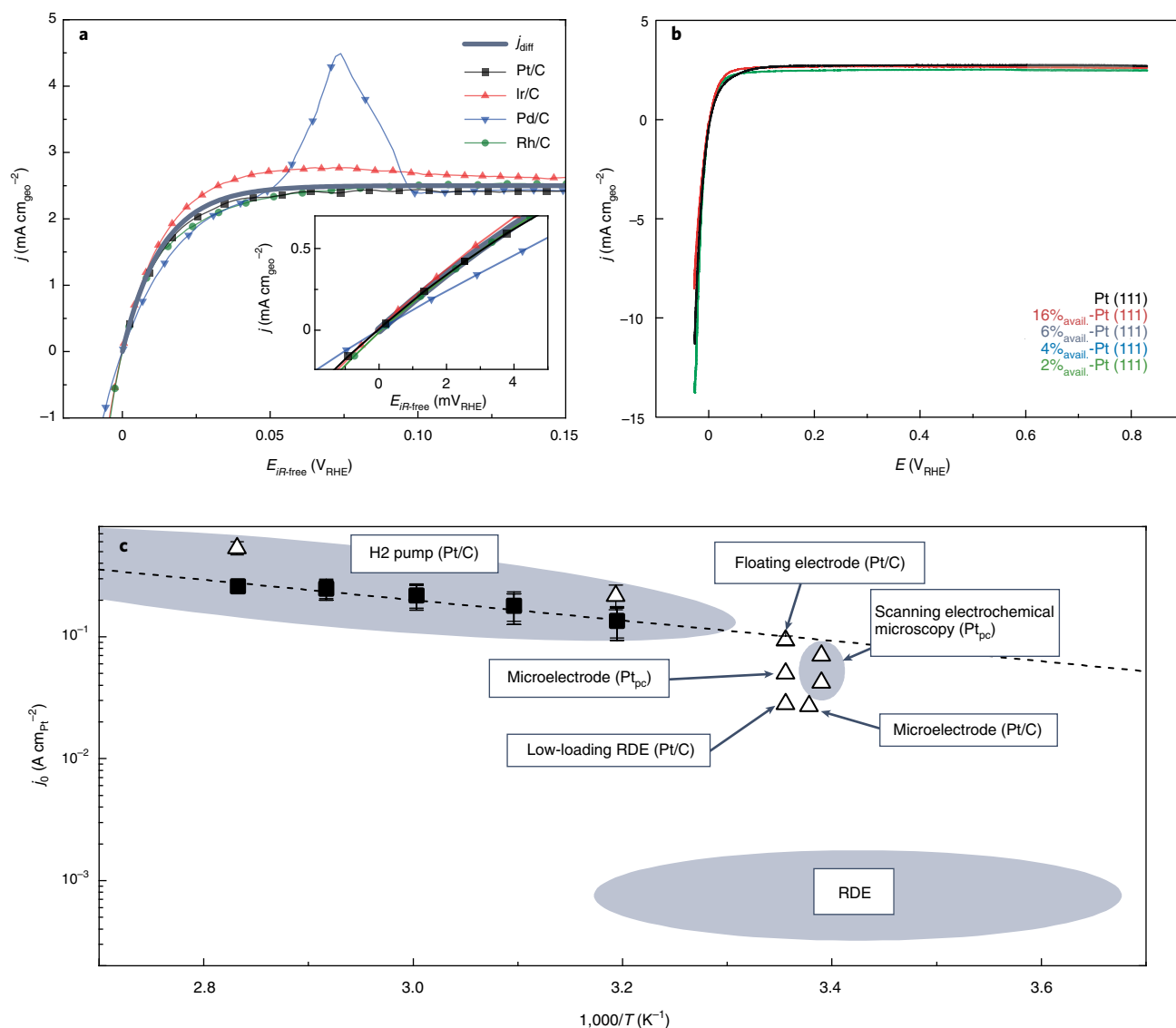


**Fig. 2 | Limited mass transport rates restricting RDE-based HOR/HER measurements of the Nernstian diffusion overpotential. a,b**, RDE-based HER/HOR polarization curves recorded in  $\text{H}_2$ -saturated  $0.1\text{M HClO}_4$  for Pt/C, Ir/C, Rh/C and Pd/C (scan rate  $\nu = 20\text{ mV s}^{-1}$ ,  $T = 313\text{ K}$  and rotation rate  $\omega = 1,600\text{ r.p.m.}$ ) with the theoretical diffusion current density derived from equation (4) for  $j_{\text{lim}} = 2.4\text{ mA cm}_{\text{geo}}^{-2}$  (a) and for a Pt (111) disc with calix[4] arene surface poisoning (b). In b, the remaining surface area available according to hydrogen underpotential deposition is given in %<sub>avail.</sub>. c,  $j_0$  values obtained for Pt/C from PEMFC-based  $\text{H}_2$  pump measurements and compared with other high mass transport set-ups and RDE measurements for Pt/C and polycrystalline Pt (Pt<sub>pc</sub>) showing the systematic underestimation of kinetic data obtained from the RDE set-up due to its mass transport limitation. Panels adapted with permission from: a,c, ref. 45, under a Creative Commons licence CC BY 4.0; b, ref. 48, Springer Nature Ltd.

validated across different laboratories<sup>4,12,13</sup>. These works detailed meticulously, among many other factors, the importance of electrolyte purity, thin-film preparation and scan and rotation rates, and should be relied on for all ORR catalyst benchmarking. Note that although absolute activity values still do not match those obtained by MEA techniques, activity trends generally hold across both set-ups. Furthermore, the intrinsic catalyst activity can be gleaned more easily from RDE testing, as unrelated influences from the membrane or anode are excluded, making the RDE an essential tool for rapidly screening small sample quantities.

In recent years, optimizing the lattice strain and electronic effects of catalysts has enabled more than tenfold improvements in mass activity compared with state-of-the-art Pt/C catalysts, as demonstrated by RDE measurements<sup>3,15,57,58</sup>. However, ORR mass activities are much lower when integrating such advanced materials into MEAs, typically improving mass activity by only a factor of three

compared with Pt/C (refs. 3,15). The exact reason for these observations is a matter of ongoing debate<sup>2,59</sup>, but the main differences are found in the catalyst/electrolyte interface and the harsher conditions in MEAs (such as higher temperatures and lower pH), under which the stabilization and utilization of optimized active sites proved challenging. In Pt alloys, the TM often de-alloys during testing, which results not only in the loss of active sites but also in TM<sup>2+</sup> contamination of the system. It has been shown for Pt alloy catalysts that the discrepancy in the initial performances of the RDE and MEA measurements could partially be eliminated by pre-leaching the catalyst, which resulted in lower RDE activities but improved the MEA performance<sup>10</sup>. To obtain a more reliable estimate of potential performance improvements in MEAs, a leaching step that mimics fuel cell operation (for example, by stirring multiple times for  $\geq 8\text{ h}$  in  $\geq 0.5\text{ M H}_2\text{SO}_4$  at  $\geq 80^\circ\text{C}$ ) is highly recommended before activity testing.

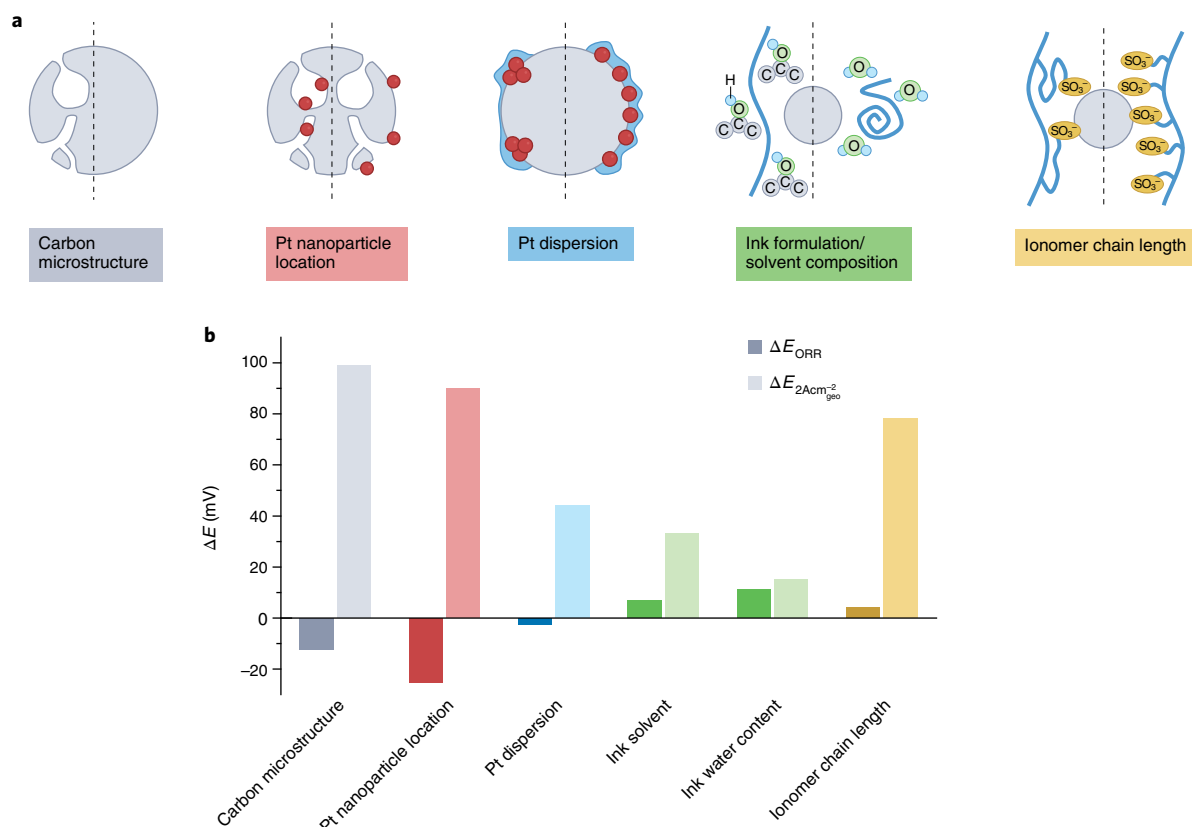


**Fig. 3 | Structural influences on ORR catalyst activity and MEA performance. a, b,** Conceptual overview of literature-reported catalyst and electrode morphologies that improve MEA performance (**a**) and their respective effect at low current density (ORR kinetics) and high current density (mass transport; **b**). Solid bars ( $\Delta E_{\text{ORR}}$ ) represent the expected ORR overpotential changes calculated from the reported difference in mass activity at  $0.9\text{ V}_{\text{RHE}}$  ( $j_{\text{m}}^{0.9\text{V}}$ ) and a theoretical Tafel slope of  $70\text{ mV dec}^{-1}$ . Light-shaded bars ( $\Delta E_{2\text{Acm}_{\text{geo}}^{-2}}$ ) show the observed changes in cell voltage at high current density ( $2\text{ A cm}_{\text{geo}}^{-2}$ ), taken from  $\text{H}_2/\text{air}$  polarization curves. Calculations are based on the following materials, as referred to in their original publications (from left to right): HSC-f versus HSC-g (ref. <sup>82</sup>), Pt/ $\text{KB}_{\text{TKK}}$  versus Pt/ $\text{KB}_{\text{PO}}$  (ref. <sup>74</sup>),  $0.05\text{ mg}_{\text{Pt}}\text{ cm}^{-2}$  (10%) versus  $0.05\text{ mg}_{\text{Pt}}\text{ cm}^{-2}$  (50%)<sup>75</sup>, 16 wt%  $\text{H}_2\text{O}$  in 1-propanol versus 16 wt%  $\text{H}_2\text{O}$  in 2-propanol<sup>80</sup>, 16 wt%  $\text{H}_2\text{O}$  in 1-propanol versus 65 wt%  $\text{H}_2\text{O}$  in 1-propanol<sup>80</sup> and SSC-870 EW versus LSC-1100 EW (ref. <sup>79</sup>).

Beyond standardized procedures, which have not reliably yielded matching RDE- and MEA-based activities so far, bridging techniques such as FETs and GDEs have opened a promising path to reconciliation. Comparative studies have shown that the ORR activities of Pt(alloy)/C catalysts obtained from FET and GDE experiments match MEA-based measurements owing to comparable catalyst loadings, mass-specific current densities and mass transport phenomena<sup>9,20,60</sup>. Although these techniques have yet to be applied to those advanced catalyst designs that so far have not replicated their outstanding improvements in MEAs, their low catalyst requirements and ease and speed of characterization make FETs and GDEs interesting candidates for intermediate techniques where single-cell testing cannot be realized.

**Stability and durability of Pt (alloy) catalysts.** Electrode durability is mainly compromised by a loss of Pt surface area due to various particle growth phenomena and Pt dissolution, as well as by a collapse of the carbon support following electrochemical oxidation. In both RDE and MEA investigations, a catalyst's susceptibility to such degradation is assessed by ASTs, typically by cycling the electrode potential within defined limits. What insights can such ASTs reliably generate? RDE ASTs play an essential role in the qualitative understanding of degradation pathways, particularly in conjunction with advanced characterization techniques. For example, coupling RDE ASTs with identical location transmission electron microscopy (IL-TEM) has provided visual evidence for Ostwald ripening,

particle coalescence and detachment, as well as their prevalence as a function of potential window, particle deposition method and carbon support type<sup>61,62</sup>. This mechanistic understanding is fundamental for designing mitigation strategies. Quantifying catalyst degradation using RDE ASTs has been less successful despite the existence of standardized procedures defined by the United States Department of Energy (DoE) and the Fuel Cell Commercialization Conference of Japan (FCCJ). Among 20 studies employing the same DoE protocol, end-of-test activity retention was anywhere between 0 and 84% of the respective beginning-of-test value<sup>63</sup>.

Caution must further be taken when projecting the degradation trends (or even rates) observed in RDE ASTs to established MEA ASTs<sup>56,64</sup>. Although upper and lower voltage limits constitute the primary characteristics of ASTs, degradation processes are highly sensitive to testing conditions and the local environment. RDEs are often operated at ambient temperature because temperature control requires additional hardware. Under these conditions, an RDE AST evaluating carbon corrosion on different supports found no difference in degradation rates, contrary to observations gathered in MEA measurements. The expected trends in carbon oxidation-induced loss of electrochemically accessible surface area (ECSA) only became apparent on increasing the temperature to  $60\text{ }^\circ\text{C}$ , demonstrating that potential windows and scan rates alone are insufficient as control variables in ASTs<sup>65</sup>. Note that even at appropriate temperatures, RDE ASTs still cannot replicate the collapse of an oxidatively weakened carbon structure under the compressive force applied

**Table 1 | Summary of the discussed aspects of the OER, HOR, HER and ORR reactions, regarding transferability between RDE and MEA, suggested protocols, the main issues that prevent comparable results and possible alternatives to MEA measurements**

Reaction	Aspect	Transferability	Protocol (RDE)	Protocol (MEA)	Main issues	Alternatives
OER	Activity	Yes	Alia et al. <sup>45</sup>	Alia et al. <sup>34</sup> , Fathi Tovini et al. <sup>14</sup>	• Excessive potential cycling results in activity decay	MRDE <sup>19</sup> , GDE <sup>8</sup>
	Durability	No	-	Spöri et al. <sup>81</sup>	• Blockage of active sites (bubble formation and passivation)	MRDE <sup>19</sup>
HOR	Activity	No	-	Stühmeier et al. <sup>55</sup>	• Mass transport limitation	GDE <sup>52</sup> , FET <sup>44</sup> , alkaline RDE <sup>53</sup>
HER	Activity	No	-	Stühmeier et al. <sup>55</sup>	• Mass transport limitation • Blockage of active sites	GDE <sup>52</sup> , FET <sup>44</sup> , alkaline RDE <sup>53</sup>
HOR/HER	Durability	No	-	-	• Activity loss immeasurable	-
ORR	Activity	Trends only	Shinozaki et al. <sup>4</sup> Kocha et al. <sup>13</sup>	Gasteiger et al. <sup>10</sup>	• Different local environment • Active site instability (advanced catalysts)	GDE, FET
	Durability	No (some trends)	Riese et al. <sup>65</sup>	DoE (Table P.1/P.2) <sup>56</sup> Stariha et al. <sup>64</sup>	• Dissolution/redeposition rates • Non-CL degradation not replicable in RDE	GDE (not yet standardized)
	High current density	No	-	Baker et al. <sup>72</sup> Ramaswamy et al. <sup>82</sup>	• Different Pt-specific currents • Influencing factors hard to isolate in other set-ups	-

to a single cell or stack, which is the predominant failure mode in start-up/shut-down-induced carbon corrosion<sup>66</sup>. The second important class of degradation tests, ASTs targeting the loss of Pt surface area, is strongly governed by the competing rates of Pt dissolution and redeposition. In aqueous electrolytes, the ionic mobility of Pt<sup>2+</sup> is an order of magnitude higher than in a solid ionomer, making it easier for dissolved Pt to diffuse away from the catalyst layer. Equally, the rotation of the RDE tip during ASTs has been found to lessen Pt redeposition due to the forced convective flow, which is absent in MEAs<sup>67</sup>. Catalyst layer thickness, which is substantially greater in MEAs than in RDEs, has an opposite effect and is known to mitigate Pt loss because longer diffusion paths favour redeposition<sup>68</sup>. When comparing ASTs at identical temperatures, for example, 80 °C, these three factors lead to a systematic overestimation of ECSA loss in RDE experiments compared with MEA observations. Analogous to carbon corrosion ASTs, ECSA loss also exhibits an Arrhenius-type dependency on temperature (activation energy  $E_a = 28.6 \text{ kJ mol}^{-1}$ )<sup>69</sup>, and thus RDE ASTs carried out under ambient conditions typically underestimate degradation rates compared with MEA ASTs run at 80 °C, despite the lower set-up-specific redeposition rates in RDEs.

Although no dedicated protocols to harmonize RDE and MEA ASTs exist so far, half-cell testing using GDEs might prove to be a suitable intermediate mimicking realistic MEA degradation rates. The elevated cell temperatures, thicker catalyst layers and ionic diffusion in a solid electrolyte closely resemble MEA conditions, and GDE ASTs have already demonstrated comparable rates of Pt particle growth<sup>68</sup>. However, GDE ASTs are still very much in their infancy, such that standardized protocols and degradation benchmarks have yet to be established.

The difference in electrolyte type and diffusion rates also concerns the fate of TM cations leached from Pt alloy nanoparticles (see above for details on contamination effects), which introduce

a thermodynamic penalty and lead to currents that are effectively proton transport limited<sup>26,27</sup>. Importantly, established mitigation steps such as acid washing may not entirely prevent continuous leaching over the entire lifetime of the cell, even if beginning-of-life performance appears satisfactory<sup>28</sup>. This highlights the criticality of secondary degradation phenomena affecting cell components other than the catalyst itself. Holistic assessments of catalyst durability through MEA ASTs are therefore essential, both because degradation mechanisms are highly sensitive to stressors that are difficult to reproduce in an RDE, and because cation contamination plays an increasingly important role on longer timescales.

**Mass transport-limited operation at high current density.** Parallel to ORR activity improvements, fuel cell operation at high current density ( $>2 \text{ A cm}_{\text{geo}}^{-2}$ ) has been a high-priority research area throughout the past decade<sup>70,71</sup>. Performance in this regime is primarily governed by resistances related to mass transport, with a major contribution arising from local oxygen gradients at the active Pt surface. Normalizing the oxygen-limiting current density to the available Pt surface translates to a specific current density of  $30 \text{ mA cm}_{\text{Pt}}^{-2}$  for a typical MEA set-up ( $2 \text{ A cm}_{\text{geo}}^{-2}$ ,  $0.1 \text{ mg}_{\text{Pt}} \text{ cm}_{\text{geo}}^{-2}$  and  $70 \text{ m}_{\text{Pt}}^2 \text{ g}_{\text{Pt}}^{-1}$ ). In contrast to the oxygen/air atmosphere in an MEA cathode, RDEs are strongly transport limited by oxygen availability in the liquid electrolyte, even at high rotation rates, which restricts the maximum geometric current density to approximately  $6 \text{ mA cm}_{\text{geo}}^{-2}$ . Achieving the same Pt-specific current density in this set-up would require lowering the catalyst loading on the electrode disk to  $<0.5 \mu\text{g cm}_{\text{geo}}^{-2}$ . Such minute amounts of catalyst are highly susceptible to impurities and also unlikely to deposit as a homogeneous film, both of which would pose major challenges to experimental reproducibility.

MEAs are much better suited to operating reliably at such high current densities, in both absolute and Pt-specific terms. Beyond

simple polarization curves, robust diagnostic protocols allow quantification of mass transport characteristics, that is, oxygen transport resistance and proton conduction resistivity, which have an outsized impact at low electrode loadings ( $<0.1 \text{ mg}_{\text{Pt}} \text{ cm}_{\text{geo}}^{-2}$ )<sup>72,73</sup>. This tool-kit has enabled a comprehensive understanding of different voltage loss contributions to the overall performance. In particular, efficient mass transport has been found to hinge on Pt particle accessibility<sup>74</sup> and dispersion<sup>75</sup>, carbon pore morphology<sup>76–78</sup>, ionomer structure<sup>79</sup> and ink formulation with respect to solvent and water content<sup>80</sup> (depicted in Fig. 3a). Current state-of-the-art catalysts are the result of carefully optimizing such structure–performance relationships. As demonstrated in Fig. 3b, these factors may yield up to 70–90 mV in additional cell voltage at high current densities; this would be equivalent to an order-of-magnitude improvement in ORR catalyst kinetics, illustrating the importance of transport resistance optimization at high current densities. At the same time, the corresponding change in ORR overpotential does not reliably reflect either magnitude or direction of the cell voltage gains at high current density. Mass activities, evaluated by either RDE or MEA measurements, are therefore insufficient proxies for high current density performance. We thus deem catalyst layer design guided by MEA testing indispensable for future breakthroughs in PEMFC power density.

## Conclusions

The widespread commercialization of PEMFCs and PEMWEs hinges in no small part on further advances in electrocatalyst development, achieving outstanding activity and durability with ever lower quantities of PGMs. Here, the ubiquitous use of the RDE technique to quickly characterize novel catalysts prepared from milligram amounts of material remains important in pre-selecting promising catalyst designs at scale, but catalysts must ultimately demonstrate their performance and durability in MEA testing, which very closely resembles the actual application. The projection of RDE-obtained results to MEA performance, however, often only applies to trends, but not absolute values. In certain instances, the RDE-based determination systematically leads to measurement artefacts instead of actual catalyst properties. This gap in transferability between both techniques poses a major obstacle towards the rapid integration of promising electrocatalyst designs into actual PEM systems.

In this Perspective, we have juxtaposed RDE and MEA set-ups and highlighted their fundamental differences. Key factors, such as the nature of the electrolyte, the local environment of the catalyst and the governing mode of mass transport, directly determine what can and cannot be reliably measured in an RDE set-up. We have provided a concise summary of RDE–MEA transferability and its limitations for the fundamental reactions of PEMFCs and PEMWEs in Table 1. Wherever possible, cross-validated testing protocols are recommended to the reader, but their awareness is also brought to fields of study where those protocols do not (yet) exist or even may never exist due to the fundamental limitations of the RDE. Here, researchers should consider integrating MEA testing into earlier stages of catalyst development. Where this remains unfeasible due to prohibitively high time and capital requirements, method development and standardized benchmarking of bridging techniques, such as FETs, MRDEs and GDEs, is a logical focal point for future research endeavours.

Received: 26 June 2021; Accepted: 24 March 2022;

Published online: 23 May 2022

## References

- Buttler, A. & Spliethoff, H. Current status of water electrolysis for energy storage, grid balancing and sector coupling via power-to-gas and power-to-liquids: a review. *Renew. Sustain. Energy Rev.* **82**, 2440–2454 (2018).
- Fan, J. et al. Bridging the gap between highly active oxygen reduction reaction catalysts and effective catalyst layers for proton exchange membrane fuel cells. *Nat. Energy* **6**, 475–486 (2021).
- Kodama, K., Nagai, T., Kuwaki, A., Jinnouchi, R. & Morimoto, Y. Challenges in applying highly active Pt-based nanostructured catalysts for oxygen reduction reactions to fuel cell vehicles. *Nat. Nanotechnol.* **16**, 140–147 (2021).
- Shinozaki, K., Zack, J. W., Richards, R. M., Pivovar, B. S. & Kocha, S. S. Oxygen reduction reaction measurements on platinum electrocatalysts utilizing rotating disk electrode technique: I. Impact of impurities, measurement protocols and applied corrections. *J. Electrochem. Soc.* **162**, F1144–F1158 (2015).
- Gasteiger, H. A., Panels, J. E. & Yan, S. G. Dependence of PEM fuel cell performance on catalyst loading. *J. Power Sources* **127**, 162–171 (2004).
- Schmidt, T. J. et al. Characterization of high-surface-area electrocatalysts using a rotating disk electrode configuration. *J. Electrochem. Soc.* **145**, 2354–2358 (1998).
- Wakabayashi, N., Takeichi, M., Itagaki, M., Uchida, H. & Watanabe, M. Temperature-dependence of oxygen reduction activity at a platinum electrode in an acidic electrolyte solution investigated with a channel flow double electrode. *J. Electroanal. Chem.* **574**, 339–346 (2005).
- Schröder, J. et al. The gas diffusion electrode setup as straightforward testing device for proton exchange membrane water electrolyzer catalysts. *JACS Au* **1**, 247–251 (2021).
- Ehelebe, K. et al. Evaluating electrocatalysts at relevant currents in a half-cell: the impact of Pt loading on oxygen reduction reaction. *J. Electrochem. Soc.* **166**, F1259–F1268 (2019).
- Gasteiger, H. A., Kocha, S. S., Somppalli, B. & Wagner, F. T. Activity benchmarks and requirements for Pt, Pt-alloy, and non-Pt oxygen reduction catalysts for PEMFCs. *Appl. Catal. B* **56**, 9–35 (2005).
- Bard, A. J. & Faulkner, L. R. *Electrochemical Methods: Fundamentals and Applications* Vol. 2 (Wiley, 2001).
- Garsany, Y., Ge, J., St-Pierre, J., Rocheleau, R. & Swider-Lyons, K. E. Analytical procedure for accurate comparison of rotating disk electrode results for the oxygen reduction activity of Pt/C. *J. Electrochem. Soc.* **161**, F628–F640 (2014).
- Kocha, S. S. et al. Best practices and testing protocols for benchmarking ORR activities of fuel cell electrocatalysts using rotating disk electrode. *Electrocatalysis* **8**, 366–374 (2017).
- Fathi Tovini, M., Hartig-Weiß, A., Gasteiger, H. A. & El-Sayed, H. A. The discrepancy in oxygen evolution reaction catalyst lifetime explained: RDE vs MEA - dynamics within the catalyst layer matters. *J. Electrochem. Soc.* **168**, 014512 (2021).
- Pan, L., Ott, S., Dionigi, F. & Strasser, P. Current challenges related to the deployment of shape-controlled Pt alloy oxygen reduction reaction nanocatalysts into low Pt-loaded cathode layers of proton exchange membrane fuel cells. *Curr. Opin. Electrochem.* **18**, 61–71 (2019).
- Jiang, J. & Kucernak, A. Investigations of fuel cell reactions at the composite microelectrode|solid polymer electrolyte interface. I. Hydrogen oxidation at the nanostructured Pt|Nafion<sup>®</sup> membrane interface. *J. Electroanal. Chem.* **567**, 123–137 (2004).
- Chen, S. & Kucernak, A. Electrocatalysis under conditions of high mass transport rate: oxygen reduction on single submicrometer-sized Pt particles supported on carbon. *J. Phys. Chem. B* **108**, 3262–3276 (2004).
- Zalitis, C. M., Kramer, D. & Kucernak, A. R. Electrocatalytic performance of fuel cell reactions at low catalyst loading and high mass transport. *Phys. Chem. Chem. Phys.* **15**, 4329–4340 (2013).
- Petzoldt, P. J., Kwan, J. T. H., Bonakdarpour, A. & Wilkinson, D. P. Deconvoluting reversible and irreversible degradation phenomena in OER catalyst coated membranes using a modified RDE technique. *J. Electrochem. Soc.* **168**, 026507 (2021).
- Martens, S. et al. A comparison of rotating disc electrode, floating electrode technique and membrane electrode assembly measurements for catalyst testing. *J. Power Sources* **392**, 274–284 (2018).
- Katsounaros, I. et al. The effective surface pH during reactions at the solid–liquid interface. *Electrochem. Commun.* **13**, 634–637 (2011).
- Okada, T., Möller-Holst, S., Gørseth, O. & Kjelstrup, S. Transport and equilibrium properties of Nafion<sup>®</sup> membranes with H<sup>+</sup> and Na<sup>+</sup> ions. *J. Electroanal. Chem.* **442**, 137–145 (1998).
- Ito, H., Maeda, T., Nakano, A. & Takenaka, H. Properties of Nafion membranes under PEM water electrolysis conditions. *Int. J. Hydrogen Energy* **36**, 10527–10540 (2011).
- Ehelebe, K., Escalera-López, D. & Cherevko, S. Limitations of aqueous model systems in the stability assessment of electrocatalysts for oxygen reactions in fuel cell and electrolyzers. *Curr. Opin. Electrochem.* **29**, 100832 (2021).
- Cheng, X. et al. A review of PEM hydrogen fuel cell contamination: impacts, mechanisms, and mitigation. *J. Power Sources* **165**, 739–756 (2007).
- Greszler, T. A., Moylan, T. E. & Gasteiger, H. A. in *Handbook of Fuel Cells: Fundamentals, Technology and Applications* Vol. 6: *Advances in Electrocatalysis, Materials, Diagnostics and Durability* (eds Vielstich, W. et al.) 729–748 (Wiley, 2009).
- Papadias, D. D. et al. Durability of Pt–Co alloy polymer electrolyte fuel cell cathode catalysts under accelerated stress tests. *J. Electrochem. Soc.* **165**, F3166–F3177 (2018).

28. Ahluwalia, R. K. et al. Durability of de-alloyed platinum-nickel cathode catalyst in low platinum loading membrane-electrode assemblies subjected to accelerated stress tests. *J. Electrochem. Soc.* **165**, F3316–F3327 (2018).
29. Durst, J., Chatenet, M. & Maillard, F. Impact of metal cations on the electrocatalytic properties of Pt/C nanoparticles at multiple phase interfaces. *Phys. Chem. Chem. Phys.* **14**, 13000–13009 (2012).
30. Jovanović, P. et al. New insight into platinum dissolution from nanoparticulate platinum-based electrocatalysts using highly sensitive in situ concentration measurements. *ChemCatChem* **6**, 449–453 (2014).
31. Ayers, K. et al. Perspectives on low-temperature electrolysis and potential for renewable hydrogen at scale. *Annu. Rev. Chem. Biomol. Eng.* **10**, 219–239 (2019).
32. Ohno, H. et al. Remarkable mass activities for the oxygen evolution reaction at iridium oxide nanocatalysts dispersed on tin oxides for polymer electrolyte membrane water electrolysis. *J. Electrochem. Soc.* **164**, F944–F947 (2017).
33. Hartig-Weiss, A. et al. Iridium oxide catalyst supported on antimony-doped tin oxide for high oxygen evolution reaction activity in acidic media. *ACS Appl. Nano Mater.* **3**, 2185–2196 (2020).
34. Alia, S. M. & Anderson, G. C. Iridium oxygen evolution activity and durability baselines in rotating disk electrode half-cells. *J. Electrochem. Soc.* **166**, F282–F294 (2019).
35. Bernt, M. et al. Current challenges in catalyst development for PEM water electrolyzers. *Chem. Ing. Tech.* **92**, 31–39 (2020).
36. Oakton, E. et al. IrO<sub>2</sub>-TiO<sub>2</sub>: a high-surface-area, active, and stable electrocatalyst for the oxygen evolution reaction. *ACS Catal.* **7**, 2346–2352 (2017).
37. Bernt, M. et al. Effect of the IrO<sub>x</sub> conductivity on the anode electrode/porous transport layer interfacial resistance in PEM water electrolyzers. *J. Electrochem. Soc.* **168**, 084513 (2021).
38. Geiger, S. et al. Catalyst stability benchmarking for the oxygen evolution reaction: the importance of backing electrode material and dissolution in accelerated aging studies. *ChemSusChem* **10**, 4140–4143 (2017).
39. Oh, H.-S. et al. Electrochemical catalyst-support effects and their stabilizing role for IrO<sub>x</sub> nanoparticle catalysts during the oxygen evolution reaction. *J. Am. Chem. Soc.* **138**, 12552–12563 (2016).
40. El-Sayed, H. A., Weiß, A., Olbrich, L. F., Putro, G. P. & Gasteiger, H. A. OER catalyst stability investigation using RDE technique: a stability measure or an artifact? *J. Electrochem. Soc.* **166**, F458–F464 (2019).
41. Knöppel, J. et al. On the limitations in assessing stability of oxygen evolution catalysts using aqueous model electrochemical cells. *Nat. Commun.* **12**, 2231 (2021).
42. Hartig-Weiss, A., Tovini, M. F., Gasteiger, H. A. & El-Sayed, H. A. OER catalyst durability tests using the rotating disk electrode technique: the reason why this leads to erroneous conclusions. *ACS Appl. Energy Mater.* **3**, 10323–10327 (2020).
43. Tan, X., Shen, J., Semagina, N. & Secanell, M. Decoupling structure-sensitive deactivation mechanisms of Ir/IrO<sub>x</sub> electrocatalysts toward oxygen evolution reaction. *J. Catal.* **371**, 57–70 (2019).
44. Zaltis, C. M., Sharman, J., Wright, E. & Kucernak, A. R. Properties of the hydrogen oxidation reaction on Pt/C catalysts at optimised high mass transport conditions and its relevance to the anode reaction in PEMFCs and cathode reactions in electrolyzers. *Electrochim. Acta* **176**, 763–776 (2015).
45. Durst, J., Simon, C., Hasché, F. & Gasteiger, H. A. Hydrogen oxidation and evolution reaction kinetics on carbon supported Pt, Ir, Rh, and Pd electrocatalysts in acidic media. *J. Electrochem. Soc.* **162**, F190–F203 (2015).
46. Bernt, M., Siebel, A. & Gasteiger, H. A. Analysis of voltage losses in PEM water electrolyzers with low platinum group metal loadings. *J. Electrochem. Soc.* **165**, F305–F314 (2018).
47. Sheng, W., Gasteiger, H. A. & Shao-Horn, Y. Hydrogen oxidation and evolution reaction kinetics on platinum: acid vs alkaline electrolytes. *J. Electrochem. Soc.* **157**, B1529 (2010).
48. Genorio, B. et al. Selective catalysts for the hydrogen oxidation and oxygen reduction reactions by patterning of platinum with calix[4]arene molecules. *Nat. Mater.* **9**, 998–1003 (2010).
49. Zheng, J., Yan, Y. & Xu, B. Correcting the hydrogen diffusion limitation in rotating disk electrode measurements of hydrogen evolution reaction kinetics. *J. Electrochem. Soc.* **162**, F1470–F1481 (2015).
50. Chen, Q. & Luo, L. Correlation between gas bubble formation and hydrogen evolution reaction kinetics at nanoelectrodes. *Langmuir* **34**, 4554–4559 (2018).
51. Saibi, R., Punathil Meethal, R. & Srinivasan, R. Mechanistic analysis of hydrogen evolution reaction on Pt in HClO<sub>4</sub> using inverted rotating disc electrode. *Electroanalysis* **32**, 2545–2554 (2020).
52. Elbert, K. et al. Elucidating hydrogen oxidation/evolution kinetics in base and acid by enhanced activities at the optimized Pt shell thickness on the Ru core. *ACS Catal.* **5**, 6764–6772 (2015).
53. Rheinländer, P. J., Herranz, J., Durst, J. & Gasteiger, H. A. Kinetics of the hydrogen oxidation/evolution reaction on polycrystalline platinum in alkaline electrolyte reaction order with respect to hydrogen pressure. *J. Electrochem. Soc.* **161**, F1448–F1457 (2014).
54. Zheng, J., Sheng, W., Zhuang, Z., Xu, B. & Yan, Y. Universal dependence of hydrogen oxidation and evolution reaction activity of platinum-group metals on pH and hydrogen binding energy. *Sci. Adv.* **2**, e1501602 (2016).
55. Stühmeier, B. M., Pietsch, M. R., Schwämmlein, J. N. & Gasteiger, H. A. Pressure and temperature dependence of the hydrogen oxidation and evolution reaction kinetics on Pt electrocatalysts via PEMFC-based hydrogen-pump measurements. *J. Electrochem. Soc.* **168**, 064516 (2021).
56. *Fuel Cell Technologies Program Multi-Year Research, Development, and Demonstration Plan—3.4 Fuel Cells* (US Department of Energy, 2017); <https://www.energy.gov/eere/fuelcells/downloads/hydrogen-and-fuel-cell-technologies-office-multi-year-research-development>
57. Asset, T. et al. A review on recent developments and prospects for the oxygen reduction reaction on hollow Pt-alloy nanoparticles. *ChemPhysChem* **19**, 1552–1567 (2018).
58. Zaman, S. et al. Oxygen reduction electrocatalysts toward practical fuel cells: progress and perspectives. *Angew. Chem. Int. Ed.* **60**, 2–23 (2021).
59. Ly, A., Asset, T. & Atanassov, P. Integrating nanostructured Pt-based electrocatalysts in proton exchange membrane fuel cells. *J. Power Sources* **478**, 228516 (2020).
60. Inaba, M. et al. Benchmarking high surface area electrocatalysts in a gas diffusion electrode: measurement of oxygen reduction activities under realistic conditions. *Energy Environ. Sci.* **11**, 988–994 (2018).
61. Mayrhofer, K. J. J. et al. Fuel cell catalyst degradation on the nanoscale. *Electrochem. Commun.* **10**, 1144–1147 (2008).
62. Meier, J. C. et al. Stability investigations of electrocatalysts on the nanoscale. *Energy Environ. Sci.* **5**, 9319–9330 (2012).
63. Hu, Y. et al. Revealing the genuine stability of the reference Pt/C electrocatalyst toward the ORR. *Electrochim. Acta* **391**, 138963 (2021).
64. Stariha, S. et al. Recent advances in catalyst accelerated stress tests for polymer electrolyte membrane fuel cells. *J. Electrochem. Soc.* **165**, F492–F501 (2018).
65. Riese, A., Banham, D., Ye, S. & Sun, X. Accelerated stress testing by rotating disk electrode for carbon corrosion in fuel cell catalyst supports. *J. Electrochem. Soc.* **162**, F783–F788 (2015).
66. Reiser, C. A. et al. A reverse-current decay mechanism for fuel cells. *Electrochem. Solid State Lett.* **8**, A273–A276 (2005).
67. Nagai, T., Murata, H. & Morimoto, Y. Influence of experimental conditions on the catalyst degradation in the durability test. *J. Electrochem. Soc.* **161**, F789–F794 (2014).
68. Schröder, J. et al. A new approach to probe the degradation of fuel cell catalysts under realistic conditions: combining tests in a gas diffusion electrode setup with small angle X-ray scattering. *J. Electrochem. Soc.* **167**, 134515 (2020).
69. Kneer, A. & Wagner, N. A semi-empirical catalyst degradation model based on voltage cycling under automotive operating conditions in PEM fuel cells. *J. Electrochem. Soc.* **166**, F120–F127 (2019).
70. Kongkanand, A. & Mathias, M. F. The priority and challenge of high-power performance of low-platinum proton-exchange membrane fuel cells. *J. Phys. Chem. Lett.* **7**, 1127–1137 (2016).
71. Gittleman, C. S., Kongkanand, A., Masten, D. & Gu, W. Materials research and development focus areas for low cost automotive proton-exchange membrane fuel cells. *Curr. Opin. Electrochem.* **18**, 81–89 (2019).
72. Baker, D. R., Caulk, D. A., Neyerlin, K. C. & Murphy, M. W. Measurement of oxygen transport resistance in PEM fuel cells by limiting current methods. *J. Electrochem. Soc.* **156**, B991 (2009).
73. Liu, Y. et al. Proton conduction and oxygen reduction kinetics in PEM fuel cell cathodes: effects of ionomer-to-carbon ratio and relative humidity. *J. Electrochem. Soc.* **156**, B970–B980 (2009).
74. Harzer, G. S., Orfanidi, A., El-Sayed, H., Madkikar, P. & Gasteiger, H. A. Tailoring catalyst morphology towards high performance for low Pt loaded PEMFC cathodes. *J. Electrochem. Soc.* **165**, F770–F779 (2018).
75. Owejan, J. P., Owejan, J. E. & Gu, W. Impact of platinum loading and catalyst layer structure on PEMFC performance. *J. Electrochem. Soc.* **160**, F824–F833 (2013).
76. Park, Y.-C., Tokiwa, H., Kakinuma, K., Watanabe, M. & Uchida, M. Effects of carbon supports on Pt distribution, ionomer coverage and cathode performance for polymer electrolyte fuel cells. *J. Power Sources* **315**, 179–191 (2016).
77. Yarlagadda, V. et al. Boosting fuel cell performance with accessible carbon mesopores. *ACS Energy Lett.* **3**, 618–621 (2018).
78. Lazaridis, T. & Gasteiger, H. A. Pt-catalyzed oxidation of PEMFC carbon supports: a path to highly accessible carbon morphologies and implications for start-up/shut-down degradation. *J. Electrochem. Soc.* **168**, 114517 (2021).

79. Ramaswamy, N. et al. Editors' choice—ionomer side chain length and equivalent weight impact on high current density transport resistances in PEMFC cathodes. *J. Electrochem. Soc.* **168**, 024518 (2021).
80. Orfanidi, A. et al. The key to high performance low Pt loaded electrodes. *J. Electrochem. Soc.* **164**, F418–F426 (2017).
81. Spöri, C., Kwan, J. T. H., Bonakdarpour, A., Wilkinson, D. P. & Strasser, P. The stability challenges of oxygen evolving catalysts: towards a common fundamental understanding and mitigation of catalyst degradation. *Angew. Chem. Int. Ed.* **56**, 5994–6021 (2017).
82. Ramaswamy, N., Gu, W., Ziegelbauer, J. M. & Kumaraguru, S. Carbon support microstructure impact on high current density transport resistances in PEMFC cathode. *J. Electrochem. Soc.* **167**, 064515 (2020).

### Acknowledgements

T.L. acknowledges funding from the Swiss National Foundation under the funding scheme Sinergia (project grant number 180335). B.M.S. acknowledges support by the Deutsche Forschungsgemeinschaft (DFG, German Research Foundation) under Germany's Excellence Strategy (EXC 2089/1–390776260). We thank our colleague P. Rapp for the graphic design of Fig. 1.

### Author contributions

All authors conceptualized the overall structure of this Perspective. T.L., B.M.S. and H.A.E.-S. co-wrote the manuscript, with T.L. and B.M.S. contributing the discussion of general aspects and the conclusion, H.A.E.-S. focusing on the OER section, B.M.S. drafting the HOR/HER section and T.L. discussing the ORR-specific aspects. All authors provided insights, contributed feedback and edited the manuscript.

### Competing interests

The authors declare no competing interests.

### Additional information

**Correspondence** should be addressed to Hany A. El-Sayed.

**Peer review information** *Nature Catalysis* thanks Jiujuun Zhang and the other, anonymous, reviewer(s) for their contribution to the peer review of this work.

**Reprints and permissions information** is available at [www.nature.com/reprints](http://www.nature.com/reprints).

**Publisher's note** Springer Nature remains neutral with regard to jurisdictional claims in published maps and institutional affiliations.

© Springer Nature Limited 2022

### 3.1.2. PEMFC-Based Hydrogen-Pump Measurements for the Investigation of the HOR/HER Kinetics

This section presents the article "Pressure and Temperature Dependence of the Hydrogen Oxidation and Evolution Reaction Kinetics on Pt Electrocatalysts via PEMFC-based Hydrogen Pump measurements" that was published in June 2021 in the *Journal of The Electrochemical Society*.<sup>25</sup> It is an open access article published under the terms of the Creative Commons Attribution 4.0 License (CC BY). The permanent web-link to the article is <https://doi.org/10.1149/1945-7111/ac099c>. Additionally, the paper was presented by Björn Stühmeier at the PRiME 2020 conference of *The Electrochemical Society* (October 4-9, 2020, Abstract number: 2337).<sup>161</sup>

In acidic environment, the HOR/HER on Pt electrocatalysts is extremely fast, with exchange current densities on the order of  $\approx 100 \text{ mA cm}_{\text{Pt}}^{-2}$ .<sup>25, 85, 141, 152, 162</sup> Consequently, the RDE technique cannot be used to accurately determine the kinetics of the HOR/HER on Pt catalysts due to mass transport limitations (see previous section). Thus, kinetic data can only be obtained with experimental setups that provide very fast mass transport, so that the effect of hydrogen partial pressure ( $p_{\text{H}_2}$ ) and kinetic limitations at high overpotentials are not yet fully understood. In this study, a new protocol is established to investigate the effect of temperature and pressure on the HOR/HER at low and high overpotentials, using a modification of earlier H<sub>2</sub>-pump measurement procedures by Neyerlin *et al.*<sup>152</sup> and Durst *et al.*<sup>85, 163</sup>

By employing a combination of galvanostatic and potentiostatic hold periods that include EIS measurements on ultra-low-loaded electrodes ( $\approx 1 - 2 \mu\text{g}_{\text{Pt}} \text{ cm}_{\text{MEA}}^{-2}$ ), it is possible to correct for changes in the HFR due to membrane dryout and to investigate an apparent limitation of the HOR currents ( $i_{\text{lim}}$ ) at high anodic overpotentials ( $> 100 \text{ mV}_{\text{RHE}}$ ). It is found that the HOR is heavily affected by this current limitation already at low currents ( $< 10\%$  of  $i_{\text{lim}}$ ). Especially at high temperatures and low  $p_{\text{H}_2}$ , the resulting Tafel-plots are highly asymmetric, i.e., Butler-Volmer fits with the sum of transfer coefficients fixed to one ( $\alpha_{\text{a}} + \alpha_{\text{c}} = 1$ ) for a Tafel-Volmer reaction mechanism<sup>164-166</sup> result in  $\alpha_{\text{a}} < 0.5$ . Analyzing a matrix of five temperatures (30 – 90 °C) and four partial pressures of hydrogen (100 – 450 kPa<sub>H<sub>2</sub></sub>), it is found that the apparent activation energy ( $E_{\text{A,app}}$ ) of the exchange current density increases with increasing pressure. In analogy to a Langmuir-Hinshelwood mechanism,<sup>167, 168</sup> this is

explained by a diminishing effect of the hydrogen adsorption enthalpy on the oxidation of adsorbed hydrogen atoms on the Pt surface with increasing coverage at high  $p_{\text{H}_2}$ . A direct consequence of this increase in apparent activation energy is that the reaction order with respect to  $p_{\text{H}_2}$  increases with higher temperatures as well. These results show that for PEMFC anodes with extremely low  $rf$  values, e.g., for severely aged electrodes, raising the  $\text{H}_2$  partial pressure could significantly reduce the expected HOR overpotentials, while an increase in the cell temperature has a diminishing effect on the electrode performance.

Another important aspect of the study is the investigation of the current limitation at high anodic overpotentials. We hypothesize that this limitation is either a shift of the rate-determining step to a limitation by the Tafel-reaction, i.e., the dissociative adsorption of hydrogen on the Pt-surface, or a mass transport limitation through the ionomer film that covers the Pt nanoparticles. It is found that  $i_{\text{lim}}$  is directly proportional to  $p_{\text{H}_2}$  and has a pressure independent activation energy of  $\approx 20 \text{ kJ mol}^{-1}$ . Unfortunately, both hypothesized origins for the observed HOR current limitation would yield the observed direct proportionality of  $i_{\text{lim}}$  and  $p_{\text{H}_2}$ ,<sup>167</sup> an activation energy in the range of  $17\text{--}20 \text{ kJ mol}^{-1}$ ,<sup>134,169</sup> and absolute currents on the same order of magnitude as measured in this study.<sup>134,145,170</sup> Therefore, it is currently impossible to determine which of the two mechanisms is responsible for the limiting current at high anodic overpotentials, but it seems likely that both affect the measurements to some extent.

### Author contributions

B.M.S. and M.R.P. performed the  $\text{H}_2$ -pump measurements and analyzed the data. J.N.S. started the study and did an initial parameter investigation. B.M.S. and H.A.G. wrote the manuscript. All authors discussed the results and commented on the manuscript.



# Pressure and Temperature Dependence of the Hydrogen Oxidation and Evolution Reaction Kinetics on Pt Electrocatalysts via PEMFC-based Hydrogen-Pump Measurements

Björn M. Stühmeier,<sup>\*,\*,z</sup>  Markus R. Pietsch,<sup>=</sup>  Jan N. Schwämmlein,<sup>\*</sup>  and Hubert A. Gasteiger<sup>\*\*</sup> 

Chair of Technical Electrochemistry, Department of Chemistry and Catalysis Research Center, Technical University of Munich, D-85748 Garching, Germany

The hydrogen oxidation and evolution reaction (HOR/HER) has been widely investigated due to its importance for a broad variety of applications especially in electrolysis and fuel cells. However, owing to its extremely fast kinetics, kinetic data can only be obtained with experimental setups that provide very fast mass transport, so that the effect of hydrogen partial pressure ( $p_{H_2}$ ) and kinetic limitations at high overpotentials are not yet fully understood. Here we report detailed kinetic investigations on the temperature and pressure dependence of the HOR/HER kinetics on carbon supported platinum (Pt/C) using the PEMFC-based  $H_2$ -pump approach. By using ultra-low platinum loadings, we could show that the apparent activation energy of the HOR/HER on platinum increases with increasing  $p_{H_2}$ , due to a diminishing effect of the hydrogen adsorption enthalpy with increasing coverage by adsorbed hydrogen atoms on the Pt surface. Consequently, the HOR/HER reaction order with respect to  $p_{H_2}$  also depends on the temperature. We further observed that the HOR reaches a limiting current at high HOR overpotentials that showed a direct proportionality to  $p_{H_2}$  and a pressure-independent activation energy. We ascribe this to a limitation of the hydrogen adsorption rate either by a rate limiting Tafel-reaction or mass transport limitations.

© 2021 The Author(s). Published on behalf of The Electrochemical Society by IOP Publishing Limited. This is an open access article distributed under the terms of the Creative Commons Attribution 4.0 License (CC BY, <http://creativecommons.org/licenses/by/4.0/>), which permits unrestricted reuse of the work in any medium, provided the original work is properly cited. [DOI: 10.1149/1945-7111/ac099c]



Manuscript submitted April 16, 2021; revised manuscript received June 2, 2021. Published June 23, 2021. This was paper 2337 presented during PRiME 2020, October 4–9, 2020.

Supplementary material for this article is available [online](#)

One of the main challenges of the transition to renewable energies is the development of efficient energy storage technologies at relatively low costs. Here, water electrolyzers (ELs) and hydrogen fuel cells (FCs) play a central role for the use of  $H_2$  as chemical energy storage.<sup>1–3</sup> The main performance limitation in both systems are the sluggish reactions at the oxygen electrode, i.e., the oxygen evolution reaction (OER) for electrolyzers and the oxygen reduction reaction (ORR) for fuel cells. This is especially the case for acidic systems based on proton exchange membranes (PEMs), where the hydrogen evolution reaction (HER) on the cathode of a PEMEL and the hydrogen oxidation reaction (HOR) on the anode of a PEMFC according to Eq. 1 are extremely fast.<sup>4–6</sup>

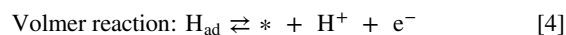
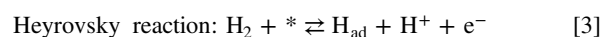
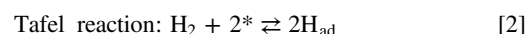


Consequently, only small amounts of Pt ( $\approx 0.025$ – $0.05 \text{ mg}_{Pt} \text{ cm}_{geo}^{-2}$ ) are required to limit the HOR/HER voltage loss contribution to only a few mV.<sup>1,6,7</sup> At such low Pt loadings, however, even a modest loss of electrochemically active surface area (ECSA) of the hydrogen catalysts due to cell-reversal and start-up and shut-down events can lead to a noticeable performance degradation.<sup>8,9</sup> Although the occurrence of these events can be reduced by system mitigation strategies,<sup>10,11</sup> a better understanding of the HOR/HER kinetics is essential for accurate durability predictions and the development of next generation system designs.

While the HOR/HER reaction rates on platinum and platinum alloy catalysts in alkaline environment can be determined precisely with rotating ring disk (RDE) measurements,<sup>12–14</sup> this is not possible at low pH due to the two orders of magnitude higher reaction rates that by far exceed the slow mass transport limited currents afforded by the RDE configuration.<sup>15–17</sup> In recent years, new experimental approaches have been developed, which allow for fast transport of hydrogen to the catalyst, thereby enabling kinetic investigations at

low pH as well.<sup>4,5,15,17–22</sup> Although a change in the hydrogen binding energy (HBE) could therefore be identified as one reason for the decrease in HOR/HER activity with pH,<sup>14,23</sup> these studies have highlighted an overall lack of fundamental understanding at the mechanistic level of the HOR/HER, especially at high overpotentials.

From a mechanistic point of view, Eq. 1 can be divided in a series of two of the following elementary steps, where a surface adsorption site (\*) is required for hydrogen adsorption.<sup>24</sup>



In order to unveil the overall reaction mechanism, it is necessary to determine the electrochemical reaction parameters, i.e., the exchange current density  $i_0$  (in  $A \text{ cm}_{Pt}^{-2}$ ), its activation energy  $E_A$  (in  $\text{kJ mol}^{-1}$ ), the anodic and cathodic transfer coefficients  $\alpha_{a/c}$  or the Tafel slopes in  $\text{mV decade}^{-1}$ , respectively, and the reaction order with regards to the hydrogen partial pressure. Knowing these parameters would allow to determine which set of the above listed reactions establish the HOR/HER equilibrium, which of these reactions constitutes the rate determining step (RDS), and how the reaction mechanism might change with overpotential.<sup>24,25</sup>

Many studies in the literature have shown that close to the equilibrium potential, the HOR/HER kinetics can be described by the Butler-Volmer equation,<sup>4,13,15,17,21,26,27</sup> which therefore is commonly used to describe the potential dependence of the HOR/HER kinetics:<sup>24,28</sup>

$$\text{Butler – Volmer kinetics: } i_{\text{spec}} = i_0 \left( e^{\frac{\alpha_a F \eta}{RT}} - e^{-\frac{\alpha_c F \eta}{RT}} \right) \quad [5]$$

with  $i_{\text{spec}}$  being the Pt surface specific current density (in  $A \text{ cm}_{Pt}^{-2}$ ),  $i_0$  the exchange current density (in  $A \text{ cm}_{Pt}^{-2}$ ),  $\alpha_a/\alpha_c$  the anodic/cathodic transfer coefficients,  $\eta$  the overpotential (in V), i.e., the difference between the electrode potential and the equilibrium

<sup>=</sup>These authors contributed equally to this work.

<sup>\*</sup>Electrochemical Society Student Member.

<sup>\*\*</sup>Electrochemical Society Fellow.

<sup>z</sup>E-mail: [bjorn.stuehmeier@tum.de](mailto:bjorn.stuehmeier@tum.de)

potential,  $F$  the Faraday constant ( $96,484 \text{ A s mol}^{-1}$ ),  $R$  the universal gas constant ( $8.314 \text{ kJ mol}^{-1} \text{ K}^{-1}$ ), and  $T$  the temperature (in K). To a first approximation, a Tafel-Volmer (TV) reaction pathway with a rate determining Volmer-step would result in a sum of the anodic and cathodic transfer coefficients of one ( $\alpha_a + \alpha_c = 1$ ), while the Heyrovsky-Volmer (HV) mechanism would yield  $\alpha_a + \alpha_c = 2$  (independent on whether Volmer or Heyrovsky are the RDS, as long as the RDS is the same for the forward and backward reaction).<sup>29,30</sup> However, a more rigorous analysis of the HV mechanism shows that it does not strictly follow Butler-Volmer kinetics. Instead, the sum of transfer coefficients changes from two to unity at higher overpotentials with the exact occurrence of this transition strongly depending on the equilibrium hydrogen coverage of the catalyst and the relative rates of the elementary steps, so that the initial state might not even be observed.<sup>25,28</sup>

While the HOR/HER mechanism has been excessively investigated for decades, many older and even some recent studies on the predominant mechanism of the HOR/HER in acid have erroneously relied on kinetic parameters from RDE measurements,<sup>31–37</sup> which have been shown to be mainly affected by  $\text{H}_2$  mass transport rates.<sup>15,16,22</sup> The validity of these earlier studies regarding a mechanistic understanding is therefore to be questioned. Most commonly, HOR/HER kinetic studies based on experimental approaches that allow for fast mass transport, a TV (Tafel-Volmer) mechanism was used for the description of the HOR/HER kinetics,<sup>4,14,15,17,18,23,38</sup> while a predominant HV (Heyrovsky-Volmer) mechanism was proposed by Zalitis et al.<sup>5</sup> With increasing overpotentials, however, the HOR/HER currents have been reported to deviate from the Butler-Volmer behavior and to reach a limiting current even under experimental conditions that allow for fast mass transport; in these cases, the appearance of a limiting current has been explained by a transition from a TV to a HV mechanism at high anodic overpotentials,<sup>25,39</sup> by a transition to a rate determining Tafel-step,<sup>15,18,38</sup> or by active site blocking.<sup>20</sup>

In this study, we report detailed kinetic investigations on the temperature and pressure dependence of the HOR/HER kinetics on a Pt/C catalyst using the  $\text{H}_2$ -pump approach. After discussing the observed differences in the measured HOR/HER currents between a dynamic measurement approach (i.e., cyclic voltammetric scans), and a static measurement approach (i.e., galvanostatic or potentiostatic conditions),  $i_0$ -values are extracted for a broad matrix of temperatures and  $\text{H}_2$  partial pressures in order to determine the  $\text{H}_2$  partial pressure ( $p_{\text{H}_2}$ ) dependent activation energies and the temperature dependent reaction orders with respect to  $p_{\text{H}_2}$ . These findings will be critically discussed with respect to the underlying reaction mechanism and the involved elementary steps. Furthermore, the extensive set of data will be used for a detailed investigation of the limiting current for the HOR at high overpotentials. Thus, the activation energy and the pressure dependence of this limiting current will be determined, followed by a critical discussion of the implications to the reaction mechanism or possible mass transport limitations.

## Experimental

**Hardware and experimental setup.**—All hydrogen-pump measurements were performed on a customized G60 test station (Greenlight Innovation Corp., USA) modified to feature pure  $\text{H}_2$  instead of air/ $\text{O}_2$  on the cathode side; the normally present connection to a CO containing gas line for CO stripping analysis was removed in order to eliminate the risk of unintended CO poisoning (CO stripping analysis was thus conducted on a different test station). The current range of the potentiostat (Reference 3000, Gamry Instruments, USA) was extended by a booster (Reference 30 K Booster, Gamry Instruments, USA). All measurements were carried out with a  $5 \text{ cm}^2$  active area single-cell hardware, using commercial graphite flow fields (7 parallel channels, one serpentine, 0.5 mm lands/channels; manufactured by Poco Graphite, Entegris GmbH, Germany, according to our design<sup>40</sup>). Gas diffusion layers

(GDLs) were the same in all experiments (H14C10, Freudenberg KG, Germany) and the GDL compression was adjusted to  $13 \pm 0.5\%$  by quasi-incompressible, PTFE-coated fiberglass gaskets (Fiberflon, Fiberflon GmbH & Co. KG, Germany), assembled at a torque of 12 Nm resulting in a contact pressure of  $\approx 1.5 \text{ MPa}$  on the active area (for details see Simon et al.<sup>41</sup>).

**Membrane electrode assembly (MEA) preparation.**—MEAs were prepared by the decal transfer method, using Vulcan carbon supported platinum catalysts (Pt/C), namely 4.8wt.% Pt/C (TEC10V50E, Tanaka, Japan) for the working electrode (WE) and 45.6wt.% Pt/C (TEC10V50E, Tanaka) for the counter electrode (CE). For the catalyst inks, a defined amount of catalyst was mixed with 1-propanol, ultrapure water, and ionomer solution (Asahi Kasei, Japan, 700 equivalent weight). The water concentration of the ink was 7wt.% (WE) or 16wt.% (CE), while the catalyst content was 0.02 (WE) or 0.04  $\text{g}_{\text{cat}} \text{ ml}_{\text{ink}}^{-1}$  (CE), respectively. The ionomer/carbon (I/C) ratio was fixed to 0.65  $\text{g}_I \text{ g}_C^{-1}$  for all electrodes. The inks were mixed by placing the bottles onto a roller mill at 60 rpm for 18 h at 25 °C. Then, the Mayer rod technique (coating machine: K Control Coater, RK PrintCoat Instruments Ltd, England) with the appropriate bar size was used to achieve loadings of  $\approx 1.2\text{--}1.6 \mu\text{g}_{\text{Pt}} \text{ cm}^{-2}_{\text{MEA}}$  (WE) and  $400 \pm 10 \mu\text{g}_{\text{Pt}} \text{ cm}^{-2}_{\text{MEA}}$  (CE) on virgin PTFE decals. The unsymmetrical MEAs were fabricated by hotpressing the air dried decals onto a 12  $\mu\text{m}$  membrane (Asahi Kasei Corp., Japan) at 155 °C for 3 min with an applied pressure of 0.11  $\text{kN cm}^{-2}$ . The platinum loadings were determined by weighing the decals before and after the catalyst layer transfer using a high-precision balance (XPE105, METTLER TOLEDO, USA); owing to the rather small mass of the deposited catalyst layer for the  $\approx 1.2\text{--}1.6 \mu\text{g}_{\text{Pt}} \text{ cm}^{-2}_{\text{MEA}}$  working electrode ( $\approx 0.21\text{--}0.27 \text{ mg}$  electrode coating for the  $5 \text{ cm}^2$  active area), the error for the quantification of the Pt loading of working electrode is estimated to be on the order of  $\pm 10\%$ . This, however, does not impact the precision of the determined exchange current densities, since these are referenced to the electrochemically active surface area (ECSA) obtained by CO stripping voltammetry (see below). The thickness of the working electrodes ranges between  $\approx 0.5\text{--}0.7 \mu\text{m}$ , based on the correlations given by Harzer et al.<sup>42</sup>

**$\text{H}_2$ -pump measurement procedure.**—In the  $\text{H}_2$ -pump experiments, the electrode with the very low Pt loadings ( $\approx 1.2\text{--}1.6 \mu\text{g}_{\text{Pt}} \text{ cm}^{-2}_{\text{MEA}}$ ) served as working electrode, while the electrode with the high Pt loadings ( $\approx 400 \mu\text{g}_{\text{Pt}} \text{ cm}^{-2}_{\text{MEA}}$ ) served both as counter electrode and as reference electrode (due to the high Pt loadings, the maximum overpotential of the working electrode at each pressure/temperature condition is estimated to be  $\approx 2 \text{ mV}$  at the highest current density). Thus, the working electrode potential is essentially at 0 V vs the reversible hydrogen electrode (RHE) potential at the given  $\text{H}_2$  partial pressure, with a maximum error of  $\approx 2 \text{ mV}$  at the highest current density. Prior to any kinetic measurements, each cell was conditioned to activate the catalyst. Due to the extremely low loading of the WE, a standard conditioning in an  $\text{H}_2$ /air setup did not lead to a stable performance. Instead, a voltage-controlled ramp-in procedure in a  $\text{H}_2/\text{H}_2$  setup (80 °C, 90% relative humidity (RH), flow rates of 2000/2000 nccm at a  $\text{H}_2$  partial pressure of 450/450  $\text{kPa}_{\text{H}_2}$ ) was used, polarizing the working electrode to the following potentials:  $+0.35 V_{\text{RHE}}$  for 20 min,  $+0.75 V_{\text{RHE}}$  for 5 min, 5 min at open circuit voltage (OCV),  $-0.2 V_{\text{RHE}}$  for 10 min, and finally again 5 min at OCV. This sequence was repeated 10 times until a constant performance was reached.

The HOR/HER kinetic measurements were then performed at each combination of temperature (30 °C, 40 °C, 60 °C, 80 °C, and 90 °C) and partial pressure of  $\text{H}_2$  (100 °C, 200 °C, 300 °C, and 450  $\text{kPa}_{\text{H}_2}$ ) in  $\text{H}_2/\text{H}_2$  (2000/2000 nccm) configuration at 90% RH (note that cell pressure is controlled to a value corresponding to the sum of the  $\text{H}_2$  partial pressure and the  $\text{H}_2\text{O}$  partial pressure calculated for 90% RH at a given temperature). At each condition, cyclic voltammograms (CVs) were recorded between  $-0.3 V_{\text{RHE}}$  and  $0.6 V_{\text{RHE}}$  at scan rates of  $100 \text{ mV s}^{-1}$  (20 cycles) and  $5 \text{ mV s}^{-1}$

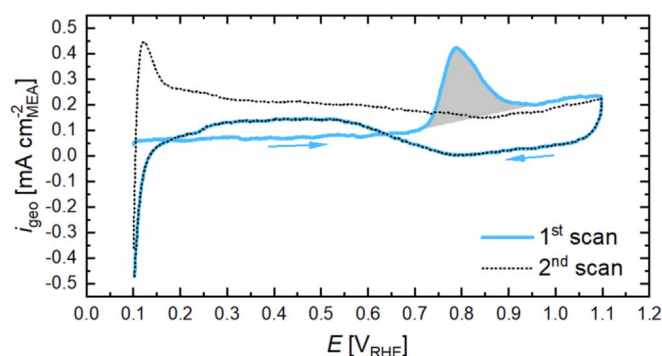


**Figure 1.** CO stripping voltammogram (blue solid line, arrows indicating the scan direction) and subsequent CV (black dotted line) of the Pt/C working electrode ( $1.4 \mu\text{g}_{\text{Pt}} \text{cm}_{\text{MEA}}^{-2}$ ) recorded after the HOR/HER kinetic measurements at a scan rate of  $50 \text{ mV s}^{-1}$  from 0.1 to 1.1  $V_{\text{RHE}}$  at 150  $\text{kPa}_{\text{abs}}$  and 40 °C (constant flows of 200 nccm 5%  $\text{H}_2/\text{Ar}$  on the CE and 5 nccm  $\text{N}_2$  on the WE). CO was adsorbed for 10 min at 0.1  $V_{\text{RHE}}$  at a flow of 10%  $\text{CO}/\text{N}_2$  (100 nccm) prior to the CV, followed by a 2 h purging procedure with  $\text{N}_2$  while maintaining the potential at 0.1  $V_{\text{RHE}}$ . To obtain the ECSA, the CO stripping current was integrated using a linear baseline (grey area) and converted to a corresponding Pt surface area using a specific capacity of  $420 \mu\text{C cm}_{\text{Pt}}^{-2}$ .

(3 cycles), followed by a galvanostatic electrochemical impedance spectroscopy (EIS) measurement at OCV with a  $2 \text{ mA cm}_{\text{MEA}}^{-2}$  AC current perturbation between 500 kHz and 1 Hz (10 points per decade) to determine the high frequency resistance (HFR; in  $\text{m}\Omega \text{ cm}_{\text{MEA}}^{-2}$ ). The HFR was used to correct the  $\text{H}_2$ -pump cell potential ( $E_{\text{cell}}$ ) for the Ohmic drop in order to obtain the  $i\text{R}$ -free cell voltage ( $E_{i\text{R-free}}$ ) that corresponds to the working electrode potential on the RHE potential scale at the given  $\text{H}_2$  partial pressure:

$$E_{i\text{R-free}} = E_{\text{cell}} - i \cdot \text{HFR} \quad [6]$$

Here,  $i$  is the geometric current density (in  $\text{A cm}_{\text{MEA}}^{-2}$ ), which is positive for the HOR and negative for the HER on the working electrode. These potentiodynamic measurements were followed by a set of galvanostatic and potentiostatic measurements. For galvanostatic measurements, a DC current was drawn for 60 s and the resulting potential response was averaged over the last 10 s; this was followed by an EIS measurement at the same current, with a current amplitude of 10% of the DC current (from 500 kHz to 1 Hz, with 10 points per decade). These measurements were performed for currents between  $\pm 0.0117 \text{ A cm}_{\text{MEA}}^{-2}$  and  $\pm 0.074 \text{ A cm}_{\text{MEA}}^{-2}$  in ascending order (4 different DC current values) by alternating between anodic and the corresponding cathodic current in order to precisely determine the reversible potential at each condition.

Following these galvanostatic measurements, potentiostatic measurements were conducted in the analogous manner by applying a given potential for 60 s and averaging the resulting current during the last 10 s, followed by a potentiostatic EIS at the same potential using a potential amplitude of 1% of the DC potential (from 500 kHz to 1 Hz, with 10 points per decade). The potentiostatic testing was performed for potentials between  $\pm 5 \text{ mV}$  and  $\pm 450 \text{ mV}$  (cathodic potentials only until  $-200 \text{ mV}$ ) in ascending order and alternating between anodic and equal cathodic potentials. After each data point (static hold plus EIS), a relaxation step of 5 or 60 s (after potentials exceeding  $\pm 0.1 \text{ V}$ ) at OCV was implemented to ensure steady-state conditions for the next point. Due to the limitations of the potentiostat, data exceeding a total current of  $>30 \text{ A}$  (corresponding to  $>6 \text{ A cm}_{\text{MEA}}^{-2}$ ) could not be recorded.

All measurements were conducted for five MEAs. The HOR/HER curves were evaluated for each MEA and each condition individually before averaging the obtained values over all MEAs (error bars represent the standard derivation). Slopes represent an error-weighted fit of the averaged data.

#### Surface area determination by CO stripping voltammetry.—

Due to the extremely low loadings, the voltammetric hydrogen under potential deposition ( $\text{H}_{\text{upd}}$ ) currents are severely overlapped by the onset of the HER and by hydrogen crossover induced HOR. Thus, the electrochemically active surface area (ECSA) was determined by CO stripping voltammetry that was performed after all kinetic measurements had been completed on a second G60 test station (Greenlight Innovation Corp., USA) to avoid CO poisoning during the  $\text{H}_2$ -pump measurements (see above). CO stripping was done according to a previously reported procedure<sup>42</sup> by adsorbing CO (using 10%  $\text{CO}$  in  $\text{N}_2$ , 100 nccm) for 10 min at 40 °C and 150  $\text{kPa}_{\text{abs}}$  while maintaining the cathode potential at 0.1  $V_{\text{RHE}}$  referenced to a nominal hydrogen partial pressure of 100  $\text{kPa}_{\text{abs}}$ . Subsequently, residual CO was removed from the cell and the gas lines by purging with nitrogen for  $\approx 2 \text{ h}$ . A CV from the CO adsorption potential to 1.1  $V_{\text{RHE}}$  at a scan rate of  $50 \text{ mV s}^{-1}$  was performed to oxidize the adsorbed CO. Two additional sweeps were recorded to verify the full oxidation and removal of CO from the electrode and the gas feed system. At the extremely low loadings used in this study, the hydrogen crossover current of  $\approx 0.18 \text{ mA cm}_{\text{MEA}}^{-2}$  severely distorts the CV shape, whereby the deactivation of the catalyst for the HOR occurs in the CO stripping region (above 0.7  $V_{\text{RHE}}$ ). Since CO poisoning prevents the oxidation of crossover hydrogen,<sup>37</sup> the conventional method of subtracting the subsequent CV as the baseline would lead to an underestimation of the ECSA due to HOR current being subtracted from CO oxidation current (overlapping grey area in Fig. 1). Instead, the ECSA was determined by integrating the area of the first anodic scan with a linear baseline rather than using a baseline based on the subsequent CV, using a specific charge of  $420 \mu\text{C cm}_{\text{Pt}}^{-2}$  (Fig. 1). The thus obtained Pt surface area of the low-loaded  $5 \text{ cm}^2$  active area electrodes falls within the range of  $7.0 \pm 1.5 \text{ cm}_{\text{Pt}}^2$ , corresponding to a so-called roughness factor ( $rf$ ) within the range of  $1.4 \pm 0.3 \text{ cm}_{\text{Pt}}^2 \text{ cm}_{\text{MEA}}^{-2}$ . Based on the Pt loading determined by weight measurements (ranging from 1.2–1.6  $\mu\text{g}_{\text{Pt}} \text{ cm}_{\text{MEA}}^{-2}$ ) and the  $rf$  value for each of the working electrodes, the ECSA of the 4.8wt.% Pt/C catalyst of the WE equates to  $104 \pm 10 \text{ m}^2 \text{ g}_{\text{Pt}}^{-1}$ ; this is in excellent agreement with the ECSA of  $104 \pm 1 \text{ m}^2 \text{ g}_{\text{Pt}}^{-1}$  obtained for the same catalyst using electrodes with a higher and therefore more precisely quantifiable loading of  $15 \mu\text{g}_{\text{Pt}} \text{ cm}_{\text{MEA}}^{-2}$ , validating the accuracy of the electrode weight measurements. In comparison, the roughness factor of the high-loaded counter electrodes is more than two orders of magnitude higher ( $\approx 240 \pm 30 \text{ cm}_{\text{Pt}}^2 \text{ cm}_{\text{MEA}}^{-2}$ ) compared to that of the low-loaded working electrodes.

## Results

#### $\text{H}_2$ -pump measurements.—

In principle, kinetic data of electrochemical reactions can be determined either by potentiodynamic measurements, i.e., cyclic voltammetry (CV) or linear sweep voltammetry, or by steady-state measurements, i.e., potentiostatically or galvanostatically measured polarization curves. The former is most commonly done using RDE or micro-electrode measurements, where the effect of ohmic resistances and mass transport limitations is either constant throughout the measurement or very well defined. The latter is most commonly done using fuel cell measurements, where high current densities often lead to time dependent effects like membrane drying or pore flooding. For reactions with very fast kinetics like the HOR/HER on Pt, the mass transport resistance in the RDE configuration is generally too high to extract kinetic information from the data,<sup>4,15,16</sup> and the so-called  $\text{H}_2$ -pump configuration (a PEM fuel cell with  $\text{H}_2$  fed to both electrodes) in combination with ultra-low catalyst loadings on the working electrode has been used, as it offers 3–4 orders of magnitude faster mass transport rates compared to the RDE configuration.<sup>4,15</sup> In previous studies evaluating the HOR/HER kinetics of Pt based catalysts using the  $\text{H}_2$ -pump configuration or other measurement techniques that offer fast mass transport rates,

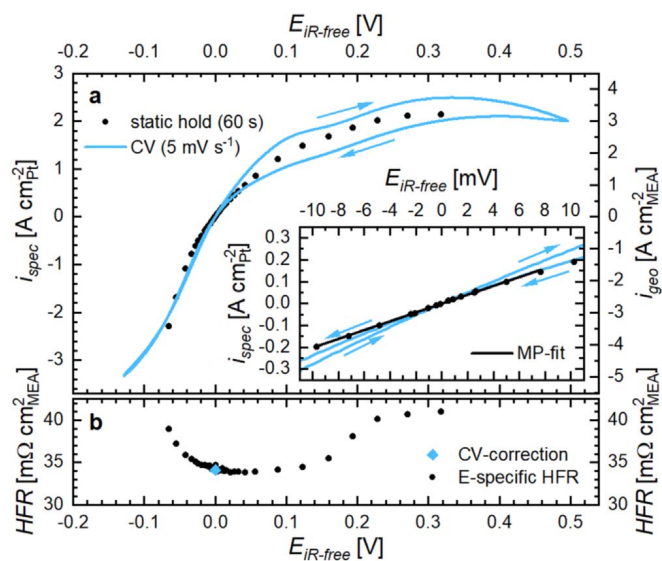


**Figure 2.** Representative hydrogen oxidation and evolution polarization curves on a Pt/C working electrode ( $1.4 \mu\text{g}_{\text{Pt}} \text{cm}_{\text{MEA}}^{-2}$ ;  $r_f = 1.5 \text{ cm}_{\text{Pt}}^2 \text{cm}_{\text{MEA}}^{-2}$ ) in a  $\text{H}_2$ -pump configuration at  $80^\circ\text{C}$ ,  $100 \text{ kPa}_{\text{H}_2}$ ,  $90\% \text{ RH}$ , and  $2000/2000 \text{ nccm H}_2$ . (a) Specific current densities (left-hand y-axis) and geometric current densities (right-hand y-axis) vs  $E_{iR\text{-free}}$  (see Eq. 6) recorded by cyclic voltammetry at  $5 \text{ mV s}^{-1}$  (blue solid lines) and by galvanostatic/potentiostatic measurements (black symbols, averaged over the last 10 s of a 60 s hold period), alternating between anodic and cathodic polarization (see Experimental section). The inset shows the micropolarization region ( $E_{iR\text{-free}} = \pm 10 \text{ mV}$ ) and a corresponding linear fit for the galvanostatic/potentiostatic measurements according to Eq. 9. (b) Corresponding HFRs used for the  $iR$ -correction of the cell potential, recorded at OCV (i.e., at 0 V) for the CV based measurement (blue diamond) and at each data point for the galvanostatic/potentiostatic measurements (black circles). The Pt/C counter electrode Pt loading was  $\approx 400 \mu\text{g}_{\text{Pt}} \text{cm}_{\text{MEA}}^{-2}$ .

both the dynamic<sup>5,15,17,20,26</sup> and the steady-state approach<sup>4,21</sup> have been used. Here, both approaches have been examined, namely CVs recorded at  $5 \text{ mV s}^{-1}$  as well as a combination of galvanostatic and potentiostatic measurements (Fig. 2).

As mentioned previously, the HOR/HER consists of a series of two of the three elementary steps shown in Eqs. 2–4. Thus, the possible reaction pathways are: (i) a Tafel-Volmer mechanism (TV), meaning a dissociative adsorption of hydrogen onto the platinum surface of the catalyst (Tafel reaction), followed by an electrochemical oxidation of the adsorbed hydrogen species (Volmer reaction); (ii) a Heyrovsky-Volmer mechanism (HV), meaning a partially oxidative adsorption of hydrogen (Heyrovsky reaction), again followed by the oxidation of the adsorbed hydrogen species (Volmer reaction); or, (iii) a combination of TV and HV. While a Tafel-Heyrovsky mechanism (TH) is conceivable, it has been argued to play no significant role.<sup>25</sup> The overall reaction rate for both the TV and the HV reaction sequences is generally assumed to follow a Butler-Volmer kinetics expression (see Eq. 5) at low HOR/HER overpotentials, i.e., close to the equilibrium potential.

Thus, an exponential relationship between the HOR/HER current density and overpotential for the anodic/cathodic branches at high overpotentials is expected. The potentiodynamic measurement (blue line in Fig. 2a), which was corrected for the HFR at OCV according to Eq. 6, clearly deviates from this behavior, as a distinct flattening of the current density vs overpotential curve could be observed at anodic/cathodic overpotentials exceeding an absolute value of  $\approx 50 \text{ mV}$ . On the anodic side, this flattening is much more pronounced than on the cathodic side, expressed by a rather constant limiting current plateau of  $\approx 3\text{--}4 \text{ A cm}_{\text{MEA}}^{-2}$  (see right-hand y-axis in Fig. 2) at high anodic overpotentials of  $\approx 250\text{--}500 \text{ mV}$ . The origin of this limiting current density could be ascribed to two different possible reasons: The first one would be a mass transport limitation

of the hydrogen reactant to the electrode, leading to a diffusion-limited current density, analogous to what is observed in RDE measurements.<sup>43</sup> However, in the here used  $\text{H}_2$ -pump configuration recorded under differential-flow conditions (at  $4 \text{ A cm}_{\text{MEA}}^{-2}$ , the supplied  $\text{H}_2$  flow of  $2000 \text{ nccm}$  corresponds to a  $\approx 14$ -fold  $\text{H}_2$  excess) with a  $\text{H}_2$  partial pressure of  $100 \text{ kPa}$ , the diffusion limited current density through the GDL and the electrode is at least an order of magnitude higher than the observed  $\approx 3\text{--}4 \text{ A cm}_{\text{MEA}}^{-2}$ . The second and at first glance more probable reason would then be a change of the rate determining step (RDS) in the HOR kinetics. This could, for example, be a switch of the RDS from a Volmer-step to either a Heyrovsky-step (in a HV mechanism) or a Tafel-step (in a TV mechanism). Considering that the current density seems to reach a rather potential-independent plateau at high anodic overpotentials,<sup>15</sup> it is more likely that here the Tafel-step becomes rate limiting (as proposed previously), as it is—other than the Heyrovsky-step—a completely potential independent adsorption process. The nature of this current limitation will be discussed in detail below.

In addition to the obvious current limitation in the HOR branch, the potentiodynamic data show a significant hysteresis between the anodic and cathodic scan direction. Although most obvious at high anodic overpotentials, this hysteresis can already be observed for small overpotentials in the micropolarization (MP) region, i.e., at small overpotentials between  $\pm 10 \text{ mV}$  (inset in Fig. 2a), resulting in slightly different slopes between the anodic-going and the cathodic-going scans. This hysteresis has already been reported in previous publications,<sup>5,15</sup> yet its origin is unclear. Due to the dependency on scan direction and scan rate (data not shown), the hysteresis is most likely caused by time and/or potential dependent effects, which could include significant dryout of the membrane over the course of the CV, differences in the local MEA temperature evolving at high current densities and high overpotentials (thus depending on the scan direction), and/or a hysteresis in anion adsorption or hydrogen coverage.<sup>5</sup>

In order to determine whether the observed difference between anodic and cathodic scans is a time dependent effect, the HOR/HER kinetics were also measured using steady-state polarization experiments. Here, a series of galvanostatic holds at low current densities (i.e., at low overpotentials) and potentiostatic holds at overpotentials of  $\geq +5 \text{ mV}$  or  $\leq -5 \text{ mV}$  were applied for 60 s hold periods (averaging the resulting potential or current over the last 10 s), whereby anodic and cathodic currents/potentials were applied in an alternating fashion (see Experimental section). This approach allowed for an equilibration of the potential/current response and of the local MEA temperature at any given current/potential and, more importantly, made it possible to determine the HFR at the end of each current/potential hold, thus resulting in a more accurate estimation of the actual HOR/HER overpotential ( $\eta$ ) via Eq. 7 (note that this is not possible for the above discussed potentiodynamic scans):

$$\eta = E_{iR\text{-free}}(E) = E_{\text{cell}} - i \cdot \text{HFR}(E) \quad [7]$$

The thus acquired current densities as well as the HFR vs  $\eta$  (i.e., vs  $E_{iR\text{-free}}$ ) are shown by the black circles in Figs. 2a and 2b, respectively. Note that previous studies have corrected the potential additionally for the effective proton sheet resistance ( $R_{\text{H}^+}^{\text{effective}}$ ; in  $\text{m}\Omega \text{ cm}_{\text{MEA}}^2$ ) via Eq. 8:<sup>4,15,44</sup>

$$R_{\text{H}^+}^{\text{effective}} = \frac{R_{\text{sheet}}}{3} = \frac{\delta_{\text{cl}}}{3 \cdot \sigma_{\text{H}^+} \cdot \varepsilon_i} \quad [8]$$

where the electrode's proton sheet resistance ( $R_{\text{sheet}}$ ) is estimated from the RH and temperature-dependent ionomer conductivity ( $\sigma_{\text{H}^+}$ , in  $\text{S cm}^{-1}$ ), the electrode's ionomer volume fraction ( $\varepsilon_i$ ), and the electrode thickness ( $\delta_{\text{cl}}$ , in cm). For the low-EW ionomer used in this study, with  $\sigma_{\text{H}^+} \approx 0.3 \text{ S cm}^{-1}$  at  $80^\circ\text{C}$  and  $100\% \text{ RH}$ ,<sup>45</sup> an effective proton sheet resistance of only  $\approx 0.3 \text{ m}\Omega \text{ cm}_{\text{MEA}}^2$  is obtained for the

low-Pt-loaded working with a thickness of  $\approx 0.5 \mu\text{m}$  ( $\varepsilon_i = 0.2$ ).<sup>4</sup> Since this would result in an error of only  $\approx 2 \text{ mV}$  at the highest current densities and is much smaller than the observed variation in the HFR measurements, the contribution of  $R_{\text{H}^+}^{\text{effective}}$  was neglected in this study.

Regarding the current density vs overpotential response, the same current limitation of the HOR at high overpotentials could be observed for this galvanostatic/potentiostatic experiment (black symbols in Fig. 2a) as in the potentiodynamic experiments (blue line). While the galvanostatic/potentiostatic data followed the cathodic branch at least in the micropolarization region (see inset in Fig. 2a), they started to deviate for higher positive overpotentials, resulting in a current density vs overpotential response that lies in between the potentiodynamic response of for anodic and cathodic scans. Despite the alternating anodic/cathodic polarization in the galvanostatic/potentiostatic approach, a smooth current density vs overpotential response was obtained, suggesting that the hysteresis in the potentiodynamic measurements is most likely due to time dependent effects (i.e., due to insufficient equilibration time at each potential). While the HFR at 0 V is the same for both measurement approaches (see Fig. 2b), the HFR values acquired in the galvanostatic/potentiostatic experiments start to increase significantly at higher anodic/cathodic current densities or overpotentials, increasing by  $7 \text{ m}\Omega \text{ cm}_{\text{MEA}}^2$  at an anodic overpotential of  $\approx 0.3 \text{ V}$ . This change in HFR is neglected when using the potentiodynamic measurement approach and, as a consequence, the HOR/HER overpotentials are overestimated in this case. The importance of this individual HFR correction at each current density becomes obvious when looking at the cathodic HER branch: while the potentiodynamic approach showed a distinct flattening of the current vs overpotential response that could be interpreted as a change in the RDS of the HER, this effect is not any more apparent for the galvanostatic/potentiostatic measurements with proper HFR correction. Thus, such inaccurate accounting of the HFR correction could lead to a misinterpretation of the reaction kinetics. Therefore, the galvanostatic/potentiostatic measurement procedure that allows for an equilibration of the reaction system and for a more precise HFR correction was chosen for the evaluation of the HOR/HER kinetics in this study.

The specific HOR/HER current densities of representative galvanostatic/potentiostatic measurements are depicted in the form of Tafel plots in Fig. 3 (upper panels) for different temperatures and pressures, whereby the overpotentials were determined from the

measured HFR values (lower panels) by means of Eq. 7. The Tafel plots in the upper panels of Fig. 3a ( $100 \text{ kPa}_{\text{H}_2}$ ) and Fig. 3b ( $450 \text{ kPa}_{\text{H}_2}$ ) show that the current density increases with increasing temperature due to faster reaction kinetics. Both the anodic and cathodic branches of the Tafel plots follow the Butler-Volmer equation at low overpotentials (lines in Fig. 3; the details of the fitting procedure are given below). In the HER branch, the kinetic data closely follow the Butler-Volmer fits over the entire measured potential interval, indicating that the associative desorption of hydrogen from the catalyst surface (Tafel reaction) is much faster than the proton reduction (Volmer reaction). On the other hand, the kinetic data in the HOR branch all exhibit the above discussed limiting current at high overpotentials (orange highlighted areas), which clearly increases with temperature and hydrogen partial pressure. Furthermore, the deviation of the kinetic data in the HOR branch from a simple Butler-Volmer relationship occurs already at rather low overpotentials, especially for low  $\text{H}_2$  partial pressures (see Fig. 3a). This is most apparent when comparing different partial pressures at the same temperature (Fig. 3c), where the HER currents increase only slightly with  $p_{\text{H}_2}$ , while the HOR currents increase significantly, thus leading to much more symmetrical Tafel plots at high  $\text{H}_2$  partial pressures. This gradual increase in HOR activity with hydrogen partial pressure correlates well with the assumption of a Tafel-limitation at high overpotentials: an increase in  $p_{\text{H}_2}$  leads to an increased rate of the Tafel reaction, resulting in a higher limiting current and delaying the change of the RDS from the potential-controlled Volmer reaction to the potential-independent Tafel reaction. The high asymmetry between the anodic and cathodic branches at small hydrogen partial pressures indicates that already at small overpotentials there is a significant effect of the apparently comparably slow dissociative hydrogen adsorption for the HOR, while the associative hydrogen desorption does not seem to limit the HER in the observed potential range.

As stated above, the HFR values were used to calculate the HOR/HER overpotentials (see Eq. 7), so that a variation of the HFR with the current density at any given operating conditions critically affects the kinetic analysis. While the HFR (bottom panels of Fig. 3) generally decreases for higher temperatures due to a higher proton conductivity of the membrane, an increase of the HFR is observed with higher overpotentials for all conditions. This HFR increase goes along with the higher current densities measured at higher overpotentials, so that it is more pronounced for

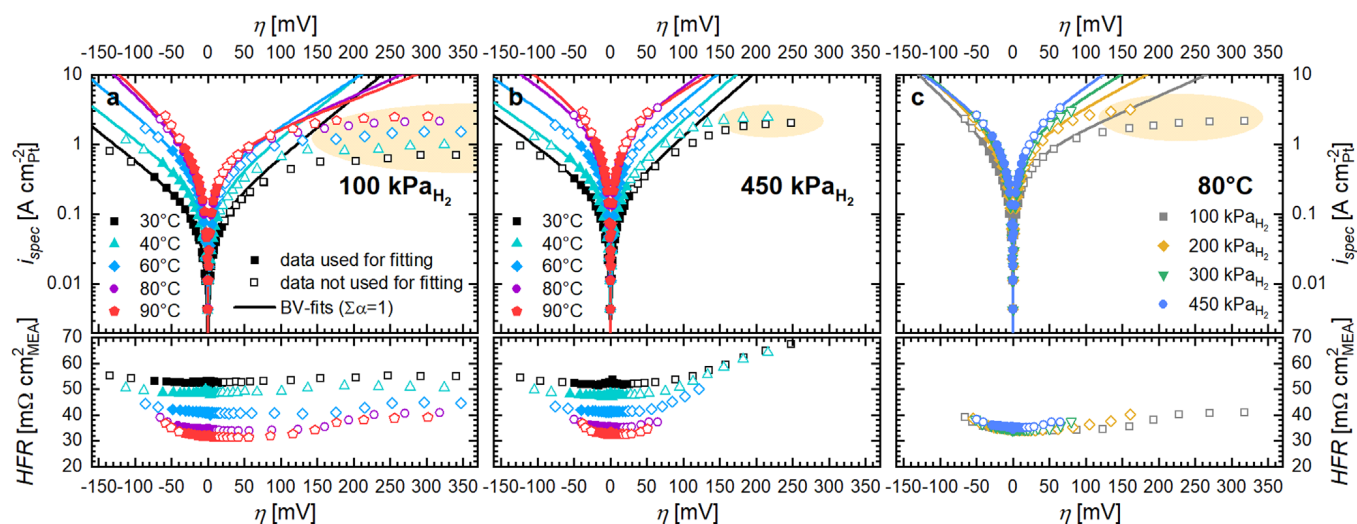


**Figure 3.** Kinetic current densities for the hydrogen oxidation and evolution reaction (top panels) and corresponding HFRs (bottom panels) of a representative MEA: temperature dependence at (a)  $100 \text{ kPa}_{\text{H}_2}$  and (b)  $450 \text{ kPa}_{\text{H}_2}$ , as well as (c)  $\text{H}_2$  partial pressure dependence at  $80^\circ\text{C}$  (all data at 90% RH and 2000/2000 nccm  $\text{H}_2$ ). The data points used (filled symbols) and excluded (open symbols) for the shown Butler-Volmer fits (lines) represent the average over the last 10 s of a 60 s galvanostatic/potentiostatic hold period (see Experimental section). The selection criteria for data to be included in the Butler-Volmer fits are: (i) a less than  $1 \text{ m}\Omega \text{ cm}_{\text{MEA}}^2$  HFR increase for the HER data; (ii) a current density of less than 10% of the limiting current density (orange shaded area) for the HOR data. Furthermore, the sum of the transfer coefficients in Eq. 5 was fixed to one (i.e.,  $\alpha_a + \alpha_c = 1$ ). The Pt/C working and counter electrode Pt loadings are  $1.4 \mu\text{g}_{\text{Pt}} \text{ cm}_{\text{MEA}}^{-2}$  and  $\approx 400 \mu\text{g}_{\text{Pt}} \text{ cm}_{\text{MEA}}^{-2}$ , respectively.

measurements at elevated temperatures and hydrogen partial pressures, as these resulted in higher current densities at a given overpotential. As the current density increases, the higher proton flux through the membrane leads to a higher water flux via electroosmotic drag, which in turn leads to a partial dry-out the membrane that results in an increase of the HFR.<sup>46</sup>

***H<sub>2</sub>-pump data analysis.***—To obtain the kinetic parameters of the HOR/HER, the following kinetic analysis was performed individually for each tested MEA (five in total), and the extracted kinetic parameters for each MEA and test condition (exchange current densities, transfer coefficients, etc.) were then averaged, rather than fitting the averaged data points from all MEAs. This was considered more accurate, since differences between individual MEAs with regards to roughness factor or HFR can be accounted for easily and accurately in individual measurements, but would introduce uncertainties in overpotential when averaging over measurements with multiple MEAs.

The exchange current density  $i_0$  has been obtained by fitting the data using the Butler-Volmer equation (Eq. 5). To limit the effect of the HOR limiting current on the kinetic evaluation, only data points with a current density of less than 10% of the corresponding limiting current density were used for fitting; where the limiting current density could not be determined due to exceeding the current limitation of the potentiostat (30 A, corresponding to 5 A cm<sup>-2</sup>), the limiting current density was estimated using its dependence on the hydrogen partial pressure discussed in the last part of this work. Additionally, all data points with an HFR increase of more than 1 mΩ cm<sub>MEA</sub><sup>2</sup> compared to the average HFR within the range of ± 20 mV were excluded from the fit in order to ensure that the correction of the potential for the Ohmic drop was accurate under the relevant measurement conditions. Data points considered for a given Butler-Volmer fit are depicted as full symbols in Fig. 3, whereas data points that were excluded from the fit are depicted as open symbols. In order to obtain physically meaningful fits, the values of the anodic and cathodic transfer coefficients  $\alpha_a$  and  $\alpha_c$  of the Butler-Volmer equation need to be constrained in some way. For example, the sum of  $\alpha_a$  and  $\alpha_c$  can either be unity in the case of a Tafel-Volmer mechanism or a maximum of two in the case of a Heyrovsky-Volmer mechanism.<sup>28–30</sup> For the presented data, only fits with a sum of transfer coefficients of one ( $\alpha_a + \alpha_c = 1$ ) represented the data reasonably well, thus further confirming a predominant Tafel-Volmer mechanism. In previous publications by our group, the Butler-Volmer fitting of the HOR/HER kinetic data was furthermore limited to a symmetrical behavior, where both transfer coefficients were fixed to the value 0.5, assuming that both the anodic and cathodic parts of the reaction would behave symmetrical with regards to the overpotential.<sup>15,17</sup> To account for the obvious asymmetry in the Tafel-plots shown in Fig. 3, a higher degree of freedom with the sum of transfer coefficients only being fixed to one was chosen in this study, as this type of fitting represented the data much better even for data points that were excluded from fitting (see fitted curves in Fig. 3), and since we could not find a convincing explanation as to why the anodic and the cathodic branch of the reaction should be strictly symmetrical under all conditions. The obtained values for the exchange current densities are reported in Table I, while the anodic transfer coefficient are summarized in Fig. S1 (available online at [stacks.iop.org/JES/168/064516/mmedia](https://stacks.iop.org/JES/168/064516/mmedia)) in the SI, showing that the HOR/HER becomes more symmetrical at higher partial pressures of hydrogen and at lower temperatures, as  $\alpha_a$  approaches 0.5 under these conditions. To increase the comparability to other studies, all fits and data analysis were also performed using symmetrical transfer coefficients fixed to a value 0.5 (Figs. S2, S3 and S4).

Additionally, the micropolarization region (inset in Fig. 2) close to the HOR/HER equilibrium potential ( $\eta = \pm 10$  mV), where the overall influence of any mass transport limitations should be negligible, was fitted using the linearized form of the Butler-Volmer equation for

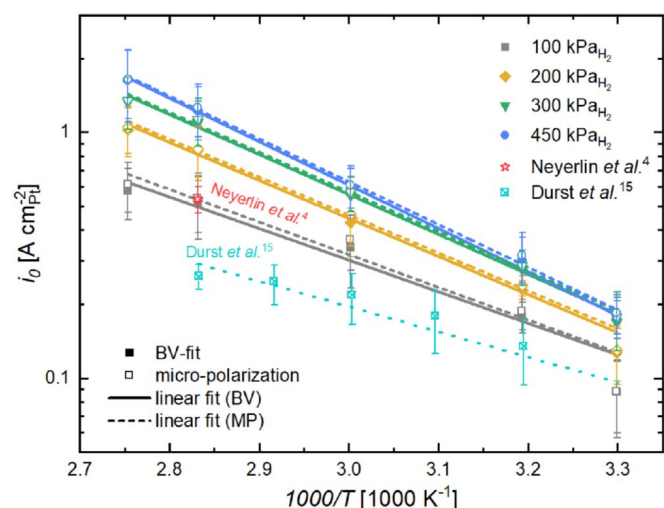


**Figure 4.** Pressure-dependent Arrhenius plots of the  $i_0$ -values of the HOR/HER on Pt/C determined in this work with the H<sub>2</sub>-pump setup and fitted from the BV-equation with the constraint  $\alpha_a + \alpha_c = 1$  (filled symbols and solid lines;  $i_0$ -values listed in Table I) and the micropolarization equation with the constraint  $\alpha_a + \alpha_c = 1$  (open symbols and dashed lines;  $i_0$ -values listed in Table SI) between 30 °C and 90 °C (averaged over five MEAs). The H<sub>2</sub>-pump based measurements at 100 kPa<sub>H<sub>2</sub></sub> from Neyerlin et al.<sup>4</sup> (red open star) and from Durst et al.<sup>15</sup> (turquoise crossed squares; from BV-fitting with the constraint  $\alpha_a = \alpha_c = 0.5$ ) are given for comparison.

small overpotentials:<sup>28</sup>

$$i_0 \cdot (\alpha_a + \alpha_c) = \frac{R \cdot T}{F} \cdot \frac{i_{\text{spec}}}{\eta} \quad [9]$$

Here, the exchange current density can be obtained from the slope in the current-potential plots when the sum of transfer coefficients is known. For the reader's convenience, the obtained exchange current densities from the BV-fits with the constraints of either  $\alpha_a + \alpha_c = 1$  or  $\alpha_a = \alpha_c = 0.5$  as well as of the micropolarization (MP) fit with the constraint  $\alpha_a + \alpha_c = 1$  are compared in Table SI in the SI.

To investigate the temperature dependency of the HOR/HER, the apparent activation energy  $E_{A,\text{app}}$  (in kJ mol<sup>-1</sup>) of the exchange current density for any given H<sub>2</sub> partial pressure can be determined according to:

$$\left( \frac{\partial \log(i_0)}{\partial(1/T)} \right)_{\text{pH}_2} = - \frac{E_{A,\text{app}}}{2.303 \cdot R} \quad [10]$$

Figure 4 shows the Arrhenius plots of  $i_0$  vs  $T^{-1}$  for different p<sub>H<sub>2</sub></sub> values, either for the exchange current densities determined from the micropolarization region assuming  $\alpha_a + \alpha_c = 1$  (open symbols and dashed lines) or from the asymmetric Butler-Volmer fits with  $\alpha_a + \alpha_c = 1$  (filled symbols and solid lines). As could already be seen from comparing the  $i_0$ -values in Table SI, the difference in the differently deduced  $i_0$ -values is rather negligible. Both data sets follow straight lines in the Arrhenius plot and, within the experimental error, yield the same apparent activation energies (see Table I). In comparison to previous publications that determined the HOR/HER kinetics by the H<sub>2</sub>-pump approach, it can be seen that the here obtained  $i_0$  value at 80 °C and 100 kPa H<sub>2</sub> (red open star in Fig. 4) is essentially identical with that reported by Neyerlin et al.,<sup>4</sup> on the other hand, the exchange current densities between 40 °C–80 °C and 100 kPa H<sub>2</sub> reported by Durst et al.<sup>15</sup> (see turquoise crossed squares in Fig. 4) are ≈1.5–3 times lower and yielded a significantly lower activation energy of ≈16 kJ mol<sup>-1</sup> compared to the ≈25 kJ mol<sup>-1</sup> measured here. Interestingly, the former also used a static measurement approach (galvanostatically controlled in their

**Table I.** Pressure-dependent  $i_0$ -values obtained from the Butler-Volmer fits outlined in Fig. 3, averaged for five independently prepared and measured MEAs. The apparent activation energies ( $E_{A,app}$ ) were determined in the range of 30 °C to 90 °C (see Fig. 4) based on the  $i_0$ -values obtained either from Butler-Volmer fits ( $E_{A,app}$  (BV); Eq. 5) or from the micropolarization region ( $E_{A,app}$  (MP); Eq. 9), assuming in both cases a sum of transfer coefficients of one ( $\alpha_a + \alpha_c = 1$ ).

$p_{H_2}$ [kPa]	100	200	300	450
$i_0$ at 30 °C [A cm <sub>Pt</sub> <sup>-2</sup> ]	0.088 ± 0.031	0.13 ± 0.03	0.17 ± 0.04	0.18 ± 0.03
$i_0$ at 40 °C [A cm <sub>Pt</sub> <sup>-2</sup> ]	0.18 ± 0.03	0.23 ± 0.02	0.28 ± 0.04	0.30 ± 0.07
$i_0$ at 60 °C [A cm <sub>Pt</sub> <sup>-2</sup> ]	0.34 ± 0.11	0.43 ± 0.12	0.55 ± 0.10	0.59 ± 0.12
$i_0$ at 80 °C [A cm <sub>Pt</sub> <sup>-2</sup> ]	0.52 ± 0.15	0.84 ± 0.20	1.10 ± 0.24	1.23 ± 0.30
$i_0$ at 90 °C [A cm <sub>Pt</sub> <sup>-2</sup> ]	0.58 ± 0.14	1.03 ± 0.23	1.33 ± 0.33	1.63 ± 0.53
$E_{A,app}$ (BV) [kJ mol <sup>-1</sup> ]	24.6 ± 2.8	29.6 ± 1.8	31.1 ± 1.1	33.9 ± 1.0
$E_{A,app}$ (MP) [kJ mol <sup>-1</sup> ]	25.4 ± 3.3	29.5 ± 1.8	30.9 ± 1.0	33.3 ± 1.1

case) as performed in this study, whereas the latter used a potentiodynamic approach (at 2 mV s<sup>-1</sup>), which may (at part) be the reason for the lower exchange current densities and the lower apparent activation energy reported in the latter. However, the most striking observation from the Arrhenius plots in Fig. 4 is that the slope of the fitting lines increases with increasing hydrogen partial pressures, equating to an increase of the apparent activation energy from 24.6 ± 2.8 kJ mol<sup>-1</sup> at 100 kPa<sub>H<sub>2</sub></sub> up to 33.9 ± 1.0 kJ mol<sup>-1</sup> at 450 kPa<sub>H<sub>2</sub></sub> for the BV-fitting based data reported in Table I (this trend is only slightly smaller when based on the MP-fitting, with 25.4 ± 3.3 kJ mol<sup>-1</sup> at 100 kPa<sub>H<sub>2</sub></sub> increasing to 33.3 ± 1.1 kJ mol<sup>-1</sup> at 450 kPa<sub>H<sub>2</sub></sub>). Thus, the HOR/HER kinetics exhibit an apparently non-constant activation energy, which increases gradually with hydrogen partial pressure.

## Discussion

In the following, we will more closely examine the possible origin of the H<sub>2</sub> partial pressure dependence of the activation energy of  $i_0$  deduced from Fig. 4 and given in Table I, determine the reaction order of the HOR/HER kinetics with respect to H<sub>2</sub> partial pressure, and discuss two different mechanisms that could lead to the observed limiting current for the HOR at high anodic overpotentials.

**H<sub>2</sub> partial pressure dependence of the activation energy.**—At first glance, the H<sub>2</sub> partial pressure dependence of the activation energy of  $i_0$  (see Table I) at low anodic and cathodic overpotentials is surprising, since the rate determining Volmer reaction does not involve gaseous H<sub>2</sub> and would thus be expected to be independent of  $p_{H_2}$ . However, when considering that the presumed rate determining Volmer reaction is preceded by a Tafel reaction that is in equilibrium, the effect of  $p_{H_2}$  on  $i_0$  can be rationalized. In this case, when describing the Tafel reaction by a dissociative Langmuir adsorption isotherm, an increase in H<sub>2</sub> partial pressure at any given overpotential would be expected to result in an increase in the H<sub>ads</sub> coverage, which in turn was found to somewhat lower the H<sub>ads</sub> adsorption energy and bond strength;<sup>47–50</sup> for a Volmer rate determining step, the latter effect would be expected to lead to the observed increase of  $i_0$  with  $p_{H_2}$  (see Fig. 4).

An alternative view would be to consider the mechanistic analogy between a Tafel-Volmer mechanism and a “potential dependent” Langmuir-Hinshelwood mechanism with a dissociative adsorption step. The rate of the HOR,  $r_{HOR}(\eta, p_{H_2})$ , would then depend on the potential dependent rate constant of the Volmer reaction for the HOR,  $k_{HOR}(\eta)$ , and the potential dependent surface coverage,  $\theta_H(\eta, p_{H_2})$ :

$$r_{HOR}(\eta, p_{H_2}) = k_{HOR}(\eta) \cdot \theta_H(\eta, p_{H_2}) \quad [11]$$

While these dependencies cannot be determined from the here presented kinetic data, assuming a Langmuir-Hinshelwood mechanism might nevertheless help to understand the pressure dependency of the determined activation energies. At the HOR/HER

equilibrium potential, the Volmer-step has exactly the same absolute rate for the HER and the HOR, so that the H<sub>ads</sub> surface coverage remains constant and is only controlled by the equilibrium coverage established through the Tafel reaction. As the overall reaction at 0 V vs RHE is not driven by potential (as  $\eta = 0$ ), a potential independent or classical Langmuir-Hinshelwood mechanism can be considered as a reasonable approximation. In this case, the adsorption enthalpy  $\Delta H_{ads}$  (marked in orange in Fig. 5) affects the measurable apparent activation energy  $E_{A,app}$  (marked in blue).<sup>51,52</sup> While the true activation energy of the Volmer reaction  $E_A$  (marked in black), i.e., the energy difference between the transition state and H<sub>ads</sub>, is roughly constant (clearly only a first-order estimate, as discussed above), the effect of  $\Delta H_{ads}$  at the equilibrium potential ( $\eta = 0$ ) would depend on the surface coverage of H<sub>ads</sub> ( $\theta_H$ ), which in turn is a function of the H<sub>2</sub> partial pressure according to Eq. 12 (this corresponds to Eq. 126 in ref. 51) and Eq. 13 (adapted for Eq. 11 in this work according to eqs. 48–52 in ref. 51) with the equilibrium constant K in units of Pa<sup>-1</sup>:

$$\theta_H(\eta = 0) = \frac{\sqrt{K \cdot p_{H_2}}}{1 + \sqrt{K \cdot p_{H_2}}} \quad [12]$$

$$\begin{aligned} E_{A,app}(\eta = 0) &= E_A + \Delta H_{ads} - \theta_H \cdot \Delta H_{ads} \\ &= E_A + \Delta H_{ads} \cdot (1 - \theta_H) \end{aligned} \quad [13]$$

As our experiments do not allow for a direct measure of the H<sub>ads</sub> coverage during the HOR/HER, the apparent activation energy can only be determined as a function of H<sub>2</sub> partial pressure. Since  $\Delta H_{ads}$  is a negative quantity and since  $\theta_H$  will increase with increasing  $p_{H_2}$ ,  $E_{A,app}$  is expected to increase with pressure, consistent with the values listed in Table I; eventually,  $E_{A,app}$  should approach the activation energy of the Volmer reaction ( $E_A$ ) at very high H<sub>2</sub> partial pressures. In summary, the experimentally observed decrease of  $E_{A,app}$  with increasing  $p_{H_2}$  can at least be qualitatively rationalized by drawing an analogy to the Langmuir-Hinshelwood mechanism.

**Estimation of the reaction order with respect to hydrogen partial pressure.**—The increase in the apparent activation energy of  $i_0$  with  $p_{H_2}$  has unexpected implications on the HOR/HER kinetics with respect to H<sub>2</sub> partial pressure. The exchange current density,  $i_0$ , is expected to depend on the hydrogen concentration  $c_{H_2}$  on the catalyst surface, i.e., on the H<sub>2</sub> concentration in the ionomer phase that is considered to cover the Pt particles. Assuming Henry’s Law, the H<sub>2</sub> concentration in the ionomer phase should be directly proportional to the hydrogen partial pressure  $p_{H_2}$ :<sup>28</sup>

$$\frac{i_0}{i_0^*} \propto \left( \frac{c_{H_2}}{c_{H_2}^*} \right)^m \propto \left( \frac{p_{H_2}}{p_{H_2}^*} \right)^m \quad [14]$$

Here,  $i_0^*$  stands for the exchange current density measured at a reference concentration  $c_{H_2}^*$ , e.g., the concentration obtained at the

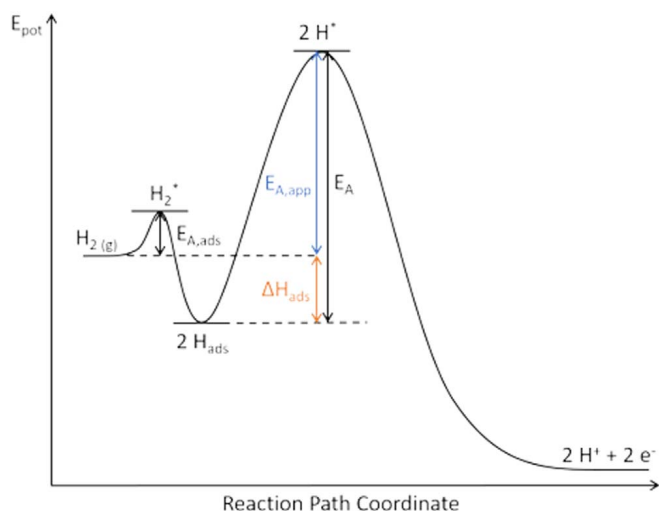


**Figure 5.** Scheme of the potential energy diagram for the catalytic oxidation of hydrogen with a dissociative adsorption of  $H_2$  (Tafel reaction) with the activation energy  $E_{A,ads}$  preceding the oxidation of  $H_{ads}$  (Volmer reaction) with its activation energy  $E_A$  being composed of the measureable apparent activation energy  $E_{A,app}$  (blue) and a surface coverage dependent contribution of the adsorption enthalpy  $\Delta H_{ads}$  (orange). Figure combined and adapted from *Concepts of Modern Catalysis and Kinetics*,<sup>51</sup> and *Fundamental Concepts in Heterogeneous Catalysis*.<sup>52</sup>

reference pressure of  $p_{H_2}^* = 100$  kPa. Thus, we can obtain the reaction order with respect to  $p_{H_2}$  (i.e.,  $m$ ) from the slope in the double logarithmic plot of  $i_0$  vs  $p_{H_2}$  at any given reaction temperature, which is shown in Fig. 6. As revealed by the values of these slopes marked in Fig. 6, the reaction order  $m$  also increases with temperature. This is a direct consequence of the increase in apparent activation energy with  $H_2$  partial pressure, as this results in a larger pressure induced spread in the  $i_0$ -values at higher temperatures. An exception to this here observed trend is the rather high slope of  $0.47 \pm 0.08$  for data recorded at 30 °C. At this temperature, the measured  $i_0$ -values for all pressures were lower than one would expect from the Arrhenius plot (Fig. 4), with the deviation being most severe for low pressures. This might be the result of operating at the limit of the test station's capabilities with respect to a tight control of both the cell temperature and the dewpoint (i.e., the humidification), due to the small difference between room temperature ( $\approx 25$  °C) and the set cell and dewpoint temperatures; furthermore, at this lowest  $H_2$  partial pressure of 100 kPa, the required total cell pressure of 104 kPa (considering a water vapor pressure of  $\approx 4$  kPa at 30 °C and 90% RH) is very close to the ambient pressure. That these difficulties are a likely problem for the measurements at 30 °C, particularly at 100 kPa  $H_2$ , is also reflected by the larger standard deviation between the five measurements at this condition.

**HOR limiting currents at high anodic overpotentials.**—As discussed above, the Butler-Volmer plots in Fig. 3 clearly show a limiting HOR current at high anodic overpotentials (orange marked areas). The cell temperature and  $H_2$  partial pressure dependent values of the limiting current densities referenced to the electrochemically active Pt surface area ( $i_{lim}$ ) were determined from the HOR/HER data at anodic overpotentials of at least 150 mV, using as a criterion that the increase in the current density with increasing overpotential remain below 10% (for the thus determined values see Table SII in the SI). Analogous limiting currents for the HOR have been observed in several other studies, and were mostly attributed to a limitation by the Tafel reaction,<sup>15,18,38</sup> while the only study that explicitly addressed this limiting current by Zalitis et al. concluded that it is most likely a limitation due to a rate limiting Heyrovsky reaction.<sup>5</sup> The latter can be excluded based on the data in the present study, since a rate limiting Heyrovsky reaction would result in a

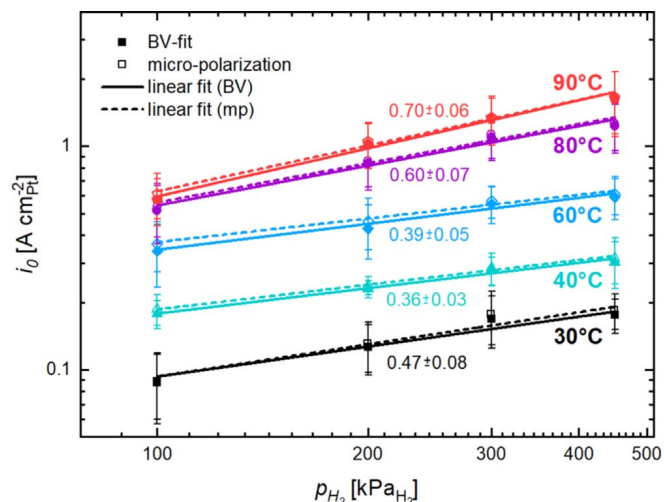


**Figure 6.** Double-logarithmic relation between the hydrogen partial pressure ( $p_{H_2}$ ) and the exchange current density ( $i_0$ ) estimated from the Butler-Volmer fits (filled symbols and solid lines, with the constraint  $\alpha_a + \alpha_c = 1$ ) or from the fits in the micropolarization region (open symbols and dashed lines, with the constraint  $\alpha_a + \alpha_c = 1$ ) at temperatures from 30 °C to 90 °C (averaged over five MEAs). The slopes represent the reaction order ( $m$ ) with respect to  $p_{H_2}$ , which are given by the numbers in the plot based on the  $i_0$ -values obtained from the BV-fits.

Tafel slope of 120 mV decade<sup>-1</sup>, whereas the hydrogen pump data shown in Fig. 3 reached a current density plateau that is independent of potential. Therefore, only two other possible causes can result in the observed limiting currents for the HOR: (i) the RDS being the dissociative adsorption of hydrogen, i.e., the Tafel reaction; and/or, (ii) a hydrogen mass transport limitation. With regards to the latter, at least bulk diffusion limitations through the diffusion medium and the electrode can be excluded for the here used  $H_2$ -pump experiments with ultra-thin working electrodes ( $\approx 0.5$ – $0.7$   $\mu\text{m}$ ), ultra-low Pt roughness factors ( $1.4 \pm 0.3$   $\text{cm}_{Pt}^{-2}$   $\text{cm}_{MEA}^{-2}$ ), and with pure  $H_2$ : the bulk diffusion limited current densities in this case should be on the order of 50–100  $\text{A cm}^{-2}_{MEA}$  (corresponding to at least  $\approx 30$ – $60$   $\text{A cm}^{-2}_{Pt}$ ), and are thus at least an order of magnitude larger than the observed  $i_{lim}$ -values (see Table SII in the SI).

Thus, we will first focus on the kinetic investigation of an assumed rate limiting Tafel reaction at high anodic overpotentials. In this case, the H-adsorption rate of the Tafel reaction ( $r_{ads}$  in  $\text{cm}_{Pt}^{-2} \text{s}^{-1}$ ) can be converted into a limiting current ( $i_{lim}(\text{Tafel})$ , in units of  $\text{A cm}^{-2}_{Pt}$ ) by means of the Faraday constant  $F$  ( $96484$   $\text{A s mol}^{-1}$ ) and the Avogadro-constant  $N_A$  ( $6.022 \cdot 10^{23}$   $\text{mol}^{-1}$ ):

$$i_{lim}(\text{Tafel}) = \frac{r_{ads}}{N_A} \cdot F \quad [15]$$

According to kinetic gas and collision theory,  $r_{ads}$  can be described by Eq. 16:<sup>51</sup>

$$r_{ads} = N_0 \cdot \frac{d\theta_H}{dt} = S(T) \cdot \frac{2 \cdot p_{H_2} \cdot (1 - \theta_H)^2}{\sqrt{2 \cdot \pi \cdot m_{H_2} \cdot k_B \cdot T}} \quad [16]$$

Here,  $N_0$  is the active site density (in units of  $\text{cm}_{Pt}^{-2}$ ),  $S(T)$  is the sticking coefficient,  $m_{H_2}$  is the molecular mass of hydrogen (2.016 u),  $k_B$  is the Boltzmann-constant ( $1.381 \cdot 10^{-23}$   $\text{J K}^{-1}$ ), and  $T$  is the temperature (in units of K). Furthermore, when the hydrogen adsorption at high anodic overpotentials is the rate determining step, one can assume that  $H_{ads}$  is instantaneously oxidized, so that the fraction of free adsorption sites ( $\theta_{\square}$ ) should be approximately one:

$$\theta_{\square} = 1 - \theta_H \approx 1 \quad [17]$$

Under these considerations, the rate of hydrogen adsorption is expected to be directly proportional to  $p_{H_2}$  according to Eq. 16,

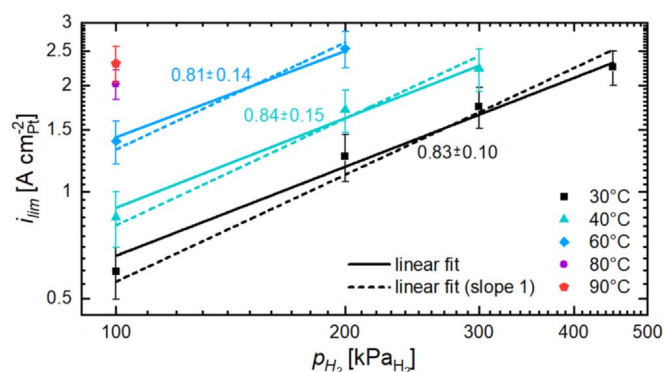


**Figure 7.** Double-logarithmic relationship between the hydrogen partial pressure ( $p_{\text{H}_2}$ ) and the limiting current density for the HOR at high anodic overpotentials ( $i_{\text{lim}}$ ), referenced to the electrochemically active Pt surface area and averaged over five independent measurements. The  $i_{\text{lim}}$ -values were obtained at anodic overpotentials of at least 150 mV, whereby data points for which the increase in current density to the next point exceeded 10% were excluded. The numerical values of the slopes determined by a linear fit (solid line, the slope represents the averaged slope obtained from five independently fitted measurements) are given in the figure and represent the reaction order with respect to  $p_{\text{H}_2}$ , while the dashed lines represent linear regression fits with a fixed slope of 1.0, i.e., assuming a direct proportionality between  $i_{\text{lim}}$  and  $p_{\text{H}_2}$ .

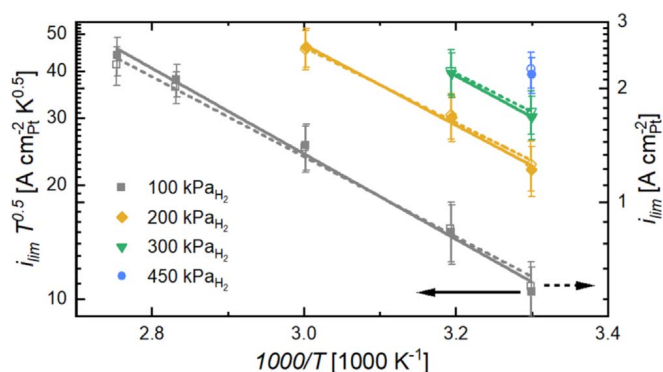


**Figure 8.** Arrhenius-type plots of the limiting HOR current density at high anodic overpotentials (from Table SII in the SI) with the temperature factor extracted from the pre-factor according to Eq. 19 ( $i_{\text{lim}} T^{0.5}$ , filled symbols and solid lines, left axis), assuming a dissociative Langmuir adsorption as the RDS; and of the limiting HOR current density directly ( $i_{\text{lim}}$ , open symbols and dashed lines, right axis).

which in turn implies that also the adsorption limited current density should be directly proportional to  $p_{\text{H}_2}$  (acc. to Eq. 15). Therefore, plotting the logarithm of the experimentally determined  $i_{\text{lim}}$ -values for the HOR (data in Table SII in the SI) vs the logarithm of  $p_{\text{H}_2}$  at a given temperature should result in straight lines with a slope of 1.0. This analysis is shown in Fig. 7 for the temperatures for which at least two limiting current density values could be determined (i.e., for 30 °C, 40 °C, and 60 °C), whereby the slopes of the linear regressions (solid lines) of 0.81–0.84 are slightly lower than the expected value of 1.0. However, since the linear fits with a fixed

slope of 1.0 (dashed lines) are still within the error range of the  $i_{\text{lim}}$  measurements (given by the vertical error bars that correspond to the standard deviation), it is reasonable to assume that  $i_{\text{lim}}$  for the HOR at high overpotentials is indeed directly proportional to  $p_{\text{H}_2}$  within the error of our measurements.

The temperature dependency of the Tafel reaction is more complex, as it not only involves the  $T^{-0.5}$  term from Eq. 16, but also the temperature dependence of the sticking coefficient  $S(T)$ . Embedded in the latter is the activation barrier for breaking the H-H-bond during the dissociative adsorption of  $\text{H}_2$ :<sup>51</sup>

$$S(T) = S_0 \cdot e^{-\frac{E_{A,\text{ads}}}{R \cdot T}} \quad [18]$$

Here,  $S_0$  ( $\leq 1$ ) is the pre-exponential factor of the sticking coefficient and  $E_{A,\text{ads}}$  is the activation energy of adsorption (see Fig. 5). Combining Eqs. 15–18 shows that  $E_{A,\text{ads}}$  can be determined directly from the slope of an Arrhenius-type plot of the limiting current density multiplied by  $T^{0.5}$ , as shown in Fig. 8 (filled symbols and solid lines). The thus determined activation energy of  $21 \pm 1 \text{ kJ mol}^{-1}$  is independent of the  $\text{H}_2$  partial pressure (see Table II), as expected for a dissociative adsorption step. This agrees well with an activation energy for the dissociative  $\text{H}_2$  adsorption on Pt of roughly  $17 \text{ kJ mol}^{-1}$  found in  $\text{H}_2$ - $\text{D}_2$  exchange experiments by Vogel et al.<sup>37</sup> These authors also reported an adsorption rate constant of  $k_{\text{ads}} \approx 2.4 \text{ cm s}^{-1}$  at 22 °C,<sup>37</sup> which would equate to a limiting current density of  $i_{\text{lim}} \approx 0.4 \text{ A cmPt}^{-2}$  at 100  $\text{kPa}_{\text{H}_2}$ , when assuming a hydrogen solubility of  $S_{\text{H}_2} \approx 8 \cdot 10^{-12} \text{ mol}_{\text{H}_2} \text{ cm}^{-3} \text{ Pa}^{-1}$  in the ionomer (from:  $i_{\text{lim}} = 2 \cdot F \cdot k_{\text{ads}} \cdot S_{\text{H}_2} \cdot p_{\text{H}_2}$ ).<sup>53</sup> This value is surprisingly close to the limiting current density of  $0.60 \pm 0.07 \text{ A cmPt}^{-2}$  at 30 °C obtained in the present study, supporting the idea that the Tafel reaction is responsible for the limiting HOR current density at high anodic overpotentials.

With these results providing strong support that the Tafel reaction is rate limiting the HOR at high anodic overpotentials, one nevertheless must reexamine the assumption that  $\text{H}_2$  mass transport limitations can indeed be ruled out (see Table II). As was already outlined above,  $\text{H}_2$  transport resistances through the diffusion medium and the electrode should be negligible, but the hydrogen transport resistance through the ionomer film covering the Pt particles might nevertheless be significant.<sup>54</sup> These film diffusion or local mass transport resistances are well known for  $\text{O}_2$  transport through the ionomer film in cathodes with low Pt loadings,<sup>55–58</sup> with any quantification being complicated by the likely inhomogeneous ionomer distribution and a presumably different morphology compared to bulk ionomer.<sup>59–61</sup> Still, the mass transport limited current density can be estimated using Fick's First Law that links the diffusive flux of  $\text{H}_2$  through the ionomer film ( $J_{\text{H}_2}$ , in  $\text{mol cm}^{-2} \text{ s}^{-1}$ ) to the diffusion coefficient ( $D_{\text{H}_2}$ , in  $\text{cm}^2 \text{ s}^{-1}$ ) and the  $\text{H}_2$  concentration gradient:<sup>51</sup>

$$J_{\text{H}_2} = -D_{\text{H}_2} \frac{dc}{dx} \quad [19]$$

The absolute value of the limiting current density is then obtained from the hydrogen maximum concentration gradient through an ionomer film of the thickness  $d_{\text{film}}$ , which occurs when the  $\text{H}_2$  concentration goes to zero at the ionomer/Pt interface, while at the

**Table II.** Pressure-dependent activation energies determined from the limiting HOR current densities at high anodic overpotentials. The values are deduced from the Arrhenius-type plots shown in Fig. 8, by two different methods, assuming two different mechanisms: (i) assuming a Tafel reaction RDS, plotting  $i_{\text{lim}} \cdot T^{0.5}$  vs  $1/T$  to obtain the activation energy for hydrogen adsorption ( $E_{A,\text{ads}}$ , see Fig. 5); (ii) assuming  $\text{H}_2$  mass transport resistance limitations through the ionomer film, plotting  $i_{\text{lim}}$  vs  $1/T$  to obtain the activation energy for  $\text{H}_2$  permeation ( $E_{A,\text{perm}}$ ). The data are averaged over 5 independent experiments.

$p_{\text{H}_2}$ [kPa]	100	200	300	450	Average
$E_{A,\text{ads}}$ [ $\text{kJ mol}^{-1}$ ] ( $i_{\text{lim}} \cdot T^{0.5}$ )	$21.6 \pm 1.0$	$20.4 \pm 1.6$	$\approx 20.7$	—	$21 \pm 1$
$E_{A,\text{perm}}$ [ $\text{kJ mol}^{-1}$ ] ( $i_{\text{lim}}$ )	$20.2 \pm 1.0$	$19.1 \pm 1.6$	$\approx 19.5$	—	$20 \pm 1$

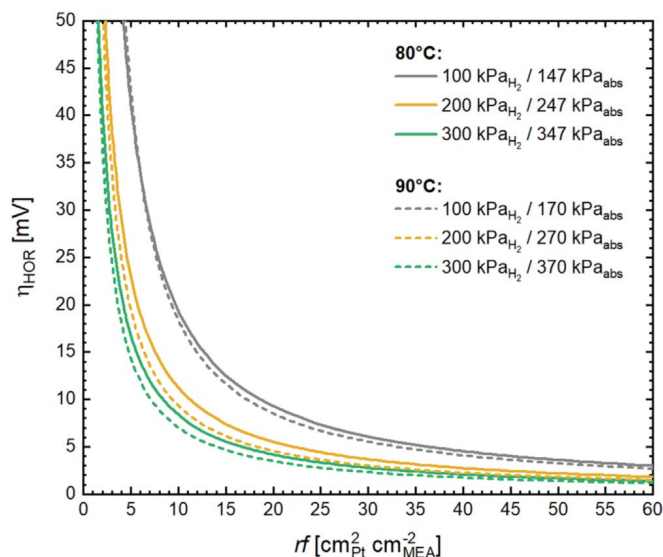


**Figure 9.** Kinetic HOR overpotential at  $3 \text{ A cm}_{\text{MEA}}^{-2}$  as a function of the anode roughness factor, calculated for  $80 \text{ }^{\circ}\text{C}$  and  $90 \text{ }^{\circ}\text{C}$  using the exchange current densities listed in Table I and the anodic transfer coefficients shown in Fig. S1. The absolute cell pressures ( $\text{kPa}_{\text{abs}}$ ) for operation at fully humidified conditions would be the sum of  $p_{\text{H}_2}$  and the water vapor saturation pressure at the respective temperature ( $47 \text{ kPa}$  at  $80 \text{ }^{\circ}\text{C}$  and  $70 \text{ kPa}$  at  $90 \text{ }^{\circ}\text{C}$ ).

gas/ionomer interface it corresponds to the product of the hydrogen solubility in the ionomer ( $S_{\text{H}_2}$ , in  $\text{mol cm}^{-3} \text{ Pa}^{-1}$ ) and  $p_{\text{H}_2}$  in the gas phase, according to Henry's Law:

$$i_{\text{lim}}(\text{diff}) = 2 \cdot F \cdot J_{\text{H}_2} = 2 \cdot F \cdot D_{\text{H}_2} \frac{S_{\text{H}_2} \cdot p_{\text{H}_2}}{d_{\text{film}}} = 2 \cdot F \cdot \frac{P_{\text{H}_2} \cdot p_{\text{H}_2}}{d_{\text{film}}} \quad [20]$$

$$P_{\text{H}_2} = D_{\text{H}_2} \cdot S_{\text{H}_2} \quad [21]$$

In Eq. 20, the permeability of hydrogen through the ionomer ( $P_{\text{H}_2}$ ) is the product of the diffusion coefficient ( $D_{\text{H}_2}$ ) and the hydrogen solubility ( $S_{\text{H}_2}$ ), according to Eq. 21.<sup>53</sup>

The permeability of hydrogen at  $80 \text{ }^{\circ}\text{C}$  has been reported to range from  $\approx 10^{-16} \text{ mol cm}^{-1} \text{ s}^{-1} \text{ Pa}^{-1}$  for dry to  $\approx 3 \cdot 10^{-16} \text{ mol cm}^{-1} \text{ s}^{-1} \text{ Pa}^{-1}$  for fully humidified ionomer membranes,<sup>53,62</sup> which according to Eq. 20 would result in limiting current densities of  $\approx 6\text{--}19 \text{ A cm}_{\text{Pt}}^{-2}$  when assuming a film thickness of  $3 \text{ nm}$  (for an I/C ratio of  $0.65 \text{ g}_I \text{ g}_C^{-1}$ )<sup>45</sup> and  $100 \text{ kPa}_{\text{H}_2}$ ; the actual water content of the ionomer film might indeed be significantly lower than that expected for  $90\%$  RH, due to a possible ionomer dry-out that is indicated by the HFR increase at high anodic overpotentials (see Fig. 3). Similarly, for the same  $\text{H}_2$  partial pressure, temperature, and ionomer film thickness, a limiting current in the range of  $\approx 1.9 \text{ A cm}_{\text{Pt}}^{-2}$  can be calculated from a local mass transport resistance ( $R_{\text{T}}$ ) of  $\approx 350 \text{ s m}^{-1}$  reported by Schuler et al.,<sup>54</sup> using the correlation of  $R_{\text{T}}$  and  $i_{\text{lim}}$  established by Baker et al. (adapted from Eq. 3 for a two-electron oxidation of  $100\% \text{ H}_2$ ):<sup>63</sup>

$$i_{\text{lim}}(\text{diff}) = \frac{2 \cdot F}{R_{\text{T}}} \cdot \frac{P_{\text{H}_2}}{R \cdot T} \quad [22]$$

As the ionomer film diffusion limited current densities ( $i_{\text{lim}}(\text{diff})$ ) estimated from the hydrogen permeability of a bulk membrane are only  $\approx 3\text{--}10$  times higher than the here measured limiting current density at  $80 \text{ }^{\circ}\text{C}$  and  $100 \text{ kPa H}_2$  ( $\approx 2.0 \text{ A cm}_{\text{Pt}}^{-2}$ ; see Table SII in the SI), and as the  $i_{\text{lim}}(\text{diff})$  estimate based on the actually measured local transport resistance yields a value that is essentially identical with the observed limiting current at high anodic overpotentials, it can unfortunately not be excluded that hydrogen mass transport

through the ionomer film might indeed affect or even govern the observed limiting HOR current at high anodic overpotentials.

One further option that we considered to distinguish whether the observed limiting currents can be ascribed to the Tafel reaction or to  $\text{H}_2$  mass transport through the ionomer film was to examine the temperature dependence of the latter. As shown in Eq. 20, the temperature dependence of the limiting current density is simply the temperature dependence of the  $\text{H}_2$  permeability, which for ionomeric membranes at a constant relative humidity is generally described by an Arrhenius-type law.<sup>62</sup> Thus, when limited by  $\text{H}_2$  mass transport through the ionomer film, plotting the logarithm of the limiting HOR current vs  $1/T$  should yield straight lines with a slope corresponding to  $-E_{\text{A,perm}}/R$ , where  $E_{\text{A,perm}}$  is the activation energy for  $\text{H}_2$  permeation through the ionomer phase and  $R$  is the gas constant. This is shown in Fig. 8 (open symbols and dashed lines, plotted vs the right-hand y-axis), yielding  $E_{\text{A,perm}} \approx 20 \pm 1 \text{ kJ mol}^{-1}$  when averaged over the data between  $100\text{--}300 \text{ kPa}_{\text{H}_2}$  (see Table II). This value is essentially identical with the activation energy for  $\text{H}_2$  permeation of  $E_{\text{A,perm}} \approx 19.7 \text{ kJ mol}^{-1}$  for  $\text{H}_2$  diffusion in Nafion at  $95\%$  RH,<sup>62</sup> and within the experimental error also the same as the activation energy for  $\text{H}_2$  adsorption ( $E_{\text{A,ads}}$ ) that was determined above when assuming a rate determining Tafel reaction (see Table II).

In summary, based on the above analysis, it is not possible to determine whether a rate limiting Tafel reaction or a  $\text{H}_2$  mass transport resistance through the ionomer film is responsible for the observed limiting HOR current density at high anodic overpotentials. One possible means to distinguish between these two phenomena would be to investigate the limiting HOR current density for different catalysts with different HOR/HER activities (e.g., platinum alloys<sup>26,64</sup>), or to examine electrodes with different I/C ratios that would result in different average ionomer film thicknesses.<sup>45</sup>

**Implications for low-loaded PEMFC anodes.**—In order to reach the current DoE target of  $125 \mu\text{g}_{\text{Pt}} \text{ cm}_{\text{MEA}}^{-2}$ ,<sup>65</sup> the state-of-the-art anode loadings of  $50 \mu\text{g}_{\text{Pt}} \text{ cm}_{\text{MEA}}^{-2}$  will likely have to be reduced to  $25 \mu\text{g}_{\text{Pt}} \text{ cm}_{\text{MEA}}^{-2}$  or even lower.<sup>66</sup> With a typical ECSA of  $\approx 60 \text{ m}^2 \text{ g}_{\text{Pt}}^{-1}$  for anode catalysts, this would correspond to an  $rf$  of 30 or  $15 \text{ cm}_{\text{Pt}}^2 \text{ cm}_{\text{MEA}}^{-2}$ , respectively, whereby ECSA losses of up to  $50\%$  due to SUSD are expected over the MEA lifetime.<sup>9</sup> To correlate the here presented kinetic investigation of the HOR/HER to the expected contribution of the HOR to the overall cell performance on these low-loaded anodes, Fig. 9 shows the kinetic HOR overpotential as a function of the anode roughness factor, calculated via the Butler-Volmer equation (Eq. 5) for a current density of  $3 \text{ A cm}_{\text{MEA}}^{-2}$ , using the  $i_0$ -values reported in Table I and the  $\alpha_a$ -values shown in Fig. S1. For an  $rf$  of  $30 \text{ cm}_{\text{Pt}}^2 \text{ cm}_{\text{MEA}}^{-2}$ , minor HOR overpotentials of  $\approx 6 \text{ mV}$  are observed even at  $3 \text{ A cm}_{\text{MEA}}^{-2}$  at  $80 \text{ }^{\circ}\text{C}$  and  $100 \text{ kPa}_{\text{H}_2}$  (corresponding to a fully humidified cell pressure of  $147 \text{ kPa}_{\text{abs}}$ ). However, when the  $rf$  decreases to  $10 \text{ cm}_{\text{Pt}}^2 \text{ cm}_{\text{MEA}}^{-2}$  with lower anode loadings or after severe degradation, the HOR overpotential would increase to  $\approx 20 \text{ mV}$ . The analysis of Fig. 9 shows that for such a low  $rf$ , raising the  $\text{H}_2$  partial pressure to 200 or even  $300 \text{ kPa}_{\text{abs}}$  could significantly reduce the expected HOR overpotentials at  $80 \text{ }^{\circ}\text{C}$  to  $\approx 11$  or  $\approx 8 \text{ mV}$ , respectively, lowering the cell voltage loss by  $\approx 10 \text{ mV}$ ; Fig. 9 also shows that raising the cell temperature to  $90 \text{ }^{\circ}\text{C}$  has a diminishing effect on the performance of low-loaded anodes.

## Conclusions

In this study, a measurement procedure that allows for a precise determination of the HOR/HER kinetics over a broad range of temperatures, pressures, and overpotentials was developed. This approach combines galvanostatic/potentiostatic (a low/high overpotentials) hold periods of 60 s with impedance measurements, thereby allowing for a precise determination of the HFR at each measurement point and thus resulting in precise and reproducible kinetic data.

It could be shown that the HOR/HER follows a Tafel-Volmer mechanism in the observed range of temperatures and pressures. At low overpotentials, the rate determining Volmer-step is affected by the preceding Tafel-step, resulting in a significantly asymmetric behavior, with the symmetry increasing with higher partial pressures of hydrogen and lower temperatures (i.e., approaching equal anodic and cathodic transfer coefficients). Furthermore, a pressure dependence of the apparent activation energy of the Volmer-step was observed due to a pressure dependent contribution of the preceding Tafel-step's hydrogen adsorption enthalpy. The effect of the hydrogen adsorption enthalpy decreases with increasing surface coverage of adsorbed hydrogen, thus leading to an apparent increase of the measured activation energy with increasing hydrogen pressures. Due to this complex interaction between activation energy and hydrogen partial pressure, the reaction order of  $i_0$  with respect to  $p_{\text{H}_2}$  increases with temperature as well.

At high anodic overpotentials, the HOR approaches a limiting current that showed a direct proportionality to  $p_{\text{H}_2}$  and exhibited an apparent activation energy  $\approx 20 \text{ kJ mol}^{-1}$ . The origin of this limiting current could either be a change of the RDS to a rate limiting adsorption of  $\text{H}_2$  (rate limiting Tafel reaction) or a mass transport limitation of  $\text{H}_2$  through the ionomer film. Since both of these limitations would be expected to show the observed direct proportionality to  $p_{\text{H}_2}$ , as well as very similar apparent activation energies, it unfortunately could not be determined which of the two mechanisms is responsible for the limiting current at high anodic overpotentials.

### ORCID

Björn M. Stühmeier  <https://orcid.org/0000-0001-7713-2261>  
 Markus R. Pietsch  <https://orcid.org/0000-0003-3872-4496>  
 Jan N. Schwämmlein  <https://orcid.org/0000-0001-8902-4508>  
 Hubert A. Gasteiger  <https://orcid.org/0000-0001-8199-8703>

### References

1. K. Ayers, N. Danilovic, R. Ouimet, M. Carmo, B. Pivovar, and M. Bornstein, *Annul. Rev. Chem. Biomol. Eng.*, **10**, 219 (2019).
2. J. P. Torreglosa, P. García, L. M. Fernández, and F. Jurado, *Energy Convers. Manage.*, **77**, 514 (2014).
3. A. Chapman et al., *Int. J. Hydrogen Energy*, **44**, 6371 (2019).
4. K. C. Neyerlin, W. Gu, J. Jorne, and H. A. Gasteiger, *J. Electrochem. Soc.*, **154**, B631 (2007).
5. C. M. Zalitis, J. Sharman, E. Wright, and A. R. Kucernak, *Electrochim. Acta*, **176**, 763 (2015).
6. M. Bernat, A. Siebel, and H. A. Gasteiger, *J. Electrochem. Soc.*, **165**, F305 (2018).
7. H. A. Gasteiger, J. E. Panels, and S. G. Yan, *J. Power Sources*, **127**, 162 (2004).
8. W. R. Baumgartner, P. Parz, S. D. Fraser, E. Wallnöfer, and V. Hacker, *J. Power Sources*, **182**, 413 (2008).
9. J. N. Schwämmlein, P. J. Rheinländer, Y. Chen, K. T. Freyer, and H. A. Gasteiger, *J. Electrochem. Soc.*, **165**, F1312 (2018).
10. R. Borup et al., *Chem. Rev.*, **107**, 3904 (2007).
11. Y. Yu, H. Li, H. Wang, X.-Z. Yuan, G. Wang, and M. Pan, *J. Power Sources*, **205**, 10 (2012).
12. G. Couturier, D. W. Kirk, P. J. Hyde, and S. Srinivasan, *Electrochim. Acta*, **32**, 995 (1987).
13. P. J. Rheinländer, J. Herranz, J. Durst, and H. A. Gasteiger, *J. Electrochem. Soc.*, **161**, F1448 (2014).
14. J. Zheng, W. Sheng, Z. Zhuang, B. Xu, and Y. Yan, *Sci. Adv.*, **2**, e1501602 (2016).
15. J. Durst, C. Simon, F. Hasché, and H. A. Gasteiger, *J. Electrochem. Soc.*, **162**, F190 (2015).
16. W. Sheng, H. A. Gasteiger, and Y. Shao-Horn, *J. Electrochem. Soc.*, **157**, B1529 (2010).
17. J. Durst, A. Siebel, C. Simon, F. Hasche, J. Herranz, and H. A. Gasteiger, *Energy Environ. Sci.*, **7**, 2255 (2014).
18. M. Wesselmarm, B. Wickman, C. Lagergren, and G. Lindbergh, *Electrochem. Commun.*, **12**, 1585 (2010).
19. H. Uchida, K. Izumi, K. Aoki, and M. Watanabe, *Phys. Chem. Chem. Phys.*, **11**, 1771 (2009).
20. C. M. Zalitis, A. R. Kucernak, J. Sharman, and E. Wright, *J. Mater. Chem. A*, **5**, 23328 (2017).
21. X. Wang, R. K. Ahluwalia, and A. J. Steinbach, *J. Electrochem. Soc.*, **160**, F251 (2013).
22. W. Sheng, Z. Zhuang, M. Gao, J. Zheng, J. G. Chen, and Y. Yan, *Nat. Commun.*, **6**, 5848 (2015).
23. J. Zheng, J. Nash, B. Xu, and Y. Yan, *J. Electrochem. Soc.*, **165**, H27 (2018).
24. H. A. Gasteiger, W. Gu, R. Makharia, M. F. Mathias, and B. Sompalli, "Handbook of fuel cells—fundamentals, technology and applications." ed. W. Vielstich, H. A. Gasteiger, A. Lamm, W. Vielstich, H. A. Gasteiger, and A. Lamm. *3 Fuel Cell Technology and Applications* (Wiley, Hoboken) p. 593 (2003).
25. A. R. Kucernak and C. Zalitis, *J. Phys. Chem. C*, **120**, 10721 (2016).
26. K. Elbert, J. Hu, Z. Ma, Y. Zhang, G. Chen, W. An, P. Liu, H. S. Isaacs, R. R. Adzic, and J. X. Wang, *ACS Catal.*, **5**, 6764 (2015).
27. J. N. Schwämmlein, B. M. Stühmeier, K. Wagenbauer, H. Dietz, V. Tileli, H. A. Gasteiger, and H. A. El-Sayed, *J. Electrochem. Soc.*, **165**, H229 (2018).
28. J. S. Newman, *Electrochemical systems* (Prentice Hall, Englewood Cliffs) (1991).
29. S. Fletcher, *J. Solid State Electrochem.*, **13**, 537 (2009).
30. R. Guidelli, G. Compton Richard, M. Felio Juan, E. Gileadi, J. Lipkowski, W. Schmickler, and S. Trasatti, *Pure Appl. Chem.*, **86**, 245 (2014).
31. M. R. Gennero de Chialvo and A. C. Chialvo, *Phys. Chem. Chem. Phys.*, **6**, 4009 (2004).
32. E. Skúlason, V. Tripkovic, M. E. Björketun, S. Gudmundsdóttir, G. Karlberg, J. Rossmeisl, T. Bligaard, H. Jónsson, and J. K. Nørskov, *J. Phys. Chem. C*, **114**, 18182 (2010).
33. J. A. Santana, J. J. Saavedra-Arias, and Y. Ishikawa, *Electrocatalysis*, **6**, 534 (2015).
34. N. M. Marković, B. N. Grgur, and P. N. Ross, *J. Phys. Chem. B*, **101**, 5405 (1997).
35. B. E. Conway and G. Jerkiewicz, *Electrochim. Acta*, **45**, 4075 (2000).
36. J. Greeley, T. F. Jaramillo, J. Bonde, I. Chorkendorff, and J. K. Nørskov, *Nat. Mater.*, **5**, 909 (2006).
37. W. Vogel, L. Lundquist, P. Ross, and P. Stonehart, *Electrochim. Acta*, **20**, 79 (1975).
38. C. Jackson, G. T. Smith, M. Markiewicz, D. W. Inwood, A. S. Leach, P. S. Whalley, A. R. Kucernak, A. E. Russell, D. Kramer, and P. B. J. Levecque, *J. Electroanal. Chem.*, **819**, 163 (2018).
39. J. X. Wang, T. E. Springer, and R. R. Adzic, *J. Electrochem. Soc.*, **153**, A1732 (2006).
40. C. Simon, F. Hasché, D. Müller, and H. A. Gasteiger, *ECSS Trans.*, **69**, 1293 (2015).
41. C. Simon, F. Hasché, and H. A. Gasteiger, *J. Electrochem. Soc.*, **164**, F591 (2017).
42. G. S. Harzer, J. N. Schwämmlein, A. M. Damjanović, S. Ghosh, and H. A. Gasteiger, *J. Electrochem. Soc.*, **165**, F3118 (2018).
43. T. J. Schmidt, H. A. Gasteiger, G. D. Stäb, P. M. Urban, D. M. Kolb, and R. J. Behm, *J. Electrochem. Soc.*, **145**, 2354 (1998).
44. K. C. Neyerlin, W. Gu, J. Jorne, A. Clark, and H. A. Gasteiger, *J. Electrochem. Soc.*, **154**, B279 (2007).
45. A. Orfanidi, P. Madkikar, H. A. El-Sayed, G. S. Harzer, T. Kratky, and H. A. Gasteiger, *J. Electrochem. Soc.*, **164**, F418 (2017).
46. W.-M. Yan, F. Chen, H.-Y. Wu, C.-Y. Soong, and H.-S. Chu, *J. Power Sources*, **129**, 127 (2004).
47. B. W. J. Chen and M. Mavrikakis, *Catalysis Science & Technology*, **10**, 671 (2020).
48. K. Christmann, G. Ertl, and T. Pignet, *Surf. Sci.*, **54**, 365 (1976).
49. L. Xu, Y. Ma, Y. Zhang, B. Teng, Z. Jiang, and W. Huang, *Science China Chemistry*, **54**, 745 (2011).
50. F. G. Will, *J. Electrochem. Soc.*, **112**, 451 (1965).
51. I. Chorkendorff and J. W. Niemantsverdriet, *Concepts of Modern Catalysis and Kinetics* (Wiley, Weinheim) (2003).
52. J. K. Nørskov, F. Studt, F. Abild-Pedersen, and T. Bligaard, *Fundamental Concepts in Heterogeneous Catalysis* (Wiley, Hoboken) (2014).
53. H. Ito, T. Maeda, A. Nakano, and H. Takenaka, *Int. J. Hydrogen Energy*, **36**, 10527 (2011).
54. T. Schuler, A. Chowdhury, A. T. Freiberg, B. Sneed, F. B. Spingler, M. C. Tucker, K. L. More, C. J. Radke, and A. Z. Weber, *J. Electrochem. Soc.*, **166**, F3020 (2019).
55. W. Yoon and A. Z. Weber, *J. Electrochem. Soc.*, **158**, B1007 (2011).
56. T. Suzuki, K. Kudo, and Y. Morimoto, *J. Power Sources*, **222**, 379 (2013).
57. G. S. Harzer, A. Orfanidi, H. El-Sayed, P. Madkikar, and H. A. Gasteiger, *J. Electrochem. Soc.*, **165**, F770 (2018).
58. J. P. Owejan, J. E. Owejan, and W. Gu, *J. Electrochem. Soc.*, **160**, F824 (2013).
59. F. C. Cetinbas, R. K. Ahluwalia, N. Kariuki, V. De Andrade, D. Fongalland, L. Smith, J. Sharman, P. Ferreira, S. Rasouli, and D. J. Myers, *J. Power Sources*, **344**, 62 (2017).
60. K. Karan, *Curr. Opin. Electrochem.*, **5**, 27 (2017).
61. S. A. Eastman, S. Kim, K. A. Page, B. W. Rowe, S. Kang, C. L. Soles, and K. G. Yager, *Macromolecules*, **45**, 7920 (2012).
62. C. K. Mittelsteadt and H. Liu, "Handbook of fuel cells—fundamentals, technology and applications." ed. W. Vielstich, H. A. Gasteiger, H. Yokokawa, W. Vielstich, H. A. Gasteiger, and H. Yokokawas *5 Advances in Electrocatalysis, Materials, Diagnostics and Durability* (Wiley, Hoboken) p. 345 (2009).
63. D. R. Baker, D. A. Caulk, K. C. Neyerlin, and M. W. Murphy, *J. Electrochem. Soc.*, **156**, B991 (2009).
64. G. Shi, H. Yano, D. A. Tryk, A. Iiyama, and H. Uchida, *ACS Catal.*, **7**, 267 (2017).
65. U.S. Department of Energy, "Fuel Cell Technologies Program Multi-Year Research, Development, and Demonstration Plan" by the U.S. Department of Energy (2012), <https://energy.gov/eere/fuelcells/downloads/hydrogen-and-fuel-cell-technologies-office-multi-year-research-development>.
66. A. Kongkanand and M. F. Mathias, *J. Phys. Chem. Lett.*, **7**, 1127 (2016).

## 3.2. Novel Catalyst Concepts for PEMFCs

In this section, novel catalyst concepts based on metal oxide supports will be presented. The overarching aim is to address the PEMFC durability and performance issues discussed in Section 1.1, with a focus on the mitigation of detrimental corrosion of the carbon support of the cathode catalyst. The first publication presents a novel way of using the polyol process for the surface reduction of metal oxide supports, which might enable the subsequent deposition of a thin film of an active metal and thus make carbon-free oxide supports with high PGM utilization available. Furthermore, the unique properties of an SMSI were used to develop a novel catalyst system consisting of Pt/TiO<sub>x</sub> aggregates on a carbon support, yielding a catalyst that is selective for the HOR, i.e., that exhibits a significantly suppressed ORR activity while maintaining a similar HOR activity compared to conventional Pt/C catalysts. Finally, this catalyst concept was adapted for Ru nanoparticles to investigate the effect of the SMSI on the surface electrochemistry and the HOR activity of less surface oxidation resistant noble metals.

### 3.2.1. Metal Oxide Thin-Film Reduction via the Polyol Process

This section presents the article "Extending the Polyol Reduction Process into the Second Dimension: Oxide Thin Film Reduction" that was published in January 2021 in the *Journal of The Electrochemical Society*.<sup>70</sup> It is an open access article published under the terms of the Creative Commons Attribution Non-Commercial No Derivatives 4.0 License (CC BY-NC ND). The permanent web-link to the article is <https://doi.org/10.1149/1945-7111/abda22>.

As described in Section 1.1, one of the main durability issues of PEMFCs is the stability of the cathode catalyst carbon support during SUSD and local hydrogen starvation events.<sup>123</sup> Here, contiguous Pt films on high surface area oxide supports are among the most promising structures for next generation fuel cell electrodes.<sup>171</sup> However, the deposition of metallic monolayers or extremely thin metal films ( $\leq 5$  nm) on corrosion resistant oxide surfaces is prevented by the high interfacial energy of the metal/oxide interface that results in the growth of 3D structures rather than 2D films of the deposited metal.<sup>69,172,173</sup> Thus, the metal/oxide interfacial tension has to be minimized, e.g., by reducing the outermost surface of the oxide to form a metallic buffer layer on

which metal deposition can take place.<sup>174–176</sup>

This work employs the polyol process<sup>177</sup> for the in-situ reduction of metal oxide surfaces. First, the possibility of using ethylene glycol (EG) for the reduction of three metal oxides ( $\text{SnO}_2$ ,  $\text{NiO}$ , and  $\text{Ta}_2\text{O}_5$ ) was explored by thermodynamic calculations according to Larcher and Patrice.<sup>129</sup> These showed that it might be possible to reduce  $\text{NiO}$  already at room temperature, whereas the reduction of  $\text{SnO}_2$  can only be possible when the concentration of the side products  $\text{H}_2\text{O}$  and  $\text{CO}_2$  is kept sufficiently low, while the reduction of  $\text{Ta}_2\text{O}_5$  should not be possible up to the boiling temperature of EG even under these conditions. To test this hypothesis, the reduction of the thin native oxide film on a Sn wire was monitored in-situ by measuring the open circuit potential (OCP) of the wire vs. a  $\text{Ag}/\text{AgCl}$  reference electrode. Upon heating, a drop in OCP was observed, being a clear indication for a change in the surface/electrolyte interaction that is related to the reduction of the surface of the oxide film and for the exposure of a metallic surface.<sup>178</sup> When a conductive salt, e.g., lithium bis(trifluoromethanesulfonyl)imide ( $\text{LiTFSI}$ ) was added, the reduction of the oxide could be in-situ monitored by cyclic voltammetry, whereby the native oxide feature disappeared after the OCP drop. In-situ recorded near ambient pressure X-ray photoelectron spectroscopy (XPS) directly showed the reduction of the native oxide layer on a Sn substrate by EG at elevated temperatures, thus verifying the electrochemical measurements.

Furthermore, it was shown by OCP measurements that EG can reduce the native oxides of both Sn and Ni, not only on a wire model substrate, but also on the technologically more relevant nanoparticles and even on antimony-doped  $\text{SnO}_2$  nanoparticles. However, EG is not capable of reducing Ta oxide up to the boiling temperature of EG. Thus, the oxide reduction process is independent of the oxide morphology (extended surfaces, nanoparticles and nanowires), which might make  $\text{oxide}_{\text{core-metal}}_{\text{shell}}$  structures accessible via a metallic inter-layer.

Finally, simple thermodynamic calculations indicate that by tuning the reaction conditions, e.g., reducing the concentration of the side products  $\text{H}_2\text{O}$  and  $\text{CO}_2$ , and choosing a suitable (poly)alcohol, it is possible to reduce the surface of a broad range of metal oxides (note that these calculations obviously neglect the complexity of the reduction reaction).<sup>179, 180</sup>

### **Author contributions**

B.M.S., V.S., L.S., and L.H.T. performed the electrochemical measurements. M.T.G. performed the XPS measurements. J.N.S. performed pre-experiments that were crucial for the understanding of the polyol reduction process. B.M.S. and H.A.E. wrote the manuscript. All authors discussed the results and commented on the manuscript.



## Extending the Polyol Reduction Process into the Second Dimension: Oxide Thin Film Reduction

Björn M. Stühmeier,<sup>1,\*</sup>  Mark T. Greiner,<sup>2</sup> Vignesh Sureshwaran,<sup>1</sup> Lukas Schuster,<sup>1</sup> Li Hui Tiah,<sup>1</sup> Jan N. Schwämmlein,<sup>1,\*a</sup>  Hubert A. Gasteiger,<sup>1,\*\*</sup>  and Hany A. El-Sayed<sup>1,z</sup>

<sup>1</sup>Chair of Technical Electrochemistry, Department of Chemistry, Technische Universität München, München, Germany

<sup>2</sup>Department of Heterogeneous Reactions, Max-Planck Institute for Chemical Energy Conversion, Mülheim an der Ruhr, Germany

The formation of extended metal thin films (<5 nm) or monolayers on oxide surfaces, for applications in (electro-)catalysis, has never been achieved due to the high interfacial energy of the metal/oxide interface that always results in a 3D growth of the deposited metal. To realize 2D growth, the outermost surface of the oxide must be reduced prior to metal deposition in the same system. Here, we demonstrate that the polyol method, typically used for metal nanoparticles synthesis, can be used for the reduction of oxide thin films. The reduction of the oxide layer upon heating in ethylene glycol was electrochemically monitored in situ by measuring the open circuit potential and confirmed by cyclic voltammetry and near ambient pressure X-ray photoelectron spectroscopy. The reduction of oxide thin films could be verified for nanoparticles of Sn, Ni and Sb-doped SnO<sub>2</sub> in accordance with thermodynamic calculations. This method will enable the formation of metal thin films and monolayers on oxide substrates for applications in (electro-)catalysis.

© 2021 The Author(s). Published on behalf of The Electrochemical Society by IOP Publishing Limited. This is an open access article distributed under the terms of the Creative Commons Attribution Non-Commercial No Derivatives 4.0 License (CC BY-NC-ND, <http://creativecommons.org/licenses/by-nc-nd/4.0/>), which permits non-commercial reuse, distribution, and reproduction in any medium, provided the original work is not changed in any way and is properly cited. For permission for commercial reuse, please email: [permissions@iopublishing.org](mailto:permissions@iopublishing.org). [DOI: [10.1149/1945-7111/abda22](https://doi.org/10.1149/1945-7111/abda22)]



Manuscript submitted October 26, 2020; revised manuscript received December 17, 2020. Published January 15, 2021.

Supplementary material for this article is available [online](#)

Metal/oxide interfaces play important roles in several applications including microelectronics, materials science, and chemical applications, where the metal over-layer is in the form of particles, such as in catalysis, or thick films (>50 nm), such as in the semiconductor industry. The deposition of metallic monolayers or extremely thin films (<5 nm) on oxide surfaces, for applications in heterogeneous catalysis and electrocatalysis, has never been achieved due to the high interfacial energy of the metal/oxide interface that always results in a 3D morphology growth of the deposited metal.<sup>1–4</sup> To realize these structures, the metal/oxide interfacial tension has to be minimized, for example, by reducing the outermost surface of the oxide support before metal deposition.

In general, oxide reduction is achieved by either heating an oxide in the presence of a reducing agent, or by electrochemical means, such as aqueous or molten salt electrolysis.<sup>5–10</sup> In fine materials processing methods, electrochemical reduction has several advantages over gas phase reduction, including ease of use, precise control over the morphology, the possibility to accurately monitor the process via electrochemical means, and the ability to perform additional processing steps, such as metal deposition, in situ.<sup>9–12</sup> Such in situ techniques have been extensively used in synthesizing core-shell metallic nano-structures for application in the fields of (electro-)catalysis,<sup>13–18</sup> biology,<sup>19</sup> materials chemistry,<sup>20,21</sup> and sensors.<sup>22,23</sup>

Continuous metal films on high surface area supports are among the most promising structures for next generation electrode production in batteries and fuel cells.<sup>24–29</sup> To obtain these structures on oxide support materials, the outermost surface of the oxide must be reduced to form a metallic buffer layer on which metal deposition takes place. However, most surfaces re-oxidize after reduction treatment once the reducing agent is removed. Thus, successful pre-reduction should be performed directly before subsequent metallization steps, without removing the material from the reductant.

One wet chemical reduction method that has been extensively employed in the synthesis of (metal) nanoparticles,<sup>30–34</sup> could be very suitable for in situ surface processing steps. This method is based on polyols, such as ethylene glycol (EG), di-, tri-, and tetraethylene glycol, or glycerol.<sup>31</sup> The polyols act as both solvent and reducing agent. They reduce solvated precursors to form metallic nanoparticles, and protect the nanoparticle surfaces from re-oxidation to enable subsequent metal deposition steps.<sup>29,35–38</sup> This technology would be very useful in electrode processing, if the reduction step can be additionally applied to solid surfaces, as it allows for uniform metallization of high surface area supports.

Here, we demonstrate that the polyol method can be used to reduce solid-state ions, specifically metal oxide surfaces, which is a completely new application of the polyol process. We show that metal oxide thin films, formed on bulk metallic substrates, metallic nanoparticles, and metal oxide nanoparticles, can be reduced by simply heating them in the appropriate polyalcohol, which would allow for a subsequent metal deposition step in the same solvent. In this system, the oxide reduction process can be in situ monitored, by measuring the electrode potential as a function of the temperature. The electrochemical means to monitor oxide reduction were confirmed by in situ near ambient pressure X-ray photoelectron spectroscopy (XPS) measurements. This polyol processing technique offers a low cost, easy to use, and highly adaptable method for a broad range of systems,<sup>31–33</sup> and will be a key processing technique in next generation fuel cell and battery electrode preparation.

### Experimental

A modified polyol setup to monitor oxide reduction.—In order to investigate the reduction of an oxide thin film by monitoring the potential of the working electrode (a Sn oxide/Sn wire in this case) against a reference electrode (RE) as a function of solvent temperature, a typical polyol setup was modified as schematically shown in Fig. 1a. As the most suitable solvent for this study, EG was chosen as the most basic polyol and due to its dominant role in the synthesis of noble metal nanoparticles.<sup>31</sup> To avoid the high temperature of the system upon heating, a Ag/AgCl RE was not directly placed in the EG but separated by two electrolyte bridges (EBs) filled with the same polyol. Figure 1b shows the temperature

\*Electrochemical Society Student Member.

\*\*Electrochemical Society Fellow.

<sup>a</sup>Present address: Mercedes-Benz Fuel Cell GmbH, 73230 Kirchheim/Teck-Nabern, Germany.

<sup>z</sup>E-mail: [hany.el-sayed@tum.de](mailto:hany.el-sayed@tum.de)

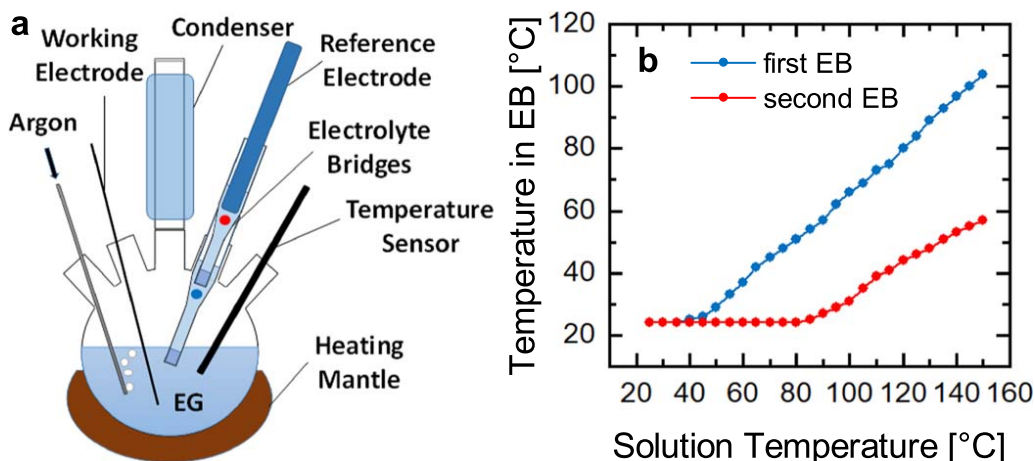


**Figure 1.** (a) Modified polyol setup used for monitoring the potential of the working electrode during the reduction by ethylene glycol; (b) temperature measured in the first and the second electrolyte bridge while heating the solution at  $1\text{ }^{\circ}\text{C min}^{-1}$ .

inside the first and second EBs, represented by the blue and red dots, respectively, as a function of EG temperature. Clearly, a single EB is not sufficient to prevent the RE from reaching the boiling temperature of the water-based RE electrolyte. However, when using two EBs, measurements until  $180\text{ }^{\circ}\text{C}$  can easily be achieved. Ar purging for 90 min with a flow rate of ca.  $20\text{ l h}^{-1}$  was necessary to remove most soluble oxygen from the EG solvent. The potential of the working electrode was monitored at room temperature during the Ar purging. It was found that the potential gradually moves to more negative values with the Ar purging until a steady state potential was obtained indicating a constant concentration of oxygen in the solvent. This also suggests that the potential of the Sn electrode is mainly controlled by the  $\text{O}_2/\text{H}_2\text{O}$  redox equilibrium at room temperature. After 90 min of Ar purging the flow rate was reduced to  $10\text{ l h}^{-1}$  during the experiment. The temperature of the system was increased with a ramp rate of  $1\text{ }^{\circ}\text{C min}^{-1}$  until the temperature reached the desired endpoint after which the system was allowed to cool down to room temperature at a rate of  $1\text{ }^{\circ}\text{C min}^{-1}$ . For measurements on nanoparticles,  $10\text{ }\mu\text{l}$  of an ink consisting of  $1.0\text{ mg}$  nanoparticles in  $3.3\text{ ml}$  2-propanol was drop casted onto the polished end of a glassy carbon rod ( $5\text{ mm}$  diameter), which served as the working electrode.

**Cyclic voltammetry in the modified polyol setup.**—All Cyclic voltammetry (CV) measurements were performed at room temperature in the modified polyol setup described above with a scan rate of  $25\text{ mV s}^{-1}$ . For CV measurements at intermediate points during the heating cycle, the heating was interrupted at the indicated temperature and the reaction was flash-cooled to room temperature using an ice bath. To measure the potential more accurately, the EBs were removed and the RE was placed directly in the reaction vessel. A curled up gold wire was used as the counter electrode for the CV measurements. The measured currents were normalized to the exposed surface of the wire (calculated from the thickness and the electrolyte exposed length) or the area of the GC rod ( $0.196\text{ cm}^2$ ), respectively.

**X-ray photoelectron spectroscopy (XPS).**—In-situ XPS measurements were performed using a Phoibos NAP-150 hemispherical analyzer from SPECS Surface Nanoanalysis GmbH. The excitation source was a monochromated Al  $k\text{-}\alpha$ . A  $1\text{ cm} \times 1\text{ cm}$  piece of Sn foil was mounted onto a stainless steel sample holder. Prior to loading, the foil was cleaned by ultrasonication in acetone and deionized water. The sample was first measured in vacuum, as-loaded. The sample was then heated to  $150\text{ }^{\circ}\text{C}$  in an atmosphere of  $0.1\text{ mbar}$  of EG. Heating was accomplished by illuminating the back-side of the sample holder with an infrared laser. Temperature was controlled using a calibration curve, whereby  $3\text{ W}$  were required to heat the sample to  $150\text{ }^{\circ}\text{C}$ . The  $0.1\text{ mbar}$  vapor pressure of EG was accomplished by dosing EG through an ultra-high vacuum leak

valve. EG was placed into a glass container, welded to a DN16-CF type flange, which was connected to the leak valve. The EG was degassed by several freeze-pump-thaw cycles, pumping to a turbo-molecular pump, having a base pressure of  $1 \times 10^{-6}\text{ mbar}$ . At room temperature, the ultimate pressure achievable when dosing EG was only  $0.04\text{ mbar}$ . Therefore, we heated the EG up to  $70\text{ }^{\circ}\text{C}$  by wrapping the glass vessel in heating tape. At  $70\text{ }^{\circ}\text{C}$  a pressure of  $0.1\text{ mbar}$  could be reached in the analysis chamber. A mass spectrometer (Pfeiffer Prisma), attached to the analysis chamber confirmed that EG, was being filled into the chamber. The mass spectrum showed a molecular peak of  $62\text{ AMU}$ , as expected for EG.

**Thermodynamic Calculations.**—To examine the possibility of reducing bulk metal oxides, we first consider the thermodynamics of metal oxide reduction in a polyol medium (ethylene glycol). By considering the full reduction of the metal oxide  $\text{MO}_x$  to the corresponding metal (Eq. 1) and the full oxidation of EG to  $\text{CO}_2$  (Eq. 2), and assuming standard conditions at the boiling point of the solvent, the Gibbs free energies ( $\Delta G_{\text{red}}$ ) for the reduction of numerous oxides were estimated previously.<sup>39</sup>



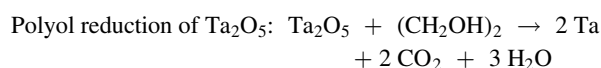
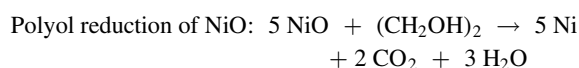
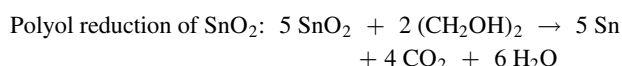
While the oxidation of EG during the polyol process follows a much more complex reaction pathway,<sup>40–42</sup> such calculations provide a useful indication of what might thermodynamically be possible. Thus, the Gibbs free energies of the reduction of three metal oxides (tin, nickel, and tantalum oxides) using EG were calculated as a function of temperature ( $\Delta_{\text{red}}G(T)$ ) under otherwise standard conditions (pressures/activities) using the standard enthalpy of formation ( $\Delta_f H_i^{\ominus}$ ) for the reactants and the standard entropy ( $S_i^{\ominus}$ ) for each compound at  $25\text{ }^{\circ}\text{C}$ , assuming that the entropy term is not a function of temperature within the investigated temperature range (Eq. 3).<sup>43</sup> For the calculation of the Gibbs free energy of reduction under more realistic conditions, the initial activities ( $a_i$ ) of reactants and products were taken into account (Eq. 4) using Raoult's law (Eq. 5).<sup>43</sup> In our experimental setup, an initial concentration of  $100\text{ ppm}$  of  $\text{H}_2\text{O}$  was measured by Karl Fischer titration and the maximum partial pressure ( $p_i$ ) of  $\text{CO}_2$  was estimated to be  $40\text{ ppm}$ , i.e.,  $10\%$  of the partial pressure of  $\text{CO}_2$  in air (under the condition of continuous purging with Ar). The activities of EG and all solid reactants were assumed to equal 1.

$$\Delta_{\text{red}}G(T) = \sum_i \nu_i \Delta_f H_i^{\ominus} - T \sum_i \nu_i S_i^{\ominus} \quad [3]$$

$$\Delta_{\text{red}}G(T, a_i) = \sum_i \nu_i \Delta_f H_i^\ominus - T \sum_i \nu_i S_i^\ominus + RT \ln \left( \prod_i a_i^{\nu_i} \right) \quad [4]$$

$$a_i = \frac{P_i}{P_i^\ominus} \approx \chi_i \quad [5]$$

Exemplarily, the Gibbs free energy was calculated for the reduction of tin, nickel and tantalum oxide assuming the following reaction equations (thermodynamic values given in Table S1 available online at [stacks.iop.org/JES/168/014506/mmedia](https://stacks.iop.org/JES/168/014506/mmedia)):



When comparing the Gibbs free energies of reduction under standard conditions (Fig. 2a) to more realistic conditions, taking the initial activities of reactants and products into account (Fig. 2b), it can be seen that, while nickel oxide may be reduced by EG even at room temperature and standard conditions, tantalum oxide cannot be reduced even up to the boiling temperature of EG. The calculations for tin oxide showed that, at standard conditions, it cannot be reduced by EG up to 200 °C. However, when reduced activities for CO<sub>2</sub> and H<sub>2</sub>O were considered, the results suggested that tin oxide could be reduced by EG even at room temperature.

## Results

The measurement of such reduction processes is not trivial for oxide nanoparticles dispersed and heated in EG. To facilitate the monitoring of oxide reduction, initial experiments were carried out to reduce oxide thin films on their corresponding metal substrates. This was achieved by dipping a Sn wire covered with native Sn oxide (Sn oxide/Sn) of an approximate thickness of 2-4 nm (a surface oxide thickness expected after long time exposure to air)<sup>44,45</sup> in EG and monitoring the potential vs a reference electrode. Lithium bis(trifluoromethanesulfonyl)imide (LiTFSI) was added to the EG to ensure sufficient ionic conductivity for in situ electrochemical characterization, while oxygen was removed by purging with argon to prevent re-oxidation.

The potential in any system is the result of a charge separation across the interface of two conducting phases.<sup>46</sup> Thus, a sudden change in potential would be expected upon reduction of the oxide layer, due to the different surface-electrolyte interaction between a semiconducting oxide and a metal electrode.<sup>47</sup> Figure 3a shows the change in the Sn oxide/Sn electrode potential, vs Ag/AgCl, as a function of EG temperature (1 °C min<sup>-1</sup> ramp rate).

It can be clearly seen that there are three distinguishable stages during the heating ramp. At stage I, a linear behavior of the potential vs temperature was observed, followed by a sudden decrease in the measured potential (stage II), and then a steady-state potential was obtained (stage III). The potential drop may indicate oxide thin film reduction, and a steady-state potential most likely indicates that no further changes (namely oxide reduction) are taking place,<sup>46</sup> although the temperature is still increasing, which suggests that the oxide reduction process has been completed.

Based on a typical polyol method, in which solvated metal ions are reduced to form metal nanoparticles, the behavior observed here is what is expected for the reduction of an oxide. For a metal ion to be reduced by a polyol, as long as it is thermodynamically favorable, a reaction barrier between the reduction potential of metal ions and the oxidation potential of polyol must be overcome by heating the polyol.<sup>44</sup> Therefore, in metal ion reduction, no substantial physical changes are observed until a significant reduction takes place at a threshold temperature, after which the color of the solution changes dramatically, indicating the formation of nanoparticles. Thermodynamically, oxide reduction can start at temperatures as low as 30 °C (Fig. 2b), but the reaction might still be kinetically hindered. This can be attributed to the time needed to reduce the oxide film and reveal the metal underneath it. According to our hypothesis, the potential drop starts only when the underlying metal is exposed to the EG, which requires reduction of the oxide film on top. In other words, it is possible that oxide reduction starts at low temperature, but the potential drop takes place only after consuming enough oxide to reveal the underlying metal.

In fact, clear signs of reduction, i.e. a change in the slope of the OCP-temperature profile resulting in a sudden potential drop, start at a threshold temperature of around 60 °C and continue until the oxide film has been fully reduced, after which a steady-state potential is reached. Upon cooling, this steady-state potential is maintained, indicating that the surface does not re-oxidize in the Ar-saturated electrolyte, confirming that the reduction is indeed kinetically hindered rather than the reduced surface being thermodynamically instable.

When performing a second heating cycle, following the reduction, the potential decrease is marginal compared to the distinct drop during the first heating ramp. This shows that the reduction had been

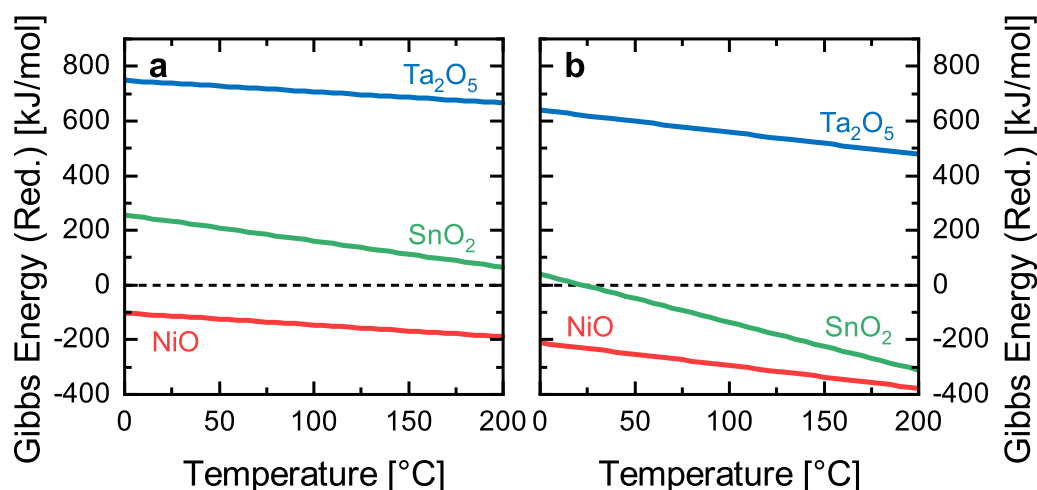


**Figure 2.** Gibbs free energy calculated for oxide reduction with EG to the corresponding metal at (a) standard conditions and (b) non-standard conditions (40 ppm CO<sub>2</sub> and 100 ppm H<sub>2</sub>O).

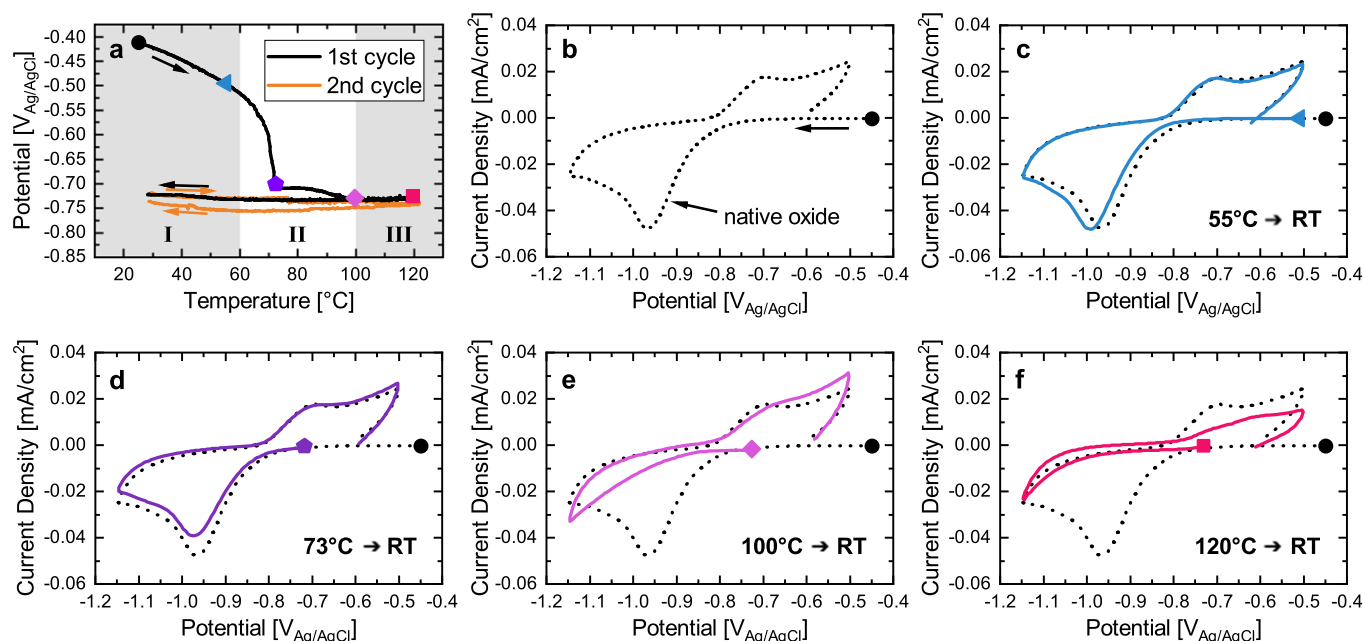


**Figure 3.** Chemical reduction of the native oxide thin layer on a Sn wire in ethylene glycol containing 0.25 M LiTFSI; (a) OCP-temperature profile with three distinguishable stages (I–III) and intermediate points used for electrochemical characterization; (b) CV of a fresh Sn wire; (c)–(f) CVs recorded at intermediate points during the reduction (after flash-cooling from the indicated temperature to room temperature) compared to the fresh wire showing increasing reduction of the native oxide. All CVs were recorded at room temperature (RT, 15–25 °C) at 25 mV s<sup>-1</sup>.

completed during the first cycle, and little to no re-oxidation by residual oxygen had occurred. To check this hypothesis, cyclic voltammetry (CV) measurements were performed at various stages of the reduction process (Figs. 3b–3f) using a fresh wire for each experiment and normalizing the current to the surface area exposed

to the electrolyte. CVs were conducted in the polyol solution in the presence of a conducting salt at room temperature after flash-cooling the solution from different temperature points of the heating cycle. When starting at the open circuit potential (OCP) of a fresh Sn wire, a reductive peak at  $-0.96$  V (vs Ag/AgCl;  $V_{\text{Ag/AgCl}}$ ) is observed

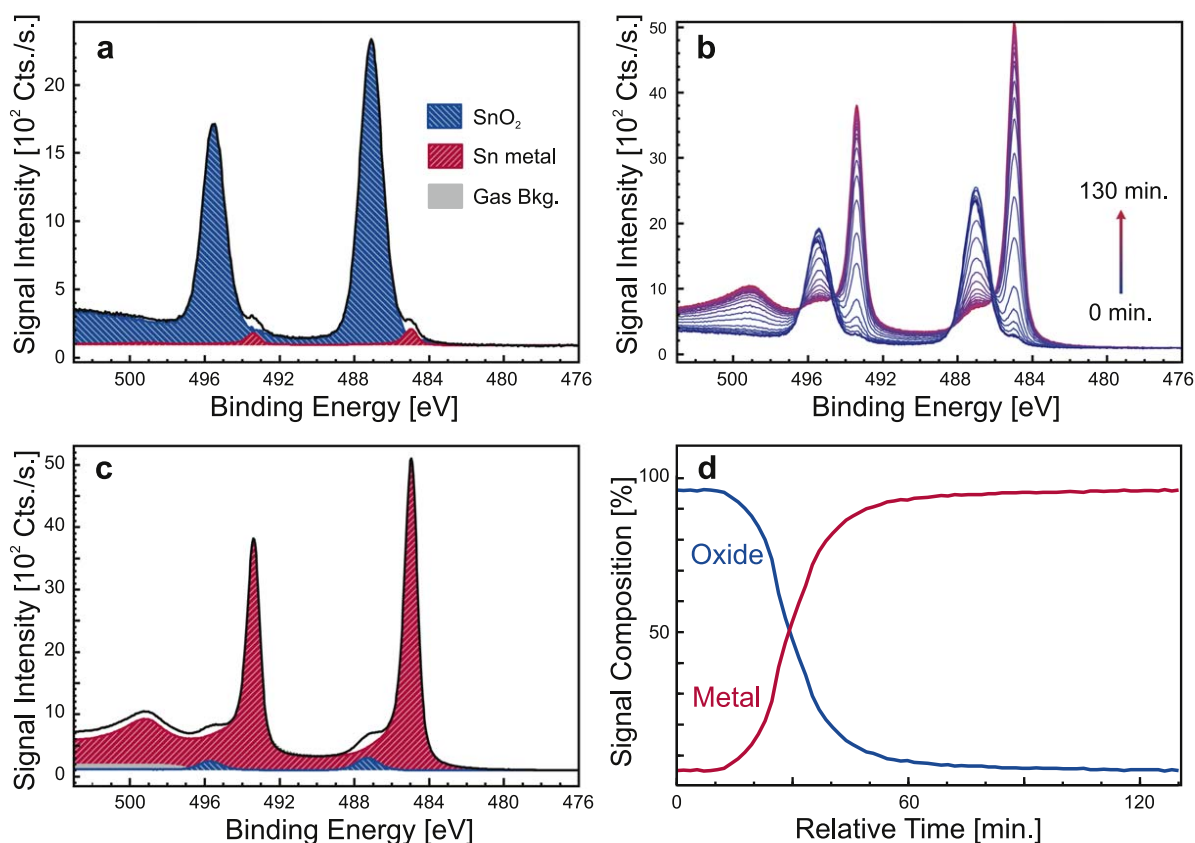


**Figure 4.** Near ambient pressure XPS showing the reduction of the native tin oxide thin film by EG. (a) Sn 3d signal of a fresh sample showing mainly tin oxide; (b) development of the Sn 3d signal upon heating to 150 °C in 0.1 mbar EG atmosphere; (c) Sn 3d signal after reduction; (d) partial contributions of the tin oxide and the elemental tin signal as a function of heating time.

during the negative going scan, corresponding to the reduction of the native oxide thin film (Fig. 3b). At the end of stage I (Fig. 3c), the reductive feature had shifted to slightly more negative potentials, most likely due to flash-cooling the solution below room temperature resulting in slower reduction kinetics,<sup>48</sup> but the total charge remained the same, indicating that no reduction has occurred. After the initial potential drop at  $\approx 70^\circ\text{C}$  (Fig. 3d), the reductive feature had decreased slightly compared to that of a fresh Sn wire, indicating the onset of the reduction. This implies that the potential drop is due to the oxide reduction, revealing metallic Sn, and that the intermediate potential plateau during stage II could be the result of a mixed potential region with Sn oxide and Sn surface being exposed while the reduction continues. After the second potential drop of stage II at  $\approx 100^\circ\text{C}$ , the reductive feature had mostly disappeared (Fig. 3e), and when the wire had been heated to the final temperature of  $120^\circ\text{C}$ , no further reduction could be observed during the CV (Fig. 3f), proving that the oxide reduction process has been completed on all surfaces that were in contact with EG and in turn electrochemically accessible by the electrolyte. A similar drop in the OCP has been observed when heating a Sn wire in pure EG indicating that the method of measuring the OCP can be applied to systems without additional conducting salts as well (Fig. S1). However, due to the low ionic conductivity in pure EG, the reduction could not be verified by measuring CVs.

To confirm that the reduction of  $\text{SnO}_2$  occurs in pure EG, near ambient pressure XPS was performed on a Sn foil to monitor the reduction in situ. The initial spectra of the sample, upon loading into vacuum from air, showed that the sample exhibited no signs of contamination except for the “adventitious carbon” signal typical for samples having been exposed to air.<sup>49</sup> The Sn 3d signal revealed signs of a thin native oxide layer formed on the foil, as evident from the oxidized Sn signal at a binding energy of ca. 487.1 eV.<sup>50</sup> One can also discern a weak signal from metallic Sn, at a binding energy of ca. 485.0 eV (Fig. 4a).<sup>51</sup> These observations suggest that the metallic Sn is buried under an oxide of ca. 6 nm thickness (based on the  $\text{Sn}^0$  relative to the  $\text{Sn}^{4+}$  signal intensity, and assuming an inelastic mean free path of 2 nm, for electrons with 1000 eV kinetic energy in  $\text{SnO}_2$ ). Note that an accurate determination of the Sn:O stoichiometry in the oxide film was not possible, due to the presence of the adventitious carbon (which also contains oxygen), and due to the fact that the oxide film was so thin, its signal has not converged to its bulk value. Nonetheless, a rough approximation of the Sn:O ratio, whereby these factors are ignored, gives a Sn-to-O ratio of 3:7, which is close to the 3:6 ratio one would expect for  $\text{SnO}_2$ . Thus we conclude that the native oxide was likely composed of  $\text{SnO}_2$ .

After heating the Sn foil in EG (0.1 mbar) to  $150^\circ\text{C}$ , the Sn 3d signal of the metallic component slowly starts to rise, while the signal of the oxidized component slowly decreases (Fig. 4b). The transition continues, and slows down to a near steady state after ca. 120 min (Fig. 4c). After this time, some small amount of oxidized Sn could still be discerned in the spectrum, equating to roughly 5% of the initial  $\text{SnO}_2$  signal intensity (Fig. 4d). Presumably, a higher pressure of EG or a higher temperature would eventually completely reduce this species. These results with EG vapor further prove that the reduction of the oxide film is achieved without dissolving the metal ions as it would be the case in a classical polyol process.<sup>34</sup>

## Discussion

Having shown that EG is capable of reducing the native oxide layer on bulk Sn by two in situ techniques, the potential of Sn nanoparticles (NPs,  $<150\text{ nm}$ ), drop-casted onto a glassy carbon (GC) disc, was measured in the LiTFSI-modified polyol setup to check whether this method can be applied to nanoparticles as well. Sn nanoparticles are also covered with a thin layer of Sn oxide, where the composition/thickness of this oxide depends on the synthesis method.<sup>52</sup> The OCP-temperature profile shows a potential drop that starts around  $95^\circ\text{C}$ , followed by a second potential drop beginning at  $150^\circ\text{C}$  (Fig. 5a). This indicates that the Sn oxide thin

film on nanoparticles might be more resistive to reduction than that on a flat Sn substrate, as would be expected due to the particle size effect on the surface energy that shifts the redox equilibrium towards the oxide for smaller particles.<sup>53</sup> Additionally, the contact between the nanoparticles forming the film may result in a reduced accessibility by EG, thus requiring more time and higher temperatures for the reduction. The absence of a hysteresis between the first and the second heating ramps in addition to a potential difference of about 470 mV between initial and final state indicate that oxide reduction has successfully taken place. Again, the reduction could be confirmed by the disappearance of the native oxide reduction feature in the CV after the heating cycle (Fig. 5b).

The thermodynamic calculations (Fig. 2) suggested that the reduction of NiO by EG should be possible, while  $\text{Ta}_2\text{O}_5$  should be unreducible even at  $200^\circ\text{C}$ . Having established that a distinct drop in potential shows the reduction of the native oxide thin film, further experiments were carried out to prove the general applicability of the method. As expected, the initial potential drop, indicating the start of oxide reduction, occurred at a relatively low temperature of  $\approx 40^\circ\text{C}$  when using a Ni wire (Fig. 6a). Interestingly, the potential during the second heating cycle perfectly overlapped with the cooling branch of the first cycle, indicating that the reductive strength of EG was sufficient to prevent any re-oxidation of nickel by traces of oxygen in the system. Again, for nickel nanoparticles ( $<100\text{ nm}$ ), the reduction took place at higher temperatures compared to a flat substrate, with no further reduction observable during a second heating cycle (Fig. 6c). On the contrary, the potential returned to the initial state when a tantalum wire was heated in EG, indicating that no reduction of tantalum oxide had taken place (Fig. 6b). Still, a hysteresis in the potential-temperature profile was observed which may hint towards a reversible interaction between EG and tantalum oxide that is kinetically hindered.

To this point, surface oxide reduction has merely been shown on native oxide thin films on metal substrates. However, the general applicability of using the polyol process for the reduction of surface oxides would require that it is possible to reduce the surface of bulk oxides as well. Thus, nanoparticles of antimony-doped tin oxide (ATO,  $<50\text{ nm}$ ), which are sufficiently conductive to allow for monitoring the potential, were investigated (Fig. 6d). According to the previous observations, the two distinct potential drops, starting at  $\approx 60^\circ\text{C}$  and  $\approx 140^\circ\text{C}$ , respectively, and a potential difference of  $\approx 170\text{ mV}$  at room temperature after the heating cycle strongly indicate that the reduction of the ATO surface was successful.

To demonstrate the general applicability of the newly discovered phenomenon, Fig. 7 shows the Gibbs free energy of reduction of a large number of oxides, using EG, plotted against temperature (both at standard and non-standard conditions). Figure 7a shows that there is a broad spectrum of oxides that can be readily reduced by EG, even at room temperature, for instance, NiO, CuO,  $\text{Co}_3\text{O}_4$ ,  $\text{IrO}_2$  and  $\text{MoO}_3$ . Some oxides, like  $\text{Fe}_2\text{O}_3$ , can be reduced by EG at elevated temperatures, and numerous oxides cannot be reduced even at EG's boiling temperature, e.g.,  $\text{SnO}_2$ ,  $\text{WO}_3$ ,  $\text{Al}_2\text{O}_3$  and ZnO. We have shown earlier that Sn oxide can be reduced by EG if the non-standard conditions are considered in the calculation.

Figure 7b, in which the non-standard conditions were considered in the calculation, shows that other than  $\text{SnO}_2$ , there are a few metal oxides that can be reduced by EG when the water content and  $\text{CO}_2$  concentrations are low enough. These oxides include  $\text{In}_2\text{O}_3$ ,  $\text{Fe}_3\text{O}_4$ , and  $\text{WO}_3$ . The comparison between Fig. 7a and b shows that the lines representing these metal oxides have moved below the zero line and thus they thermodynamically can be reduced by EG (if a full oxidation to  $\text{CO}_2$  is assumed). In Fig. 7c, the reduction of  $\text{SnO}_2$  to Sn is calculated for a variety of (poly)alcohols assuming full oxidation to  $\text{CO}_2$  and  $\text{H}_2\text{O}$ , and non-standard conditions (the calculations needed to obtain this figure are provided in the SI). While these thermodynamic calculations obviously neglect the complexity of the reduction reaction, they indicate that by tuning the reaction conditions, e.g. reducing the concentration of the side products  $\text{H}_2\text{O}$  and  $\text{CO}_2$ , and choosing a suitable (poly)alcohol, it is possible to reduce

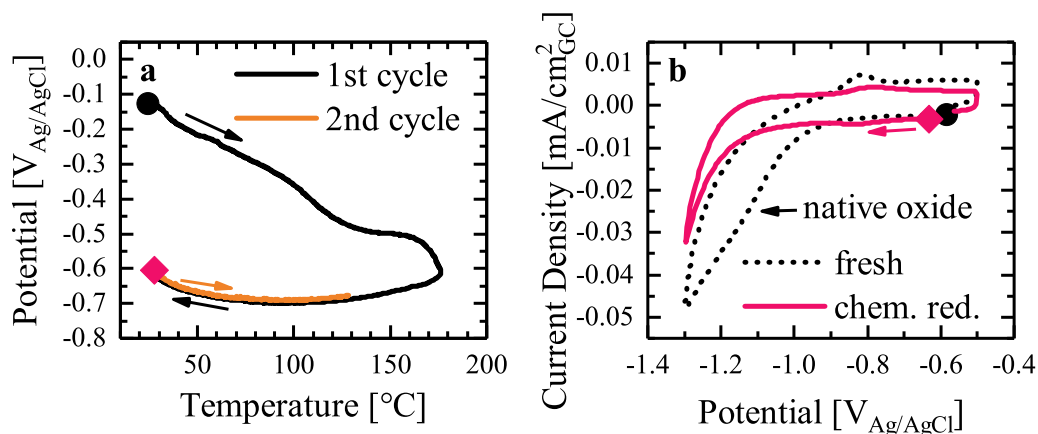


**Figure 5.** Chemical reduction of the native oxide thin layer on Sn nanoparticles in ethylene glycol containing 0.25 M LiTFSI; (a) OCP-temperature profile of the chemical reduction and electrochemical characterization points; (b) comparison of the CVs of fresh vs chemically reduced Sn nanoparticles (scan rate:  $25\text{ mV s}^{-1}$ ).

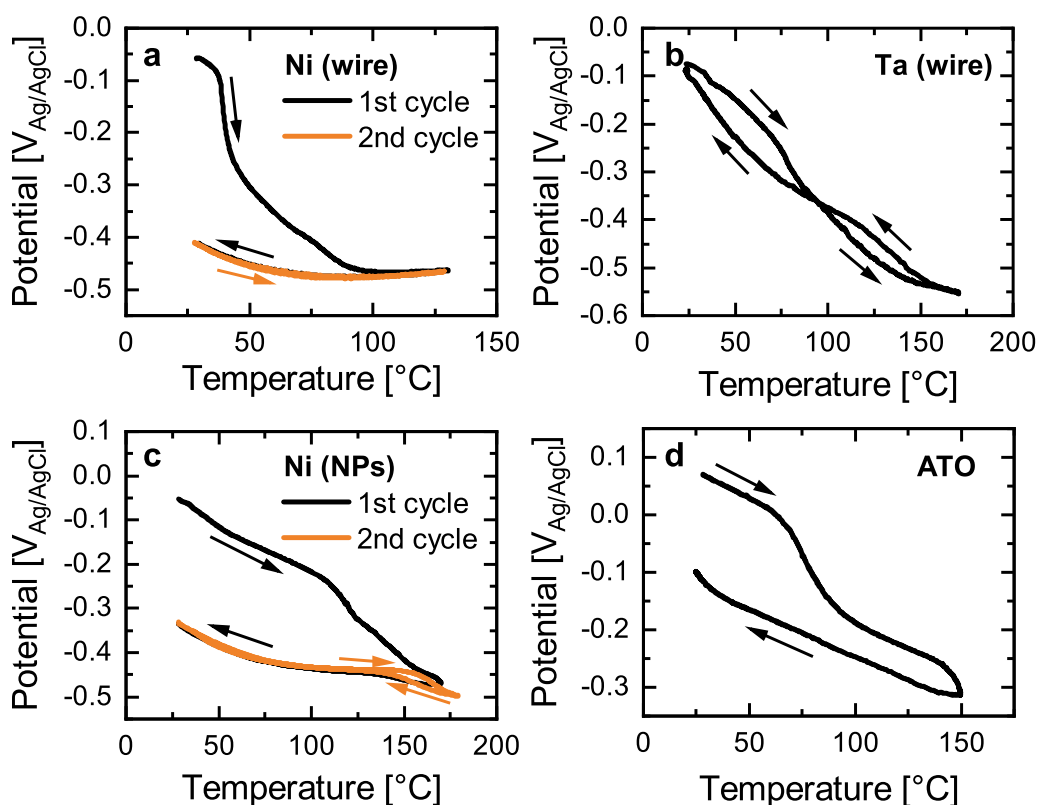


**Figure 6.** OCP-temperature profiles of (a) a Ni wire; (b) a Ta wire; (c) Ni nanoparticles; and (d) Sb-doped Sn oxide (ATO) nanoparticles while heated in ethylene glycol containing 0.25 M LiTFSI.

the surface of a broad range of metal oxides. It could be confirmed by near ambient pressure XPS that indeed methanol is capable of reducing the native  $\text{SnO}_2$  layer on a Sn substrate (data not shown).

### Conclusions

The results presented in this study clearly demonstrate that the polyol method is an efficient process in reducing oxide thin films on extended surfaces as well as on nanostructures. It was further shown that the reduction of these oxides can be in situ monitored by cyclic voltammetry when adding a conductive salt, e.g. LiTFSI. A drop in OCP was established as a clear indication for the reduction of an oxide thin film, thus allowing for a simple method to monitor the reduction process. In-situ recorded near ambient pressure XPS directly showed the reduction of the native oxide layer on a Sn

substrate by EG at elevated temperatures, thus verifying the electrochemical measurements. By OCP measurements, we have shown that EG can reduce both Sn and Ni oxides, but it is not capable of reducing Ta oxide under relevant conditions, and up to the boiling temperature of the solvent. The new oxide reduction process is independent of the oxide morphology (extended surfaces, nanoparticles and nanowires), so it can have a technological impact on metal coatings on oxide surfaces where the coating can be now done through a metallic buffer layer as shown here. Oxide<sub>core</sub>-metal<sub>shell</sub> structures may now be obtained on any oxide particle shape, which was limited in the past to surface modified metal oxides<sup>54</sup> or the use of metallic nanoparticles as intermediates for the shell formation.<sup>55,56</sup> Using this new approach, the surface of oxide particles of various shapes can be reduced, and so a metal

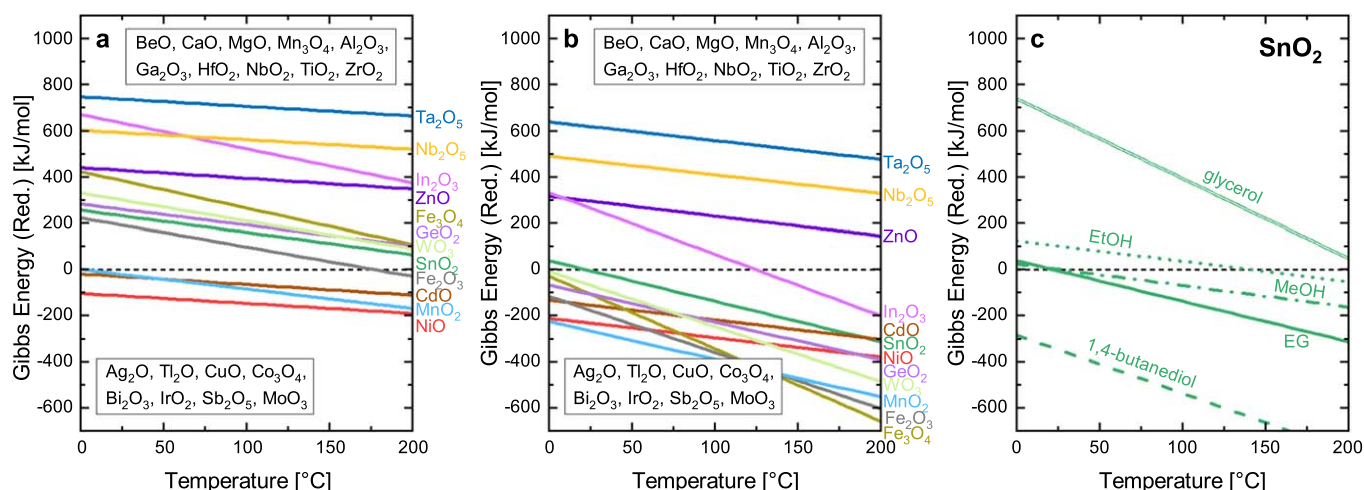


**Figure 7.** Gibbs free energy calculated for the reduction with EG to the corresponding metal at (a) standard conditions and (b) non-standard conditions (40 ppm CO<sub>2</sub> and 100 ppm H<sub>2</sub>O). Metal oxides given in the boxes have a clearly positive (top right) or negative (bottom left) Gibbs free energy of reduction; (c) Gibbs free energy for the reduction of SnO<sub>2</sub> by various (poly)alcohols at non-standard conditions.

layer may be coated on top of it via the polyol method, which is a process we are currently investigating.

### Acknowledgments

The financial support in the frame of the European Community's Seventh Framework Program (FP7/2013–2016) for the Fuel Cell and Hydrogen Joint Technology Initiative under grant agreement CATAPULT n°.325268 and that of the innoKA project (BMW, 03ET6096A) is acknowledged.

### ORCID

Björn M. Stühmeier <https://orcid.org/0000-0001-7713-2261>  
 Jan N. Schwämmlein <https://orcid.org/0000-0001-8902-4508>  
 Hubert A. Gasteiger <https://orcid.org/0000-0001-8199-8703>

### References

- Q. Fu and T. Wagner, *Surf. Sci. Rep.*, **62**, 431 (2007).
- J. Lu, K.-B. Low, Y. Lei, J. A. Libera, A. Nicholls, P. C. Stair, and J. W. Elam, *Nat. Commun.*, **5**, 3264 (2014).
- N. W. Kwak, S. J. Jeong, H. G. Seo, S. Lee, Y. Kim, J. K. Kim, P. Byeon, S.-Y. Chung, and W. Jung, *Nat. Commun.*, **9**, 4829 (2018).
- K. Sarakinos, *Thin Solid Films*, **688**, 137312 (2019).
- A. F. Hollemann, E. Wiberg, and N. Wiberg, *Lehrbuch der anorganischen Chemie, 102. Auflage* (Walter de Gruyter, Berlin, New York) (2007).
- S. Luidold and H. Antrekowitsch, *JOM*, **59**, 20 (2007).
- C. R. O'Connor, M. A. van Spronsen, T. Egle, F. Xu, H. R. Kersell, J. Oliver-Meseguer, M. Karatok, M. Salmeron, R. J. Madix, and C. M. Friend, *Nat. Commun.*, **11**, 1844 (2020).
- A. Borgschulte, O. Sambalova, R. Delmelle, S. Jenatsch, R. Hany, and F. Nüesch, *Sci. Rep.*, **7**, 40761 (2017).
- W. Xiao and D. Wang, *Chem. Soc. Rev.*, **43**, 3215 (2014).
- J. N. Schwämmlein, P. A. L. Torres, H. A. Gasteiger, and H. A. El-Sayed, *Sci. Rep.*, **10**, 59 (2020).
- G. Z. Chen, D. J. Fray, and T. W. Farthing, *Nature*, **407**, 361 (2000).
- A. M. Abdelkader, K. T. Kilby, A. Cox, and D. J. Fray, *Chem. Rev.*, **113**, 2863 (2013).
- J. Kibsgaard, Z. Chen, B. N. Reinecke, and T. F. Jaramillo, *Nat. Mater.*, **11**, 963 (2012).
- M. B. Gawande, A. Goswami, T. Asefa, H. Guo, A. V. Biradar, D.-L. Peng, R. Zboril, and R. S. Varma, *Chem. Soc. Rev.*, **44**, 7540 (2015).
- L. Tzounis, C. Gravalidis, A. Papamichail, and S. Logothetidis, *Materials Today: Proceedings*, **3**, 832 (2016).
- R. Jiang, S. o. Tung, Z. Tang, L. Li, L. Ding, X. Xi, Y. Liu, L. Zhang, and J. Zhang, *Energy Storage Mater.*, **12**, 260 (2018).
- M. Luo, Y. Yang, Y. Sun, Y. Qin, C. Li, Y. Li, M. Li, S. Zhang, D. Su, and S. Guo, *Mater. Today*, **23**, 45 (2019).
- W. Lamai, A. Bunphung, I. Junjapun, and A. Wongkaew, *Materials Today: Proceedings*, **17**, 1396 (2019).
- A.-M. Hada, M. Potara, S. Suarasan, A. Vulpoi, T. Nagy-Simon, E. Licarete, and S. Astilean, *Nanotechnology*, **30**, 315701 (2019).
- A. Pajor-Świerzy, D. Gaweł, E. Drzymała, R. Socha, M. Parlińska-Wojtan, K. Szczepanowicz, and P. Warszyński, *Nanotechnology*, **30**, 015601 (2018).
- P. Bhatia, S. S. Verma, and M. M. Sinha, *Chem. Phys. Lett.*, **745**, 137272 (2020).
- A. Härtl, E. Schmich, J. A. Garrido, J. Hernando, S. C. R. Catharino, S. Walter, P. Feulner, A. Kromka, D. Steinmüller, and M. Stutzmann, *Nat. Mater.*, **3**, 736 (2004).
- P. K. Kalambate, Dhanjai, Z. Huang, Y. Li, Y. Shen, M. Xie, Y. Huang, and A. K. Srivastava, *TrAC, Trends Anal. Chem.*, **115**, 147 (2019).
- S. H. Joo, J. Y. Park, C.-K. Tsung, Y. Yamada, P. Yang, and G. A. Somorjai, *Nat. Mater.*, **8**, 126 (2009).
- D. F. van der Vliet, C. Wang, D. Tripkovic, D. Strmcnik, X. F. Zhang, M. K. Debe, R. T. Atanasoski, N. M. Markovic, and V. R. Stamenkovic, *Nat. Mater.*, **11**, 1051 (2012).
- K. Y. Cho, Y. S. Yeom, H. Y. Seo, P. Kumar, K.-Y. Baek, and H. G. Yoon, *J. Mater. Chem. A*, **5**, 3129 (2017).
- H. Wang, H. Yu, S. Yin, Y. Xu, X. Li, Y. Yamauchi, H. Xue, and L. Wang, *J. Mater. Chem. A*, **6**, 12744 (2018).
- Z. Wang, Q. Gao, P. Lv, X. Li, X. Wang, and B. Qu, *J. Mater. Sci. Technol.*, **38**, 119 (2020).
- Y.-C. Hsieh et al., *Nat. Commun.*, **4**, 2466 (2013).
- S. Alayoglu, A. U. Nilekar, M. Mavrikakis, and B. Eichhorn, *Nat. Mater.*, **7**, 333 (2008).
- F. Fiévet, S. Ammar-Merah, R. Brayner, F. Chau, M. Giraud, F. Mammeri, J. Peron, J. Y. Piquemal, L. Sicard, and G. Viau, *Chem. Soc. Rev.*, **47**, 5187 (2018).
- S. Nam, B. Park, and B. D. Condon, *RSC Adv.*, **8**, 21937 (2018).
- I. Favier, D. Pla, and M. Gómez, *Chem. Rev.*, **120**, 1146 (2020).
- H. Dong, Y. C. Chen, and C. Feldmann, *Green Chem.*, **17**, 4107 (2015).
- G. Park, D. Seo, J. Jung, S. Ryu, and H. Song, *J. Phys. Chem. C*, **115**, 9417 (2011).
- N. V. Long, T. Asaka, T. Matsubara, and M. Nogami, *Acta Mater.*, **59**, 2901 (2011).
- H. Zhu, X. Li, and F. Wang, *Int. J. Hydrogen Energy*, **36**, 9151 (2011).
- J. N. Schwämmlein, B. M. Stühmeier, K. Wagenbauer, H. Dietz, V. Tileli, H. A. Gasteiger, and H. A. El-Sayed, *J. Electrochem. Soc.*, **165**, H229 (2018).
- D. Larcher and R. Patrice, *J. Solid State Chem.*, **154**, 405 (2000).
- M. J. González, C. T. Hable, and M. S. Wrighton, *J. Phys. Chem. B*, **102**, 9881 (1998).
- T. Matsumoto, K. Takahashi, K. Kitagishi, K. Shinoda, J. L. Cuya Huaman, J.-Y. Piquemal, and B. Jayadevan, *New J. Chem.*, **39**, 5008 (2015).
- H. A. El-Sayed, V. M. Burger, M. Miller, K. Wagenbauer, M. Wagenhofer, and H. A. Gasteiger, *Langmuir*, **33**, 13615 (2017).
- P. N. Atkins and J. De Paula, *Atkins' Physical Chemistry* 10th edn. ed. (Oxford Univ. Press, Oxford) (2014).
- S. Cho, J. Yu, S. K. Kang, and D.-Y. Shih, *J. Electron. Mater.*, **34**, 635 (2005).
- P. Song and D. Wen, *J. Phys. Chem. C*, **113**, 13470 (2009).
- A. J. Bard and L. R. Faulkner, *Electrochemical Methods: Fundamentals and Applications* (Wiley, Hoboken) (2001).
- N. Sato, *Electrochemistry at Metal and Semiconductor Electrodes* (Elsevier, Amsterdam) (1998).
- S. Hadži-Jordanov, *J. Electrochem. Soc.*, **125**, 1471 (1978).
- T. L. Barr and S. Seal, *J. Vac. Sci. Technol. A*, **13**, 1239 (1995).
- M. A. Stranick and A. Moskwa, *Surf. Sci. Spectra*, **2**, 50 (1993).
- J. F. Moulder, W. F. Stickle, and P. E. Sobol, *Handbook of X-ray Photoelectron Spectroscopy* (Perkin-Elmer, Physical Electronics Division, Eden Prairie) (1993).
- S. Nakayama, T. Sugihara, J. Matsumoto, T. Notoya, and T. Osakai, *J. Electrochem. Soc.*, **158**, C341 (2011).
- A. Navrotsky, C. Ma, K. Lilova, and N. Birkner, *Science*, **330**, 199 (2010).
- E. A. Kwizera, E. Chaffin, Y. Wang, and X. Huang, *RSC Adv.*, **7**, 17137 (2017).
- J. C. M. Silva, R. F. B. De Souza, L. S. Parreira, E. T. Neto, M. L. Calegario, and M. C. Santos, *Appl. Catal., B*, **99**, 265 (2010).
- V. M. Dhavale and S. Kurungot, *J. Phys. Chem. C*, **116**, 7318 (2012).

### 3.2.2. SMSI-Induced HOR-Selectivity of Pt/TiO<sub>x</sub> Catalysts

This section presents the article "Highly Selective Pt/TiO<sub>x</sub> Catalysts for the Hydrogen Oxidation Reaction" that was published in August 2019 in *ACS Applied Energy Materials*.<sup>118</sup> It is an open access article that is reprinted with permission from *ACS Appl. Energy Mater.* 2019, 2, 5534-5539. Copyright 2019 American Chemical Society. The permanent web-link to the article is <https://dx.doi.org/10.1021/acsaem.9b00718>. Additionally, the paper was presented by Björn Stühmeier at the 70<sup>th</sup> Annual Meeting of the *International Society of Electrochemistry* (August 4-9, 2019, Durban, South Africa, Abstract number: ise185364).

As described in Section 1.3, the SMSI between a Pt nanoparticle and a reducible oxide can significantly alter the electrocatalytic properties of the catalyst. For instance, Banham *et al.* showed that Pt supported on Nb-doped TiO<sub>2</sub> develops a reduced ORR activity upon cycling the catalyst between 1.0 – 1.4 V, while maintaining its HOR activity.<sup>103</sup> A similarly suppressed ORR activity has been shown by Hsieh *et al.* after heating their Pt/TiO<sub>2</sub> catalyst in reductive atmosphere.<sup>114</sup> As mentioned in Section 1.1, an anode catalyst that has a high HOR activity but at the same time a low ORR activity should result in a significantly reduced degradation of the carbon support of the cathode catalyst during SUSD events.<sup>59</sup> However, the implementation of an oxide supported catalyst is challenging, as oxides often lack the porous structure and electrical conductivity that render carbon to be the essentially exclusively used support material for PEMFC catalysts.<sup>66</sup> In this study, we aim to combine the SMSI-driven superior HOR-selectivity of Pt/TiO<sub>x</sub> ( $x \leq 2$ ) with the advantages of a carbon support. This is achieved by depositing Pt nanoparticles synthesized by the polyol process on nanoparticles of TiO<sub>x</sub> that are obtained from the hydrolysis of titanium(IV)isopropoxide. The Pt/TiO<sub>x</sub> agglomerates are then deposited on a high surface area Vulcan carbon support that ensures the structural integrity and large-range electrical conductivity of the final catalyst layer in an MEA. The SMSI is achieved by heating the catalyst to 400 °C in 5% H<sub>2</sub>/Ar.

Compared to a Pt/C reference catalyst, the Pt/TiO<sub>x</sub>/C catalyst shows almost no Pt oxidation features and a significantly reduced ORR activity ( $\approx 10$ -times lower mass activity for the as-synthesized catalyst and  $\approx 50$ -times lower activity after the heat-treatment), which agrees well with previous observations by other groups.<sup>101,102,114</sup> The SMSI formation is confirmed by high resolution TEM images that show an en-

capsulation of the Pt particles after the heat-treatment. Interestingly, the catalyst shows not only an HOR activity that is higher than what can be measured with an RDE setup, but also maintains the mass transport limited current up to  $1.5 V_{\text{RHE}}$ , whereas the Pt/C reference loses its HOR activity above  $1.0 V_{\text{RHE}}$  due to Pt surface oxidation. The HOR/HER kinetics obtained from polarization curves in 0.1M NaOH, where the HOR/HER kinetics are roughly two orders of magnitude slower,<sup>181</sup> show that with an exchange current density of  $57 \pm 14 \text{ A g}_{\text{Pt}}^{-1}$ , the heat-treated Pt/TiO<sub>x</sub>/C catalyst is only  $\approx 3$  times less active compared to Pt/C ( $161 \pm 18 \text{ A g}_{\text{Pt}}^{-1}$ ). Thus, the selectivity, i.e., the ratio between HOR and ORR activity, of the Pt/TiO<sub>x</sub>/C<sup>400°C, H<sub>2</sub></sup> catalyst is  $\approx 18$  times higher compared to Pt/C, which should make it a suitable SUSD mitigation catalyst (this will be tested in Section 3.3.1).

#### **Author contributions**

B.M.S. synthesized the catalyst and performed the electrochemical testing. S.S. did the TEM measurements. M.U.M.P. and T.N.G. performed pre-experiments that were crucial for the synthesis of titanium oxide nanoparticles and the electrochemical understanding of the SMSI. B.M.S., H.A.E., and H.A.G. developed the catalyst concept and wrote the manuscript. All authors discussed the results and commented on the manuscript.

# Highly Selective Pt/TiO<sub>x</sub> Catalysts for the Hydrogen Oxidation Reaction

Björn M. Stühmeier,<sup>\*,†</sup> Sören Selve,<sup>‡</sup> Manu U. M. Patel,<sup>†</sup> Timon N. Geppert,<sup>†</sup> Hubert A. Gasteiger,<sup>†</sup> and Hany A. El-Sayed<sup>†</sup>

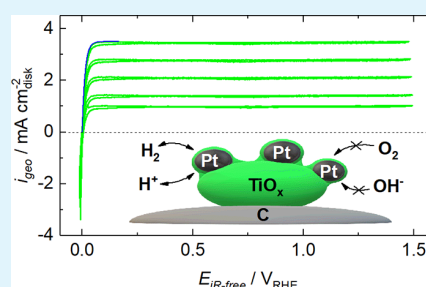
<sup>†</sup>Chair of Technical Electrochemistry, Department of Chemistry and Catalysis Research Center, Technical University of Munich, Lichtenbergstr. 4, 85748 Garching, Germany

<sup>‡</sup>Center for Electron Microscopy (ZELMI), Technical University of Berlin, Straße des 17. Juni 135, 10623 Berlin, Germany

## Supporting Information

**ABSTRACT:** Reducing the cathode degradation in proton exchange membrane fuel cells during start-up and shut-down events (where the anode is filled with H<sub>2</sub> and air) is crucial for its widespread automotive implementation. The use of selective catalysts for the hydrogen oxidation reaction (HOR) that sparingly reduce oxygen on the anode could significantly reduce the carbon corrosion on the cathode. Herein, we report a novel system of carbon supported Pt/TiO<sub>x</sub> catalysts that combines the unique properties of a strong metal–support interaction (SMSI) with the known advantages of a carbon support. High-resolution transmission electron microscopy of the selective catalyst shows the encapsulation of the Pt nanoparticles (NPs) by a TiO<sub>x</sub> layer resulting from the SMSI. Rotating disk electrode experiments confirmed that Pt oxidation and oxygen reduction are hindered due to the TiO<sub>x</sub> layer. Furthermore, a high HOR activity that is retained even at high potentials proved the superior HOR selectivity of the catalyst.

**KEYWORDS:** electrochemistry, fuel cells, hydrogen oxidation reaction, oxygen reduction reaction, strong metal–support interaction, start-up/shut-down



## 1. INTRODUCTION

A major durability issue of proton exchange membrane fuel cells (PEMFCs) is the long-term stability of the cathode, especially during start-up and shut-down (SUSD) events, where a H<sub>2</sub>/air gas front passes through the anode, which leads to the oxygen reduction reaction (ORR) in the air-filled anode segment. At the adjacent segment of the cathode, carbon oxidation and H<sub>2</sub>O oxidation take place, leading to its degradation.<sup>1,2</sup> Shintani et al. showed that if the ORR on the anode is hindered due to a change in the support's conductivity upon switching from H<sub>2</sub> to air, i.e., the Pt being electrically insulated at high potentials, the degradation of the cathode can be significantly reduced.<sup>3</sup> Furthermore, Durst et al. showed for Ir/C vs Pt/C that an anode catalyst selective for the hydrogen oxidation reaction (HOR) compared to the ORR could significantly reduce SUSD-induced performance losses.<sup>4</sup> Still, only a few other HOR-selective catalysts have been proposed, focusing mainly on highly dispersed Pt catalysts<sup>5,6</sup> or selective poisoning of the Pt surface.<sup>7,8</sup> A promising approach in this direction is the modification of the catalytic properties of oxide-supported Pt-NPs by strong metal–support interaction (SMSI) effects. SMSI has long been known in heterogeneous catalysis<sup>9</sup> but only recently gained interest in electrocatalysis, revealing, e.g., an exceptional CO oxidation activity for Au/TiO<sub>2</sub> vs Au/C<sup>10</sup> or a strongly enhanced ORR activity for Pt/doped-SnO<sub>2</sub> vs Pt/C.<sup>11</sup> Recent results for Nb-

doped TiO<sub>2</sub>-supported Pt further showed that the ORR activity can be reduced upon cycling at high potentials, apparently without affecting the HOR activity; this was explained by selective Pt site blocking through the dissolution and redeposition of the oxide support.<sup>12</sup> Here, we present a novel system of Pt/TiO<sub>x</sub>/C ( $x \leq 2$ ) catalysts that combine the SMSI-driven superior HOR-selectivity of Pt/TiO<sub>x</sub> with the advantages of a carbon support (high conductivity and low packing density, yielding highly porous electrodes).

## 2. EXPERIMENTAL SECTION

The Pt/TiO<sub>x</sub>/C catalysts were synthesized by using a multistep synthesis method. First, titania-NPs were obtained by the dropwise addition of 1.15 mL of titanium(IV) isopropoxide dissolved in 50 mL of absolute ethanol to 50 mL of water at 80 °C. After addition of 50 mL of ethylene glycol (EG), ethanol and water were removed *in vacuo*. In a second flask, Pt-NPs were obtained by polyol synthesis from 425 mg of potassium tetrachloroplatinate(II) dissolved in 250 mL of EG at a pH of  $\approx 10$  (adjusted using 0.1 M NaOH<sub>(EG)</sub>). The solution was heated (4 °C min<sup>-1</sup>) to 130 °C, kept at this temperature for 90 min, and then cooled to room temperature. Subsequently, both vessels were sonicated for 10 min, and one-half of the Pt NP solution was added to the titania dispersion, while the other half was added to a suspension of 150 mg of Vulcan carbon in 100 mL of EG to obtain

**Received:** April 8, 2019

**Accepted:** July 24, 2019

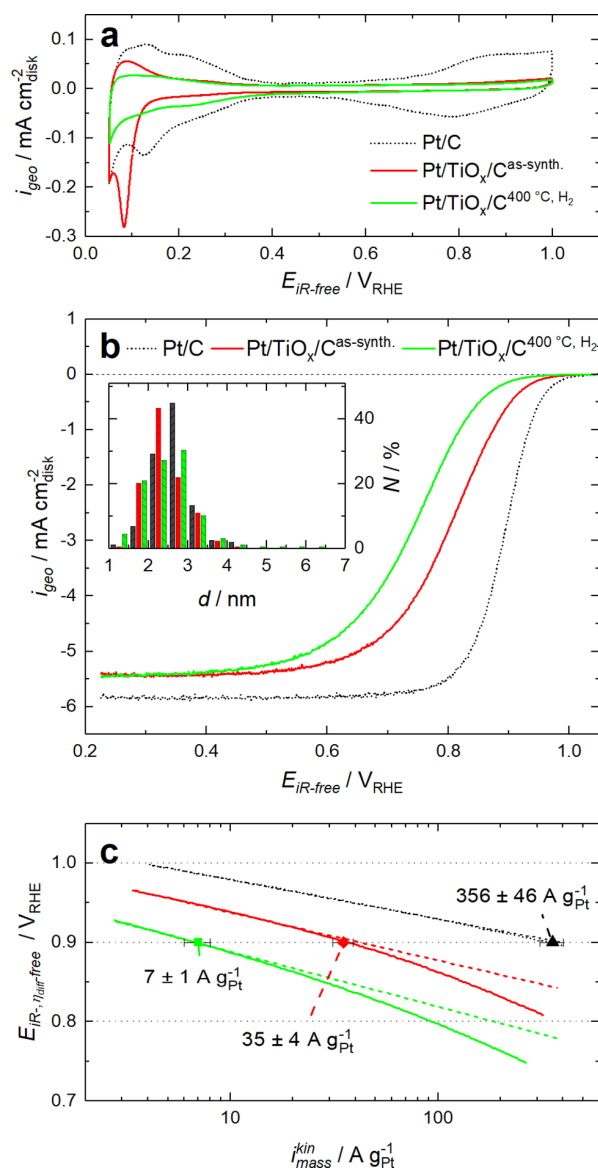
**Published:** August 5, 2019

the Pt/C reference catalyst. The pH of both mixtures was adjusted to  $\approx 4$  by adding 0.1 M  $\text{H}_2\text{SO}_4(\text{EG})$ . The centrifugation of  $\approx 0.5$  mL of the freshly prepared and pH-adjusted Pt +  $\text{TiO}_x$  mixture led to a white precipitation of  $\text{TiO}_x$  and a brown centrifugate of well-dispersed Pt-NPs. After 16 h of stirring, however, the same test resulted in a brown precipitate and a colorless clear solution, thus indicating a successful supporting of the Pt-NPs on the  $\text{TiO}_x$ . Furthermore, a solution of Pt-NPs stirred under the same conditions for 16 h without a support still resulted in a stable brown solution after the centrifugation, indicating that only when most of the Pt-NPs were successfully supported on  $\text{TiO}_x$ , a clear centrifugate could be observed. The Pt/ $\text{TiO}_x$  suspension was then added to a suspension of 150 mg of Vulcan carbon in 100 mL of EG and stirred for another 48 h. The catalysts were then separated by centrifugation, washed three times with acetone, and dried at 70 °C in air. Finally, 60 mg of the as-synthesized Pt/ $\text{TiO}_x$ /C<sup>as-synth.</sup> were heat-treated for 1 h at 400 °C (10 K min<sup>-1</sup>) in a reductive atmosphere (5%  $\text{H}_2/\text{Ar}$ ) to obtain Pt/ $\text{TiO}_x$ /C<sup>400°C,H<sub>2</sub></sup>. Inductively coupled plasma mass spectrometry (ICP-MS) was used to determine the Pt content of the catalysts.

### 3. RESULTS AND DISCUSSION

Rotating disk electrode (RDE) experiments were performed to evaluate the electrochemical properties of the catalysts (for details see our previous publications<sup>13,14</sup> and the Supporting Information). Figure 1a shows the cyclic voltammograms (CVs) of the catalysts in Ar-saturated 0.1 M  $\text{HClO}_4$ . In agreement with the literature,<sup>13,15</sup> Pt/C (dotted line) exhibits hydrogen underpotential deposition ( $\text{H}_{\text{upd}}$ ) features at  $< 0.4$  V vs the reversible hydrogen potential (RHE) as well as platinum oxidation ( $\text{Pt}_{\text{ox}}$ ) and corresponding reduction features at  $> 0.6$  V<sub>RHE</sub>. These features are suppressed for both Pt/ $\text{TiO}_x$ /C catalysts, and a reductive feature at 0.09 V<sub>RHE</sub> is observed for Pt/ $\text{TiO}_x$ /C<sup>as-synth.</sup> (red line) in the negative going scan. The charge is not fully compensated in the positive going scan, which can be explained by hydrogen spillover ( $\text{H}_{\text{so}}$ ) from Pt onto the oxide supports, which is well-known in heterogeneous catalysis.<sup>16,17</sup> This leads to the observed imbalance between anodic and cathodic charges (note that this imbalance disappears after a large number of scans; data not shown). This charge imbalance is not as pronounced for Pt/ $\text{TiO}_x$ /C<sup>400°C,H<sub>2</sub></sup> since the support is already partially reduced after the heat treatment in  $\text{H}_2$ . The  $\text{Pt}_{\text{ox}}$  features are suppressed completely for both Pt/ $\text{TiO}_x$ /C catalysts, similar to what has been reported for Pt/ $\text{TiO}_x$ ,<sup>18,19</sup> heat-treated Pt/ $\text{TiO}_2$ ,<sup>20</sup> and cycled Pt/(Nb)/ $\text{TiO}_2$ .<sup>12,21</sup>

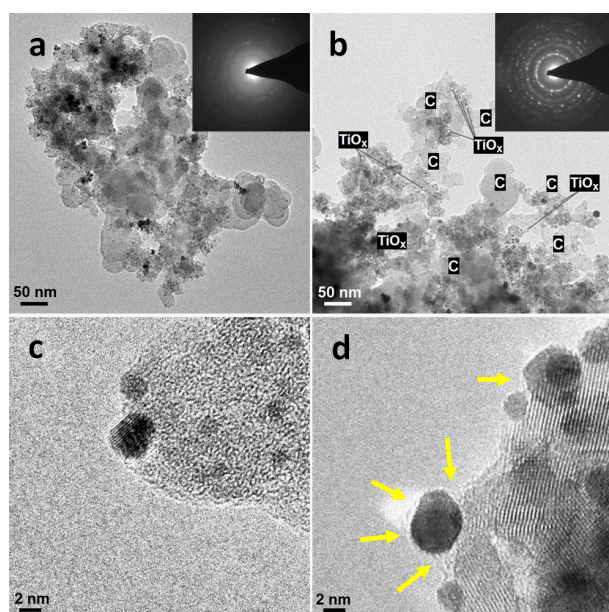
Figure 1b shows the RDE-based ORR activity of the catalysts, whereby the mass-transport-limited current densities are within 10% of previously reported values,<sup>14,22</sup> thus confirming the high quality of the coatings. Quite clearly, compared to the Pt/C catalyst, the ORR activities of the Pt/ $\text{TiO}_x$ /C catalysts are substantially lower, particularly after hydrogen treatment (Pt/ $\text{TiO}_x$ /C<sup>400°C,H<sub>2</sub></sup>). To extract kinetic data from the ORR polarization curves, corrections for the diffusion overpotential and oxygen mass transport were applied (details in the Supporting Information).<sup>14,22</sup> Unfortunately, the electrochemically accessible surface area (ECSA) of the Pt/ $\text{TiO}_x$ /C catalysts cannot be determined reliably by using the  $\text{H}_{\text{upd}}$  area due to the SMSI-induced  $\text{H}_{\text{so}}$  effects, nor can it be quantified by CO stripping voltammetry, as SMSI effects significantly hinder CO chemisorption.<sup>23</sup> Therefore, the ORR activities are normalized to the Pt mass throughout this study, which is reasonable considering the essentially identical transmission electron microscopy (TEM) derived Pt particle



**Figure 1.** Comparison of Pt/ $\text{TiO}_x$ /C<sup>as-synth.</sup> (red line,  $16.7 \mu\text{g}_{\text{Pt}} \text{cm}_{\text{disk}}^{-2}$ ), Pt/ $\text{TiO}_x$ /C<sup>400°C,H<sub>2</sub></sup> (green line,  $20.5 \mu\text{g}_{\text{Pt}} \text{cm}_{\text{disk}}^{-2}$ ), and Pt/C (dotted line,  $14.8 \mu\text{g}_{\text{Pt}} \text{cm}_{\text{disk}}^{-2}$ ). All measurements were conducted at room temperature with a scan rate of  $10 \text{ mV s}^{-1}$  and with an ionomer/carbon mass ratio of  $\text{I/C} = 0.1$ . (a) CVs in Ar-saturated 0.1 M  $\text{HClO}_4$  at 0 rpm. (b) Capacitively corrected ORR polarization curves recorded in  $\text{O}_2$ -saturated 0.1 M  $\text{HClO}_4$  at 1600 rpm (only the positive-going scan is shown); inset: particle size distribution obtained by TEM. (c) Tafel plot of diffusion overpotential-corrected,  $iR$ -free potential vs mass-specific kinetic current density, whereby the given numerical mass activity values at 0.9 V<sub>RHE</sub> are the average of at least two separate measurements.

size distributions (Figure 1b, inset) with Sauter diameters ( $\equiv \sum d_i^3 \cdot (\sum d_i^2)^{-1}$ ) and thus specific surface areas being very similar (2.6 nm for Pt/ $\text{TiO}_x$ /C<sup>as-synth.</sup>, 2.8 nm for Pt/C, and 3.0 nm for Pt/ $\text{TiO}_x$ /C<sup>400°C,H<sub>2</sub></sup>). Figure 1c shows the Tafel plot of the diffusion overpotential- and  $iR$ -corrected potential vs the mass-specific kinetic current density. The ORR mass activity is  $\approx 10$ -fold reduced upon the introduction of  $\text{TiO}_x$  and by  $\approx 50$ -fold after catalyst heat treatment in  $\text{H}_2$ . Based on the TEM

analysis, the strongly reduced ORR activity cannot be explained by Pt sintering,<sup>20</sup> but rather by a SMSI effect, as observed by Hsieh et al.,<sup>20</sup> or by an atmospheric switching resistive mechanism (ASRM), as proposed by Shintani et al.<sup>3</sup> However, the latter is unlikely to be the cause in the presented experiments, as a carbon support was used. The current path through the  $\text{TiO}_x$  is therefore only a few nanometers as compared to a few micrometers in the case of a purely Ta- $\text{TiO}_2$ -based electrode used by Shintani et al.<sup>3</sup> An increase in resistance by about an order of magnitude<sup>3</sup> on such short current paths will not lead to a complete insulation of Pt at high positive potentials. Since Hsieh et al.<sup>20</sup> and Banham et al.<sup>12</sup> have both clearly demonstrated a deactivation of their respective catalysts without changing the support or the atmosphere, there must be an effect other than the ASRM. The observed behavior cannot be explained by the formation of a PtTi alloy either, as this would lead to no significant change in the Pt oxidation features and an increase in ORR activity.<sup>24</sup>



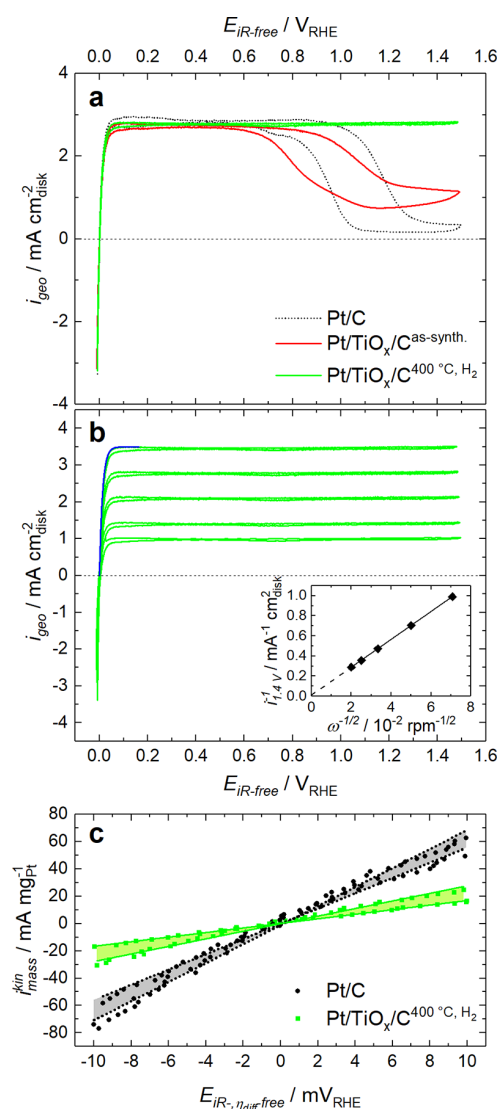
**Figure 2.** (HR) TEM images of  $\text{Pt}/\text{TiO}_x/\text{C}^{\text{as-synth.}}$  and  $\text{Pt}/\text{TiO}_x/\text{C}^{400^\circ\text{C},\text{H}_2}$ . (a) TEM image of the  $\text{Pt}/\text{TiO}_x/\text{C}^{\text{as-synth.}}$  catalyst showing areas with a high Pt content and Pt-free areas. The SAED pattern shows a low  $\text{TiO}_x$  crystallinity of the sample together with sharp reflections from Pt single crystals. The contrast does not allow for a differentiation between the titania and carbon. (b) TEM image and corresponding SAED pattern of the  $\text{Pt}/\text{TiO}_x/\text{C}^{400^\circ\text{C},\text{H}_2}$  catalyst. Because of the increased  $\text{TiO}_x$  crystallinity (SAED), a differentiation (by EDX) is possible for this sample. Pt-containing areas consist of  $\text{TiO}_x$ , while Pt-free areas are the carbon support. (c) HR-TEM of a Pt particle on titania on the as-synthesized sample showing the absence of any surface layer on Pt-NPs. (d) HR-TEM of the  $\text{Pt}/\text{TiO}_x/\text{C}^{400^\circ\text{C},\text{H}_2}$  catalyst showing the formation of a  $\text{TiO}_x$  surface layer on Pt-NPs (indicated by yellow arrows).

Figure 2 shows TEM images (experimental details in the Supporting Information) of  $\text{Pt}/\text{TiO}_x/\text{C}^{\text{as-synth.}}$  (left) and  $\text{Pt}/\text{TiO}_x/\text{C}^{400^\circ\text{C},\text{H}_2}$  (right). Before the heat treatment, a differentiation between the titania and the carbon support is challenging due to a low contrast and the low crystallinity of the  $\text{TiO}_x$  (Figure 2a). The images show areas with high Pt

content and others that are Pt-free, indicating the presence of Pt exclusively on  $\text{TiO}_x$ , as expected from the synthesis. The representative selected area electron diffraction (SAED), corresponding TEM image in Figure S1a) pattern merely shows reflections from Pt-NPs. After heat treatment, the  $\text{TiO}_x$  becomes crystalline, as seen by additional strong rutile phase reflections in the SAED (Figure 2b and Figure S1b). Probing different areas by energy dispersive X-ray spectroscopy (EDX) shows that the Pt-containing areas consist mainly of Pt and  $\text{TiO}_x$ , while the Pt-free areas are carbon. Thus, the Pt-NPs are exclusively supported on  $\text{TiO}_x$ , and the  $\text{Pt}/\text{TiO}_x$  material is well-distributed on the C support. The high-resolution (HR) TEM images indicate another difference between the two samples. For the as-synthesized catalyst, the lattice fringes of the titania-adsorbed Pt-NPs extend to the edge of the particle (Figure 2c). However, after reductive heat treatment, a thin layer of  $\text{TiO}_x$  covering the Pt particles is observed (indicated by yellow arrows in Figure 2d). The encapsulation of Pt-NPs during reductive heat treatment is widely known to occur with SMSI formation.<sup>20,25–27</sup> It has been shown that the encapsulation of Pt by  $\text{TiO}_x$  takes place, regardless of the Pt particle size, while it was found to be faster for smaller particles.<sup>25</sup> Because of analytical constraints, an unambiguous detection of Pt encapsulation was only possible for larger Pt particles; however, this does not exclude that it may occur also for smaller Pt particles. Otherwise, the overall decrease in the ORR activity cannot be explained, particularly since it was recently shown that removing the  $\text{TiO}_x$  layer by etching with hydrofluoric acid restores the ORR performance.<sup>20</sup>

$\text{TiO}_x$  layers have been discussed to be permselective, allowing for  $\text{H}_2$  chemisorption to partially take place.<sup>28</sup> Additionally, Hsieh et al. observed that the  $\text{H}_{\text{upd}}$  process is hindered less than  $\text{Pt}_{\text{ox}}$  formation, concluding that the  $\text{TiO}_x$  layer must be permeable for protons but not for hydroxyl groups.<sup>20</sup> Taking these observations into account, the hydrogen evolution reaction (HER) and the HOR would be expected to take place even on encapsulated Pt particles. To examine this hypothesis, HER/HOR polarization curves were recorded for all catalysts in  $\text{H}_2$ -saturated 0.1 M  $\text{HClO}_4$  at 1600 rpm (Figure 3a). Clearly, all catalysts reach 99% of the mass-transport-limited current density at 60  $\text{mV}_{\text{RHE}}$ , thus being limited exclusively by the diffusion overpotential, which implies that the HOR/HER activity is too high to be quantifiable by RDE.<sup>29</sup> As is well-known, the HOR activity of the Pt/C catalyst decreases above 0.7  $\text{V}_{\text{RHE}}$  and vanishes at 1.0  $\text{V}_{\text{RHE}}$  due to  $\text{Pt}_{\text{ox}}$  formation. This also occurs for the  $\text{Pt}/\text{TiO}_x/\text{C}^{\text{as-synth.}}$  catalyst, even though its activity remains finite even at  $>1.0 \text{ V}_{\text{RHE}}$ . Quite surprisingly, no such HOR/HER activity loss is observed for  $\text{Pt}/\text{TiO}_x/\text{C}^{400^\circ\text{C},\text{H}_2}$ , even at 1.5  $\text{V}_{\text{RHE}}$ , which we ascribe to SMSI effects with the  $\text{TiO}_x$  layer preventing Pt oxidation without electrically insulating the catalyst. Although Pt stabilization against oxidation by  $\text{TiO}_2$  was suggested by Gebauer et al.,<sup>30</sup> the possibility to oxidize  $\text{H}_2$  at such high potentials represents a finding, which, to the best of our knowledge, has not previously been reported.

For this reason, HER/HOR polarization curves were recorded at different rpm for  $\text{Pt}/\text{TiO}_x/\text{C}^{400^\circ\text{C},\text{H}_2}$  (Figure 3b). The Koutecký–Levich plot (inset) relating the reciprocal current density at 1.4  $\text{V}_{\text{RHE}}$  and the inverse square root of the rpm shows a linear relation and an essentially zero  $y$ -axis intercept, thus confirming that the current densities are purely mass transport limited,<sup>29</sup> indicated by the blue line in Figure



**Figure 3.** HER/HOR polarization curves recorded in  $\text{H}_2$ -saturated electrolytes at room temperature and  $10 \text{ mV s}^{-1}$  ( $I/C = 0.1$ ). (a) Comparison of Pt/TiO<sub>x</sub>/C<sup>as-synth.</sup> (red line,  $16.7 \mu\text{g}_{\text{Pt}} \text{ cm}_{\text{disk}}^{-2}$ ), Pt/TiO<sub>x</sub>/C<sup>400°C, H<sub>2</sub></sup> (green line,  $20.5 \mu\text{g}_{\text{Pt}} \text{ cm}_{\text{disk}}^{-2}$ ), and Pt/C (dotted line,  $14.8 \mu\text{g}_{\text{Pt}} \text{ cm}_{\text{disk}}^{-2}$ ) at 1600 rpm in 0.1 M HClO<sub>4</sub>. (b) Rotation rate dependency (top to bottom: 2500, 1600, 900, 400, and 200 rpm) for the Pt/TiO<sub>x</sub>/C<sup>400°C, H<sub>2</sub></sup> catalyst in 0.1 M HClO<sub>4</sub>. The polarization curve at 2500 rpm directly follows the HOR diffusion overpotential (blue line), indicating that the kinetics are too fast to be quantified by RDE. The inset shows a Koutecký–Levich plot of the inverse of the current density at  $1.4 V_{\text{RHE}}$  vs the inverse square root of the electrode rotation speed  $\omega$ . (c) Mass-specific kinetic current density vs diffusion overpotential- and  $iR$ -free potential in the micropolarization region obtained from HER/HOR polarization curves in 0.1 M NaOH at 1600 rpm for Pt/TiO<sub>x</sub>/C<sup>400°C, H<sub>2</sub></sup> and Pt/C (same loadings as above). Depicted are the negative-going scans (points) and linear fits (lines) of two separate measurements each.

3b, which represents the pure Nernstian diffusion overpotential at 2500 rpm.<sup>13</sup> The ability to perform HOR at these high potentials is of great interest for PEM water electrolysis applications, where hydrogen crossover is a critical safety issue, as the Ir-based oxygen evolution catalyst has no HOR activity.

A typical solution for such problem is the use of platinumized anode current collectors to promote the recombination/oxidation of crossed-over  $\text{H}_2$ .<sup>31</sup>

Because of the fast HOR/HER kinetics on Pt in acidic electrolytes, no HOR/HER kinetics can be obtained from RDE data. This makes it impossible to quantify changes in the HOR selectivity in acid electrolytes, a fact which has been ignored in previous studies.<sup>5–8</sup> Thus, we conducted measurements in an alkaline electrolyte, where the catalyst shows similarly reduced ORR activity and high potential stability for the HOR (Figure S2). While many studies suggest that the HER/HOR follows a different mechanism involving hydroxide ions in an alkaline environment,<sup>32–34</sup> recent studies suggest that the HER/HOR follows the same microscopic steps involving protons as compared to acidic environment.<sup>13,29,35–37</sup> Thus, the HER/HOR activity of the catalyst is not significantly reduced at high pH although the TiO<sub>x</sub> layer hinders the hydroxide ions from reaching the Pt surface. As the HER/HOR kinetics on Pt are  $\approx 100$ -fold slower in an alkaline environment, the exchange current density  $i_0$  (in  $\text{A g}_{\text{Pt}}^{-1}$ ) can be obtained from the micropolarization region ( $\pm 10 \text{ mV}$ ) by using the linearized form of the Butler–Volmer equation:<sup>13,38</sup>

$$i_{\text{mass}}^{\text{kin}} \approx i_0 \frac{(\alpha_a + \alpha_c)F}{RT} \eta \quad (1)$$

with the mass-specific kinetic current  $i_{\text{mass}}^{\text{kin}}$ , the anodic/cathodic transfer coefficients  $\alpha_a/\alpha_c$ , the Faraday constant  $F$ , the ideal gas constant  $R$ , the temperature  $T$ , and the reaction overpotential  $\eta$  that is equal to the diffusion overpotential- and  $iR$ -corrected potential. According to earlier results for Pt-based catalysts in alkaline media, the sum of  $\alpha_a$  and  $\alpha_c$  is 1.<sup>13,38,39</sup> Thus,  $i_0$  can be extracted from the micropolarization region by using eq 1. The negative-going scans (points) and the corresponding linear fits (lines) of the measurements indicating highest/lowest obtained activities for Pt/C and Pt/TiO<sub>x</sub>/C<sup>400°C, H<sub>2</sub></sup> are shown in Figure 3c. The obtained activity of  $161 \pm 18 \text{ A g}_{\text{Pt}}^{-1}$  for Pt/C is in good agreement with that reported by Schwämmlein et al. ( $182 \pm 7 \text{ A g}_{\text{Pt}}^{-1}$ ) for a similar Pt particle size.<sup>38</sup> With an  $i_0$  of  $57 \pm 14 \text{ A g}_{\text{Pt}}^{-1}$ , Pt/TiO<sub>x</sub>/C<sup>400°C, H<sub>2</sub></sup> is only  $\approx 3$ -fold less active. This may be due to various effects which we cannot yet quantify: (i) a lower Pt surface area (see Figure 1a), (ii) the encapsulation of Pt with TiO<sub>x</sub> hindering  $\text{H}_2/\text{H}^+$  transport, and/or (iii) the low conductivity of the TiO<sub>x</sub> particles, leading to electron transport resistances between the Pt-NPs and the carbon support.

While previous studies on HOR-selective catalysts showed reduced ORR activity without properly quantifying the HOR activity,<sup>5–8,12</sup> we can now estimate the changes in the HOR selectivity by assuming that the above shown HOR activity differences in NaOH are representative of the those in HClO<sub>4</sub> or in a PEMFC. Thus, we here define the selectivity  $S$  as the ratio of the HER/HOR exchange current density obtained in 0.1 M NaOH and the ORR activity obtained at  $0.9 V_{\text{RHE}}$  in 0.1 M HClO<sub>4</sub> (note that the ORR at the anode during SUSD occurs at an absolute potential of  $\approx 0.8–0.9 V_{\text{RHE}}$ ):<sup>4</sup>

$$S = \frac{i_0(\text{HER/HOR})}{i_{\text{mass}}^{\text{kin}}(\text{ORR})} \quad (2)$$

The thus-defined selectivity value of  $8.1 \pm 3.2$  for the Pt/TiO<sub>x</sub>/C<sup>400°C, H<sub>2</sub></sup> catalyst is by far superior compared to  $0.45 \pm 0.11$  for Pt/C. While this does not correspond to the actual

selectivity in a PEMFC, the  $\approx 18$ -fold difference between these selectivities is a reasonable estimate of what one might expect. Nevertheless, a clear answer requires the measurement of the HOR/HER and ORR kinetics in a PEMFC as well as actual SUSD experiments, which will be conducted in a follow-up study.

#### 4. CONCLUSION

To summarize, an HOR-selective catalyst based on Pt/TiO<sub>x</sub> was synthesized via a multistep synthesis combined with a reductive heat treatment, which leads to the (partial) encapsulation of the Pt-NPs of this catalyst (Pt/TiO<sub>x</sub>/C<sup>400°C,H<sub>2</sub></sup>) as observed by HR-TEM. The  $\approx 50$ -fold lower ORR activity of the Pt/TiO<sub>x</sub>/C<sup>400°C,H<sub>2</sub></sup> catalyst compared to a Pt/C catalyst was confirmed by RDE in 0.1 M HClO<sub>4</sub>. Furthermore, the surface oxidation of Pt particles of the here synthesized catalysts was strongly suppressed, concomitant with a high HOR activity even at high positive potentials. Measurements in alkaline electrolyte confirmed an only  $\approx 3$ -fold lower HER/HOR exchange current density of Pt/TiO<sub>x</sub>/C<sup>400°C,H<sub>2</sub></sup> compared to conventional Pt/C. Consequently, we estimate that the former has a superior HOR selectivity compared to Pt/C. Because of these unique properties, this novel catalyst system is interesting for the application in both electrolyzers and fuel cells.

#### ■ ASSOCIATED CONTENT

##### Supporting Information

The Supporting Information is available free of charge on the ACS Publications website at DOI: 10.1021/acsaem.9b00718.

Experimental procedures; TEM images corresponding to the SAED patterns; elemental analysis data; electrochemical testing and correction details; alkaline RDE results (PDF)

#### ■ AUTHOR INFORMATION

##### Corresponding Author

\*(B.M.S.) E-mail: [bjorn.stuehmeier@tum.de](mailto:bjorn.stuehmeier@tum.de).

##### ORCID

Björn M. Stühmeier: 0000-0001-7713-2261

Hubert A. Gasteiger: 0000-0001-8199-8703

Hany A. El-Sayed: 0000-0002-8769-8258

##### Notes

The authors declare no competing financial interest.

#### ■ ACKNOWLEDGMENTS

We thank the Centrum Baustoffe und Materialprüfung at TUM for their fast determination of the catalysts' elemental composition by ICP-MS, especially Dr. Harald Hilbig. Financial support in the frame of the innoKA project (BMW, 03ET6096A) is acknowledged.

#### ■ REFERENCES

- (1) Reiser, C. A.; Bregoli, L.; Patterson, T. W.; Yi, J. S.; Yang, J. D.; Perry, M. L.; Jarvi, T. D. A Reverse-Current Decay Mechanism for Fuel Cells. *Electrochem. Solid-State Lett.* **2005**, *8* (6), A273–A276.
- (2) Mittermeier, T.; Weiß, A.; Hasché, F.; Hübner, G.; Gasteiger, H. A. PEM Fuel Cell Start-up/Shutdown Losses vs Temperature for Non-Graphitized and Graphitized Cathode Carbon Supports. *J. Electrochem. Soc.* **2017**, *164* (2), F127–F137.

- (3) Shintani, H.; Kojima, Y.; Kakinuma, K.; Watanabe, M.; Uchida, M. Novel strategy to mitigate cathode catalyst degradation during air/air startup cycling via the atmospheric resistive switching mechanism of a hydrogen anode with a platinum catalyst supported on tantalum-doped titanium dioxide. *J. Power Sources* **2015**, *294*, 292–298.

- (4) Durst, J.; Orfanidi, A.; Rheinländer, P. J.; Hasché, F.; Eickes, C.; Suchsland, P.; Binder, M.; Gasteiger, H. A. Selective Hydrogen Oxidation Catalyst for Reduced Startup/Shutdown Degradation in Low Temperature Fuel Cells. *ECS Trans.* **2015**, *69* (17), 67–76.

- (5) Kamai, R.; Kamiya, K.; Hashimoto, K.; Nakanishi, S. Oxygen-Tolerant Electrodes with Platinum-Loaded Covalent Triazine Frameworks for the Hydrogen Oxidation Reaction. *Angew. Chem., Int. Ed.* **2016**, *55* (42), 13184–13188.

- (6) Luo, J.; Tang, H.; Tian, X.; Hou, S.; Li, X.; Du, L.; Liao, S. Highly Selective TiN-Supported Highly Dispersed Pt Catalyst: Ultra Active toward Hydrogen Oxidation and Inactive toward Oxygen Reduction. *ACS Appl. Mater. Interfaces* **2018**, *10* (4), 3530–3537.

- (7) Genorio, B.; Strmcnik, D.; Subbaraman, R.; Tripkovic, D.; Karapetrov, G.; Stamenkovic, V. R.; Pejovnik, S.; Marković, N. M. Selective catalysts for the hydrogen oxidation and oxygen reduction reactions by patterning of platinum with calix[4]arene molecules. *Nat. Mater.* **2010**, *9*, 998–1003.

- (8) Yun, S. W.; Park, S. A.; Kim, T. J.; Kim, J. H.; Pak, G. W.; Kim, Y. T. Hydrogen Oxidation-Selective Electrocatalysis by Fine Tuning of Pt Ensemble Sites to Enhance the Durability of Automotive Fuel Cells. *ChemSusChem* **2017**, *10* (3), 489–493.

- (9) Tauster, S.; Fung, S.; Garten, R. L. Strong Metal-Support Interactions. Group 8 Noble Metals Supported on TiO<sub>2</sub>. *J. Am. Chem. Soc.* **1978**, *100* (1), 170–175.

- (10) Hayden, B. E. Particle Size and Support Effects in Electrocatalysis. *Acc. Chem. Res.* **2013**, *46* (8), 1858–1866.

- (11) Jiménez-Morales, I.; Cavaliere, S.; Jones, D.; Rozière, J. Strong metal-support interaction improves activity and stability of Pt electrocatalysts on doped metal oxides. *Phys. Chem. Chem. Phys.* **2018**, *20* (13), 8765–8772.

- (12) Banham, D.; Ye, S.; O'Toole, A.; Lemke, A.; Eisenbraun, E. Unexpected hydrogen oxidation selectivity of Pt/NbTiO<sub>2</sub> catalysts. *Nano Energy* **2016**, *27*, 157–166.

- (13) Rheinländer, P. J.; Herranz, J.; Durst, J.; Gasteiger, H. A. Kinetics of the Hydrogen Oxidation/Evolution Reaction on Polycrystalline Platinum in Alkaline Electrolyte Reaction Order with Respect to Hydrogen Pressure. *J. Electrochem. Soc.* **2014**, *161* (14), F1448–F1457.

- (14) Mittermeier, T.; Madkikar, P.; Wang, X.; Gasteiger, H. A.; Piana, M. ZrO<sub>2</sub> Based Oxygen Reduction Catalysts for PEMFCs: Towards a Better Understanding. *J. Electrochem. Soc.* **2016**, *163* (14), F1543–F1552.

- (15) Birss, V. I.; Chang, M.; Segal, J. Platinum oxide film formation—reduction: an in-situ mass measurement study. *J. Electroanal. Chem.* **1993**, *355* (1), 181–191.

- (16) Khoobiar, S. Particle to Particle Migration of Hydrogen Atoms on Platinum—Alumina Catalysts from Particle to Neighboring Particles. *J. Phys. Chem.* **1964**, *68* (2), 411–412.

- (17) Prins, R. Hydrogen Spillover. *Chem. Rev.* **2012**, *112* (5), 2714–2738.

- (18) Hayden, B. E.; Pletcher, D.; Suchsland, J.-P.; Williams, L. J. The influence of Pt particle size on the surface oxidation of titania supported platinum. *Phys. Chem. Chem. Phys.* **2009**, *11* (10), 1564–1570.

- (19) Hayden, B. E.; Pletcher, D.; Suchsland, J.-P.; Williams, L. J. The influence of support and particle size on the platinum catalysed oxygen reduction reaction. *Phys. Chem. Chem. Phys.* **2009**, *11* (40), 9141–9148.

- (20) Hsieh, B.-J.; Tsai, M.-C.; Pan, C.-J.; Su, W.-N.; Rick, J.; Chou, H.-L.; Lee, J.-F.; Hwang, B.-J. Tuning metal support interactions enhances the activity and durability of TiO<sub>2</sub>-supported Pt nanocatalysts. *Electrochim. Acta* **2017**, *224*, 452–459.

- (21) Eckardt, M.; Gebauer, C.; Jusys, Z.; Wassner, M.; Hüsing, N.; Behm, R. J. Oxygen reduction reaction activity and long-term stability

of platinum nanoparticles supported on titania and titania-carbon nanotube composites. *J. Power Sources* **2018**, *400*, 580–591.

(22) Gasteiger, H. A.; Kocha, S. S.; Sompalli, B.; Wagner, F. T. Activity benchmarks and requirements for Pt, Pt-alloy, and non-Pt oxygen reduction catalysts for PEMFCs. *Appl. Catal., B* **2005**, *56* (1), 9–35.

(23) Tauster, S. Strong Metal-Support Interactions. *Acc. Chem. Res.* **1987**, *20* (11), 389–394.

(24) Duan, H.; Hao, Q.; Xu, C. Hierarchical nanoporous PtTi alloy as highly active and durable electrocatalyst toward oxygen reduction reaction. *J. Power Sources* **2015**, *280*, 483–490.

(25) Pesty, F.; Steinrück, H.-P.; Madey, T. E. Thermal stability of Pt films on TiO<sub>2</sub>(110): evidence for encapsulation. *Surf. Sci.* **1995**, *339* (1), 83–95.

(26) Iddir, H.; Disko, M. M.; Ogut, S.; Browning, N. D. Atomic scale characterization of the Pt/TiO<sub>2</sub> interface. *Micron* **2005**, *36* (3), 233–241.

(27) Zhang, J.; Zhang, M.; Jin, Z.; Wang, J.; Zhang, Z. Study of high-temperature hydrogen reduced Pt<sup>0</sup>/TiO<sub>2</sub> by X-ray photoelectron spectroscopy combined with argon ion sputtering—Diffusion-encapsulation effect in relation to strong metal–support interaction. *Appl. Surf. Sci.* **2012**, *258* (8), 3991–3999.

(28) Logan, A. D.; Braunschweig, E. J.; Datye, A. K.; Smith, D. J. Direct Observation of the Surfaces of Small Metal Crystallites: Rhodium Supported on TiO<sub>2</sub>. *Langmuir* **1988**, *4* (4), 827–830.

(29) Durst, J.; Simon, C.; Hasché, F.; Gasteiger, H. A. Hydrogen Oxidation and Evolution Reaction Kinetics on Carbon Supported Pt, Ir, Rh, and Pd Electrocatalysts in Acidic Media. *J. Electrochem. Soc.* **2015**, *162* (1), F190–F203.

(30) Gebauer, C.; Jusys, Z.; Behm, R. J. On the Role of the Support in Pt Anode Catalyst Degradation under Simulated H<sub>2</sub> Fuel Starvation Conditions. *J. Electrochem. Soc.* **2018**, *165* (15), J3342–J3349.

(31) Ito, H.; Miyazaki, N.; Ishida, M.; Nakano, A. Cross-permeation and consumption of hydrogen during proton exchange membrane electrolysis. *Int. J. Hydrogen Energy* **2016**, *41* (45), 20439–20446.

(32) Schmidt, T. J.; Ross, P. N.; Markovic, N. M. Temperature dependent surface electrochemistry on Pt single crystals in alkaline electrolytes: Part 2. The hydrogen evolution/oxidation reaction. *J. Electroanal. Chem.* **2002**, *524–525*, 252–260.

(33) Sheng, W.; Gasteiger, H. A.; Shao-Horn, Y. Hydrogen Oxidation and Evolution Reaction Kinetics on Platinum: Acid vs Alkaline Electrolytes. *J. Electrochem. Soc.* **2010**, *157* (11), B1529–B1536.

(34) Strmcnik, D.; Uchimura, M.; Wang, C.; Subbaraman, R.; Danilovic, N.; van der Vliet, D.; Paulikas, A. P.; Stamenkovic, V. R.; Markovic, N. M. Improving the hydrogen oxidation reaction rate by promotion of hydroxyl adsorption. *Nat. Chem.* **2013**, *5*, 300–306.

(35) Durst, J.; Siebel, A.; Simon, C.; Hasche, F.; Herranz, J.; Gasteiger, H. A. New insights into the electrochemical hydrogen oxidation and evolution reaction mechanism. *Energy Environ. Sci.* **2014**, *7* (7), 2255–2260.

(36) Elbert, K.; Hu, J.; Ma, Z.; Zhang, Y.; Chen, G.; An, W.; Liu, P.; Isaacs, H. S.; Adzic, R. R.; Wang, J. X. Elucidating Hydrogen Oxidation/Evolution Kinetics in Base and Acid by Enhanced Activities at the Optimized Pt Shell Thickness on the Ru Core. *ACS Catal.* **2015**, *5* (11), 6764–6772.

(37) Zheng, J.; Sheng, W.; Zhuang, Z.; Xu, B.; Yan, Y. Universal dependence of hydrogen oxidation and evolution reaction activity of platinum-group metals on pH and hydrogen binding energy. *Sci. Adv.* **2016**, *2* (3), No. e1501602.

(38) Schwämmlein, J. N.; Stühmeier, B. M.; Wagenbauer, K.; Dietz, H.; Tileli, V.; Gasteiger, H. A.; El-Sayed, H. A. Origin of Superior HOR/HER Activity of Bimetallic Pt-Ru Catalysts in Alkaline Media Identified via Ru@Pt Core-Shell Nanoparticles. *J. Electrochem. Soc.* **2018**, *165* (5), H229–H239.

(39) Nash, J.; Zheng, J.; Wang, Y.; Xu, B.; Yan, Y. Mechanistic Study of the Hydrogen Oxidation/Evolution Reaction over Bimetallic PtRu Catalysts. *J. Electrochem. Soc.* **2018**, *165* (15), J3378–J3383.

### 3.2.3. Suppression of the Ruthenium Surface Oxide Formation by SMSI Effects

This section presents the article "Modification of the Electrochemical Surface Oxide Formation and the Hydrogen Oxidation Activity of Ruthenium by Strong Metal Support Interactions" that was published in March 2022 in the *Journal of The Electrochemical Society*.<sup>120</sup> It is an open access article published under the terms of the Creative Commons Attribution 4.0 License (CC BY). The permanent web-link to the article is <https://doi.org/10.1149/1945-7111/ac58c9>.

Based on the stabilization of the HOR activity at high positive potentials for TiO<sub>2</sub>-supported Pt, this study explores whether Ru could be stabilized against surface oxidation in a similar fashion. Thus, the established synthesis procedure is adapted to obtain a Ru/TiO<sub>x</sub>/C<sup>as-synth.</sup> catalyst and, after a subsequent reductive heat-treatment, the final Ru/TiO<sub>x</sub>/C<sup>400°C,H<sub>2</sub></sup> catalyst, whereby the Ru nanoparticles sinter significantly during the latter process, with the Sauter mean diameter increasing from 2.0 to 4.4 nm. It is confirmed by tomographic TEM imaging and EDX mappings that the catalyst consists mostly of agglomerated Ru/TiO<sub>x</sub>-composites adsorbed on the Vulcan carbon support structure. Similarly, it is confirmed by CVs that the oxidation of Ru is indeed suppressed for the Ru/TiO<sub>x</sub>/C<sup>400°C,H<sub>2</sub></sup> catalyst. This stabilization of the Ru surface to remain in its metallic state at high positive potentials is furthermore confirmed by XPS, whereby the catalysts are polarized for 600 s in 0.1 M HClO<sub>4</sub> and even after polarization at 1.3 V<sub>RHE</sub>, the Ru 3d<sub>5/2</sub> peak of the Ru/TiO<sub>x</sub>/C<sup>400°C,H<sub>2</sub></sup> catalyst remains at the binding energy of Ru(0), while the Ru/C reference catalyst is fully oxidized to Ru(IV). In conventional RDE experiments, the Ru/TiO<sub>x</sub>/C<sup>400°C,H<sub>2</sub></sup> catalyst showed an excellent stabilization of the HOR activity up to the onset of the OER at 1.3 V<sub>RHE</sub>, whereas the HOR activity of the Ru/C reference quickly decays after reaching the mass transport limited current density at 0.11 V<sub>RHE</sub>. This stabilization of metallic Ru by SMSI results in a suppression of the OER activity above 1.3 V<sub>RHE</sub>, where the Ru/C reference catalyst outperforms the heat-treated catalyst.

Finally, the HOR/HER kinetics of the catalysts are determined by H<sub>2</sub>-pump measurements. Here, the stabilization of the HOR activity of the Ru/TiO<sub>x</sub>/C<sup>400°C,H<sub>2</sub></sup> catalyst can be confirmed, whereby at an overpotential of  $\approx 0.1$  V, a maximum HOR current plateau of  $\approx 9$  A mg<sub>Ru</sub><sup>-1</sup> is reached and maintained up to an overpotential of  $\approx 0.45$  V.

With an exchange current density of  $8.2 \pm 0.3 \text{ A mg}_{\text{Ru}}^{-1}$ , the Ru/TiO<sub>x</sub>/C<sup>400°C,H<sub>2</sub></sup> catalyst proves to be three times more active than Ru/C ( $2.5 \pm 0.2 \text{ A mg}_{\text{Ru}}^{-1}$ ), but roughly two orders of magnitude less active than Pt/C under the same conditions.<sup>25</sup> In summary, it is shown that Ru can be stabilized for the HOR/HER by an SMSI, but the low activity and limited stability of both Ru<sup>182,183</sup> and TiO<sub>2</sub><sup>121</sup> prevent this type of catalyst from representing a feasible alternative to conventional Pt/C catalysts.

#### **Author contributions**

R.J.S. synthesized the catalyst. R.J.S. and B.M.S. performed the RDE testing. B.M.S. performed the MEA testing. L.H. measured XPS and S.S. did the TEM measurements. B.M.S., H.A.E. and H.A.G. designed the Ru/TiO<sub>x</sub>/C catalyst concept. B.M.S. and H.A.G. wrote the manuscript. All authors discussed the results and commented on the manuscript.



# Modification of the Electrochemical Surface Oxide Formation and the Hydrogen Oxidation Activity of Ruthenium by Strong Metal Support Interactions

Björn M. Stühmeier,<sup>1,\*,z</sup> Robin J. Schuster,<sup>1,=</sup> Louis Hartmann,<sup>1,\*</sup> Sören Selve,<sup>2</sup>  
Hany A. El-Sayed,<sup>1,a</sup> and Hubert A. Gasteiger<sup>1,\*\*</sup>

<sup>1</sup>Chair of Technical Electrochemistry, Department of Chemistry and Catalysis Research Center, Technical University of Munich, 85748 Garching, Germany

<sup>2</sup>Center for Electron Microscopy (ZELMI), Technical University of Berlin, 10623 Berlin, Germany

A major hurdle for the wide spread commercialization of proton exchange membrane based fuel cells (PEMFCs) and water electrolyzers are the durability and high cost of noble metal catalysts. Here, alternative support materials might offer advantages, as they can alter the properties of a catalyst by means of a strong metal support interaction (SMSI) that has been shown to prevent platinum oxidation and suppress the oxygen reduction reaction on titanium oxide supported platinum nanoparticles deposited on a carbon support (Pt/TiO<sub>x</sub>/C). Herein, we report a novel Ru/TiO<sub>x</sub>/C catalyst that according to tomographic transmission electron microscopy analysis consists of partially encapsulated Ru particles in a Ru/TiO<sub>x</sub>-composite matrix supported on a carbon support. It is shown by cyclic voltammetry and X-ray photoelectron spectroscopy that ruthenium oxidation is mitigated by an SMSI between Ru and TiO<sub>x</sub> after reductive heat-treatment (Ru/TiO<sub>x</sub>/C<sup>400°C,H<sub>2</sub></sup>). As a result, the catalyst is capable of oxidizing hydrogen up to the onset of oxygen evolution reaction, in stark contrast to a Ru/C reference catalyst. PEMFC-based hydrogen pump measurements confirmed the stabilization of the hydrogen oxidation reaction (HOR) activity on Ru/TiO<sub>x</sub>/C<sup>400°C,H<sub>2</sub></sup> and showed a ≈3-fold higher HOR activity compared to Ru/C, albeit roughly two orders of magnitude less active than Pt/C.

© 2022 The Author(s). Published on behalf of The Electrochemical Society by IOP Publishing Limited. This is an open access article distributed under the terms of the Creative Commons Attribution 4.0 License (CC BY, <http://creativecommons.org/licenses/by/4.0/>), which permits unrestricted reuse of the work in any medium, provided the original work is properly cited. [DOI: 10.1149/1945-7111/ac58c9]



Manuscript submitted November 17, 2021; revised manuscript received February 4, 2022. Published March 16, 2022.

Supplementary material for this article is available [online](#)

Water electrolyzers and hydrogen powered fuel cells are expected to play a key role in energy storage and production when transitioning to a carbon neutral economy based on renewable energy to combat climate change.<sup>1,2</sup> For both technologies, a major hurdle for wide-spread commercialization are the high system costs, whereby a significant fraction results from the use of noble metal based electrocatalysts. Proton exchange membrane fuel cells (PEMFCs) rely on Pt-based catalysts for the hydrogen oxidation reaction (HOR) and the oxygen reduction reaction (ORR).<sup>3</sup> Similarly, Pt-based hydrogen evolution reaction (HER) and Ir-based oxygen evolution reaction (OER) catalysts are used in proton exchange membrane water electrolyzers (PEMWEs).<sup>4</sup> Due to the sluggish kinetics of the ORR and OER, the main focus of catalyst development for these devices has been on reducing the noble metal loading of the respective oxygen electrodes by seeking to develop Pt-free ORR catalysts as well as highly active and durable Pt-alloy catalysts for low-loaded PEMFC cathodes,<sup>5,6</sup> and to reduce the anode loading of PEMWE systems.<sup>7</sup> On the contrary, the hydrogen side is often neglected with regards to potential catalyst cost savings. This is due to the extremely fast kinetics of the HER/HOR (Eq. 1) that allows for the use of metal loadings of ≈ 0.025–0.05 mg<sub>Pt</sub> cm<sub>geo</sub><sup>-2</sup>,<sup>8–10</sup> which should be sufficient to reach target loadings of ≈ 0.125 mg<sub>Pt</sub> cm<sub>geo</sub><sup>-2</sup> for the whole membrane electrode assembly (MEA) of PEMFC systems.<sup>11,12</sup>



At such low Pt loadings, however, even a modest loss of electrochemically active surface area (ECSA) of either of the electrodes due to cell-reversal (CR) or start-up and shut-down (SUSD) events can lead to a noticeable performance degradation of the PEMFC.<sup>6,13–16</sup>

In this respect, Ru might offer advantages as an anode catalyst as it might mitigate some of the most detrimental ECSA degradation phenomena in PEMFCs: Ru in the form of ruthenium oxide is well known to be a highly active oxygen evolution catalyst,<sup>17,18</sup> and employing an OER catalyst on the anode has been shown to significantly increase the system durability in CR events.<sup>19</sup> Additionally, Ru is essentially inactive for the ORR,<sup>20</sup> which could significantly reduce cathode degradation during SUSD events, as was shown for iridium catalysts that have a high HOR activity and a low ORR activity.<sup>21</sup> Finally, it exhibits a high CO tolerance, which might reduce the required purification efforts to remove CO from reformat gas.<sup>22</sup> However, the HOR on ruthenium catalysts is inhibited by hydroxide adsorption even at low overpotentials,<sup>23,24</sup> preventing its use as a commercial anode catalyst. In order to enable the use of ruthenium as an alternative to platinum based HOR catalyst, the (surface-)oxidation of metallic ruthenium would have to be suppressed and the thus stabilized catalyst would need to have at least 10% of the mass activity of Pt ( $i_0 = 540 \pm 160 \text{ A mg}_{\text{Pt}}^{-1}$ )<sup>25</sup> and a similar long term stability in order to be of any practical advantage.

In recent years, the field of oxide supported metal nanoparticles has gained interest due to the unique properties of a strong metal-support interaction (SMSI) effect that can dramatically alter the catalytic properties of the metal. The SMSI is characterized by a modified bonding interaction between the metal and a partially reduced oxide support that in most cases results in an encapsulation of the metal nanoparticles by a thin (sub-)oxide layer.<sup>26–29</sup> The driving force for this encapsulation is widely considered to be the minimization of the surface energy of the nanoparticles.<sup>30,31</sup> When it comes to the alteration of the electrocatalytic behavior of such systems, it was shown that when a Nb-doped TiO<sub>2</sub> supported Pt catalyst was exposed to voltage cycling between 1.0–1.4 V vs the reversible hydrogen electrode (RHE), Pt oxidation features and ORR activity were apparently reduced without affecting the HOR activity; this was explained by selective Pt-site blocking through the dissolution and re-deposition of a very thin layer of the oxide support (on the order of one to a few monolayers) on the Pt surface.<sup>32</sup> Depending on the thickness, such thin oxide layers might significantly affect the charge transport mechanism and therefore

<sup>=</sup>Equal Contribution.

<sup>\*</sup>Electrochemical Society Student Member.

<sup>\*\*</sup>Electrochemical Society Fellow.

<sup>a</sup>Current Address: Freudenberg Fuel Cell e-Power Systems GmbH, Bayerwaldstr. 3, 81737 München, Germany.

<sup>z</sup>E-mail: [bjorn.stuehmeier@tum.de](mailto:bjorn.stuehmeier@tum.de)

alter the electrochemical reactivity of the catalyst.<sup>33</sup> Similarly, a TiO<sub>2</sub> supported Pt catalyst that was exposed to reductive conditions during the atomic layer deposition of Pt or in H<sub>2</sub> atmosphere showed an HOR activity of Pt that was stabilized up to 1.5 V<sub>RHE</sub>, while the ORR activity was almost completely suppressed.<sup>34,35</sup> While some of these effects have been explained by a change in conductivity of the oxide support material depending on the atmosphere,<sup>36</sup> other studies suggest that a proton conducting monolayer-thick film of (sub-)oxide encapsulates the nanoparticles and prevents oxygenated species from reaching the metal surface, thereby stabilizing the reduced state of the metal nanoparticles.<sup>32,34,35,37,38</sup> It seems reasonable to speculate that the HOR activity of other HER/HOR active metals such as Ru might be preserved in a similar fashion at potentials where a deactivation due to surface oxidation would occur otherwise. Indeed, it was recently shown by Zhou et al. that Ru clusters can be stabilized against oxidation in a TiO<sub>2</sub> matrix while remaining active for the HOR beyond 0.5 V<sub>RHE</sub> even when poisoned by CO.<sup>39</sup>

In this study, we present a novel Ru/TiO<sub>x</sub>/C (x ≤ 2) catalyst that is capable of oxidizing hydrogen up to the onset of the OER at 1.3 V<sub>RHE</sub>. This catalyst is based on the deposition of Ru nanoparticles on nano-sized titanium oxide particles, the subsequent adsorption of the resulting Ru/TiO<sub>x</sub> particles onto high-surface area carbon Vulcan carbon (Ru/TiO<sub>x</sub>/C), and a reductive treatment in H<sub>2</sub>-containing atmosphere at 400 °C (Ru/TiO<sub>x</sub>/C<sup>400°C,H<sub>2</sub></sup>). After a detailed structural investigation of the hierarchical catalyst by transmission electron microscopy (TEM) using a tomographic tilt-series in combination with selective area electron diffraction (SAED), the stability against oxidation of the catalyst is compared to a Ru/C reference catalyst by means of rotating disk electrode (RDE) measurements and ex-situ X-ray photoelectron spectroscopy (XPS). Based on the differences in oxidation behavior, the retention of the HOR activity and the effect of the SMSI on the OER activity, as observed in RDE, is discussed. Finally, catalysts were implemented in membrane electrode assemblies (MEAs) in order to quantify their HOR/HER activity via PEMFC-based hydrogen pump measurements. The implications on the usability of Ru-based catalysts for the hydrogen side of PEMFC will be discussed.

## Experimental

**Catalyst synthesis.**—The Ru/TiO<sub>x</sub>/C catalysts were prepared based on a previously reported multistep synthesis procedure for Pt/TiO<sub>x</sub>/C catalysts,<sup>35</sup> whereby the key synthesis steps and adaptations are described in the following. First, Ru-nanoparticles (Ru-NP) were prepared using the polyol reduction method: 150 mg RuCl<sub>3</sub> (45%–55% Ru content, Sigma Aldrich) and 75 mg polyvinylpyrrolidone (PVP, average Mw ≈ 55000, Sigma Aldrich) were dissolved in 500 ml of water-free ethylene glycol (EG, 99.8%, anhydrous, Sigma Aldrich), deaerated by argon (6.0-grade, Westfalen AG), then the solution was heated from room temperature to 155 °C at a constant rate of 4 °C min<sup>-1</sup> (controlled by a temperature controller; model 310, J-KEM), kept there for 90 min, and subsequently was allowed to cool down to room temperature. Meanwhile, a solution of 0.84 ml titanium(IV)isopropoxide (≥97%, Sigma Aldrich Corp.) in 75 ml ethanol (EtOH, 99.8%, absolute, Sigma Aldrich Corp.) was added dropwise over the course of ca. 10 min to 75 ml of high purity water (H<sub>2</sub>O, 15 MΩ·cm, E-POD, Merck Millipore KGaA) held at 80 °C. After stirring for 60 min, 150 ml EG were added and the titania dispersion was allowed to cool down to room temperature.

Then, H<sub>2</sub>O and EtOH were evaporated using a rotary evaporator (Hei-VAP Value; Heidolph Instruments GmbH & CO. KG.) resulting in a titania dispersion in the remaining EG. Subsequently, the Ru-NP suspension was added to the titania dispersion and stirred for 24 h at room temperature. The suspension of the resulting Ru/TiO<sub>x</sub>-composite (x ≤ 2, whereby TiO<sub>x</sub> might be partially hydrated)<sup>35</sup> was added to a suspension of 108 mg Vulcan carbon (XC-72R, Tanaka Kikinoku International K. K., Japan) dispersed by ultrasonication in 150 ml EG and stirred for another 48 h. Afterwards, the volume of the suspension was doubled with acetone (≥98%, Sigma Aldrich Corp.), stirred for another 12 h, and centrifuged at 11000 rpm at 10 °C in an ultra-centrifuge (5810 R, Eppendorf) to separate the Ru/TiO<sub>x</sub>/C catalyst and the solvent. Finally, the catalyst was washed three times with a 50/50 (v/v) acetone/water mixture and dried at 70 °C in air to obtain the Ru/TiO<sub>x</sub>/C<sup>as-synth.</sup> catalyst. Finally, a heat treatment at 400 °C (10 K min<sup>-1</sup>) for 1 h under reductive atmosphere (5% H<sub>2</sub>/Ar) was performed to obtain the Ru/TiO<sub>x</sub>/C<sup>400°C,H<sub>2</sub></sup> catalyst.

The elemental composition of Ru/C and Ru/TiO<sub>x</sub>/C<sup>400°C,H<sub>2</sub></sup> was determined by inductively coupled plasma mass spectrometry (ICP-MS) after acid digestion (aqua regia according to the procedure proposed by Suoranta et al.<sup>40</sup> for Ru and sulfuric acid for Ti), and by carbon oxidation at elevated temperatures in air. The results are given in Table I. Note that the samples were analyzed as stored under ambient conditions. Thus, the total masses add up to less than 100% when considering only Ru, TiO<sub>2</sub>, and C due to water adsorption and, in the case of Ru/C, ruthenium bulk oxidation.

### Transmission electron microscopy and electron diffraction.—

The powders of each specimen were dispersed in pure ethanol and sonicated for 5 min 3 μl of the dispersion was drop-casted on 300 mesh lacey-carbon copper grids and air-dried at 40 °C. TEM, high resolution (HR-)TEM, and electron diffraction investigations were performed at an FEI TECNAI G<sup>2</sup>20 S-Twin transmission electron microscope with LaB<sub>6</sub> emitter, operated at 200 kV. TEM images were acquired with a Gatan 1kx1k MSP794 P CCD-camera. The microscope is further equipped with an EDAX r-TEM SUTW EDX detector, a customized DISS6 scan unit by point electronic GmbH, and a combined BF-ADF-HAADF-STEM detector from PN-Detector for STEM investigations and qualitative elemental mappings.

Tomographic tilt-series were acquired in TEM-mode for alpha-tilts between -60° and +70° using a Fischione Dual-Axis Tomography Holder Model 2040. For tomographic data processing, the IMOD and etomo software were used; DigitalMicrograph was used for evaluating HR-/TEM images and diffraction patterns; the EDAX Genesis Software was used for EDX-data acquisition and evaluation.

**Rotating disk electrode, hardware and preparation.**—The electrode and ink preparation, as well as the setup and measurement procedure were already reported in previous publications by our group.<sup>41–43</sup> For the preparation of the electrolytes and for the rinsing of the measurement components, 18.2 MΩ cm deionized water (Milli-Q Integral 5, Merck Millipore KGaA) was used. Glassy Carbon (GC) electrodes (5 mm diameter, Pine Research Instrumentation) fixed in a PTFE-body (Pine Research Instrumentation) were used as working electrodes (WE). The GC substrates were polished with a 0.05 μm Al<sub>2</sub>O<sub>3</sub> polishing suspension (Bühler AG) and sonicated various times in

**Table I.** Weight percentages of Ru, Ti, and C in the catalyst samples as obtained by ICP-MS and carbon oxidation. The remaining mass percentages up to 100% are due to the oxygen in the titanium oxide, the largely oxidized form of ruthenium NPs, and adsorbed water.

Catalyst	Ru-Content [wt.%]	Ti-Content [wt.%]	C-Content [wt.%]
Ru/C	17.1	—	67.6
Ru/TiO <sub>x</sub> /C <sup>400°C,H<sub>2</sub></sup>	8.8	28.6	23.3

Milli-Q water. Inks were prepared by adding high purity acetone ( $\geq 99.9\%$ , Chromasolv Plus, for HPLC, Sigma Aldrich Corp.) to the dry catalyst. The catalyst content in the ink was adjusted to achieve Ru loadings of  $\approx 20 \mu\text{g}_{\text{Ru}} \text{cm}_{\text{disk}}^{-2}$  (corresponding to  $\approx 0.09 \text{mg}_{\text{Vulcan}} \text{cm}_{\text{disk}}^{-2}$ , which yields a catalyst layer film thickness of  $\approx 3 \mu\text{m}$  (based on a packing density of  $\approx 28 \mu\text{m} (\text{mg}_{\text{Vulcan}} \text{cm}_{\text{disk}}^{-2})^{-1}$  on the glassy carbon disk).<sup>44</sup> The catalyst suspension was sonicated in a sonication bath (Elmasonic S 30 H, Elma Schmidbauer GmbH), maintaining the bath temperature at less than  $25 \text{ }^\circ\text{C}$  to avoid evaporation of the solvent. Nafion (5 wt.% in lower aliphatic alcohols, 15%–20%  $\text{H}_2\text{O}$ , Sigma Aldrich Corp.) was then added to the suspension, resulting in an ionomer to support (C +  $\text{TiO}_x$ ) ratio of  $0.1 \text{ g}_I \text{ g}_S^{-1}$ , followed by sonication in a weaker sonication bath (USC100T, VWR International GmbH) for at least  $10 \text{ min}$   $10 \mu\text{l}$  of ink were dropped on a GC disk, which was subsequently covered with a small glass vial. As still some catalyst ( $\approx 5\%$ – $10\%$ ) remained as an unsuspended sediment,  $10 \mu\text{l}$  of ink were dropped in parallel on each of six aluminum foil pieces (10 mm diameter), whose blank weight prior to applying the ink had been determined with an ultra-high precision balance (XP6, Mettler-Toledo GmbH). After drying at room temperature, the actual catalyst loading on the disk was inferred to be  $17 \pm 2 \mu\text{g}_{\text{Ru}} \text{cm}_{\text{disk}}^{-2}$  based on the mass of the catalyst deposits on the aluminum foil samples.

Electrolyte solutions were prepared from high purity  $\text{HClO}_4$  (60%, Guaranteed Reagent, Kanto Chemical Co., Inc., Japan) by addition of ultrapure water. Argon and hydrogen gases used for purging the electrolyte were of high purity (6.0-grade, Westfalen AG). A glass cell with a Pt mesh as the counter electrode that was separated by a glass frit from the working electrode compartment was used. As reference electrode (RE), a static hydrogen RE was used as a reversible hydrogen electrode (RHE), consisting of a Pt wire (1.0 mm diameter;  $>99.99\%$  purity, ADVENT Research Materials Ltd., UK) sealed into a glass tube that was partially filled with the same electrolyte as that used for the RDE measurements and whose other end was drawn to a capillary; a hydrogen bubble was evolved electrolytically inside the glass tube prior to usage.<sup>45</sup> The capillary was immersed into the electrolyte and, separated from the RDE compartment with an electrolyte bridge. This reference electrode (RE) was freshly prepared each day and calibrated against a polycrystalline Pt disk electrode in  $\text{H}_2$  saturated electrolyte and. Electrochemical measurements were performed using an Autolab potentiostat (PGSTAT302N, Metrohm AG, Switzerland) equipped with an analog potential scan module, a frequency response analyzer, and a bipotentiostat module. A rotator with a polyether ether ketone shaft (Pine Research Instrumentation, USA) was used.

**Rotating disk electrode measurements.**—Prior to any measurements, the catalysts were cleaned by cycling the potential 25 times between 0.0 and  $1.0 V_{\text{RHE}}$  at  $100 \text{ mV s}^{-1}$  in an Ar-saturated electrolyte, after which steady-state CVs were obtained, directly followed by CV measurements (3 cycles each) at  $20 \text{ mV s}^{-1}$  with a lower potential limit of  $0.02 V_{\text{RHE}}$  and an upper potential limit increasing in  $0.1 \text{ V}$  steps from  $0.6$  to  $1.3 V_{\text{RHE}}$ . The high frequency resistance (HFR in  $\Omega$ ) between WE and RE was determined by electrochemical impedance spectroscopy (EIS) from  $100 \text{ kHz}$  to  $100 \text{ Hz}$  at the open circuit voltage (OCV) with an amplitude of  $10 \text{ mV}$ . Potentials corrected according to Eq. 2 are denominated  $E_{\text{IR-free}}$ , whereby E is the potential and I the current (note that cathodic currents are taken to be negative):

$$E_{\text{IR-free}} = E - I \cdot \text{HFR} \quad [2]$$

The geometric current density  $i_{\text{geo}}$  (Eq. 3) is normalized by the area of the electrode ( $A_{\text{disk}} = 0.196 \text{ cm}^2$ ).

$$i_{\text{geo}} = I \cdot A_{\text{electrode}}^{-1} \quad [3]$$

Prior to the HER/HOR measurements, the electrolyte was saturated with  $\text{H}_2$ . While recording the HER/HOR polarization curves, the  $\text{H}_2$  flow was set to blanketing the cell head space. The potential was

cycled between  $-0.05$  and  $1.3 V_{\text{RHE}}$  at rotation rates going from  $2500$  to  $200 \text{ rpm}$ , followed by a single HER/HOR curve up to  $1.5 V_{\text{RHE}}$  at  $1600 \text{ rpm}$ .

**X-ray photoelectron spectroscopy measurements.**—Nafion-free dispersions of Ru/C and  $\text{Ru}/\text{TiO}_x/\text{C}^{400^\circ\text{C.H}_2}$  were prepared as described for the TEM measurements and the catalysts were drop-casted in close proximity of each other on gold foils ( $0.025 \text{ mm}$  thickness,  $99.99\%$  purity, ADVENT Research Materials Ltd., UK). Subsequently, the samples containing the catalysts were submerged in Ar-saturated  $0.1 \text{ M HClO}_4$  and polarized to  $0.02 V_{\text{RHE}}$  for  $600 \text{ s}$ , followed by an oxidation at either  $0.8$ ,  $1.0$ , or  $1.3 V_{\text{RHE}}$  for another  $600 \text{ s}$ . The samples were then dipped three times in an excess of Milli-Q water and dried in vacuo at  $70 \text{ }^\circ\text{C}$  overnight.

The surface analysis of these samples was carried out by X-ray photoelectron spectroscopy (Axis, Supra, Kratos, UK). A PEEK-sample holder in a floating ground configuration was used to avoid differential charging. The samples were kept in the antechamber until a pressure of  $\approx 10^{-8}$  Torr and were then transferred to the sample analysis chamber (SAC) where the pressure was always kept at  $\approx 10^{-9}$  Torr during the whole measurement period. Sample irradiation was carried out with monochromatic Al  $K\alpha$  radiation ( $1486.6 \text{ eV}$ ) with an emission current of  $15 \text{ mA}$ . For the Ag  $3d_{5/2}$  line, the full width at half-maximum (FWHM) was  $1.02 \text{ eV}$  under the recording conditions (using a pass energy of  $0.05 \text{ eV}$ ). Elemental spectra were recorded with a step size of  $0.05 \text{ eV}$  and an emission current of  $15 \text{ mA}$  and a pass energy of  $0.05 \text{ eV}$ . Low energy electrons were used for charge neutralization and the spectra were calibrated to the elemental Au  $4f_{7/2}$  peak from the substrate with a binding energy (BE) of  $83.95 \text{ eV}$ . To avoid any errors in charge neutralization, the binding energy differences of the different elemental peaks in the survey spectra were compared. Short acquisition time spectra in the O  $1s$  region were recorded before and after each set of experiments in order to check that the samples did not suffer from radiation damage.

The XPS data analysis was performed using the Casa XPS software. A Shirley function was used as background. As it is reported that Ru  $3d$  spectra exhibit a distinct asymmetric line shape, a Functional Lorentzian line shape was used for metallic ruthenium and for ruthenium oxides, with the parameters set to  $A(0.5,1,0)GL(0)$ .<sup>46</sup> The fits of the doublets of Ru  $3d_{5/2}$  and Ru  $3d_{3/2}$  were fixed to have the same FWHM and to have a  $(3d_{5/2})/(3d_{3/2})$  peak area ratio of  $3:2$  with a fixed separation of the peak maxima of  $4.17 \text{ eV}$ .<sup>46</sup> The C  $1s$  peaks were fitted using a mixture of a Lorentzian (30%) and Gaussian (70%) shape function<sup>47</sup>; the constraints on binding energy and full width at half maximum (FWHM) for the different species are given in Table. II. For the ease of the reader only the Ru-fits are shown below. In-house reference spectra of  $\text{TiO}_2$ , carbon, metallic Ru and anhydrous  $\text{RuO}_2$  were used to determine the binding energy and FWHM.

**Table II. XPS peak fitting parameters used for identification and quantification of the different surface species of the measured samples.**

Element/ Region	Assigned Species	Binding Energy [eV] (constrained range)	FWHM [eV] (constrained range)
Ruthenium Ru 3d	$\text{Ru}^0$	$280.1 (\pm 0.1)$	$0.7\text{--}1.0$
	$\text{Ru}^{4+}$	$281.3 (\pm 0.1)$	$0.7\text{--}1.0$
Carbon C 1s	C–C $\text{sp}^2$	$284.8 (\pm 0.1)$	$1.0\text{--}1.3$
	C–C $\text{sp}^3$	$284.4 (\pm 0.1)$	$1.0\text{--}1.3$
	C–O	$289.8 (\pm 0.1)$	$1.5\text{--}2.25$
Gold Au 4f	$\text{Au}^0$	$83.95$ (fixed)	$1.5\text{--}2.25$

**Fuel cell hardware & MEA preparation.**—All hydrogen-pump measurements were performed on a customized G60 test station (Greenlight Innovation Corp., USA) modified to feature pure H<sub>2</sub> instead of air/O<sub>2</sub> on the cathode side; there were also no CO gas connections in order to avoid any unintentional poisoning with CO. The current range of the potentiostat (Reference3000, Gamry Instruments, USA) was extended by a booster (Reference 30K Booster, Gamry Instruments, USA). All measurements were carried out with an in-house designed 5 cm<sup>2</sup> active area single-cell hardware, using commercial graphite flow fields (7 parallel channels, one serpentine, 0.5 mm lands/channels; manufactured by Poco Graphite, Entegris GmbH, Germany, according to our design).<sup>48</sup> Gas diffusion layers (GDLs) were the same in all experiments (H14C10, Freudenberg KG, Germany) and the GDL compression was adjusted to 13 ± 1% by quasi-incompressible, PTFE-coated fiberglass gaskets (Fiberflon, Fiberflon GmbH & Co. KG, Germany), assembled at a torque of 12 Nm, resulting in a contact pressure of ≈1.5 MPa on the active area (for details see Simon et al.).<sup>49</sup>

MEAs were prepared by the decal transfer method. The catalyst inks were prepared by ball milling (200 rpm, 3 min on, 5 min off, 5 cycles) a defined amount of catalyst (Ru/C or Ru/TiO<sub>x</sub>/C<sup>400°C,H<sub>2</sub></sup>) with 1-propanol in a 20 ml jar containing 16 g of ZrO<sub>2</sub> beads (2 mm diameter) with a solid content of 0.03 g mL<sup>-1</sup>. Afterwards, the catalyst dispersion was transferred into a smaller bottle, to which an ionomer solution (low equivalent weight, Asahi Kasai Corp.) corresponding to an I/S ratio of 0.65/1 g<sub>I</sub> g<sub>S</sub><sup>-1</sup> (based on the weight of the transferred ink) was added, and the ink mixing was completed by placing the bottles onto a roller-mill at 100 rpm for 18 h at 25 °C. For the CE, a Pt/C catalyst (45.6wt.% Pt, TEC10V50E, Tanaka) was directly mixed with 1-propanol and ionomer solution on the-roller mill (water concentration: 16wt.%; solid content: 0.04 g mL<sup>-1</sup>; I/C: 0.65/1 g<sub>I</sub> g<sub>C</sub><sup>-1</sup>). Then, the Mayer rod technique (K Control Coater, RK PrintCoat Instruments Ltd., England) with the appropriate bar size was used to achieve loadings of ≈ 50 μg<sub>Ru</sub> cm<sup>-2</sup><sub>MEA</sub> (WE) and 0.39 ± 0.02 mg<sub>Pt</sub> cm<sup>-2</sup><sub>MEA</sub> (CE) on virgin PTFE decals. The unsymmetrical MEAs were fabricated by hotpressing the air-dried decals onto a 15 μm membrane (W. L. Gore & Associates GmbH) at 155 °C for 3 min with an applied pressure of 0.11 kN cm<sup>-2</sup>.

**H<sub>2</sub>-pump measurement procedure.**—The measurement procedure was already reported in a previous publication by our group.<sup>25</sup> Prior to any kinetic measurements, each cell was conditioned to activate the catalyst using a voltage-controlled ramp-in procedure in a H<sub>2</sub>/H<sub>2</sub> setup (80 °C, 90% relative humidity (RH), flow rates of 2000/2000 nccm at a H<sub>2</sub> partial pressure of 450/450 kPa<sub>H<sub>2</sub></sub>): -0.35 V for 15 min, 5 min at open circuit voltage (OCV), and 0.35 V for 10 min. This sequence was repeated four times until a constant performance was reached. The kinetic measurements were then performed at 80 °C and 100 kPa<sub>H<sub>2</sub></sub> in H<sub>2</sub>/H<sub>2</sub> (2000/2000 nccm) configuration at 90% RH. Cyclic voltammograms (CVs) were recorded between -0.3 V and +0.6 V at scan rates of 100 mV s<sup>-1</sup> (20 cycles) and then at 5 mV s<sup>-1</sup> (3 cycles), followed by a galvanostatic electrochemical impedance spectroscopy (EIS) at OCV with a 2 mA cm<sub>MEA</sub><sup>-2</sup> AC current perturbation between 500 kHz and 1 Hz (10 points per decade) to determine the HFR (in mΩ cm<sub>MEA</sub><sup>2</sup>) that was used for correcting the cell potential E<sub>cell</sub> for the Ohmic drop, yielding the iR-free cell voltage (E<sub>iR-free</sub>) according to Eq. 2. These potentiodynamic measurements were followed by a set of galvanostatic and potentiostatic measurements. For galvanostatic measurements, a DC current was drawn for 60 s and the resulting potential response was averaged over the last 10 s; this was followed by an EIS measurement at the same current, with a current amplitude of 10% of the DC current (from 500 kHz to 1 Hz, with 10 points per decade). These measurements were performed for four currents between ±0.0117 A cm<sub>MEA</sub><sup>-2</sup> and ±0.074 A cm<sub>MEA</sub><sup>-2</sup> in ascending order by alternating between anodic and the corresponding cathodic current in order to precisely determine the reversible potential at each condition.

Following these galvanostatic measurements, potentiostatic measurements were conducted in the analogous manner by applying a given potential for 60 s and averaging the resulting current during the last 10 s, followed by a potentiostatic EIS at the same potential using a potential amplitude of 1% of the DC potential (from 500 kHz to 1 Hz, with 10 points per decade). The potentiostatic testing was performed for potentials between ±5 mV and in the range between -200 mV and +450 mV; this was done in ascending order and by alternating between anodic and equal cathodic potentials. Each data point was corrected for the HFR at this specific potential. Considering that the WE was very thin (ca. 6 μm) and that the HOR/HER overpotential of the high-loaded Pt based CE is negligible, the HFR-corrected cell voltage very closely represents the HOR/HER overpotential η:

$$\eta = E_{iR-free}(E) = E_{cell} - i \times HFR(E_{cell}) \quad [4]$$

After each data point (static hold plus EIS), a relaxation step of 5 or 30 s (after potentials exceeding ±0.1 V) at OCV was implemented to ensure steady-state conditions for the next point.

Finally, CVs of the WE were recorded between 0.05 and 1.0 V<sub>RHE</sub> at a scan rate of 100 mV s<sup>-1</sup>, at 40 °C and ambient pressure. The CE was fed with 200 nccm of fully humidified 5% H<sub>2</sub> in Ar, and the WE was initially purged with dry N<sub>2</sub> at 50 nccm, while interrupting the gas flow to record the CVs.

## Results and Discussion

**Structural characterization by transmission electron microscopy.**—To ensure that the catalyst synthesis steps would yield the desired structural characteristics, the morphology of the as-synthesized Ru/TiO<sub>x</sub>/C<sup>as-synth.</sup> catalyst, consisting of Ru-NPs supported on larger TiO<sub>x</sub> nanoparticles which in turn are supported on Vulcan carbon, and of the subsequently reduced Ru/TiO<sub>x</sub>/C<sup>400°C,H<sub>2</sub></sup> catalyst was analyzed by TEM (Fig. 1). For comparison, a carbon supported ruthenium catalyst prepared from the same Ru-NPs and the same Vulcan carbon support (Ru/C) served as reference catalyst and as a baseline for the characterization of the Ru/TiO<sub>x</sub>/C catalysts, as it allows for a precise analysis of Ru-NP shape, size, and distribution. Furthermore, the non-heat-treated Ru/TiO<sub>x</sub>/C<sup>as-synth.</sup> catalyst was examined to monitor the distribution of Ru-NPs throughout the catalyst, offering a way to confirm the targeted Ru-NP deposition onto the TiO<sub>x</sub> particles. At the end, the final Ru/TiO<sub>x</sub>/C<sup>400°C,H<sub>2</sub></sup> catalyst was investigated for the effect of the reductive heat-treatment on the catalyst morphology.

The Ru-NPs were prepared by the polyol reduction method with PVP as a capping agent that resulted in spherical particles. The TEM image of the Ru/C reference catalyst (Fig. 1a) displays a homogeneous distribution of Ru-NPs and small agglomerates thereof on the surface of the Vulcan carbon support. Using higher magnified images (one representative example shown in Fig. 1e), the Ru particle diameter (d<sub>i</sub> in nm) was determined for at least 100 particles (Fig. 1h, green bars). The Sauter mean diameter (SMD) was calculated according to Eq. 5 as ≈2.2 nm for the Ru/C catalyst.

$$SMD = \frac{\sum d_i^3}{\sum d_i^2} \quad [5]$$

This small particle size was desired to achieve a high electrochemically active surface area (ECSA), which in the spherical particle approximation would be inversely proportional to the SMD (i.e., ECSA = 6/(SMD · ρ<sub>Ru</sub>), with ρ<sub>Ru</sub> = 12.2 · 10<sup>6</sup> g m<sup>-3</sup>).

The preparation route for the Ru/TiO<sub>x</sub>/C<sup>as-synth.</sup> catalyst was designed to deposit the Ru-NPs on TiO<sub>x</sub> ("Ru/TiO<sub>x</sub>-composite") to enable the later formation of an SMSI, which is not possible for Ru-NPs supported on carbon. The TEM images of the Ru/TiO<sub>x</sub>/C<sup>as-synth.</sup> catalyst (Figs. 1b and 1f) indicate that the synthesis strategy to support Ru/TiO<sub>x</sub>-composites on the carbon was largely successful. While the weak contrast of Ru ↔ TiO<sub>x</sub> and TiO<sub>x</sub> ↔ C complicates the

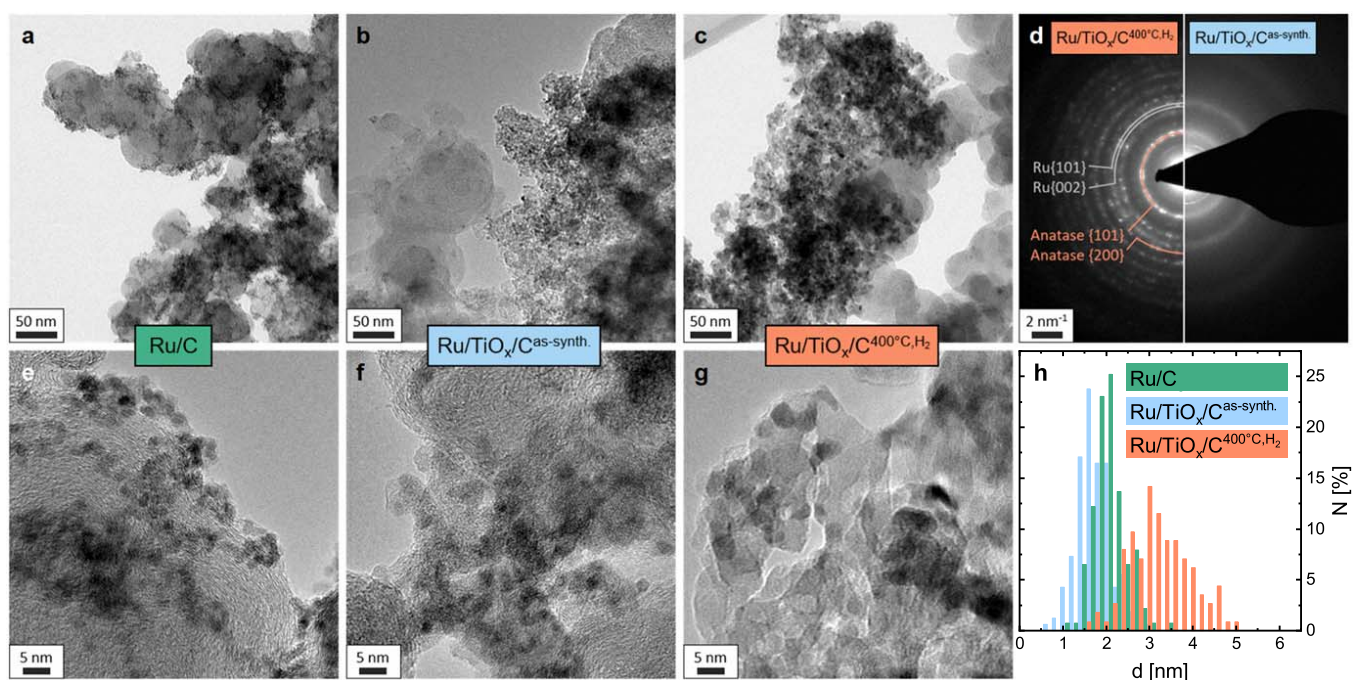


**Figure 1.** (HR) TEM images of the various prepared catalysts. (a) and (e) Ru/C, showing the distribution of Ru nanoparticles and small agglomerates on the carbon support; (b) and (f) Ru/TiO<sub>x</sub>/C<sup>as-synth.</sup>, with the Ru/TiO<sub>x</sub>-composites attached to the carbon support, showing only few isolated Ru-NPs on the carbon; and, (c) and (g) Ru/TiO<sub>x</sub>/C<sup>400°C,H<sub>2</sub></sup> consisting of agglomerates of larger Ru particles and crystalline TiO<sub>x</sub> that are supported on carbon. Panel (d) shows a comparison of the SAED patterns of Ru/TiO<sub>x</sub>/C<sup>400°C,H<sub>2</sub></sup> (left half of the image) and of Ru/TiO<sub>x</sub>/C<sup>as-synth.</sup> (right half), emphasizing the high crystallinity of Ru and anatase type TiO<sub>2</sub> after the heat-treatment. Panel (h) shows the Ru particle size distributions for the three catalysts, showing small particles on the as-synthesized samples (green and blue bars) and severe sintering after the heat-treatment at 400 °C (orange bars).

interpretation, the structural differences of the well-defined carbon spheres compared to the irregular shape of the Ru/TiO<sub>x</sub> agglomerates nevertheless allow to distinguish between Ru/TiO<sub>x</sub>-composites and the mostly Ru-NP-free carbon although a few isolated Ru particles can be seen on the carbon support in Fig. 1b. A tomographic TEM tilt series was recorded to explore the large-scale three-dimensional (3D) catalyst structure (see the file RuTiO<sub>x</sub>C\_TOMO.avi, with a scale bar of 100 nm, in the supporting information (available online at [stacks.iop.org/JES/169/034519/mmedia](https://stacks.iop.org/JES/169/034519/mmedia))). Here, the differently sized and irregularly shaped Ru/TiO<sub>x</sub>-composites are clearly deposited on and between the spherical primary particles of the carbon support and even some of the smaller particles on the carbon seem to be Ru/TiO<sub>x</sub>-composites that did not aggregate to larger agglomerates based on the 3D structure. The determined particle size distribution (Fig. 1h, blue) has a similar shape as that of the Ru/C reference catalyst, with a calculated SMD of  $\approx 2.0$  nm. This minor decrease in average particle size can be explained by the fact that a fresh batch of Ru-NPs was prepared for each catalyst and small deviations were therefore expected. Additionally, the particle size determination for Ru-NPs on TiO<sub>x</sub> was further complicated by the poor contrast, which could potentially have resulted in a systematic underestimation of the particle size, as the particle edge was not well defined in all cases.

The Ru/TiO<sub>x</sub>/C<sup>as-synth.</sup> catalyst was heat-treated at 400 °C under reductive atmosphere (5% H<sub>2</sub> in Ar, see experimental section) to obtain the final Ru/TiO<sub>x</sub>/C<sup>400°C,H<sub>2</sub></sup> catalyst. The overall catalyst morphology consisting of Ru/TiO<sub>x</sub>-composite agglomerates on the carbon support was maintained after the heat treatment (see Fig. 1c and the file RuTiO<sub>x</sub>C-400\_TOMO.avi, with a scale bar of 200 nm, in the SI (available online at [stacks.iop.org/JES/169/034519/mmedia](https://stacks.iop.org/JES/169/034519/mmedia))). This was confirmed by EDX mappings, where a Ru signal was always accompanied by a strong Ti signal proving the preferential deposition of Ru on the TiO<sub>x</sub> support (see Fig. A-1). However, the structure of the Ru/TiO<sub>x</sub>-composites was significantly altered (Fig. 1g): While the TiO<sub>x</sub> had been mostly amorphous in the as-synthesized catalyst, the heat-treatment resulted in mostly

crystalline TiO<sub>2</sub> particles of the anatase-type (see indicated anatase-TiO<sub>2</sub>{101}, and anatase-TiO<sub>2</sub>{200} lattice planes), as seen in the selected area electron diffraction (SAED) patterns (Fig. 1d). For Ru/TiO<sub>x</sub>/C<sup>as-synth.</sup> (right half of the image), the SAED only showed almost amorphous rings of low intensity, whereas for Ru/TiO<sub>x</sub>/C<sup>400°C,H<sub>2</sub></sup> (left half), the intensity of the rings was much higher and additional Bragg-reflexes could be observed for both Ru (see indicated Ru{101} and Ru{002} lattice planes) and TiO<sub>2</sub>. While the TiO<sub>2</sub> particles clearly increased in crystallinity as seen from the TEM images, the pronounced reflexes of Ru might at part be the result of a severe increase in particle size after the heat-treatment due to particle sintering as well. The low contrast of Ru $\leftrightarrow$ TiO<sub>2</sub> in combination with a thickness contrast in TEM images complicated the identification of Ru-NPs. The Ru particle size (Fig. 1h, orange) was thus determined from a high-resolution tomographic TEM tilt series (see file HR\_RuTiO<sub>x</sub>C-400\_TOMO.avi, with a scale bar of 20 nm, in the SI (available online at [stacks.iop.org/JES/169/034519/mmedia](https://stacks.iop.org/JES/169/034519/mmedia))) by identifying individual Ru particles from TEM images recorded at slightly different angles (see Fig. A-2 for examples). The resulting particle size distribution was much broader, with an SMD of 4.4 nm. Interestingly, some of the Ru particles seem to be incorporated into the TiO<sub>2</sub> structure rather than sitting on the surface. While it cannot be excluded that this might be the result of Ru sitting in cavities of the TiO<sub>2</sub> flakes/particles, it is likely the result of an encapsulation of the Ru-NPs by a thin TiO<sub>x</sub> ( $x \leq 2$ ) layer that is well known to occur when an SMSI is formed.<sup>27,29,50,51</sup>

**Electrochemical characterization in aqueous HClO<sub>4</sub> electrolyte.**—To investigate whether an SMSI between Ru and TiO<sub>2</sub> in the Ru/TiO<sub>x</sub>/C<sup>400°C,H<sub>2</sub></sup> catalyst might also prevent the surface oxidation of ruthenium and thereby stabilize the HOR activity at high potentials, analogous to what had been observed for a similarly prepared Pt/TiO<sub>x</sub>/C<sup>400°C,H<sub>2</sub></sup> catalyst,<sup>35</sup> RDE measurements in 0.1 M HClO<sub>4</sub> were performed. Figure 2 shows the cyclic voltammograms (CVs) of the Ru/C (green line), the Ru/TiO<sub>x</sub>/C<sup>as-synth.</sup> (blue line), and the Ru/TiO<sub>x</sub>/C<sup>400°C,H<sub>2</sub></sup> (orange line) catalysts recorded in

Ar-saturated electrolyte. One difficulty in analyzing the voltammetric response of Ru-based catalysts is the distinction between hydrogen underpotential deposition ( $H_{\text{upd}}$ ), double layer capacity, and surface oxidation that all overlap in the same potential regions.<sup>52</sup> It is known that the Ru-surface oxidation to  $\text{RuO}_2$  is a complex multistep process via  $\text{RuO}$  and  $\text{Ru}_2\text{O}_3$  that starts above  $0.2 V_{\text{RHE}}$  in the anodic scan.<sup>53</sup> While an increasing extent of surface oxidation with increasing potential is clearly visible for the Ru/C reference catalyst, this process seems to be strongly suppressed for both Ru/TiO<sub>x</sub>/C catalysts. Since the Ru to carbon ratio was similar in all catalysts, the capacitive contribution of the carbon support can be estimated by recording a CV of the corresponding amount of Vulcan-carbon on the GC (gray dashed line in Fig. 2). Thus, the much lower currents above  $0.3 V_{\text{RHE}}$  for the Ru/TiO<sub>x</sub>/C catalysts cannot result from the carbon support double layer capacity but must be related to the surface properties of the ruthenium. The high voltammetric currents of the Ru/C catalyst above  $0.3 V_{\text{RHE}}$  (green line, Fig. 2) are generally ascribed to the continuous Ru-surface oxidation, which occurs up to the formation of bulk  $\text{RuO}_2$  above  $1.1 V_{\text{RHE}}$ .<sup>23,52</sup> Analogous oxidation features would be expected also for the Ru/TiO<sub>x</sub>/C<sup>as-synth.</sup> catalyst that has not yet undergone any reductive heat treatment, but in this case all voltammetric features are strongly suppressed, despite the fact that the SMD of the Ru-NPs and thus the expected ECSA of the Ru/TiO<sub>x</sub>/C<sup>as-synth.</sup> catalyst is essentially identical with that of the Ru/C catalyst. The origin of this difference is unclear and might be related to either remaining surface contaminants from the synthesis process, a very low conductivity of the amorphous TiO<sub>x</sub> particles, and/or a higher amount of surface oxidation of Ru in Ru/TiO<sub>x</sub>/C<sup>as-synth.</sup>. For the Ru/TiO<sub>x</sub>/C<sup>400°C,H<sub>2</sub></sup> catalyst, the Ru surface oxidation is similarly suppressed, which could be the result of the ECSA loss due to particle sintering (yielding a  $\approx 2$ -fold lower SMD), a reduced conductivity of TiO<sub>x</sub> at higher potentials,<sup>36</sup> or the desired SMSI effect.<sup>34,35</sup> The pronounced  $H_{\text{upd}}$ -like features below  $0.3 V_{\text{RHE}}$  indicate that the reduced ECSA cannot be the sole reason for the reduced Ru surface oxidation currents above  $0.3 V_{\text{RHE}}$  and that a significant change in the Ru surface chemistry must have occurred compared to the Ru/C reference following the reductive heat-treatment of the catalyst that resulted in the reduction of the Ru particles and the formation of an SMSI.

To further investigate the different oxidation behavior and obtain insights into the contributions of surface reduction and  $H_{\text{upd}}$  in the low potential region, each catalyst was cycled to a stepwise increasing upper cutoff potential from  $0.6 V_{\text{RHE}}$  up to  $1.3 V_{\text{RHE}}$  (Fig. 3). For the Ru/C reference catalyst, the cycling is reversible up to an upper cutoff potential of  $1.1 V_{\text{RHE}}$  (Fig. 3a). However, surpassing this upper potential limit, the surface passivation becomes irreversible, which is shown by the decreasing oxidative current in the anodic scan of the steady-state CVs, i.e., steady state CVs with a higher upper potential limit do not follow the anodic CVs of measurements with a lower upper potential limit even within that range. Simultaneously, the reduction feature that starts below  $\approx 0.4 V_{\text{RHE}}$  during the cathodic scan are shifting to lower potentials with increasing upper potential limit, thus indicating that higher overpotentials are required to reduce the Ru-NPs again (indicated by the arrow in Fig. 3a).

In contrast, the Ru/TiO<sub>x</sub>-based catalysts could be cycled to an upper potential limit of  $1.3 V_{\text{RHE}}$  with significantly improved reversibility. While the Ru/TiO<sub>x</sub>/C<sup>as-synth.</sup> catalyst showed a certain degree of irreversibility when cycled to  $1.3 V_{\text{RHE}}$ , the reductive peak at  $\approx 0.2 V_{\text{RHE}}$  does not shift to lower potentials. Thus, already by introducing a TiO<sub>x</sub> support, Ru could be stabilized in its metallic state up to high positive potential limits (Fig. 3b). This might be the result of an electrochemical SMSI formation by hydrogen spillover induced reduction or the TiO<sub>x</sub> support or the dissolution and subsequent redeposition of TiO<sub>x</sub> within the first 25 cleaning cycles.<sup>35,37,54,55</sup> The stabilization is more pronounced after an SMSI was formed (Fig. 3c). Here, the decreased surface oxidation

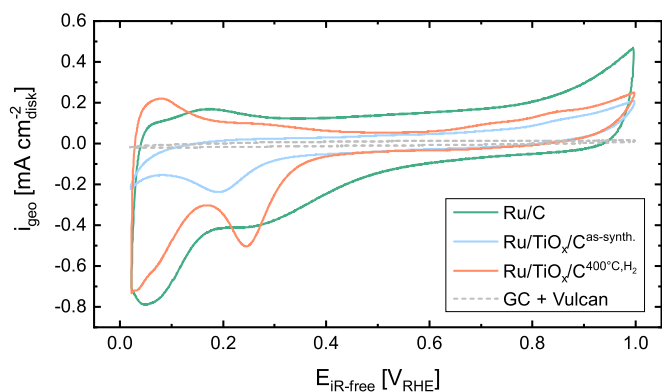


**Figure 2.** CVs of Ru/C (green), Ru/TiO<sub>x</sub>/C<sup>as-synth.</sup> (blue), Ru/TiO<sub>x</sub>/C<sup>400°C,H<sub>2</sub></sup> (orange), and the corresponding Vulcan-carbon baseline (gray dashed) in Ar-saturated 0.1 M HClO<sub>4</sub> at 0 rpm. All measurements were recorded in an RDE setup at 25 °C with a scan rate of 20 mV s<sup>-1</sup>, a loading of  $17 \pm 2 \mu\text{g}_{\text{Ru}} \text{cm}_{\text{disk}}^{-2}$  and an ionomer/support (C + TiO<sub>x</sub>) ratio of  $I/S = 0.1$ . The potential was corrected for the HFR of the setup. The loading of the pure Vulcan carbon electrode was  $\approx 45 \mu\text{g}_{\text{C}} \text{cm}_{\text{disk}}^{-2}$  and thus closely matched that in the Ru/TiO<sub>x</sub>/C catalysts.

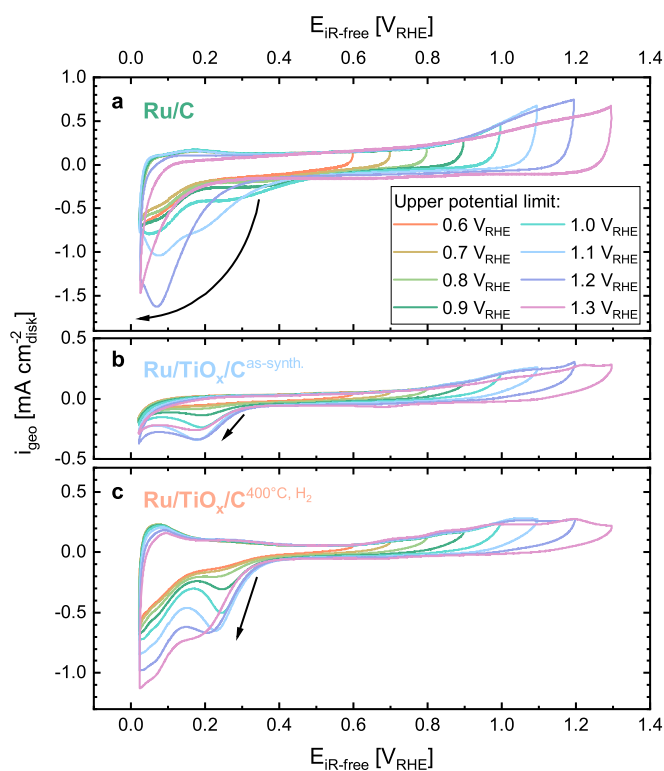


**Figure 3.** Steady state CVs of the various catalysts in Ar-saturated 0.1 M HClO<sub>4</sub> with increasing upper potential limits: (a) Ru/C; (b) Ru/TiO<sub>x</sub>/C<sup>as-synth.</sup>; and (c) Ru/TiO<sub>x</sub>/C<sup>400°C,H<sub>2</sub></sup> recorded. All measurements were recorded at 25 °C, in an RDE setup at 0 rpm with a scan rate of 20 mV s<sup>-1</sup>, a Ru loading of  $17 \pm 2 \mu\text{g}_{\text{Ru}} \text{cm}_{\text{disk}}^{-2}$ , and an ionomer/support (C + TiO<sub>x</sub>) ratio of  $I/S = 0.1$ ; the potentials were corrected for the HFR of the setup.

of Ru was found fully reversible, whereby the reduction feature at  $\approx 0.25 V_{\text{RHE}}$  does not exhibit a negative shift except for the highest upper cutoff potential of  $1.3 V_{\text{RHE}}$ , where a negative shift of  $\approx 20$  mV could be observed. At low potentials ( $< 0.3 V_{\text{RHE}}$ ), the Ru/TiO<sub>x</sub>/C<sup>400°C,H<sub>2</sub></sup> catalyst clearly features a mixed region, where  $H_{\text{upd}}$  (indicated by the positive currents in the anodic scan that are missing in the other catalysts), Ru oxide reduction, and the onset of the HER overlap.

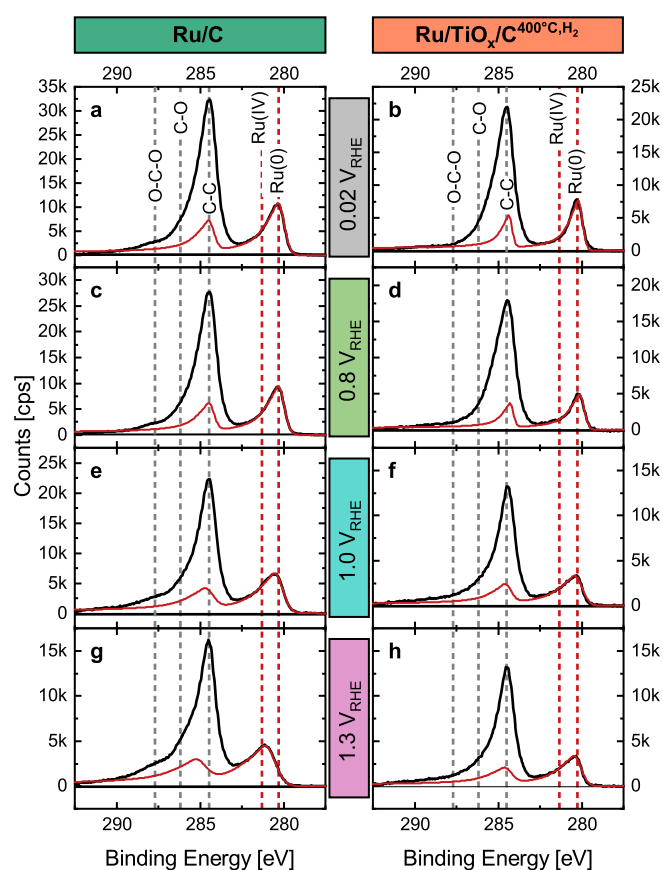


**Figure 4.** XPS of Ru/C (left) and Ru/TiO<sub>x</sub>/C<sup>400°C,H<sub>2</sub></sup> (right) drop-casted on a gold foil and polarized in 0.1 M HClO<sub>4</sub> at different potentials for 600 s: (a) and (b) 0.02 V<sub>RHE</sub>; (c) and (d) 0.8 V<sub>RHE</sub>; (e) and (f) 1.0 V<sub>RHE</sub>; and, (g) and (h) 1.3 V<sub>RHE</sub>. The catalysts were reduced at 0.02 V<sub>RHE</sub> for 600 s before being exposed to oxidative potentials. Due to an overlap with the C 1s peaks (only peak positions indicated for clarity), the Ru 3d<sub>3/2</sub> peak was fixed to the 3d<sub>5/2</sub> peak and the doublet was jointly fitted (red lines, details see experimental section). The black lines mark the total measured XPS counts.

**Oxidation state analysis by XPS.**—To get more insight into the Ru (surface) oxidation behavior of the Ru/C and the Ru/TiO<sub>x</sub>/C<sup>400°C,H<sub>2</sub></sup> catalysts, they were pre-polarized at 0.02, 0.8, 1.0, and 1.3 V<sub>RHE</sub> in 0.1 M HClO<sub>4</sub> for 600 s, then emersed from the electrolyte, dried, and finally examined by XPS. To ensure that the oxidation state of the Ru-NPs is due to the effect of the oxidation potential rather than the storage conditions before conducting these experiments, a 600 s hold at 0.02 V<sub>RHE</sub> was implemented prior to any oxidative polarization (for details see experimental section). While XPS is technically a surface sensitive technique with a penetration depth of  $\approx 3$  nm for a kinetic energy of  $\approx 1200$  eV of the photo electrons (i.e., in the R 3d region using an Al X-ray source),<sup>56</sup> the small particle size of the Ru-NPs implies that the XPS signal comprises a major contribution from the bulk of the Ru-NPs particles in addition to their surface. Although the Ru 3d<sub>3/2</sub> signal overlaps with the main C 1s feature from the Vulcan carbon support (at 284.4 eV<sup>47</sup>), the stronger Ru 3d<sub>5/2</sub> peak is located at sufficiently low binding energy so that it does not overlap with the C 1s feature. Note that the Ru 3p<sub>3/2</sub> signal (461.7–463.2 eV, depending on the oxidation state)<sup>46</sup> overlaps completely with the much stronger Ti 2p features (Ti(IV)<sub>3/2</sub> at 458.5 eV and Ti(IV)<sub>1/2</sub> at 464.2 eV, data not shown), so that this spectral region was not considered and the following XPS analysis is focusing on the Ru 3d region (for details see Table II).

Thus, Fig. 4 shows the Ru 3d XPS spectra of the Ru/C (left) and the Ru/TiO<sub>x</sub>/C<sup>400°C,H<sub>2</sub></sup> (right) catalysts after polarization. After emersion at the lowest potential of 0.02 V<sub>RHE</sub>, the Ru 3d<sub>5/2</sub> peaks

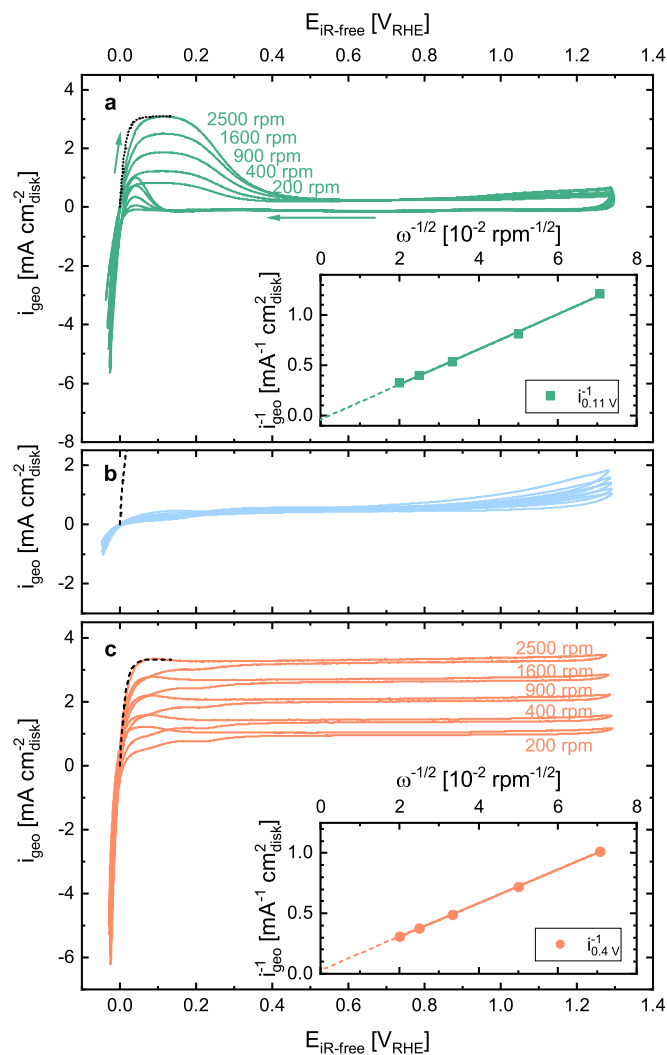


**Figure 5.** Rotation rate dependent HER/HOR polarization curves in H<sub>2</sub>-saturated 0.1 M HClO<sub>4</sub> at 25 °C: (a) Ru/C; (b) Ru/TiO<sub>x</sub>/C<sup>as-synth.</sup>; (c) Ru/TiO<sub>x</sub>/C<sup>400°C,H<sub>2</sub></sup>. All measurements were recorded in an RDE setup at a scan rate of 20 mV s<sup>-1</sup>, with a loading of  $17 \pm 2 \mu\text{g}_{\text{Ru}} \text{cm}_{\text{disk}}^{-2}$  and an ionomer/support (C + TiO<sub>x</sub>) ratio of I/S = 0.1, and were corrected for the HFR of the setup. The dashed black lines represent the pure Nernstian diffusion overpotentials for the positive-going scan at 2500 rpm. The insets show Koutecký-Levich plots of the inverse of the current density vs the inverse square root of the electrode rotation speed  $\omega$ : in (a) for the Ru/C catalyst at the current maximum, taken at 0.11 V<sub>RHE</sub>; in (c) for the Ru/TiO<sub>x</sub>/C<sup>400°C,H<sub>2</sub></sup> catalyst at the stable plateau, taken at 0.4 V<sub>RHE</sub>.

at 280.3 eV for Ru/C (Fig. 4a) and 280.2 eV for Ru/TiO<sub>x</sub>/C<sup>400°C,H<sub>2</sub></sup> (Fig. 4b) correspond to Ru(0), thus confirming that the Ru-NPs are fully reduced to metallic Ru at this potential.<sup>46</sup> After the polarization at 0.8 V<sub>RHE</sub>, the spectra remain essentially identical (Fig. 4c and d), although a partial oxidation of the Ru surface would have been expected for the Ru/C catalyst based on its CV (green line in Fig. 2). This might be the result of a reversible hydroxide adsorption by water discharge at these potentials,<sup>32</sup> whereby no stable oxide is formed and the majority of Ru atoms therefore remain in metallic state after vacuum drying of the sample. After polarization at 1.0 V<sub>RHE</sub>, a small peak shift of 0.2 eV to higher binding energies was detectable for both catalysts, which might indicate partial oxidation of Ru (Figs. 4e and 4f), as would be expected from the CV measurements (see Figs. 3a and 3c). After polarization to 1.3 V<sub>RHE</sub>, the Ru-NPs of the Ru/C reference are largely oxidized, as is indicated by a peak shift to 281.2 eV (corresponding to Ru(IV), Fig. 4g), while the Ru-NPs of the Ru/TiO<sub>x</sub>/C<sup>400°C,H<sub>2</sub></sup> catalyst still show the characteristic Ru(0) peak at 280.2 eV (Fig. 4h). These

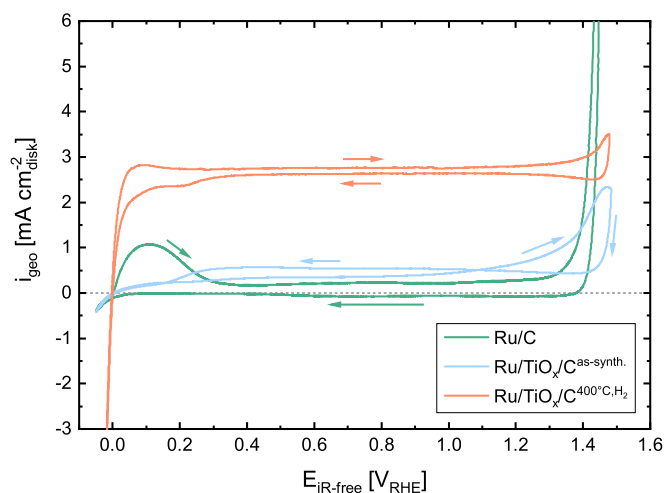


**Figure 6.** HER/HOR polarization curves in  $\text{H}_2$ -saturated 0.1 M  $\text{HClO}_4$  at 1600 rpm and 25 °C that are extended into the OER potential window of the Ru/C (green), the  $\text{Ru/TiO}_x/\text{C}^{\text{as-synth.}}$  (blue), and the  $\text{Ru/TiO}_x/\text{C}^{400^\circ\text{C},\text{H}_2}$  (orange) catalysts. All measurements were recorded after the rotation rate dependent HER/HOR polarization curves under identical conditions (see Fig. 5).

results confirm the observations from the CV measurements that Ru oxidation is significantly suppressed for the  $\text{Ru/TiO}_x/\text{C}^{400^\circ\text{C},\text{H}_2}$  compared to the Ru/C reference catalyst. Whether this stabilization is the result of a  $\text{TiO}_x$  encapsulation could unfortunately not be verified by investigating the Ti 2p spectrum, as the fraction of Ti in such a thin film would have an insignificant contribution compared to the bulk  $\text{TiO}_2$  of the support structure. No changes in the Ti 2p spectrum could therefore be observed, except for a potential dependent shift of the shoulder corresponding to the Ru  $3p_{3/2}$  signal (data not shown).

**HER/HOR investigation by RDE.**—In the case of similarly prepared  $\text{Pt/TiO}_x/\text{C}^{400^\circ\text{C},\text{H}_2}$  catalysts, the analogously observed suppression of the surface oxide formation was accompanied by an extension of the HOR activity of Pt to very high positive potentials.<sup>35</sup> Therefore, we will next examine whether this will also hold true for the  $\text{Ru/TiO}_x/\text{C}^{400^\circ\text{C},\text{H}_2}$  catalyst, using RDE experiments at different rotation rates in 0.1 M  $\text{HClO}_4$ . For the Ru/C reference catalyst, a high HER activity is observed, but its HOR activity quickly decreases above 0.15  $V_{\text{RHE}}$  due to surface oxidation (Fig. 5a), analogous to what had been observed for a ruthenium metal disk.<sup>23</sup> A Koutechý-Levich analysis relating the reciprocal current density maximum (at 0.11  $V_{\text{RHE}}$ ) and the inverse square root of the rotation rate shows an essentially zero y-axis intercept, thus confirming that the HOR currents are mostly mass-transport limited at 0.11  $V_{\text{RHE}}$  (Fig. 5a inset). However, when comparing the actual oxidation currents below 0.11  $V_{\text{RHE}}$  with those predicted by the purely Nernstian diffusion overpotential for the HOR<sup>57</sup> for the positive-going scan at 2500 rpm (see dashed black line in Fig. 5a), it becomes clear that the HOR on the Ru/C catalyst in this region is still affected by kinetic limitations. As the potential reaches  $\approx 0.5 V_{\text{RHE}}$  during the positive-going scan, the HOR activity of the Ru-NPs has vanished to zero, and only once the Ru surface is polarized again below 0.1  $V_{\text{RHE}}$  during the negative-going scan, some HOR activity can again be observed. The HER activity at negative potentials is sufficiently good to reach a mostly mass-transport controlled current profile that is expected for highly active HER catalysts in acidic RDE measurements.<sup>58</sup>

As discussed previously, the  $\text{Ru/TiO}_x/\text{C}^{\text{as-synth.}}$  catalyst appeared to suffer from a poor conductivity and/or from poisoning by surface adsorbates from the synthesis, which also seems limit its ability to

oxidize hydrogen (Fig. 5b). Independent on the rotation rate, the catalyst showed almost no HOR activity and never reached the mass-transport limited current densities. Since any residual organic surface contaminations would be expected to be oxidized upon cycling to 1.3  $V_{\text{RHE}}$  multiple times but the HOR performance did not increase, it is more likely that the suppressed HOR activity is the result of the poor conductivity of the as-synthesized  $\text{TiO}_x$  that results in most of the Ru particles being electrically insulated.

In contrast to the Ru/C catalyst, the polarization curve of the  $\text{Ru/TiO}_x/\text{C}^{400^\circ\text{C},\text{H}_2}$  catalyst shows a steady HOR activity up to 1.3  $V_{\text{RHE}}$  (Fig. 5c). The zero y-axis intercept in the Koutechý-Levich analysis at 0.4  $V_{\text{RHE}}$  (to exclude  $\text{H}_{\text{upd}}$  contributions) shows that even at higher potentials, the currents are purely mass-transport limited (Fig. 5c inset). In contrast to the Ru/C catalyst, the HOR currents of the  $\text{Ru/TiO}_x/\text{C}^{400^\circ\text{C},\text{H}_2}$  catalyst are now exclusively limited by the Nernstian diffusion overpotential (black dashed line in Fig. 5c) rather than kinetics, which means its true HOR kinetics cannot be assessed by RDE measurements (see below for kinetic investigation in an MEA setup).<sup>57</sup>

Since the SMSI in  $\text{Ru/TiO}_x/\text{C}^{400^\circ\text{C},\text{H}_2}$  prevents the (surface) oxidation of Ru and thereby enables continuous hydrogen oxidation even at 1.3  $V_{\text{RHE}}$ , it will likely also impact the OER performance of the catalyst, as was observed for a Pt/ $\text{TiO}_x$  based catalyst.<sup>34</sup> Thus, the OER activity of the Ru/C,  $\text{Ru/TiO}_x/\text{C}^{\text{as-synth.}}$ , and  $\text{Ru/TiO}_x/\text{C}^{400^\circ\text{C},\text{H}_2}$  catalysts was examined by extending the upper potential limit in the HER/HOR polarization curves to 1.5  $V_{\text{RHE}}$  (Fig. 6). The OER on the Ru/C reference catalyst readily starts above 1.3  $V_{\text{RHE}}$ , as shown by the steep current increase. As these measurements had been performed after the HER/HOR polarization curves at different rotation rates up to 1.3  $V_{\text{RHE}}$ , the HOR activity of Ru/C has already severely degraded compared to the initial experiments shown in Fig. 5. This limited stability of Ru in acidic environment is well known and Ru dissolution poses a major issue for the implementation of any Ru containing catalyst in PEMFCs and similar systems.<sup>59,60</sup> The mass-transport limited current density was therefore not reached anymore even in the first scan. After the catalyst had been exposed to even higher potentials of 1.5  $V_{\text{RHE}}$ , the overpotential for Ru reduction apparently has shifted to even more negative potentials, continuing the trend observed in Fig. 3a and thereby nearly completely deactivating the HER activity of the Ru/C catalyst. In contrast, the  $\text{Ru/TiO}_x/\text{C}^{400^\circ\text{C},\text{H}_2}$  catalyst maintains its superior HOR activity as well as its high HER activity when polarized up to 1.5  $V_{\text{RHE}}$ , but its OER activity is strongly suppressed, as is indicated by the observation that the current upper potential limit of 1.5  $V_{\text{RHE}}$  barely exceeds the HOR current plateau. This observation and the fact that the HER/HOR activity is maintained even after harsh oxidative potentials confirm the successful stabilization of Ru in its metallic state. The OER activity of the  $\text{Ru/TiO}_x/\text{C}^{400^\circ\text{C},\text{H}_2}$  catalyst still exceeds that of a similarly stabilized Pt/ $\text{TiO}_x/\text{C}^{400^\circ\text{C},\text{H}_2}$  catalyst,<sup>35</sup> which is most likely the result of a small fraction of Ru-NPs that are located on the carbon support and thus are not affected by the SMSI effect. While the HOR activity of  $\text{Ru/TiO}_x/\text{C}^{\text{as-synth.}}$  remained almost completely suppressed, the catalyst showed a surprisingly high activity for the OER that by far exceeded that of the heat-treated catalyst. These observations confirm that the stabilization of Ru against (surface) oxidation is indeed the result of an encapsulation of the Ru particles due to SMSI effects after the reductive heat-treatment, thereby enabling a high HOR activity at potentials where surface passivation by (surface) oxide formation would otherwise have occurred.

**CV characterization of the catalysts in MEAs.**—As the HER/HOR rates on platinum group metal catalysts with high HOR/HER activity (e.g., Pt or Ir) cannot be determined precisely in acidic liquid electrolyte using an RDE setup,<sup>57</sup> the HER/HOR kinetics of the  $\text{Ru/TiO}_x/\text{C}^{400^\circ\text{C},\text{H}_2}$  catalyst (and of the Ru/C catalyst as a reference) were investigated using a PEMFC-based hydrogen pump approach,

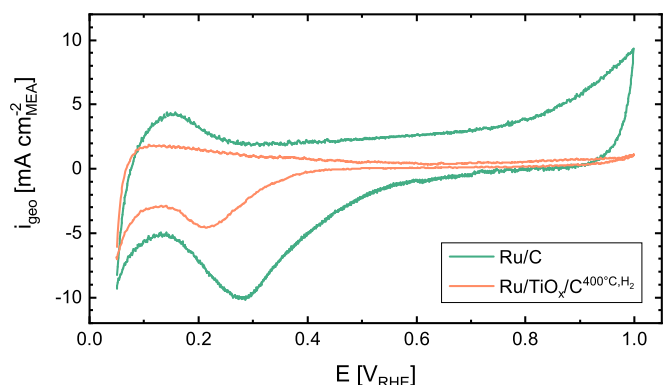


**Figure 7.** Cyclic voltammograms of Ru/C (green,  $56 \mu\text{g}_{\text{Ru}} \text{cm}_{\text{MEA}}^{-2}$ ) and Ru/TiO<sub>x</sub>/C<sup>400°C,H<sub>2</sub></sup> (orange,  $44 \mu\text{g}_{\text{Ru}} \text{cm}_{\text{MEA}}^{-2}$ ) working electrodes recorded in a 5 cm<sup>2</sup> single-cell PEM fuel cell at a scan rate of 100 mV s<sup>-1</sup> from 0.05 to 1.0 V<sub>RHE</sub> at ambient pressure and 40 °C. The CE compartment was purged with 200 nccm 5% H<sub>2</sub>/Ar (humidified at 90% RH), while the WE compartment was purged with 50 nccm dry N<sub>2</sub> (set to zero flow when recording the CV).

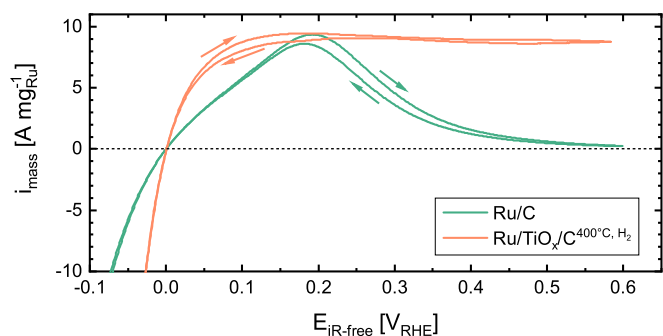


**Figure 8.** Mass normalized potentiodynamic HER/HOR polarization curves at 5 mV s<sup>-1</sup> on the Ru/C (green) and Ru/TiO<sub>x</sub>/C<sup>400°C,H<sub>2</sub></sup> (orange) catalyst in a 5 cm<sup>2</sup> single-cell PEMFC, with the potential corrected for the HFR at OCV ( $E_{\text{IR-free}}$ ). The data were recorded at 80 °C, 100 kPa<sub>H<sub>2</sub></sub>, 90% RH and 2000/2000 nccm H<sub>2</sub> (through the WE/CE compartments). Electrode loadings of the MEAs:  $56 \mu\text{g}_{\text{Ru}} \text{cm}_{\text{MEA}}^{-2}$  for the Ru/C WE and  $44 \mu\text{g}_{\text{Ru}} \text{cm}_{\text{MEA}}^{-2}$  for the Ru/TiO<sub>x</sub>/C<sup>400°C,H<sub>2</sub></sup> WE; the Pt loading of the Pt/C CE was  $0.39 \pm 0.02 \text{ mg}_{\text{Pt}} \text{cm}_{\text{MEA}}^{-2}$ .

where much higher H<sub>2</sub> mass-transport rates can be achieved.<sup>25</sup> Figure 7 compares the CVs of the Ru/C (green line) and Ru/TiO<sub>x</sub>/C<sup>400°C,H<sub>2</sub></sup> (orange line) catalysts as working electrode (WE) in an MEA (with a Pt/C counter electrode (CE)), obtained in a 5 cm<sup>2</sup> single-cell, with the WE held under N<sub>2</sub> and the CE compartment purged with humidified 5% H<sub>2</sub>/Ar. While the Ru/C CV is very similar to that recorded in Ar-saturated 0.1 M HClO<sub>4</sub> (Fig. 2), with similar oxidative and reductive features, the voltammetric currents of the Ru/TiO<sub>x</sub>/C<sup>400°C,H<sub>2</sub></sup> catalyst measured in the MEA are only similar to those obtained in the 0.1 M HClO<sub>4</sub> electrolyte in the hydrogen adsorption/desorption region, but almost vanish at potentials above  $\approx 0.5 \text{ V}_{\text{RHE}}$ . This could be the result of several factors. First, the liquid electrolyte in the RDE setup might access the Ru surface better than the ionomer, especially when Ru is supported and encapsulated by TiO<sub>x</sub>. It has frequently been observed that the ECSA determined by RDE differs from that observed for the same catalyst in an MEA,<sup>57,61</sup> and it is likely that this effect will be more pronounced for a catalyst with a more complex structure like that of the Ru/TiO<sub>x</sub>/C<sup>400°C,H<sub>2</sub></sup> catalyst. Secondly, the interaction of the two support materials with the ionomer might be different, causing the ionomer to adsorb preferentially on either C or TiO<sub>2</sub>,<sup>62,63</sup> thus leading to selective electrochemical accessibility of Ru particles being supported on either of the support materials. In either case, it is

clear that the difference in Ru loading ( $44 \mu\text{g}_{\text{Ru}} \text{cm}_{\text{MEA}}^{-2}$  for Ru/TiO<sub>x</sub>/C<sup>400°C,H<sub>2</sub></sup> compared to  $56 \mu\text{g}_{\text{Ru}} \text{cm}_{\text{MEA}}^{-2}$  for Ru/C) is too small to result in such different CVs, especially considering that the H<sub>upd</sub> features of Ru/TiO<sub>x</sub>/C<sup>400°C,H<sub>2</sub></sup> (orange line, Fig. 7) are significantly enhanced compared to the overall capacitive currents.

**H<sub>2</sub>-pump measurements in a single-cell PEMFC configuration.**—In a first set of experiments to determine the HER/HOR mass activity of the catalysts, CVs were recorded potentiodynamically at 5 mV s<sup>-1</sup> in a H<sub>2</sub>-pump configuration, scanning the potential from -0.3 to 0.6 V<sub>RHE</sub> (Fig. 8). Again, the Ru/C catalyst (green line) strongly deactivates above 0.2 V<sub>RHE</sub>, whereas the Ru/TiO<sub>x</sub>/C<sup>400°C,H<sub>2</sub></sup> (orange line) catalyst maintains its activity up to the highest investigated potential of 0.6 V<sub>RHE</sub>. Although the H<sub>upd</sub> features in Fig. 7 indicated less ECSA for the Ru/TiO<sub>x</sub>/C<sup>400°C,H<sub>2</sub></sup> catalyst, its HER/HOR activity at low overpotentials ( $\leq 30 \text{ mV}$ ) by far outperforms that of the Ru/C reference catalyst. For the HOR on the Ru/TiO<sub>x</sub>/C<sup>400°C,H<sub>2</sub></sup> the performance curve quickly deviates from the expected Butler-Volmer behavior and reaches a current plateau of  $\approx 9 \text{ A mg}_{\text{Ru}}^{-1}$  (corresponding to  $\approx 0.4 \text{ A cm}_{\text{MEA}}^{-2}$ ) at high overpotentials above  $\approx 0.2 \text{ V}_{\text{RHE}}$ . For Pt catalysts, similar limitations in current density have been discussed to be due to a change from a rate determining Volmer-step to a Tafel-limited<sup>25,57,64,65</sup> or a Heyrovsky-limited step,<sup>66</sup> or due to a hydrogen mass-transport limitation through the ionomer film covering the catalyst surface.<sup>25</sup> In the latter case, the specific current density at which mass transport resistances through the ionomer film could be limiting was estimated to be  $\approx 2 \text{ A cm}_{\text{Pt}}^{-2}$  for a Pt/C catalyst.<sup>25</sup> Based on the ECSA of  $\approx 110 \text{ m}^2 \text{ g}_{\text{Ru}}^{-1}$  that can be estimated from the measured SMD of  $\approx 4.4 \text{ nm}$  (using the spherical approximation) and the Ru loading of  $44 \mu\text{g}_{\text{Ru}} \text{cm}_{\text{MEA}}^{-2}$ , the Ru roughness factor of the Ru/TiO<sub>x</sub>/C<sup>400°C,H<sub>2</sub></sup> catalyst can be estimated to be  $\approx 50 \text{ cm}_{\text{Ru}}^{-2} \text{ cm}_{\text{MEA}}^{-2}$ , which then would convert to a limiting specific current density of  $\approx 8 \text{ mA cm}_{\text{Ru}}^{-2}$  for the data in Fig. 8. As this is nearly three orders of magnitude lower than the expected mass transport limitation near a specific current density of  $\approx 2 \text{ A cm}_{\text{Ru}}^{-2}$ , mass-transport resistances through the ionomer film can be ruled out as the origin of the current plateau observed in Fig. 8. However, an encapsulation of Ru, as it was discussed above and has been suggested for similar oxide supported Pt catalysts,<sup>32,34,35,37</sup> might be another source for a significant local hydrogen transport resistance to the active site. This hypothesis is supported by a suppressed chemisorption of hydrogen that has been reported for a SMSI between Ru and TiO<sub>2</sub>.<sup>67</sup>

On the other hand, in the case of a limitation by a rate determining adsorption step, the current limitation would be given by the rate of adsorption, whereby the current plateau of only  $9 \text{ A mg}_{\text{Ru}}^{-1}$  could result from slow hydrogen adsorption kinetics on the Ru surface. In the case of Pt, an adsorption rate constant of  $\approx 2.4 \text{ cm s}^{-1}$  at 22 °C determined from H<sub>2</sub>-D<sub>2</sub> exchange experiments by Vogel et al. would predict a limiting specific current density of  $\approx 0.40 \text{ A cm}_{\text{Pt}}^{-2}$  at 100 kPa<sub>H<sub>2</sub></sub>,<sup>25,68</sup> i.e., of the same order of magnitude as the estimated transport limiting current density through the ionomer film (see above), so that for a Pt catalyst the observed limiting current may originate from either kinetic or local transport limitations (or both). To the best of our knowledge there is only the study by Lu et al. that reports a hydrogen adsorption rate constant for Ru, but only states that it exceeds their detection limit of  $10^{-3} \text{ cm s}^{-1}$  at 25 °C (H<sub>2</sub>-D<sub>2</sub> exchange experiments).<sup>69</sup> If the hydrogen adsorption rate were to be responsible for the specific current density limitation of  $\approx 8 \text{ mA cm}_{\text{Ru}}^{-2}$  observed in Fig. 8 (see above), it would have to be on the order of  $10^{-2} \text{ cm s}^{-1}$ .

Since the current density maximum reached by the Ru/C reference catalyst (green line, Fig. 8) coincides with that of the Ru/TiO<sub>x</sub>/C<sup>400°C,H<sub>2</sub></sup> catalyst (orange line, Fig. 8), a distinction between a Ru-specific limitation and a limitation induced by the interaction of Ru and TiO<sub>x</sub> is not possible at this point. Still, it is most likely that the equal mass normalized current density maximum

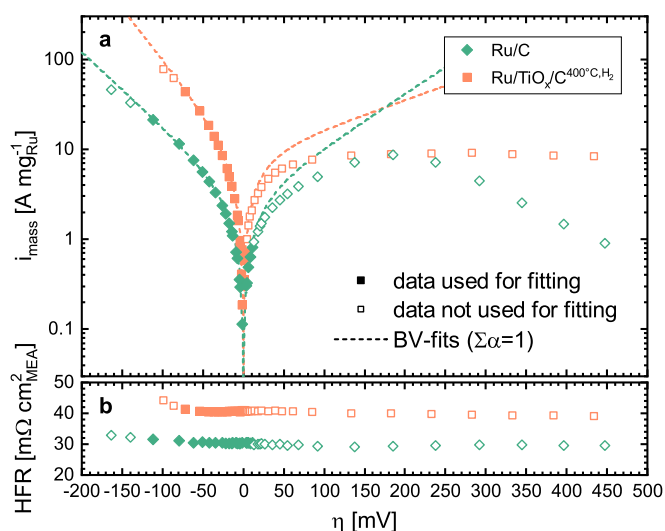


**Figure 9.** Mass normalized kinetic current densities for the HER/HOR (a) and corresponding HFRs (b) of representative MEAs of with Ru/C (green) and Ru/TiO<sub>x</sub>/C<sup>400°C,H<sub>2</sub></sup> (orange) WEs, recorded by a combination of galvanostatic/potentiostatic measurements (all data at 80 °C, 90% RH, 100 kPa<sub>H<sub>2</sub></sub>, and 2000/2000 ncm H<sub>2</sub>). The overpotential  $\eta$  was calculated from the HFRs according to Eq. 4. The data points used (filled symbols) and excluded (open symbols) for the shown Butler-Volmer fits (dashed lines) represent the average over the last 10 s of a 60 s galvanostatic/potentiostatic hold period (see Experimental section). The selection criteria for data to be included in the Butler-Volmer fits are: (i) a less than 1 m $\Omega$  cm<sub>MEA</sub><sup>-2</sup> HFR increase for the HER data; (ii) a current density of less than 10% of the maximum current density for the HOR data. Furthermore, the sum of the transfer coefficients in Eq. 6 was fixed to one (i.e.,  $\alpha_a + \alpha_c = 1$ ). Electrode loadings of the MEAs: 56  $\mu\text{g}_{\text{Ru}}$  cm<sub>MEA</sub><sup>-2</sup> for the Ru/C WE and 44  $\mu\text{g}_{\text{Ru}}$  cm<sub>MEA</sub><sup>-2</sup> for the Ru/TiO<sub>x</sub>/C<sup>400°C,H<sub>2</sub></sup> WE; the Pt loading of the Pt/C CE was 0.39 ± 0.02 mg<sub>Pt</sub> cm<sub>MEA</sub><sup>-2</sup>.

is a coincidence rather than an intrinsic property of the Ru catalysts, as the MEA roughness factors of the two Ru catalysts differ by a factor of  $\approx 2.5$  (due to the differences in Ru loading and the Ru-NP SMD), which means that the estimated specific limiting current density maximum also differs by the same factor, while hydrogen adsorption limitations would be expected to scale with the specific current density. In any case, the currents of the Ru/C reference decrease drastically with increasing potential after having reached the maximum current density at  $\approx 0.2 V_{\text{RHE}}$ , whereby the catalyst deactivates almost completely upon reaching 0.4  $V_{\text{RHE}}$ . On the contrary, the current density plateau is maintained up to 0.6  $V_{\text{RHE}}$  for the stabilized Ru/TiO<sub>x</sub>/C<sup>400°C,H<sub>2</sub></sup>.

For a more accurate determination of the HER/HOR kinetics, a steady-state approach was chosen to avoid time dependent artifacts such as HFR variations due to membrane dry-out.<sup>25</sup> HER/HOR polarization curves were recorded using a static measurement approach that allows for the system to equilibrate at each point, whereby the HFR is determined by EIS directly after every hold period (Fig. 9). The HFRs of all MEAs with Ru/TiO<sub>x</sub>/C<sup>400°C,H<sub>2</sub></sup> (orange symbols, Fig. 9b) were roughly 10 m $\Omega$  cm<sub>MEA</sub><sup>-2</sup> higher than of MEAs with Ru/C (green symbols, Fig. 9b). As differences in electrode thickness were accounted for when assembling the cells, contact resistances can most likely be ruled out as the origin of this offset. Instead, ionic contamination from TiO<sub>2</sub> dissolution might be the cause for the slightly higher HFR of the MEAs with the Ru/TiO<sub>x</sub>/C<sup>400°C,H<sub>2</sub></sup> catalyst, as according to the Pourbaix diagram (given for 25 °C), bulk TiO<sub>2</sub> has a low but finite solubility of  $\approx 10^{-8}$  mol l<sup>-1</sup> at pH 0 (the approximate pH of a PFSA membrane) at the negative iR-free potential limit of  $-0.2 V_{\text{RHE}}$  that was used in these H<sub>2</sub>-pump experiments,<sup>70</sup> considering that the solubility will likely be higher at 80 °C and for the nano-sized TiO<sub>x</sub> support, a

significant dissolution of titanium species is quite plausible. While low concentrations of cation contamination would reduce the membrane conductivity without severely affecting the performance, higher concentrations would lead to significant voltage losses in the system.<sup>71,72</sup> Furthermore, the detrimental effect of TiO<sub>2</sub> on the long term durability of PEMFC systems has recently been shown by Zhang et al.,<sup>73</sup> which limits the overall applicability of the here presented catalyst system and might require the use of a more stable oxide support that still develops an SMSI, such as tungsten oxide.<sup>74,75</sup>

With the differences in HFR accounted for according to Eq. 4, a representative dataset of the mass normalized kinetic HER/HOR currents obtained from the static measurement approach is depicted in the form of a Tafel plot in Fig. 9a for the Ru/TiO<sub>x</sub>/C<sup>400°C,H<sub>2</sub></sup> catalyst and for the Ru/C reference catalyst. Both the anodic and cathodic branches of the Tafel plots show a behavior according to the Butler-Volmer equation (Eq. 6) at low overpotentials:<sup>44,76</sup>

$$i_{\text{kin}} = i_0 \cdot \left( e^{\frac{\alpha_a F \eta}{RT}} - e^{-\frac{\alpha_c F \eta}{RT}} \right) \quad [6]$$

with  $i_{\text{kin}}$  being the kinetic current density in A mg<sub>Ru</sub><sup>-1</sup>,  $i_0$  the exchange current density in A mg<sub>Ru</sub><sup>-1</sup>,  $\alpha_a/\alpha_c$  the anodic/cathodic transfer coefficients,  $\eta$  the overpotential in V (i.e., the difference between the potential and the equilibrium potential),  $F$  the Faraday constant (96,484 A s mol<sup>-1</sup>),  $R$  the universal gas constant (8.314 kJ mol<sup>-1</sup> K<sup>-1</sup>), and  $T$  the temperature in K. While the HER part was seemingly unlimited over the complete potential interval, the HOR currents reached the same maximum value that was observed in the potentiodynamic experiments (see Fig. 8), whereby the HOR activity of the Ru/C reference catalyst (green symbols) rapidly decreased above an HOR overpotential of  $\approx 0.2$  V, while the Ru/TiO<sub>x</sub>/C<sup>400°C,H<sub>2</sub></sup> catalyst (orange symbols) maintained this maximum activity up to highest measured overpotential of 0.45 V.

The exchange current density  $i_0$  has been obtained by fitting the data to the Butler-Volmer equation with a sum of transfer coefficients of one ( $\alpha_a + \alpha_c = 1$ , dashed lines), representing a predominant Tafel-Volmer mechanism that is most often assumed for platinum group metals.<sup>57,76-79</sup> According to our established protocol,<sup>25</sup> exclusively data points with currents of less than 10% of the current maximum were fitted to minimize the effect of the HOR current limitation on the kinetic evaluation, and all data points with an HFR increase of more than 1 m $\Omega$  cm<sub>MEA</sub><sup>-2</sup> (compared to the average HFR in the overpotential range of  $\pm 20$  mV) were excluded for fitting in order to ensure that the correction of the potential for the Ohmic drop was accurate under the relevant measurement conditions. Data points considered for fitting are depicted as full symbols, whereas data points that were excluded from the fits are depicted as open symbols in Fig. 9. While the fit for the Ru/C catalyst (green line, Fig. 9a) showed a high degree of symmetry, the Ru/TiO<sub>x</sub>/C<sup>400°C,H<sub>2</sub></sup> catalyst (orange line, Fig. 9a) seems to be severely affected by the HOR limitation already at low overpotentials ( $\leq 30$  mV), resulting in highly asymmetrical fits with  $\alpha_a$ -values of  $0.26 \pm 0.03$ . An analogous behavior has previously been observed for a carbon supported Pt catalyst, where it was not possible to determine whether the observed limiting HOR current is due to an intrinsic kinetic effect or due to H<sub>2</sub> mass transport restrictions through the ionomer film.<sup>25</sup> For the  $\approx 50$ -fold lower limiting current when evaluated in terms of specific current density in the case of the Ru/TiO<sub>x</sub>/C<sup>400°C,H<sub>2</sub></sup> catalyst ( $\approx 8$  mA cm<sub>Ru</sub><sup>-2</sup> vs  $\approx 400$  mA cm<sub>Pt</sub><sup>-2</sup> in the case of Pt/C, as discussed above), a limitation by H<sub>2</sub> transport can be excluded, so that it must be due to a kinetic limitation (e.g., by hydrogen adsorption/dissociation).

The exchange current densities at 80 °C determined from the Butler-Volmer fits (dashed lines in Fig. 9), are roughly three times higher for the Ru/TiO<sub>x</sub>/C<sup>400°C,H<sub>2</sub></sup> catalyst ( $i_0 = 8.2 \pm 0.3$  A mg<sub>Ru</sub><sup>-1</sup>) compared to the Ru/C reference catalyst ( $i_0 = 2.5 \pm 0.2$  A mg<sub>Ru</sub><sup>-1</sup>).

Thus, the exchange current density of the Ru/TiO<sub>x</sub>/C<sup>400°C,H<sub>2</sub></sup> catalyst is similar to those of Rh/C and Pd/C (both  $\approx 15 \text{ A mg}_{\text{metal}}^{-1}$  for the catalysts studied by Durst et al.<sup>57</sup>), but roughly two orders of magnitude lower than for Pt/C ( $i_0 = 540 \pm 160 \text{ A mg}_{\text{Pt}}^{-1}$ )<sup>25</sup> under the same conditions. Consequently, loadings of  $\approx 1 \text{ mg}_{\text{Ru}} \text{ cm}_{\text{MEA}}^{-2}$  would be required to limit the HER/HOR overpotentials to  $< 10 \text{ mV}$  at  $2 \text{ A cm}^{-2}$  in a PEMFC or PEMWE, while this can be achieved with the currently used Pt/C catalysts for loading of  $< 0.05 \text{ mg}_{\text{Pt}} \text{ cm}_{\text{MEA}}^{-2}$ . These high loadings annihilate the cost advantage of Ru compared to conventional Pt catalysts for the hydrogen side of PEM systems.

### Conclusions

In this study, an HOR active Ru/TiO<sub>x</sub>/C catalyst was synthesized via a multi-step synthesis route and subsequent reductive heat-treatment. According to tomographic TEM imaging, the catalyst consists mostly of agglomerated Ru/TiO<sub>x</sub>-composites adsorbed on the Vulcan carbon support structure. The heat-treatment of the catalyst (Ru/TiO<sub>x</sub>/C<sup>400°C,H<sub>2</sub></sup>) leads to severe sintering of the Ru nanoparticles (Ru-NPs), increasing their Sauter mean diameter (SMD) from 2.0 to 4.4 nm, and results in an increased crystallinity of the TiO<sub>x</sub> support, accompanied by a partial encapsulation of the Ru particles due to strong metal support interaction (SMSI).

It was shown by cyclic voltammetry that Ru oxidation was suppressed for the Ru/TiO<sub>x</sub>/C<sup>400°C,H<sub>2</sub></sup> catalyst compared to a Ru/C reference catalyst. This stabilization of Ru in its metallic state at high positive potentials was confirmed by XPS, whereby the Ru 3p<sub>5/2</sub> peak remained at the binding energy of Ru(0) even after polarization at  $1.3 \text{ V}_{\text{RHE}}$  of the Ru/TiO<sub>x</sub>/C<sup>400°C,H<sub>2</sub></sup> catalyst, while the Ru/C reference catalyst was fully oxidized to Ru(IV).

In RDE experiments, the Ru/TiO<sub>x</sub>/C<sup>400°C,H<sub>2</sub></sup> catalyst showed an excellent stabilization of the HOR activity up to the onset of the OER at  $1.3 \text{ V}_{\text{RHE}}$ , whereas the HOR activity of the Ru/C reference quickly deactivated after reaching the mass-transport limited current density at  $0.11 \text{ V}_{\text{RHE}}$ . This stabilization of metallic Ru by SMSI resulted in a suppression of the OER activity above  $1.3 \text{ V}_{\text{RHE}}$ , where the Ru/C reference catalyst outperformed the heat-treated catalyst, with Ru/C exhibiting by far the highest OER activity.

The HER/HOR kinetics of the catalysts were determined by PEMFC-based hydrogen-pump measurements. These confirmed the stabilization of the HOR activity of the Ru/TiO<sub>x</sub>/C<sup>400°C,H<sub>2</sub></sup> catalyst, whereby at an overpotential of  $\approx 0.1 \text{ V}$  a maximum HOR current plateau of  $\approx 9 \text{ A mg}_{\text{Ru}}^{-1}$  was reached and maintained up to an overpotential of  $\approx 0.45 \text{ V}$ . This limiting current can clearly be ascribed to a kinetic limitation. With an exchange current density of  $8.2 \pm 0.3 \text{ A mg}_{\text{Ru}}^{-1}$ , the Ru/TiO<sub>x</sub>/C<sup>400°C,H<sub>2</sub></sup> catalyst proved to be three times more active than Ru/C ( $2.5 \pm 0.2 \text{ A mg}_{\text{Ru}}^{-1}$ ), but roughly two orders of magnitude less active than Pt/C under the same conditions. In summary, it was shown that Ru can be stabilized for the HER/HOR by an SMSI, but the low activity and limited stability of both Ru and TiO<sub>2</sub> prevent this type of catalyst from representing a feasible alternative to conventional Pt/C catalysts.

### Acknowledgments

The authors would like to thank Thomas Bein (LMU) and Markus Döblinger (LMU) for their support in the initial stages of the project and for conducting combined HAADF-STEM and EDX mappings. Financial support in the frame of the innoKA project funded by the German Federal Ministry for Economic Affairs and Energy (BMWi; funding number 03ET6096A) and by the Deutsche Forschungsgemeinschaft (DFG, German Research Foundation) under Germany's Excellence Strategy (EXC 2089/1–390776260) is acknowledged. Financial support by the BASF SE through its Research Network on Electrochemistry and Batteries is gratefully acknowledged by L. H.

### Appendix

For TEM/EDX mappings, Ru/TiO<sub>x</sub>/C<sup>400°C,H<sub>2</sub></sup> was dispersed in ethanol and drop-coated on a copper grid covered with a holey carbon film. STEM measurements were carried out on a probe corrected FEI Titan Themis operated at 300 kV in high-angle annular dark-field (HAADF) mode. Elemental maps were acquired with a Super-X energy-dispersive X-ray spectrometer and processed using the Velox V 3.0 software.

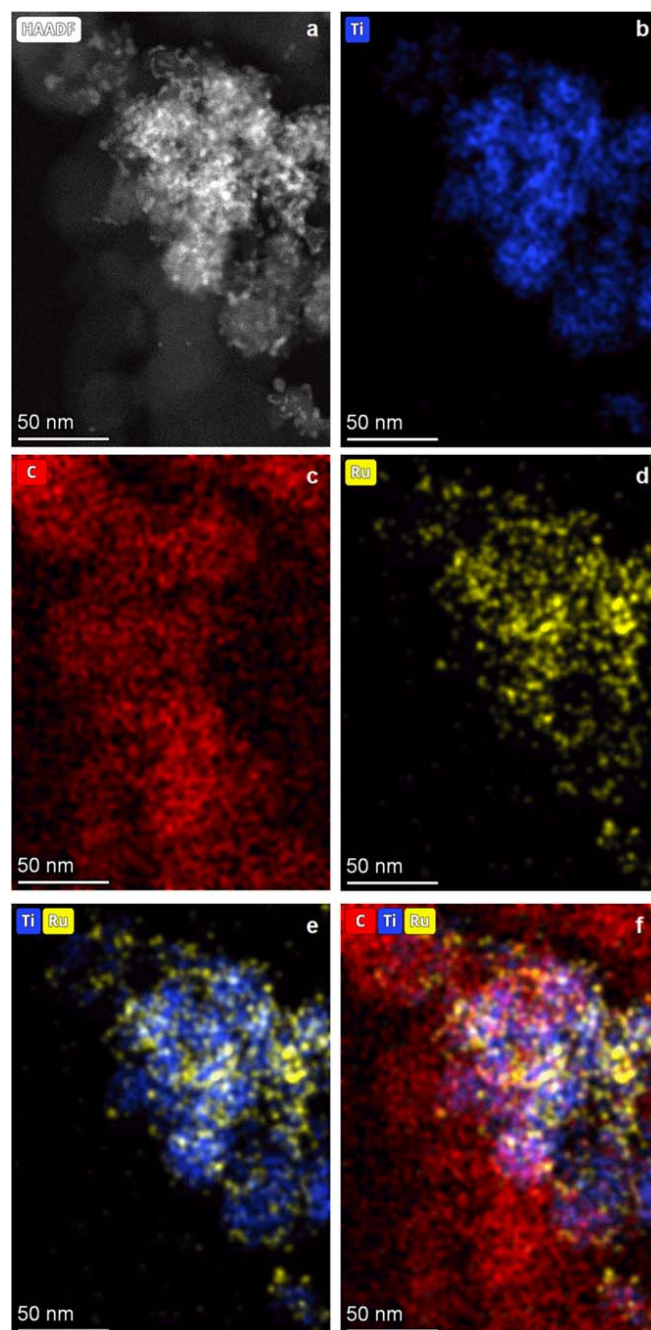


**Figure A.1.** Combined HAADF-STEM image and EDX mapping of the Ru/TiO<sub>x</sub>/C<sup>400°C,H<sub>2</sub></sup> catalyst. Elements with a higher atomic number appear brighter in the HAADF image (a). The EDX mapping illustrates the location of Ti (b), C (c), Ru (d), and the combined locations of Ti and Ru (e), and C, Ti, and Ru (f), respectively. The combined EDX mappings clearly show that most of the Ru nanoparticles are located on TiO<sub>x</sub>, whereas the carbon is mostly Ru free.

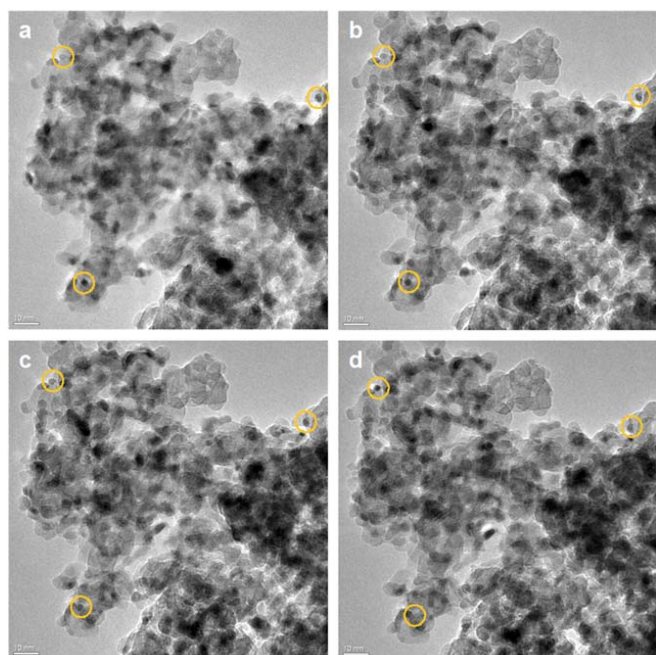


**Figure A-2.** Example of the use of individual images from the high resolution tomographic TEM series of Ru/TiO<sub>x</sub>/C<sup>400°C,H<sub>2</sub></sup> (see file HR\_RuTiOx-400\_TOMO.avi in the SI) for the determination of the Ru particle size, whereby the angle of the sample holder was varied by 2° for each frame from (a) to (d). Exemplarily, the circles indicate the position of three individual Ru particles in each frame, whereby the comparison of the images enables the identification of Ru particles and the assessment of the particle size distribution depicted in Fig. 1h.

### ORCID

Björn M. Stühmeier <https://orcid.org/0000-0001-7713-2261>

Robin J. Schuster <https://orcid.org/0000-0003-4144-8680>

Louis Hartmann <https://orcid.org/0000-0002-3964-1935>

Hubert A. Gasteiger <https://orcid.org/0000-0001-8199-8703>

### References

- S. van Renssen, *Nat. Clim. Change*, **10**, 799 (2020).
- M. Noussan, P. P. Raimondi, R. Scita, and M. Hafner, *Sustainability*, **13**, 298 (2021).
- M. M. Whiston, I. L. Azevedo, S. Litster, K. S. Whitefoot, C. Samaras, and J. F. Whitacre, *Proc. Natl. Acad. Sci. USA*, **116**, 4899 (2019).
- A. T. Mayyas, M. F. Ruth, B. S. Pivovar, G. Bender, and K. B. Wipke, *Manufacturing cost analysis for proton exchange membrane water electrolyzers NREL/TP-6A20-72740*, National Renewable Energy Lab. (NREL), Golden, CO (United States) (2019).
- L. Du, V. Prabhakaran, X. Xie, S. Park, Y. Wang, and Y. Shao, *Adv. Mater.*, **33**, 1908232 (2021).
- R. L. Borup, A. Kusoglu, K. C. Neyerlin, R. Mukundan, R. K. Ahluwalia, D. A. Cullen, K. L. More, A. Z. Weber, and D. J. Myers, *Curr. Opin. Electrochem.*, **21**, 192 (2020).
- M. Bernt, A. Hartig-Weiß, M. F. Tovini, H. A. El-Sayed, C. Schramm, J. Schröter, C. Gebauer, and H. A. Gasteiger, *Chem. Ing. Tech.*, **92**, 31 (2020).
- M. Bernt, A. Siebel, and H. A. Gasteiger, *J. Electrochem. Soc.*, **165**, F305 (2018).
- H. A. Gasteiger, J. E. Panels, and S. G. Yan, *J. Power Sources*, **127**, 162 (2004).
- K. Ayers, N. Danilovic, R. Ouimet, M. Carmo, B. Pivovar, and M. Bornstein, *Annu. Rev. Chem. Biomol. Eng.*, **10**, 219 (2019).
- 'Fuel Cell Technologies Program Multi-Year Research, Development, and Demonstration Plan', U.S. Department of Energy (2005, revision: 2012, accessed: 11/12/2021) (<https://energy.gov/eere/fuelcells/downloads/hydrogen-and-fuel-cell-technologies-office-multi-year-research-development>).
- A. Kongkanand and M. F. Mathias, *J. Phys. Chem. Lett.*, **7**, 1127 (2016).
- J. N. Schwämmlein, P. J. Rheinländer, Y. Chen, K. T. Freyer, and H. A. Gasteiger, *J. Electrochem. Soc.*, **165**, F1312 (2018).
- W. R. Baumgartner, P. Parz, S. D. Fraser, E. Wallnöfer, and V. Hacker, *J. Power Sources*, **182**, 413 (2008).
- C. A. Reiser, L. Bregoli, T. W. Patterson, J. S. Yi, J. D. Yang, M. L. Perry, and T. D. Jarvi, *Electrochem. Solid-State Lett.*, **8**, A273 (2005).
- G. S. Harzer, J. N. Schwämmlein, A. M. Damjanović, S. Ghosh, and H. A. Gasteiger, *J. Electrochem. Soc.*, **165**, F3118 (2018).
- S. Trasatti, *J. Electroanal. Chem. Interf. Electrochem.*, **111**, 125 (1980).
- Y. Lee, J. Suntivich, K. J. May, E. E. Perry, and Y. Shao-Horn, *J. Phys. Chem. Lett.*, **3**, 399 (2012).
- S. D. Knights, K. M. Colbow, J. St-Pierre, and D. P. Wilkinson, *J. Power Sources*, **127**, 127 (2004).
- N. A. Anastasijević, Z. M. Dimitrijević, and R. R. Adžić, *Electrochim. Acta*, **31**, 1125 (1986).
- J. Durst, A. Orfanidi, P. J. Rheinländer, F. Hasché, C. Eickes, P. Suchsland, M. Binder, and H. A. Gasteiger, *ECS Trans.*, **69**, 67 (2015).
- C. Bracchini, V. Indovina, S. D. Rossi, and L. Giorgi, *Catal. Today*, **55**, 45 (2000).
- H. A. Gasteiger, N. M. Markovic, and P. N. Ross, *J. Phys. Chem.*, **99**, 8290 (1995).
- M. S. Rau, M. R. Gennero de Chialvo, and A. C. Chialvo, *Electrochim. Acta*, **55**, 5014 (2010).
- B. M. Stühmeier, M. R. Pietsch, J. N. Schwämmlein, and H. A. Gasteiger, *J. Electrochem. Soc.*, **168**, 064516 (2021).
- G. L. Haller and D. E. Resasco, *Advances in Catalysis*, ed. D. D. Eley et al. (Academic, New York, NY) 36, p. 173 (1989).
- S. Tauster, *Acc. Chem. Res.*, **20**, 389 (1987).
- J. Zhang, M. Zhang, Z. Jin, J. Wang, and Z. Zhang, *Appl. Surf. Sci.*, **258**, 3991 (2012).
- A. D. Logan, E. J. Braunschweig, A. K. Datye, and D. J. Smith, *Langmuir*, **4**, 827 (1988).
- Q. Fu and T. Wagner, *Surf. Sci. Rep.*, **62**, 431 (2007).
- C.-J. Pan, M.-C. Tsai, W.-N. Su, J. Rick, N. G. Akalework, A. K. Agegnehu, S.-Y. Cheng, and B.-J. Hwang, *J. Taiwan Inst. Chem. Eng.*, **74**, 154 (2017).
- D. Banham, S. Ye, A. O'Toole, A. Lemke, and E. Eisenbraun, *Nano Energy*, **27**, 157 (2016).
- V. Viswanathan, K. L. Pickrahn, A. C. Luntz, S. F. Bent, and J. K. Nørskov, *Nano Lett.*, **14**, 5853 (2014).
- T. N. Geppert, M. Bosund, M. Putkonen, B. M. Stühmeier, A. T. Pasanen, P. Heikkilä, H. A. Gasteiger, and H. A. El-Sayed, *J. Electrochem. Soc.*, **167**, 084517 (2020).
- B. M. Stühmeier, S. Selve, M. U. M. Patel, T. N. Geppert, H. A. Gasteiger, and H. A. El-Sayed, *ACS Appl. Energy Mater.*, **2**, 5534 (2019).
- H. Shintani, Y. Kojima, K. Kakinuma, M. Watanabe, and M. Uchida, *J. Power Sources*, **294**, 292 (2015).
- E. Hornberger et al., *ACS Catal.*, **8**, 9675 (2018).
- B.-J. Hsieh, M.-C. Tsai, C.-J. Pan, W.-N. Su, J. Rick, H.-L. Chou, J.-F. Lee, and B.-J. Hwang, *Electrochim. Acta*, **224**, 452 (2017).
- Y. Zhou, Z. Xie, J. Jiang, J. Wang, X. Song, Q. He, W. Ding, and Z. Wei, *Nat. Catal.*, **3**, 454 (2020).
- T. Suoranta, M. Niemelä, and P. Perämäki, *Talanta*, **119**, 425 (2014).
- T. Mittermeier, P. Madkikar, X. Wang, H. A. Gasteiger, and M. Piana, *J. Electrochem. Soc.*, **163**, F1543 (2016).
- J. N. Schwämmlein, B. M. Stühmeier, K. Wagenbauer, H. Dietz, V. Tileli, H. A. Gasteiger, and H. A. El-Sayed, *J. Electrochem. Soc.*, **165**, H229 (2018).
- P. J. Rheinländer, J. Herranz, J. Durst, and H. A. Gasteiger, *J. Electrochem. Soc.*, **161**, F1448 (2014).
- H. A. Gasteiger, W. Gu, R. Makharia, M. F. Mathias, and B. Sompalli, "Handbook of fuel cells—fundamentals, technology and applications.", ed. W. Vielstich, H. A. Gasteiger, and A. Lamm *Fuel Cell Technology and Applications* (Wiley, Hoboken, New York) 3, p. 593 (2003).
- T. Mittermeier, A. Weiß, H. A. Gasteiger, and F. Hasché, *J. Electrochem. Soc.*, **164**, F1081 (2017).
- D. J. Morgan, *Surf. Interface Anal.*, **47**, 1072 (2015).
- A. Fujimoto, Y. Yamada, M. Koinuma, and S. Sato, *Anal. Chem.*, **88**, 6110 (2016).
- C. Simon, F. Hasché, D. Müller, and H. A. Gasteiger, *ECS Trans.*, **69**, 1293 (2015).
- C. Simon, F. Hasché, and H. A. Gasteiger, *J. Electrochem. Soc.*, **164**, F591 (2017).
- S. Bernal, J. J. Calvino, M. A. Cauqui, J. M. Gatica, C. L. Cartes, J. A. P. Omil, and J. M. Pintado, *Catal. Today*, **77**, 385 (2003).
- S. Tauster, S. Fung, and R. L. Garten, *J. Am. Chem. Soc.*, **100**, 170 (1978).
- H. A. Gasteiger, N. Markovic, P. N. Ross, and E. J. Cairns, *J. Phys. Chem.*, **97**, 12020 (1993).
- Y. Sugawara, A. P. Yadav, A. Nishikata, and T. Tsuru, *J. Electrochem. Soc.*, **155**, B897 (2008).
- R. Prins, *Chem. Rev.*, **112**, 2714 (2012).
- W. Karim, C. Spreafico, A. Kleibert, J. Gobrecht, J. VandeVondele, Y. Ekinci, and J. A. van Bokhoven, *Nature*, **541**, 68 (2017).
- M. P. Seah and W. A. Dench, *Surf. Interface Anal.*, **1**, 2 (1979).
- J. Durst, C. Simon, F. Hasché, and H. A. Gasteiger, *J. Electrochem. Soc.*, **162**, F190 (2015).
- J. Zheng, Y. Yan, and B. Xu, *J. Electrochem. Soc.*, **162**, F1470 (2015).
- L. Ganes, B. N. Hult, N. Hakim, and S. Mukerjee, *Electrochem. Solid-State Lett.*, **10**, B150 (2007).
- P. Piela, C. Eickes, E. Brosha, F. Garzon, and P. Zelenay, *J. Electrochem. Soc.*, **151**, A2053 (2004).
- S. Martens et al., *J. Power Sources*, **392**, 274 (2018).
- A. Kusoglu, D. Kushner, D. K. Paul, K. Karan, M. A. Hickner, and A. Z. Weber, *Adv. Funct. Mater.*, **24**, 4763 (2014).
- M. A. Modestino, A. Kusoglu, A. Hexemer, A. Z. Weber, and R. A. Segalman, *Macromolecules*, **45**, 4681 (2012).

64. C. Jackson, G. T. Smith, M. Markiewicz, D. W. Inwood, A. S. Leach, P. S. Whalley, A. R. Kucernak, A. E. Russell, D. Kramer, and P. B. J. Levecque, *J. Electroanal. Chem.*, **819**, 163 (2018).
65. M. Wesselmark, B. Wickman, C. Lagergren, and G. Lindbergh, *Electrochem. Commun.*, **12**, 1585 (2010).
66. C. M. Zalitis, J. Sharman, E. Wright, and A. R. Kucernak, *Electrochim. Acta*, **176**, 763 (2015).
67. H.-Y. Lin and Y.-W. Chen, *Thermochim. Acta*, **419**, 283 (2004).
68. W. Vogel, L. Lundquist, P. Ross, and P. Stonehart, *Electrochim. Acta*, **20**, 79 (1975).
69. K. Lu, Y. J. Kuo, and B. J. Tatarchuk, *J. Catal.*, **116**, 373 (1989).
70. M. J. Muñoz-Portero, J. García-Antón, J. L. Guiñón, and R. Leiva-García, *Corros. Sci.*, **53**, 1440 (2011).
71. M. Sulek, J. Adams, S. Kaberline, M. Ricketts, and J. R. Waldecker, *J. Power Sources*, **196**, 8967 (2011).
72. T. A. Greszler, T. E. Moylan, and H. A. Gasteiger, "Handbook of fuel cells—fundamentals, technology and applications." ed. W. Vielstich, H. Yokokawa, and H. A. Gasteiger *Advances in Electrocatalysis, Materials, Diagnostics and Durability* (Wiley, Hoboken) 6, p. 729 (2009).
73. J. Zhang, F. Coms, and S. Kumaraguru, *J. Electrochem. Soc.*, **168**, 024520 (2021).
74. H. Tian, X. Cui, and J. Shi, *Chem. Eng. J.*, **421**, 129430 (2021).
75. A. Lewera, L. Timperman, A. Roguska, and N. Alonso-Vante, *J. Phys. Chem. C*, **115**, 20153 (2011).
76. J. S. Newman, *Electrochemical Systems* (Prentice Hall, Englewood Cliffs) (1991).
77. J. Zheng, J. Nash, B. Xu, and Y. Yan, *J. Electrochem. Soc.*, **165**, H27 (2018).
78. J. Zheng, W. Sheng, Z. Zhuang, B. Xu, and Y. Yan, *Sci. Adv.*, **2**, e1501602 (2016).
79. J. Durst, A. Siebel, C. Simon, F. Hasche, J. Herranz, and H. A. Gasteiger, *Energy Environ. Sci.*, **7**, 2255 (2014).

### 3.3. PEMFC Cathode Durability Aspects

As discussed in Section 1.1.3, the durability of the cathode catalyst layer remains a critical challenge for the wide spread commercialization of PEMFC systems.<sup>41</sup> This section focuses on the most detrimental effects that limit the lifetime of the cathode catalyst, namely the carbon corrosion during SUSD events and the loss of *ECSA* or *r<sub>f</sub>* resulting from repeated load cycling.

#### 3.3.1. Mitigation of SUSD-Induced Cathode Degradation in PEMFCs via HOR-Selective Anodes

This section presents the manuscript "Selective Anode Catalysts for the Mitigation of Start-Up/Shut-Down Induced Cathode Degradation in Proton Exchange Membrane Fuel Cells" that will be submitted to the *Journal of The Electrochemical Society* in the near future. The manuscript was presented by Björn Stühmeier at the 240th ECS Meeting (October 10-14, 2021, Abstract number: 1185).<sup>184</sup>

The HOR-selective Pt/TiO<sub>2</sub>/C catalyst (note that the nomenclature is adapted from Pt/TiO<sub>x</sub>/C<sup>400°C,H<sub>2</sub></sup> for the sake of simplicity and because the catalyst is found to contain mostly anatase-type TiO<sub>2</sub>) that was developed in Section 3.2.2, was identified as a suitable candidate for an anode-based SUSD-mitigation strategy.<sup>118</sup> Therefore, the synthesis procedure is upscaled to obtain a sufficient catalyst quantity for implementation in MEAs. In order to validate the upscaling process, the CV, ORR activity, and HOR stability of the upscaled catalyst are investigated by RDE experiments, whereby the new batch of the Pt/TiO<sub>2</sub>/C catalyst shows a  $\approx$  30-fold lower ORR activity compared to Pt/C when using no ionomer in the ink preparation, whereas the ORR activity is only  $\approx$  14-fold reduced when the catalysts are poisoned by ionomer. This discrepancy is most likely due to the different accessibility of the Pt surface, where the encapsulation can be considered to either poison the Pt or prevent the ionomer from adsorbing on the Pt surface. In H<sub>2</sub>-pump measurements, Pt/TiO<sub>2</sub>/C exhibits a  $\approx$  2-fold lower HOR activity compared to Pt/C, which is largely the result of the difference in *ECSA*.

However, upon MEA implementation of the catalyst at a typical anode loading of  $\approx$  45  $\mu\text{g}_{\text{Pt}} \text{cm}_{\text{MEA}}^{-2}$ , the ORR activity of Pt/TiO<sub>2</sub>/C is found to be essentially identical

to a Pt/C electrode with a three times lower loading and therefore similar HOR activity ( $\approx 15 \mu\text{g}_{\text{Pt}} \text{cm}_{\text{MEA}}^{-2}$ , indicated as Pt/C<sub>LL</sub>). Therefore, the selectivity advantage of the catalyst that is expected from the RDE experiments cannot be confirmed in an MEA. Furthermore, the beginning-of-test performance of MEAs with Pt/TiO<sub>2</sub>/C anodes shows additional voltage losses of  $\approx 35 \text{ mV}$  at  $2 \text{ A cm}_{\text{MEA}}^{-2}$  in H<sub>2</sub>/O<sub>2</sub> polarization curves and when the cell was polarized in H<sub>2</sub>/H<sub>2</sub> atmosphere. Based on H<sub>2</sub>-pump measurements, these losses cannot be attributed to kinetic HOR overpotentials, but are rather the result of a TiO<sup>2+</sup> contamination due to TiO<sub>2</sub> dissolution that leads to a pH gradient in the MEA under load.<sup>74,122</sup> Accordingly, Ti is found to be distributed throughout membrane and cathode catalyst layer in EDX mappings of cross-sectioned MEAs after the initial characterization.

Finally, the degradation during SUSD events is investigated for MEAs with a regular anode loading of  $\approx 45 \mu\text{g}_{\text{Pt}} \text{cm}_{\text{MEA}}^{-2}$  for Pt/C (referred to as Pt/C<sub>HL</sub>) and for the “selective” Pt/TiO<sub>2</sub>/C catalyst, as well as the lower loaded Pt/C anode with  $\approx 15 \mu\text{g}_{\text{Pt}} \text{cm}_{\text{MEA}}^{-2}$  (referred to as Pt/C<sub>LL</sub>) that has an ORR activity comparable to the Pt/TiO<sub>2</sub>/C anodes. Surprisingly, the MEAs with Pt/TiO<sub>2</sub>/C show an 8-fold reduced SUSD degradation compared to Pt/C<sub>HL</sub>, while a lower Pt/C<sub>LL</sub> loading increases the durability only by a factor of two, in agreement with the kinetic model introduced by Mittermeier *et al.*<sup>57</sup> Interestingly, the significant advantage of a Pt/TiO<sub>2</sub>/C anode agrees well with the difference in selectivity observed from RDE measurements, but the reason for this behavior is not yet understood.

### Author contributions

B.M.S. synthesized the catalyst and performed the RDE testing. B.M.S. and A.M.D. performed MEA testing. A.M.D. and K.R. analyzed the MEA cross sections by SEM/EDX. B.M.S. and A.M.D. wrote the manuscript. All authors discussed the results and commented on the manuscript.

# Selective Anode Catalysts for the Mitigation of Start-Up/Shut-Down Induced Cathode Degradation in Proton Exchange Membrane Fuel Cells

Björn M. Stühmeier,<sup>1,=,\*</sup> Ana Marija Damjanović,<sup>1,=</sup> Katia Rodewald,<sup>2</sup> Hubert A. Gasteiger<sup>1</sup>

1) Chair of Technical Electrochemistry, Department of Chemistry and Catalysis Research Center, Technical University of Munich, D-85748 Garching, Germany

2) WACKER-Chair for Macromolecular Chemistry, Department of Chemistry and Catalysis Research Center, Technical University of Munich, D-85748 Garching, Germany

<sup>=</sup>Equal contribution.

<sup>\*</sup>Corresponding author

## Abstract

Reducing cathode degradation during start-up and shut-down (SUSD) events is one of the remaining challenges for the wide spread application of proton exchange membrane fuel cells (PEMFC). An anode catalyst that is selective for the hydrogen oxidation reaction (HOR) while its activity for the oxygen reduction reaction (ORR) is severely reduced, could substantially prolong the SUSD lifetime of the cathode. Herein, we report on single cell measurements with a Pt/TiO<sub>2</sub>/C catalyst that has been shown to be HOR selective by rotating disk electrode (RDE) measurements. The HOR activity of the catalyst is compared to conventional Pt/C by ultra-low-loaded H<sub>2</sub>-pump measurement. The ORR activity of Pt/TiO<sub>2</sub>/C was compared to Pt/C anodes with high and low Pt loadings, thereby showing a diminished selectivity in MEA vs RDE measurements. The negative impact of TiO<sub>2</sub> dissolution on the PEMFC performance was investigated by a voltage loss analysis of the oxygen polarization curves and ex-situ analysis of the MEAs. Finally, the successful mitigation of cathode carbon corrosion was shown over the course of 3200 SUSD cycles, whereby the retention of the electrochemically active surface area of the cathode catalyst when using a Pt/TiO<sub>2</sub>/C anode by far exceeded the improvements expected from the reduced ORR kinetics.

## Introduction

The durability of the cathode catalyst layer continues to be one of the main challenges for the wide spread commercialization of proton exchange membrane fuel cells (PEMFCs) for transportation applications.<sup>1-3</sup> Especially start-up and shut-down (SUSD) events, where a H<sub>2</sub>/air gas front passes through the anode, have a detrimental effect on the long term stability of the cathode carbon support. This is caused by a polarization of the anode between a hydrogen-filled segment, where hydrogen oxidation reaction (HOR) takes place, and an air-filled segment, in which the oxygen reduction reaction (ORR) occurs. Due to the poor in-plane proton conductivity of the catalyst layers and distances of several mm-cm between the respective anode segments, an oxidative current is forced on the adjacent cathode that is only separated by a 10-50 μm thick membrane, which leads to cathode-sided carbon oxidation in the air/air-filled section of the cell.<sup>4, 5</sup>

While system based approaches have been developed to minimize SUSD induced cathode degradation, catalyst based mitigation strategies are still required to reach current durability and cost targets.<sup>6-8</sup> This might be achieved either by increasing the tolerance of the cathode catalyst layer against the detrimental oxidative currents during SUSD events, or by modifying the anode in a way that reduces its ORR activity and therefore the resulting polarization of the cathode. Following the former approach, it has been shown that using graphitized carbon can increase the tolerance against the carbon oxidation reaction (COR) by orders of magnitude,<sup>5, 6, 9</sup> but the implementation of well performing graphitized supports remains challenging. Other studies have replaced carbon by metal oxide supports that cannot be further oxidized, therefore eliminating the detrimental effects of SUSD events.<sup>10-12</sup> However, these oxide based catalysts often lack the excellent conductivity and structural advantages of carbon supports thereby resulting in severe performance penalties.<sup>8, 13</sup>

For the anode, HOR-selective catalysts, i.e. catalysts that feature a reduced ORR activity while maintaining their HOR performance, have recently gained interest as a potential mitigation strategy against SUSD-induced cathode degradation.<sup>14-18</sup> Durst *et al.* compared Ir/C and Pt/C and showed that the lower ORR activity of the former lead to significantly reduced performance losses during SUSD events.<sup>19</sup> Similar results were obtained by selectively poisoning the ORR activity of conventional Pt/C with dodecanethiol.<sup>17</sup> Furthermore, it has been shown that if the ORR on the anode is hindered due to a change in the support's conductivity upon switching from H<sub>2</sub> to air, i.e. the Pt being electrically insulated at high potentials, the degradation of the cathode can be significantly reduced.<sup>14, 20</sup> Similarly, it has been shown for titanium oxide supported platinum nanoparticles that a strong metal-support interaction (SMSI) led to an encapsulation of the Pt particles with a thin layer of TiO<sub>x</sub> (x≤2), which significantly reduced the catalyst's ORR activity.<sup>21</sup><sup>22</sup> This encapsulation has been shown to occur either under reductive conditions during the synthesis procedure,<sup>21-23</sup> or in-situ as a result of oxide support dissolution and redeposition on the Pt surface during voltage cycling.<sup>24-26</sup> While the SMSI reduced the ORR activity of the catalyst by more than an order of magnitude, the HOR activity was shown to be mostly maintained making TiO<sub>2</sub> supported Pt an ideal candidate for an anode based SUSD mitigation catalyst.<sup>22-24</sup>

In this study, we upscaled a previously reported Pt/TiO<sub>2</sub>/C catalyst, that combines the HOR selectivity of the SMSI between Pt and TiO<sub>2</sub> with the conductivity and structural integrity of a carbon support,<sup>23</sup> for testing in PEMFC membrane electrode assemblies (MEAs). After confirming the successful upscaling by rotating disk electrode (RDE) measurements, the catalyst is introduced in MEAs, where the selectivity is compared to a conventional Pt/C catalyst by determining the HOR kinetics in ultra-low loaded H<sub>2</sub>-pump measurements and evaluating the anodes' ORR performance in air. The performance of MEAs with Pt/TiO<sub>2</sub>/C is then compared to MEAs with conventional Pt/C anodes of the same loading and the same ORR activity (at a lower loadings), respectively. These findings will be critically discussed with respect to the intrinsic stability of TiO<sub>2</sub>. Lastly, SUSD degradation tests will be conducted on all MEAs to investigate the effect of using a selective Pt/TiO<sub>2</sub>/C

catalyst vs simply reducing the anode loading to yield a lower ORR activity.

## Experimental

**Catalyst Synthesis.**– The Pt/TiO<sub>2</sub>/C catalyst was prepared according to a previously reported synthesis procedure:<sup>23</sup> First, 4.6 mL titanium(IV) isopropoxide (≥97%, Sigma Aldrich Corp.) in 200 mL ethanol (99.8%, absolute, Sigma Aldrich Corp.) were added dropwise to 400 mL of high purity water (15 MΩ cm, E-POD, Merck Millipore KGaA) at 80 °C. After stirring for 60 min, 400 mL ethylene glycol (EG, 99.8%, anhydrous, Sigma Aldrich Corp.) were added and subsequently, ethanol and water were evaporated using a rotary evaporator (Hei-VAP Value; Heidolph Instruments GmbH & CO. KG.). Simultaneously, two identical batches of Pt nanoparticles were each synthesized by heating 850 mg K<sub>2</sub>PtCl<sub>4</sub> (99.99% [metal basis], Sigma Aldrich Corp.), dissolved in 500 mL EG and with the pH adjusted to 10 by 1 M NaOH (99.99% [metal basis], Sigma Aldrich Corp.; dissolved in EG), at a rate of 1.5 K/min to 130 °C for 90 min using an automated temperature controlling device (Model 310, J-KEM, Inc.). When the Pt nanoparticle solutions had cooled down to 60 °C, they were added to the titania dispersion (also at 60 °C), the pH was adjusted to ≈4 using a 1 M solution of H<sub>2</sub>SO<sub>4</sub> (95%, VWR) in EG and the mixture was stirred for 16 h. Then, the Pt/TiO<sub>2</sub> mixture was added to 2.5 g Vulcan carbon (XC-72R, Tanaka Kikinokoku International K. K., Japan) that had been dispersed in 600 mL EG overnight and the mixture was stirred for 72 h before 2 L of acetone (≥98%, Sigma Aldrich Corp.) were added to reduce the solution's polarity and the catalyst was separated from the solvents using an ultra-centrifuge (5810 R, Eppendorf). The thus obtained catalyst was washed four times in 0.5 L of a 50/50-acetone/water mixture and dried in air at 70 °C. Subsequently, a heat treatment at 400 °C (10 K/min) for 1 h under reductive atmosphere (5% H<sub>2</sub>/Ar, 1 L/min) was conducted in a tube furnace (HST 12/400, Carbolite Gero GmbH & Co. KG). Finally, 4 g of the catalyst were ball milled (30 cycles, 200 rpm, 2 min on, 5 min break, 30 g of 3 mm ZrO<sub>2</sub> beads in a 20 mL ZrO<sub>2</sub> container, Pulverisette 7, Fritsch GmbH).

The elemental composition of Pt/TiO<sub>2</sub>/C was determined by inductively coupled plasma mass spectrometry (ICP-MS) after acid digestion (aqua regia for Pt and sulfuric

acid for Ti), and by carbon oxidation at elevated temperatures in air: Pt (13.0wt.%), Ti (21.6wt.%), and C (41 wt.%).

**Rotating disk electrode (RDE) measurements.**– The setup and measurement procedure for RDE measurements was already reported in previous publications by our group (for details see Mittermeier *et al.*<sup>27</sup> and Stühmeier *et al.*<sup>23</sup>). In short, electrolyte solutions were prepared from high purity HClO<sub>4</sub> (60%, Guaranteed Reagent, Kanto Chemical Co., Inc., Japan) by addition of ultrapure water (18.2 MΩ cm, Milli Q Integral 5, Merck Millipore KGaA). Argon, hydrogen and oxygen used for purging the electrolyte were of high purity (6.0 grade, Westfalen AG). A glass cell with a Pt mesh as the counter electrode, separated by a glass frit from the working electrode compartment, and a freshly prepared trapped hydrogen electrode (Pt wire of 1.0 mm diameter sealed into a glass plug with the end drawn to a capillary, >99.99% purity, Advent Research Materials, Eynsham, UK), separated with an electrolyte bridge, as the reference electrode (RE) was used.

Inks were prepared by adding high purity acetone (≥99.9%, Chromasolv Plus, for HPLC, Sigma Aldrich Corp.) and, unless specified otherwise, ionomer solution (Asahi Kasei, Japan, 700 equivalent weight) to the dry catalyst. The ionomer to support (TiO<sub>2</sub>+C) ratio (I/S) was adjusted to 0.55 g/g<sub>s</sub> for Pt/TiO<sub>2</sub>/C or 0.65 g/g<sub>s</sub> for the Vulcan carbon supported platinum reference catalyst (19.8wt.% Pt/C, TEC10V20E, Tanaka Kikinokoku International K. K., Japan), respectively. After at least 10 min of sonication, 10 μL of the ink were dropped on a Glassy Carbon (GC) electrode substrate (5 mm diameter, Pine Research Instrumentation) to achieve a loading of 20 μg<sub>Pt</sub>/cm<sub>disk</sub><sup>2</sup> and left to dry at room temperature. The uniformity of the resulting catalyst layer was controlled using an optical microscope (Stemi 2000-C, Carl Zeiss Microscopy GmbH).

All potentials are given on the reversible hydrogen electrode reference scale (V<sub>RHE</sub>), whereby the zero current intercept of the hydrogen oxidation and evolution reaction (HOR/HER) polarization curves was used to calibrate the RE during each measurement. Electrochemical measurements were performed using an Autolab potentiostat (PGSTAT302N, Metrohm AG, Switzerland) and a rotator

with a polyether ether ketone shaft (Pine Research Instrumentation, USA). Prior to any measurements, the catalysts were cleaned by cycling the potential 50 times between 0.05 and 1.0 V<sub>RHE</sub> at 100 mV/s in an Ar-saturated electrolyte, directly followed by cyclic voltammetry (CV) measurements (5 cycles) at 10 mV/s in the potential region of 0.05-1.0 V<sub>RHE</sub> and 0.2-1.05 V<sub>RHE</sub>. Then, ORR polarization curves between 0.2 and 1.05 V<sub>RHE</sub> were recorded in O<sub>2</sub>-saturated electrolyte, followed by HER/HOR measurements between -0.025 and 1.5 V<sub>RHE</sub> after H<sub>2</sub>-saturation, all at 10 mV/s and 1600 rpm. For ORR activity determinations, the positive-going scan was used and CVs recorded in the Ar-saturated electrolyte in the same potential region were used for baseline corrections. The high frequency resistance (*HFR* in Ω cm<sup>2</sup>) between WE and RE was determined by electrochemical impedance spectroscopy (EIS) from 100 kHz to 100 Hz at open circuit voltage (OCV) with an amplitude of 10 mV. Potentials corrected this way (eq. 1) are denominated *E*<sub>*iR-free*</sub>, whereby *E* is the potential and *i*<sub>*geo*</sub> the geometric current density (normalized to *A*<sub>*disk*</sub> = 0.196 cm<sup>2</sup> for RDE measurements):

$$E_{iR-free} = E - i \cdot HFR \quad [1]$$

ORR polarization curves were further corrected for the diffusion overpotential  $\eta_{diff}$  according to eq. 2, whereby *R* is the universal gas constant, *T* the temperature, *F* the Faraday constant, *i*<sub>*meas*</sub> the measured and *i*<sub>*lim*</sub> the limiting current density:<sup>28</sup>

$$E_{iR-, \eta_{diff}-free} = E_{iR-free} - \frac{R \cdot T}{4 \cdot F} \cdot \ln \left( 1 - \frac{i_{meas}}{i_{lim}} \right) \quad [2]$$

After capacitive baseline correction, the mass-specific kinetic current density *i*<sub>*mass*</sub> (eq. 3) is obtained using the mass-transport correction for RDE measurements and normalizing to the Pt loading *L*:<sup>29</sup>

$$i_{mass} = \frac{i_{lim} \cdot i_{meas}}{i_{lim} - i_{meas}} \cdot L^{-1} \quad [3]$$

However, the corrections are only reliable for measured current densities smaller than *i*<sub>*lim*</sub>/2 where the mass-transport corrections according to eq. 3 are less than a factor of 2.<sup>29</sup> Additionally, current densities smaller than 1% of the limiting current have been neglected for the ORR in order to minimize the error of the capacitive baseline corrections.

**Fuel cell hardware and experimental setup.**– All MEA

measurements were performed on a customized G60 test station (Greenlight Innovation Corp., USA). For recording  $H_2/H_2$  polarization curves during the SUSD study, the cathode gas supply was disconnected from the cell hardware and the anode gas was connected to the cathode side by a U-piece instead. For  $H_2$ -pump and anode ORR measurements, the current range of the potentiostat (Reference3000, Gamry Instruments, USA) was extended by a booster (Reference 30K Booster, Gamry Instruments, USA). All measurements were carried out with a 5 cm<sup>2</sup> active area single-cell hardware, using commercial graphite flow fields (7 parallel channels, one serpentine, 0.5 mm lands/channels; manufactured by Poco Graphite, Entegris GmbH, USA, according to our design<sup>30</sup>). Gas diffusion layers (GDLs) were the same in all experiments (H14C7, Freudenberg KG, Germany) and the GDL compression was adjusted to 18±1% by quasi-incompressible, PTFE-coated fiber-glass gaskets (Fiberflon, Fiberflon GmbH & Co. KG, Germany), assembled at a torque of 12 Nm resulting in a contact pressure of ≈1.5 MPa on the active area (for details see Simon *et al.*<sup>31</sup>).

**Membrane electrode assembly preparation.**— MEAs were prepared by the decal transfer method, using Pt/TiO<sub>2</sub>/C or a Vulcan carbon supported platinum catalyst (Pt/C, 19.8wt.% Pt/C, TEC10V20E, Tanaka Kikinzoku International K. K., Japan) for the anode electrode, and 45.6wt.% Pt/C (TEC10V50E, Tanaka Kikinzoku International K. K., Japan) was used for the cathode electrode. For the catalyst inks, a defined amount of catalyst was mixed with 1-propanol and ionomer solution (Asahi Kasei, Japan, 700 equivalent weight). The ionomer/support (I/S) ratio was fixed to 0.65 g/g<sub>s</sub> for Pt/C electrodes and 0.55 g/g<sub>s</sub> for Pt/TiO<sub>2</sub>/C electrodes. The inks were mixed by placing the bottles onto a roller mixer at 60 rpm for 18 h at room temperature. Then, the Mayer rod technique (coating machine: K Control Coater, RK PrintlCoat Instruments Ltd., England) with the appropriate bar size was used to achieve loadings of 45±5 μg<sub>Pt</sub>/cm<sub>MEA</sub><sup>2</sup> (Pt/TiO<sub>2</sub>/C and Pt/C<sub>HL</sub> anodes), 15±2 μg<sub>Pt</sub>/cm<sub>MEA</sub><sup>2</sup> (Pt/C<sub>LL</sub> anodes) and 0.4 mg<sub>Pt</sub>/cm<sub>MEA</sub><sup>2</sup> (±10%, cathodes), respectively, on virgin PTFE decals unless mentioned otherwise. The MEAs were fabricated by hotpressing the air dried decals onto a 15 μm membrane (chemically mitigated, W. L. Gore &

Associates GmbH, Germany) at 155 °C for 3 min with an applied pressure of 0.11 kN/cm<sup>2</sup>.

**Hydrogen pump measurement procedure.**— The  $H_2$ -pump measurements were performed according to a previously reported procedure.<sup>32</sup> Thus, the test station was modified to feature pure  $H_2$  instead of air/O<sub>2</sub> on the cathode side. Electrodes with very low Pt loadings of 2.2±0.4 μg<sub>Pt</sub>/cm<sub>MEA</sub><sup>2</sup> (Pt/C or Pt/TiO<sub>2</sub>/C) served as working electrodes (WE, nominally “anode”), while an electrode with high Pt loadings (≈0.4 mg<sub>Pt</sub>/cm<sub>MEA</sub><sup>2</sup>, nominally “cathode”) served both as counter electrode and as RE. Prior to any kinetic measurements, each cell was conditioned in a  $H_2/H_2$  setup (80 °C, 90% RH, flow rates of 2000/2000 nccm at 170 kPa<sub>abs</sub>) by polarizing the working electrode to the following potentials: +0.35 V<sub>RHE</sub> for 20 min, +0.75 V<sub>RHE</sub> for 5 min, 5 min at open circuit voltage (OCV), -0.2 V<sub>RHE</sub> for 10 min, and finally again 5 min at OCV. This sequence was repeated 10 times until a constant performance was reached. The HOR/HER kinetic measurements were then performed under the same conditions by a set of galvanostatic and potentiostatic measurements. For galvanostatic measurements, a DC current was drawn for 60 s and the resulting potential response was averaged over the last 10 s; this was followed by an EIS measurement at the same current, with a current amplitude of 10% of the DC current (from 500 kHz to 1 Hz, with 10 points per decade). These measurements were performed for currents between ±0.0117 A/cm<sub>MEA</sub><sup>2</sup> and ±0.074 A/cm<sub>MEA</sub><sup>2</sup> in ascending order (4 different DC current values) by alternating between anodic and the corresponding cathodic current in order to precisely determine the reversible potential at each condition. At each point, the *HFR* was used to correct the  $H_2$ -pump cell potential for the ohmic drop according to eq. 1 in order to obtain the *iR*-free cell voltage that corresponds to the HOR/HER overpotential  $\eta$  at this specific measurement point.<sup>32</sup>

Following these galvanostatic measurements, potentiostatic measurements were conducted in the analogous manner by applying a given potential for 60 s and averaging the resulting current during the last 10 s, followed by a potentiostatic EIS at the same potential using a potential amplitude of 1% of the DC potential (from 500 kHz to 1 Hz, with 10 points per decade). The potentiostatic testing was performed for potentials between

$\pm 5$  mV and  $\pm 1.1$  V (cathodic potentials only until -200 mV) in ascending order and alternating between anodic and equal cathodic potentials. After each data point (static hold plus EIS), a relaxation step of 5 or 60 s (after potentials exceeding  $\pm 0.1$  V) at OCV was implemented to ensure steady-state conditions for the next point.

**SUSD aging procedure and diagnostic measurements.**– All MEAs were conditioned prior to testing, using a voltage-controlled ramp-in procedure ( $H_2$ /air flows of 1390/3320 nccm at 80 °C, 100% RH, and 150 kPa<sub>abs</sub>): 0.6 V for 20 min and 10 min at 0.85 V. This sequence was repeated 8 times, after which a constant performance was reached. The conditioning step was followed by a  $H_2/H_2$  polarization curve similar to the previously described  $H_2$ -pump measurements. The cathode inlet and outlet tubes were connected in a way to bypass the cell and purged with  $N_2$  at 170 kPa<sub>abs</sub>. Anode outlet of the cell was connected to the cathode inlet of the cell by a metal U-piece that was thermally isolated and heated (electrical heating wire, Horst GmbH). The U-piece was heated to 100 °C to prevent the possibility of the water condensation in the cell connections. The purpose of this procedure is to evaluate the HOR overpotential on the anode over the course of aging, thus, the polarization of the anode was conducted in galvanostatic mode at the same current densities as air and  $O_2$  polarization curves recorded in the standard fuel cell mode (details in the following paragraphs). At each current density, galvanostatic electrochemical impedance spectroscopy (GEIS) was conducted for the HFR evaluation. The  $H_2/H_2$  polarization further served as a recovery step after aging that reduced the cathode electrode prior to its characterization.

CVs of the cathode electrode were recorded between 0.07 and 1.00 V<sub>RHE</sub> at a scan rate of 20, 50, 100 and 150 mV/s, at 40 °C and ambient pressure. The cathode ECSA was evaluated from CVs recorded with 20 mV/s by integrating the hydrogen under-potential deposition ( $H_{upd}$ ) region and averaging the H-desorption and H-adsorption charge (using a specific charge,  $q_{Pt}$  of 210  $\mu C/cm^2_{Pt}$ ) as follows:

$$ECSA_{ads./des.} = \frac{A_{ads./des.}}{v * q_{Pt} * L} \quad [4]$$

where  $A_{ads./des.}$  is H-adsorption/-desorption,  $v$  is a scan rate and  $L$  is Pt loading of the electrode.

The counter/reference electrode was fed with 200 nccm of fully humidified 5%  $H_2$  in  $N_2$ , and the working electrode was initially purged with dry  $N_2$  at 50 nccm, while interrupting the gas flow to record the CVs. Anode CVs were recorded in the same potential range as cathode CVs at a scan rate of 50, 100, 150 and 300 mV/s, at 40 °C and ambient pressure. The ECSA of the anode was evaluated from CVs recorded at 50 mV/s scan rate in the same way as the cathode ECSA. The counter/reference electrode (nominally cathode) was fed with 200 nccm of fully humidified 5%  $H_2$  in Ar, and the working electrode (nominally anode) was purged with fully humidified  $N_2$  at 50 nccm, while interrupting the gas flow while recording the CVs.

The proton conduction resistance of the cathode electrode,  $R_{H^+, cath}$  was determined from AC impedance spectra recorded in blocking conditions ( $H_2/N_2$  in anode and cathode respectively) at 0.2 V with a peak-to-peak perturbation of 3.5 mV between 500 kHz and 0.2 Hz (20 points per decade) based on a transmission line model.<sup>33</sup> In order to ensure reproducibility, the measurement was repeated three times. This measurement was conducted at 90% RH, with 270 kPa<sub>abs</sub> under differential flow conditions ( $H_2/N_2$  at 1000/1000 nccm) at 80 °C.

Differential flow polarization curves were recorded in galvanostatic mode at 80 °C, 170 kPa<sub>abs</sub> inlet-controlled pressure, 90% RH for both reactants, and constant flows of 2000 nccm of  $H_2$  on the anode and 5000 nccm of  $O_2$  or air on the cathode. Anode and cathode were operated in counter flow mode. Each current density point was held constant for 5 min and the resulting voltage was averaged over the final 30 s. The ORR kinetics were determined from  $H_2/O_2$  polarization curves after application of four corrections: i) the potential was corrected for the  $iR$ -drop, using the high frequency resistance (HFR) obtained from the x-axis intersect in the Nyquist plot measured by GEIS in the frequency range from 100 kHz to 10 Hz at each current density (applying a 10% AC amplitude with respect to the current); ii) HOR polarization potential determined from  $H_2/H_2$  polarization curves (polarization curve corrected only for the  $iR$ -drop:  $E_{iR-free}^{H_2/H_2} = E_{cell} - iR_{HFR}$ ) and iii) proton conduction resistance

through the cathode catalyst layer; according to the following equation:

$$E_{iR/R_{H^+, cath} - free} + E_{iR-free}^{H_2/H_2} \\ = E_{cell} + iR_{HFR} + iR_{H^+, cath}^{eff} + E_{iR-free}^{H_2/H_2} \quad [5]$$

The current was corrected for the ohmic short of the membrane, as well as for the H<sub>2</sub> crossover, both determined in H<sub>2</sub>/N<sub>2</sub> (150/600 nccm) at 170 kPa<sub>abs</sub>, 80 °C, and 90% RH by applying a constant potential of 0.2, 0.3, 0.4, 0.5, 0.6 and 0.7 V for 2 min each, and Pt loading normalized.

The SUSD protocol was adapted from the previous study in our group.<sup>5</sup> The gas flow during the measurement was 500 nccm (air on the cathode; air and H<sub>2</sub> on the anode) at 170 kPa<sub>abs</sub> gas pressure, 80 °C cell temperature and 90% RH, resulting in a short residence time of the H<sub>2</sub>/air front of only 0.02 s generated on the anode side. Fast gas exchange on the anode was ensured by operating with separate secondary anode humidifier and mass flow controller. One SUSD cycle was comprised of 60 s in standard FC mode (H<sub>2</sub>/air) at OCV, followed by a shut-down step of 60 s with air on the anode (air/air). Finally, the next cycle was started with a start-up step, where H<sub>2</sub> was purged to the cell.

**Electrode thickness and Ti distribution determination by SEM and EDX.**– The electrode cross-section samples for ex-situ thickness evaluation by scanning electron microscope (SEM) and energy dispersive X-ray analysis (EDX) were prepared in a cooled cross-section polisher (IB-19520CCP, Jeol GmbH, Germany). Fresh and aged MEAs (together with the GDLs) were cut in rectangular pieces (0.5 mm x 0.75 mm) and placed in the sample holder. The cutting protocol was conducted at 6.0 kV accelerating voltage of the ion beam and 4.0 kV Ar flow at -80 °C (to avoid thermal damage, constant cooling was ensured by liquid N<sub>2</sub>) and under vacuum (5 mPa) for 4 h (with 10 s alteration between beam on and off mode). At the end, a fine polishing protocol was conducted with 4.0 kV beam accelerating voltage and 6.0 kV Ar flow for 2 h (again 10 s alteration between beam on and off mode). The SEM images were taken under vacuum in secondary electron mode at 10 kV accelerating voltage and a magnification of 2200x at five

arbitrarily chosen locations for each MEA (given errors represent the standard deviation of all thickness measurements on one MEA).

Additional SEM/EDX measurements were conducted on an MEA containing a Pt/TiO<sub>2</sub>/C anode after the initial electrochemical characterization (the MEA was not tested for SUSD durability). A line scan across the MEA was recorded with an accelerating voltage of 15 kV, which was sufficient for the analysis of the Ti K-shell, and 2200x magnification.

## Results and Discussion

### **Catalyst characterization by rotating disk electrode measurements.**

– The Pt/TiO<sub>2</sub>/C catalyst resembled an up-scaled version of a previously reported catalyst.<sup>23</sup> To ensure that the catalyst featured the previously reported characteristics, namely suppressed Pt oxidation, stabilization of a high HOR activity up to 1.5 V<sub>RHE</sub>, and a significantly reduced ORR activity, it was investigated by rotating disk electrode (RDE) measurements (fig. 1). As can be seen by CVs recorded in Ar-saturated 0.1 M HClO<sub>4</sub>, Pt/TiO<sub>2</sub>/C featured a reduced capacity in the H<sub>upd</sub> region below 0.4 V<sub>RHE</sub> compared to the Pt/C reference (fig. 1a). A lower ECSA of 28±7 (Pt/TiO<sub>2</sub>/C) vs 81±1 m<sup>2</sup>/g<sub>Pt</sub> (Pt/C) obtained from the H<sub>upd</sub> charge according to eq. 4 has been discussed to result from particle sintering during the reductive heat treatment at 400 °C and a reduced accessibility of the particles due to SMSI.<sup>23</sup> The large uncertainty in determining the ECSA originates in parts from the imbalance of anodic and cathodic H<sub>upd</sub> charge and overall less defined H<sub>upd</sub> features that complicate the evaluation.<sup>21, 23</sup> An almost complete suppression of platinum oxidation at potentials above 0.7 V<sub>RHE</sub> on Pt/TiO<sub>2</sub>/C compared to Pt/C has likewise been explained by an encapsulation of the Pt particles by a thin titanium sub-oxide (TiO<sub>x</sub>, x≤2) layer.<sup>22, 23</sup> Such layers have been proposed to be permeable for H<sub>2</sub> and protons but not oxygenated species, thereby suppressing Pt oxidation and ORR alike, while maintaining the HER/HOR activity of the catalyst.<sup>21, 25</sup> As both Pt oxidation and ORR require a surface accessibility for oxygenated species, it has been speculated in previous works that the ORR activity of Pt catalysts effected by SMSI correlates with the suppression of Pt oxidation.<sup>21, 22, 26</sup> The mass specific oxidation charge was therefore calculated by integrating the positive going scan from 0.6 to 1.0 V<sub>RHE</sub> analogous to eq. 4.

With  $14 \pm 3$  mC/mg<sub>Pt</sub>, Pt oxidation was roughly 12-fold reduced on Pt/TiO<sub>2</sub>/C compared to Pt/C ( $168 \pm 2$  mC/mg<sub>Pt</sub>). This would indicate that the ORR is more suppressed than one would expect from the reduced ECSA.

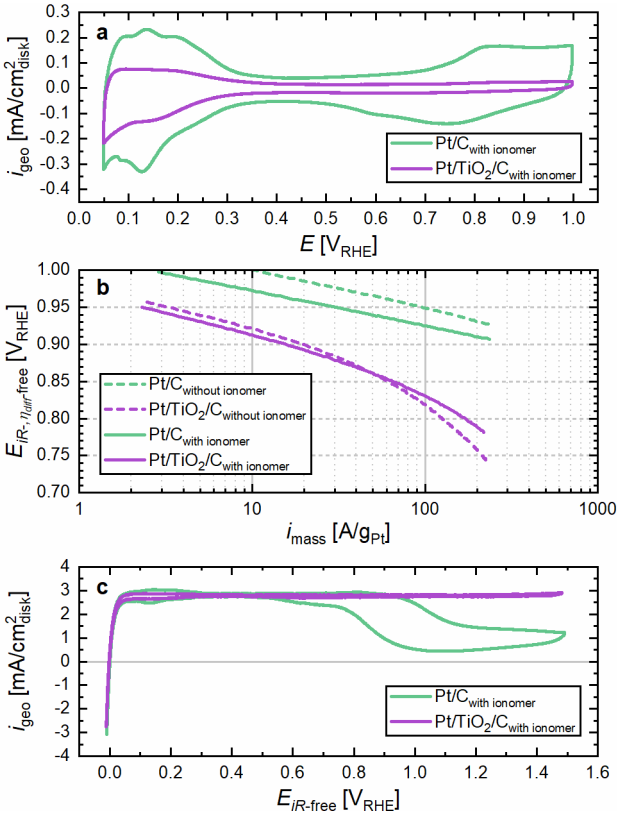


**Figure 1.** RDE measurements comparing Pt/TiO<sub>2</sub>/C (purple) and Pt/C (green) in 0.1 M HClO<sub>4</sub>. a) CVs in Ar-saturated electrolyte; b) Tafel plots of diffusion overpotential corrected,  $iR$ -free potential vs. mass-specific kinetic ORR current density with (solid lines) and without ionomer (dashed lines), recorded at 1600 rpm in O<sub>2</sub>-saturated electrolyte; c) HER/HOR polarization curves recorded in H<sub>2</sub>-saturated electrolyte at 1600 rpm. All measurements were recorded at room temperature with a scan rate of 10 mV/s, a loading of 20  $\mu\text{g}_{\text{Pt}}/\text{cm}_{\text{disk}}^2$ , and an I/S ratio (Asahi Kasei ionomer) of 0.55 (Pt/TiO<sub>2</sub>/C) or 0.65 (Pt/C), respectively.

Indeed, the ORR activity of Pt/TiO<sub>2</sub>/C is significantly reduced compared to Pt/C (fig. 1b, for applied corrections see experimental section). When no ionomer was used, Pt/C (green dashed line) featured a mass activity of  $99 \pm 2$  A/g<sub>Pt</sub> at 0.95 V<sub>RHE</sub> (note that the catalyst was too active to obtain reliable results at 0.9 V<sub>RHE</sub> with the used loadings). In contrast, Pt/TiO<sub>2</sub>/C had a  $\approx 30$ -fold lower mass activity at  $2.9 \pm 0.4$  A/g<sub>Pt</sub> under these conditions (purple dashed line). However, this gap narrowed to a  $\approx 14$ -fold reduced activity once ionomer was used,

whereby Pt lost 70% of its activity due to ionomer poisoning ( $30 \pm 1$  A/g<sub>Pt</sub>, green solid line), whereas Pt/TiO<sub>2</sub>/C maintained most of its activity at  $2.2 \pm 0.1$  A/g<sub>Pt</sub> (purple solid line). Most likely, this is a result of the TiO<sub>x</sub>-encapsulation that would prevent ionomer poisoning by separating active sites and sulfonate groups and could itself be considered as severe catalyst poisoning. The degree of activity reduction correlates well with the  $\approx 12$ -fold reduced Pt oxidation charge, which indicates that the origin of the reduction is indeed a reduced accessibility of the surface for oxygenated species.

Another result of the TiO<sub>x</sub>-encapsulation is that the HOR activity of Pt/TiO<sub>2</sub>/C (purple line) is maintained up to 1.5 V<sub>RHE</sub>, whereby the deactivation of the catalyst due to platinum oxidation at high potentials (confer Pt/C, green line) is mitigated (fig. 1c). A determination of the HOR exchange current density according to the Butler-Volmer equation is not possible by RDE measurements in acidic electrolytes due to the setup's slow mass transport in combination with the extremely fast rates of the HER/HOR.<sup>34</sup> Thus, the HER/HOR activity of Pt/TiO<sub>2</sub>/C had been estimated in a previous work in 0.1 M NaOH, where the HER/HOR kinetics on Pt-based catalysts are two orders of magnitude lower,<sup>35</sup> to be roughly three times lower than Pt/C.<sup>23</sup> In first approximation, this difference in activity can be explained by the ECSA differences between the two catalysts. To estimate the selectivity of a catalyst and therefore its usefulness as SUSD mitigation catalyst, a selectivity factor  $S$  that correlates the HER/HOR exchange current density  $i_0$  and the ORR mass activity can be defined (eq. 6):<sup>23</sup>

$$S \approx \frac{i_0 \text{ (HER/HOR)}}{i_{\text{mass}} \text{ (ORR)}} \quad [6]$$

Assuming that the HOR activity is indeed reduced by roughly a factor of three, a 14-fold lower ORR activity would result in a  $\approx 5$  times higher selectivity of Pt/TiO<sub>2</sub>/C versus Pt/C.

**HOR activity determination by hydrogen pump measurements.**– To investigate whether the selectivity observed in RDE measurements can be confirmed on the application level, HOR and ORR activities need to be obtained in an MEA setup. The overpotential for the anode reaction is typically in the order of less than 10 mV for electrodes with roughness factors ( $rfs$ ) of more than

$20 \text{ cm}_{\text{Pt}}^2/\text{cm}_{\text{MEA}}^2$  due to the fast HOR kinetics on Pt catalysts.<sup>32</sup> Thus, H<sub>2</sub>-pump measurements were performed on ultra-low-loaded electrodes ( $2.2 \pm 0.4 \mu\text{g}_{\text{Pt}}/\text{cm}_{\text{MEA}}^2$ ), whereby pure hydrogen is supplied to both sides of the MEA that is then polarized to accurately determine the HER/HOR kinetics (fig. 2).

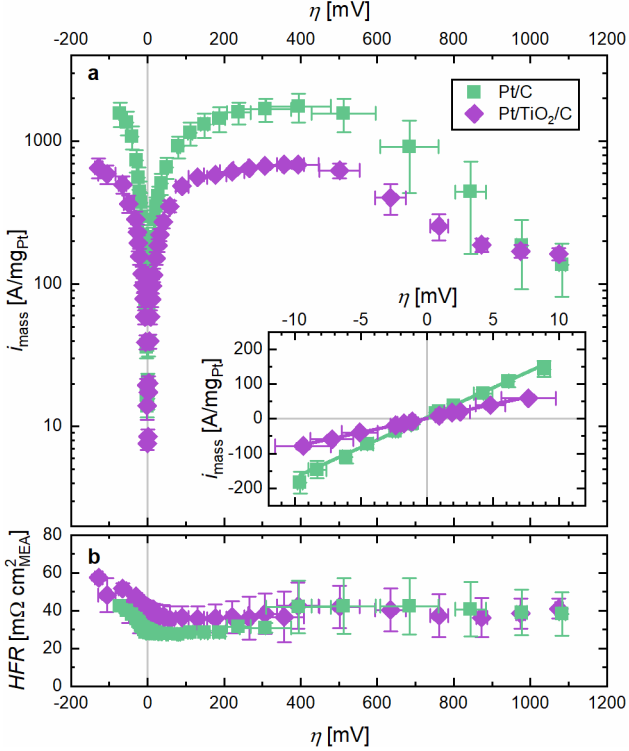


**Figure 2.** HER/HOR activity of Pt/C and Pt/TiO<sub>2</sub>/C recorded by PEMFC-based H<sub>2</sub>-pump measurements. a) Mass normalized kinetic current densities for the hydrogen oxidation and evolution reaction of Pt/C (green squares) and Pt/TiO<sub>2</sub>/C (purple diamonds); inset: micropolarization region ( $\leq 10 \text{ mV}_{\text{RHE}}$ ) with linearized Butler-Volmer fits according to eq. 7; b) corresponding HFRs used for correcting the  $iR$ -drop. Data averaged over two MEAs for each catalyst measured at 80 °C, 100 kPa<sub>H<sub>2</sub></sub>, and 90% RH with 2000/2000 nccm H<sub>2</sub> on both sides. The working and counter electrode Pt loadings are  $2.2 \pm 0.4 \mu\text{g}_{\text{Pt}}/\text{cm}_{\text{MEA}}^2$  and  $\approx 0.4 \text{ mg}_{\text{Pt}}/\text{cm}_{\text{MEA}}^2$ , respectively.

A galvano-/potentiostatic measurement approach was used that allows for a determination of the HFR (fig. 2b) and therefore for an accurate  $iR$ -correction for each data point according to eq. 1 (for details see experimental section). A much higher counter electrode loading of  $\approx 0.4 \text{ mg}_{\text{Pt}}/\text{cm}_{\text{MEA}}^2$  ensured that the measured potentials can be attributed exclusively to the WE. Since the contributions of proton conduction in the WE and mass transport to the electrode can be neglected under the chosen conditions, the overpotential  $\eta$  (in V) of the

HER/HOR is assumed to equal the  $iR$ -free voltage.<sup>32</sup> The exchange current density  $i_0$  can then be calculated from the micropolarization region ( $|\eta| \leq \pm 10 \text{ mV}$ , inset in fig. 2a) using the linearized form of the Butler-Volmer equation (eq. 7),<sup>36</sup> whereby the sum of the transfer coefficients ( $\alpha_a + \alpha_c$ ) is assumed to equal 1 for a Tafel-Volmer reaction mechanism.<sup>37, 38</sup>

$$i_0 \cdot (\alpha_a + \alpha_c) = \frac{R \cdot T}{F} \cdot \frac{i_{\text{mass}}}{\eta} \quad [7]$$

With an  $i_0$  of  $0.25 \pm 0.03 \text{ A}/\mu\text{g}_{\text{Pt}}$ , Pt/TiO<sub>2</sub>/C is indeed roughly two times less active for the HER/HOR than Pt/C ( $0.54 \pm 0.12 \text{ A}/\mu\text{g}_{\text{Pt}}$ , tab. 2), thus confirming the previously from alkaline RDE measurements estimated trend. However, the stabilization at high positive potentials could not be confirmed. After reaching a current plateau at roughly 200 mV overpotential, both catalysts started to deactivate above 400 mV. The current plateau has been discussed to result either from a change in the rate determining step to an adsorption limitation (Tafel reaction) or a mass transport limitation through the ionomer film, both of which would scale with ECSA, therefore explaining the difference in current density.<sup>32, 34, 39, 40</sup> The deactivation seems to be more pronounced for Pt/C (green squares) as it crosses Pt/TiO<sub>2</sub>/C (purple diamonds) at 1.1 V<sub>RHE</sub>. Still, the overlapping error bars from two measurements indicate that this is not a clear trend. The HOR activity on Pt/TiO<sub>2</sub>/C seemed to reach a second plateau at  $\approx 1 \text{ V}$  overpotential, which might explain the observed behavior in RDE. Considering that the currents in the H<sub>2</sub>-pump measurements were much higher than the  $\approx 140 \mu\text{A}/\mu\text{g}_{\text{Pt}}$  required to reach the limiting current density in RDE measurements (at a loading of  $20 \mu\text{g}_{\text{Pt}}/\text{cm}^2$ ), it is likely that both catalysts deactivate to some extent and that Pt/TiO<sub>2</sub>/C just maintained enough activity to reach the limiting current density even at 1.5 V<sub>RHE</sub> due to suppressed Pt oxidation.

**Anode ORR activity.**— Having confirmed the high HOR activity of Pt/TiO<sub>2</sub>/C by ultra-low loaded H<sub>2</sub>-pump measurements, regular MEAs with an anode loading of  $45 \pm 5 \mu\text{g}_{\text{Pt}}/\text{cm}_{\text{MEA}}^2$  and a cathode loading of  $0.4 \text{ mg}_{\text{Pt}}/\text{cm}_{\text{MEA}}^2$  were prepared. Fig. 3a shows CVs of the respective anodes. While the overall CV shape was maintained for both catalysts, the difference in H<sub>upd</sub> charge was smaller than observed in RDE with Pt/TiO<sub>2</sub>/C having an ECSA of  $44 \pm 2 \text{ m}^2/\text{g}_{\text{Pt}}$  compared to Pt/C with

$78 \pm 1 \text{ m}^2/\text{g}_{\text{Pt}}$ . The origin of this discrepancy between the *EC*SA determined by RDE vs. MEA for Pt/TiO<sub>2</sub>/C is not clear at this point and multiple factors might play a role: A) proton conduction through the TiO<sub>x</sub> layer could have improved due to the higher temperature making more of the Pt surface accessible; B) the conditioning under pure hydrogen might have been sufficient to partially reduce the TiO<sub>2</sub> support by hydrogen-spillover,<sup>41</sup> thereby improving its conductivity and making formerly isolated particles accessible;<sup>20</sup> C) longer times and higher temperatures under conditions, where TiO<sub>2</sub> is not fully stable (pH<6),<sup>42</sup> might have led to a partial dissolution of the TiO<sub>x</sub> layers, which exposed more of the Pt surface. The later factor does not seem to be the main reason for the increased *EC*SA as the CV shape would be expected to resemble more closely a conventional Pt CV once the TiO<sub>x</sub>-encapsulation is removed,<sup>21</sup> whereas Pt oxidation remained suppressed in this case. The larger *EC*SA of Pt/TiO<sub>2</sub>/C is most likely responsible for the only two times lower HOR/HER activity of the catalyst, which exceeded the expectations from previous RDE experiments.

In order to investigate the selectivity of the catalysts, the connections of anode and cathode were switched after conditioning of the cells, i.e., the high loaded nominal “cathode” was supplied with H<sub>2</sub> and the low loaded nominal “anode” with air. In fig. 3b, the air performance of Pt/TiO<sub>2</sub>/C ( $45 \pm 5 \text{ } \mu\text{g}_{\text{Pt}}/\text{cm}_{\text{MEA}}^2$ , purple line) is compared to Pt/C with the same loading (Pt/C<sub>HL</sub>, green line) and a lower loading of  $14 \pm 2 \text{ } \mu\text{g}_{\text{Pt}}/\text{cm}_{\text{MEA}}^2$  (Pt/C<sub>LL</sub>, orange line). Surprisingly, a significant reduction in ORR activity due to the SMSI was no longer observed when implementing the catalyst in an MEA. Instead, the catalyst showed a roughly 3-fold reduced mass activity at 0.85 V in air (tab. 2). As a result of the unexpectedly high ORR activity, Pt/TiO<sub>2</sub>/C showed only an insignificant advantage in selectivity, i.e., the ratio of HER/HOR exchange current density over ORR activity (eq. 6), compared to Pt/C but rather an overall lower activity (tab. 2). Only at current densities above  $50 \text{ mA}/\text{cm}_{\text{MEA}}^2$ , there seemed to be a difference between Pt/TiO<sub>2</sub>/C and Pt/C<sub>LL</sub> with the former being more mass transport limited. This indicates that a hindered oxidation of Pt as observed in the CVs does not necessarily result in significantly reduced ORR kinetics at low current densities but might still hinder the ORR

by additional mass transport resistances through the encapsulating layer.

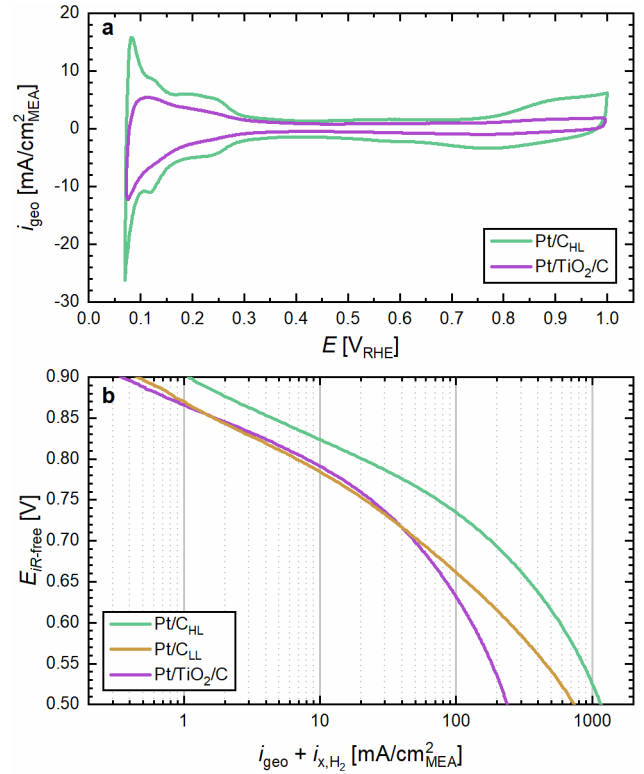


**Figure 3.** Characterization of the anodes after conditioning. a) CVs of Pt/TiO<sub>2</sub>/C (purple) and Pt/C<sub>HL</sub> (green) anode catalyst layers recorded at 40 °C between 0.07–1.00 V<sub>RHE</sub> at a scan rate of 150 mV/s, using a constant flow of 5 nccm dry N<sub>2</sub> in the anode compartment and 500 nccm fully humidified 5% H<sub>2</sub> in Ar in the cathode compartment at ambient pressure; b) differential flow H<sub>2</sub>/air (2000/5000 nccm) polarization of the respective anodes in Tafel plot representation of geometric current density, corrected by the *HFR*, the H<sub>2</sub> crossover and the capacitive currents (obtained from CVs under H<sub>2</sub>/N<sub>2</sub>), measured with a scan rate of 20 mV/s between 0.3–1.0 V, at a pressure of 170 kPa<sub>abs</sub>, a temperature of 80 °C, and an *RH* of 90%. The anode loadings were  $45 \pm 5 \text{ } \mu\text{g}_{\text{Pt}}/\text{cm}_{\text{MEA}}^2$  (Pt/C<sub>HL</sub> and Pt/TiO<sub>2</sub>/C) and  $14 \pm 2 \text{ } \mu\text{g}_{\text{Pt}}/\text{cm}_{\text{MEA}}^2$  (Pt/C<sub>LL</sub>), with a cathode loading of  $0.4 \text{ mg}_{\text{Pt}}/\text{cm}_{\text{MEA}}^2$ .

**Table 2.** Summary of the HER/HOR and ORR activities (recorded under air) of the investigated anode catalysts obtained by PEMFC-based MEA measurements and the resulting selectivity according to eq. 6.

Catalyst	$i_0$ (HER/HOR) [A/ $\mu\text{g}_{\text{Pt}}$ ]	$i_{\text{mass}}(\text{air}) @$ 0.85 V [mA/mg <sub>Pt</sub> ]	$S$ := $\frac{i_0(\text{HER/HOR})}{i_{\text{mass}}(\text{air}) \cdot 10^3}$
Pt/C	$0.54 \pm 0.12$	$102 \pm 10$	$5.3 \pm 1.7$
Pt/TiO <sub>2</sub> /C	$0.25 \pm 0.03$	$34 \pm 2$	$7.4 \pm 1.3$

To estimate whether this might still have an effect on the SUSD durability of the MEA, the expected COR current densities during SUSD events were calculated via a kinetic model (for details on the used equations and input parameters see Mittermeier *et al.*<sup>5</sup>). Hereby, the cell is formally split into a galvanic (fuel cell operation) and an electrolytic cell compartment (COR on the cathode and ORR on the anode side). Since the only difference between the investigated MEAs is the anode composition with insignificant contributions of the HOR overpotentials (see fig. 2), the polarization curve of the FC compartment (black dotted line in fig. 4) was modeled for an MEA with a cathode loading of  $0.4 \text{ mPt/cm}_{\text{MEA}^2}$  (50wt.% Pt/C), an *HFR* of  $30 \text{ m}\Omega \text{ cm}_{\text{MEA}^2}$  and a  $\text{H}_2$ -crossover of  $5 \text{ mA/cm}_{\text{MEA}^2}$ . The COR branch of the electrolytic cell compartment was modeled for the same cathode according to Mittermeier *et al.*,<sup>5</sup> while the data depicted in fig. 3b was used for the anode's ORR overpotential resulting in the electrolytic polarization curves (i.e., the potential difference between COR and anode ORR potentials, solid lines) shown in fig. 4.

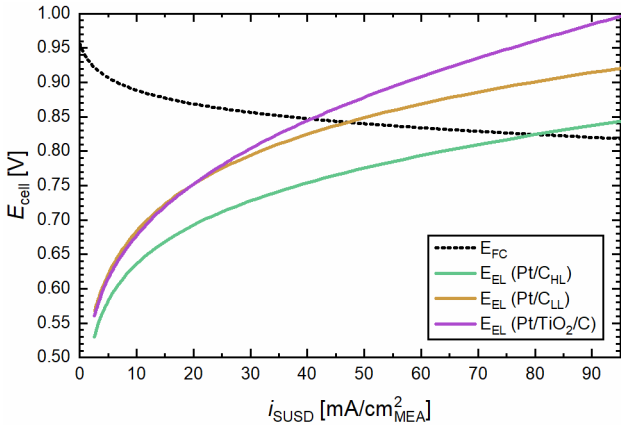


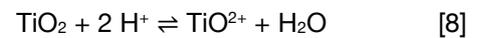
**Figure 4.** Modeled polarization curves for both the fuel cell (dotted black line) and the electrolytic part of the cell (full lines) during an SUSD event based on the anode ORR polarization curves depicted in fig. 3b. This plot is based on a  $\text{H}_2/\text{air}$  anode location  $\tau = 0.5$  (i.e., the cell is divided equally in the electrolytic and galvanic sections), plotting  $E_{\text{cell}}$  vs the SUSD current normalized by the entire cell area (i.e.,  $i_{\text{SUSD}}/A_{\text{cell}}$ ) for MEAs with a cathode loading of  $0.4 \text{ mgPt/cm}_{\text{MEA}^2}$  at  $80 \text{ }^\circ\text{C}$ ,  $70 \text{ kPa}_g$  and full humidification based on the kinetic model and input parameters reported by Mittermeier *et al.*<sup>5</sup>

The crossover point of the cell potentials is the expected SUSD current density  $i_{\text{SUSD}}$  (in  $\text{mA/cm}_{\text{MEA}^2}$ ) for an anode  $\text{H}_2/\text{air}$ -front location  $\tau$  of 0.5 (i.e., equally sized galvanic

and electrolytic cell compartments). A 3-fold lower anode loading and therefore equally reduced ORR activity for  $\text{Pt/C}_{\text{LL}}$  would result in an SUSD current of  $\approx 45 \text{ mA/cm}_{\text{MEA}^2}$  compared to  $\approx 80 \text{ mA/cm}_{\text{MEA}^2}$  for  $\text{Pt/C}_{\text{HL}}$  leading to roughly a doubling of the life time. As expected from the ORR curves, a  $\text{Pt/TiO}_2/\text{C}$  anode should yield only a slight improvement over  $\text{Pt/C}_{\text{LL}}$  with an  $i_{\text{SUSD}}$  of  $\approx 40 \text{ mA/cm}_{\text{MEA}^2}$  due to the onset of mass transport limitations. Still, the kinetic model suggests that the SUSD current densities fall into a region where other effects than pure kinetics start to impact the  $\text{Pt/TiO}_2/\text{C}$  MEAs. Thus, the cell performance and SUSD induced cathode degradation was investigated for the three MEA compositions to decouple the effect of a lower anode activity and effects due to the use of a  $\text{TiO}_2$  support.

**Beginning of test performance.**— Having characterized the anode performance, the beginning of test (BoT) cell performance was investigated before proceeding with the SUSD degradation study. Thus, polarization curves in  $\text{H}_2/\text{O}_2$  configuration were recorded for freshly ramped-in MEAs (fig. 5). The characterization was preceded by polarization curves in  $\text{H}_2/\text{H}_2$  configuration that served as a recovery step and to verify the anode performance. While slight variations in *HFR* (fig. 5b) and performance (fig. 5a) could be observed, the MEAs with Pt/C anodes showed essentially the same behavior, whereas the MEAs with a  $\text{Pt/TiO}_2/\text{C}$  anode additionally lost  $\approx 35 \text{ mV}$  at  $2 \text{ A/cm}_{\text{MEA}^2}$ . Interestingly, this loss could be observed in the *iR*-corrected  $\text{H}_2/\text{H}_2$  polarization curves as well (fig. 5c), although losses of less than  $10 \text{ mV}$  would be expected for  $50 \text{ A/mgPt}$  (corresponding to  $2 \text{ A/cm}_{\text{MEA}^2}$  at  $40 \text{ }\mu\text{gPt/cm}_{\text{MEA}^2}$ ) according to the HER/HOR kinetics determined in the  $\text{H}_2$ -pump measurements. Indeed, the  $\text{Pt/C}_{\text{LL}}$  anode that should have a similar HOR activity showed the expected *iR*-free potential of less than  $10 \text{ mV}$  (orange cycles in fig. 5c).

The additional  $\approx 35 \text{ mV}$  therefore cannot be explained by kinetic overpotentials but must have a different origin. As previously discussed,  $\text{TiO}_2$  is to some extent instable at low pH, whereby  $\text{TiO}^{2+}$  ions are formed according to eq. 8:<sup>42</sup>



These cations would lead to a contamination of the ionomer phase where protons are replaced by  $\text{TiO}^{2+}$ . Under load, ion migration to the cathode would result in the

build-up of a pH gradient across the MEA, which shifts the cathode equilibrium potential and results in an additional thermodynamic penalty.<sup>43</sup> Since the same current densities were used in the H<sub>2</sub>/H<sub>2</sub> and the H<sub>2</sub>/O<sub>2</sub> polarization curves, the reduction reaction (HER or ORR) occurred on the cathode in both cases, and the Nernst shift with pH is the same for all reactions, a cation contamination would be expected to result in the same additional overpotential in both polarization curves, as it was observed in this case. Thus, the *iR*-free potential in H<sub>2</sub>/H<sub>2</sub> polarization curves cannot be used to evaluate the kinetic HOR voltage losses of the anode when using a TiO<sub>2</sub> support.

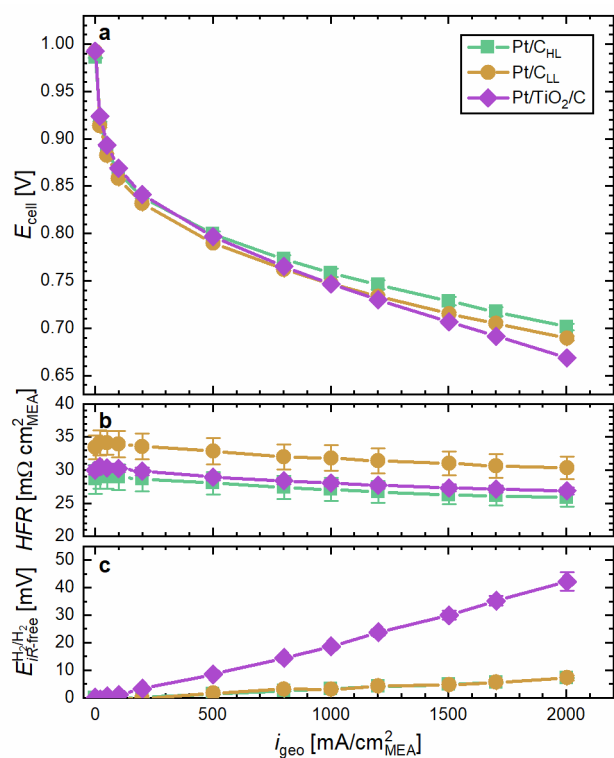


**Figure 5.** Beginning of test performance of MEAs with anode loadings of  $45 \pm 5 \mu\text{g}_{\text{Pt}}/\text{cm}_{\text{MEA}}^2$  for Pt/C<sub>HL</sub> (green squares) and Pt/TiO<sub>2</sub>/C (purple diamonds) or  $14 \pm 2 \mu\text{g}_{\text{Pt}}/\text{cm}_{\text{MEA}}^2$  (Pt/C<sub>LL</sub>, orange circles) and a cathode loading of  $0.4 \text{ mg}_{\text{Pt}}/\text{cm}_{\text{MEA}}^2$ . a) uncorrected H<sub>2</sub>/O<sub>2</sub> (2000/5000 nccm) polarization curve; b) corresponding HFR values recorded by GEIS; c) absolute, HFR-corrected cell potential in H<sub>2</sub>/H<sub>2</sub> (2000/2000 nccm) polarization curves. All measurements recorded at a pressure of 170 kPa<sub>abs</sub>, a temperature of 80 °C, and an RH of 90%.

If a TiO<sup>2+</sup> contamination would be the origin for the additional voltage losses, titanium should be detectable in the cathode catalyst layer. Thus, scanning electron microscopy (SEM) coupled with energy dispersive X-ray

spectroscopy (EDX) was used to analyze the cross-section of a Pt/TiO<sub>2</sub>/C containing MEA after initial performance characterization (fig. 6). In the SEM image (fig. 6a), the anode can be seen as a  $4.6 \pm 0.7 \mu\text{m}$  thin layer separated from the  $8.6 \pm 0.3 \mu\text{m}$  thick cathode by the reinforced membrane.

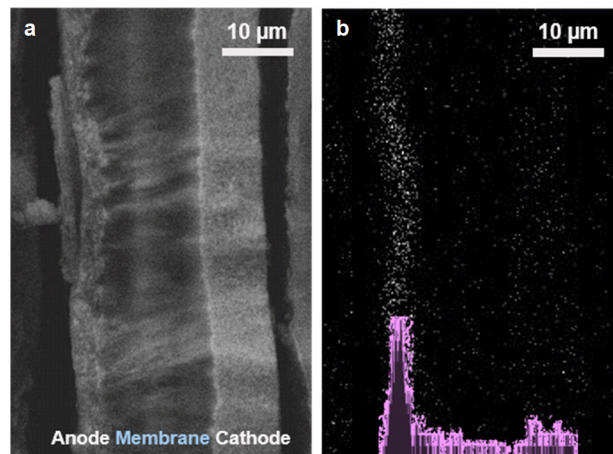


**Figure 6.** Cross section of an MEA with a Pt/TiO<sub>2</sub>/C anode after beginning of test performance characterization. a) SEM image showing anode catalyst layer, reinforced membrane and cathode catalyst layer; b) corresponding EDX spectrum showing the Ti distribution in the sample with a representative line spectrum recorded through the MEA depicted in purple.

As expected, the corresponding EDX detection in a line scan of the Ti K-shell signal (fig. 6b) showed that, while the majority of Ti remained in the anode catalyst layer, its signal was also recorded throughout the membrane and cathode catalyst layer. The line signal through the MEA (represented by the purple bar diagram in fig. 6b) showed a high concentration in the anode but also the distribution throughout membrane and cathode catalyst layer, whereby an accumulation in the cathode catalyst layer could be observed to some extent. Although it is not possible to tell which titanium species was present in the MEA, it seems likely that it would be a dissolved cationic species capable of migrating through the ionomer phase. The mobility of such Ti<sup>z+</sup> species in an MEA was recently shown by Zhang *et al.*, where the use of a TiO<sub>2</sub> supported catalyst lead to severe membrane degradation as a result of titanium ions catalyzing the Fenton reaction.<sup>44</sup>

With Ti having been demonstrated within the cathode catalyst layer, it seems likely that the origin for the sur-

prisingly high voltage losses in the  $\text{H}_2/\text{H}_2$  and  $\text{H}_2/\text{O}_2$  polarization curves was indeed a cation induced pH gradient throughout the MEA. Since this effect of the contamination is expected to affect both polarization curves the same way, i.e., the pH dependency of the HOR and the ORR is the same, the voltage difference should disappear when the  $iR$ -free potential from the  $\text{H}_2/\text{H}_2$  polarization curves ( $E_{iR\text{-free}}^{\text{H}_2/\text{H}_2}$ ) is used to correct the oxygen polcurves (see experimental section). Furthermore, the proton sheet resistance measurement for the cathode would be affected by a cationic contamination as well, as the ionic resistance in the electrode would increase at the membrane-electrode interface due to proton depletion. For such an increased proton resistance at the interface, a deviation from the  $45^\circ$  line and a shift to higher apparent proton sheet resistances would be expected from the transition line model.<sup>45</sup> Indeed, this behavior was observed for MEAs with a  $\text{Pt}/\text{TiO}_2/\text{C}$  anode (see Appendix-A), whereby the deviation from the  $45^\circ$  line expected in combination with the unknown extend of the conductivity gradient made a determination of a reliable proton sheet resistance value impossible.

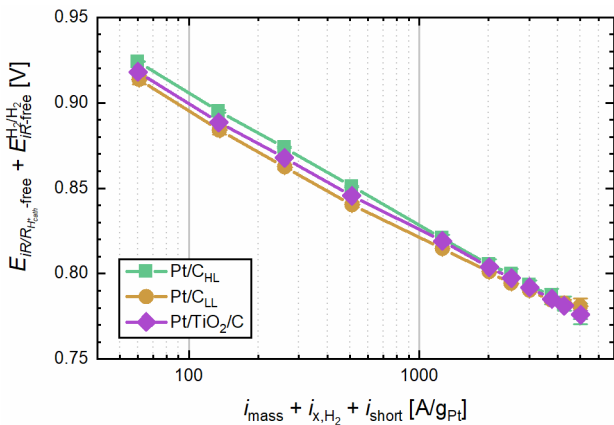


**Figure 7.** Beginning of test  $\text{H}_2/\text{O}_2$  performance of MEAs with anode loadings of  $45 \pm 5 \mu\text{g}_{\text{Pt}}/\text{cm}_{\text{MEA}}^2$  for  $\text{Pt}/\text{C}_{\text{HL}}$  (green squares) and  $\text{Pt}/\text{TiO}_2/\text{C}$  (purple diamonds) or  $14 \pm 2 \mu\text{g}_{\text{Pt}}/\text{cm}_{\text{MEA}}^2$  ( $\text{Pt}/\text{C}_{\text{LL}}$ , orange circles) and a cathode loading of  $0.4 \text{ mg}_{\text{Pt}}/\text{cm}_{\text{MEA}}^2$  in mass normalized Tafel representation. The potential was corrected for the  $HFR$ , a proton sheet resistance of  $25 \text{ m}\Omega \text{ cm}_{\text{MEA}}^2$  (obtained for  $\text{Pt}/\text{C}_{\text{HL}}$ ), and the  $HFR$ -free potential of the  $\text{H}_2/\text{H}_2$  polarization curves; the current was corrected for  $\text{H}_2$  crossover and the shorting current. All measurements recorded in differential flow configuration at a pressure of  $170 \text{ kPa}_{\text{abs}}$ , a temperature of  $80^\circ \text{C}$ , and an  $RH$  of  $90\%$ .

However, the effect of this changed proton conductivity

in the cathode should affect the  $\text{H}_2/\text{H}_2$  polarization in a similar manner and should therefore be accounted for in  $E_{iR\text{-free}}^{\text{H}_2/\text{H}_2}$ . Thus, the proton sheet resistance of  $\approx 25 \text{ m}\Omega \text{ cm}_{\text{MEA}}^2$  obtained from the  $\text{Pt}/\text{C}$  MEAs was used to correct the  $\text{H}_2/\text{O}_2$  polcurves of the  $\text{Pt}/\text{TiO}_2/\text{C}$  MEAs as well. Once all of these corrections have been applied, the curves for all MEAs fall on top of each other without additional unassigned losses (fig. 7). The cell performance is therefore a combination of the expected ohmic resistances and cathode overpotentials, cation contamination effects from dissolved  $\text{TiO}_2$  and kinetic overpotentials from the HOR in the range of  $<10 \text{ mV}$ .

**Start-up and shut-down degradation.**— Having identified the origin of the beginning of life performance losses from using a  $\text{Pt}/\text{TiO}_2/\text{C}$  anode, SUSD measurements were performed to test how the catalyst affects the degradation rate. While the degradation originates mainly from carbon corrosion, a decay in  $ECSA$  due to particle loss and dissolution has been shown to correlate well with the overall cathode degradation.<sup>5, 46</sup> As expected, when using an anode with a high ORR activity ( $\text{Pt}/\text{C}_{\text{HL}}$ , fig. 8a), the cathode quickly lost  $ECSA$  with progressing SUSD cycling. In comparison, the use of an anode with a lower ORR activity by either reducing the loading ( $\text{Pt}/\text{C}_{\text{LL}}$ , fig. 8b) or the intrinsic activity of the catalyst in the case of  $\text{Pt}/\text{TiO}_2/\text{C}$  (fig. 8c) resulted in a stabilization of the cathode as shown by the smaller changes in the CVs throughout the SUSD degradation study. For  $\text{Pt}/\text{C}$  anodes, the  $ECSA$  degradation rate seemed to correlate well with the ORR activity of the anode (fig. 9). The reduction of the ORR activity by a factor of 3 for  $\text{Pt}/\text{C}_{\text{LL}}$  nearly exactly doubled the lifetime of the MEA, as expected from fig. 4. The cathode  $ECSA$  of  $24 \pm 3 \text{ m}^2/\text{g}_{\text{Pt}}$  that remained after 3200 SUSD cycles for  $\text{Pt}/\text{C}_{\text{LL}}$  was reached by  $\text{Pt}/\text{C}_{\text{HL}}$  MEAs already after 1600 SUSD cycles ( $25 \pm 2 \text{ m}^2/\text{g}_{\text{Pt}}$ ) while the value dropped further to only  $17 \pm 1 \text{ m}^2/\text{g}_{\text{Pt}}$  at the end of aging. In contrast, MEAs with a  $\text{Pt}/\text{TiO}_2/\text{C}$  anode maintained a cathode  $ECSA$  of  $40 \pm 2 \text{ m}^2/\text{g}_{\text{Pt}}$  after 3200 SUSD cycles, with  $\text{Pt}/\text{C}_{\text{HL}}$  MEAs having fallen below this value already after 400 SUSD cycles, resulting in an 8-fold increased durability by the use of the selective  $\text{Pt}/\text{TiO}_2/\text{C}$  anodes. This unexpectedly high lifetime prolongation is most likely the result of effects that are not considered in the kinetic model but might affect the SUSD currents when using a  $\text{TiO}_2$  sup-

ported catalyst. As described in the experimental section, the use of a 5 cm<sup>2</sup> active area cell hardware meant that the SUSD front residence time was limited to only 0.02 s in order to maintain a sharp potential jump. At these extremely short intervals, additional mass transport resistances due to the TiO<sub>x</sub>-encapsulation (see fig. 3) might have significantly reduced the SUSD currents.

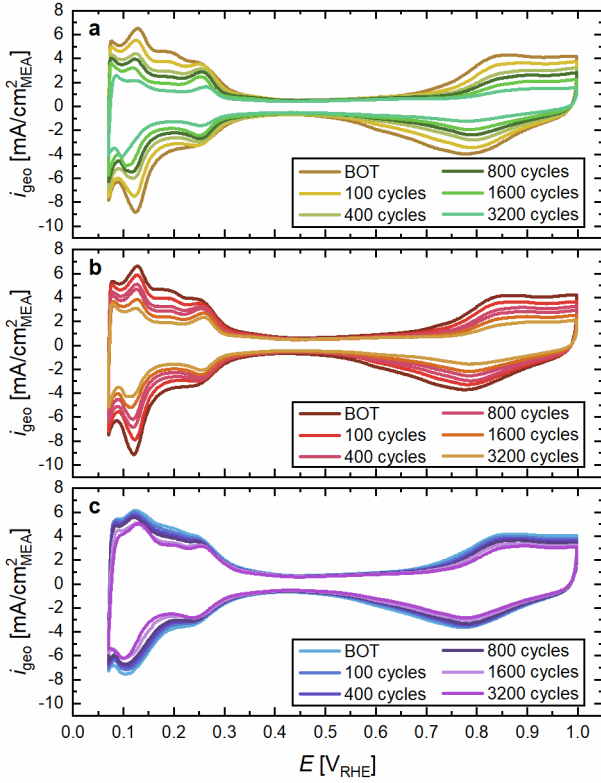


**Figure 8.** CVs of the cathode catalyst layers after different numbers of SUSD cycles with a) Pt/C<sub>HL</sub>, b) Pt/C<sub>LL</sub>, and c) Pt/TiO<sub>2</sub>/C anodes, respectively; recorded between 0.07-1.00 V<sub>RHE</sub> at a scan rate of 20 mV/s at 40 °C, using a constant flow of 5 nccm dry N<sub>2</sub> in the cathode compartment and 500 nccm fully humidified 5% H<sub>2</sub> in N<sub>2</sub> in the anode compartment.

Additionally, it has been shown that on Pt adsorbed hydrogen atoms reversibly spill over onto the TiO<sub>2</sub> support.<sup>41, 47</sup> This might lead to two pseudo-capacitive effects when the front residence times are extremely short: A) spilled over hydrogen might migrate back to the Pt particles once H<sub>2</sub> is replaced by air, whereby ORR and HOR can take place at the same time in the same section of the cell; B) when air is replaced by H<sub>2</sub>, adsorbed hydrogen might in parts spill over to the TiO<sub>2</sub> support, thereby reducing it while HOR supplies the current at the

same time. Both of these effects would prevent the reverse-current decay mechanism because oxidation and reduction take place at the same electrode section. However, since the reverse-current mechanism is a continuous process that occurs as long as the anode is partially filled with hydrogen and air,<sup>4</sup> such capacitive effects of a TiO<sub>2</sub> support will most likely not be transferrable to large active area cells where the front residence times are much larger. Because these effects would not lead to an external current and we were not able to prolong the front residence times in our setup, it was unfortunately not possible to test the hypothesis of pseudo-capacitive effects.

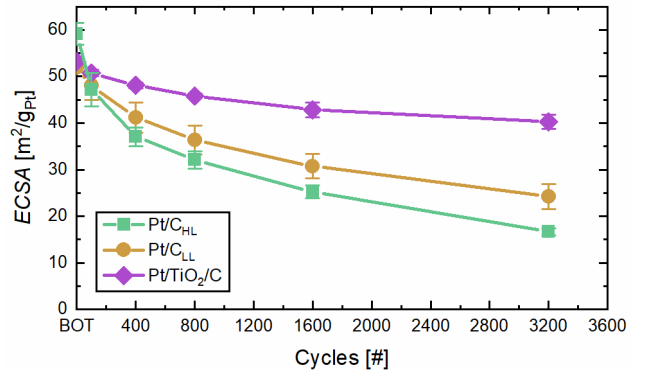


**Figure 9.** Cathode ECSA vs number of SUSD cycles dependent on the used anode electrode, evaluated from the averaged H<sub>upd</sub> charge from CVs with a limited potential window of 0.07-0.55 V<sub>RHE</sub> recorded at a scan rate of 20 mV/s at 40 °C, using a constant flow of 5 nccm dry N<sub>2</sub> in the cathode compartment and 500 nccm fully humidified 5% H<sub>2</sub> in N<sub>2</sub> in the anode compartment.

As expected from the ECSA degradation, the performance in the H<sub>2</sub>/air polarization curves decayed quickly for Pt/C<sub>HL</sub> with an additional loss of 180±35 mV at 2 A/cm<sub>MEA</sub><sup>2</sup> after 3200 SUSD cycles (fig. 10a). Carbon corrosion lead to a thinning of the cathode from initially ≈8.6±0.3 μm (see fig. 3) to 8.0±0.5 μm (inset in fig. 10a) that also lead to a gradual increase in HFR with progressing SUSD cycling (fig. 10d). MEAs with a Pt/C<sub>LL</sub> anode started with essentially the same performance as MEAs with a higher loaded anode but lost only 62±3 mV at 2 A/cm<sub>MEA</sub><sup>2</sup> in agreement with the better ECSA retention. Although a thinning of the cathode could not be observed within the measurement errors (8.6±0.6 μm after 3200 cycles), the HFR increased slightly (fig. 10e), which would indicate cathode thinning. Additionally, a Pt band had formed in the membrane (indicated by the bright line

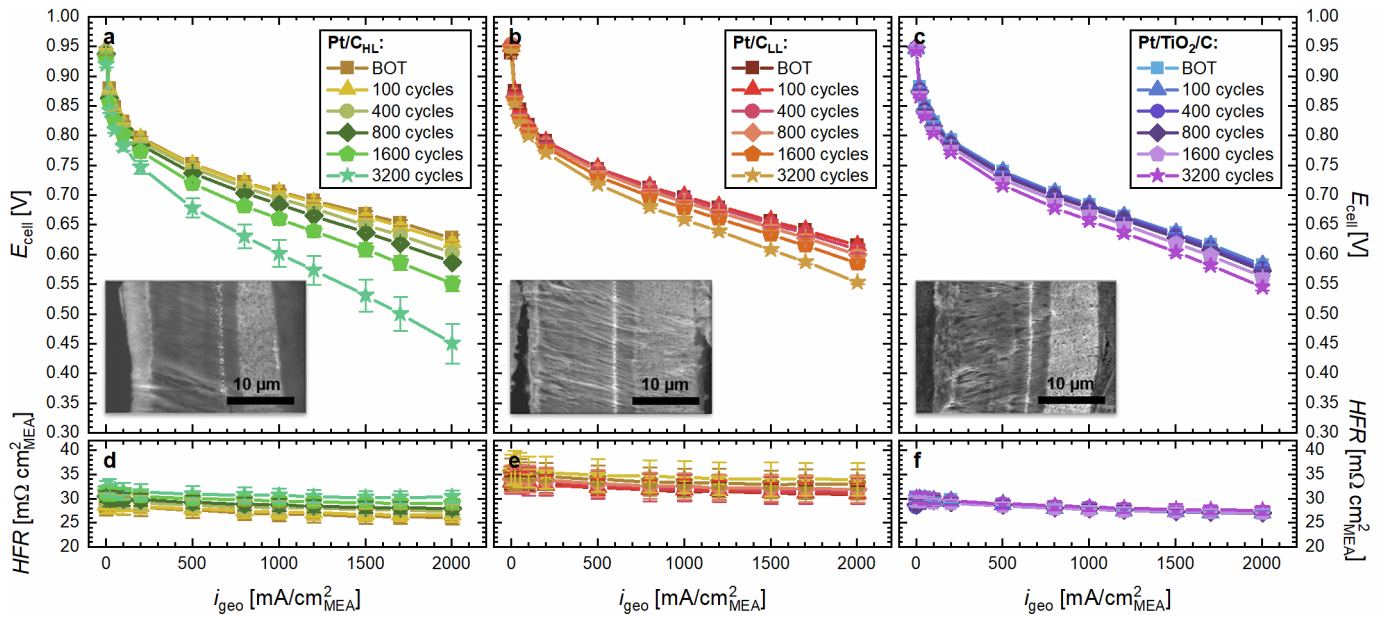


**Figure 10.** Differential flow  $\text{H}_2/\text{air}$  (2000/5000 nccm) performance and the corresponding HFR values after different SUSD degradation stages of MEAs with  $\text{Pt}/\text{C}_{\text{HL}}$  (a&d),  $\text{Pt}/\text{C}_{\text{LL}}$  (b&e), and  $\text{Pt}/\text{TiO}_2/\text{C}$  (c&f) anodes; the insets show the SEM image of a MEA cross section after 3200 SUSD cycles. All measurements were recorded at  $80^\circ\text{C}$ ,  $170\text{ kPa}_{\text{abs}}$ , and  $90\% \text{ RH}$  for MEAs with a cathode loading of  $0.4\text{ mg}_{\text{Pt}}/\text{cm}_{\text{MEA}}^2$ .

in the SEM inset in fig. 10b), where dissolved Pt from the cathode catalyst redeposited after being reduced by crossover  $\text{H}_2$  from the anode side.<sup>48</sup> This loss of Pt was most likely responsible for a significant fraction of the ECSA degradation, especially when a low activity anode ( $\text{Pt}/\text{C}_{\text{LL}}$  or  $\text{Pt}/\text{TiO}_2/\text{C}$ ) was used. The Pt band formation and a lack of electrode thinning ( $8.6 \pm 0.2\ \mu\text{m}$ , inset in fig. 10c) was also observed with a  $\text{Pt}/\text{TiO}_2/\text{C}$  anode. Here, the HFR remained constant during the SUSD study (fig. 10f), thus confirming the mitigation of carbon corrosion on the cathode. Again, the previously discussed dissolution of  $\text{TiO}_2$  affected the  $\text{H}_2/\text{air}$  polarization curves, whereby MEAs with  $\text{Pt}/\text{TiO}_2/\text{C}$  suffered the aforementioned  $\approx 35\text{ mV}$  performance penalty at beginning of test with a cell potential of  $583 \pm 1\text{ mV}$  at  $2\text{ A}/\text{cm}_{\text{MEA}}^2$  compared to  $615 \pm 1\text{ mV}$  for  $\text{Pt}/\text{C}_{\text{LL}}$ . After 3200 SUSD cycles, the MEAs lost another  $38 \pm 5\text{ mV}$  at  $2\text{ A}/\text{cm}_{\text{MEA}}^2$ . This loss can (in part) be attributed to the ECSA loss of the cathode and to a combination of anode degradation and further  $\text{TiO}_2$  dissolution that led to additional overpotentials of  $\approx 16\text{ mV}$  in the  $\text{H}_2/\text{H}_2$  polarization curves compared to an increase of only  $\approx 5\text{ mV}$  for  $\text{Pt}/\text{C}_{\text{LL}}$ . In summary, the cathode degradation seemed to be exclusively a function of the anode ORR activity when using a  $\text{Pt}/\text{C}$  anode, while the  $\text{Pt}/\text{TiO}_2/\text{C}$  catalyst seemingly lost its selectivity

for the HOR but still mitigated SUSD degradation, most likely due to pseudo-capacitive effects.

## Conclusions

In this study, we presented an HOR selective anode catalyst for mitigation of SUSD induced cathode degradation based on a SMSI between Pt and  $\text{TiO}_2$  that resulted in an encapsulation of the Pt nanoparticles by a thin titanium suboxide layer. In RDE experiments, this  $\text{Pt}/\text{TiO}_2/\text{C}$  catalyst showed a  $\approx 30$ -fold lower ORR activity compared to  $\text{Pt}/\text{C}$  when no ionomer was used, whereas the ORR activity was only  $\approx 14$ -fold reduced when the catalysts were poisoned by ionomer due to the different accessibility of the Pt surface. In ultra-low loaded  $\text{H}_2$ -pump measurements,  $\text{Pt}/\text{TiO}_2/\text{C}$  exhibited a 2-fold lower HOR activity compared to  $\text{Pt}/\text{C}$  that can be explained by the difference in ECSA. However, when the ORR activity of the anode was measured in an MEA setup,  $\text{Pt}/\text{TiO}_2/\text{C}$  showed essentially the same performance as a  $\text{Pt}/\text{C}$  electrode with a 3-times lower loading ( $\text{Pt}/\text{C}_{\text{LL}}$ ). The higher selectivity of the catalyst that was expected from RDE experiments could therefore not be confirmed in an MEA.

The BoT performance of MEAs with  $\text{Pt}/\text{TiO}_2/\text{C}$  anodes showed additional voltage losses of  $\approx 35\text{ mV}$  at

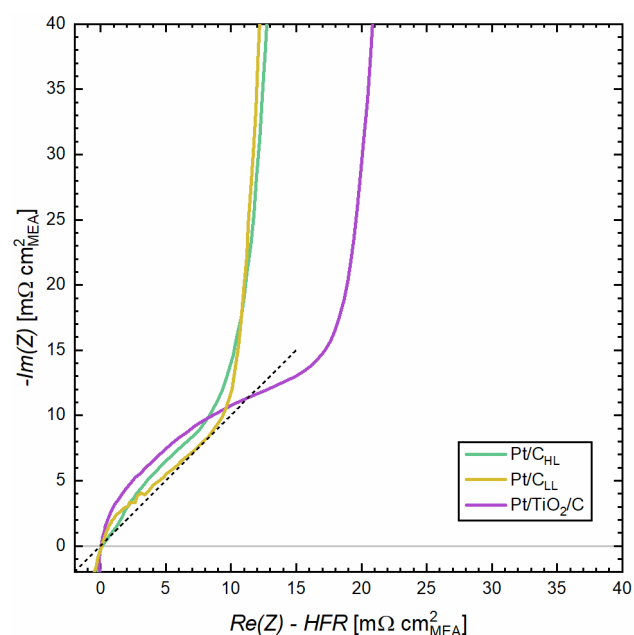
$2A/cm_{MEA}^2$  in oxygen polarization curves and when the cell was polarized in  $H_2/H_2$  atmosphere. These losses could not be attributed to kinetic HOR overpotentials according to the  $H_2$ -pump measurements, but rather a  $TiO^{2+}$  contamination due to  $TiO_2$  dissolution that led to a pH gradient in the MEA under load. Accordingly, Ti was found to be distributed throughout membrane and cathode catalyst layer by EDX mapping of cross sectioned MEAs after initial characterization.

Finally, the degradation during SUSD events was investigated for MEAs with a regular Pt/C anode loading of  $\approx 45 \mu g_{Pt}/cm_{MEA}^2$  (Pt/C<sub>HL</sub>), the “selective” Pt/TiO<sub>2</sub>/C catalyst and a lower loaded anode ( $\approx 15 \mu g_{Pt}/cm_{MEA}^2$ , Pt/C<sub>LL</sub>) that had the same ORR activity as the Pt/TiO<sub>2</sub>/C catalyst. Surprisingly, the MEAs with Pt/TiO<sub>2</sub>/C showed an 8-fold reduced SUSD degradation compared Pt/C<sub>HL</sub> while the use of Pt/C<sub>LL</sub> increased the durability only by a factor of 2 as expected for the reduced ORR activity according to the kinetic model. Interestingly, the significant advantage of a Pt/TiO<sub>2</sub>/C anode agrees well with the difference in selectivity observed from RDE measurements but the questions remain, why a reduced ORR activity could not be reproduced in an MEA and whether the proposed pseudo-capacitive effects are the true origin of the improved durability.

## Acknowledgments

We would like to thank Hany El-Sayed for the fruitful discussions on catalyst synthesis and stability. Furthermore, we would like to thank Jozsef Speder (Greenenergy) for his help with optimizing the electrode preparation procedure and supplying electrodes in the early stages of the project, and Anne Berger for the help in sample preparation for the ex-situ analysis. Financial support in the frame of the innoKA project funded by the German Federal Ministry for Economic Affairs and Energy (BMWFi; funding number 03ET6096A) is acknowledged.

## Appendix



**Appendix-A.** PEIS measurements of the cathode electrode recorded at 0.2 V showing the effect of  $TiO^{2+}$  contamination on the proton sheet resistance in MEAs with a Pt/TiO<sub>2</sub>/C anode (purple line). While Pt/C<sub>HL</sub> (green line) and Pt/C<sub>LL</sub> (orange line) show the expected 45° line, an additional semicircle appeared for the Pt/TiO<sub>2</sub>/C containing MEAs, leading to an apparently higher proton sheet resistance. Measurements recorded at 90% RH, 80 °C and 270 kPa<sub>abs</sub> gas pressure both for hydrogen and nitrogen on anode and cathode respectively.  $Re(Z)$  was shifted by the zero intercept of the x-axis to allow for an easier comparison between the measurements.

## References

1. C. S. Gittleman, A. Kongkanand, D. Masten, and W. Gu, *Curr. Opin. Electrochem.*, **18** 81-89 (2019).
2. R. L. Borup, A. Kusoglu, K. C. Neyerlin, R. Mukundan, R. K. Ahluwalia, D. A. Cullen, K. L. More, A. Z. Weber, and D. J. Myers, *Curr. Opin. Electrochem.*, **21** 192-200 (2020).
3. K. Kodama, T. Nagai, A. Kuwaki, R. Jinnouchi, and Y. Morimoto, *Nat. Nanotechnol.*, **16** (2), 140-147 (2021).
4. C. A. Reiser, L. Bregoli, T. W. Patterson, J. S. Yi, J. D. Yang, M. L. Perry, and T. D. Jarvi, *Electrochem. Solid-State Lett.*, **8** (6), A273-A276 (2005).
5. T. Mittermeier, A. Weiß, F. Hasché, G. Hübner, and H. A. Gasteiger, *J. Electrochem. Soc.*, **164** (2), F127-F137 (2017).
6. Y. Yu, H. Li, H. Wang, X.-Z. Yuan, G. Wang, and M. Pan,

- J. Power Sources*, **205** 10-23 (2012).
7. T. Zhang, P. Wang, H. Chen, and P. Pei, *Applied Energy*, **223** 249-262 (2018).
  8. J. Zhao, Z. Tu, and S. H. Chan, *J. Power Sources*, **488** 229434 (2021).
  9. P. T. Yu, W. Gu, R. Makharia, F. T. Wagner, and H. A. Gasteiger, *ECS Trans.*, **3** (1), 797-809 (2006).
  10. A. Bauer, R. Hui, A. Ignaszak, J. Zhang, and D. J. Jones, *J. Power Sources*, **210** 15-20 (2012).
  11. C. Gebauer, Z. Jusys, M. Wassner, N. Hüsing, and R. J. Behm, *ChemPhysChem*, **15** (10), 2094-2107 (2014).
  12. J. Parrondo, T. Han, E. Niangar, C. Wang, N. Dale, K. Adjemian, and V. Ramani, *Proc. Natl. Acad. Sci. U.S.A.*, **111** (1), 45-50 (2014).
  13. L. Du, Y. Shao, J. Sun, G. Yin, J. Liu, and Y. Wang, *Nano Energy*, **29** 314-322 (2016).
  14. S.-M. Jung, S.-W. Yun, J.-H. Kim, S.-H. You, J. Park, S. Lee, S. H. Chang, S. C. Chae, S. H. Joo, Y. Jung, J. Lee, J. Son, J. Snyder, V. Stamenkovic, N. M. Markovic, and Y.-T. Kim, *Nat. Catal.*, **3** (8), 639-648 (2020).
  15. R. Kamai, K. Kamiya, K. Hashimoto, and S. Nakanishi, *Angew. Chem. Int. Ed.*, **55** (42), 13184-13188 (2016).
  16. B. Genorio, D. Strmcnik, R. Subbaraman, D. Tripkovic, G. Karapetrov, V. R. Stamenkovic, S. Pejovnik, and N. M. Marković, *Nat. Mater.*, **9** 998-1003 (2010).
  17. S. W. Yun, S. A. Park, T. J. Kim, J. H. Kim, G. W. Pak, and Y. T. Kim, *ChemSusChem*, **10** (3), 489-493 (2017).
  18. J. Jang, M. Sharma, D. Choi, Y. S. Kang, Y. Kim, J. Min, H. Sung, N. Jung, and S. J. Yoo, *ACS Appl. Mater. Interfaces*, **11** (31), 27735-27742 (2019).
  19. J. Durst, A. Orfanidi, P. J. Rheinländer, F. Hasché, C. Eickes, P. Suchsland, M. Binder, and H. A. Gasteiger, *ECS Trans.*, **69** (17), 67-76 (2015).
  20. H. Shintani, Y. Kojima, K. Kakinuma, M. Watanabe, and M. Uchida, *J. Power Sources*, **294** 292-298 (2015).
  21. B.-J. Hsieh, M.-C. Tsai, C.-J. Pan, W.-N. Su, J. Rick, H.-L. Chou, J.-F. Lee, and B.-J. Hwang, *Electrochim. Acta*, **224** 452-459 (2017).
  22. T. N. Geppert, M. Bosund, M. Putkonen, B. M. Stühmeier, A. T. Pasanen, P. Heikkilä, H. A. Gasteiger, and H. A. El-Sayed, *J. Electrochem. Soc.*, **167** (8), 084517 (2020).
  23. B. M. Stühmeier, S. Selve, M. U. M. Patel, T. N. Geppert, H. A. Gasteiger, and H. A. El-Sayed, *ACS Appl. Energy Mater.*, **2** (8), 5534-5539 (2019).
  24. D. Banham, S. Ye, A. O'Toole, A. Lemke, and E. Eisenbraun, *Nano Energy*, **27** 157-166 (2016).
  25. E. Hornberger, A. Bergmann, H. Schmies, S. Kühl, G. Wang, J. Drnec, D. J. S. Sandbeck, V. Ramani, S. Cherevko, K. J. J. Mayrhofer, and P. Strasser, *ACS Catal.*, **8** (10), 9675-9683 (2018).
  26. M. Eckardt, C. Gebauer, Z. Jusys, M. Wassner, N. Hüsing, and R. J. Behm, *J. Power Sources*, **400** 580-591 (2018).
  27. T. Mittermeier, P. Madkikar, X. Wang, H. A. Gasteiger, and M. Piana, *J. Electrochem. Soc.*, **163** (14), F1543-F1552 (2016).
  28. J. Newman, *J. Electrochem. Soc.*, **113** (12), 1235-1241 (1966).
  29. H. A. Gasteiger, S. S. Kocha, B. Sompalli, and F. T. Wagner, *Appl. Catal., B*, **56** (1), 9-35 (2005).
  30. C. Simon, F. Hasché, D. Müller, and H. A. Gasteiger, *ECS Trans.*, **69** (17), 1293-1302 (2015).
  31. C. Simon, F. Hasché, and H. A. Gasteiger, *J. Electrochem. Soc.*, **164** (6), F591-F599 (2017).
  32. B. M. Stühmeier, M. R. Pietsch, J. N. Schwämmlein, and H. A. Gasteiger, *J. Electrochem. Soc.*, **168** (6), 064516 (2021).
  33. Y. Liu, M. W. Murphy, D. R. Baker, W. Gu, C. Ji, J. Jorne, and H. A. Gasteiger, *J. Electrochem. Soc.*, **156** (8), B970-B980 (2009).
  34. J. Durst, C. Simon, F. Hasché, and H. A. Gasteiger, *J. Electrochem. Soc.*, **162** (1), F190-F203 (2015).
  35. J. Durst, A. Siebel, C. Simon, F. Hasche, J. Herranz, and H. A. Gasteiger, *Energy Environ. Sci.*, **7** (7), 2255-2260 (2014).
  36. J. S. Newman, *Electrochemical systems*, Prentice Hall, Englewood Cliffs (1991).
  37. S. Fletcher, *J. Solid State Electrochem.*, **13** (4), 537-549 (2009).
  38. R. Guidelli, G. Compton Richard, M. Feliu Juan, E. Gileadi, J. Lipkowski, W. Schmickler, and S. Trasatti, *Pure Appl. Chem.*, **86** (2), 245-258 (2014).
  39. C. Jackson, G. T. Smith, M. Markiewicz, D. W. Inwood, A. S. Leach, P. S. Whalley, A. R. Kucernak, A. E. Russell, D. Kramer, and P. B. J. Levecque, *J. Electroanal. Chem.*, **819** 163-170 (2018).
  40. M. Wesselmarm, B. Wickman, C. Lagergren, and G. Lindbergh, *Electrochem. Commun.*, **12** (11), 1585-1588 (2010).
  41. R. Prins, *Chem. Rev.*, **112** (5), 2714-2738 (2012).
  42. M. J. Muñoz-Portero, J. García-Antón, J. L. Guiñón, and R. Leiva-García, *Corros. Sci.*, **53** (4), 1440-1450 (2011).

43. T. A. Greszler, T. E. Moylan, and H. A. Gasteiger, in *Handbook of Fuel Cells – Fundamentals, Technology and Applications*, W. Vielstich, H. Yokokawa and H. A. Gasteiger, Editors, Vol. 6: Advances in Electrocatalysis, Materials, Diagnostics and Durability, p. 729-748, John Wiley & Sons Ltd, Hoboken (2009).
44. J. Zhang, F. Coms, and S. Kumaraguru, *J. Electrochem. Soc.*, **168** (2), 024520 (2021).
45. R. Morasch, J. Landesfeind, B. Suthar, and H. A. Gasteiger, *J. Electrochem. Soc.*, **165** (14), A3459-A3467 (2018).
46. J. N. Schwämmlein, P. J. Rheinländer, Y. Chen, K. T. Freyer, and H. A. Gasteiger, *J. Electrochem. Soc.*, **165** (16), F1312-F1322 (2018).
47. C. Spreafico, W. Karim, Y. Ekinci, J. A. van Bokhoven, and J. VandeVondele, *J. Phys. Chem. C*, **121** (33), 17862-17872 (2017).
48. P. J. Ferreira, G. J. la O', Y. Shao-Horn, D. Morgan, R. Makharia, S. Kocha, and H. A. Gasteiger, *J. Electrochem. Soc.*, **152** (11), A2256 (2005).

### 3.3.2. Correlation Between Voltage Cycling-Induced Cathode Degradation and H<sub>2</sub>/Air Performance Losses

This section presents the manuscript "Universal Correlation between Cathode Roughness Factor and H<sub>2</sub>/Air Performance Losses in Voltage Cycling-based Accelerated Stress Tests" that was published in April 2022 in the *Journal of The Electrochemical Society*.<sup>53</sup> It is an open access article published under the terms of the Creative Commons Attribution 4.0 License (CC BY). The permanent web-link to the article is <https://doi.org/10.1149/1945-7111/ac67b8>.

The loss of cathode *ECSA* during load cycling remains a major durability issue for PEMFCs.<sup>41,123</sup> The cathode durability is therefore often studied by using voltage cycling based ASTs that simulate load cycles during PEMFC operation. Thus, the mechanisms and accelerating factors for the voltage cycling induced Pt *ECSA* losses are well understood,<sup>50,159,185–192</sup> but to date, only a small fraction of studies has additionally investigated the various voltage loss terms during aging, whereby it is mostly found that harsher aging conditions lead to lower Pt *ECSA*s and higher H<sub>2</sub>/air performance losses.<sup>51,52,193</sup>

In this study, the degradation of low-loaded cathodes ( $0.1 \text{ mg}_{\text{Pt}} \text{ cm}_{\text{MEA}}^{-2}$ , resulting in *rf* values in  $\text{cm}_{\text{Pt}}^2 \text{ cm}_{\text{MEA}}^{-2}$  that are equal to the *ECSA* of the catalyst in  $\text{m}^2 \text{ g}_{\text{Pt}}^{-1}$ ) is investigated by voltage cycling based ASTs in H<sub>2</sub>/N<sub>2</sub> (anode/cathode) configuration, whereby the upper potential limit (UPL, 0.85–1.0 V) and the hold time (1, 2, and 8 s) of the square wave voltage cycling profiles are varied. A full voltage loss analysis is performed over the course of cycling (three times per decade of cycles, over up to 500,000 cycles), determining: i) the *rf* via CO-stripping; ii) the H<sub>2</sub>-crossover; iii) the cathode electrode's proton conduction resistance; iv) the H<sub>2</sub>/O<sub>2</sub> and H<sub>2</sub>/air performance; and v) the O<sub>2</sub>-transport resistance. Similar to other studies, we find that aging protocols with higher UPL and longer hold times induce higher cathode *ECSA* or *rf* losses per cycle, resulting in faster H<sub>2</sub>/air performance degradation. Interestingly, after a mostly AST-independent *ECSA* or *rf* loss in the first 100 cycles, a linear trend of the *ECSA* or *rf* loss is observed when plotting it vs the logarithm of either the number of cycles or the time at UPL. This linearity can be used to predict the *ECSA* or *rf* loss after extended cycling by an extrapolation of the trend line.

When investigating the individual voltage loss contributions that govern the H<sub>2</sub>/air performance, it is observed that the H<sub>2</sub>-crossover, the HFR, and the proton conduction resistance remain unchanged over the course of aging, while the ORR mass and specific activity as well as the O<sub>2</sub>-transport resistances correlate exclusively with the cathode  $rf$  (independent of the investigated UPLs and hold times). As expected, the ORR mass activity decreases with decreasing cathode  $rf$ , while the specific activity increases due to the particle size effect. The pressure-independent O<sub>2</sub>-transport resistance ( $R_{O_2}^{PI}$ ) is shown to be strongly affected by the local O<sub>2</sub>-transport resistance that scales with  $rf^{-1}$  (see eq. 2.6), whereas the pressure-dependent O<sub>2</sub>-transport resistance ( $R_{O_2}^{PD}$ ) remains unchanged over the course of the ASTs. For all measurements, an  $rf$  of  $\approx 10 \text{ cm}_{Pt}^2 \text{ cm}_{MEA}^{-2}$  proves to be a critical value, below which a reliable determination of the ORR mass activity and the oxygen mass transport resistances is no longer possible. In summary, the individual voltage losses are found to be either unaffected by the aging (H<sub>2</sub>-crossover and proton conduction resistance) or to depend exclusively on the cathode  $rf$  (mass/specific activity and O<sub>2</sub> transport resistances), independent of the AST procedure. This results in a universal correlation between H<sub>2</sub>/air performance and  $rf$  over the course of voltage cycling based ASTs.

The combination of the linear cathode  $rf$  loss behavior and the AST protocol independent correlation between H<sub>2</sub>/air performance and  $rf$  implies that data acquired using a harsh cycling protocol (i.e., conducted with an UPL of 0.95 – 1.0 V) can be used to predict the H<sub>2</sub>/air performance losses over a large number of voltage cycles under application-relevant conditions (i.e., UPLs of < 0.9 V).

### Author contributions

R.K.F.D.B. performed the electrochemical testing. B.M.S. designed the study and developed the measurement procedure. R.K.F.D.B. and B.M.S. evaluated the data and wrote the manuscript. All authors discussed the results and commented on the manuscript.



# Universal Correlation between Cathode Roughness Factor and H<sub>2</sub>/Air Performance Losses in Voltage Cycling-Based Accelerated Stress Tests

Roberta K. F. Della Bella,<sup>\*,\*</sup> Björn M. Stühmeier,<sup>\*,\*z</sup> and Hubert A. Gasteiger<sup>\*\*</sup>

Chair of Technical Electrochemistry, Department of Chemistry and Catalysis Research Center, Technical University of Munich, D-85748 Garching, Germany

The loss of electrochemically active surface area (ECSA) in the cathode during load cycling remains a major durability issue for proton exchange membrane fuel cells (PEMFCs). Here, the degradation of low-loaded cathodes (0.1 mg<sub>Pt</sub> cm<sup>-2</sup><sub>MEA</sub>) was investigated by accelerated stress tests (ASTs) in H<sub>2</sub>/N<sub>2</sub> configuration, varying the upper potential limit (UPL, 0.85–1.0 V) and the hold time (1, 2, or 8 s) of the square wave voltage cycling profiles. A full voltage loss analysis was performed at beginning-of-life and after 100, 300, 1 k, 2 k, 5 k, 10 k, 20 k, 50 k, 100 k, 200 k, and 500 k cycles, determining: (i) the roughness factor (*rf*) via CO-stripping; (ii) the H<sub>2</sub>-crossover; (iii) the cathode electrode's proton conduction resistance; (iv) the H<sub>2</sub>/O<sub>2</sub> and H<sub>2</sub>/air performance; and, (v) the O<sub>2</sub> transport resistance. It was found that the ECSA/*rf* deteriorates linearly vs the logarithm of the number of cycles or time at UPL, with higher slopes for harsher ASTs. The individual voltage losses were found to be either unaffected by the aging (H<sub>2</sub>-crossover and proton conduction resistance) or depend exclusively on the cathode *rf* (mass/specific activity and O<sub>2</sub> transport resistances), independent of the AST procedure. This results in a universal correlation between H<sub>2</sub>/air performance and *rf* during voltage cycling ASTs.

© 2022 The Author(s). Published on behalf of The Electrochemical Society by IOP Publishing Limited. This is an open access article distributed under the terms of the Creative Commons Attribution 4.0 License (CC BY, <http://creativecommons.org/licenses/by/4.0/>), which permits unrestricted reuse of the work in any medium, provided the original work is properly cited. [DOI: 10.1149/1945-7111/ac67b8]



Manuscript submitted February 9, 2022; revised manuscript received April 14, 2022. Published April 27, 2022.

The durability of the cathode catalyst layer remains a major challenge for the wide spread application of proton exchange membrane fuel cells (PEMFCs). The U.S. Department of Energy (DoE) set lifetime targets of at least 5,000 h for light-duty vehicles (LDV) and 30,000 h for heavy-duty vehicles (HDV) under drive cycle operation.<sup>1</sup> Hereby, many factors affect the durability of the membrane electrode assembly (MEA), namely cell reversal events that cause anode degradation, mechanical and chemical degradation of membrane and ionomer, corrosion of the carbon support of the cathode catalyst during start-up/shut-down or local hydrogen starvation events, and finally the loss of electrochemically active surface area (ECSA) of platinum in the cathode as a result of load cycling.<sup>2–7</sup> While many of these mechanisms can be mitigated to a significant degree by PEMFC system design, which has led to substantial improvements of PEMFC durability, the lifetime prediction based on accelerated stress tests (ASTs) remains challenging, particularly for the long lifetimes required for HDVs. In this study, we will therefore focus on the analysis of ASTs that mimic the Pt ECSA loss in the cathode electrode due to load cycling.

In order to simulate load cycling between relevant operation points, current research focuses on the development of appropriate voltage cycling (VC) based ASTs.<sup>8–10</sup> In general, load variations between low and high load, corresponding to high and low cathode potentials, respectively, cause repetitive surface oxidation and reduction of the Pt nanoparticles. This results in Pt dissolution and subsequent redeposition, which leads to a loss of electrochemically accessible platinum surface area due to both Pt nanoparticle growth via Ostwald ripening and platinum loss into the membrane phase that leads to the so-called Pt-band formation.<sup>4,11,12</sup> Due to their higher surface energies, the Pt dissolution/redeposition processes are more pronounced for smaller Pt nanoparticles, which therefore are more susceptible to Pt ECSA loss during load cycling.<sup>4,12,13</sup> Beside the effect of particle size, some studies highlight the importance of the interparticle distance for the various particle growth and migration phenomena, whereby an increase in interparticle distance (via, e.g., lowering the Pt loading on a given carbon support) enhances Pt dissolution phenomena, while a decrease in interparticle distance (via, e.g., increasing the Pt loading

of the carbon support) will in contrast promote Pt nanoparticle agglomeration and coalescence.<sup>14,15</sup> It has further been shown that the overall loss of active Pt surface area is not homogenous across the thickness of the electrode: in the part of the electrode that is closest to the membrane, a depletion of Pt due to Pt loss into the membrane phase occurs, whereas in the part of the electrode that is closest to the gas diffusion layer (GDL), the platinum particle growth is the predominant cause of the Pt ECSA loss.<sup>4</sup> More recently, similar observations have also been made by Kneer et al.<sup>16</sup> The concomitant Pt ECSA loss during MEA aging by voltage cycling ASTs leads to severe H<sub>2</sub>/air performance losses. At low current densities (<500 mA cm<sup>-2</sup><sub>MEA</sub>), the induced voltage losses are mainly due to a loss in the activity of the platinum catalyst towards the oxygen reduction reaction (ORR), while in the middle and high current density region, additional O<sub>2</sub> mass transport resistances dominate the induced voltage losses. Here, the reduced roughness factor (*rf*), i.e., the reduced electrochemically active Pt surface area per geometric electrode area (in units of cm<sup>2</sup><sub>Pt</sub> cm<sup>-2</sup><sub>MEA</sub>), implies that higher local O<sub>2</sub> and proton fluxes are required to sustain the ORR at a given geometric current density. These transport resistances, also known as Pt-specific or local O<sub>2</sub> mass transport resistances ( $R_{O_2}^{local}$ ), have been reported to be especially pronounced for low-loaded cathodes, as they are predominantly inversely proportional to the *rf*.<sup>17–19</sup>

To evaluate the performance and ECSA losses during load cycle operation, the impact of different VC profiles on the degradation rate has been studied both in half-cell configuration with aqueous acidic electrolytes<sup>2,20–22</sup> and in membrane electrode assemblies (MEAs).<sup>2,8,10,16,23,24</sup> Despite the existence of standardized procedures, quantifying catalyst degradation with VC-based rotating disk electrode (RDE) experiments has proven challenging, as among 20 studies employing the same DoE protocol, the ORR mass activity retention was anywhere between 0 and 85% of the respective beginning-of-life (BoL) value.<sup>22</sup> Focusing on voltage cycling ASTs conducted in the PEM fuel cell environment, a variety of different voltage cycling profiles has been used in the literature, which complicates determining the reproducibility between different degradation studies. Still, when similar protocols are used with carbon supported Pt catalysts (Pt/C) with a comparable BoL ECSA, as it is the case in the studies of Stariha et al.<sup>25</sup> and Padgett et al.<sup>23</sup> for a ≈20 wt.% Pt catalyst supported on Vulcan carbon (Pt/V; TEC10V20E from Tanaka), or for analogous studies on Pt/C and

<sup>†</sup>Equal contribution.

<sup>\*</sup>Electrochemical Society Student Member.

<sup>\*\*</sup>Electrochemical Society Fellow.

<sup>z</sup>E-mail: [bjorn.stuehmeier@tum.de](mailto:bjorn.stuehmeier@tum.de)

Pt-alloy/C catalysts with an  $ECSA$  of  $\approx 45 \text{ m}^2 \text{ g}_{\text{Pt}}^{-1}$ ,<sup>26–28</sup> the  $ECSA$  losses are reasonably comparable. Due to extensive research in recent years, the impact of gas composition (i.e.,  $\text{H}_2/\text{N}_2$  or  $\text{H}_2/\text{air}$  on anode/cathode), scan rate, hold time, temperature, relative humidity ( $RH$ ), and the upper potential limit (UPL) on the  $ECSA$  degradation during VC-ASTs is well understood. Hereby, higher temperatures, high  $RH$ -values and high UPLs clearly accelerate  $ECSA$  loss, whereas the cathode gas composition does not affect the degradation rate.<sup>8–10,16,24,29,30</sup> Slower scan rates in case of triangular wave (TW, cyclic voltammetry based) profiles and longer hold times in case of square wave (SW, chronoamperometry based) profiles were shown to enhance the Pt  $ECSA$  loss per cycle but reduce the Pt  $ECSA$  loss per time, indicating that the number of cycles is a stronger stressor than the time at UPL.<sup>8,31</sup> Examining the impact of different voltage profiles, Harzer et al. found that mostly the UPL and the vertex hold times were responsible for the  $ECSA$  losses, whereby the degradation using a trapezoidal wave (TW-H, combination of linear scan and vertex holds) or a SW profile was essentially identical and much harsher compared to a TW profile.<sup>10</sup> In a similar study by Kneer et al., it was furthermore shown by asymmetric SW profiles that the hold time at UPL has a much more degrading effect than the hold time at the lower potential limit (LPL).<sup>24</sup> The role of the carbon support of the catalyst is an ongoing debate, whereby significant stability improvements for a porous carbon support have been shown in a study by Padgett et al.,<sup>23</sup> whereas Stariha et al.<sup>25</sup> did not find any significant differences between carbon supports. Finally, Ramaswamy et al.<sup>27</sup> showed that Pt particles originally placed within the nanopores of a porous carbon support become increasingly accessible upon voltage cycling.

While the mechanisms and accelerating factors for the Pt  $ECSA$  loss are well understood, only a small fraction of studies focusing on voltage cycling AST protocols additionally incorporate measurements for the determination of the various voltage loss terms during aging.<sup>8,10,28</sup> In fact, most of the published works concentrate on monitoring the  $ECSA$  by cyclic voltammetry (CV) or CO-stripping during the AST, while only comparing the air performance, catalyst activity and/or mass transport resistances at the end-of-life (EoL).<sup>9,23,27–29,31</sup> It is generally found that higher  $ECSA$  losses, i.e. harsher aging conditions, correlate with increased voltage losses from a reduced mass activity and increased oxygen mass transport resistances, while the specific activity increases due to particle growth.<sup>8–10,23,27–29,31</sup> However, in order to use voltage cycling ASTs for reliable lifetime predictions, a direct correlation of the Pt  $ECSA$  and the  $\text{H}_2/\text{air}$  performance losses for a given catalyst/MEA type, independent of the specific voltage cycling conditions, would be desired.

In this study, the development of the Pt  $ECSA$  and the individual voltage loss contributions was studied for  $5 \text{ cm}^2$  MEAs with a commercial Pt/Vulcan catalyst using SW-based ASTs with different hold times and UPLs in order to find a suitable degradation model. For this, the  $ECSA$  was determined by CO-stripping, the ORR mass and specific activity were extracted from  $\text{H}_2/\text{O}_2$  polarization curves, the  $\text{O}_2$  mass transport resistances were calculated from limiting current measurements, and the proton conduction resistance in the cathode catalyst layer (CCL) was determined by electrochemical impedance spectroscopy (EIS). The development of these voltage losses is compared for all aging procedures at similar degrees of  $rf$ -losses. Based on the findings for the individual voltage loss contributions, a universal correlation between  $rf$  and the  $\text{H}_2/\text{air}$  performance of the cell will be shown. Finally, we will propose a new combined AST protocol for efficient lifetime prediction of VC-induced degradation based on the  $\text{H}_2/\text{air}$  performance targets.

## Experimental

Experimental details about the setup and measurement procedures can be found in previous publications,<sup>10,32–35</sup> but for reader's convenience, the most relevant information is summarized here.

**Fuel cell hardware and MEA preparation.**—All measurements were performed on a customized G60 test station (Greenlight Innovation Corp., USA) equipped with a potentiostat (Reference3000, Gamry, UK), using a  $5 \text{ cm}^2$  active area single-cell hardware with graphite flow fields (7 parallel channels, one serpentine, 0.5 mm lands/channels; manufactured by Poco Graphite, Entegris GmbH, USA, according to our design<sup>33</sup>). Gas diffusion layers (GDLs, H14C10, Freudenberg KG, Germany) with a thickness of  $170 \pm 5 \mu\text{m}$  were compressed by  $14 \pm 1\%$  by means of quasi-incompressible, PTFE-coated fiberglass gaskets (Fiberflon, Fiberflon GmbH & Co. KG, Germany). The cells were assembled at a torque of 12 Nm resulting in a GDL compression of  $\approx 1.5 \text{ MPa}$  on the active area (for details see Simon et al.<sup>34</sup>).

MEAs were prepared by the decal transfer method: The catalyst inks were prepared by mixing a commercial 19.8 wt.% Pt/V (TEC10V20E, Tanaka, Japan) catalyst, 1-propanol, and a water-based ionomer dispersion (700 EW, Asahi Kasei, Japan) in a 15 ml HDPE bottle containing 25.5 g of 5 mm  $\text{ZrO}_2$  grinding balls. The carbon content of the dispersion was adjusted to  $30 \text{ mg}_c \text{ mL}_{\text{ink}}^{-1}$  and the ionomer to carbon mass ratio ( $I/C$ ) was set to  $0.65 \text{ g}_I \text{ g}_C^{-1}$ . The inks were mixed on a roller mill at 60 rpm for 18 h at  $25 \text{ }^\circ\text{C}$  before being coated onto virgin PTFE foils with a  $130 \mu\text{m}$  Mayer rod using an automated coater (K Control Coater, RK PrintCoat Instruments Ltd., England). Symmetrical MEAs were prepared by hot-pressing two  $5 \text{ cm}^2$  decals at  $155 \text{ }^\circ\text{C}$  for 3 min onto a  $15 \mu\text{m}$  thick reinforced membrane (low EW, mitigated GORE-SELECT<sup>®</sup>, W. L. Gore & Associates GmbH, Germany). To minimize the deviation in the cathode loading between measurements, the electrodes were assigned to the cathode ( $0.103 \pm 0.005 \text{ mg}_{\text{Pt}} \text{ cm}_{\text{MEA}}^{-2}$ ) and the anode electrode ( $0.10 \pm 0.01 \text{ mg}_{\text{Pt}} \text{ cm}_{\text{MEA}}^{-2}$ ) after the respective loadings were determined. The thickness of the cathodes was  $\approx 7.5 \mu\text{m}$  according to scanning electron microscopy (SEM) images of MEA cross-sections (see Fig. A-1).

**Voltage cycling procedure and MEA characterization measurements.**—The experimental testing procedure is summarized in the scheme shown in Fig. 1. The measurement procedure was optimized to minimize the amount of gas composition changes, unintended voltage cycles, and required  $\text{N}_2$  purges. Unless otherwise specified, the cell was kept at 95%  $RH$  at all times to ensure operation close to full humidification, while avoiding flooding of the cell with liquid water. Furthermore, note that all pressures were measured and controlled at the inlet of the fuel cell and are stated as absolute pressures, and that potentials are given as cell potentials unless specified otherwise.

All MEAs were conditioned prior to testing by 8 cycles of the following voltage-controlled ramp-in procedure ( $\text{H}_2/\text{air}$  flow rates of 1390/3320 nccm (anode/cathode),  $80 \text{ }^\circ\text{C}$ , 100%  $RH$ , and  $150 \text{ kPa}_{\text{abs}}$ ):  $0.6 \text{ V}$  (45 min), open circuit voltage (OCV, 5 min), and  $0.85 \text{ V}$  (10 min).

Cathode CVs were recorded between  $0.07\text{--}1.00 \text{ V}$  vs the reversible hydrogen electrode reference potential ( $V_{\text{RHE}}$ , corrected by the Nernst shift of the counter electrode to a nominal hydrogen partial pressure of  $100 \text{ kPa}$ ), using a scan rate of  $150 \text{ mV s}^{-1}$  at  $40 \text{ }^\circ\text{C}$  and  $100 \text{ kPa}_{\text{abs}}$ . During the measurement, the anode was fed with 200 nccm of fully humidified 5%  $\text{H}_2/\text{Ar}$ , while the cathode was flushed with a dry nitrogen flow of 200 nccm (reduced to 5 nccm while recording CVs).

In order to determine the proton conduction resistance in the cathode layer ( $R_{\text{H}^+, \text{cath}}$  in units of  $\Omega \text{ cm}_{\text{MEA}}^2$ ), three AC impedance spectra were recorded in blocking conditions (1000/1000 nccm  $\text{H}_2/\text{N}_2$  flows at anode/cathode) at  $80 \text{ }^\circ\text{C}$ , 95%  $RH$ ,  $270 \text{ kPa}_{\text{abs}}$ , and at a potential of  $0.2 \text{ V}$  (peak-to-peak perturbation of  $3.5 \text{ mV}$ ,  $200 \text{ kHz}$  to  $0.2 \text{ Hz}$ , 20 points per decade). The AC impedance response of the cathode electrode was then fitted to a transmission line model (using constant phase elements, ionic conduction resistances, and assuming negligible electrical resistances) in order to extract the proton

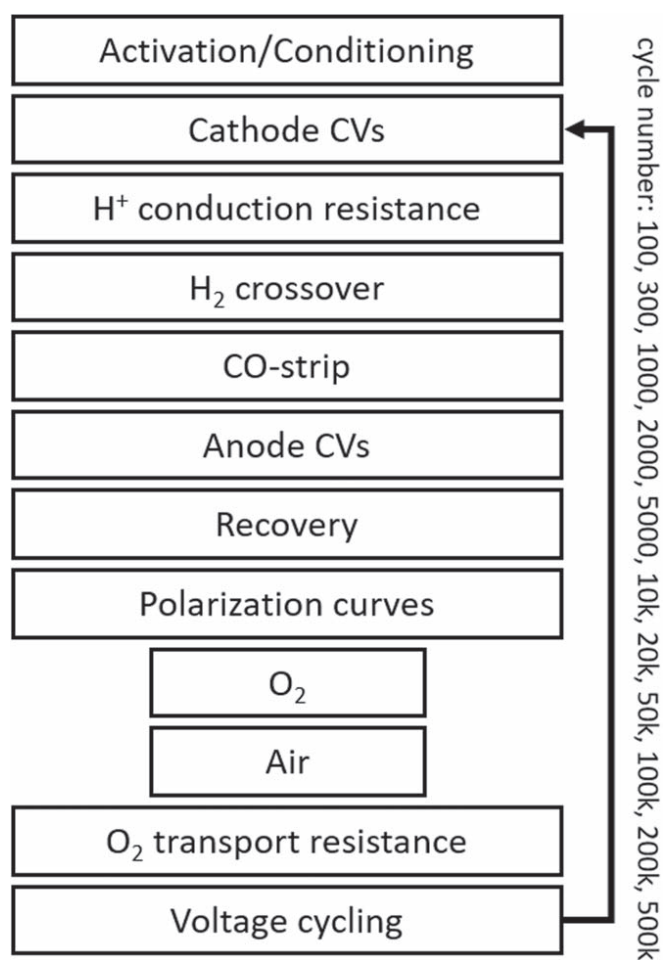


**Figure 1.** Scheme of the experimental procedure for the voltage cycling based MEA ASTs, whereby a full characterization was performed after each of the listed cycle numbers.

conduction resistance of the cathode electrode,  $R_{\text{H}^+, \text{cath}}$  (for details see Liu et al.);<sup>36–39</sup> considering the cathode utilization,  $R_{\text{H}^+, \text{cath}}$  was used to calculate the effective proton conduction resistance of the cathode electrode,  $R_{\text{H}^+, \text{cath}}^{\text{eff}}$ , from which the associated voltage losses can be determined.<sup>40</sup> The ohmic short of the membrane and the  $\text{H}_2$ -crossover were determined from measurements in  $\text{H}_2/\text{N}_2$  (150/600 nccm) at 170 kPa<sub>abs</sub>, 80 °C, and 95% RH by sequentially applying constant potentials of 0.3, 0.4, 0.5, 0.6 and 0.7 V for 2 min each.

CO-stripping measurements were performed by adsorbing CO (100 nccm flow of 10% CO in  $\text{N}_2$ ) for 3 min at 40 °C and 150 kPa<sub>abs</sub>, while holding a constant cathode potential of 0.1 V<sub>RHE</sub>. After CO adsorption, the cell was purged with high purity  $\text{N}_2$  (5.0) for  $\approx 1$  h to remove residual CO from the cell and the gas lines. A CV was recorded from the holding potential to 1.1 V<sub>RHE</sub> at a scan rate of 100 mV s<sup>-1</sup> to oxidize the adsorbed CO. Afterwards, two subsequent sweeps were recorded to ensure complete oxidation of CO from the catalyst surface. The area between the first anodic scan and its subsequent sweep was then used to determine the  $rf$ , using a specific charge of 420  $\mu\text{C cm}^{-2}$ . For the CO-stripping measurements, the anode was purged with 5%  $\text{H}_2/\text{Ar}$  at 200 nccm.

After CO-stripping, anode CVs were recorded between 0.07–1.00 V<sub>RHE</sub> (anode potential) using a scan rate of 150 mV s<sup>-1</sup> at 40 °C and 100 kPa<sub>abs</sub>. During the measurement, the anode was fed with a dry nitrogen flow of 200 nccm (reduced to 5 nccm while recording CVs), while the cathode was flushed with fully humidified 5%  $\text{H}_2/\text{Ar}$  at 200 nccm. This step was implemented to ensure that crossover CO, i.e., CO coming from the cathode side during the CO-stripping could

not accumulate on the anode catalyst surface, where it would poison the hydrogen oxidation reaction (HOR) activity and might lead to increasing overpotentials over the course of aging.

Prior to each set of polarization curves (see scheme in Fig. 1), a MEA recovery step was introduced to recover reversible losses at the cathode electrode. It consisted of a hold in  $\text{H}_2/\text{air}$  (2000/5000 nccm) at 0.3 V for 2 h at 40 °C and 270 kPa<sub>abs</sub> under fully humidified conditions (100% RH). Afterwards, differential flow polarization curves in  $\text{H}_2/\text{O}_2$  and  $\text{H}_2/\text{air}$  were carried out at 80 °C, 95% RH and 170 kPa<sub>abs</sub> with a flow rate of 2000/5000 nccm. The polarization curves were recorded in current controlled mode from low to high current densities up to 2.5 A cm<sub>MEA</sub><sup>-2</sup>. To ensure reduction of Pt-oxides, the potential was held at 0.75 V for 15 min before each polarization curve. Stabilization of the resulting cell voltage was received by holding each current density point constant for 5 min and averaging the data points over the final 30 s. Afterwards, galvanostatic electrochemical impedance spectroscopy (GEIS) measurements were performed in the frequency range from 100 kHz to 10 Hz (amplitude adjusted to 10% of the applied current with a minimum of 20 mA cm<sub>MEA</sub><sup>-2</sup>) to extract the high frequency resistance ( $HFR$ ) from the  $x$ -axis intersect in the Nyquist plot.  $HFR$  and  $R_{\text{H}^+, \text{cath}}$  (i.e., its effective contribution  $R_{\text{H}^+, \text{cath}}^{\text{eff}}$ ) were used to correct the cell voltage in  $\text{H}_2/\text{O}_2$  polarization curves for ohmic resistances and, additionally, the current density was corrected for the membrane short and  $\text{H}_2$ -crossover currents to obtain kinetic data (mass activity, specific activity, Tafel slope).

The total  $\text{O}_2$  mass transport resistance ( $R_{\text{O}_2}^{\text{total}}$ ) was obtained from limiting current measurements at 80 °C and 95% RH under differential flow conditions using 2000 nccm  $\text{H}_2$  and 5000 nccm of  $\text{O}_2/\text{N}_2$  mixtures on the anode and cathode, respectively. For each dry  $\text{O}_2$  mole fraction of 2, 4, 7 and 11%  $\text{O}_2$  in  $\text{N}_2$ , the cell potential was varied between 0.4 V and 0.05 V in steps of 0.05 V to determine the mass transport limited current densities (for details see Simon et al.<sup>34</sup>). To deconvolute  $R_{\text{O}_2}^{\text{total}}$  into a pressure dependent ( $R_{\text{O}_2}^{\text{PD}}$ ) and a pressure independent ( $R_{\text{O}_2}^{\text{PI}}$ ) part according to Baker et al.,<sup>41</sup> limiting current measurements were conducted at 170, 270, and 400 kPa<sub>abs</sub>.

Voltage cycling induced aging was performed at 80 °C, 95% RH, 100 kPa<sub>abs</sub>, and  $\text{H}_2/\text{N}_2$  flows of 200/75 nccm on anode/cathode. The SW voltage cycling ASTs were controlled by the Reference3000 potentiostat, whereby the potential step was completed in less than 0.1 s. The lower potential limit (LPL) was kept at 0.6 V, while the upper potential limit (UPL) was varied between 0.85 and 1.0 V, using hold times of 1, 2, or 8 s at each vertex potential. Here, the UPL of 1.0 V (at 8 s hold) was selected as comparison to the study of Harzer et al.,<sup>10</sup> while an UPL of 0.95 V resembles the open-circuit-voltage under  $\text{H}_2/\text{air}$  operation that was chosen as UPL in the studies by Kneer et al.<sup>9,16,24</sup> Finally, an UPL of 0.85 V was suggested by Ahluwalia et al. as a realistic value for load cycling in automotive applications.<sup>42</sup> The employed voltage cycling profiles and the end-of-life cycle numbers (EoL CN) are summarized in Table I. For each AST condition, two MEAs were prepared and evaluated; the measured MEA properties ( $\text{H}_2/\text{air}$  performance, ORR activities, etc.) are represented as average of these two measurements and the error bars represent the min/max values.

**Post-mortem MEA analysis.**—Scanning electron microscopy (SEM) images of ion-milled MEA cross-sections were taken for fresh as well as aged MEAs. In order to compare the cathode catalyst layer thickness before and after aging, the pristine MEA was subjected to the above mentioned conditioning step (confer Fig. 1) to ensure a more realistic comparability and to exclude any effects of cell assembly on the catalyst layer thickness. Prior to the ion-milling step, the GDL was peeled off and the 3-layer MEAs were fixed on adhesive Cu tape. Cross-sections were then prepared in an IB-19520 cryo cross-section polisher (JEOL Ltd., Japan) at -80 °C, using a multiple step polishing procedure with a first 3 h rough polishing (6.0 kV, 10/10 s on/off), followed by a 2 h fine polishing (4.0 kV,

**Table I. Characteristic parameters of the square wave (SW) profiles used for the voltage cycling based MEA ASTs that were performed at 100 kPa<sub>abs</sub>, 80 °C, 95% RH, and H<sub>2</sub>/N<sub>2</sub> flows of 200/75 nccm (anode/cathode). For all procedures, the lower potential limit (LPL) was kept constant at 0.6 V, while the upper potential limit (UPL), the hold time at each potential, and the end-of-life cycle number (EoL CN) were varied.**

AST procedure	LPL [V]	UPL [V]	hold time [s]	EoL CN [#]
1.00 V–8s	0.6	1.0	8	10 k
0.95 V–1s	0.6	0.95	1	50 k
0.85 V–8s	0.6	0.85	8	50 k
0.85 V–2s	0.6	0.85	2	100 k
0.85 V–1s	0.6	0.85	1	500 k

5/10 on/off). For thickness determination, SEM micrographs of the polished cross-sections were taken on a FE-SEM JSM 7500F (JEOL Ltd. Japan) in the secondary electron mode at 1 kV acceleration voltage and with a magnification of 2500× at 3 arbitrarily chosen locations for each cross-sectioned MEA. The thickness of the electrode was determined by integration of the electrode area with ImageJ (version 1.53 k) and dividing by the length of the image. In order to get more insights into the distribution of platinum across the MEA before and after voltage cycling based ASTs, SEM images were also taken in backscattering mode at 15 kV acceleration voltage and a magnification of 2500× at the same position as the ones used in the secondary electron mode.

## Results and Discussion

**ECSA determination.**—During voltage cycling based ASTs with Pt based catalysts, the ECSA is known to decrease substantially depending on the aging procedure. This effect can be seen exemplarily in Fig. 2a, which shows the cathode CVs of an MEA exposed to SW-aging between 0.6 and 1.0 V (see Table I). At BoL (black line), the characteristic Pt/C features of the hydrogen underpotential deposition (H<sub>upd</sub>, region below 0.4 V<sub>RHE</sub>) and of the Pt oxidation/reduction (starting above 0.75 V<sub>RHE</sub>) are clearly visible. Over the course of cycling, the features decrease substantially due to a decrease in the cathode roughness factor (*rf*), resulting from the aforementioned Pt dissolution/redeposition mechanism. After 10,000 cycles between 0.6 and 1.0 V and with a hold time of 8 s (further on referred to as “1.00 V–8s”), the characteristic platinum features are no longer visible (orange line in Fig. 2a). Instead, the double layer capacity of the carbon support is observed, exhibiting the characteristic hydroquinone/quinone feature at ≈0.6 V<sub>RHE</sub>.<sup>43</sup> The fact that this feature does not grow indicates that carbon corrosion does not play a significant role when using a SW cycling protocol up to 1.0 V, which agrees with the findings of Harzer et al.<sup>10</sup>

While the ECSA can be obtained from the H<sub>upd</sub> region, an increasing contribution of hydrogen evolution currents, that are mostly controlled thermodynamically at potentials near 0 V<sub>RHE</sub><sup>44</sup> and thus will not be affected by the aging induced degradation mechanism,<sup>45</sup> will lead to increasing errors in the quantification of the ECSA by H<sub>upd</sub> with decreasing cathode *rf* values.<sup>46</sup> Thus, CO-stripping is often used especially for the characterization of low-loaded or aged electrodes.<sup>45,47</sup> Representative CO-stripping voltammograms are given in Fig. 2b after subtraction of the second scan as baseline. As the second scan exhibits H<sub>upd</sub> features in the potential region below 0.4 V<sub>RHE</sub>, the subtracted CO-stripping voltammograms would show negative currents in this region and thus, only data above 0.6 V<sub>RHE</sub> are shown. Similar to the H<sub>upd</sub> feature development, the CO oxidation peak decreases with increasing cycle number. The integration of the CO oxidation peaks is shown in Figs. 2c and 2d for the pristine and aged (10,000 cycles) cathode, respectively. When comparing the CO oxidation peak (see Fig. 2d) with the H<sub>upd</sub> features (orange line in Fig. 2a) for the same aged cathode, the

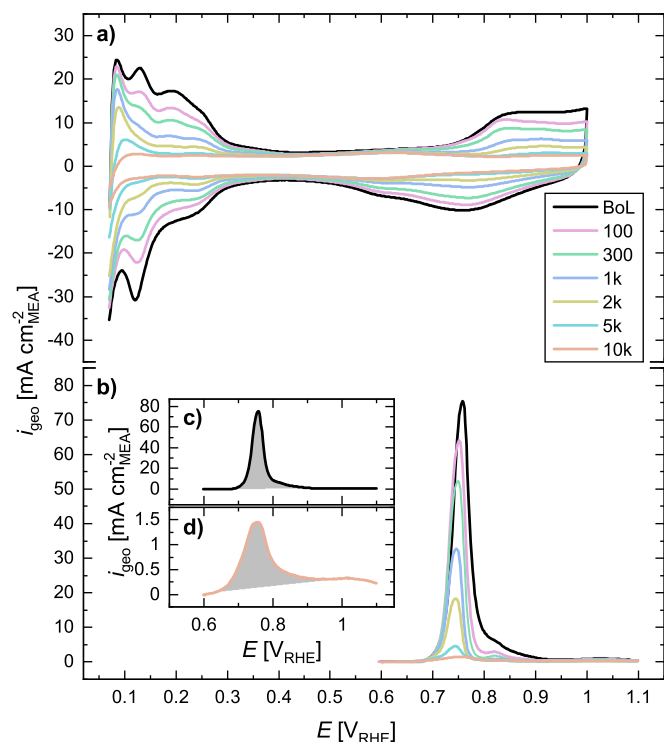


**Figure 2.** (a) CVs of the cathode after various cycles of aging during a SW based AST between 0.6 and 1.0 V with 8 s dwell time at each potential (further on referred to as 1.00 V–8s). CVs were measured at a scan rate of 150 mV s<sup>-1</sup> from 0.07 to 1.00 V<sub>RHE</sub> at ambient pressure and 40 °C under fully humidified conditions (see Experimental section). (b) Representative CO stripping voltammograms after subtraction of the subsequent anodic sweep for pristine and aged cathodes shown in the voltage range of 0.6–1.1 V<sub>RHE</sub> to exclude negative currents due to subtracted H<sub>upd</sub> features from the second scan. In addition, the zoomed-in CO-stripping voltammograms are shown: (c) at BoL and (d) at EoL. CO-stripping voltammograms were recorded at 100 mV s<sup>-1</sup> up to 1.1 V<sub>RHE</sub> at 150 kPa<sub>abs</sub>, 40 °C, and 95% RH with 200 nccm 5% H<sub>2</sub>/Ar and 5 nccm N<sub>2</sub> on anode and cathode, respectively. CO was adsorbed by introducing 10% CO/N<sub>2</sub> (100 nccm flow) for 3 min, followed by a N<sub>2</sub> purge for 1 h, while maintaining a constant cell potential of 0.1 V<sub>RHE</sub> at all times.

advantage of the CO-stripping method becomes obvious: even for a catalyst exhibiting very low *rf* values that does not show distinguishable H<sub>upd</sub> features anymore, the CO oxidation peak is still distinct and clearly visible, which allows for a reliable *rf* determination. However, it was observed that the CO-stripping current, i.e., the difference between first and second scan, did not return to zero after the CO-strip but remained fairly constant at ≈0.2–0.3 mA cm<sup>-2</sup><sub>MEA</sub> (see Fig. 2d). This offset was observed in all cases and could also be reproduced for a pristine MEA without introducing CO, i.e., after the respective potential hold at 0.1 V<sub>RHE</sub> for 1 h in pure N<sub>2</sub> (5.0 purity), which means that it is most likely a partially irreversible oxidation of the carbon support rather than a CO oxidation current. While this offset does not have a significant effect on the ECSA determination at BoL (see Fig. 2c), the contribution of this current is significant after extended aging (see Fig. 2d). Therefore, the integration was conducted with a linear baseline between 0.6 and 1.0 V<sub>RHE</sub> even after having subtracted the subsequent scan as a first baseline (see gray areas in Figs. 2c and 2d).

Since a reliable determination of the ECSA for cathodes with very low *rf* values by the H<sub>upd</sub> method is no longer possible and since CO-stripping generally yields slightly higher ECSAs than H<sub>upd</sub>,<sup>48</sup> the ECSA results are solely determined by CO-stripping measurements throughout this study.

**ECSA development over the course of VC-ASTs.**—The development of the ECSA normalized to the initial BoL ECSA (ECSA<sub>BoL</sub>)

for the different aging protocols (see Table I) vs the number of cycles (CN) or vs the time at the upper potential limit (UPL) is shown in Figs. 3a and 3b, respectively. As expected from previous studies, a higher UPL and longer hold times accelerate the *ECSA* loss per cycle (Fig. 3a), whereby the mildest aging protocol (0.85 V–1s, violet hexagon symbols) leads to the highest *ECSA* retention after 10,000 cycles, whereas the harshest aging protocol (1.00 V–8s, orange squares) shows the most pronounced decline in *ECSA*, reaching less than 5% of the initial *ECSA* after 10,000 cycles. When comparing the degradation after 10,000 cycles to other studies by Stariha et al.<sup>25</sup> and Padgett et al.<sup>23</sup> that used the same  $\approx 20$  wt.% Pt/V catalyst and an UPL of 0.95 V, their *ECSA* loss of  $\approx 50\%$  and  $\approx 65\%$ , respectively, was slightly lower than the *ECSA* loss of  $\approx 75\%$  found in our study (red triangle at 10,000 cycles in Fig. 3a). These discrepancies are most likely the result of slightly different protocols and setups. A degradation caused by the excessive characterization procedure in this study can be excluded on the basis of reference measurements that yielded the exact same *ECSA* after 10,000 cycles when the extensive MEA characterization steps were only performed at BoL and after 10,000 cycles (data not shown).

Interestingly, very similar values of  $82 \pm 2\%$  normalized *ECSA* were observed after a settle-in phase in the first 100 cycles for all aging procedures with an UPL below 1 V (see Table II); only the harshest procedure with an UPL of 1.00 V and a hold time of 8 s showed a significantly lower normalized *ECSA* of  $74 \pm 1\%$  after 100 cycles. An initial *ECSA* decay independent of the used aging condition has already been observed by Harzer et al., although they did not explicitly comment on it.<sup>10</sup> However, for the same Pt/V catalyst that is used here, they showed that the pristine Pt/V catalyst contained a significant fraction of sub-1.5 nm diameter Pt particles. Thus, when considering the reported particle size effects,<sup>12,49,50</sup> it

seems likely that these smallest Pt particles would be sufficiently instable, so that within the first 100 cycles they are likely to dissolve even under relatively mild cycling conditions, leading to the here observed initial *ECSA* losses.

Another universal behavior is the linear *ECSA* decay after 100 cycles in all cases when plotting the normalized *ECSA* (i.e.,  $ECSA/ECSA_{BoL}$ ) against the logarithm of the cycle number (CN), a behavior which has already been observed previously.<sup>13</sup> This linearity differs strongly from the 1st order decay rate that was found in earlier studies by Debe et al.<sup>51</sup> and Bi et al.<sup>52,53</sup> for VC-ASTs with an UPL of 1.2  $V_{RHE}$  and resulted in a linear behavior when plotting the logarithm of the normalized *ECSA* against the CN. Based on these works, Kneer and Wagner proposed a modified 1st order kinetic rate model for VC-ASTs with lower UPLs but in most cases, the model underestimated the *ECSA* loss up to  $\approx 50\%$  of the BoL *ECSA* and overestimated the *ECSA* loss thereafter,<sup>9</sup> thus indicating that the model does not accurately describe the *ECSA* degradation at limited UPLs ( $\leq 1.0 V_{RHE}$ ). The most likely explanation of these different *ECSA* loss behaviors is the different origins of the Pt *ECSA* losses with carbon corrosion and Pt detachment/migration/coalescence being the dominating degradation mechanisms when using an UPL of 1.2  $V_{RHE}$ , whereas Pt dissolution/redeposition dominates at limited UPLs ( $\leq 1.0 V_{RHE}$ ).<sup>4,6,13</sup> Only below a normalized *ECSA* of  $\approx 12.5\%$  (horizontal red dashed line in Fig. 3) that corresponds to a *rf* of  $\approx 10 \text{ cm}^2_{Pt} \text{ cm}^{-2}_{MEA}$  (the reasoning for this specific value will be discussed in detail later), a deviation from the linear behavior is observed. This apparent stabilization of very small *ECSA* values after extended cycling has been discussed to be due to a thermodynamic stabilization of larger Pt particles.<sup>10</sup> This observed linear trend can be used to determine a phenomenological normalized *ECSA*-loss rate constant ( $k_{ECSA-loss}$ ) that is an empirical measure of

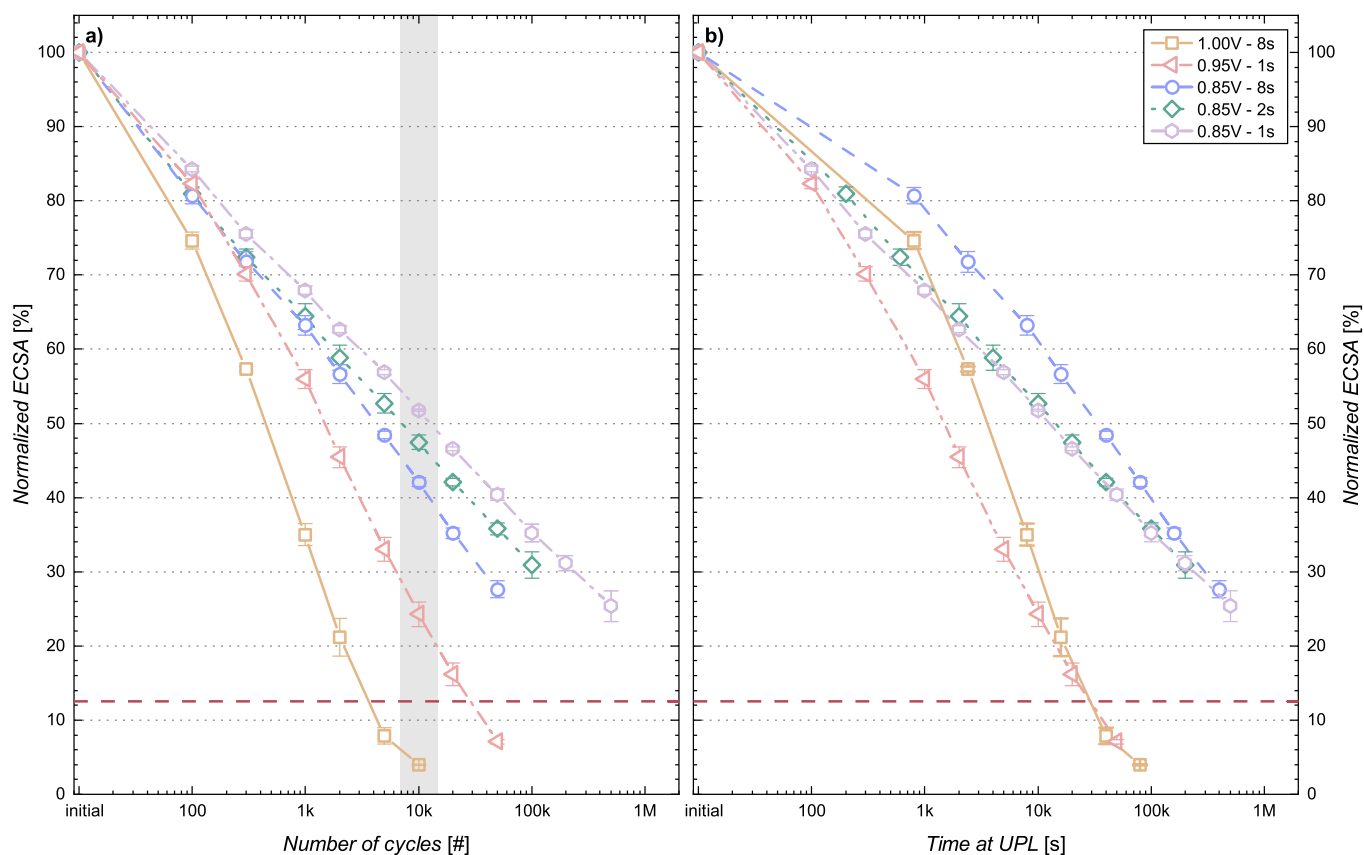


**Figure 3.** Loss of normalized cathode *ECSA* (i.e.,  $ECSA/ECSA_{BoL}$ ) plotted either vs: (a) the number of cycles, or (b) the time at the upper potential limit (UPL). The initial BoL value of the *ECSA* for all cathodes is  $ECSA_{BoL} = 75.2 \pm 0.6 \text{ m}^2 \text{ g}_{Pt}^{-1}$ , corresponding to *rf* values of  $79.0 \pm 4.4 \text{ cm}^2_{Pt} \text{ cm}^{-2}_{MEA}$  at Pt cathode loadings of  $0.103 \pm 0.005 \text{ mg}_{Pt} \text{ cm}^{-2}_{MEA}$ . The horizontal red dashed line at 12.5% normalized *ECSA* (corresponding to a *rf* of  $\approx 10 \text{ cm}^2_{Pt} \text{ cm}^{-2}_{MEA}$ ) marks the lower limit that was used for the linear fits the normalized *ECSA* vs. the logarithm of the cycle number (see Eq. 1 and Table II). The gray shaded area marks the *ECSA* values after 10,000 cycles.

**Table II.** Least-squares regression parameters for the relationship between the normalized ECSA ( $ECSA/ECSA_{BoL}$ ) and the logarithm of the number of cycles (see Eq. 1) for the different voltage cycling ASTs shown in Fig. 3a. The normalized ECSA data were fitted between their normalized value at 100 cycles ( $ECSA_{100CN}/ECSA_{BoL}$ ) and all the measured  $ECSA/ECSA_{BoL}$  values that were higher than 12.5% (i.e., above the horizontal red dashed line in Fig. 3a). The resulting parameter fits of the  $ECSA_{100CN}/ECSA_{BoL}$  values and of the slopes ( $k_{ECSA-loss}$ ) are given below.

UPL of the VC-AST hold time at UPL	1.0 V	0.95 V	0.85 V		
	8 s	1 s	8 s	2 s	1 s
$ECSA_{100CN}/ECSA_{BoL}$ [%]	$74.6 \pm 1.2$	$82.3 \pm 0.7$	$80.7 \pm 1.1$	$80.9 \pm 1.0$	$84.3 \pm 0.4$
$k_{ECSA-loss}$ [% dec <sup>-1</sup> ]	$40.3 \pm 2.3$	$28.8 \pm 0.5$	$19.9 \pm 0.4$	$16.7 \pm 0.1$	$16.2 \pm 0.1$

how harsh an aging protocol is (Eq. 1).

$$ECSA/ECSA_{BoL} = ECSA_{100CN}/ECSA_{BoL} - k_{ECSA-loss} \cdot \log(CN) \quad [1]$$

For the  $ECSA$  data obtained from the different AST protocols shown in Fig. 3a, the  $k_{ECSA-loss}$  values obtained from linear regression fits of the normalized  $ECSA$  data obtained between 100 cycles ( $ECSA_{100CN}/ECSA_{BoL}$ ) and the number of cycles up to which the normalized  $ECSA$  values remain above 12.5% are given in Table II. The slopes gradually increase with longer hold times from 1 to 8 s and with higher UPLs from 0.85 to 1.0 V, thereby confirming the Pt  $ECSA$  trends that were observed in previous voltage cycling studies.<sup>8–10</sup>

The assumption that Pt dissolution/redeposition is the dominating aging mechanism for voltage cycling ASTs with an UPL of  $\leq 1.0$  V<sub>RHE</sub> is confirmed by post-mortem analysis of MEA cross-sections via scanning electron microscopy (SEM) in backscattered mode (see Fig. 4). While Pt is distributed homogeneously throughout the cathode catalyst layer at BoL (see Fig. 4a), a pronounced anisotropy of the Pt distribution across the cathode catalyst layer (depicted on top of the images in Fig. 4) is observed after voltage-cycling. For the severely degraded cathode after 10,000 cycles of the 1.00 V–8s AST protocol (see Fig. 4b), a pronounced Pt band can be seen at the membrane-electrode interface, whereas the electrode is completely depleted of Pt close to the membrane. According to Zhang et al.,<sup>54</sup> the position of the Pt band is governed by the partial pressures of H<sub>2</sub> and O<sub>2</sub> in anode and cathode compartment, respectively, and since the O<sub>2</sub> partial pressure is 0 kPa during voltage cycling in H<sub>2</sub>/N<sub>2</sub> configuration, the Pt band position is expected to be directly at the electrode-membrane interface. According to Ferreira et al.,<sup>4</sup> the observed depletion of Pt adjacent to the membrane with Pt being maintained next to the GDL is a clear indication for a dominating Pt dissolution/redeposition mechanism. On the other hand, others reported that Pt coalescence would contribute to the overall  $ECSA$  losses even when the UPL is limited to  $\leq 1.0$  V<sub>RHE</sub>.<sup>23</sup> While we believe that the latter mechanism might be a significant factor in the Pt particle growth-dominated region (close to the cathode/GDL interface), the origin of the Pt depletion next to the membrane must be caused by Pt dissolution and loss into the membrane phase. For the less severe aging protocols with an UPL of 0.85 V<sub>RHE</sub> and hold times of 8 s (Fig. 4c) or 1 s (Fig. 4d), a similar but less pronounced trend of Pt band formation and Pt depletion adjacent to the membrane is observed at EoL, in accordance with the less severe  $ECSA$  degradation at EoL for these protocols. Within the measurement accuracy, the initial cathode catalyst layer thickness was maintained after the ASTs (see Table III), which confirms that carbon corrosion did not contribute significantly to the cathode degradation.

As mentioned previously, the hold time at the UPL has been reported to affect the degradation differently, depending on whether it is looked at as a function of CN or the time at UPL ( $t_{UPL}$ ). In Fig. 3b, the normalized  $ECSA$  is shown over the logarithm of the time at UPL, whereby the time at UPL is the product of CN and hold time ( $t_{hold}$ ). Due to the nature of the logarithmic scale, this results in a right-shift of all data points by the factor  $\log(t_{hold})$  and the

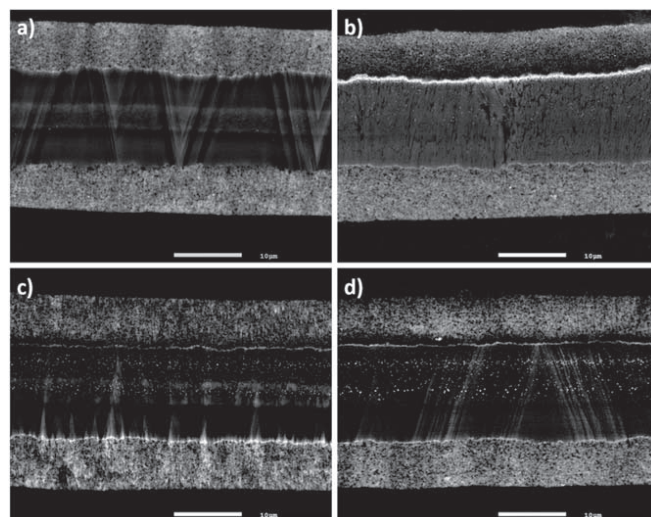


**Figure 4.** Post-mortem SEM cross-section images of MEAs after (a) BoL characterization as well as after voltage cycling ASTs using the (b) 1.00 V–8s, (c) 0.85 V–8s, or (d) 0.85 V–1s protocols. Images were taken by SEM at a magnification of 2500 $\times$  in electron back-scattering mode. The cathode catalyst layer of the MEA is shown in each image at the top; the white scale bar at the bottom of each image represents 10  $\mu$ m.

$k_{ECSA-loss}$  values representing the slope in % dec<sup>-1</sup> (Table II) remain the same (Eq. 2).

$$\log(t_{UPL}) = \log(t_{hold} \cdot CN) = \log(t_{hold}) + \log(CN) \quad [2]$$

Still, this representation allows for some interesting conclusions. First, the normalized  $ECSA$  of the harshest protocol (1.00 V–8s, orange squares in Fig. 3b) is higher than that for the fast cycling to a lower potential of 0.95 V (0.95 V–1s, red triangles) in the whole linear region, which indicates that for a given  $t_{UPL}$  value, a few long OCV periods are less detrimental than many short high/low-load cycles. The same holds true when the UPL is the same, as can be seen for the AST data with UPL = 0.85 V: for the same  $t_{UPL}$  value, a few cycles with long hold times (8 s, blue circles) induce significantly lower  $ECSA$  loss compared to more cycles with shorter hold times of 2 s (green diamonds) or 1 s (pink hexagons). This indicates that the number of cycles is a stronger trigger for degradation than the total time at UPL. However, due to the higher slope for longer hold periods, there is a crossover point at which the  $ECSA$  degradation is the same for different hold times. In this case, the crossover point occurred after  $\approx 500,000$  cycles with  $\approx 25\%$   $ECSA$  remaining, i.e., at a point that would be considered past EoL.

The effect of the hold time at the same UPL can be examined by the data taken for the same UPL of 0.85 V but for different hold times (see Fig. 3b). Assuming that the anodic and the cathodic potential steps lead to a transient dissolution of platinum, as suggested by rotating ring disk electrode measurements<sup>55,56</sup> and by online mass spectrometry,<sup>57</sup> one would expect that the  $t_{hold}$ -averaged amount of dissolved platinum would decrease with increasing  $t_{hold}$ , so that the  $ECSA$  loss vs  $t_{hold}$  should decrease with increasing time at

**Table III.** Averaged cathode catalyst layer thicknesses for MEAs after conditioning (BoL) or after a given number of AST cycles (CN) with different UPLs values (0.85 V or 1.00 V) and hold times (1 or 8 s). These ASTs represent the most harsh (1.00 V–8s) and least harsh aging protocols (0.85 V–8/1s) and the MEAs from these ASTs were therefore chosen for further investigation using SEM imaging. The averaged cathode electrode thickness values were calculated by dividing the integrated electrode area by the length of the SEM cross-section images taken in the secondary electron mode (confer Fig. A-1); the error bars represent the standard deviation of the thus obtained thicknesses from at least three images taken at arbitrarily chosen positions on the same cross-sectioned MEA.

MEA history	CN [#]	Cathode thickness [ $\mu\text{m}$ ]
BoL	0	$7.2 \pm 0.5$
1.00 V–8s AST	10 k	$7.5 \pm 0.3$
0.85 V–8s AST	50 k	$7.5 \pm 0.4$
0.85 V–1s AST	500 k	$7.2 \pm 0.4$

UPL. This would explain why the *EC*SA loss vs time at UPL is lower for the 0.85 V–8s compared to the 0.85 V–2s AST (see Fig. 3b). It is inconsistent, however, with the observation that the *EC*SA loss vs time at UPL is essentially identical for the 0.85 V–2s and the 0.85 V–1s AST data (see Fig. 3b). One possible explanation might be that at very short hold times the typically significant platinum loss into the membrane/ionomer phase during voltage cycling<sup>4,52</sup> is reduced due to an insufficient mobility of dissolved platinum ions in the ionomer phase, thereby reducing the platinum loss into the membrane/ionomer phase per cycle. Whether this is the case could be determined by estimating the diffusion length ( $x$ ) of dissolved platinum ions in the ionomer phase of the cathode electrode over the hold time (via  $x \approx (D_{\text{Pt, eff}} \cdot t_{\text{hold}})^{0.5}$ ), but this requires that the effective diffusion coefficient of platinum ions in the membrane/ionomer phase ( $D_{\text{Pt, eff}}$ ) be known. Unfortunately, the  $D_{\text{Pt, eff}}$  values in the ionomer phase of the catalyst layer that are used in voltage cycling models vary widely (from  $1 \cdot 10^{-6} \text{ cm}^2 \text{ s}^{-1}$ <sup>58</sup> to  $1.5 \cdot 10^{-9} \text{ cm}^2 \text{ s}^{-1}$ <sup>53</sup>), and to our knowledge only two actual measurements exist for the platinum diffusion coefficient in Nafion<sup>®</sup> membranes ( $D_{\text{Pt}}$ ) at 25 °C:  $\approx 4 \cdot 10^{-7} \text{ cm}^2 \text{ s}^{-1}$ <sup>59</sup> (determined by online mass spectrometry) and  $\approx 1.4 \cdot 10^{-8} \text{ cm}^2 \text{ s}^{-1}$  (measured for  $(\text{PtCl}_6)^{2-}$  ions<sup>60</sup>). In order to obtain the  $D_{\text{Pt, eff}}$  values in the ionomer phase of the catalyst layer at 80 °C, these  $D_{\text{Pt}}$  values must be multiplied by the typical ionomer volume fraction in the electrode ( $\varepsilon_{\text{ionomer}} \approx 0.2$ <sup>4</sup>) and the  $\approx 5$ -fold increase for ionic diffusion coefficients in a Nafion<sup>®</sup> membrane between 25 and 80 °C (measured for  $\text{Co}^{2+}$  and  $\text{Ce}^{3+}$ <sup>61</sup>). Coincidentally, both corrections cancel each other, so that the measured membrane  $D_{\text{Pt}}$  values at 25 °C and the estimated  $D_{\text{Pt, eff}}$  values in the catalyst layer at 80 °C turn out to be numerically identical, i.e.,  $D_{\text{Pt, eff}} \approx (1.4\text{--}40) \cdot 10^{-8} \text{ cm}^2 \text{ s}^{-1}$ . For this range, the  $x$  values for  $t_{\text{hold}} = 1 \text{ s}$  would range between  $\approx 1.2\text{--}6 \mu\text{m}$ , which is less than the cathode electrode thickness ( $\approx 7.5 \mu\text{m}$ , see Table III), making it plausible that the loss of platinum into the membrane/ionomer phase per cycle could be reduced for such short hold times, which in turn could explain the observed reduced *EC*SA losses per cycle and the similar *EC*SA losses per time at UPL for very short  $t_{\text{hold}}$  values. According to the post mortem analysis of cross-sectioned MEAs by SEM, the fraction of Pt lost into the membrane/ionomer phase and the depletion of platinum in the cathode electrode in the vicinity of the membrane (appearing as dark region in in Figs. 4c and 4d) seems to be essentially the same for hold times of 8 and 1 s, indicating that the hold time does not significantly affect the degradation mechanism when comparing two MEAs with similar remaining *EC*SA values.

Finally, it should be noted that most studies take the *EC*SA loss during voltage cycling ASTs as primary parameter to describe the aging of the cathode electrode and the associated fuel performance degradation. In order to allow for an easier comparison with the literature, this convention has been adopted in the preceding section

as well. Here, the *EC*SA is generally obtained by quantifying the cathode roughness factor (in  $\text{cm}^2_{\text{Pt}} \text{ cm}^{-2}_{\text{MEA}}$ ), namely by  $H_{\text{upd}}$  or CO-stripping measurements that are then normalized by the initial Pt loading of the cathode electrode (in  $\text{mg}_{\text{Pt}} \text{ cm}^{-2}_{\text{MEA}}$ ). Here, the term “*EC*SA,” i.e., the mass normalized Pt surface area of a catalyst, is usually associated with specific property of a catalyst, reflecting its platinum particle size distribution. However, as voltage cycling progresses, platinum in the cathode electrode is increasingly lost into the membrane/ionomer phase<sup>4,52</sup> (illustrated, e.g., by the Pt-band formation in the membrane, see Fig. 4b), resulting both in a loss of platinum from the electrode into the membrane/ionomer phase and in a variation of the platinum concentration (see Fig. 4) and the Pt particle size across the cathode electrode thickness,<sup>4</sup> so that the nominally calculated “*EC*SA” does not anymore represent a catalyst-specific property, i.e., an *EC*SA of  $50 \text{ m}^2 \text{ g}_{\text{Pt}}^{-1}$  after aging describes a completely different situation with regards to the platinum catalyst than the same *EC*SA value for a pristine catalyst taken at BoL. In contrast, the *rf* value (i.e., the active Pt area per geometric area) is associated with the properties of the catalyst layer rather than the catalyst that comprises the catalyst layer, and thus remains an accurate representation of the state of the MEA (i.e., represents a direct measurement). Since the *rf* avoids the false impression of an underlying average particle size that would be associated with the *EC*SA, the *rf* will be used as the main state-of-health descriptor in the following parts of our study.

**Qualitative assessment of voltage losses in  $H_2$ /air polarization curves.**— $H_2$ /air polarization curves of pristine and aged catalysts after 10,000 cycles are shown in Fig. 5. As expected, more severely degraded MEAs, i.e., MEAs with larger normalized *EC*SA losses (see gray area in Fig. 3a for reference), showed higher performance losses compared to the BoL performance (black squares). An exception to this trend is the essentially identical performance of the MEAs subjected to the 0.85 V–8s AST (blue circles) and to the 0.85 V–2s AST (green diamonds). This, unfortunately, is the result of a slightly below average BoL performance of the MEAs that had been used for the 0.85 V–2 s measurement series ( $\approx 25 \text{ mV}$  at the highest current density; confer right-most green diamonds in Fig. 12), resulting in a  $H_2$ /air performance after 10,000 cycles that is the same as that of the MEAs subjected to the harsher 0.85 V–8s AST that experienced a higher *EC*SA loss. The most severe differences can be observed in the high current density region, where increasing oxygen mass transport overpotentials directly correlate with the decrease in the normalized *EC*SA (see Fig. 3a) and thus the roughness factor. For the most degraded catalyst with a *rf* of only  $\approx 3 \text{ cm}^2_{\text{Pt}} \text{ cm}^{-2}_{\text{MEA}}$  (1.00 V–8s, orange squares in Fig. 5), this results in a maximum current density of only  $500 \text{ mA cm}^{-2}_{\text{MEA}}$  before the cell potential goes below the specified cutoff of 0.2 V. In contrast to the mass transport penalties at low *rf* values, ORR kinetic overpotentials should have a minor contribution to the overall voltage losses due to the logarithmic nature of the Tafel kinetics, where a 90% *rf*-loss is required for an overpotential increase by  $\approx 70 \text{ mV}$ .<sup>62,63</sup> Indeed, for an *EC*SA or *rf* loss of  $\approx 53\%$  (0.85 V–2s, green diamonds), the potential at  $500 \text{ mA cm}^{-2}_{\text{MEA}}$  decreased by less than 10 mV, which is less than the  $\approx 20 \text{ mV}$  one would expect based on simple Tafel kinetics with a constant exchange current density, and thus already hints at an increase of the ORR specific activity that has been observed in previous studies.<sup>10,23,64</sup>

For all MEAs, *HFR* values of 26–33  $\text{m}\Omega \text{ cm}^{-2}_{\text{MEA}}$  were obtained at BoL and stayed constant for an individual MEA over aging (Fig. 5b). Similarly, the  $H_2$ -crossover current density stayed constant at  $\approx 5\text{--}6 \text{ mA cm}^{-2}_{\text{MEA}}$  for all MEAs during aging, except for a decrease to  $\approx 2\text{--}3 \text{ mA cm}^{-2}_{\text{MEA}}$  at extremely low *rf* values ( $< 10 \text{ cm}^2_{\text{Pt}} \text{ cm}^{-2}_{\text{MEA}}$ ). The origin of this decrease is unknown as measurements in  $H_2/N_2$  configuration cannot replicate the  $H_2\text{--}O_2$  recombination effect of a Pt-band in the membrane that might cause

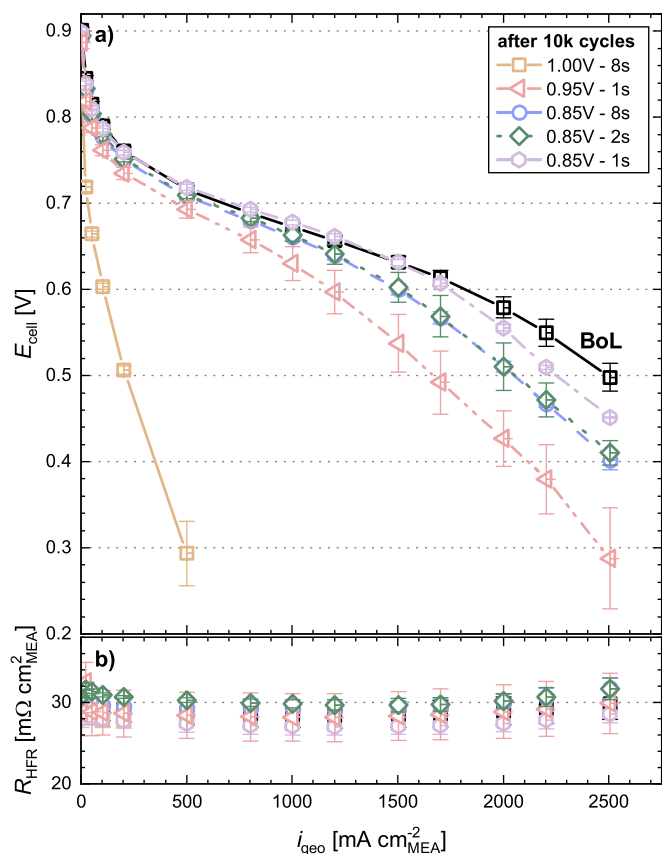


**Figure 5.** (a) Differential flow  $\text{H}_2/\text{air}$  (2000/5000 nccm) polarization curves at 170 kPa<sub>abs</sub>, 80 °C, and 95% RH of MEAs with  $0.103 \pm 0.05 \text{ mg}_{\text{Pt}} \text{ cm}^{-2}_{\text{MEA}}$  cathode loadings at BoL (black symbols) and after 10,000 aging cycles (for respective ECSA losses see gray highlighted area in Fig. 3a); (b) corresponding high frequency resistance (HFR) values. After 10,000 cycles, the error bars represent the mean absolute deviation of two independent measurements, while the BoL data are averaged over all 10 MEAs and error bars represent the standard deviation.

a reduced  $\text{H}_2$ -crossover during  $\text{H}_2/\text{air}$  operation and the HOR activity of the cathode should be sufficiently high for  $\text{H}_2$ -crossover measurements even at these low  $rf$  values.<sup>47</sup> Considering the constant HFR values and the very low  $\text{H}_2$ -crossover currents, a significant degradation of the membrane over the course of the ASTs can be excluded.

Finally, the proton conduction resistance of the cathode electrode ( $R_{\text{H}^+, \text{cath}}$ ) remained rather constant for the MEAs subjected to different aging protocols over the course of aging ( $\approx 20$ – $25 \text{ m}\Omega \text{ cm}^{-2}_{\text{MEA}}$ ; see Fig. 6), i.e., did not vary significantly despite the large changes in ECSA or  $rf$  (see Fig. 3). Therefore, ionomer degradation induced changes in the proton conduction pathway that have been shown to result in reversible and irreversible voltage losses after dry operation can be excluded as a major voltage loss contribution.<sup>65</sup>

Overall, ohmic resistances were found to be unaffected by aging, which leaves changes in the catalytic activity and increasing mass transport resistances as the main causes for the deteriorating  $\text{H}_2/\text{air}$  performance. Both aspects will be discussed in detail below.

**Dependence of the ORR activity losses on cathode  $rf$ .**—To evaluate the cathode activity,  $\text{H}_2/\text{O}_2$  polarization curves were recorded under differential flow conditions. The Tafel plots of the HFR- and  $R_{\text{H}^+, \text{cath}}$ -corrected voltage against the logarithm of the specific current density that was corrected by the  $\text{H}_2$ -crossover ( $i_{\text{H}_2\text{-cross}}$ ) and the ohmic short current ( $i_{\text{short}}$ ) are shown in Fig. 7 for the pristine and for the most severely degraded MEAs of each AST protocol with a final  $rf > 10 \text{ cm}^2_{\text{Pt}} \text{ cm}^{-2}_{\text{MEA}}$  (Fig. 7a) or with a final  $rf$

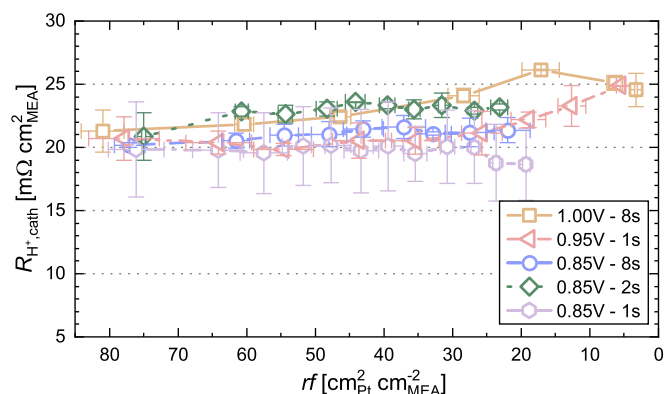


**Figure 6.** Variation of the proton conduction resistance ( $R_{\text{H}^+, \text{cath}}$ ) of the cathode electrode as a function of  $rf$  over the course of the various voltage cycling ASTs (see Table I), determined from transition line model fits of AC impedance spectra that were recorded in  $\text{H}_2/\text{N}_2$  (150/600 nccm) configuration at 270 kPa<sub>abs</sub>, 80 °C, and 95% RH. Error bars represent the mean absolute deviation between two independent measurements.

$< 10 \text{ cm}^2_{\text{Pt}} \text{ cm}^{-2}_{\text{MEA}}$  (Fig. 7b). This distinction is made based on the empirically found linear relationship between the normalized ECSA (or the  $rf$ ) and the logarithm of the cycle number that holds until the  $rf$  decreases to below  $\approx 10 \text{ cm}^2_{\text{Pt}} \text{ cm}^{-2}_{\text{MEA}}$  (see horizontal red dashed line in Fig. 3a); this limit seems to mark a change in the degradation behavior and, furthermore, below this limit a characterization of the MEA with regard to specific surface area (see Fig. 2) and limiting current measurements (shown later in Fig. 9) becomes challenging and error prone.

Overall, a similar development can be seen for all cycling procedures when comparing the Tafel plots at BoL (black squares, averaged over all MEAs) to that of the aged MEAs (procedure and respective CN given in the legend of Fig. 7a). As long as the  $rf$  remains above  $10 \text{ cm}^2_{\text{Pt}} \text{ cm}^{-2}_{\text{MEA}}$  (Fig. 7a), a constant Tafel slope of  $75 \pm 3 \text{ mV dec}^{-1}$  was found, similar to previously reported values for the same catalyst and setup;<sup>10,66</sup> it is slightly higher than the  $70 \text{ mV dec}^{-1}$  that correspond to a cathodic transfer coefficient of  $\alpha_c = 1$  for the ORR (gray line for reference) and that has often been assumed for carbon supported Pt catalysts.<sup>63,67</sup> Over the course of aging, the Tafel curves gradually shift towards higher potentials (only the (near-)EoL curves are depicted for clarity), indicating an increase in specific activity with decreasing  $rf$ , i.e., with increasing Pt particle size. However, at current densities higher than  $\approx 0.1 \text{ A cm}^{-2}_{\text{Pt}}$  (only reached for  $rf < 25 \text{ cm}^2_{\text{Pt}} \text{ cm}^{-2}_{\text{MEA}}$  for the maximum current density of  $2.5 \text{ A cm}^{-2}_{\text{MEA}}$ ), the curves start to deviate from the initial Tafel slope, leading to additional overpotentials. Similar deviations from the expected Tafel kinetics at low  $rf$  values have been reported by other researchers for pristine<sup>68,69</sup> and aged electrodes<sup>10</sup> alike. The origin of these losses at high specific current densities are still debated, but the proposed causes include a limited dissolution of oxygen into the ionomer phase, an intrinsically high transport resistance of the thin ionomer phase covering the Pt nanoparticles, a limited effective ionomer surface, or a decrease of the ORR kinetics at low cathode potentials.<sup>19,48,70–74</sup>

An even more pronounced deviation from the  $\approx 70 \text{ mV dec}^{-1}$  Tafel slope is observed for aged MEAs with ultra-low  $rf$  values of  $< 10 \text{ cm}^2_{\text{Pt}} \text{ cm}^{-2}_{\text{MEA}}$  (Fig. 7b). Already in the low specific current density range, i.e., up to  $0.03 \text{ A cm}^{-2}_{\text{Pt}}$ , a much higher Tafel slope of  $\approx 120 \text{ mV dec}^{-1}$  was found. This apparent increase in Tafel slope has previously been ascribed to a shift in the rate determining step of the ORR, leading to an increase in Tafel slope from  $70 \text{ mV dec}^{-1}$  ( $\alpha_c = 1$ ) to  $140 \text{ mV dec}^{-1}$  ( $\alpha_c = 0.5$ ).<sup>74,75</sup> However, this increase had been hypothesized to be due to a potential dependent change in the surface coverage of Pt with oxygen-containing species,<sup>74,75</sup> which clearly cannot explain the higher Tafel slopes at potentials

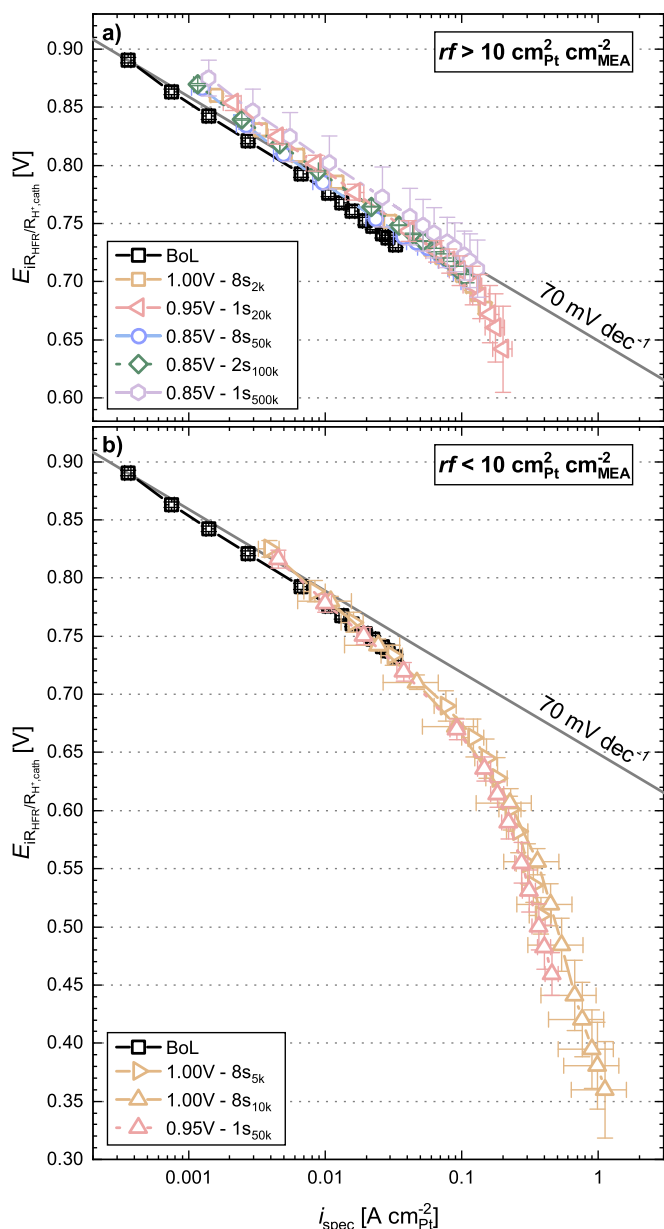


**Figure 7.** Tafel plot representation of HFR- and  $R_{H^+, cath}$ -corrected potential vs specific current density of differential flow  $H_2/O_2$  (2000/5000 nccm) polarization curves at 170 kPa<sub>abs</sub>, 80 °C, and 95% RH after different ASTs (in the figure, the respective cycle numbers are given as indices for each AST protocol). (a) Aged cathodes with  $rf > 10 \text{ cm}^2_{Pt} \text{ cm}^2_{MEA}$  (corresponding to either the  $H_2$ /air performance at EoL or near EoL, i.e., above the horizontal red dashed line in Fig. 3); (b) aged cathodes with  $rf < 10 \text{ cm}^2_{Pt} \text{ cm}^2_{MEA}$  (corresponding to three data sets below the horizontal red dashed line in Fig. 3). Error bars represent the mean absolute deviation between two independent measurements (aged electrodes), or the standard deviation of all MEAs (BoL). The black solid line with a slope of  $70 \text{ mV dec}^{-1}$  that very closely describes the BoL performance serves as a guide-to-the-eye. Error bars represent the mean absolute deviation between two independent measurements.

above 0.75 V (i.e., between 0.005–0.030  $\text{A cm}^{-2}_{Pt}$  in Fig. 7b). It has also been suggested that higher Tafel slopes might be the result of additional local proton conduction resistances in the vicinity of the Pt nanoparticles, which would not be captured by through-plane proton conduction resistance measurements (i.e., by the thus determined  $R_{H^+, cath}$  value).<sup>76</sup> While a  $\approx 50 \text{ mV dec}^{-1}$  increase in Tafel slope (i.e., from  $\approx 70$  to  $\approx 120 \text{ mV dec}^{-1}$ ) is quite severe, it should be noted that in a Pt dissolution/redeposition degradation mechanism, where reversible Pt dissolution/redeposition concurs

with irreversible Pt loss into the membrane, it may be possible that the last remaining large Pt particles in the cathode electrode (at extremely low  $rf$ ) could be poorly contacted by the proton conducting ionomer, which would also lead to an additional voltage loss that is not captured by the commonly used diagnostics.

For all electrodes shown in Fig. 7, very large deviations from the  $\approx 70 \text{ mV dec}^{-1}$  Tafel slope are observed at specific current densities above  $\approx 0.10 \text{ A cm}^{-2}_{Pt}$  (Fig. 7a) or already above  $\approx 0.03 \text{ A cm}^{-2}_{Pt}$  in case of very low roughness factors (Fig. 7b), with apparent Tafel slopes of several hundreds of  $\text{mV dec}^{-1}$ . This cannot be explained by a change in the reaction mechanism alone anymore, and is most likely the result of a Pt-specific oxygen mass transport resistance. Although oxygen mass transport in the gas phase can be neglected for the here shown measurements with pure  $O_2$ , additional local  $O_2$  transport resistances at the Pt/ionomer interface have widely been reported in the literature.<sup>17,19,48,71</sup> These local  $O_2$  transport resistances that are inversely proportional to the  $rf$  value will be discussed in detail in the next section.

To determine the kinetic ORR activity, a linear regression performed in the current range between 50–500  $\text{mA cm}^{-2}_{MEA}$  for  $rf$  values  $> 10 \text{ cm}^2_{Pt} \text{ cm}^2_{MEA}$  (see Fig. 7a) or 50  $\text{mA cm}^{-2}_{MEA}$  – 50  $\text{mA cm}^{-2}_{Pt}$  for  $rf$  values  $< 10 \text{ cm}^2_{Pt} \text{ cm}^2_{MEA}$  (see Fig. 7b) was used to extrapolate the current density to 0.9 V. Hereby, the lower current density limit was chosen to ensure a ten-fold higher ORR than the  $H_2$ -crossover current, while the upper limit was chosen to ensure an accurate representation of the first Tafel slope. The obtained current densities normalized to the Pt mass then yield the ORR mass activities ( $i_{0.9V}^{mass}$  in  $\text{A g}_{Pt}^{-1}$ ; normalized to the initial Pt mass in the cathode catalyst layer) or, when normalized to the roughness factor, yield the specific ORR activities ( $i_{0.9V}^{spec}$  in  $\text{mA cm}^{-2}_{Pt}$ ). Both are summarized in Fig. 8 as a function of  $rf$ ; the gray shaded area indicates  $rf$  values below  $10 \text{ cm}^2_{Pt} \text{ cm}^2_{MEA}$ , where only semi-quantitative values for  $rf$  and the ORR activity can be obtained due to large errors in the ECSA evaluation (see Fig. 2) and in the extrapolation to 0.9 V. The BoL ORR mass activities of  $\approx 170$ – $200 \text{ A g}_{Pt}^{-1}$  (left-most points in Fig. 8a) and specific activities of  $\approx 0.24 \text{ mA cm}^{-2}_{Pt}$  (left-most points in Fig. 8b) are essentially identical with those reported in a recent voltage cycling study by Padgett et al.<sup>23</sup> for the same catalyst (TEC10V20E from Tanaka), but are  $\approx 30\%$  higher than previously reported by our group ( $115$ – $135 \text{ A g}_{Pt}^{-1}$ ).<sup>10</sup> Over the course of voltage cycling, the mass activity gradually decreased down to  $\approx 27 \text{ A g}_{Pt}^{-1}$  for the lowest  $rf$  value of  $\approx 3 \text{ cm}^2_{Pt} \text{ cm}^2_{MEA}$ . Although a decrease in ORR mass activity with decreasing available Pt surface area is expected,<sup>64</sup> it clearly is not directly proportional to  $rf$ . After the first 100 aging cycles, an  $i_{0.9V}^{mass}$  loss of  $\approx 10\%$  compared to BoL is observed (see second points from the left in Fig. 8a), although the ECSA losses and thus the  $rf$  losses range between  $\approx 15\%$ – $25\%$  (see Table II). This is related to an increase in Pt particle size upon voltage cycling, whereby the higher specific activity of larger Pt particles partially compensates for the lower  $rf$ .<sup>63,64,77</sup> After these first 100 cycles, the mass activity observed in this study agrees reasonably well with the activity observed by Harzer et al. after the same  $rf$  loss ( $140$ – $160 \text{ A g}_{Pt}^{-1}$ ), indicating that their BoL values were the result of an incomplete activation, as they observed a gain in  $i_{0.9V}^{mass}$  in the first 100 cycles.

Over the course of the cycling ASTs, all mass activity curves follow the same trend and show a  $\approx 10$ -fold reduced mass activity at the lowest measured  $rf$  values. Again, Padgett et al.<sup>23</sup> reported similar results for  $i_{0.9V}^{mass}$  after voltage cycling between 0.6 and 0.95 V using trapezoidal voltage profiles (hold time of 2.5 s and ramp time of 0.5 s), with a remaining mass activity of  $\approx 70 \text{ A g}_{Pt}^{-1}$  at  $24 \pm 2\%$  ECSA retention (EoL) compared to  $\approx 85 \text{ A g}_{Pt}^{-1}$  at  $20 \text{ cm}^2_{Pt} \text{ cm}^2_{MEA}$  ( $\approx 25\%$  ECSA retention) obtained in this study. This comparability of different aging procedures (trapezoidal vs square wave profiles, and variations in hold time and UPL) used by different groups with

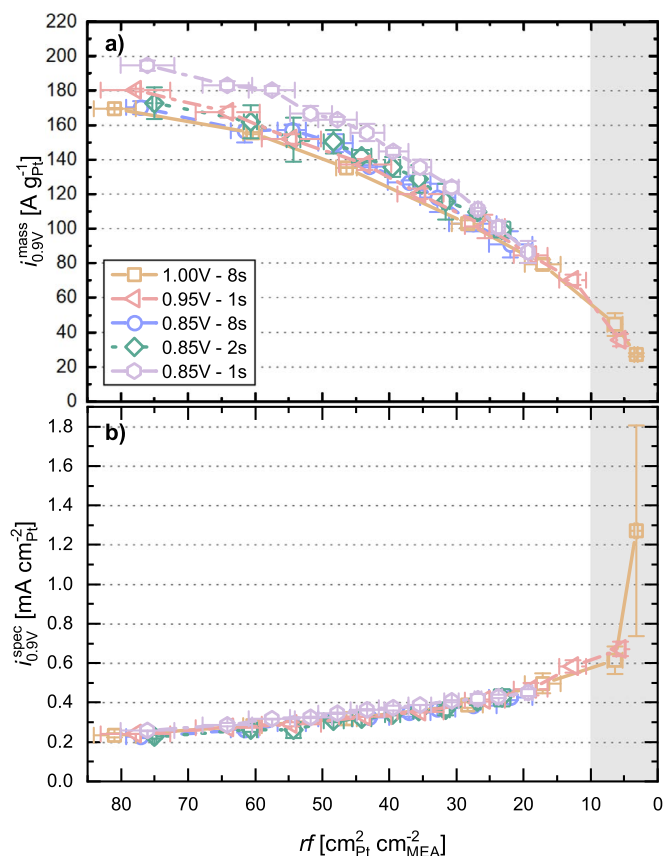


**Figure 8.** Variation of the ORR activity of the cathode catalyst determined at 80 °C, 0.9 V, and 125 kPa O<sub>2</sub> partial pressure over the course of voltage cycling ASTs as a function of  $rf$  (the left-most values represent BoL): (a) ORR mass activity ( $i_{0.9V}^{mass}$ ) and (b) ORR specific activity ( $i_{0.9V}^{spec}$ ). The ORR activity data were extracted from HFR- and  $R_{H^+, cath}$ -corrected Tafel plots by linear extrapolation to 0.9 V of the data between 50–500 mA cm<sub>MEA</sub><sup>-2</sup> (for  $rf > 10$  cm<sub>Pt</sub><sup>2</sup> cm<sub>MEA</sub><sup>-2</sup>) or between 50 mA cm<sub>MEA</sub><sup>-2</sup> – 50 mA cm<sub>Pt</sub><sup>2</sup> (for  $rf < 10$  cm<sub>Pt</sub><sup>2</sup> cm<sub>MEA</sub><sup>-2</sup>). The gray shaded area marks the data for which the  $rf$  value and the ORR activity at 0.9 V could only be determined semi-quantitatively. Error bars represent the mean absolute deviation between two independent measurements.

different setups, yielding similar mass activity values at the same  $rf$  and ECSA loss for the same catalyst and catalyst loading, reveals that voltage cycling ASTs under the specified conditions (e.g., UPL ≤ 1.0 V, no RH cycling) result in a similar aging mechanism. The degradation rate can be enhanced with increasing UPL and hold times, but it will reveal similar catalyst characteristics, i.e., essentially identical ORR mass activities at same cathode  $rf$ , as shown in Fig. 8a.

This conclusion is reinforced by comparing the specific ORR activities for the employed ASTs as a function of cathode  $rf$  (Fig. 8b). Overall,  $i_{0.9V}^{spec}$  increases with decreasing  $rf$ , which is again consistent with the increase in Pt particle size, as the initially smaller nanoparticles have a large amount of less active edge and corner sites compared to larger particles and thus exhibit lower specific ORR activity.<sup>63,64,77</sup> Again, the values obtained in this study correlate well with other studies, where for a  $rf$  of  $\approx 20$  cm<sub>Pt</sub><sup>2</sup> cm<sub>MEA</sub><sup>-2</sup> the here determined specific activity of  $\approx 0.45$  mA cm<sub>Pt</sub><sup>-2</sup> (see Fig. 8b) compares well with those by Padgett et al.<sup>23</sup> ( $\approx 0.37$  mA cm<sub>Pt</sub><sup>-2</sup>) and by Harzer et al.<sup>10</sup> ( $\approx 0.43$  mA cm<sub>Pt</sub><sup>-2</sup>); the BoL values here and in these other two studies are all at  $\approx 0.2$  mA cm<sub>Pt</sub><sup>-2</sup>.

However, it is surprising that all curves lie perfectly on top of each other. While the same specific activity would be expected for Pt particles of the same size, the  $rf$  loss is the combined result of Pt loss into the membrane/ionomer phase and a Pt particle size increase due

to Oswald ripening. The fact that the same specific activity is observed at identical  $rf$  values for vastly different aging procedures, e.g., at  $\approx 28$  cm<sub>Pt</sub><sup>2</sup> cm<sub>MEA</sub><sup>-2</sup> (corresponding to  $\approx 35\%$  normalized ECSA in Fig. 3a) after 1,000 cycles for the 1.00 V–8s AST (orange squares in Fig. 8b) and after 100,000 cycles for the 0.85 V–1s AST (violet hexagon symbols), indicates that they result in the same Pt particle size distribution and that therefore the fraction of Pt lost into the membrane/ionomer phase must be essentially the same for the different ASTs here examined (see Figs. 4c and 4d). Importantly, this implies that the here used voltage cycling ASTs with limited UPL (≤1.0 V) and nearly full humidification (95% RH) accelerate the exact same degradation mechanism, as long as other degradation mechanisms like carbon support corrosion (relevant at UPLs above 1.0 V) and/or ionomer/membrane degradation (relevant at low RH) do not play a significant role. As the different UPL values and the hold times should cover reasonably well the transient voltage profiles encountered in PEMFC applications (in the absence of start-up/shut-down events), the very same degradation mechanism would be expected for real applications.

Finally, it needs to be emphasized that the strong and sudden increase in  $i_{0.9V}^{spec}$  for very low  $rf$  values in Fig. 8b (see gray shaded area) is, as discussed above, a likely artefact due to the above discussed measurement uncertainties, so that the respective values should be treated with caution.

**Dependence of O<sub>2</sub> transport resistances on cathode  $rf$ .**—Based on the established method from Baker et al.,<sup>41</sup> the O<sub>2</sub> transport resistances were measured by limiting current measurements over the course of the voltage cycling ASTs (see scheme in Fig. 1). Exemplarily, Fig. 9a shows the limiting current densities ( $i_{lim}$ ) that were recorded at 170 kPa<sub>abs</sub> for the same MEA at BoL ( $rf \approx 80$  cm<sub>Pt</sub><sup>2</sup> cm<sub>MEA</sub><sup>-2</sup>, filled squares) as well as after 2,000 cycles ( $rf \approx 15$  cm<sub>Pt</sub><sup>2</sup> cm<sub>MEA</sub><sup>-2</sup>, half-filled triangles) and 10,000 cycles ( $rf \approx 3$  cm<sub>Pt</sub><sup>2</sup> cm<sub>MEA</sub><sup>-2</sup>, empty triangles) of the 1.00 V–8s AST procedure. As expected, the limiting current density is nearly vertical for the pristine MEA between 0.2 V and 0.1 V for all oxygen concentrations, and up to 0.3 V for the lower O<sub>2</sub> concentration of 2, 4, and 7%. At 0.05 V, the limiting current density slightly increases due to additional hydrogen evolution.<sup>48</sup>

With decreasing  $rf$ , the now lower currents start to deviate from their potential independence at low potentials. To highlight this, a close-up of the limiting current data for the aged cathode with a remaining  $rf$  of only  $\approx 3$  cm<sub>Pt</sub><sup>2</sup> cm<sub>MEA</sub><sup>-2</sup> is shown in Fig. 9b. Here, a “Z-shape” form of current vs potential is clearly observed for all oxygen concentration, with an apparent minimum value of the currents at  $\approx 0.15$ –0.2 V. This introduces an obvious ambiguity with regard to the determination of the “correct” limiting current density. Greszler et al. observed similar trends for the limiting current data of a low-loaded MEA with a Pt/Vulcan cathode catalyst (0.03 mg<sub>Pt</sub> cm<sub>MEA</sub><sup>-2</sup>), showing a decrease (“turn-back”) in limiting current from 0.2 to 0.1 V, before increasing again below 0.1 V. They attributed this to a transition from the typical four-electron oxygen reduction (water formation) to a two-electron process (hydrogen peroxide formation), which reduces the number of electrons per oxygen molecule and therefore the mass transport limited current density.<sup>48</sup> This is consistent with rotating ring disk electrode measurements by other researchers, who showed an increasing formation of hydrogen peroxide at low potentials with a decrease in ECSA (i.e., with decreasing  $rf$ ).<sup>78,79</sup> As this “Z-shape” introduces large ambiguity in the determination of the limiting current density, the maximum current density obtained at potentials >0.1 V (to avoid effects from the hydrogen evolution reaction) was taken in this study as the best possible approximation of the limiting current density. Therefore, the thus estimated  $i_{lim}$  value is clearly less than the true  $i_{lim}$  value, which in turn means that it will lead to an overestimation of the O<sub>2</sub> transport resistance (see below).

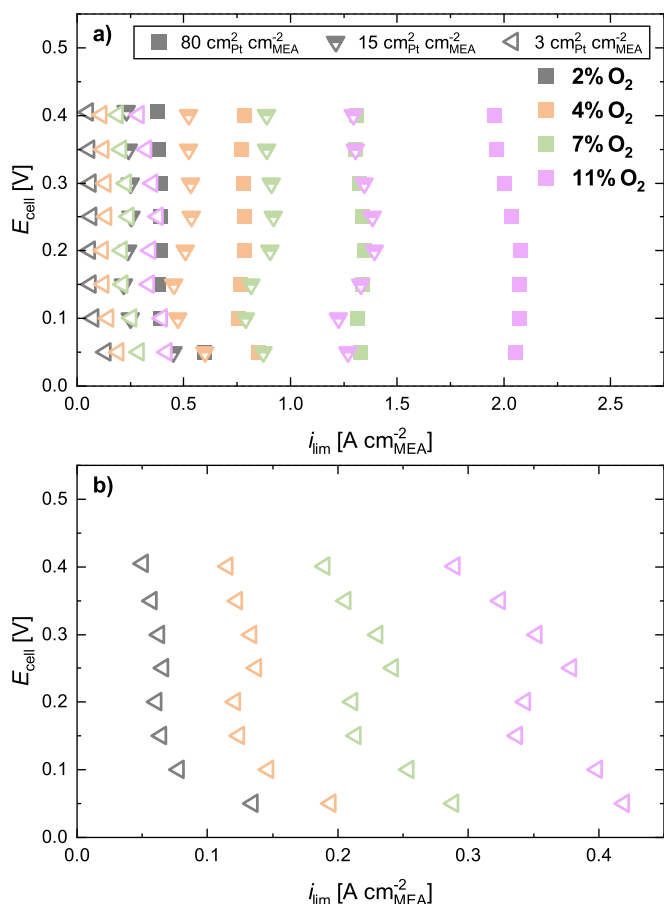


**Figure 9.** (a) Limiting current measurement in the potential range between 0.40 V and 0.05 V using  $O_2$  concentrations of 2% (gray), 4% (orange), 7% (green) and 11% (magenta) in  $N_2$  (on a dry gas basis) for a representative cathode at BoL ( $\approx 80 \text{ cm}_{Pt}^2 \text{ cm}_{MEA}^{-2}$ , filled squares), after 2,000 cycles ( $\approx 15 \text{ cm}_{Pt}^2 \text{ cm}_{MEA}^{-2}$ ; half-filled triangles), and after 10,000 cycles ( $\approx 3 \text{ cm}_{Pt}^2 \text{ cm}_{MEA}^{-2}$ , empty triangles) of the 1.00 V–8s voltage cycling AST. (b) Zoomed-in view at low current densities for the data after 10,000 cycles ( $\approx 3 \text{ cm}_{Pt}^2 \text{ cm}_{MEA}^{-2}$ ), showing a pronounced “Z-shape.” The measurements were performed at 170  $kPa_{abs}$ , 80 °C, and 95% RH using 2000 nccm  $H_2$  and 5000 nccm ( $O_2$  in  $N_2$ ) on anode and cathode, respectively.

At each pressure, the total  $O_2$  transport resistance ( $R_{O_2}^{total}$ ) was then calculated from the determined/approximated limiting currents ( $i_{lim}$ ) at each oxygen concentration ( $c_{O_2}$ ) according to Eq. 3, where  $F$  is the faradaic constant ( $96485 \text{ C mol}^{-1}$ ),<sup>41</sup>

$$R_{O_2}^{total} = \frac{4Fc_{O_2}}{i_{lim}} \quad [3]$$

For low oxygen concentrations, the transport mechanism is generally characterized by oxygen transport in the so-called “dry region,”<sup>80</sup> in which  $R_{O_2}^{total}$  vs the limiting current density is constant and therefore independent of the oxygen concentration at any given pressure. This independence of  $R_{O_2}^{total}$  vs  $i_{lim}$  (and vs  $c_{O_2}$ ) can be seen in Fig. 10a for the BoL data with  $rf \approx 80 \text{ cm}_{Pt}^2 \text{ cm}_{MEA}^{-2}$  (solid squares), marked by the horizontal lines for each pressure (the corresponding  $i_{lim}$  data at 170  $kPa_{abs}$  are shown in Fig. 9a). The same is observed for the MEA after 2,000 cycles of the 1.00 V–8s voltage cycling AST ( $rf \approx 15 \text{ cm}_{Pt}^2 \text{ cm}_{MEA}^{-2}$ ; half-filled triangles). However, after 10,000 cycles of the 1.00 V–8s AST ( $rf \approx 3 \text{ cm}_{Pt}^2 \text{ cm}_{MEA}^{-2}$ , empty triangles), this independence of  $R_{O_2}^{total}$  on  $i_{lim}$  is not anymore observed, and the  $R_{O_2}^{total}$  data show a significant scatter. This must be due to the above described issue that the true value of  $i_{lim}$  cannot

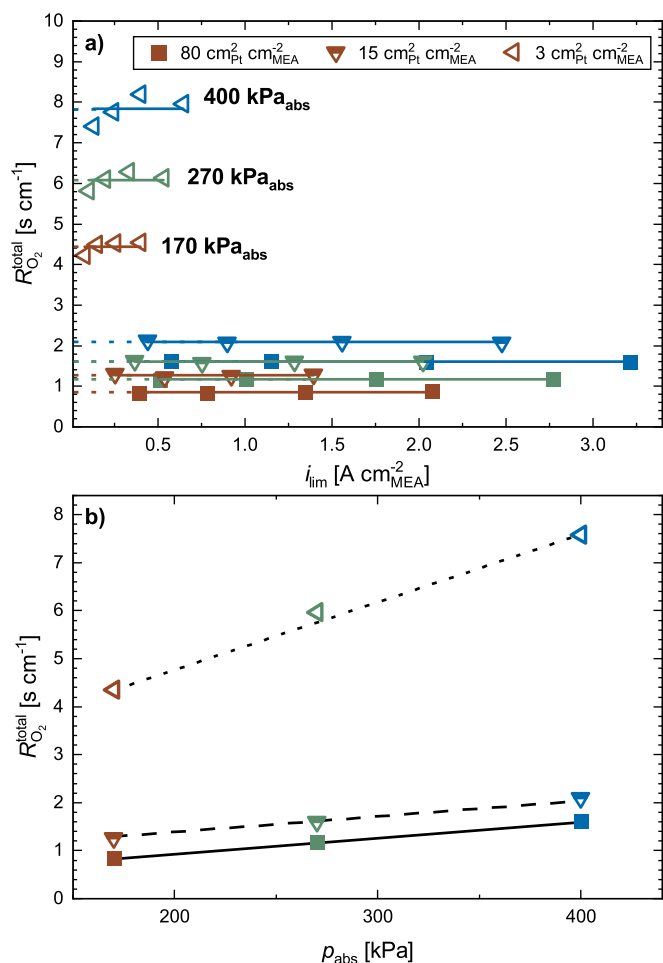


**Figure 10.** (a) Total  $O_2$  transport resistance ( $R_{O_2}^{total}$ ) vs limiting current density ( $i_{lim}$ ) for a representative cathode at BoL ( $\approx 80 \text{ cm}_{Pt}^2 \text{ cm}_{MEA}^{-2}$ , filled squares), after 2,000 cycles ( $\approx 15 \text{ cm}_{Pt}^2 \text{ cm}_{MEA}^{-2}$ ; half-filled triangles), and after 10,000 cycles ( $\approx 3 \text{ cm}_{Pt}^2 \text{ cm}_{MEA}^{-2}$ , empty triangles) of the 1.00 V–8s voltage cycling procedure (same as in Fig. 9), recorded at pressures of 170, 270, and 400  $kPa_{abs}$  with 2, 4, 7, and 11%  $O_2$  in  $N_2$  (dry gas basis). The measurements were performed at 80 °C and 95% RH, and the horizontal lines show the averaged values of  $R_{O_2}^{total}$  for the various conditions. (b) Plot of  $R_{O_2}^{total}$  of the different cathodes as a function of pressure, used for the deconvolution of  $R_{O_2}^{total}$  into a pressure-dependent ( $R_{O_2}^{PD}$ ) and a pressure-independent ( $R_{O_2}^{PI}$ ) term according to Baker et al.<sup>41</sup>

be reliably determined at low  $rf$  values, so that the estimated  $R_{O_2}^{total}$  values only represent their uppermost limit.

According to Baker et al., the total  $O_2$  transport resistance can be divided in a pressure-independent contribution ( $R_{O_2}^{PI}$ ) and a pressure-dependent contribution ( $R_{O_2}^{PD}$ ) via a linear regression of  $R_{O_2}^{total}$  vs the absolute pressure (see Fig. 10b).<sup>41</sup> The pressure-independent  $O_2$  transport resistance consists of various contributions, namely Knudsen diffusion in the small pores of the catalyst layer and the microporous layer (MPL) as well as the so-called local  $O_2$  resistance ( $R_{O_2}^{local}$ ), which is a function of  $rf$  and that is often associated to diffusion in the ionomer and liquid water phase.<sup>48,69,73,81</sup> On the other hand, the pressure-dependent transport resistance is mostly associated with the molecular diffusion of  $O_2$  in the GDL and, in part, in the MPL and in the catalyst layer.  $R_{O_2}^{PD}$  is therefore expected to remain constant as long as the pore structure of GDL, MPL, and catalyst layer are not affected, i.e., in the absence of conditions that lead to a corrosion of the catalyst carbon support (or the MPL/GDL). Since  $R_{O_2}^{PD}$  is characterized by the slope of  $R_{O_2}^{total}$  as a function of pressure, the slope is expected to remain constant throughout the

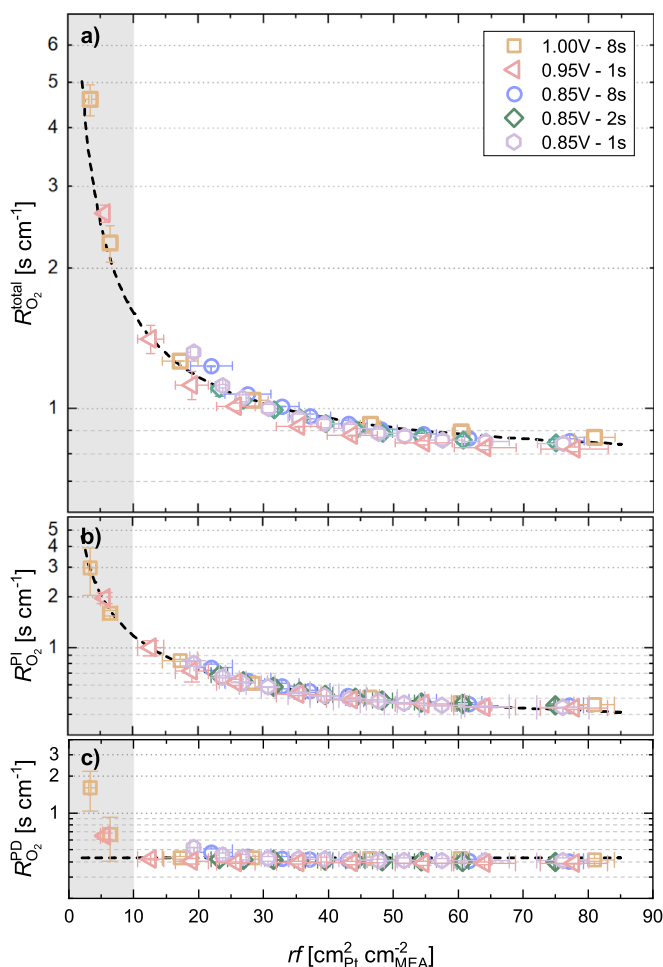


**Figure 11.** Variation of the O<sub>2</sub> mass transport resistance at 170 kPa<sub>abs</sub> with the cathode *rf* value over the course of the different voltage cycling ASTs: (a) total O<sub>2</sub> transport resistance ( $R_{O_2}^{total}$ ), (b) pressure-independent O<sub>2</sub> transport resistance ( $R_{O_2}^{PI}$ ), and (c) pressure-dependent O<sub>2</sub> transport resistance ( $R_{O_2}^{PD}$ ). The dashed black line in panel c corresponds to the averaged  $R_{O_2}^{PD}$  value of  $0.42 \pm 0.02 \text{ s cm}^{-1}$  (excluding the data in the gray shaded area). The dashed black line in panel b represents the fit of the  $R_{O_2}^{PI}$  data to Eq. 4 (excluding data in the gray shaded area), yielding  $R_{O_2}^{PI}|_{rf \rightarrow \infty} = 0.32 \pm 0.01 \text{ s cm}^{-1}$  and  $R_{O_2}^{local} = 8.6 \pm 0.2 \text{ s cm}^{-1}$ . The dashed black line in panel a is based on Eq. 5, using the above determined values of  $R_{O_2}^{PD}$ ,  $R_{O_2}^{PI}|_{rf \rightarrow \infty}$ , and  $R_{O_2}^{local}$  to calculate  $R_{O_2}^{total}$  vs cathode *rf*. The gray shaded area marks the *rf* region for which the calculated O<sub>2</sub> transport resistances are considered inaccurate due to the undefined limiting current values (see Fig. 9b) and the higher errors in the determination of the cathode *rf* values (see Fig. 2).

aging, which is observed as long as  $R_{O_2}^{total}$  could be determined reliably, i.e., for  $rf > 10 \text{ cm}^2_{Pt} \text{ cm}^{-2}_{MEA}$  (see half-filled triangles and solid squares in Fig. 10b). However, data for the MEAs with a lower *rf* did not fit the linear model quite as good, and the slope is much higher (empty triangles in Fig. 10b).

The obtained values for  $R_{O_2}^{total}$ ,  $R_{O_2}^{PI}$ , and  $R_{O_2}^{PD}$  at 170 kPa<sub>abs</sub> vs cathode *rf* over the course of the different voltage cycling ASTs are summarized in Fig. 11. Quite strikingly, the values for the oxygen transport related resistances do not depend on the aging procedure but exclusively depend on the cathode *rf*, thereby again suggesting that the different here examined voltage cycling ASTs apparently induce the same degradation mechanism. Over the course of aging, i.e., with decreasing cathode *rf*, the total oxygen transport resistance increases (Fig. 11a), similar to the increase of  $R_{O_2}^{total}$  with decreasing cathode catalyst loading (i.e., with decreasing cathode *rf*) that was observed by Greszler et al.<sup>48</sup> On the other hand,  $R_{O_2}^{PD}$  remains essentially constant for all *rf* values of  $>10 \text{ cm}^2_{Pt} \text{ cm}^{-2}_{MEA}$

(Fig. 11c), as would be expected under conditions where the corrosion of the cathode catalyst carbon support is negligible (i.e., for UPL  $\leq 1.0 \text{ V}$ ); the apparent increase of  $R_{O_2}^{PD}$  at lower *rf* values (data points in the gray shaded area in Fig. 11c) is, we believe, caused by the large errors in the quantification of  $i_{lim}$  (see Fig. 9b) and *rf* (see Fig. 2) at very low *rf* values (further substantiated below). An analogous increase of  $R_{O_2}^{PD}$  with decreasing cathode *rf* was also observed in other voltage cycling AST studies<sup>10</sup> as well as for pristine MEAs that were prepared with different catalysts and/or different catalyst loadings<sup>18</sup> (i.e., with different BoL cathode *rf*).

Therefore, Fig. 11 shows that the increase in  $R_{O_2}^{total}$  with decreasing cathode *rf* is mainly the result of an increasing  $R_{O_2}^{PI}$  (see Fig. 11b), which in turn results from the *rf*-dependent contribution of the so-called local O<sub>2</sub> resistance ( $R_{O_2}^{local}$ ).<sup>10,17,48</sup> As mentioned earlier, the contribution of  $R_{O_2}^{local}$  has been reported to be inversely proportional to  $rf$ .<sup>48</sup> It is therefore possible to disentangle the *rf*-independent fraction of  $R_{O_2}^{PI}$ , namely the Knudsen diffusion in catalyst layer and MPL that would still be expected for a hypothetical infinite cathode *rf* ( $R_{O_2}^{PI}|_{rf \rightarrow \infty}$ ), and  $R_{O_2}^{local}$  by fitting  $R_{O_2}^{PI}$  to Eq. 4:

$$R_{O_2}^{PI} = R_{O_2}^{PI}|_{rf \rightarrow \infty} + \frac{R_{O_2}^{local}}{rf} \quad [4]$$

A least-squares fit of all the measured  $R_{O_2}^{PI}$  data for a cathode *rf* of  $>10 \text{ cm}^2_{Pt} \text{ cm}^{-2}_{MEA}$  (i.e., excluding the data in the gray shaded area in Fig. 11) is given by the black dashed line in Fig. 11b, whereby a *rf*-independent fraction of  $R_{O_2}^{PI}|_{rf \rightarrow \infty} = 0.32 \pm 0.01 \text{ s cm}^{-1}$  and a local oxygen transport resistance of  $R_{O_2}^{local} = 8.6 \pm 0.2 \text{ s cm}^{-1}$  were obtained. This  $R_{O_2}^{local}$  value at 80 °C and 95% RH agrees reasonably well with the local oxygen transport resistance of  $\approx 12 \text{ s cm}^{-1}$  that was obtained at 80 °C and 62% RH by Greszler et al.,<sup>48</sup> perhaps suggesting a slight decrease of  $R_{O_2}^{local}$  with RH. According to the above discussion, an average  $R_{O_2}^{PD}$  of  $0.42 \pm 0.02 \text{ s cm}^{-1}$  (indicated by the dashed black line in Fig. 11c) was obtained at 170 kPa<sub>abs</sub> for all data points (excluding those in the gray shaded area). Taking all of these observations into account, the pressure- and *rf*-dependence of the total O<sub>2</sub> transport resistance can be summarized by Eq. 5 (dashed line in Fig. 11a):

$$R_{O_2}^{total} = R_{O_2}^{PD} + R_{O_2}^{PI} = R_{O_2}^{PD} + R_{O_2}^{PI}|_{rf \rightarrow \infty} + \frac{R_{O_2}^{local}}{rf} \quad [5]$$

Using the above determined values of  $R_{O_2}^{PD}$ ,  $R_{O_2}^{PI}|_{rf \rightarrow \infty}$ , and  $R_{O_2}^{local}$ , the values of  $R_{O_2}^{total}$  vs *rf* calculated by Eq. 5 are shown by the black dashed line in Fig. 11a. Even at values that were excluded from the fits because the determination of  $i_{lim}$  was deemed unreliable at  $rf < 10 \text{ cm}^2_{Pt} \text{ cm}^{-2}_{MEA}$  (gray shaded area in Fig. 11), the  $R_{O_2}^{total}$  values predicted by Eq. 5 represent the measured  $R_{O_2}^{total}$  values surprisingly well. It can therefore be concluded that although the limiting current measurements for severely degraded cathodes (i.e., cathodes with  $rf < 10 \text{ cm}^2_{Pt} \text{ cm}^{-2}_{MEA}$ ) are prone to errors due to the increasing impact of HER currents and a possible H<sub>2</sub>O<sub>2</sub> reaction pathway, a reasonably accurate experimental quantification of  $R_{O_2}^{total}$  seems to be still possible but that a distinction between  $R_{O_2}^{PI}$  and  $R_{O_2}^{PD}$  is not.

**Dependence of the H<sub>2</sub>/air performance on cathode.**—As discussed above, the H<sub>2</sub>/air performance deteriorates over the course of a voltage cycling AST (see Fig. 5), owing to a combination of decreasing Pt ECSA (see Fig. 3), decreasing ORR mass activity (see Fig. 8a), and increasing oxygen transport resistance (see Fig. 11).

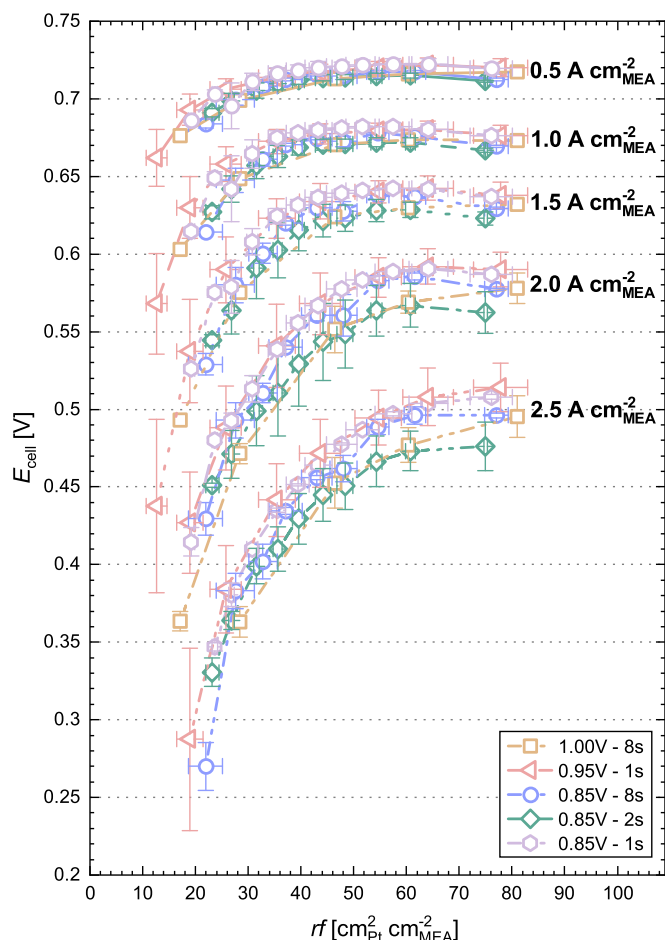


**Figure 12.** Measured cell voltages in differential flow  $\text{H}_2/\text{air}$  polarization curves for various geometric current densities (0.5, 1.0, 1.5, 2.0, and  $2.5 \text{ A cm}^{-2}_{\text{MEA}}$ ) as a function of cathode  $rf$  over the course of the different voltage cycling ASTs (see legend in the figure). The measurements were performed in  $\text{H}_2/\text{air}$  (2000/5000 nccm) at  $170 \text{ kPa}_{\text{abs}}$ ,  $80^\circ \text{C}$ , and  $95\% \text{ RH}$  (cell voltages for  $rf < 10 \text{ cm}^2_{\text{Pt}} \text{ cm}^2_{\text{MEA}}$  are not shown). The BoL performance corresponds to the right-most data point for each AST procedure, and error bars represent the mean absolute deviation between two independent measurements.

Based on the pronounced correlation of all the investigated voltage loss contributions with cathode  $rf$  (except for the  $HFR$  and the cathode proton conduction resistance, which are unaffected by voltage cycling), this section now aims to correlate the PEMFC performance in  $\text{H}_2/\text{air}$  with the cathode  $rf$ .

Figure 12 shows the measured  $\text{H}_2/\text{air}$  cell voltages at different geometric current densities as a function of  $rf$ , plotting the data obtained over the course of all of the five examined voltage cycling ASTs (see Table I). Overall, it can be seen for each current density that the measured cell voltages match surprisingly well between the different AST protocols (see Table IV), whereby the scatter between the measurements is mostly the result of variations in the BoL performance (see right-most data points in Fig. 12, with the largest BoL performance deviation observed for the MEAs used for the  $0.85 \text{ V}-2\text{s}$  AST (green diamonds)). As discussed in the preceding sections, ORR mass activities and oxygen mass transport resistances solely depend on the cathode  $rf$ , so that also the kinetic and transport induced overpotentials must be exclusive functions of the cathode  $rf$ . Especially in the high current density region, the  $\text{H}_2/\text{air}$  cell voltage is most strongly affected by the oxygen mass transport resistance that increases with decreasing cathode  $rf$ , as seen for the highest current density (i.e., at  $2.5 \text{ A cm}^{-2}_{\text{MEA}}$ ; lowermost curve in Fig. 12), where the  $\text{H}_2/\text{air}$  cell voltage curve already starts to bend downwards once the roughness factor has decreased to  $\approx 55 \text{ cm}^2_{\text{Pt}} \text{ cm}^2_{\text{MEA}}$

(corresponding to an  $ECSA/rf$  loss of  $\approx 30\%$ ). At a cathode  $rf$  of  $\approx 30 \text{ cm}^2_{\text{Pt}} \text{ cm}^2_{\text{MEA}}$ , the average cell voltage loss at  $2.5 \text{ A cm}^{-2}_{\text{MEA}}$  compared to BoL already amounts to  $\approx 100 \text{ mV}$  (see last row in Table IV). In contrast, at low current densities (e.g.,  $0.5 \text{ A cm}^{-2}_{\text{MEA}}$ ; uppermost curves in Fig. 12), the performance losses are mostly governed by ORR mass activity losses and the  $\text{H}_2/\text{air}$  cell voltage remains therefore rather constant up to low  $rf$  values, amounting to only  $\approx 10 \text{ mV}$  at  $\approx 30 \text{ cm}^2_{\text{Pt}} \text{ cm}^2_{\text{MEA}}$  (see second row in Table IV). However, even at  $0.5 \text{ A cm}^{-2}_{\text{MEA}}$ , substantial mass transport losses become apparent below  $rf \approx 30 \text{ cm}^2_{\text{Pt}} \text{ cm}^2_{\text{MEA}}$ , as indicated by the sharp downturn of the cell voltage curve.

All in all, a surprisingly universal correlation between  $\text{H}_2/\text{air}$  performance and cathode  $rf$  was found for the five different voltage cycling ASTs with upper potentials between  $0.85$  and  $1.0 \text{ V}$  and with hold times of  $1$  to  $8 \text{ s}$ . This strongly suggests that the governing aging mechanisms are the same under the here chosen conditions (viz., Pt dissolution/redeposition), which however should represent those in actual PEMFC systems in the absence of start-up/shut-down events and ionomer degradation. Under these constraints (no start-up/shut-down events and high  $RH$  to avoid chemical degradation of the ionomer), this correlation should allow for the prediction of voltage losses arising from load cycling.

#### Voltage cycling induced $\text{H}_2/\text{air}$ performance loss prediction over large cycle numbers.—

For the examined upper potential limits ( $0.85$ – $1.0 \text{ V}$ ) and hold times ( $1$ – $8 \text{ s}$ ), the above analysis shows that the cathode  $rf$  loss uniquely governs the loss in  $\text{H}_2/\text{air}$  performance (see Fig. 12). This can be used to project the voltage cycling induced  $\text{H}_2/\text{air}$  performance losses up to very large cycle numbers under application-relevant conditions where the degradation is slow (e.g., low UPL values), considering the following two observations: (i) The empirical correlation that the cathode  $rf$  (or  $ECSA$ ) after the first  $100$  cycles decreases linearly with the logarithm of the cycle number (until  $rf \approx 10 \text{ cm}^2_{\text{Pt}} \text{ cm}^2_{\text{MEA}}$ ; see Fig. 3a), so that the change of  $ECSA/rf$  can be extrapolated over quite a large cycle number range; (ii) The finding that the cathode  $rf$  loss can be accelerated by high UPL values (but restricted to  $\leq 1.0 \text{ V}$  in order to avoid carbon corrosion) and by shorter hold times (down to  $1 \text{ s}$ ) without affecting the  $\text{H}_2/\text{air}$  performance vs cathode  $rf$  correlation (see Fig. 12).

Based on these observations, we propose a novel approach to predict the load cycling limited lifetime of MEAs based on two sets of measurements, which is schematically depicted in Fig. 13. In order to reduce the measurement time that would be required to determine the voltage cycling induced degradation under application-relevant operating conditions (i.e.,  $\text{UPL} < 0.9 \text{ V}$ ), a voltage cycling AST is first conducted under harsh cycling conditions (i.e.,  $0.95$ – $1.0 \text{ V}$  UPL and  $1 \text{ s}$  hold time), thereby enabling a characterization of the full  $rf$  range down to low  $rf$  values within a low number of cycles that require relatively little measurement time (see step 1 in Fig. 13a). In a second set of measurements, an application-relevant voltage cycling protocol (i.e., with a UPL of  $0.85 \text{ V}$  or below) is employed to determine the characteristic cathode  $rf$  degradation rate under application-relevant conditions (step 2 in Fig. 13a). This procedure is performed within a limited experimental time frame, whereby it is essential that the cathode  $rf$  degradation rate after the initial procedure-independent settle-in phase (i.e., an  $ECSA$  loss of  $\approx 15\%$ – $20\%$ , which with the here used Pt/Vulcan catalyst occurs after the first  $100$  cycles) is determined with great accuracy; subsequently, the voltage cycling procedure is continued until a cathode  $rf$  loss of  $\approx 40\%$ – $50\%$  is obtained. In this case, the cathode  $rf$  loss for a larger number of cycles can then be predicted by linear extrapolation of cathode  $rf$  vs the logarithm of the cycle number (step 3 in Fig. 13a), which has been observed to hold until  $\approx 10\%$ – $15\%$  of the initial cathode  $ECSA$  value (see Fig. 3). It should be noted that the settle-in phase is greatly important for this analysis: e.g., one could think of two (hypothetical) electrodes that have the same characteristic slope and  $rf$  value after the initial settle-in phase,

**Table IV.** Cell voltages obtained from H<sub>2</sub>/air performance measurements at geometric current densities of 0.5, 1.5, and 2.5 A cm<sup>-2</sup><sub>MEA</sub> for high, medium, and low cathode *rf* values, averaged over all measurements, i.e., over 5 different ASTs (see Table I) and two independent measurements per AST protocol. The given variation represents the standard deviation of the in total 10 independent measurements.

<i>rf</i> [cm <sup>2</sup> <sub>Pt</sub> cm <sup>-2</sup> <sub>MEA</sub> ]	E <sub>cell</sub> at 0.5 A cm <sup>-2</sup> <sub>MEA</sub>	E <sub>cell</sub> at 1.5 A cm <sup>-2</sup> <sub>MEA</sub>	E <sub>cell</sub> at 2.5 A cm <sup>-2</sup> <sub>MEA</sub>
77.4 ± 3.3 (BoL)	716 ± 5 mV	632 ± 7 mV	498 ± 16 mV
49.2 ± 3.6	717 ± 4 mV	633 ± 8 mV	470 ± 17 mV
30.2 ± 3.2	705 ± 8 mV	592 ± 20 mV	395 ± 24 mV

but in one case, this initial phase might require 10 times more cycles, resulting in a right-shift of the blue curve in Fig. 13a by one order of magnitude, and therefore in a 10-fold higher cycle number to reach a cathode *rf* loss of ≈40%-50% (this will be shown in a future publication).

The harsh AST experiment (purple symbols in Fig. 13a) should provide a good estimate of the H<sub>2</sub>/air performance vs cathode *rf* throughout the whole *rf* range (exemplarily shown in Fig. 13b for 1.0 and 2.0 A cm<sup>-2</sup><sub>MEA</sub>). This means that the expected *rf* for a defined EoL performance, e.g., 0.5 V at 2.0 A cm<sup>-2</sup><sub>MEA</sub> (pink shaded area in Fig. 13b, step 4), can be extracted from the H<sub>2</sub>/air cell voltage (at defined current densities) vs *rf* curve obtained for the harsh AST. In the example given in Fig. 13, this target of 0.5 V at 2.0 A cm<sup>-2</sup><sub>MEA</sub> would correspond to a final cathode *rf* of ≈27 cm<sup>2</sup><sub>Pt</sub> cm<sup>-2</sup><sub>MEA</sub> (pink area, step 5 in Fig. 13b). Finally, the projected number of cycles after which the EoL criteria of 0.5 V at 2.0 A cm<sup>-2</sup><sub>MEA</sub> would be expected to be reached for the application-relevant (i.e., less harsh) voltage cycling protocol is obtained by extrapolating the cathode *rf* vs logarithm of the cycle number line to the same *rf* of ≈27 cm<sup>2</sup><sub>Pt</sub> cm<sup>-2</sup><sub>MEA</sub> (crossing of the blue dashed line and the pink area in Fig. 13a; step 6), which in this example would be ≈300,000 cycles. As mentioned above, this is only valid if all other degradation mechanisms can be considered negligible.

**Expected behavior for different MEA types and different AST conditions.**—While this study did not investigate the dependence of the performance degradation over the course of voltage cycling ASTs conducted at different temperature, *RH*, lower potential limit, cathode gas composition (N<sub>2</sub> or air), or voltage cycle profiles, the impact of these factors is generally well understood.<sup>8–10,65,82,83</sup> Thus, it seems reasonable to assume that a linear behavior of the cathode *rf* vs the logarithm of the cycle number and the observed unique H<sub>2</sub>/air performance vs *rf* profile will be observed for other voltage cycling AST protocols with the same cathode electrode as long as the degradation is dominated by the platinum dissolution/redeposition mechanism. This should be the case within the following boundary conditions: (i) the UPL is low enough that the carbon corrosion rate at the respective temperature is negligible over the experiment duration;<sup>84,85</sup> (ii) chemical degradation of the ionomer/membrane that occurs during H<sub>2</sub>/air operation at low *RH* is avoided; (iii) mechanical and thermal degradation of the ionomer/membrane is prevented (limited number of *RH* cycles and operating temperatures <150 °C);<sup>86</sup> and (iv) absence of carbon support corrosion due to start-up/shut-down or (local) H<sub>2</sub> starvation events.<sup>3,5,84–86</sup> Within these restrictions, it should be possible to determine accelerating factors for a wide range of voltage/load cycling conditions by comparing the characteristic slopes for the same BoL configuration, i.e., the same MEA composition (particularly with respect to the cathode catalyst and the ionomer type/content in the cathode electrode) and the same cell hardware.

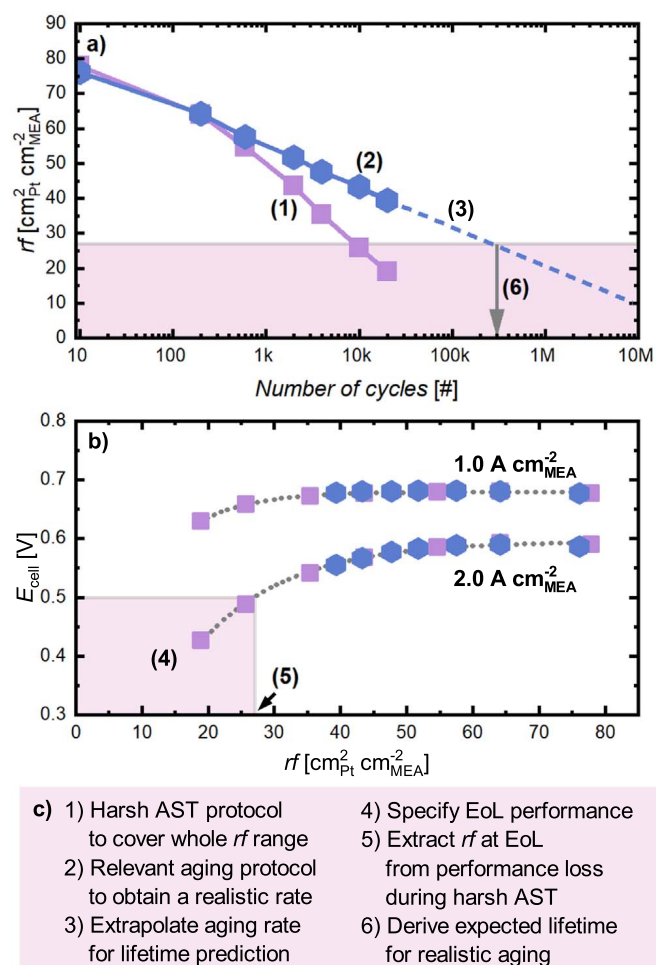


**Figure 13.** Scheme of the proposed approach to predict the voltage cycling losses of the H<sub>2</sub>/air performance over a large number of voltage cycles under application-relevant conditions (i.e., UPLs of <0.9 V) based on the data acquired for a harsh cycling protocol (i.e., conducted with an UPL of 0.95–1.0 V). (a) Cathode *rf* degradation for a harsh voltage cycling AST (purple squares) and for an application-relevant “mild” voltage cycling AST (blue hexagons). (b) H<sub>2</sub>/air performance as a function of cathode *rf* for two current densities. (c) Outline of the step-wise procedure to estimate the number of cycles after which the EoL criteria (here assumed to be 0.5 V at 2 A cm<sup>-2</sup><sub>MEA</sub>) are reached for the mild voltage cycling AST on the basis of the harsh voltage cycling AST data. The actual data points are taken from the 0.95 V–1s AST (purple squares) and from the 0.85 V–1s AST (blue hexagons).

Similarly, it should be possible to compare the degradation for different cathode electrodes, (i.e., with regard to the carbon support morphology of the catalyst, the Pt content and the Pt particle size distribution of the catalyst, the ionomer type/content, the electrode thickness, or the Pt loading) by employing the same set of voltage cycling AST protocols. However, it should be noted that the individual voltage loss contributions and therefore the H<sub>2</sub>/air performance of an MEA depend strongly on the above listed cathode electrode properties (as well as the membrane type/thickness), so that one would expect to obtain different absolute values when plotting the H<sub>2</sub>/air cell voltages at different geometric current densities as a function of *rf* for different MEA types (e.g., a Ketjenblack supported catalyst will have a higher ORR activity but worse O<sub>2</sub>-transport properties compared to a Vulcan supported catalyst with the same ECSA<sup>17</sup>). Still, the trend of a quickly decaying cell voltage at high current densities compared to a mostly maintained low current density performance with decreasing cathode *rf* (confer Fig. 12) would be expected to be the same for different MEA types. Due to the anisotropic nature of the Pt dissolution/

redeposition mechanism in the through-plane direction of the electrode (see Fig. 4), differences in the H<sub>2</sub>/air performance vs *rf* correlation would also be expected when two different cathode loadings of the same catalyst are compared (corresponding to different electrode thicknesses), although the differences would most likely be less pronounced than for MEAs with different cathode catalysts. Therefore, the here observed characteristic correlation between the H<sub>2</sub>/air performance and the cathode *rf* over the course of voltage cycling ASTs needs to be established for each MEA type, whereby the H<sub>2</sub>/air cell voltage is furthermore affected by the other cell components (e.g., GDL type and compression, and flow field design) and by the operating conditions during the H<sub>2</sub>/air performance measurements (temperature, pressure, *RH*, reactant stoichiometry, etc.).

### Conclusions

In this study, the degradation of PEMFC cathodes with a loading of 0.1 mg<sub>Pt</sub> cm<sub>MEA</sub><sup>-2</sup> was investigated by square wave voltage cycling profiles between 0.6 V and different upper potential limits (UPLs of 0.85, 0.95, and 1.0 V) under H<sub>2</sub>/N<sub>2</sub> (anode/cathode) with hold times at the vertex potentials of 1, 2, or 8 s. Similar to other studies, it was found that aging protocols with higher UPL and longer hold times induce higher cathode roughness factor (*rf*) or electrochemically active surface area (*ECSA*) losses per cycle, resulting in faster H<sub>2</sub>/air performance degradation. After a mostly AST-independent *ECSA* (or cathode *rf*) loss in the first 100 cycles, a linear trend of the *ECSA* (or cathode *rf*) loss was observed in plots of the *ECSA* vs the logarithm of either the number of cycles or the time at UPL. This linearity can be used to predict the *ECSA* (or cathode *rf*) loss after extended cycling by an extrapolation of the trend line.

When investigating the individual voltage loss contributions that govern the H<sub>2</sub>/air performance over the course of the various voltage cycling ASTs, it was found that the H<sub>2</sub>-crossover, the *HFR*, and the proton conduction resistance remain unchanged, while the ORR mass and specific activity as well as the oxygen transport resistances correlate exclusively with the cathode *rf*, independent of the voltage cycling procedure (i.e., independent of the investigated UPLs and the hold times). This shows that the degradation mechanism is identical for the different AST conditions used in this study, and is restricted to Pt dissolution/redeposition, as cathode catalyst carbon support at UPLs ≤ 1.0 V and chemical ionomer degradation under nearly fully humidified conditions (95% *RH*) are negligible. As expected, the ORR mass activity decreased with decreasing cathode *rf*, while the specific activity increased due to the particle size effect. The pressure-independent part of the O<sub>2</sub> transport resistance was shown to be strongly affected by the local O<sub>2</sub> transport resistance that scales with *rf*<sup>-1</sup>, whereas the pressure-dependent O<sub>2</sub> transport resistance remained unchanged over the course of the ASTs. For all measurements, a *rf* of ≈ 10 cm<sub>Pt</sub><sup>2</sup> cm<sub>MEA</sub><sup>-2</sup> proved to be a critical value, below which a reliable determination of the ORR mass activity and the oxygen mass transport resistances was no longer possible.

The fact that the decrease of the ORR mass activity and the increase of the O<sub>2</sub> transport resistances with decreasing cathode *rf* is identical for the here examined five different voltage cycling ASTs, explains the at first sight surprising observation that the H<sub>2</sub>/air performance decreases with decreasing cathode *rf* is also identical for all five voltage cycling ASTs. In combination with the linear behavior of the cathode *rf* losses vs the logarithm of the cycle number, these findings can be used to predict the voltage cycling losses of the H<sub>2</sub>/air performance over a large number of voltage cycles under application-relevant conditions (i.e., UPLs of <0.9 V) based on the data acquired for a harsh cycling protocol (i.e., conducted with an UPL of 0.95–1.0 V).

### Acknowledgments

We would like to express our gratitude to Katia Rodewald for measuring the SEM micrographs of MEA cross-sections. Financial

support in the frame of the POREForm project funded by the German Federal Ministry for Economic Affairs and Energy (BMWi; funding number 03ET B027C) is gratefully acknowledged.

### Appendix

In order to determine whether there is any cathode thinning due to carbon support corrosion after 500,000 voltage cycles using the 0.85 V–1s AST protocol, the cathode electrode thickness was evaluated from ion-milled cross-sections of MEAs at BoL and after 500,000 cycles of the 0.85 V–1s AST. Representative cross-sections are shown in Fig. A.1.

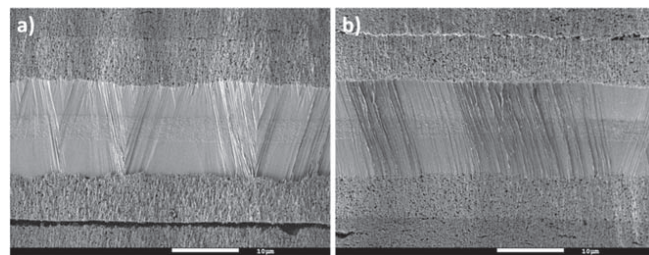


**Figure A.1.** Representative SEM micrograph of ion-milled MEA cross-sections (a) after BoL characterization and (b) after 500,000 voltage cycles using the 0.85 V–1s AST protocol. While the GDL was peeled off before the polishing step, some MPL residuals are still observed in the SEM images, directly above or below the cathode/anode (top/bottom) electrode for both MEAs. The white scale bar at the bottom of each image represents 10 μm.

### ORCID

Roberta K. F. Della Bella <https://orcid.org/0000-0002-3085-3536>  
Björn M. Stühmeier <https://orcid.org/0000-0001-7713-2261>  
Hubert A. Gasteiger <https://orcid.org/0000-0001-8199-8703>

### References

1. *Fuel Cell Technologies Program Multi-Year Research, Development, and Demonstration Plan - 3.4 Fuel Cells*, U.S. Department of Energy (2017), accessed: 11/12/2021, <https://www.energy.gov/eere/fuelcells/downloads/hydrogen-and-fuel-cell-technologies-office-multi-year-research-development>.
2. R. L. Borup, A. Kusoglu, K. C. Neyerlin, R. Mukundan, R. K. Ahluwalia, D. A. Cullen, K. L. More, A. Z. Weber, and D. J. Myers, *Curr. Opin. Electrochem.*, **21**, 192 (2020).
3. T. Patterson and R. Darling, *Electrochem. Solid-State Lett.*, **9**, A183 (2006).
4. P. J. Ferreira, G. J. la O', D. Shao-Horn, R. Morgan, S. K. Makharia, and H. A. Gasteiger, *J. Electrochem. Soc.*, **152**, A2256 (2005).
5. C. A. Reiser, L. Bregoli, T. W. Patterson, J. S. Yi, J. D. Yang, M. L. Perry, and T. D. Jarvi, *Electrochem. Solid-State Lett.*, **8**, A273 (2005).
6. L. Dubau, L. Castanheira, and F. Maillard et al., "A review of PEM fuel cell durability: materials degradation, local heterogeneities of aging and possible mitigation strategies." *WIREs Energy Environ.*, **3**, 540 (2014).
7. J. Wu, X. Z. Yuan, J. J. Martin, H. Wang, J. Zhang, J. Shen, S. Wu, and W. Merida, *J. Power Sources*, **184**, 104 (2008).
8. P. Zihrl, I. Hartung, S. Kirsch, G. Huebner, F. Hasché, and H. A. Gasteiger, *J. Electrochem. Soc.*, **163**, F492 (2016).
9. A. Kneer and N. Wagner, *J. Electrochem. Soc.*, **166**, F120 (2019).
10. G. S. Harzer, J. N. Schwämmlein, A. M. Damjanović, S. Ghosh, and H. A. Gasteiger, *J. Electrochem. Soc.*, **165**, F3118 (2018).
11. D. J. S. Sandbeck, N. M. Secher, F. D. Speck, J. E. Sørensen, J. Kibsgaard, I. Chorkendorff, and S. Cherevko, *ACS Catal.*, **10**, 6281 (2020).
12. K. Yu, D. J. Groom, X. Wang, Z. Yang, M. Gummalla, S. C. Ball, D. J. Myers, and P. J. Ferreira, *Chem. Mater.*, **26**, 5540 (2014).
13. R. Makharia, S. Kocha, P. Yu, M. Sweikart, W. Gu, F. Wagner, and H. A. Gasteiger, *ACS Transaction*, **1**, 3 (2006).
14. E. Antolini, *Appl. Catal., B*, **181**, 298 (2016).
15. D. J. S. Sandbeck et al., *J. Electrochem. Soc.*, **167**, 164501 (2020).
16. A. Kneer, J. Jankovic, D. Susac, A. Putz, N. Wagner, M. Sabharwal, and M. Secanell, *J. Electrochem. Soc.*, **165**, F3241 (2018).
17. V. Yarlagadda, M. K. Carpenter, T. E. Moylan, R. S. Kukreja, R. Koestner, W. Gu, L. Thompson, and A. Kongkanand, *ACS Energy Lett.*, **3**, 1127 (2018).
18. A. Kongkanand and M. F. Mathias, *J. Phys. Chem. Lett.*, **7**, 1127 (2016).
19. J. P. Owejan, J. E. Owejan, and W. Gu, *J. Electrochem. Soc.*, **160**, F824 (2013).
20. P. Urchaga, T. Kadyk, S. G. Rinaldo, A. O. Pistono, J. Hu, W. Lee, C. Richards, M. H. Eikerling, and C. A. Rice, *Electrochim. Acta*, **176**, 1500 (2015).
21. D. J. Myers, X. Wang, M. C. Smith, and K. L. More, *J. Electrochem. Soc.*, **165**, F3178 (2018).

22. Y. Hu, J. O. Jensen, P. Bretzler, L. N. Cleemann, J. Yu, and Q. Li, *Electrochim. Acta*, **391**, 138963 (2021).
23. E. Padgett et al., *J. Electrochem. Soc.*, **166**, F198 (2019).
24. A. Kneer, N. Wagner, C. Sadeler, A.-C. Scherzer, and D. Gerteisen, *J. Electrochem. Soc.*, **165**, F805 (2018).
25. S. Stariha, N. Macauley, B. T. Sneed, D. Langlois, K. L. More, R. Mukundan, and R. L. Borup, *J. Electrochem. Soc.*, **165**, F492 (2018).
26. D. A. Langlois, A. S. Lee, N. Macauley, S. Maurya, M. E. Hawley, S. D. Yim, and Y. S. Kim, *J. Power Sources*, **396**, 345 (2018).
27. N. Ramaswamy, S. Kumaraguru, W. Gu, R. S. Kukreja, K. Yu, D. Groom, and P. Ferreira, *J. Electrochem. Soc.*, **168**, 024519 (2021).
28. D. D. Papadias, R. K. Ahluwalia, N. Kariuki, D. Myers, K. L. More, D. A. Cullen, B. T. Sneed, K. C. Neyerlin, R. Mukundan, and R. L. Borup, *J. Electrochem. Soc.*, **165**, F3166 (2018).
29. C. Takei, K. Kakinuma, K. Kawashima, K. Tashiro, M. Watanabe, and M. Uchida, *J. Power Sources*, **324**, 729 (2016).
30. W. Bi, Q. Sun, Y. Deng, and T. F. Fuller, *Electrochim. Acta*, **54**, 1826 (2009).
31. M. Uchimura and S. S. Kocha, *ECS Trans.*, **11**, 1215 (2007).
32. Y. Liu, M. Murphy, D. Baker, W. Gu, C. Ji, J. Jorne, and H. A. Gasteiger, *ECS Trans.*, **11**, 473 (2007).
33. C. Simon, F. Hasche, D. Muller, and H. A. Gasteiger, *ECS Trans.*, **69**, 1293 (2015).
34. C. Simon, F. Hasché, and H. A. Gasteiger, *J. Electrochem. Soc.*, **164**, F591 (2017).
35. G. S. Harzer, A. Orfanidi, H. El-Sayed, P. Madkikar, and H. A. Gasteiger, *J. Electrochem. Soc.*, **165**, F770 (2018).
36. Y. Liu, M. W. Murphy, D. R. Baker, W. Gu, C. Ji, J. Jorne, and H. A. Gasteiger, *J. Electrochem. Soc.*, **156**, B970 (2009).
37. R. Makharia, M. F. Mathias, and D. R. Baker, *J. Electrochem. Soc.*, **152**, A970 (2005).
38. M. Eikerling and A. A. Kornyshev, *J. Electroanal. Chem.*, **475**, 107 (1999).
39. K. C. Neyerlin, W. Gu, J. Jorne, A. Clark, and H. A. Gasteiger, *J. Electrochem. Soc.*, **154**, B279 (2007).
40. K. C. Neyerlin, W. Gu, J. Jorne, and H. A. Gasteiger, *J. Electrochem. Soc.*, **154**, B631 (2007).
41. D. R. Baker, D. A. Caulk, K. C. Neyerlin, and M. W. Murphy, *J. Electrochem. Soc.*, **156**, B991 (2009).
42. R. K. Ahluwalia, X. Wang, J.-K. Peng, V. Konduru, S. Arisetty, N. Ramaswamy, and S. Kumaraguru, *J. Electrochem. Soc.*, **168**, 044518 (2021).
43. K. H. Kangasniemi, D. A. Condit, and T. D. Jarvi, *J. Electrochem. Soc.*, **151**, E125 (2004).
44. R. N. Carter, S. S. Kocha, F. Wagner, M. Fay, and H. A. Gasteiger, *ECS Trans.*, **11**, 403 (2019).
45. T. R. Garrick, T. E. Moylan, M. K. Carpenter, and A. Kongkanand, *J. Electrochem. Soc.*, **164**, F55 (2016).
46. K. Shinozaki, H. Yamada, and Y. Morimoto, *J. Electrochem. Soc.*, **158**, B467 (2011).
47. B. M. Stühmeier, M. R. Pietsch, J. N. Schwämmlein, and H. A. Gasteiger, *J. Electrochem. Soc.*, **168**, 064516 (2021).
48. T. A. Greszler, D. Caulk, and P. Sinha, *J. Electrochem. Soc.*, **159**, F831 (2012).
49. R. M. Darling and J. P. Meyers, *J. Electrochem. Soc.*, **150**, A1523 (2003).
50. Y. Shao-Horn, W. C. Sheng, S. Chen, P. J. Ferreira, E. F. Holby, and D. Morgan, *Top. Catal.*, **46**, 285 (2007).
51. M. K. Debe, A. K. Schmoeckel, G. D. Vernstrom, and R. Atanasoski, *J. Power Sources*, **161**, 1002 (2006).
52. W. Bi and T. F. Fuller, *J. Electrochem. Soc.*, **155**, B215 (2008).
53. W. Bi and T. F. Fuller, *J. Power Sources*, **178**, 188 (2008).
54. J. Zhang, B. A. Litteer, W. Gu, H. Liu, and H. A. Gasteiger, *J. Electrochem. Soc.*, **154**, B1006 (2007).
55. S. Kawahara, S. Mitsuhashi, K.-I. Ota, and N. Kamiya, *ECS Trans.*, **3**, 7 (2006).
56. D. C. Johnson, D. T. Napp, and S. Bruckenstein, *Electrochim. Acta*, **15**, 1493 (1970).
57. K. Ehelebe, D. Escalera-López, and S. Cherevko, *Curr. Opin. Electrochem.*, **29**, 100832 (2021).
58. R. M. Darling and J. P. Meyers, *J. Electrochem. Soc.*, **152**, A242 (2005).
59. K. Ehelebe, J. Knöppel, M. Bierling, B. Mayerhöfer, T. Böhm, N. Kulyk, S. Thiele, K. J. J. Mayrhofer, and S. Cherevko, *Angew. Chem. Int. Ed.*, **60**, 8882 (2021).
60. M. S. Kang and Y. I. Joe, *J. Power Sources*, **77**, 49 (1999).
61. F. Coms, H. Xu, T. McCallum, and C. Mittelsteadt, *ECS Trans.*, **50**, 907 (2013).
62. H. A. Gasteiger, J. E. Panels, and S. G. Yan, *J. Power Sources*, **127**, 162 (2004).
63. H. A. Gasteiger, S. S. Kocha, B. Sompalli, and F. T. Wagner, *Appl. Catal., B*, **56**, 9 (2005).
64. K. Kinoshita, *J. Electrochem. Soc.*, **137**, 845 (1990).
65. F. Du et al., *J. Electrochem. Soc.*, **167**, 144513 (2020).
66. A. Orfanidi, P. Madkikar, H. A. El-Sayed, G. S. Harzer, T. Kratky, and H. A. Gasteiger, *J. Electrochem. Soc.*, **164**, F418 (2017).
67. K. C. Neyerlin, W. Gu, J. Jorne, and H. A. Gasteiger, *J. Electrochem. Soc.*, **153**, A1955 (2006).
68. N. P. Subramanian, T. Greszler, J. Zhang, W. Gu, and R. R. Makharia, *ECS Trans.*, **41**, 985 (2011).
69. Y. Ono, T. Mashio, S. Takaichi, A. Ohma, H. Kanesaka, and K. Shinohara, *ECS Trans.*, **28**, 69 (2010).
70. T. V. Reshетенко and J. St-Pierre, *J. Electrochem. Soc.*, **161**, F1089 (2014).
71. S. Shukla, D. Stanier, M. S. Saha, J. Stumper, and M. Secanell, *J. Electrochem. Soc.*, **163**, F677 (2016).
72. K. Kudo, T. Suzuki, and Y. Morimoto, *ECS Trans.*, **33**, 1495 (2010).
73. N. Nonoyama, S. Okazaki, A. Z. Weber, Y. Ikogi, and T. Yoshida, *J. Electrochem. Soc.*, **158**, B416 (2011).
74. N. P. Subramanian, T. A. Greszler, J. Zhang, W. Gu, and R. Makharia, *J. Electrochem. Soc.*, **159**, B531 (2012).
75. J. X. Wang, F. A. Uribe, T. E. Springer, J. Zhang, and R. R. Adzic, *Faraday Discuss.*, **140**, 347 (2008).
76. T. Lazaridis and H. A. Gasteiger, *J. Electrochem. Soc.*, **168**, 114517 (2021).
77. K. J. J. Mayrhofer, D. Strmcnik, B. B. Blizanac, V. Stamenkovic, M. Arenz, and N. M. Markovic, *Electrochim. Acta*, **53**, 3181 (2008).
78. M. Inaba, H. Yamada, J. Tokunaga, and A. Tasaka, *Electrochem. Solid-State Lett.*, **7**, A474 (2004).
79. K. Ono, K. Sekizawa, N. Takeuchi, T. Yoshida, and M. Sudoh, *ECS Trans.*, **50**, 33 (2013).
80. D. A. Caulk and D. R. Baker, *J. Electrochem. Soc.*, **157**, B1237 (2010).
81. T. Schuler, A. Chowdhury, A. T. Freiberg, B. Sneed, F. B. Spingler, M. C. Tucker, K. L. More, C. J. Radke, and A. Z. Weber, *J. Electrochem. Soc.*, **166**, F3020 (2019).
82. R. Petrone, D. Hissel, M. C. Péra, D. Chamagne, and R. Gouriveau, *Int. J. Hydrog. Energy*, **40**, 12489 (2015).
83. S. Jomori, K. Komatsubara, N. Nonoyama, M. Kato, and T. Yoshida, *J. Electrochem. Soc.*, **160**, F1067 (2013).
84. J. P. Meyers and R. M. Darling, *J. Electrochem. Soc.*, **153**, A1432 (2006).
85. P. T. Yu, W. Gu, R. Makharia, F. T. Wagner, and H. A. Gasteiger, *ECS Trans.*, **3**, 797 (2006).
86. A. Collier, H. Wang, X. Zi Yuan, J. Zhang, and D. P. Wilkinson, *Int. J. Hydrogen Energy*, **31**, 1838 (2006).

## 4. Conclusions

This PhD thesis focused on the investigation of the activity, selectivity, and durability of catalysts for proton exchange membrane fuel cells (PEMFCs). Hereby, the three main aspects were the development of suitable measurement protocols, the investigation and implementation of novel catalyst concepts, and elucidating the correlation between catalyst degradation and the H<sub>2</sub>/air performance losses.

In the first part of the thesis, the two most commonly used setups for the investigation of PEMFC catalysts, namely the rotating disk electrode (RDE) technique and membrane electrode assembly (MEA) based single-cell measurements, were discussed with respect to their capabilities and limitations in accessing the catalyst properties that are most critical for PEMFC operation. We concluded that the RDE is an easily accessible tool that is essential for the initial screening of new catalyst materials that are only available in small quantities as well as for fundamental studies on the reaction mechanism of the ORR and on the degradation of fuel cell catalysts. However, the RDE technique is limited in its capabilities by the slow mass transport rates in the liquid environment, so that an evaluation of the application-relevant high current density performance of ORR catalysts and of the fast kinetics of the HOR/HER is not possible. While bridging techniques address some of these shortcomings, MEA measurements that require several grams of catalyst, complex and expensive instrumentation, and elaborate experimental procedures are often essential to elucidate the role of the carbon support morphology, the interaction between ionomer and Pt nanoparticles, and MEA-specific secondary effects of catalyst degradation. Due to the high complexity of MEA measurements, special emphasis was placed on the optimization of measurement procedures for low-loaded electrodes that are susceptible to artifacts from CO contamination, semi-irreversible support oxidation, H<sub>2</sub>-crossover, and changes in the ORR mechanism. Furthermore, a practical guideline for the time-efficient characterization of 5 cm<sup>2</sup> MEAs was given.

Since RDE measurements were found to be unsuitable for determining the HOR/HER

kinetics in acidic environment,<sup>85,152</sup> an optimized procedure for PEMFC based H<sub>2</sub>-pump measurements was developed in order to investigate the HOR/HER mechanism. A measurement procedure using a mix of galvanostatic and potentiostatic measurements allowed us to correct the potential of each individual data point via impedance spectroscopy. This way, we could investigate the reaction kinetics on highly asymmetrically loaded electrodes not only in dependence of the temperature, but for the first time also in dependence of the hydrogen partial pressure ( $p_{\text{H}_2}$ ). Thus, the HOR/HER activity on Pt/C catalysts was benchmarked for a broad matrix of measurement conditions from 30–90 °C and 100–450 kPa<sub>H<sub>2</sub></sub>. Thereby, the apparent activation energy of the HOR/HER was found to increase with increasing  $p_{\text{H}_2}$  due to a diminishing effect of the hydrogen adsorption enthalpy with increasing coverage by adsorbed hydrogen atoms on the Pt surface.<sup>167,168</sup> Consequently, the HOR/HER reaction order with respect to  $p_{\text{H}_2}$  also depends on the temperature. Furthermore, the HOR eventually reached a limiting current at high anodic overpotentials that showed a direct proportionality to the hydrogen partial pressure as well as a temperature-dependent behavior with a constant, i.e., pressure-independent, activation energy. We ascribed this effect to a limitation of the hydrogen adsorption rate by a rate limiting Tafel-reaction or local mass transport limitations.

Having established suitable measurement protocols for the screening of new catalysts by RDE and the more advanced characterization of the HOR/HER activity in MEA measurements, novel catalyst concepts based on oxide support materials were explored in the second part of this thesis. In a first study, the polyol process was established as a method for the in-situ reduction of surface oxide films, with the aim to create a metallic inter-layer onto which a thin contiguous platinum film could be deposited. We showed that by heating in ethylene glycol, the native thin oxide film on a Sn wire can be reduced, whereby in-situ cyclic voltammetry and reference measurements using near-ambient pressure XPS showed that a drop in the open circuit potential (OCP) of the wire vs. a Ag/AgCl reference electrode was a clear indication that a surface reduction had occurred. Using this OCP drop as an indicator, the reduction of the native oxides could be proven for Sn and Ni wire model substrates, for technologically more relevant Sn and Ni nanoparticles, and even for oxide nanoparticles (Sb-doped SnO<sub>2</sub>). Thus, it was shown that the oxide reduction process is independent of the oxide morphology (extended surfaces, nanoparticles, and nanowires), which might make oxide<sub>core</sub> metal<sub>shell</sub> structures accessible via a metallic inter-layer.

---

Using a different approach, the strong metal-support interaction (SMSI) effect on the electrochemical surface oxide formation and the electrochemical reactivity of Pt and Ru was explored in two studies. The respective platinum group metal (PGM) was supported on  $\text{TiO}_x$  ( $x \leq 2$ ) and the PGM/ $\text{TiO}_x$  agglomerates were then adsorbed on a Vulcan carbon support that guaranteed a sufficient electrical conductivity and high porosity of the electrodes prepared with the PGM/ $\text{TiO}_x$ /C catalysts. After a reductive heat-treatment (400 °C, 5%  $\text{H}_2/\text{Ar}$ ), the SMSI formation resulted in the encapsulation of the PGM nanoparticles and, for both metals, the electrochemical formation of a surface oxide was found to be almost completely suppressed compared to the respective PGM/C reference catalyst. This led to a stabilization of the HOR activity at high anodic potentials ( $> 1.0 \text{ V}_{\text{RHE}}$ ), where the oxidation would otherwise result in a deactivation of the catalysts for the HOR. Unfortunately,  $\text{H}_2$ -pump measurements with the Ru/ $\text{TiO}_x$ /C catalyst showed that although the catalyst proved to be three times more active than the Ru/C reference, the activity was two orders of magnitude lower compared to Pt/C, which makes this catalyst unattractive for the implementation in PEMFC systems. On the other hand, the ORR activity of Pt/ $\text{TiO}_x$ /C was found to be suppressed by 98%, which in combination by an only  $\approx 3$  times lower HOR activity (determined by alkaline RDE measurements) resulted in a unique selectivity of the catalyst for the HOR, which is considered to be beneficial for the mitigation of start-up/shut-down (SUSD) induced carbon corrosion on the cathode of a PEMFC.<sup>59,103</sup>

In the last section of the thesis, the cathode degradation during SUSD events and operation over the course of extended load cycling was investigated using small active area PEMFC single-cells. First, the HOR-selective Pt/ $\text{TiO}_2$ /C catalyst was implemented as an anode catalyst to test the hypothesized mitigation of SUSD-induced corrosion of the carbon support of the cathode catalyst. While we could show by  $\text{H}_2$ -pump measurements that the HOR activity of the Pt/ $\text{TiO}_2$ /C catalyst is indeed only twofold lower compared to Pt/C, the significantly lower ORR activity could unfortunately not be reproduced in an MEA, resulting in an overall lower activity of Pt/ $\text{TiO}_2$ /C rather than it being an HOR-selective catalyst. Furthermore, the stability of  $\text{TiO}_2$  proved to be a severe issue that resulted in a cationic contamination of the cathode catalyst layer and, consequently, in performance penalties of  $\approx 35 \text{ mV}$  at  $2 \text{ A cm}_{\text{MEA}}^{-2}$ . The necessity to avoid  $\text{TiO}_2$  in a PEMFC has also been highlighted in a recent study by Zhang *et al.*<sup>121</sup> that was published during the final phase of the data collection for

our most recent study on TiO<sub>2</sub>-based catalysts. Nevertheless, the Pt/TiO<sub>2</sub>/C anodes still proved to be advantageous during SUSD events, whereby the *ECSA* retention was significantly improved over the Pt/C references, although the loss in selectivity when implemented in an MEA would have predicted otherwise, the reason for this is still unclear.

Finally, we investigated the effect of voltage cycling based accelerated stress tests (ASTs) on the PEMFC H<sub>2</sub>/air performance losses. Hereby, we made two key observations that will greatly impact the design of voltage cycling based ASTs in the future: first of all, it was found that the *ECSA* or *rf* deteriorate linearly versus the logarithm of the number of cycles or the time at UPL, with higher slopes for harsher ASTs. This linearity can be used to predict the *ECSA* (or cathode *rf*) loss after extended voltage cycling by an extrapolation of the trend line. Moreover, the individual voltage losses were found to be either unaffected by the aging (H<sub>2</sub>-crossover and proton conduction resistance) or to depend exclusively on the cathode *rf* (mass/specific activity and O<sub>2</sub>-transport resistances), independent of the AST procedure. This results in an universal correlation between the H<sub>2</sub>/air performance and the *rf* over the course of voltage cycling ASTs. Consequently, the combination of the linear cathode *rf* loss behavior and the AST protocol-independent correlation between H<sub>2</sub>/air performance and *rf* can be used to predict the H<sub>2</sub>/air performance losses over a large number of voltage cycles under application-relevant conditions by employing a harsh aging protocol (see fig. 4.1).

In summary, this PhD thesis has contributed in several ways to a better understanding of the activity, selectivity, and durability of PEMFC catalyst materials. The perspective is a handy guideline for researchers that summarizes the capabilities and limitations of the RDE technique and of single-cell MEA measurements, and also proposes appropriate protocols for the screening and characterization of newly synthesized catalysts. The HOR/HER investigation provides not only valuable insights into the reaction mechanism and potential limitations at low electrode *rf* values, but also supplies a comprehensive set of anode performance data for PEMFC system design and modeling. Although they are not yet mature, the novel catalyst concepts presented in this thesis have the potential to significantly improve the long-term durability of PEMFC systems. While extended Pt (or Pt-alloy) thin films covering an oxide support material are certainly a far-future alternative, composite materials with an SMSI-induced selectivity might be available in the near future, if a metal oxide

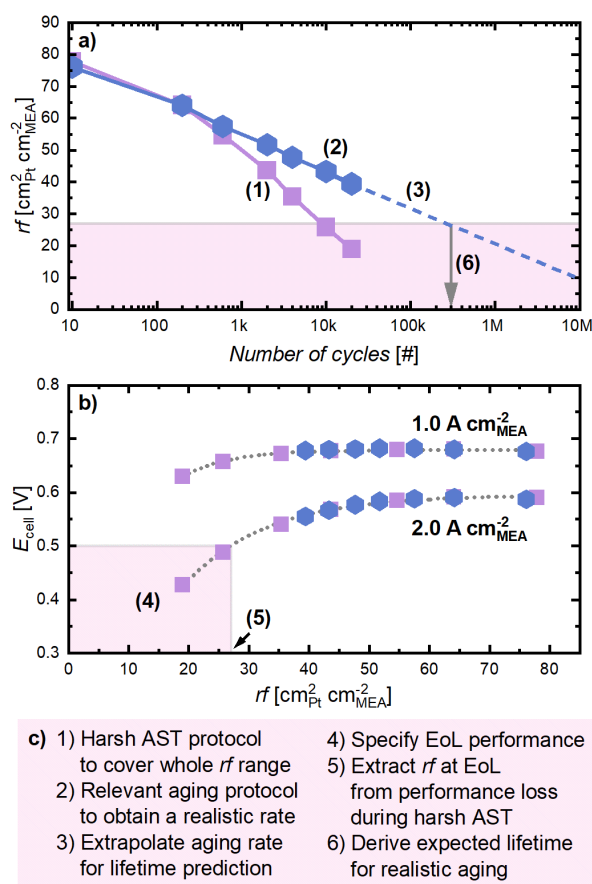


**Figure 4.1.** Scheme of the proposed approach to predict the voltage cycling losses of the  $\text{H}_2/\text{air}$  performance over a large number of voltage cycles under application-relevant conditions (i.e., UPLs of  $< 0.9 \text{ V}$ ) based on the data acquired for a harsh cycling protocol (i.e., conducted with an UPL of  $0.95 - 1.0 \text{ V}$ ); a) cathode  $rf$  degradation for a harsh voltage cycling AST (purple squares) and for an application-relevant “mild” voltage cycling AST (blue hexagons); b)  $\text{H}_2/\text{air}$  performance as a function of cathode  $rf$  for two current densities; c) outline of the step-wise procedure to estimate the number of cycles after which the end of life (EoL) criteria (here assumed to be  $0.5 \text{ V}$  at  $2 \text{ A cm}^2_{\text{MEA}}$ ) are reached for the mild voltage cycling AST on the basis of the harsh voltage cycling AST data. The figure is reprinted from Della Bella and Stühmeier *et al.* (see Section 3.3.2).<sup>53</sup>

can be found that proves to be stable under PEMFC operating conditions ( $\text{WO}_3$  and  $\text{Nb}_2\text{O}_5$  being the most promising candidates). Finally, the seminal finding that there is a universal correlation between the cathode  $rf$  and the  $\text{H}_2/\text{air}$  performance during voltage cycling based ASTs will allow researchers and manufacturers to significantly accelerate the durability testing that is required to reliably predict system lifetime and performance and to determine the necessary constraints on the operating conditions with regard to upper potential limit and temperature.



# References

- [1] Bundesministerium für Umwelt, Naturschutz, nukleare Sicherheit und Verbraucherschutz (BMUV), “Treibhausgasemissionen sinken 2020 um 8,7 Prozent”, Pressemitteilung Nr. 042/21 (gemeinsame Pressemitteilung mit dem Umweltbundesamt, 16.03.2021).
- [2] L.-M. Alfeis, P. Deierling, T. Gödecke, S. Mevers, T. Zimmermann, S. F. Andres, A. Bedrunka, U. Lüdersen, “Co<sub>2</sub>rona Effekt - Sektorspezifische Betrachtung in Deutschland 2020”, Tech. Rep., Hochschule Hannover, **2020**, DOI: 10.25968/opus-1671.
- [3] L. Menut, B. Bessagnet, G. Siour, S. Mailler, R. Pennel, A. Cholakian, “Impact of lockdown measures to combat Covid-19 on air quality over western Europe”, *Science of The Total Environment*, **2020**, *741*, 140426.
- [4] B. R. Parida, S. Bar, D. Kaskaoutis, A. C. Pandey, S. D. Polade, S. Goswami, “Impact of COVID-19 induced lockdown on land surface temperature, aerosol, and urban heat in Europe and North America”, *Sustainable Cities and Society*, **2021**, *75*, 103336.
- [5] “Climate Change 2021: The Physical Science Basis. Contribution of Working Group I to the Sixth Assessment Report of the Intergovernmental Panel on Climate Change”, Tech. Rep., The Intergovernmental Panel on Climate Change (IPCC), **2021**, Cambridge University Press, <https://www.ipcc.ch/report/sixth-assessment-report-working-group-i/> (accessed: 05.03.2022).
- [6] European Environment Agency (EEA), “Trends and projections in Europe 2021”, EEA Report No 13/2021, DOI: 10.2800/80374.
- [7] Bundesministerium für Wirtschaft und Energie (BMWi), “Die Nationale Wasserstoffstrategie”, June 2020, <https://www.bmwi.de/Redaktion/DE/Publikationen/Energie/die-nationale-wasserstoffstrategie.html> (accessed: 05.03.2022).
- [8] A. Choudhury, H. Chandra, A. Arora, “Application of solid oxide fuel cell technology for power generation—A review”, *Renewable and Sustainable Energy Reviews*, **2013**, *20*, 430–442.
- [9] L. Fan, Z. Tu, S. H. Chan, “Recent development of hydrogen and fuel cell technologies: A review”, *Energy Reports*, **2021**, *7*, 8421–8446.

- [10] W. Sheng, H. A. Gasteiger, Y. Shao-Horn, “Hydrogen Oxidation and Evolution Reaction Kinetics on Platinum: Acid vs Alkaline Electrolytes”, *Journal of The Electrochemical Society*, **2010**, *157*, B1529–B1536.
- [11] W. Sheng, Z. Zhuang, M. Gao, J. Zheng, J. G. Chen, Y. Yan, “Correlating hydrogen oxidation and evolution activity on platinum at different pH with measured hydrogen binding energy”, *Nature Communications*, **2015**, *6*, 5848.
- [12] S. Gottesfeld, D. R. Dekel, M. Page, C. Bae, Y. Yan, P. Zelenay, Y. S. Kim, “Anion exchange membrane fuel cells: Current status and remaining challenges”, *Journal of Power Sources*, **2018**, *375*, 170–184.
- [13] P. Shirvastian, A. Loh, S. Sluijter, X. Li, “Novel components in anion exchange membrane water electrolyzers (AEMWE’s): Status, challenges and future needs. A mini review”, *Electrochemistry Communications*, **2021**, *132*, 107140.
- [14] T. Yoshida, K. Kojima, “Toyota MIRAI Fuel Cell Vehicle and Progress Toward a Future Hydrogen Society”, *The Electrochemical Society Interface*, **2015**, *24*, 45–49.
- [15] B. K. Hong, S. H. Kim, “(Invited) Recent Advances in Fuel Cell Electric Vehicle Technologies of Hyundai”, *ECS Transactions*, **2018**, *86*, 3–11.
- [16] K. Kodama, T. Nagai, A. Kuwaki, R. Jinnouchi, Y. Morimoto, “Challenges in applying highly active Pt-based nanostructured catalysts for oxygen reduction reactions to fuel cell vehicles”, *Nature Nanotechnology*, **2021**, *16*, 140–147.
- [17] M. Doyle, G. Rajendran, “Perfluorinated membranes” in *Handbook of Fuel Cells – Fundamentals, Technology and Applications 1st ed., Vol. 3: Fuel Cell Technology and Applications*, W. Vielstich, H. A. Gasteiger, A. Lamm (Eds.), John Wiley & Sons Ltd, Hoboken, **2003**, pp. 351–395.
- [18] T. R. Ralph, D. E. Barnwell, P. J. Bouwman, A. J. Hodgkinson, M. I. Petch, M. Pollington, “Reinforced Membrane Durability in Proton Exchange Membrane Fuel Cell Stacks for Automotive Applications”, *Journal of The Electrochemical Society*, **2008**, *155*, B411–B422.
- [19] C. S. Gittleman, A. Kongkanand, D. Masten, W. Gu, “Materials research and development focus areas for low cost automotive proton-exchange membrane fuel cells”, *Current Opinion in Electrochemistry*, **2019**, *18*, 81–89.
- [20] W. Gu, D. R. Baker, Y. Liu, H. A. Gasteiger, “Proton exchange membrane fuel cell (PEMFC) down-the-channel performance model” in *Handbook of Fuel Cells – Fundamentals, Technology and Applications 1st ed., Vol. 6: Advances in Electrocatalysis, Materials, Diagnostics and Durability*, W. Vielstich, H. Yokokawa, H. A. Gasteiger (Eds.), John Wiley & Sons Ltd, Chichester, **2009**, pp. 631–657.

- [21] Y. Liu, M. W. Murphy, D. R. Baker, W. Gu, C. Ji, J. Jorne, H. A. Gasteiger, “Proton Conduction and Oxygen Reduction Kinetics in PEM Fuel Cell Cathodes: Effects of Ionomer-to-Carbon Ratio and Relative Humidity”, *Journal of The Electrochemical Society*, **2009**, *156*, B970–B980.
- [22] J. P. Owejan, J. E. Owejan, W. Gu, “Impact of Platinum Loading and Catalyst Layer Structure on PEMFC Performance”, *Journal of The Electrochemical Society*, **2013**, *160*, F824–F833.
- [23] Y.-C. Park, H. Tokiwa, K. Kakinuma, M. Watanabe, M. Uchida, “Effects of carbon supports on Pt distribution, ionomer coverage and cathode performance for polymer electrolyte fuel cells”, *Journal of Power Sources*, **2016**, *315*, 179–191.
- [24] A. Orfanidi, P. Madkikar, H. A. El-Sayed, G. S. Harzer, T. Kratky, H. A. Gasteiger, “The Key to High Performance Low Pt Loaded Electrodes”, *Journal of The Electrochemical Society*, **2017**, *164*, F418–F426.
- [25] B. M. Stühmeier, M. R. Pietsch, J. N. Schwämmlein, H. A. Gasteiger, “Pressure and Temperature Dependence of the Hydrogen Oxidation and Evolution Reaction Kinetics on Pt Electrocatalysts via PEMFC-based Hydrogen-Pump Measurements”, *Journal of The Electrochemical Society*, **2021**, *168*, 064516.
- [26] L. Pan, S. Ott, F. Dionigi, P. Strasser, “Current challenges related to the deployment of shape-controlled Pt alloy oxygen reduction reaction nanocatalysts into low Pt-loaded cathode layers of proton exchange membrane fuel cells”, *Current Opinion in Electrochemistry*, **2019**, *18*, 61–71.
- [27] S. Zaman, L. Huang, A. I. Douka, H. Yang, B. You, B. Y. Xia, “Oxygen Reduction Electrocatalysts toward Practical Fuel Cells: Progress and Perspectives”, *Angewandte Chemie International Edition*, **2021**, *60*, 2–23.
- [28] T. Lazaridis, B. M. Stühmeier, H. A. Gasteiger, H. A. El-Sayed, “Capabilities and limitations of rotating disk electrodes versus membrane electrode assemblies in the investigation of electrocatalysts”, *Nature Catalysis*, **2022**, DOI: 10.1038/s41929-022-00776-5.
- [29] R. Subbaraman, D. Strmcnik, V. Stamenkovic, N. M. Markovic, “Three Phase Interfaces at Electrified Metal-Solid Electrolyte Systems 1. Study of the Pt(hkl)-Nafion Interface”, *The Journal of Physical Chemistry C*, **2010**, *114*, 8414–8422.
- [30] K. Shinozaki, Y. Morimoto, B. S. Pivovar, S. S. Kocha, “Suppression of oxygen reduction reaction activity on Pt-based electrocatalysts from ionomer incorporation”, *Journal of Power Sources*, **2016**, *325*, 745–751.
- [31] V. Yarlagadda, M. K. Carpenter, T. E. Moylan, R. S. Kukreja, R. Koestner, W. Gu, L. Thompson, A. Kongkanand, “Boosting Fuel Cell Performance with Accessible Carbon Mesopores”, *ACS Energy Letters*, **2018**, *3*, 618–621.

- [32] T. Takeshita, Y. Kamitaka, K. Shinozaki, K. Kodama, Y. Morimoto, “Evaluation of ionomer coverage on Pt catalysts in polymer electrolyte membrane fuel cells by CO stripping voltammetry and its effect on oxygen reduction reaction activity”, *Journal of Electroanalytical Chemistry*, **2020**, 871, 114250.
- [33] A. Kongkanand, M. F. Mathias, “The Priority and Challenge of High-Power Performance of Low-Platinum Proton-Exchange Membrane Fuel Cells”, *The Journal of Physical Chemistry Letters*, **2016**, 7, 1127–1137.
- [34] Y. Ono, T. Mashio, S. Takaichi, A. Ohma, H. Kanesaka, K. Shinohara, “The Analysis of Performance Loss with Low Platinum Loaded Cathode Catalyst Layers”, *ECS Transactions*, **2010**, 28, 69–78.
- [35] N. Nonoyama, S. Okazaki, A. Z. Weber, Y. Ikogi, T. Yoshida, “Analysis of Oxygen-Transport Diffusion Resistance in Proton-Exchange-Membrane Fuel Cells”, *Journal of The Electrochemical Society*, **2011**, 158, B416–B423.
- [36] T. A. Greszler, D. Caulk, P. Sinha, “The Impact of Platinum Loading on Oxygen Transport Resistance”, *Journal of The Electrochemical Society*, **2012**, 159, F831–F840.
- [37] N. Ramaswamy, W. Gu, J. M. Ziegelbauer, S. Kumaraguru, “Carbon Support Microstructure Impact on High Current Density Transport Resistances in PEMFC Cathode”, *Journal of The Electrochemical Society*, **2020**, 167, 064515.
- [38] T. Lazaridis, H. A. Gasteiger, “Pt-Catalyzed Oxidation of PEMFC Carbon Supports: A Path to Highly Accessible Carbon Morphologies and Implications for Start-Up/Shut-Down Degradation”, *Journal of The Electrochemical Society*, **2021**, 168, 114517.
- [39] M. Ko, E. Padgett, V. Yarlagadda, A. Kongkanand, D. A. Muller, “Revealing the Nanostructure of Mesoporous Fuel Cell Catalyst Supports for Durable, High-Power Performance”, *Journal of The Electrochemical Society*, **2021**, 168, 024512.
- [40] A. Kobayashi, T. Fujii, C. Harada, E. Yasumoto, K. Takeda, K. Kakinuma, M. Uchida, “Effect of Pt and Ionomer Distribution on Polymer Electrolyte Fuel Cell Performance and Durability”, *ACS Applied Energy Materials*, **2021**, 4, 2307–2317.
- [41] “Fuel Cell Technologies Program Multi-Year Research, Development, and Demonstration Plan”, Tech. Rep., U.S. Department of Energy, **2005 (revision: 2012)**, <https://www.energy.gov/eere/fuelcells/downloads/hydrogen-and-fuel-cell-technologies-office-multi-year-research-development> (accessed: 11.12.2021).
- [42] S. D. Knights, K. M. Colbow, J. St-Pierre, D. P. Wilkinson, “Aging mechanisms and lifetime of PEFC and DMFC”, *Journal of Power Sources*, **2004**, 127, 127–134.

- [43] P. J. Ferreira, G. J. la O', Y. Shao-Horn, D. Morgan, R. Makharia, S. Kocha, H. A. Gasteiger, "Instability of Pt/C Electrocatalysts in Proton Exchange Membrane Fuel Cells", *Journal of The Electrochemical Society*, **2005**, *152*, A2256–A2271.
- [44] C. A. Reiser, L. Bregoli, T. W. Patterson, J. S. Yi, J. D. Yang, M. L. Perry, T. D. Jarvi, "A Reverse-Current Decay Mechanism for Fuel Cells", *Electrochemical and Solid-State Letters*, **2005**, *8*, A273–A276.
- [45] T. W. Patterson, R. M. Darling, "Damage to the Cathode Catalyst of a PEM Fuel Cell Caused by Localized Fuel Starvation", *Electrochemical and Solid-State Letters*, **2006**, *9*, A183–A185.
- [46] R. Borup, J. Meyers, B. Pivovar, Y. S. Kim, R. Mukundan, N. Garland, D. Myers, M. Wilson, F. Garzon, D. Wood, P. Zelenay, K. More, K. Stroh, T. Zawodzinski, J. Boncella, J. E. McGrath, M. Inaba, K. Miyatake, M. Hori, K. Ota, Z. Ogumi, S. Miyata, A. Nishikata, Z. Siroma, Y. Uchimoto, K. Yasuda, K.-i. Kimijima, N. Iwashita, "Scientific Aspects of Polymer Electrolyte Fuel Cell Durability and Degradation", *Chemical Reviews*, **2007**, *107*, 3904–3951.
- [47] J. Wu, X. Z. Yuan, J. J. Martin, H. Wang, J. Zhang, J. Shen, S. Wu, W. Merida, "A review of PEM fuel cell durability: Degradation mechanisms and mitigation strategies", *Journal of Power Sources*, **2008**, *184*, 104–119.
- [48] K. Ehelebe, J. Knöppel, M. Bierling, B. Mayerhöfer, T. Böhm, N. Kulyk, S. Thiele, K. J. J. Mayrhofer, S. Cherevko, "Platinum Dissolution in Realistic Fuel Cell Catalyst Layers", *Angewandte Chemie International Edition*, **2021**, *60*, 8882–8888.
- [49] K. Yu, D. J. Groom, X. Wang, Z. Yang, M. Gummalla, S. C. Ball, D. J. Myers, P. J. Ferreira, "Degradation Mechanisms of Platinum Nanoparticle Catalysts in Proton Exchange Membrane Fuel Cells: The Role of Particle Size", *Chemistry of Materials*, **2014**, *26*, 5540–5548.
- [50] R. Makharia, S. Kocha, P. Yu, M. A. Sweikart, W. Gu, F. Wagner, H. A. Gasteiger, "Durable PEM Fuel Cell Electrode Materials: Requirements and Benchmarking Methodologies", *ECS Transactions*, **2006**, *1*, 3–18.
- [51] P. Zihrul, I. Hartung, S. Kirsch, G. Huebner, F. Hasché, H. A. Gasteiger, "Voltage Cycling Induced Losses in Electrochemically Active Surface Area and in H<sub>2</sub>/Air-Performance of PEM Fuel Cells", *Journal of The Electrochemical Society*, **2016**, *163*, F492–F498.
- [52] G. S. Harzer, J. N. Schwämmlein, A. M. Damjanović, S. Ghosh, H. A. Gasteiger, "Cathode Loading Impact on Voltage Cycling Induced PEMFC Degradation: A Voltage Loss Analysis", *Journal of The Electrochemical Society*, **2018**, *165*, F3118–F3131.

- [53] R. K. F. Della Bella, B. M. Stühmeier, H. A. Gasteiger, “Universal Correlation between Cathode Roughness Factor and H<sub>2</sub>/Air Performance Losses in Voltage Cycling-based Accelerated Stress Tests”, *Journal of The Electrochemical Society*, **2022**, *169*, 044528.
- [54] S. G. Bratsch, “Standard Electrode Potentials and Temperature Coefficients in Water at 298.15 K”, *Journal of Physical and Chemical Reference Data*, **1989**, *18*, 1–21.
- [55] J. P. Meyers, R. M. Darling, “Model of Carbon Corrosion in PEM Fuel Cells”, *Journal of The Electrochemical Society*, **2006**, *153*, A1432–A1442.
- [56] P. T. Yu, W. Gu, R. Makharia, F. T. Wagner, H. A. Gasteiger, “The Impact of Carbon Stability on PEM Fuel Cell Startup and Shutdown Voltage Degradation”, *ECS Transactions*, **2006**, *3*, 797–809.
- [57] T. Mittermeier, A. Weiß, F. Hasché, G. Hübner, H. A. Gasteiger, “PEM Fuel Cell Start-up/Shut-down Losses vs Temperature for Non-Graphitized and Graphitized Cathode Carbon Supports”, *Journal of The Electrochemical Society*, **2017**, *164*, F127–F137.
- [58] T. Zhang, P. Wang, H. Chen, P. Pei, “A review of automotive proton exchange membrane fuel cell degradation under start-stop operating condition”, *Applied Energy*, **2018**, *223*, 249–262.
- [59] J. Durst, A. Orfanidi, P. J. Rheinländer, F. Hasché, C. Eickes, P. Suchsland, M. Binder, H. A. Gasteiger, “Selective Hydrogen Oxidation Catalyst for Reduced Startup/Shutdown Degradation in Low Temperature Fuel Cells”, *ECS Transactions*, **2015**, *69*, 67–76.
- [60] H. Shintani, Y. Kojima, K. Kakinuma, M. Watanabe, M. Uchida, “Novel strategy to mitigate cathode catalyst degradation during air/air startup cycling via the atmospheric resistive switching mechanism of a hydrogen anode with a platinum catalyst supported on tantalum-doped titanium dioxide”, *Journal of Power Sources*, **2015**, *294*, 292–298.
- [61] T. Ioroi, Z. Siroma, N. Fujiwara, S.-i. Yamazaki, K. Yasuda, “Sub-stoichiometric titanium oxide-supported platinum electrocatalyst for polymer electrolyte fuel cells”, *Electrochemistry Communications*, **2005**, *7*, 183–188.
- [62] S.-Y. Huang, P. Ganesan, S. Park, B. N. Popov, “Development of a Titanium Dioxide-Supported Platinum Catalyst with Ultrahigh Stability for Polymer Electrolyte Membrane Fuel Cell Applications”, *Journal of the American Chemical Society*, **2009**, *131*, 13898–13899.

- [63] T. Ioroi, T. Akita, S.-i. Yamazaki, Z. Siroma, N. Fujiwara, K. Yasuda, “Corrosion-Resistant PEMFC Cathode Catalysts Based on a Magnéli-Phase Titanium Oxide Support Synthesized by Pulsed UV Laser Irradiation”, *Journal of The Electrochemical Society*, **2011**, *158*, C329–C334.
- [64] T. Ioroi, T. Akita, M. Asahi, S.-i. Yamazaki, Z. Siroma, N. Fujiwara, K. Yasuda, “Platinum–titanium alloy catalysts on a Magnéli-phase titanium oxide support for improved durability in Polymer Electrolyte Fuel Cells”, *Journal of Power Sources*, **2013**, *223*, 183–189.
- [65] I. Savych, S. Subianto, Y. Nabil, S. Cavaliere, D. Jones, J. Roziere, “Negligible degradation upon in situ voltage cycling of a PEMFC using an electrospun niobium-doped tin oxide supported Pt cathode”, *Physical Chemistry Chemical Physics*, **2015**, *17*, 16970–16976.
- [66] L. Du, Y. Shao, J. Sun, G. Yin, J. Liu, Y. Wang, “Advanced catalyst supports for PEM fuel cell cathodes”, *Nano Energy*, **2016**, *29*, 314–322.
- [67] D. F. van der Vliet, C. Wang, D. Tripkovic, D. Strmcnik, X. F. Zhang, M. K. Debe, R. T. Atanasoski, N. M. Markovic, V. R. Stamenkovic, “Mesostructured thin films as electrocatalysts with tunable composition and surface morphology”, *Nature Materials*, **2012**, *11*, 1051–1058.
- [68] K. Y. Cho, Y. S. Yeom, H. Y. Seo, P. Kumar, K.-Y. Baek, H. G. Yoon, “A facile synthetic route for highly durable mesoporous platinum thin film electrocatalysts based on graphene: morphological and support effects on the oxygen reduction reaction”, *Journal of Materials Chemistry A*, **2017**, *5*, 3129–3135.
- [69] K. Sarakinos, “A review on morphological evolution of thin metal films on weakly-interacting substrates”, *Thin Solid Films*, **2019**, *688*, 137312.
- [70] B. M. Stühmeier, M. T. Greiner, V. Sureshwaran, L. Schuster, L. H. Tiah, J. N. Schwämmlein, H. A. Gasteiger, H. A. El-Sayed, “Extending the Polyol Reduction Process into the Second Dimension: Oxide Thin Film Reduction”, *Journal of The Electrochemical Society*, **2021**, *168*, 014506.
- [71] T. R. Ralph, S. Hudson, D. P. Wilkinson, “Electrocatalyst Stability In PEMFCs And The Role Of Fuel Starvation And Cell Reversal Tolerant Anodes”, *ECS Transactions*, **2006**, *1*, 67–84.
- [72] F. T. Wagner, S. G. Yan, P. T. Yu, “Catalyst and catalyst-support durability” in *Handbook of Fuel Cells – Fundamentals, Technology and Applications 1st ed., Vol. 5: Advances in Electrocatalysis, Materials, Diagnostics and Durability*, W. Vielstich, H. A. Gasteiger, H. Yokokawa (Eds.), John Wiley & Sons Ltd, Hoboken, **2009**, pp. 250–263.

- [73] A. Collier, H. Wang, X. Zi Yuan, J. Zhang, D. P. Wilkinson, “Degradation of polymer electrolyte membranes”, *International Journal of Hydrogen Energy*, **2006**, *31*, 1838–1854.
- [74] T. A. Greszler, T. E. Moylan, H. A. Gasteiger, “Modeling the impact of cation contamination in a polymere electrolyte membrane fuel cell” in *Handbook of Fuel Cells – Fundamentals, Technology and Applications 1st ed., Vol. 6: Advances in Electrocatalysis, Materials, Diagnostics and Durability*, W. Vielstich, H. Yokokawa, H. A. Gasteiger (Eds.), John Wiley & Sons Ltd, Hoboken, **2009**, pp. 729–748.
- [75] E. Endoh, S. Terazono, H. Widjaja, Y. Takimoto, “Degradation Study of MEA for PEMFCs under Low Humidity Conditions”, *Electrochemical and Solid-State Letters*, **2004**, *7*, A209–A211.
- [76] A. B. LaConti, M. Hamdan, R. C. McDonald, “Mechanisms of membrane degradation” in *Handbook of Fuel Cells – Fundamentals, Technology and Applications 1st ed., Vol. 3: Fuel Cell Technology and Applications*, W. Vielstich, H. A. Gasteiger, A. Lamm (Eds.), John Wiley & Sons Ltd, Hoboken, **2003**, pp. 647–662.
- [77] E. Endoh, “Highly durable PFSA membranes” in *Handbook of Fuel Cells – Fundamentals, Technology and Applications 1st ed., Vol. 5: Advances in Electrocatalysis, Materials, Diagnostics and Durability*, W. Vielstich, H. A. Gasteiger, H. Yokokawa (Eds.), John Wiley & Sons Ltd, Hoboken, **2009**, pp. 361–374.
- [78] A. J. Bard, L. R. Faulkner, *Electrochemical Methods: Fundamentals and Applications*, Vol. 2 of *Electrochemical Methods*, John Wiley & Sons, Hoboken, **2001**.
- [79] Y. Garsany, J. Ge, J. St-Pierre, R. Rocheleau, K. E. Swider-Lyons, “Analytical Procedure for Accurate Comparison of Rotating Disk Electrode Results for the Oxygen Reduction Activity of Pt/C”, *Journal of The Electrochemical Society*, **2014**, *161*, F628–F640.
- [80] T. J. Schmidt, H. A. Gasteiger, “Rotating thin-film method for supported catalysts” in *Handbook of Fuel Cells – Fundamentals, Technology and Applications 1st ed., Vol. 2: Electrocatalysis*, W. Vielstich, H. A. Gasteiger, A. Lamm (Eds.), John Wiley & Sons Ltd, Hoboken, **2003**, pp. 316–333.
- [81] K. Shinozaki, J. W. Zack, R. M. Richards, B. S. Pivovar, S. S. Kocha, “Oxygen Reduction Reaction Measurements on Platinum Electrocatalysts Utilizing Rotating Disk Electrode Technique: I. Impact of Impurities, Measurement Protocols and Applied Corrections”, *Journal of The Electrochemical Society*, **2015**, *162*, F1144–F1158.
- [82] S. S. Kocha, K. Shinozaki, J. W. Zack, D. J. Myers, N. N. Kariuki, T. Nowicki, V. Stamenkovic, Y. Kang, D. Li, D. Papageorgopoulos, “Best Practices and

- Testing Protocols for Benchmarking ORR Activities of Fuel Cell Electrocatalysts Using Rotating Disk Electrode”, *Electrocatalysis*, **2017**, *8*, 366–374.
- [83] H. A. Gasteiger, S. S. Kocha, B. Sompalli, F. T. Wagner, “Activity benchmarks and requirements for Pt, Pt-alloy, and non-Pt oxygen reduction catalysts for PEMFCs”, *Applied Catalysis B: Environmental*, **2005**, *56*, 9–35.
- [84] J. Newman, “Current Distribution on a Rotating Disk below the Limiting Current”, *Journal of The Electrochemical Society*, **1966**, *113*, 1235–1241.
- [85] J. Durst, C. Simon, F. Hasché, H. A. Gasteiger, “Hydrogen Oxidation and Evolution Reaction Kinetics on Carbon Supported Pt, Ir, Rh, and Pd Electrocatalysts in Acidic Media”, *Journal of The Electrochemical Society*, **2015**, *162*, F190–F203.
- [86] K. C. Neyerlin, W. Gu, J. Jorne, A. Clark, H. A. Gasteiger, “Cathode Catalyst Utilization for the ORR in a PEMFC”, *Journal of The Electrochemical Society*, **2007**, *154*, B279–B287.
- [87] D. R. Baker, D. A. Caulk, K. C. Neyerlin, M. W. Murphy, “Measurement of Oxygen Transport Resistance in PEM Fuel Cells by Limiting Current Methods”, *Journal of The Electrochemical Society*, **2009**, *156*, B991–B1003.
- [88] T. R. Garrick, T. E. Moylan, V. Yarlagadda, A. Kongkanand, “Characterizing Electrolyte and Platinum Interface in PEM Fuel Cells Using CO Displacement”, *Journal of The Electrochemical Society*, **2017**, *164*, F60–F64.
- [89] K. Shinozaki, H. Yamada, Y. Morimoto, “Relative Humidity Dependence of Pt Utilization in Polymer Electrolyte Fuel Cell Electrodes: Effects of Electrode Thickness, Ionomer-to-Carbon Ratio, Ionomer Equivalent Weight, and Carbon Support”, *Journal of The Electrochemical Society*, **2011**, *158*, B467–B475.
- [90] C. M. Zalitis, D. Kramer, A. R. Kucernak, “Electrocatalytic performance of fuel cell reactions at low catalyst loading and high mass transport”, *Physical Chemistry Chemical Physics*, **2013**, *15*, 4329–4340.
- [91] J. T. H. Kwan, A. Bonakdarpour, G. Afonso, D. P. Wilkinson, “Bridging Fundamental Electrochemistry with Applied Fuel Cell Testing: A Novel and Economical Rotating Disk Electrode Tip for Electrochemical Assessment of Catalyst-Coated Membranes”, *Electrochimica Acta*, **2017**, *258*, 208–219.
- [92] B. A. Pinaud, A. Bonakdarpour, L. Daniel, J. Sharman, D. P. Wilkinson, “Key Considerations for High Current Fuel Cell Catalyst Testing in an Electrochemical Half-Cell”, *Journal of The Electrochemical Society*, **2017**, *164*, F321–F327.
- [93] M. Inaba, A. W. Jensen, G. W. Sievers, M. Escudero-Escribano, A. Zana, M. Arenz, “Benchmarking high surface area electrocatalysts in a gas diffusion

- electrode: measurement of oxygen reduction activities under realistic conditions”, *Energy & Environmental Science*, **2018**, *11*, 988–994.
- [94] K. Ehelebe, D. Escalera-López, S. Cherevko, “Limitations of aqueous model systems in the stability assessment of electrocatalysts for oxygen reactions in fuel cell and electrolyzers”, *Current Opinion in Electrochemistry*, **2021**, *29*, 100832.
- [95] S. Tauster, S. Fung, R. L. Garten, “Strong Metal-Support Interactions. Group 8 Noble Metals Supported on TiO<sub>2</sub>”, *Journal of the American Chemical Society*, **1978**, *100*, 170–175.
- [96] S. Tauster, “Strong Metal-Support Interactions”, *Accounts of Chemical Research*, **1987**, *20*, 389–394.
- [97] C.-J. Pan, M.-C. Tsai, W.-N. Su, J. Rick, N. G. Akalework, A. K. Agegnehu, S.-Y. Cheng, B.-J. Hwang, “Tuning/exploiting Strong Metal-Support Interaction (SMSI) in Heterogeneous Catalysis”, *Journal of the Taiwan Institute of Chemical Engineers*, **2017**, *74*, 154–186.
- [98] S. Bernal, J. J. Calvino, M. A. Cauqui, J. M. Gatica, C. López Cartes, J. A. Pérez Omil, J. M. Pintado, “Some contributions of electron microscopy to the characterisation of the strong metal–support interaction effect”, *Catalysis Today*, **2003**, *77*, 385–406.
- [99] A. Lewera, L. Timperman, A. Roguska, N. Alonso-Vante, “Metal–Support Interactions between Nanosized Pt and Metal Oxides (WO<sub>3</sub> and TiO<sub>2</sub>) Studied Using X-ray Photoelectron Spectroscopy”, *The Journal of Physical Chemistry C*, **2011**, *115*, 20153–20159.
- [100] A. Beck, X. Huang, L. Artiglia, M. Zabilskiy, X. Wang, P. Rzepka, D. Palagin, M.-G. Willinger, J. A. van Bokhoven, “The dynamics of overlayer formation on catalyst nanoparticles and strong metal-support interaction”, *Nature Communications*, **2020**, *11*, 3220.
- [101] B. E. Hayden, D. Pletcher, J.-P. Suchsland, L. J. Williams, “The influence of Pt particle size on the surface oxidation of titania supported platinum”, *Physical Chemistry Chemical Physics*, **2009**, *11*, 1564–1570.
- [102] B. E. Hayden, D. Pletcher, J.-P. Suchsland, L. J. Williams, “The influence of support and particle size on the platinum catalysed oxygen reduction reaction”, *Physical Chemistry Chemical Physics*, **2009**, *11*, 9141–9148.
- [103] D. Banham, S. Ye, A. O’Toole, A. Lemke, E. Eisenbraun, “Unexpected hydrogen oxidation selectivity of Pt/NbTiO<sub>2</sub> catalysts”, *Nano Energy*, **2016**, *27*, 157–166.
- [104] M. Eckardt, C. Gebauer, Z. Jusys, M. Wassner, N. Hüsing, R. J. Behm, “Oxygen reduction reaction activity and long-term stability of platinum nanoparticles

- supported on titania and titania-carbon nanotube composites”, *Journal of Power Sources*, **2018**, *400*, 580–591.
- [105] E. Hornberger, A. Bergmann, H. Schmies, S. Kühl, G. Wang, J. Drnec, D. J. S. Sandbeck, V. Ramani, S. Cherevko, K. J. J. Mayrhofer, P. Strasser, “In Situ Stability Studies of Platinum Nanoparticles Supported on Ruthenium-Titanium Mixed Oxide (RTO) for Fuel Cell Cathodes”, *ACS Catalysis*, **2018**, *8*, 9675–9683.
- [106] Y.-J. Wang, D. P. Wilkinson, J. Zhang, “Noncarbon Support Materials for Polymer Electrolyte Membrane Fuel Cell Electrocatalysts”, *Chemical Reviews*, **2011**, *111*, 7625–7651.
- [107] A. Bauer, R. Hui, A. Ignaszak, J. Zhang, D. J. Jones, “Application of a composite structure of carbon nanoparticles and Nb–TiO<sub>2</sub> nanofibers as electrocatalyst support for PEM fuel cells”, *Journal of Power Sources*, **2012**, *210*, 15–20.
- [108] C. Gebauer, Z. Jusys, M. Wassner, N. Hüsing, R. J. Behm, “Membrane Fuel Cell Cathode Catalysts Based on Titanium Oxide Supported Platinum Nanoparticles”, *ChemPhysChem*, **2014**, *15*, 2094–2107.
- [109] V. T. T. Ho, C.-J. Pan, J. Rick, W.-N. Su, B.-J. Hwang, “Nanostructured Ti<sub>0.7</sub>Mo<sub>0.3</sub>O<sub>2</sub> Support Enhances Electron Transfer to Pt: High-Performance Catalyst for Oxygen Reduction Reaction”, *Journal of the American Chemical Society*, **2011**, *133*, 11716–11724.
- [110] V. T. T. Ho, K. C. Pillai, H.-L. Chou, C.-J. Pan, J. Rick, W.-N. Su, B.-J. Hwang, J.-F. Lee, H.-S. Sheu, W.-T. Chuang, “Robust non-carbon Ti<sub>0.7</sub>Ru<sub>0.3</sub>O<sub>2</sub> support with co-catalytic functionality for Pt: enhances catalytic activity and durability for fuel cells”, *Energy & Environmental Science*, **2011**, *4*, 4194–4200.
- [111] A. Kumar, V. Ramani, “Strong Metal–Support Interactions Enhance the Activity and Durability of Platinum Supported on Tantalum-Modified Titanium Dioxide Electrocatalysts”, *ACS Catalysis*, **2014**, *4*, 1516–1525.
- [112] I. Jiménez-Morales, S. Cavaliere, D. Jones, J. Rozière, “Strong metal–support interaction improves activity and stability of Pt electrocatalysts on doped metal oxides”, *Physical Chemistry Chemical Physics*, **2018**, *20*, 8765–8772.
- [113] I. Jiménez-Morales, F. Haidar, S. Cavaliere, D. Jones, J. Rozière, “Strong Interaction between Platinum Nanoparticles and Tantalum-Doped Tin Oxide Nanofibers and Its Activation and Stabilization Effects for Oxygen Reduction Reaction”, *ACS Catalysis*, **2020**, *10*, 10399–10411.
- [114] B.-J. Hsieh, M.-C. Tsai, C.-J. Pan, W.-N. Su, J. Rick, H.-L. Chou, J.-F. Lee, B.-J. Hwang, “Tuning metal support interactions enhances the activity and durability of TiO<sub>2</sub>-supported Pt nanocatalysts”, *Electrochimica Acta*, **2017**, *224*, 452–459.

- [115] S. Labich, E. Taglauer, H. Knözinger, “Metal–support interactions on rhodium model catalysts”, *Topics in Catalysis*, **2000**, *14*, 153–161.
- [116] G. Cognard, G. Ozouf, C. Beauger, L. Dubau, M. López-Haro, M. Chatenet, F. Maillard, “Insights into the stability of Pt nanoparticles supported on antimony-doped tin oxide in different potential ranges”, *Electrochimica Acta*, **2017**, *245*, 993–1004.
- [117] C. Gebauer, Z. Jusys, R. J. Behm, “On the Role of the Support in Pt Anode Catalyst Degradation under Simulated H<sub>2</sub> Fuel Starvation Conditions”, *Journal of the Electrochemical Society*, **2018**, *165*, J3342–J3349.
- [118] B. M. Stühmeier, S. Selve, M. U. M. Patel, T. N. Geppert, H. A. Gasteiger, H. A. El-Sayed, “Highly Selective Pt/TiO<sub>x</sub> Catalysts for the Hydrogen Oxidation Reaction”, *ACS Applied Energy Materials*, **2019**, *2*, 5534–5539.
- [119] T. N. Geppert, M. Bosund, M. Putkonen, B. M. Stühmeier, A. T. Pasanen, P. Heikkilä, H. A. Gasteiger, H. A. El-Sayed, “HOR Activity of Pt-TiO<sub>2-γ</sub> at Unconventionally High Potentials Explained: The Influence of SMSI on the Electrochemical Behavior of Pt”, *Journal of The Electrochemical Society*, **2020**, *167*, 084517.
- [120] B. M. Stühmeier, R. J. Schuster, L. Hartmann, S. Selve, H. A. El-Sayed, H. Gasteiger, “Modification of the Electrochemical Surface Oxide Formation and the Hydrogen Oxidation Activity of Ruthenium by Strong Metal Support Interactions”, *Journal of The Electrochemical Society*, **2022**, *169*, 034519.
- [121] J. Zhang, F. Coms, S. Kumaraguru, “Editors’ Choice—Necessity to Avoid Titanium Oxide as Electrocatalyst Support in PEM Fuel Cells: A Membrane Durability Study”, *Journal of The Electrochemical Society*, **2021**, *168*, 024520.
- [122] M. J. Muñoz-Portero, J. García-Antón, J. L. Guñón, R. Leiva-García, “Pourbaix diagrams for titanium in concentrated aqueous lithium bromide solutions at 25°C”, *Corrosion Science*, **2011**, *53*, 1440–1450.
- [123] R. L. Borup, A. Kusoglu, K. C. Neyerlin, R. Mukundan, R. K. Ahluwalia, D. A. Cullen, K. L. More, A. Z. Weber, D. J. Myers, “Recent developments in catalyst-related PEM fuel cell durability”, *Current Opinion in Electrochemistry*, **2020**, *21*, 192–200.
- [124] G. S. Harzer, Dissertation, Technische Universität München, München, **2018**.
- [125] J. N. Schwämmlein, Dissertation, Technische Universität München, München, **2020**.
- [126] B. M. Stühmeier, A. M. Damjanović, K. Rodewald, H. A. Gasteiger, “Selective Anode Catalysts for the Mitigation of Start-Up/Shut-Down Induced Cathode Degradation in Proton Exchange Membrane Fuel Cells”, *to be submitted*, **2022**.

- 
- [127] N. T. K. Thanh, N. Maclean, S. Mahiddine, “Mechanisms of Nucleation and Growth of Nanoparticles in Solution”, *Chemical Reviews*, **2014**, *114*, 7610–7630.
- [128] H. A. El-Sayed, V. M. Burger, M. Miller, K. Wagenbauer, M. Wagenhofer, H. A. Gasteiger, “Ionic Conductivity Measurements—A Powerful Tool for Monitoring Polyol Reduction Reactions”, *Langmuir*, **2017**, *33*, 13615–13624.
- [129] D. Larcher, R. Patrice, “Preparation of Metallic Powders and Alloys in Polyol Media: A Thermodynamic Approach”, *Journal of Solid State Chemistry*, **2000**, *154*, 405–411.
- [130] F. Fiévet, S. Ammar-Merah, R. Brayner, F. Chau, M. Giraud, F. Mammeri, J. Peron, J. Y. Piquemal, L. Sicard, G. Viau, “The polyol process: a unique method for easy access to metal nanoparticles with tailored sizes, shapes and compositions”, *Chemical Society Reviews*, **2018**, *47*, 5187–5233.
- [131] H. Dong, Y. C. Chen, C. Feldmann, “Polyol synthesis of nanoparticles: status and options regarding metals, oxides, chalcogenides, and non-metal elements”, *Green Chemistry*, **2015**, *17*, 4107–4132.
- [132] M. Shao, J. H. Odell, S.-I. Choi, Y. Xia, “Electrochemical surface area measurements of platinum- and palladium-based nanoparticles”, *Electrochemistry Communications*, **2013**, *31*, 46–48.
- [133] Umweltbundesamt - Fachgebiet II 4.2 ”Beurteilung der Luftqualität”, “Kohlenmonoxid (CO) im Jahr 2019”, [https://www.umweltbundesamt.de/sites/default/files/w21ad\\_luftdaten/annualtabulation/PDF/co\\_2019.pdf](https://www.umweltbundesamt.de/sites/default/files/w21ad_luftdaten/annualtabulation/PDF/co_2019.pdf) (accessed: 18.01.2022).
- [134] W. Vogel, L. Lundquist, P. Ross, P. Stonehart, “Reaction pathways and poisons—II: The rate controlling step for electrochemical oxidation of hydrogen on Pt in acid and poisoning of the reaction by CO”, *Electrochimica Acta*, **1975**, *20*, 79–93.
- [135] C. Simon, F. Hasché, D. Müller, H. A. Gasteiger, “Influence of the Gas Diffusion Layer Compression on the Oxygen Mass Transport in PEM Fuel Cells”, *ECS Transactions*, **2015**, *69*, 1293–1302.
- [136] C. Simon, F. Hasché, H. A. Gasteiger, “Influence of the Gas Diffusion Layer Compression on the Oxygen Transport in PEM Fuel Cells at High Water Saturation Levels”, *Journal of The Electrochemical Society*, **2017**, *164*, F591–F599.
- [137] M. Inaba, H. Yamada, J. Tokunaga, A. Tasaka, “Effect of Agglomeration of Pt/C Catalyst on Hydrogen Peroxide Formation”, *Electrochemical and Solid-State Letters*, **2004**, *7*, A474–A476.

- [138] P. Zihrul, P. Weber, J. Durst, H. A. Gasteiger, F. Hasché, “Impact of Hydrogen Bleeding into the Cathode Feed of a PEM Fuel Cell”, *Journal of The Electrochemical Society*, **2017**, *164*, F209–F216.
- [139] T. J. Schmidt, H. A. Gasteiger, G. D. Stäb, P. M. Urban, D. M. Kolb, R. J. Behm, “Characterization of High-Surface-Area Electrocatalysts Using a Rotating Disk Electrode Configuration”, *Journal of The Electrochemical Society*, **1998**, *145*, 2354–2358.
- [140] H. A. Gasteiger, J. E. Panels, S. G. Yan, “Dependence of PEM fuel cell performance on catalyst loading”, *Journal of Power Sources*, **2004**, *127*, 162–171.
- [141] C. M. Zalitis, J. Sharman, E. Wright, A. R. Kucernak, “Properties of the hydrogen oxidation reaction on Pt/C catalysts at optimised high mass transport conditions and its relevance to the anode reaction in PEFCs and cathode reactions in electrolyzers”, *Electrochimica Acta*, **2015**, *176*, 763–776.
- [142] S. Martens, L. Asen, G. Ercolano, F. Dionigi, C. Zalitis, A. Hawkins, A. Martinez Bonastre, L. Seidl, A. C. Knoll, J. Sharman, P. Strasser, D. Jones, O. Schneider, “A comparison of rotating disc electrode, floating electrode technique and membrane electrode assembly measurements for catalyst testing”, *Journal of Power Sources*, **2018**, *392*, 274–284.
- [143] K. Elbert, J. Hu, Z. Ma, Y. Zhang, G. Chen, W. An, P. Liu, H. S. Isaacs, R. R. Adzic, J. X. Wang, “Elucidating Hydrogen Oxidation/Evolution Kinetics in Base and Acid by Enhanced Activities at the Optimized Pt Shell Thickness on the Ru Core”, *ACS Catalysis*, **2015**, *5*, 6764–6772.
- [144] K. Ehelebe, D. Seeberger, M. T. Y. Paul, S. Thiele, K. J. J. Mayrhofer, S. Cherevko, “Evaluating Electrocatalysts at Relevant Currents in a Half-Cell: The Impact of Pt Loading on Oxygen Reduction Reaction”, *Journal of The Electrochemical Society*, **2019**, *166*, F1259–F1268.
- [145] H. Ito, T. Maeda, A. Nakano, H. Takenaka, “Properties of Nafion membranes under PEM water electrolysis conditions”, *International Journal of Hydrogen Energy*, **2011**, *36*, 10527–10540.
- [146] S. M. Alia, G. C. Anderson, “Iridium Oxygen Evolution Activity and Durability Baselines in Rotating Disk Electrode Half-Cells”, *Journal of The Electrochemical Society*, **2019**, *166*, F282–F294.
- [147] M. Bernt, A. Hartig-Weiß, M. F. Tovini, H. A. El-Sayed, C. Schramm, J. Schröter, C. Gebauer, H. A. Gasteiger, “Current Challenges in Catalyst Development for PEM Water Electrolyzers”, *Chemie Ingenieur Technik*, **2020**, *92*, 31–39.

- [148] M. Fathi Tovini, A. Hartig-Weiß, H. A. Gasteiger, H. A. El-Sayed, “The Discrepancy in Oxygen Evolution Reaction Catalyst Lifetime Explained: RDE vs MEA - Dynamicity within the Catalyst Layer Matters”, *Journal of the Electrochemical Society*, **2021**, *168*, 014512.
- [149] H. A. El-Sayed, A. Weiß, L. F. Olbrich, G. P. Putro, H. A. Gasteiger, “OER Catalyst Stability Investigation Using RDE Technique: A Stability Measure or an Artifact?”, *Journal of The Electrochemical Society*, **2019**, *166*, F458–F464.
- [150] J. Knöppel, M. Möckl, D. Escalera-López, K. Stojanovski, M. Bierling, T. Böhm, S. Thiele, M. Rzepka, S. Cherevko, “On the limitations in assessing stability of oxygen evolution catalysts using aqueous model electrochemical cells”, *Nature Communications*, **2021**, *12*, 2231.
- [151] P. J. Petzoldt, J. T. H. Kwan, A. Bonakdarpour, D. P. Wilkinson, “Deconvoluting Reversible and Irreversible Degradation Phenomena in OER Catalyst Coated Membranes Using a Modified RDE Technique”, *Journal of The Electrochemical Society*, **2021**, *168*, 026507.
- [152] K. C. Neyerlin, W. Gu, J. Jorne, H. A. Gasteiger, “Study of the Exchange Current Density for the Hydrogen Oxidation and Evolution Reactions”, *Journal of The Electrochemical Society*, **2007**, *154*, B631–B635.
- [153] J. Zheng, Y. Yan, B. Xu, “Correcting the Hydrogen Diffusion Limitation in Rotating Disk Electrode Measurements of Hydrogen Evolution Reaction Kinetics”, *Journal of The Electrochemical Society*, **2015**, *162*, F1470–F1481.
- [154] J. Zheng, W. Sheng, Z. Zhuang, B. Xu, Y. Yan, “Universal dependence of hydrogen oxidation and evolution reaction activity of platinum-group metals on pH and hydrogen binding energy”, *Science Advances*, **2016**, *2*, e1501602.
- [155] Q. Chen, L. Luo, “Correlation between Gas Bubble Formation and Hydrogen Evolution Reaction Kinetics at Nanoelectrodes”, *Langmuir*, **2018**, *34*, 4554–4559.
- [156] K. J. J. Mayrhofer, D. Strmcnik, B. B. Blizanac, V. Stamenkovic, M. Arenz, N. M. Markovic, “Measurement of oxygen reduction activities via the rotating disc electrode method: From Pt model surfaces to carbon-supported high surface area catalysts”, *Electrochimica Acta*, **2008**, *53*, 3181–3188.
- [157] J. C. Meier, I. Katsounaros, C. Galeano, H. J. Bongard, A. A. Topalov, A. Kostka, A. Karschin, F. Schüth, K. J. J. Mayrhofer, “Stability investigations of electrocatalysts on the nanoscale”, *Energy & Environmental Science*, **2012**, *5*, 9319–9330.
- [158] A. Riese, D. Banham, S. Ye, X. Sun, “Accelerated Stress Testing by Rotating Disk Electrode for Carbon Corrosion in Fuel Cell Catalyst Supports”, *Journal of The Electrochemical Society*, **2015**, *162*, F783–F788.

- [159] S. Stariha, N. Macauley, B. T. Sneed, D. Langlois, K. L. More, R. Mukundan, R. L. Borup, “Recent Advances in Catalyst Accelerated Stress Tests for Polymer Electrolyte Membrane Fuel Cells”, *Journal of The Electrochemical Society*, **2018**, *165*, F492–F501.
- [160] N. Ramaswamy, S. Kumaraguru, R. Koestner, T. Fuller, W. Gu, N. Kariuki, D. Myers, P. J. Dudenas, A. Kusoglu, “Editors’ Choice—Ionomer Side Chain Length and Equivalent Weight Impact on High Current Density Transport Resistances in PEMFC Cathodes”, *Journal of The Electrochemical Society*, **2021**, *168*, 024518.
- [161] B. M. Stühmeier, M. R. Pietsch, J. N. Schwämmlein, H. A. Gasteiger, “Pressure Dependency of the Hydrogen Oxidation and Evolution Reaction Kinetics on Carbon Supported Pt Catalysts Using a PEMFC Based Hydrogen Pump Approach”, *ECS Meeting Abstracts*, **2020**, *MA2020-02*, 2337–2337.
- [162] M. Bernt, A. Siebel, H. A. Gasteiger, “Analysis of Voltage Losses in PEM Water Electrolyzers with Low Platinum Group Metal Loadings”, *Journal of The Electrochemical Society*, **2018**, *165*, F305–F314.
- [163] J. Durst, A. Siebel, C. Simon, F. Hasche, J. Herranz, H. A. Gasteiger, “New insights into the electrochemical hydrogen oxidation and evolution reaction mechanism”, *Energy & Environmental Science*, **2014**, *7*, 2255–2260.
- [164] S. Fletcher, “Tafel slopes from first principles”, *Journal of Solid State Electrochemistry*, **2009**, *13*, 537–549.
- [165] R. Guidelli, G. Compton Richard, M. Feliu Juan, E. Gileadi, J. Lipkowski, W. Schmickler, S. Trasatti, “Defining the transfer coefficient in electrochemistry: An assessment (IUPAC Technical Report)”, *Pure and Applied Chemistry*, **2014**, *86*, 245–258.
- [166] J. S. Newman, *Electrochemical systems 2nd ed.*, Prentice Hall, Englewood Cliffs, **1991**.
- [167] I. Chorkendorff, J. W. Niemantsverdriet, *Concepts of Modern Catalysis and Kinetics*, John Wiley & Sons, Inc., Weinheim, **2003**.
- [168] J. K. Nørskov, F. Studt, F. Abild-Pedersen, T. Bligaard, *Fundamental Concepts in Heterogeneous Catalysis*, John Wiley & Sons, Inc., Hoboken, **2014**.
- [169] C. K. Mittelsteadt, H. Liu, “Conductivity, permeability, and ohmic shorting of ionomeric membranes” in *Handbook of Fuel Cells – Fundamentals, Technology and Applications 1st ed., Vol. 5: Advances in Electrocatalysis, Materials, Diagnostics and Durability*, W. Vielstich, H. A. Gasteiger, H. Yokokawa (Eds.), John Wiley & Sons Ltd, Hoboken, **2009**, pp. 345–357.

- [170] T. Schuler, A. Chowdhury, A. T. Freiberg, B. Sneed, F. B. Spingler, M. C. Tucker, K. L. More, C. J. Radke, A. Z. Weber, “Fuel-Cell Catalyst-Layer Resistance via Hydrogen Limiting-Current Measurements”, *Journal of The Electrochemical Society*, **2019**, *166*, F3020–F3031.
- [171] S. H. Joo, J. Y. Park, C.-K. Tsung, Y. Yamada, P. Yang, G. A. Somorjai, “Thermally stable Pt/mesoporous silica core-shell nanocatalysts for high-temperature reactions”, *Nature Materials*, **2009**, *8*, 126–131.
- [172] Q. Fu, T. Wagner, “Interaction of nanostructured metal overlayers with oxide surfaces”, *Surface Science Reports*, **2007**, *62*, 431–498.
- [173] J. Lu, K.-B. Low, Y. Lei, J. A. Libera, A. Nicholls, P. C. Stair, J. W. Elam, “Toward atomically-precise synthesis of supported bimetallic nanoparticles using atomic layer deposition”, *Nature Communications*, **2014**, *5*, 3264.
- [174] N. V. Long, T. Asaka, T. Matsubara, M. Nogami, “Shape-controlled synthesis of Pt–Pd core-shell nanoparticles exhibiting polyhedral morphologies by modified polyol method”, *Acta Materialia*, **2011**, *59*, 2901–2907.
- [175] G. Park, D. Seo, J. Jung, S. Ryu, H. Song, “Shape Evolution and Gram-Scale Synthesis of Gold@Silver Core-Shell Nanopolyhedrons”, *The Journal of Physical Chemistry C*, **2011**, *115*, 9417–9423.
- [176] J. N. Schwämmlein, B. M. Stühmeier, K. Wagenbauer, H. Dietz, V. Tileli, H. A. Gasteiger, H. A. El-Sayed, “Origin of Superior HOR/HER Activity of Bimetallic Pt-Ru Catalysts in Alkaline Media Identified via Ru@Pt Core-Shell Nanoparticles”, *Journal of The Electrochemical Society*, **2018**, *165*, H229–H239.
- [177] H. Dong, Y. C. Chen, C. Feldmann, “Polyol synthesis of nanoparticles: status and options regarding metals, oxides, chalcogenides, and non-metal elements”, *Green Chemistry*, **2015**, *17*, 4107–4132.
- [178] N. Sato, *Electrochemistry at Metal and Semiconductor Electrodes*, Elsevier, Amsterdam, **1998**.
- [179] M. J. González, C. T. Hable, M. S. Wrighton, “Electrocatalytic Oxidation of Small Carbohydrate Fuels at Pt-Sn Modified Electrodes”, *The Journal of Physical Chemistry B*, **1998**, *102*, 9881–9890.
- [180] T. Matsumoto, K. Takahashi, K. Kitagishi, K. Shinoda, J. L. Cuya Huaman, J.-Y. Piquemal, B. Jeyadevan, “Dissolution and reduction of cobalt ions in the polyol process using ethylene glycol: identification of the active species and its role”, *New Journal of Chemistry*, **2015**, *39*, 5008–5018.
- [181] P. J. Rheinländer, J. Herranz, J. Durst, H. A. Gasteiger, “Kinetics of the Hydrogen Oxidation/Evolution Reaction on Polycrystalline Platinum in Alkaline

- Electrolyte Reaction Order with Respect to Hydrogen Pressure”, *Journal of The Electrochemical Society*, **2014**, *161*, F1448–F1457.
- [182] P. Piela, C. Eickes, E. Brosha, F. Garzon, P. Zelenay, “Ruthenium Crossover in Direct Methanol Fuel Cell with Pt-Ru Black Anode”, *Journal of The Electrochemical Society*, **2004**, *151*, A2053–A2059.
- [183] L. Gancs, B. N. Hult, N. Hakim, S. Mukerjee, “The Impact of Ru Contamination of a Pt/C Electrocatalyst on Its Oxygen-Reducing Activity”, *Electrochemical and Solid-State Letters*, **2007**, *10*, B150–B154.
- [184] B. M. Stühmeier, A. M. Damjanović, P. A. Loichet, S. Selve, H. A. Gasteiger, “Mitigation of the Start-up and Shut-down Degradation in Pemfcs By Means of a Selective H<sub>2</sub> Oxidation Catalyst”, *ECS Meeting Abstracts*, **2021**, *MA2021-02*, 1185–1185.
- [185] M. Uchimura, S. S. Kocha, “The Impact of Cycle Profile on PEMFC Durability”, *ECS Transactions*, **2007**, *11*, 1215–1226.
- [186] C. Takei, K. Kakinuma, K. Kawashima, K. Tashiro, M. Watanabe, M. Uchida, “Load cycle durability of a graphitized carbon black-supported platinum catalyst in polymer electrolyte fuel cell cathodes”, *Journal of Power Sources*, **2016**, *324*, 729–737.
- [187] A. Kneer, J. Jankovic, D. Susac, A. Putz, N. Wagner, M. Sabharwal, M. Se-canell, “Correlation of Changes in Electrochemical and Structural Parameters due to Voltage Cycling Induced Degradation in PEM Fuel Cells”, *Journal of The Electrochemical Society*, **2018**, *165*, F3241–F3250.
- [188] A. Kneer, N. Wagner, C. Sadeler, A.-C. Scherzer, D. Gerteisen, “Effect of Dwell Time and Scan Rate during Voltage Cycling on Catalyst Degradation in PEM Fuel Cells”, *Journal of The Electrochemical Society*, **2018**, *165*, F805–F812.
- [189] A. Kneer, N. Wagner, “A Semi-Empirical Catalyst Degradation Model Based on Voltage Cycling under Automotive Operating Conditions in PEM Fuel Cells”, *Journal of The Electrochemical Society*, **2019**, *166*, F120–F127.
- [190] D. A. Langlois, A. S. Lee, N. Macauley, S. Maurya, M. E. Hawley, S. D. Yim, Y. S. Kim, “A rejuvenation process to enhance the durability of low Pt loaded polymer electrolyte membrane fuel cells”, *Journal of Power Sources*, **2018**, *396*, 345–354.
- [191] E. Padgett, V. Yarlagadda, M. E. Holtz, M. Ko, B. D. A. Levin, R. S. Kukreja, J. M. Ziegelbauer, R. N. Andrews, J. Ilavsky, A. Kongkanand, D. A. Muller, “Mitigation of PEM Fuel Cell Catalyst Degradation with Porous Carbon Supports”, *Journal of The Electrochemical Society*, **2019**, *166*, F198–F207.

- [192] N. Ramaswamy, S. Kumaraguru, W. Gu, R. S. Kukreja, K. Yu, D. Groom, P. Ferreira, “High-Current Density Durability of Pt/C and PtCo/C Catalysts at Similar Particle Sizes in PEMFCs”, *Journal of The Electrochemical Society*, **2021**, *168*, 024519.
- [193] D. D. Papadias, R. K. Ahluwalia, N. Kariuki, D. Myers, K. L. More, D. A. Cullen, B. T. Sneed, K. C. Neyerlin, R. Mukundan, R. L. Borup, “Durability of Pt-Co Alloy Polymer Electrolyte Fuel Cell Cathode Catalysts under Accelerated Stress Tests”, *Journal of The Electrochemical Society*, **2018**, *165*, F3166–F3177.



# List of Figures

1.1. Components and assembly of the 5 cm <sup>2</sup> active area PEMFC hardware that was used throughout this thesis for the characterization of PEMFC single-cells. . . . .	4
1.2. Cross-sectional image of a symmetrical MEA with anode and cathode loadings of 0.1 mg <sub>Pt</sub> cm <sup>-2</sup> <sub>MEA</sub> coated on a reinforced 15 μm thick PFSA membrane. The image was taken by scanning electron microscopy (SEM) at 10 kV and a magnification of 1,600x. . . . .	5
1.3. Schematic of a SUSD event in a PEMFC, sketching the passage of a H <sub>2</sub> /air <sub>anode</sub> front through the anode flow-field (H <sub>2</sub> -filled regions in red, air-filled regions in blue) while the cathode flow-field is filled with air. a) Illustration of the reactions occurring during the SUSD event, with sketched pathways of electrons (in green) through the electrode, diffusion medium (DM) and flow-field (FF) as well as of protons (in orange) across the membrane; b) Conceptual separation into a fuel cell (FC) segment and an electrolytic cell (EL) segment (H <sub>2</sub> -filled and air-filled flow-field segments are indicated in red and in blue, respectively). In-plane proton conduction is only possible within very short distances from the H <sub>2</sub> /air <sub>anode</sub> front (≈ 120 μm for a 20 μm thick membrane) and not over extended distances, which is indicated by the crossed-out arrows. The figure is reprinted from Mittermeier <i>et al.</i> under the terms of the CC BY-NC-ND License. <sup>57</sup> . . . . .	11
1.4. Comparison of RDE (left) and 5-layer MEA (right) setups, including a table that highlights the main differences between the techniques. a) Local environment of an RDE working electrode (WE); b) scheme of a 3-electrode RDE setup; c) 5-layer MEA setups consisting either of a CCM sandwiched between two GDLs or a PEM between two GDEs; d) local environment in an MEA with the porous catalyst layer (CL) consisting of catalyst particles (black) and ionomer (light blue). The table summarizes typical specifications for both setups (exceptions might apply). The figure is adapted from Lazaridis and Stühmeier <i>et al.</i> (see Section 3.1.1). <sup>28</sup> . . . . .	15

1.5.	TEM images of Pt/TiO <sub>x</sub> /C (a – c) and Ru/TiO <sub>x</sub> /C (d – g) after the reductive heat-treatment at 400 °C in 5% H <sub>2</sub> /Ar atmosphere. a) TEM image of the Pt/TiO <sub>x</sub> /C catalyst that consists of Pt/TiO <sub>x</sub> agglomerates (characterized by their rough morphology and the dark Pt particles) supported on the Vulcan carbon structure (primary agglomerates of round and smooth carbon spheres); b & c) high resolution TEM images showing the encapsulation of the Pt particles by a thin layer of TiO <sub>x</sub> (indicated by the yellow arrows). d) Scanning transmission electron microscopy (STEM) images of the Ru/TiO <sub>x</sub> /C catalyst in high angle annular dark field (HAADF) mode whereby heavy elements appear brighter; corresponding energy dispersive X-ray spectroscopy (EDX) mappings of e) Ru, f) Ru & Ti, and g) Ru, Ti & C, showing the successful deposition of Ru on TiO <sub>x</sub> . Panels d – g adapted from Stühmeier and Schuster <i>et al.</i> (see Section 3.2.3). <sup>120</sup> . . . . .	22
2.1.	Temperature profile for the reductive heat-treatment of PGM/TiO <sub>2</sub> /C catalysts. First, the tube furnace is flushed with Ar (1 L min <sup>-1</sup> ), followed by a temperature ramp of 10 K min <sup>-1</sup> and a 60 min hold at 400 °C in 5% H <sub>2</sub> /Ar (0.5 – 1 L min <sup>-1</sup> , depending on the sample size), and finally, the furnace is allowed to cool down in Ar atmosphere (1 L min <sup>-1</sup> ). . . . .	27
2.2.	CO-stripping measurement for a 0.1 mg <sub>Pt</sub> cm <sup>-2</sup> <sub>MEA</sub> MEA with an <i>rf</i> of 78 cm <sup>2</sup> <sub>Pt</sub> cm <sup>-2</sup> <sub>MEA</sub> : a) CO-stripping and subsequent CV recorded at 100 mV s <sup>-1</sup> ; b) baseline (second scan) corrected CO-stripping peak; the measurements were performed at 40 °C and 95% <i>RH</i> . . . . .	29
2.3.	Simplified flow diagram of the relevant connections, valves and mass flow controllers for CO measurements. Here, N <sub>2</sub> (main) refers to N <sub>2</sub> from the house line that is obtained from a liquid N <sub>2</sub> tank, whereas N <sub>2</sub> (5.0) is obtained from gas bottles (≥ 99.999% gas purity). . . . .	30
2.4.	Investigation of the gas purity by comparing measurements with regular N <sub>2</sub> (main) from the house line connected to the test station (left) and with N <sub>2</sub> (5.0) connected to both N <sub>2</sub> inlets (right); a & b) proper CO-stripping measurements including CO introduction into the system; c & d) CO <sub>free</sub> -stripping experiments consisting of the full purging procedure (including potential hold) without the preceding introduction of CO; e & f) CO <sub>free</sub> -stripping procedure after purging all lines for 12 h with N <sub>2</sub> (5.0). The CO-stripping peak in the CO <sub>free</sub> measurements is indicative of the remaining CO in the N <sub>2</sub> gas lines; the measurements were performed at 40 °C and 95% <i>RH</i> on cells with an active area of 5 cm <sup>2</sup> . . . . .	32

- 
- 2.5. All three cycles of cathode CVs that were recorded after N<sub>2</sub> purges following a) anode CVs (cathode filled with 5% H<sub>2</sub>/Ar), or b) polarization curves (cathode filled with air), respectively. A CO-oxidation peak in the first scan indicates CO accumulation on the Pt surface. The CVs were recorded at 50 mV s<sup>-1</sup>, 5 nccm N<sub>2</sub> (main), 40 °C, 95% RH, and ambient pressure with 5% H<sub>2</sub>/Ar on the anode (100 nccm). The active area of the cell is 5 cm<sup>2</sup>. . . . . 33
- 2.6. All three cycles of anode CVs that were recorded after a) a CO-strip on the cathode, or b) cathode CVs without CO, respectively. A CO-oxidation peak in the first scan indicates CO accumulation on the Pt surface. The anode was purged with N<sub>2</sub> (main) for ≈ 30 min to remove H<sub>2</sub> from the cell before recording the CVs at 50 mV s<sup>-1</sup>, 5 nccm N<sub>2</sub> (main), 40 °C, 95% RH, and ambient pressure with 5% H<sub>2</sub>/Ar on the cathode (100 nccm). The active area of the cell is 5 cm<sup>2</sup>. . . . . 34
- 2.7. CO-stripping measurement of a severely degraded cathode with an *rf* of ≈ 5 cm<sub>Pt</sub><sup>2</sup> cm<sub>MEA</sub><sup>-2</sup> (0.1 mg<sub>Pt</sub> cm<sub>MEA</sub><sup>-2</sup>, after 50,000 square wave cycles between 0.6–0.95 V with a 1 s hold under H<sub>2</sub>/N<sub>2</sub> at 80 °C and 95% RH, see Section 3.3.2): a) CO-strip and subsequent CV recorded at 100 mV s<sup>-1</sup>; b) CO-stripping peak corrected for the second scan as the baseline (red line) and difference between first and second scan after a CO<sub>free</sub>-strip of a pristine MEA (black dotted line, data taken from fig. 2.4 f); the measurements were performed at 40 °C and 95% RH. The gray area is integrated from the difference between the first and second scan in the range of 0.6 – 1.0 V<sub>RHE</sub> with a linear baseline; the blue area is the difference between the gray area and a full integration of the red curve. The active area of the cell is 5 cm<sup>2</sup>. . . . . 35
- 2.8. CO-stripping measurement of an ultra-low-loaded (1.4 μg<sub>Pt</sub> cm<sub>MEA</sub><sup>-2</sup>) electrode (see Section 3.1.2) with an active area of 5 cm<sup>2</sup>: a) CO-strip and subsequent CV recorded at 50 mV s<sup>-1</sup> with the CO-stripping current being integrated using a linear baseline (gray area); b) comparison of the CO-stripping peak using a linear baseline (0.7 – 1.0 V<sub>RHE</sub>) for the correction (red line) and conventionally corrected for the second scan as the baseline (black dotted line); the measurements were performed at 40 °C and 95% RH. Data adapted from Stühmeier and Pietsch *et al.* (see Section 3.1.2).<sup>25</sup> . . . . . 37

2.9.	Limiting current measurements in the potential range between 0.4 V and 0.05 V using O <sub>2</sub> concentrations of 2% (gray), 4% (orange), 7% (green) and 11% (magenta) in N <sub>2</sub> (on a dry gas basis) for a cathode with an $rf$ of $\approx 3 \text{ cm}_{\text{Pt}}^2 \text{ cm}_{\text{MEA}}^{-2}$ after 10,000 cycles of a square wave voltage cycling AST with an upper potential limit of 1.0 V and a vertex hold time of 8 s at 80 °C in H <sub>2</sub> /H <sub>2</sub> . The measurements were performed at 170 kPa <sub>a,abs</sub> , 80 °C, and 95% RH using 2000 nccm H <sub>2</sub> and 5000 nccm (O <sub>2</sub> in N <sub>2</sub> ) on anode and cathode, respectively. For each concentration, the measurement was performed by going from 0.4 V down in potential, followed by going from 0.05 V back up (repeated twice, direction indicated by the arrows). The active area of the cell is 5 cm <sup>2</sup> . . . . .	39
2.10.	Optimized procedure for the characterization and full voltage loss analysis of 5 cm <sup>2</sup> PEMFC single-cells. . . . .	42
2.11.	Picture detail of fig. 1.1 showing the cathode FF and the 5-layer MEA. The deep gas distribution headers at the gas inlet and outlet of the FF are highlighted in red. . . . .	43
4.1.	Scheme of the proposed approach to predict the voltage cycling losses of the H <sub>2</sub> /air performance over a large number of voltage cycles under application-relevant conditions (i.e., UPLs of < 0.9 V) based on the data acquired for a harsh cycling protocol (i.e., conducted with an UPL of 0.95 – 1.0 V); a) cathode $rf$ degradation for a harsh voltage cycling AST (purple squares) and for an application-relevant “mild” voltage cycling AST (blue hexagons); b) H <sub>2</sub> /air performance as a function of cathode $rf$ for two current densities; c) outline of the step-wise procedure to estimate the number of cycles after which the end of life (EoL) criteria (here assumed to be 0.5 V at 2 A cm <sub>MEA</sub> <sup>-2</sup> ) are reached for the mild voltage cycling AST on the basis of the harsh voltage cycling AST data. The figure is reprinted from Della Bella and Stühmeier <i>et al.</i> (see Section 3.3.2). <sup>53</sup> . . . . .	147

## **A. Curriculum Vitae and Publication List**

A Curriculum Vitae with a list of the peer-reviewed journal articles that were published during this Doctorate project as well as a list of conference presentations can be found in the following.

## Publication List

---

- 1) T. Lazaridis,<sup>=</sup> **B. M. Stühmeier**,<sup>=</sup> H. A. Gasteiger, H. A. El-Sayed,\* “Capabilities and limitations of rotating disk electrode versus membrane electrode assembly in the investigation of electrocatalysts”, *Nat. Catal.* **2022**, DOI: 10.1038/s41929-022-00776-5.
- 2) R. K. F. Della Bella,<sup>=</sup> **B. M. Stühmeier**,<sup>=,\*</sup> H. A. Gasteiger, “Universal Correlation between Cathode Roughness Factor and H<sub>2</sub>/Air Performance Losses in Voltage Cycling-based Accelerated Stress Tests”, *J. Electrochem. Soc.* **2022**, *169*, 044528.
- 3) **B. M. Stühmeier**,<sup>=,\*</sup> R. J. Schuster,<sup>=</sup> L. Hartmann, S. Selve, H. A. El-Sayed, H. A. Gasteiger, „Modification of the Electrochemical Surface Oxide Formation and the Hydrogen Oxidation Activity of Ruthenium by Strong Metal Support Interactions”, *J. Electrochem. Soc.* **2022**, *169*, 034519.
- 4) **B. M. Stühmeier**,<sup>=,\*</sup> M. R. Pietsch,<sup>=</sup> J. N. Schwämmlein, H. A. Gasteiger, “Pressure and Temperature Dependence of the Hydrogen Oxidation and Evolution Reaction Kinetics on Pt Electrocatalysts via PEMFC-based Hydrogen-Pump Measurements”, *J. Electrochem. Soc.* **2021**, *168*, 064516.
- 5) **B. M. Stühmeier**,\* M. T. Greiner, V. Sureshwaran, L. Schuster, L. H. Tiah, J. N. Schwämmlein, H. A. Gasteiger, H. A. El-Sayed, “Extending the Polyol Reduction Process into the Second Dimension: Oxide Thin Film Reduction”, *J. Electrochem. Soc.* **2021**, *168*, 014506.
- 6) T. N. Geppert,\* M. Bosund, M. Putkonen, **B. M. Stühmeier**, A. T. Pasanen, P. Heikkilä, H. A. Gasteiger, H. A. El-Sayed, “HOR Activity of Pt-TiO<sub>2-y</sub> at Unconventionally High Potentials Explained: The Influence of SMSI on the Electrochemical Behavior of Pt”, *J. Electrochem. Soc.* **2020**, *167*, 084517.
- 7) **B. M. Stühmeier**, S. Selve, M. U. M. Patel, T. N. Geppert, H. A. Gasteiger, H. A. El-Sayed,\* “Highly Selective Pt/TiO<sub>x</sub> Catalysts for the Hydrogen Oxidation Reaction“, *ACS Appl. Energy Mater.* **2019**, *2*, 5534-5539.
- 8) J. N. Schwämmlein,\* **B. M. Stühmeier**, K. Wagenbauer, H. Dietz, V. Tileli, H. A. Gasteiger, H. A. El-Sayed, “Origin of Superior HOR/HER Activity of Bimetallic Pt-Ru Catalysts in Alkaline Media Identified via Ru@Pt Core-Shell Nanoparticles”, *J. Electrochem. Soc.* **2018**, *165*, H229-H239.
- 9) J. N. Schwämmlein,\* H. A. El-Sayed, **B. M. Stühmeier**, K. Wagenbauer, H. Dietz, H. A. Gasteiger, „Origin of Superior Activity of Ru@Pt Core-Shell Nanoparticles towards Hydrogen Oxidation in Alkaline Media”, *ECS Trans.* **2016**, *75*, 971-982.

= equal contribution

\* corresponding author

## Unpublished Manuscripts

---

- 1) **B. M. Stühmeier**,<sup>=,\*</sup> A. M. Damjanović,<sup>=</sup> K. Rodewald, H. A. Gasteiger, “Selective Anode Catalysts for the Mitigation of Start-Up/Shut-Down Induced Cathode Degradation in Proton Exchange Membrane Fuel Cells”, *to be submitted*.

= equal contribution

\* corresponding author

## Oral Presentations

---

- 1) **B. M. Stühmeier**, S. Selve, M. U. M. Patel, T. N. Geppert, H. A. Gasteiger, H. A. El-Sayed, “Highly Selective Pt/TiO<sub>x</sub> Catalysts for the Hydrogen Oxidation Reaction“, *70<sup>th</sup> Annual Meeting of the International Society of Electrochemistry (ISE)*, August 4-9, **2019**, Durban, South Africa.
- 2) **B. M. Stühmeier**, M. R. Pietsch, J. N. Schwämmlein, H. A. Gasteiger, „Pressure Dependency of the Hydrogen Oxidation and Evolution Reaction Kinetics on Carbon Supported Pt Catalysts Using a PEMFC Based Hydrogen Pump Approach“, *ECS Prime*, October 4-9, **2020**, online.
- 3) **B. M. Stühmeier**, A. M. Damjanović, P. A. Loichet, S. Selve, H. A. Gasteiger, “Mitigation of the Start-Up and Shut-Down Degradation in PEMFCs by Means of a Selective H<sub>2</sub> Oxidation Catalyst”, *240th ECS Meeting*, October 10-14, **2021**, online.